PROBING NANOSCALE STRUCTURES –
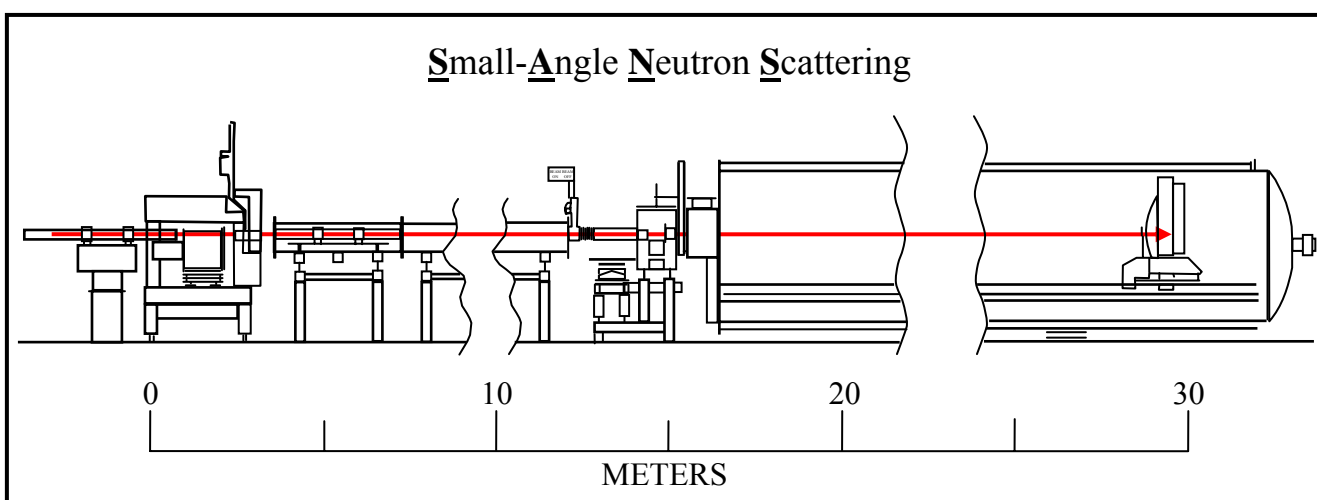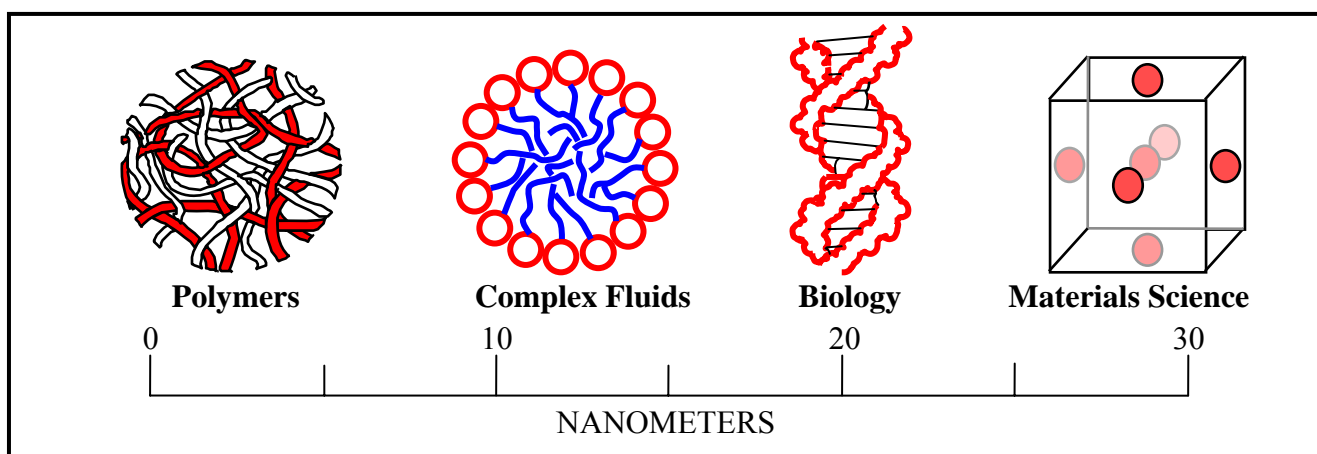
THE <u>S</u>ANS TOOLBOX

Boualem Hammouda

National Institute of Standards and Technology
Center for Neutron Research
Gaithersburg, MD 20899-6102

hammouda@nist.gov
http://www.ncnr.nist.gov/staff/hammouda/the_SANS_toolbox.pdf

Polymers   Complex Fluids   Biology   Materials Science

NANOMETERS

<u>S</u>mall-<u>A</u>ngle <u>N</u>eutron <u>S</u>cattering

METERS

LIST OF CHAPTERS

Part O. Indexes

PREFACE

This tutorial grew out of my twenty years as a Small-Angle Neutron Scattering practitioner mostly at the National Institute of Standards and Technology. I helped build, maintain, improve and schedule the 30 m SANS instruments. I also acted as local contact for a multitude of user experiments and strived to keep a healthy research program of my own using the SANS technique.

Many notes were accumulated over the years relating to topics as varied as instrumentation, experimental work and theoretical calculations. These topics were stimulated by questions from users, by lecturing needs or just by personal curiosity and research interests.

This "SANS Toolbox" has been put together in a tutorial format with a broad intended audience. It is meant to be for a wide variety of users of the SANS technique as well as for hardcore practitioners such as instrument scientists.

This work is dedicated to my colleagues and collaborators, to my dear children and to my sweetheart wife Fatima.

"When you reach the heart of maturity, you find beauty in everything".

<div align="right">Quote from Khalil Jibran.</div>

Boualem Hammouda
Gaithersburg, Maryland
February 2008

Chapter 1 - **INTRODUCTION**

Nanometer scale structures include sizes from the near atomic (nanometer) scale to the near optical (micrometer) scale. This includes most structures of interest to science for the past 100 years, i.e., since the advent of non-optical probes such as diffraction methods and electron microscopy. Before this period, the optical microscope was the main tool for observation.

Diffraction methods include neutron scattering which has found wide use in the characterization of materials. Partial deuteration has made neutron scattering unique. Use of deuterated molecules in a non-deuterated environment is comparable to the staining method used in electron microscopy and helps enhance the contrast of particular structural features.

Small-angle neutron scattering (SANS) is a well-established characterization method for microstructure investigations in various materials. It can probe inhomogeneities in the nanometer scale. Since the construction of the first SANS instrument over 35 years ago, this technique has experienced a steady growth. SANS instruments are either reactor-based using monochromated neutron beams or time-of-flight instruments at pulsed neutron sources. SANS has had major impact in many fields of research including polymer science, complex fluids, biology, and materials science. This technique has actually become a "routine" analytic characterization method used even by non-experts.

These notes are intended to help SANS users acquire (or brush up on) basic knowledge on the technique and its applications. Readers need not be experts in the various subjects covered here. Basic knowledge in areas like nuclear physics, basic chemistry, statistical mechanics and mathematics is of course helpful. The covered topics are organized into broad categories (parts) which are divided into chapters. Each chapter contains a number of related topics included as sections. Helpful questions (and answers) are included at the end of each chapter. The outlines of the various parts are color coded; blue has been chosen for introductory (or essential knowledge) sections.

After a brief review of basic neutron properties, the various methods of neutron production and various neutron sources are introduced first along with discussion of neutron flux. The major neutron sources are listed along with their overall characteristics. Production of cold neutrons (essential for SANS applications) is discussed along with description of cold neutron remoderators. Basic elements of neutron scattering follow. These include advantages and disadvantages of the technique, scattering lengths and cross sections, coherent/incoherent scattering contributions, and example calculations.
This is followed by discussion of elastic/inelastic and coherent/incoherent neutron scattering. Elements of Quantum Mechanics are used to derive the scattering cross section.

The SANS technique is described next. SANS instrumentation is examined in no great detail focusing on the major components and pointing out differences between reactor-based and spallation source-based instruments. Neutron velocity selectors and area detectors are included here along with their calibration and discussion of their performance. SANS resolution and the various elements of instrumental smearing are described next. These include contributions from the instrument focusing geometry, wavelength spread and

detector resolution as well as the effect of gravity on neutron trajectories. Instrumental resolution is also discussed when refractive optics (neutron lenses or prisms) are included.

Description of the various elements of SANS data correction and data reduction are included next. The main SANS data interpretation methods include standard plots, the use of empirical models and nonlinear least-squares fits to realistic models. Representative SANS data are presented. Elements of SANS data modeling include calculations of the radius of gyration, of the single-particle form factor and of inter-particle structure factors. The effect of polydispersity is also discussed. Since "most SANS spectra look alike", SANS is a heavily model-dependent method. The major theories used to interpret SANS data are discussed including the Random Phase Approximation (RPA) for polymer systems and the Ornstein-Zernike (OZ) equation for particulate scattering.

The major SANS research topics are covered in turn in a series of chapters. These various "parts" include: Polymers, Complex Fluids, Biology, and Other Topics that includes Materials Science. In each chapter, typical topics borrowed from the research efforts of this author are described at the tutorial level. The part on "SANS from Polymers" includes polymer solutions, polymer blends and copolymers. The Random Phase Approximation approach is described in detail and applied to realistic homogeneous polymer mixtures. The thermodynamics of phase separation are described for multi-component homogeneous polymer mixtures. The part on "SANS from Complex Fluids" includes a discussion of the phase diagram for micellar systems and contains chapters on ionic and nonionic "self-assembling systems". The main scattering features include single-particle and inter-particle contributions. Material balance equations help in the understanding of some details of the probed structures. The part on "SANS in Biology" introduces elements of biology, then covers representative basic topics such as a phospholipid membranes, the helix-to-coil transition in DNA, the structure of a protein system, and a poly(amino acid) system.

The "Other SANS Topics" part is covered next. These include solvation in mixed solvents, the effect of pressure or shear on nanoscale structures, and molecular orientation of polymeric materials. SANS measurements involving in-situ pressure or in-situ shear have been the focus of research for many years. The effects of pressure on phase separation and miscibility are discussed. In-situ shear allows investigations of the rheology and structure simultaneously.

Chapters covering review of the literature in the four main SANS research areas have been included. These draw heavily from papers published (over the past seven years) from use of the NIST Center for Neutron Research.

Two other small-angle neutron scattering techniques are discussed in no-great detail in the part on "Even Lower SANS Scales". These are the Ultra small-angle (USANS) range probing structures as large as 20 microns and the merging VSANS technique (V is for very small-angle) which bridges the two probing ranges.

A gallery of interesting SANS data images is included. These images have been collected by this author over several years. They are included here in order to show the full richness of the SANS technique and for their esthetic value. Some brief concluding topics are covered along

with two appendices; one on "Useful Mathematical Expressions" and the other on "Elements of Quantum Mechanics". These appendices gather material used throughout.

This document is meant to be used in a pdf (not print) format so that it could be searched for subject or author keywords. For this reason, no indexes have been included at the end of the book.

Part A – **NEUTRON SOURCES AND NEUTRON FLUX**

Chapter 2. The Neutron Probe
  2.1 What are Neutrons?
  2.2 Why Use Neutrons?

Chapter 3. Neutron Sources
  3.1 Introduction
  3.2 Nuclear Fission Reactions
  3.3 Nuclear Reactors
  3.4 The NIST Thermal Neutron Instruments
  3.5 The NIST Guide Hall
  3.6 The HFIR Guide Hall
  3.7 Spallation Sources
  3.8 Some Other Neutron Sources
  References
  Questions
  Answers

Chapter 4. Cold Neutron Moderators
  4.1 Cold Neutron Source
  4.2 Cold Neutron Spectrum
  References
  Questions
  Answers

Chapter 5. Neutron Flux on Sample
  5.1 The Cold Neutron Source Spectrum
  5.2 Neutron Flux on Sample
  5.3 Case of Specific Configurations
  5.4 Measured Flux on Sample
  5.5 Neutron Beam Monitor Count Rate
  References
  Questions
  Answers

Chapter 2 - **THE NEUTRON PROBE**

1. WHAT ARE NEUTRONS?

The neutron was discovered by Chadwick in 1932. It has zero charge, a mass of 1.0087 atomic mass units, a spin of 1/2 and a magnetic moment of -1.9132 nuclear magnetons. It has a half life of 894 seconds and decays into a proton, an electron and an antineutrino. Its interactions with matter are confined to the short-range nuclear and magnetic interactions. Since its interaction probability is small, the neutron usually penetrates well through matter making it a unique probe for investigating bulk condensed matter. Since the neutron can be reflected by some surfaces when incident at glancing angles, it can also be used as a surface probe. Neutrons are scattered by nuclei in samples or by the magnetic moments associated with unpaired electron spins (dipoles) in magnetic samples. The nuclear scattering potential is short range so that most neutron scattering can be described by "s wave" scattering (zero orbital angular momentum) and the scattering cross section can be described by the first Born approximation. Higher order term in the Born expansion series are required for neutron reflection from surfaces. Reflection involves the refraction (not diffraction) limit.

Some useful properties follow:

Mass: $m = 1.675*10^{-24}$ gm

Magnetic Moment: $\mu_n = 6.031*10^{-12}$ eV/gauss

Energy: $E[meV] = 81.787/\lambda^2 [\text{Å}^{-2}]$

Wavelength: $\lambda [\text{Å}] = 3955/v$ [m/sec]

Velocity: $v = 1$ m/msec (at $\lambda=4$ Å)

Useful relationship: $mv\lambda = h$.

Thermal neutrons correspond to 25 meV energies and 1.8 Å wavelength.

2. WHY USE NEUTRONS?

Neutrons are both a bulk and a surface probe for investigating both structures and dynamics. Some of the advantages of neutrons as a probe for condensed matter follow.

-- Neutrons interact through short-range nuclear interactions. They are very penetrating and do not heat up (i.e., destroy) samples. Neutrons are good probes for investigating structures in condensed matter.

-- Neutron wavelengths are comparable to atomic sizes and inter-distance spacings. Neutron energies are comparable to normal mode energies in materials (for example phonons, diffusive modes). Neutrons are good probes to investigate the dynamics of sold state and liquid materials.

-- Neutrons interactions with hydrogen and deuterium are widely different making the deuterium labeling method an advantage.

Someone once stated that "neutrons never lie!"

QUESTIONS

1. The neutron decays into what particles? How about the proton? Does it decay?
2. Why are neutrons a good probe to investigate condensed matter?
3. Can neutrons get reflected from surfaces at large angles like light does?

ANSWERS

1. The neutron decays to an electron, a proton and an anti-neutrino. The proton is stables. Its decay has not been observed.
2. Neutrons are a good probe to investigate condensed matter because it is very penetrating (due to its charge neutrality) and to its just-right typical wavelengths and kinetic energies.
3. Neutrons can be reflected from surfaces only at low glancing angles. They cannot be reflected at large angles from surfaces.

1. INTRODUCTION

Since the early days of neutron scattering, there has been an insatiable demand for higher neutron fluxes. Neutron sources are based on various processes that liberate excess neutrons in neutron rich nuclei such as Be, W, U, Ta or Pb. Presently, the highest fluxes available are around a few $*10^{15}$ n/cm^{2}sec. Even though various neutron sources exist, only a few are actually useful for scattering purposes. These are:

    -- continuous reactors
    -- spallation sources
    -- some other neutron sources.

Only minor improvements in flux increase of continuous reactors are expected because of the saturation of the technology (i.e., limit of heat removal rate and operating safety considerations). Pulsed sources are expected to go to higher fluxes (non-continuous operation allows for a better heat removal rate).

Continuous reactors operate in a continuous neutron generation mode whereas spallation source function in a pulsed (or time-of-flight) mode.

Continuous Reactors
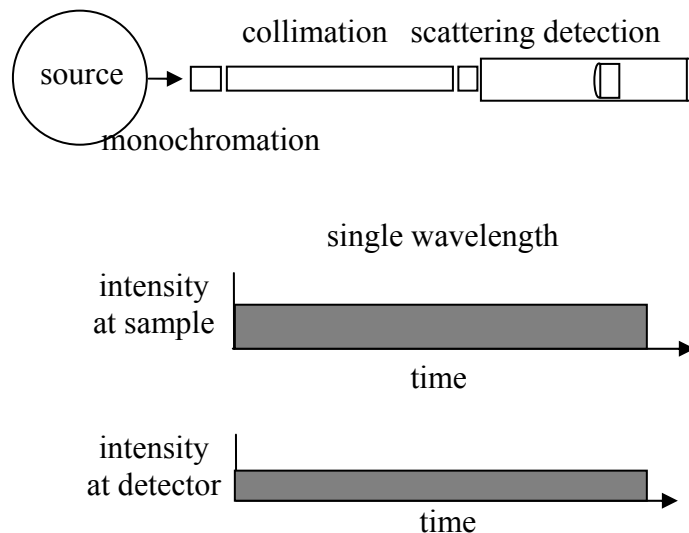
Measure some of the neutrons all of the time

Pulsed Sources
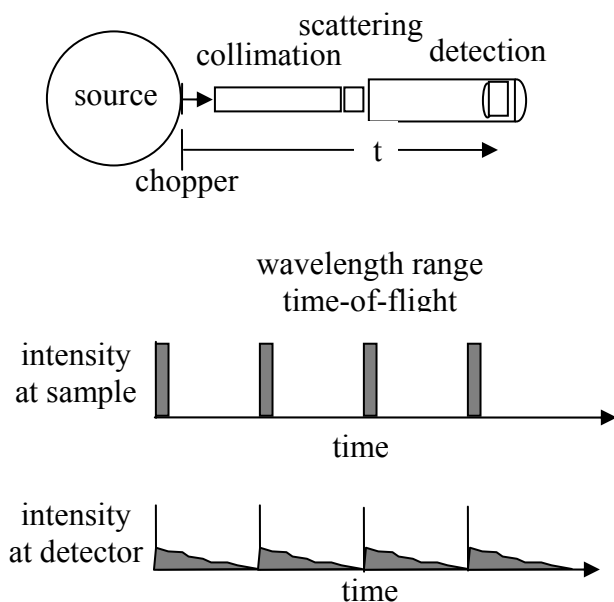
Measure all of the neutrons some of the time

Figure 1: The two main neutron sources: continuous reactors and pulsed sources. Schematic representations of SANS instruments are shown.

2. NUCLEAR FISSION REACTIONS

Some heavy nuclides undergo fission reaction into lighter ones (called fission products) upon absorption of a neutron (Duderstadt-Hamilton, 1974; Lamarsh, 1977). Known fissile nuclides are U-233, U-235, Pu-239 and Pu-241, but the most used ones are U-235 and Pu-239. Each fission event releases huge energies (200 MeV) in the form of kinetic energy of the fission fragments, gamma rays and several fast neutrons. Fission fragments are heavy and remain inside the fuel elements therefore producing the major source of heat while energetic gammas and fast neutrons penetrate most everything and are carefully shielded against. Gamma rays and fast neutrons are a nuisance to neutron scatterers and are not allowed to reach the detectors as much as possible. After being slowed down by the moderator material (usually light or heavy water) neutrons are used to sustain the fission reaction as well as in beam tubes for low energy (thermal and cold) neutron scattering.

Fission Chain Reaction
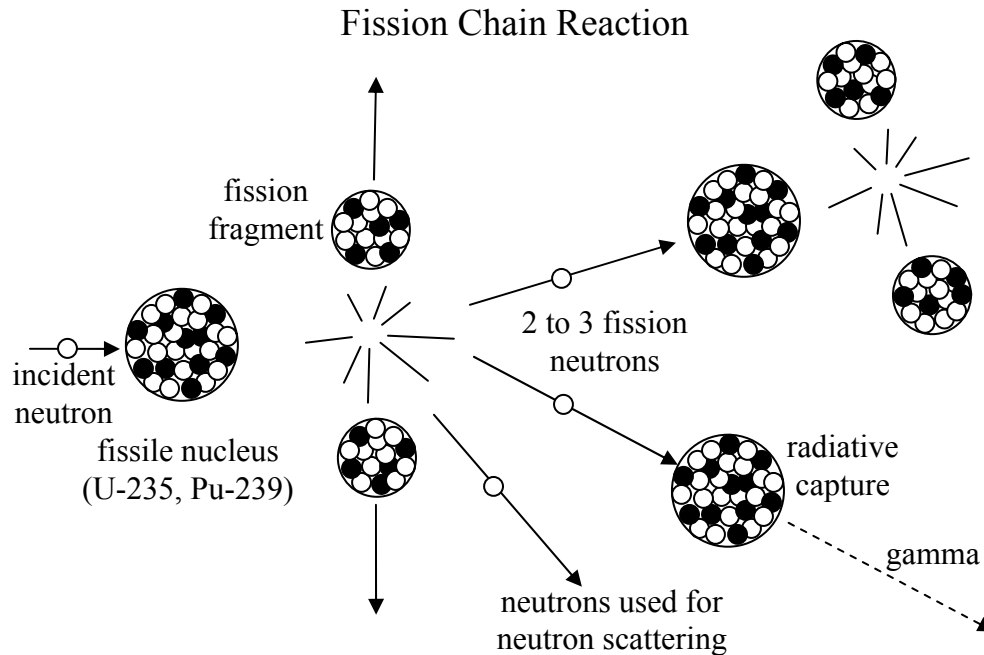
Figure 2: Typical fission chain reaction.

3. NUCLEAR REACTORS

Nuclear reactors are based on the fission reaction of U-235 (mainly) to yield 2-3 neutrons/fission at 2 MeV kinetic energies. Moderators (D_2O, H_2O) are used to slow down the neutrons to thermal (0.025 eV) energies. Reflectors (D_2O, Be, graphite) are used to maintain the core critical by reflecting neutrons back into the core. Electrical power producing reactors use wide core sizes and low fuel enrichment (2-5 % U-235), while research reactors use compact cores and highly enriched fuel (over 90 % U-235) in order to achieve high neutron fluxes. Regulatory agencies encourage the use of intermediate enrichment (20-50 %) fuel in order to avoid proliferation of weapon-grade material.

Nuclear research reactors have benefited from technological advances in power producing reactors as well as in nuclear submarines (compact cores operating with highly enriched fuel and foolproof safety control systems). The most popular of the present generation of reactors, the pressurized water reactor (PWR), operates at high pressure (70 to 150 bars) in order to achieve high operating temperatures while maintaining water in its liquid phase.

Neutrons that are produced by fission (2 MeV) can either slow down to epithermal then thermal energies, be absorbed by radiative capture, or leak out of the system. The slowing down process is maintained through collisions with low Z material (mostly water is used both as moderator and coolant) while neutron leakage is minimized by surrounding the core by a reflector (also low Z material) blanket. Most of the fission neutrons appear instantaneously (within 10^{-14} sec of the fission event); these are called prompt neutrons. However, less than 1 % of the neutrons appear with an appreciable delay time from the

subsequent decay of radioactive fission products. Although the delayed neutrons are a very small fraction of the neutron inventory, these are vital to the operation of nuclear reactors and to the effective control of the nuclear chain reaction by "slowing" the transient kinetics. Without them, a nuclear reactor would respond so quickly that it could not be controlled.

A short list of research reactors in the USA used for neutron scattering follows:

-- HFIR-Oak Ridge National Laboratory (100 MW), a horizontal cold source has recently been installed.

-- NIST-The National Institute of Standards and Technology (20 MW), contains third generation cold neutron source.

-- MURR-University of Missouri Research Reactor (10 MW), does not contain a cold neutron source.

These reactors were built during the1960's but have undergone various upgrades.

There is one major research reactor in Canada:

>   **--** CRNL-Chalk River, Canada (135 MW).

A short list of research reactors in Europe follows:

>   -- ILL-Grenoble, France (57 MW),
>   -- NERF-Petten, Netherland (45 MW),
>   -- FRM-II Munich, Germany (20 MW),
>   -- KFKI-Budapest, Hungary (15 MW),
>   -- LLB-Saclay, France (14 MW),
>   -- HMI-Berlin, Germany (10 MW),
>   -- Riso-Roskilde, Denmark (10 MW),
>   -- VVR-M Leningrad, Russia (10 MW).
>   -- GKSS Geesthacht, Germany (5 MW).

A short list of research reactors in Asia follows:

>   -- DRHUVA-Bombay, India (100 MW),
>   -- CIAE-Beijing, China (60 MW),
>   -- NLHEP-Tsukuba, Japan (50 MW),
>   -- Bhabha ARC-Bombay, India (40 MW),
>   -- HFANAR, KAERI, Hanaro, Korea (30 MW)
>   -- JRR3-Tokai Mura, Japan (20 MW),
>   -- HWRR-Chengdo, China (15 MW),

One reactor exists in Oceania. It is the Bragg Institute, ANSTO, Australia (20 MW).

Most of these facilities either have or are planning to add a cold source in order to enhance their cold neutron capability and therefore allow effective use of SANS instruments.

4. THE NIST THERMAL NEUTRON INSTRUMENTS

The NIST Center for Neutron Research (CNR) facility has a split-core geometry whereby thermal neutron beam tubes do not look at the fuel elements directly. This helps minimize epithermal neutrons and gamma radiation in the beams. There is a host of thermal neutron instruments located in the confinement building. These comprise triple axis instruments for inelastic neutron scattering, a powder diffractometer, a single crystal instrument also used for texture studies, a neutron radiography station, and a Bonse-Hart USANS instrument. Location of the cold neutron source is optimized. It is located at the peak flux position within the reflector region. A set of neutron guides transport cold neutrons to a guide hall.
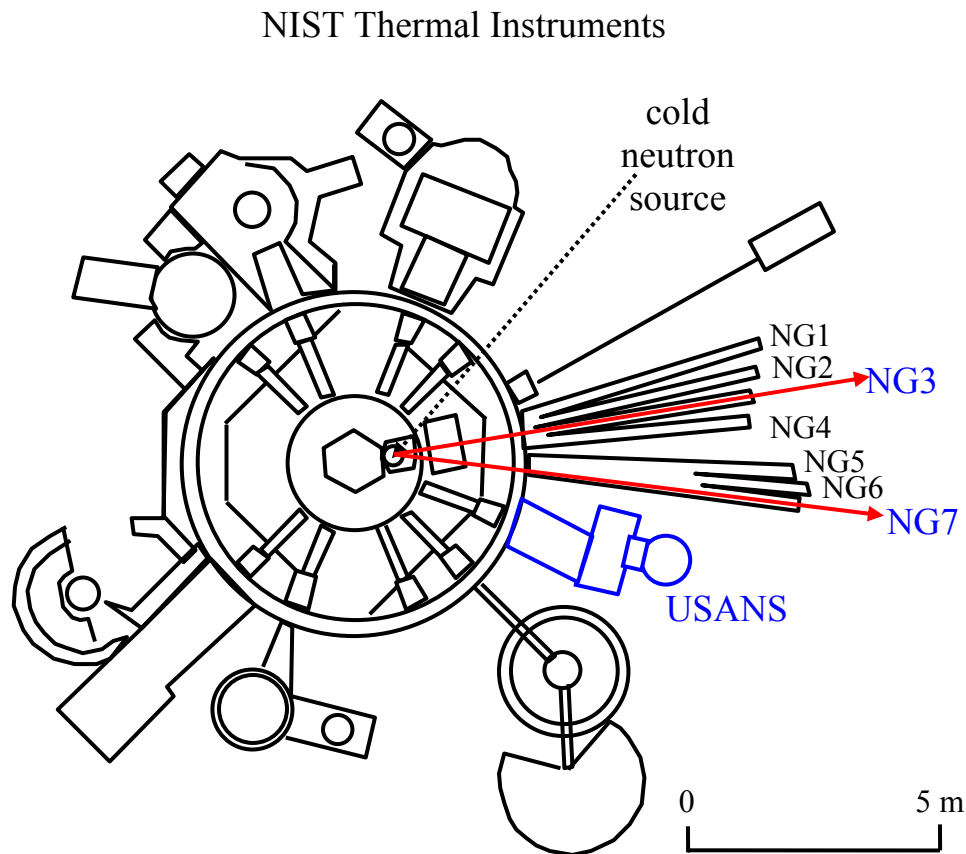
NIST Thermal Instruments

Figure 3: Schematics of the NIST confinement building showing the thermal neutron scattering instruments and the cold neutron source along with the beginning of the cold neutron guides leading to the "old" guide hall. The USANS instrument is located on a thermal neutron beam tube.

5. THE NIST GUIDE HALL

The NIST CNR guide hall contains a set of seven guides looking at the cold source. Cold neutron instruments include three SANS instruments, three reflectometers, two time-of-flight instruments, a cold triple axis, a backscattering spectrometer, a neutron spin-echo spectrometer and other fundamental physics stations (interferometry, measurement of the neutron half-life, etc).

All the guides are straight (with no curvature) and looking at the cold source directly. Guide dimensions are 12 cm*5 cm for some and 15 cm*6 cm for others. The guides' inner surfaces are coated with either natural Ni or Ni-58 on the sides and with either Ni-58 or supermirror coating on the top and bottom. The critical angle for natural Ni is 0.1 $^\circ$/Å, that for Ni-58 is 0.115 $^\circ$/Å and that for supermirror coating is 0.3 $^\circ$/Å. This critical angle for total reflection increases with neutron wavelength as $\theta_c = \gamma_c \lambda$ where $\gamma_c = \sqrt{\rho b / \pi}$ is given in terms of the atomic number density ρ and scattering length b of the reflecting material. Neutron guides are anchored onto a thick concrete base in order to decouple them from the rest of the guide hall. Neutron guides are encased in jackets that are evacuated or filled with helium. Neutron losses in neutron guides are estimated to be around 1 % per meter.

Filters are used to remove epithermal neutrons and gamma radiation from the neutron guides. Crystal filters include beryllium for neutrons and bismuth for gamma rays. They are kept at liquid nitrogen temperature. Optical filters are also used to steer the neutron beam out of the direct line-of-sight from the cold source and with minimum losses. Optical filters are characterized by high transmission gains over crystal filters for long wavelength neutrons.

Note that other facilities use curved guides that avoid the use of filters completely. Curved guides however transmit neutrons above a cutoff wavelength that depends on the guide curvature and width. A curved guide of width W and radius of curvature R has a characteristic angle $\Psi_c = \sqrt{2W/R}$. This is the minimum angle that the guide subtends (in the horizontal plane) in order to get out of the direct line-of-sight. This curved guide has a cutoff wavelength $\lambda_c = \Psi_c / \gamma_c$ below which no neutrons are transmitted.

The NIST Guide Hall

NG1
NG2
NG3
NG4
NG5
NG7
NG3-30 m SANS
NG7-30 m SANS

0   10 m
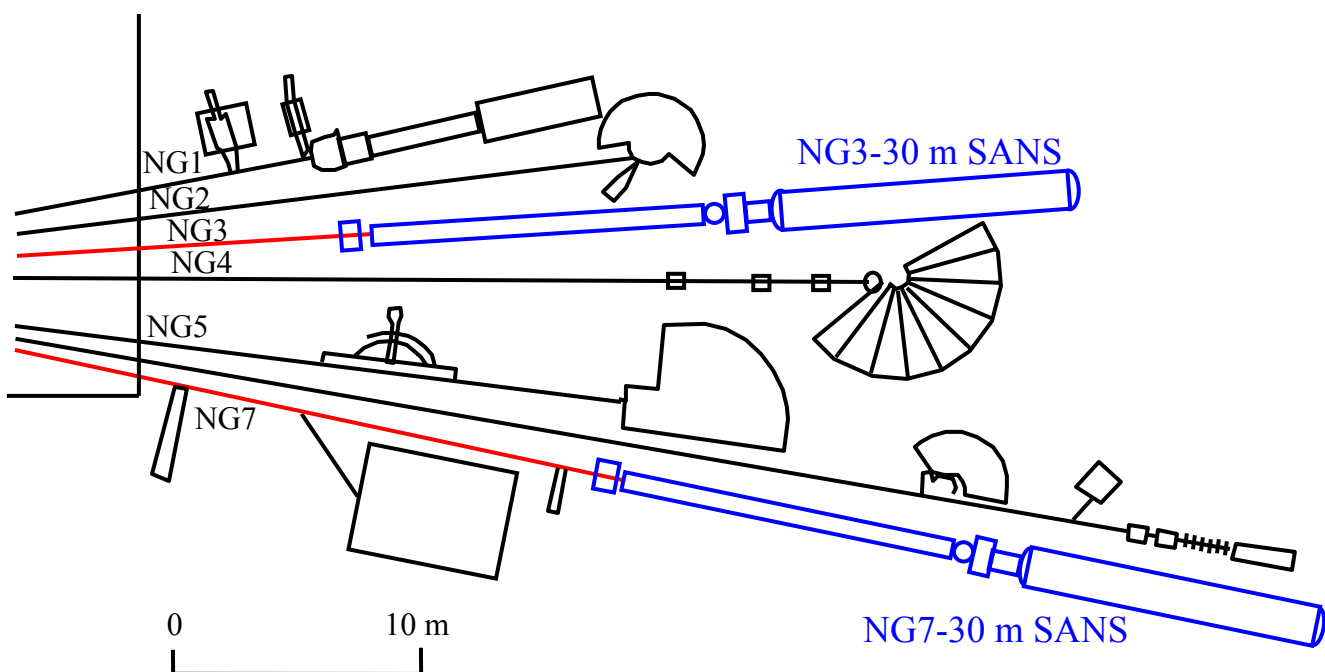
Figure 4: Schematics of the NIST "old" guide hall. Note the two 30 m SANS instruments on the NG3 and NG7 guides.
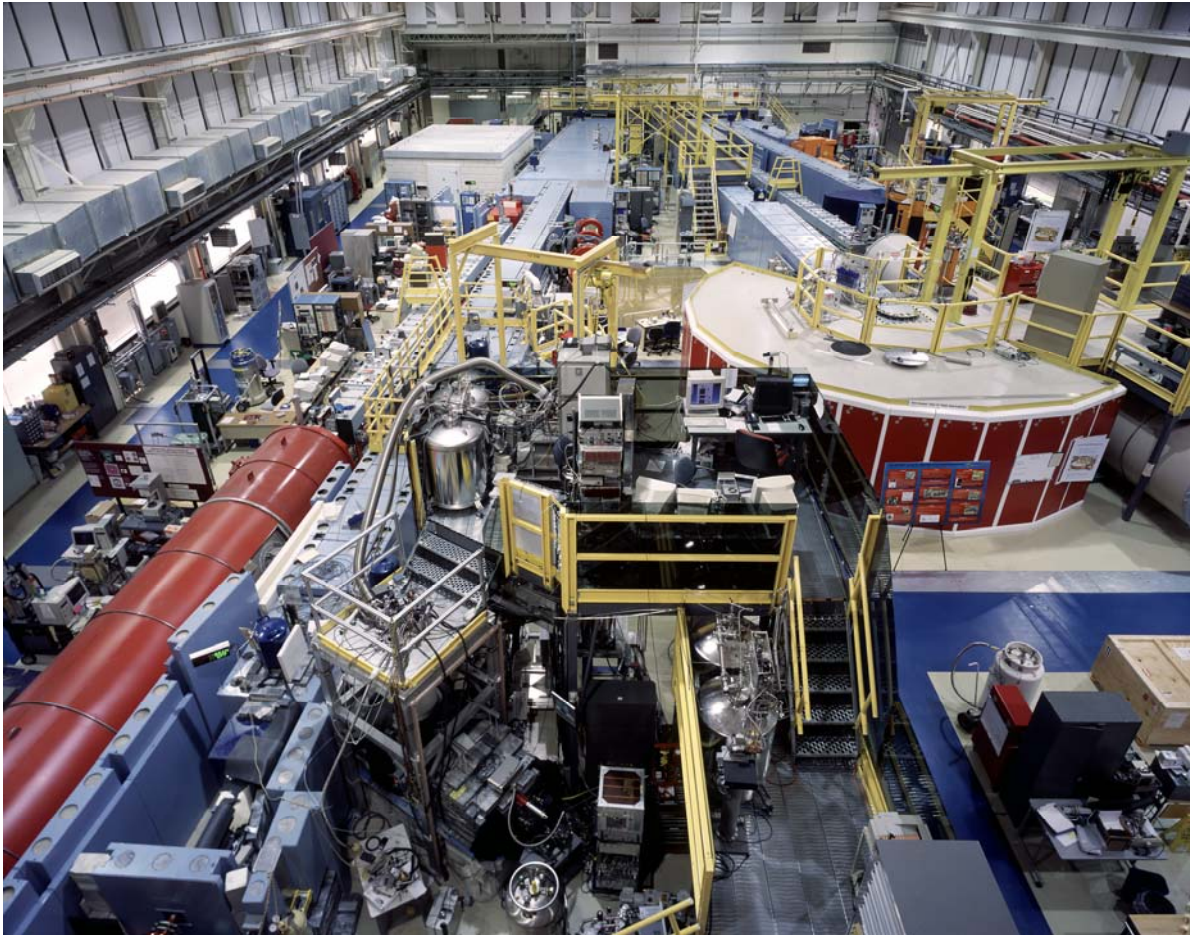
Figure 5: Photograph of the NIST CNR guide hall. The confinement building wall is at the rear end of the picture. The red color scattering vessel of the NG7 30m SANS instrument is seen to the left.

6. THE HFIR GUIDE HALL

The High Flux Isotope Reactor (HFIR) located at Oak Ridge National Lab has built two SANS instruments and a horizontal cold source. These are 35 m and 30 m long respectively and both use 1 m*1 m size area detectors.

The HFIR Guide Hall

CG2 SANS

CG3 BioSANS
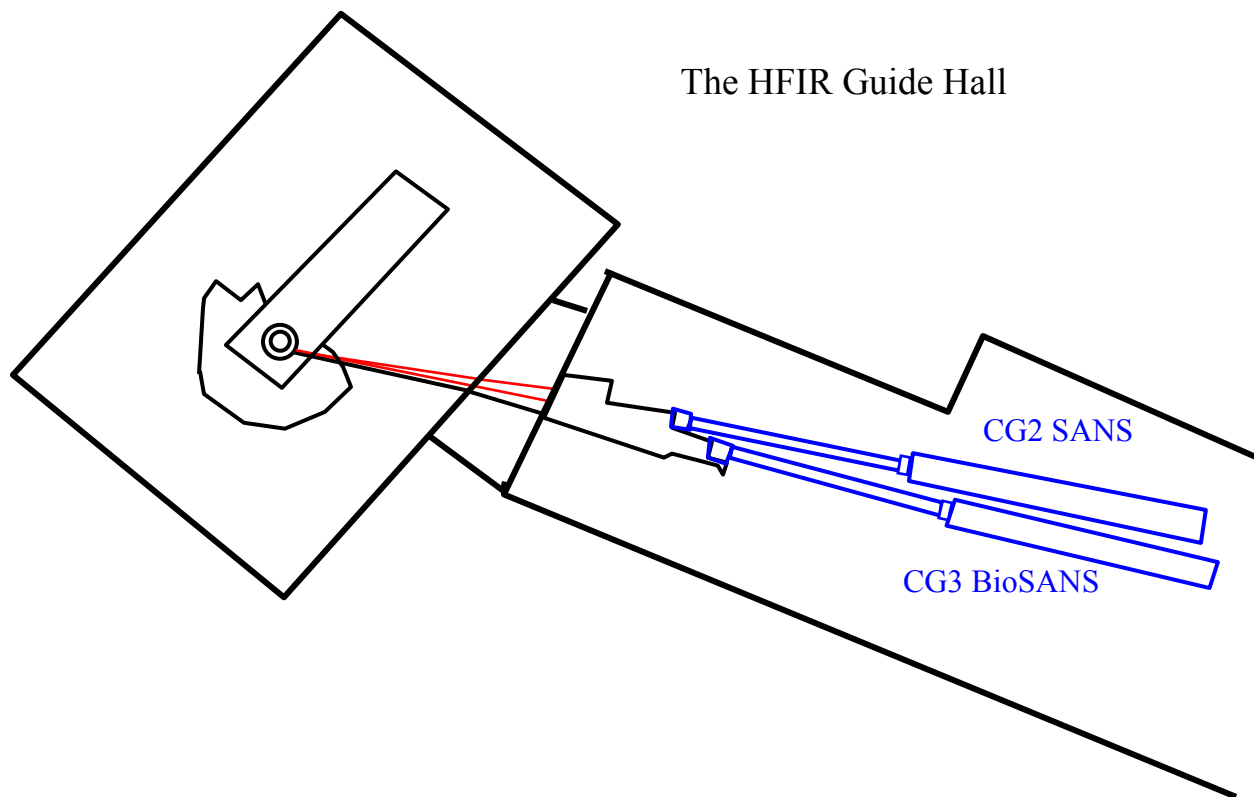
Figure 6: Schematic representation of the HFIR guide hall with the two 30 m SANS instruments. The CG2 SANS instrument is slightly longer.

7. SPALLATION SOURCES

Beams of high kinetic energy (typically 70 MeV) hydrogen ions are produced (by linear accelerator) and injected into a synchrotron ring to reach much higher energies (500-800 MeV) and then steered to hit a high Z (neutron rich) target (W-183 or U-238) and produce about 10-30 neutrons/proton with energies about 1 MeV. These neutrons are then moderated, reflected, contained, etc., as in the case of nuclear reactor. Most spallation sources operate in a pulsed mode. The spallation process produces relatively few gamma rays but the spectrum is rich in high energy neutrons. Typical fast neutron fluxes are 10^{15}-10^{16} n/sec with a 50 MeV energy deposition/neutron produced. Booster targets (enriched in U-235) give even higher neutron fluxes.

Spallation Nuclear Reaction

incident
H ion

10 to 30
neutrons
emitted

high Z nucleus
(W-183, U-238)

neutrons used for
neutron scattering
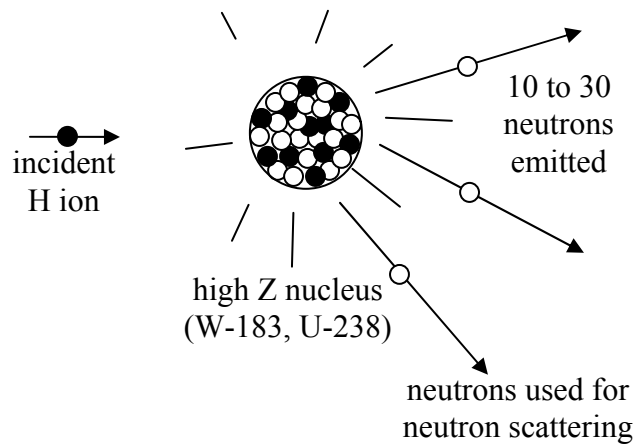
Figure 7: Spallation nuclear reaction.

Spallation sources in the USA:

-- IPNS (Argonne National Lab): 500 MeV protons, U-238 target, 12 μA (30 Hz), pulse width = 0.1 μsec, flux = $1.5*10^{15}$ n/sec, operating from 1981 till the end of 2007 when it was shutdown.

-- WNR/PSR LANSCE (Los Alamos): 800 MeV protons, W target, 100 μA (12 Hz), pulse width = 0.27 μsec, flux = $1.5*10^{16}$ n/sec, operating since 1986.

-- SNS (Oak Ridge National Lab): 1.3 GeV, Hg target, 2 mA (60 Hz), pulse width = 0.945 μsec, operation started in 2006.

Spallation sources elsewhere in the world:

-- ISIS (Rutherford, UK): 800 MeV protons, U target, 200 μA (50 Hz), pulse width = 0.27 μsec, flux = $4*10^{16}$ n/sec, operating since 1984.

-- KENS (Tsukuba, Japan): 500 MeV protons, U target, 100 μA (12 Hz), pulse width = 0.07 μsec, flux = $3*10^{14}$ n/sec, operating since 1980.

-- SINQ, Paul Scherrer Institut (PSI), Switzerland, 590 MeV protons, Pb target, 1.8 mA, flux = $5*10^{14}$ n/sec, operating since 2002.

The Intense Pulsed Neutron Source
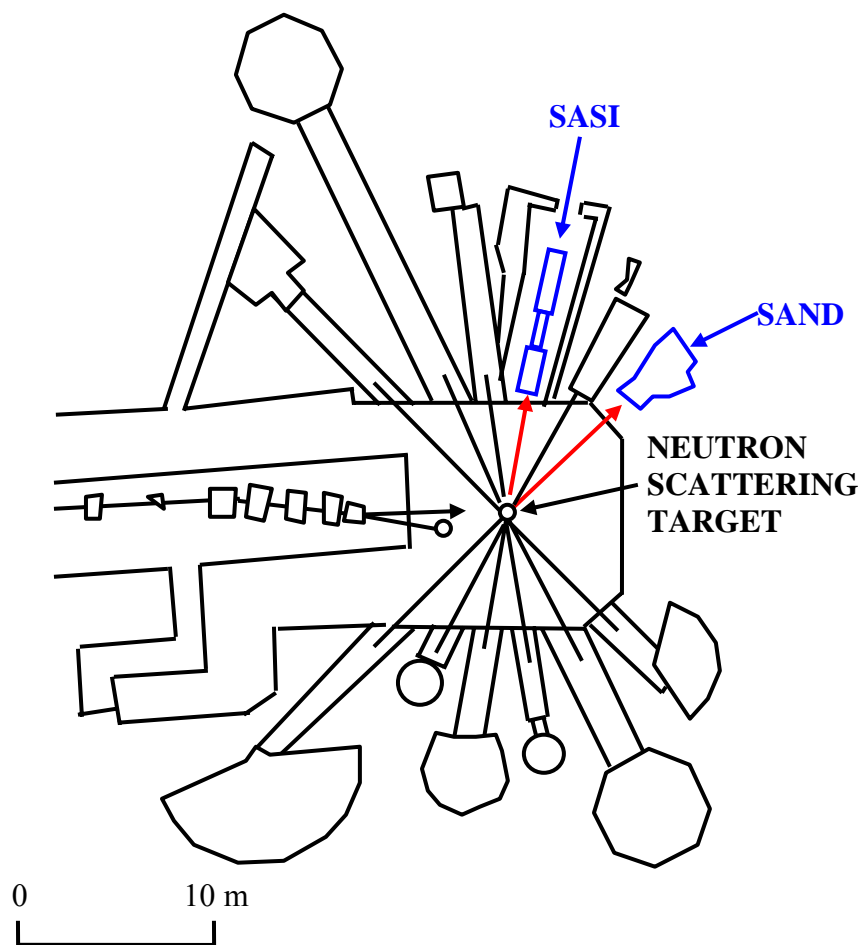
Figure 8: Schematic of the IPNS spallation source and instruments hall. Note the two SANS instruments (SASI and SAND).

Los Alamos Neutron Scattering

LQD
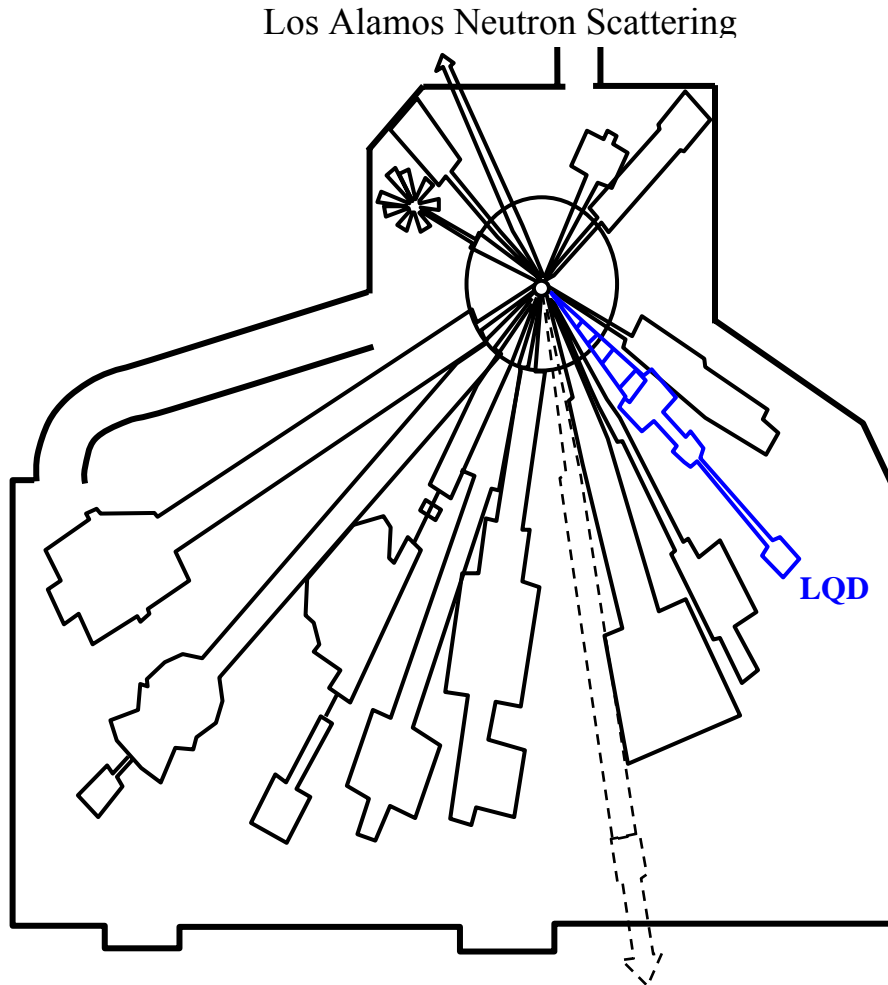
Figure 9: Schematic of the LANSCE (LANL) instruments hall. Note the SANS (LQD) instrument on the right hand side.

8. SOME OTHER NEUTRON SOURCES

"Pulsed reactors" include a moving element of fuel (or reflector material) which moves periodically causing regular variation of the reactivity. A fast rising burst of neutrons occurs when the reactivity exceeds prompt critical. One such reactor exists at:

-- IBR-II (Dubna, USSR), with mean power of 2 MW, pulse width of 50 μsec, repetition rate of 5 Hz. Neutron in pulse fluxes are of order of $5*10^{15}$ n/cm^{2}sec.

Stripping (p,n) nuclear reactions can be used to produce neutrons. The following reaction:

$$p + {}^9Be \rightarrow n + {}^9B$$
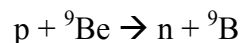
is used to produce pulsed neutrons at:

-- The Low Energy Neutron Source at the University of Indiana with pulse width between 5 μsec and 1 msec.

REFERENCES

J.J. Duderstadt and L.J. Hamilton, "Nuclear Reactor Analysis", J. Wiley and Sons, Inc., (1976).

L.R. Lamarsh, "Introduction to Nuclear Engineering", Addison Wesley Pub. Co., (1977).

International Atomic Energy Commission web site (http://www.iaea.org).

QUESTIONS

1. When was the first research reactor built?
2. Name a few applications of nuclear research reactors besides neutron scattering.
3. Why can't neutron sources be designed for much higher fluxes?
4. What is the origin of delayed neutrons?
5. Are there nuclear reactors that use non-enriched uranium?
6. Name the research reactor and the spallation source closest to your home institution.
7. Instruments at pulsed sources use a range of wavelengths whereas reactor-based instruments use single wavelength. How could the same scattering information be obtained from these two different types of instruments?
8. Why are most SANS instruments installed in neutron guide halls?
9. What is a dosimeter?

ANSWERS

1. The first nuclear reaction was performed by Enrico Fermi and his team in a sports facility close to the University of Chicago stadium in 1942. This is the first nuclear reactor built in the US called CP1 for Chicago Pile 1. A series of reactors were built at Oak Ridge, Los Alamos, Brookhaven, and Argonne National Labs and were referred to as CP2 to CP5. The first university-based research reactor was built in 1955 at Penn State University. The second one was built in 1957 at the University of Michigan.
2. There are many practical applications of nuclear research reactors besides neutron scattering. A few are mentioned here: neutron activation analysis, radioisotopes production, neutron radiography, transmutation doping of silicon, coloration of gemstones, etc.
3. Neutron sources cannot deliver much higher fluxes because they are at their limit of heat removal rate from the core (cooling rate).
4. Delayed neutrons are emitted from the decay of fission fragments. Their half-lives range from seconds to minutes.
5. The Canadian CANDU design uses U-238 (natural uranium).
6. There are two main research reactors in the US, one at the NIST Center for Neutron Research and one at the Oak Ridge High Flux Reactor.

7. Reactor-based neutron scattering instruments use some of the neutrons all of the time while spallation source-based instruments (time-of-flight) use all of the neutrons some of the time. They both measure scattered neutrons intensity with increasing scattering variable Q.

8. SANS instruments are located mostly in guide halls because they are long (30 m). Moreover guide halls are characterized by low neutron and gamma background.

9. A dosimeter is a special type of detector to monitor radiation levels and doses. It is worn by experimenters.

1. COLD NEUTRON SOURCE

"Cold" (slow) neutrons are often needed for better spatial resolution in scattering applications (long wavelength scattering). Atoms with low Z (such as H or D) are good moderators making them ideal as cold source material. Cold neutrons are generated in a neutron remoderator also called "cold source" using either hydrogen or deuterium in the liquid form, supercooled gas form, or solid form (methane or ice). The Maxwellian neutron spectral distribution (peaking at 1.8 Å for thermal neutrons) is shifted to lower energies by neutron slowing down (through inelastic scattering) processes. The mean free path (average distance between collisions) of neutrons in hydrogen (0.43 cm) is smaller than in deuterium (2.52 cm).

Liquid cold sources (hydrogen or deuterium) operate at low temperature (around 20 K) and 2 bar pressure (Russell-West, 1990). Vacuum and helium jackets isolate the remoderating liquid from the surrounding. Supercritical gas cold sources (hydrogen or deuterium) operate at 40 K and 15 bars of pressure (one phase system); thicker walls are necessary for the containment of the higher gas pressure. Solid methane at 50 K and solid ice at 35 K have been used as cold source material. Radiation damage in solid state cold sources produces stored (so called "Wigner") energy due to ionization. In order to avoid sudden release of this energy (explosion!), a recombination of radiolysis products is induced in the cold source material by warming it up on a regular basis (once every couple of days).

Use of a cold source yields high gains (one to two orders of magnitude) at high wavelengths.
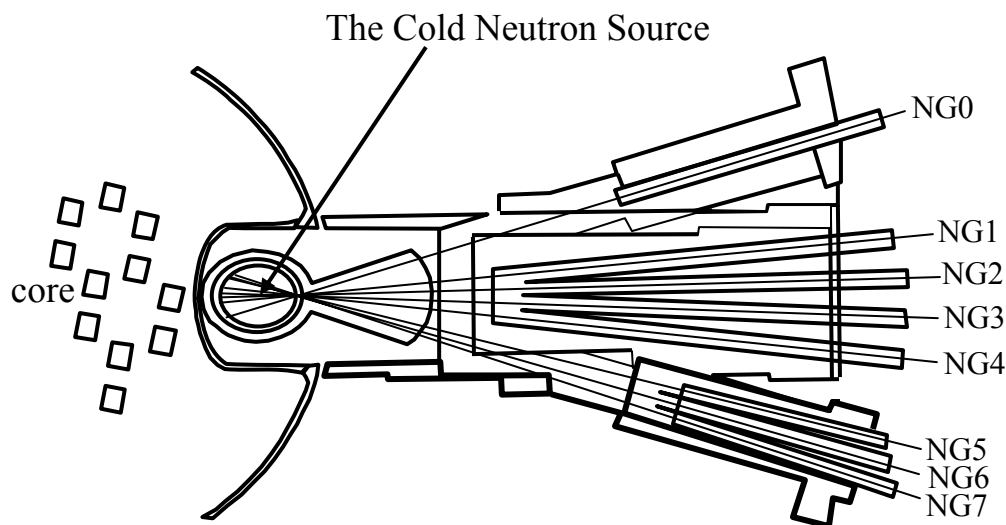
Figure 1: The NIST liquid hydrogen cold source and neutron guide system.
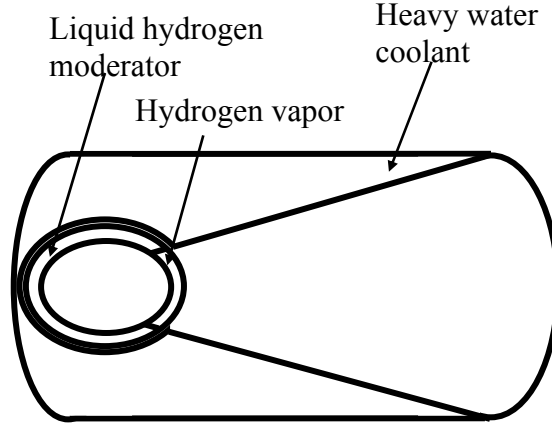
Figure 2: Schematic view of the liquid hydrogen cold source with optimized re-entrant geometry.

2. COLD NEUTRON SPECTRUM

Neutrons are produced by fission with energies around 2 MeV, then they slow down to form a Maxwellian spectrum distribution which is peaked around the moderator temperature $k_B T$ (in energy units).

The neutron flux $\varphi(E)$ is the number of neutrons crossing a unit area (1 cm^2) per second in all directions and with energies E.

$$\varphi(E) = \frac{\Phi_0}{(k_B T)^2} E \exp(-E/k_B T) . \tag{1}$$

Its integral is the neutron current (total number of neutrons produced by the cold source per second):

$$\Phi_0 = \int_0^\infty dE \, \varphi(E) . \tag{2}$$

Neutron conservation is expressed as $\varphi(E)dE = \varphi(\lambda)d\lambda$. The neutron kinetic energy E can be expressed in terms of the wavelength λ as $E = \left(\frac{h^2}{2m}\right)\frac{1}{\lambda^2}$. Using $\frac{dE}{d\lambda} = \left(\frac{h^2}{2m}\right)\frac{(-2)}{\lambda^3}$, $\varphi(\lambda)$ can be expressed as:

$$\varphi(\lambda) = \frac{\Phi_0}{(k_B T)^2} \frac{2\lambda_T^2}{\lambda^5} \exp\left(-\frac{\lambda_T^2}{\lambda^2}\right). \tag{3}$$

The variable $\lambda_T^2 = \dfrac{h^2}{2mk_B T}$ has been defined for simplicity in notation and h is Planck's constant. $\varphi(\lambda)$ is the neutron current per unit wavelength. Its units are n/s.Å. The angular spectral neutron distribution simply referred to as neutron flux (or current density) is given by $\dfrac{\varphi(\lambda)}{4\pi L_0^2}$ at a distance L_0 from the cold source. Its units are n/cm².s.ster.Å.

For high neutron wavelength λ, $\varphi(\lambda)$ decreases as $1/\lambda^5$. A cold source effectively shifts the Maxwellian peak to higher wavelengths therefore increasing the population of cold neutrons and yielding better small-angle neutron scattering resolution. For elastic scattering, this means the ability to resolve larger structures (close to micron size).

The spectral neutron distribution of the NIST Center for Neutron Research cold source is plotted (Williams-Rowe, 2002).
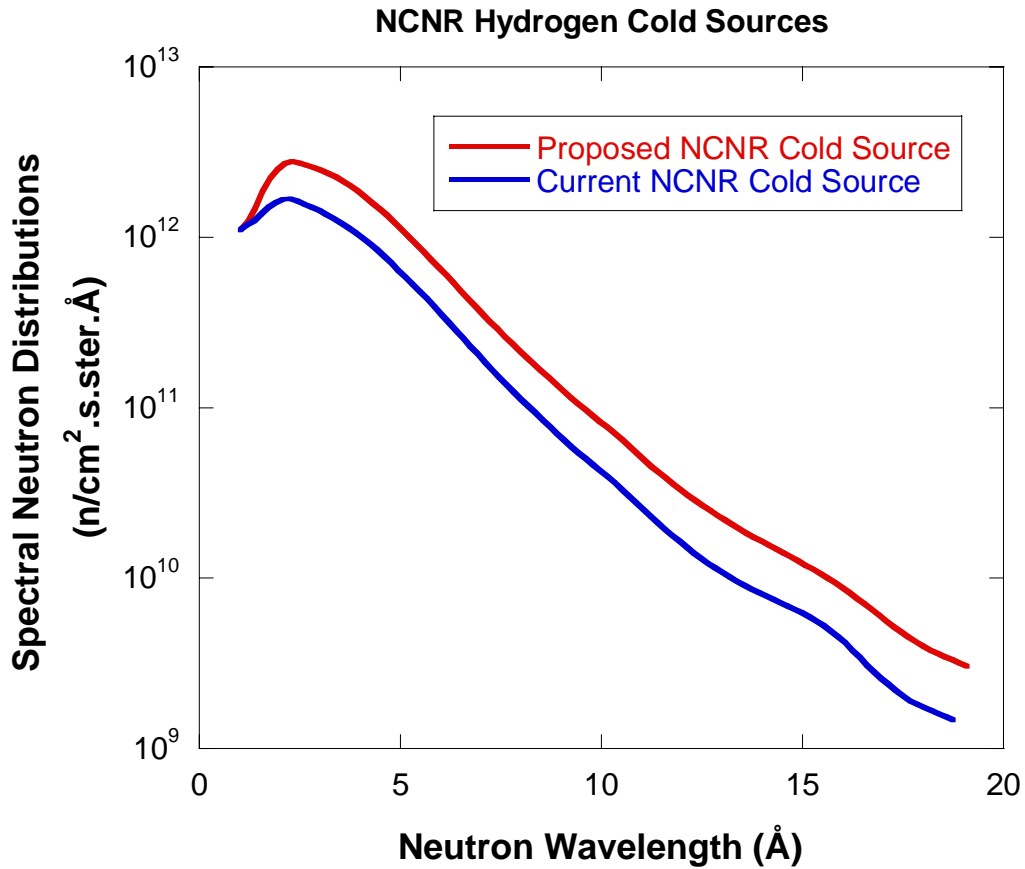
Figure 3: Spectral neutron distributions for the current and the proposed NIST Center for Neutron Research cold sources. The current one supplies neutrons to the current guide hall

and will supply the guide hall addition. The proposed smaller and brighter cold source (referred as "peewee") will supply cold neutron to one instrument inside the confinement building.

REFERENCES

G.J. Russell, and C.D. West, "International Workshop on Cold Neutron Sources", Los Alamos National Lab, March 5-8 (1990).

R. E. Williams and J. M. Rowe, "Developments in Neutron Beam Devices and an Advanced Cold Source for the NIST Research Reactor", Physica B 311, 117-122 (2002).

QUESTIONS

1. What are the main types of cold neutron sources?
2. What is the primary safety issue associated with solid cold sources?
3. What is the boiling temperature of hydrogen?
4. What is the spectral distribution of cold neutrons?
5. Why are cold neutrons necessary for the SANS technique?

ANSWERS

1. Cold sources are of the liquid, gas or solid types. Most of them use eith hydrogen or deuterium to slow down neutrons to cold energies.
2. Solid state cold sources (either solid methane or solid heavy ice) store Wigner energy that needs to be released by annealing the cold source. If not annealed, the solid cold source could explode.
3. Liquid hydrogen boils at 21 K.
4. Cold neutrons follow a Maxwellian spectral distribution with a tail varying like $1/\lambda 5$ where λ is the neutron wavelength.

Chapter 5 - **NEUTRON FLUX ON SAMPLE**

Flux on sample is an important factor in characterizing the performance of a neutron scattering instrument. It depends on many factors as discussed here.

1. THE COLD NEUTRON SOURCE SPECTRUM

The liquid hydrogen neutron cold source is characterized by the following angular spectrum distribution (neutrons/cm^2.s.Å.ster):

$$\frac{\varphi(\lambda)}{4\pi L_0^{~2}} = \frac{\Phi_0}{4\pi L_0^{~2}} \frac{2\lambda_T^{~2}}{\lambda^5} \exp\left(-\frac{\lambda_T^{~2}}{\lambda^2}\right) \tag{1}$$

It is also referred to as the "Maxwellian" distribution. λ is the neutron wavelength and λ_T is a cold source constant defined as $\lambda_T = h/\sqrt{2mk_BT}$. λ_T can be expressed as:

$$\lambda_T = A\sqrt{T_e} \; . \tag{2}$$

The constant $A = 30.9 \text{Å}\sqrt{K}$, T_e is the cold source effective temperature $T_e = 32$ K. Note that the cold source real temperature is the condensation temperature of hydrogen (around 21 K). Therefore $\lambda_T = 5.5$ Å is a good estimate in our case. Note the $1/\lambda^5$ tail behavior of the wavelength distribution. The normalization factor Φ_0 is determined through flux measurements.

2. NEUTRON FLUX ON SAMPLE

The neutron current on sample (n/s) can be estimated for a typical SANS instrument configuration as:

$$\frac{\varphi(\lambda)}{4\pi} \Delta\lambda\Delta\Omega = \frac{\varphi(\lambda)}{4\pi} \Delta\lambda \frac{A_1}{L_0^{~2}} \frac{A_2}{L_1^{~2}} \tag{3}$$

$\Delta\lambda$ is the wavelength spread, $\Delta\Omega$ is the solid angle, A_1 and A_2 are the areas of the source and sample apertures, L_0 and L_1 are the cold source-to-source aperture and source aperture-to-sample aperture distances respectively.
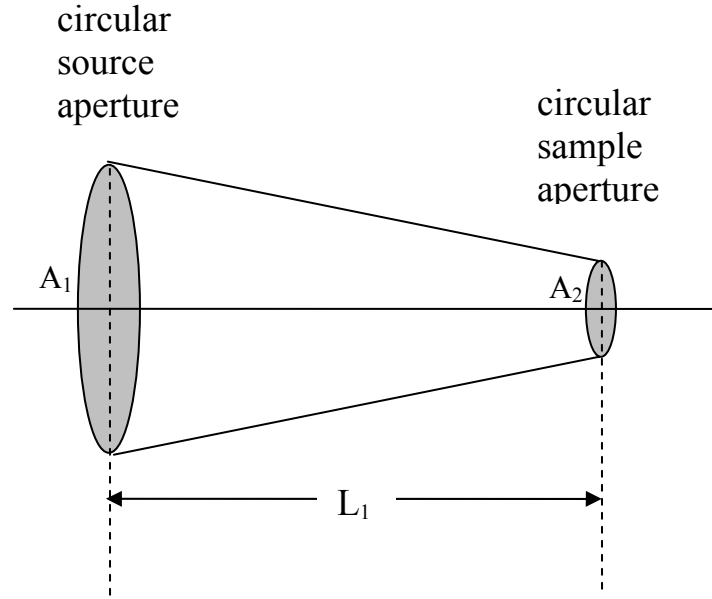
Figure 1: Typical pre-sample SANS collimation geometry. This figure is not to scale. Vertical scale is of order of centimeters while horizontal scale is of order of meters.

This quantity can be expressed as:

$$\frac{\varphi(\lambda)}{4\pi}\Delta\lambda\Delta\Omega = \frac{\Phi_0}{2\pi}\frac{\lambda_T^4}{\lambda^5}\exp\left(-\frac{\lambda_T^2}{\lambda^2}\right)\Delta\lambda\,\frac{A_1}{L_0^2}\frac{A_2}{L_1^2} \qquad (4)$$

with $\lambda_T = 5.5$ Å. In order to make the neutron flux expression match the measured flux at the NG3 SANS instrument the following factor is chosen:

$$\frac{\Phi_0}{2\pi L_0^2} = 1.65 * 10^{12}\,\text{n/cm}^2.\text{s}. \qquad (5)$$

The estimated flux (or current density) on sample (n/cm^2.s.Å) is given by:

$$\phi(\lambda) = \frac{\varphi(\lambda)}{4\pi}\Delta\lambda\frac{\Delta\Omega}{A_2} = \frac{\Phi_0}{2\pi L_0^2}\frac{\lambda_T^4}{\lambda^4}\exp\left(-\frac{\lambda_T^2}{\lambda^2}\right)\left(\frac{\Delta\lambda}{\lambda}\right)\left(\frac{A_1}{L_1^2}\right) \qquad (6)$$

$$\phi(\lambda) = \frac{1.507 * 10^{15}}{\lambda^4}\exp\left(-\frac{30.25}{\lambda^2}\right)\left(\frac{\Delta\lambda}{\lambda}\right)\left(\frac{A_1}{L_1^2}\right)$$

Consider a typical neutron wavelength and wavelength spread:

Neutron wavelength: $\lambda = 6$ Å.
Wavelength spread: $\Delta\lambda/\lambda = 0.15$.

So that::

$$\phi(6 \text{ Å}) = 7.53 * 10^{10}\left(\frac{A_1}{L_1^2}\right) \text{n/cm}^2.\text{s} \qquad (7)$$

This expression is used in the following section.

3. CASE OF SPECIFIC CONFIGURATIONS

Consider two instrument configurations both using:

Neutron wavelength: $\lambda = 6$ Å.
Wavelength spread: $\Delta\lambda/\lambda = 0.15$.

The first configuration corresponds to high flux on sample:

Source aperture radius: $R_1 = 2.5$ cm.
Area of source aperture: $A_1 = \pi\ 2.5^2 = 19.63$ cm^2.
Source-to-sample distance: $L_1 = 3.82$ m.

So that $\phi(6\text{Å}) = 1.01 * 10^7$ n/cm^2.s for the high flux configuration.

The second configuration corresponds to low flux on sample:

Source aperture radius: $R_1 = 1.9$ cm.
Area of source aperture: $A_1 = \pi\ 1.9^2 = 11.34$ cm^2.
Source-to-sample distance: $L_1 = 16.22$ m.

So that $\phi(6\text{Å}) = 3.24 * 10^5$ n/cm^2.s for the low flux configuration.

4. MEASURED FLUX ON SAMPLE

The two previously considered cases correspond to two specific configurations on the NG3 30 m-SANS instrument at NIST. Flux on sample measurements were made for these two configurations described above and for a range of wavelengths. These results are plotted here.
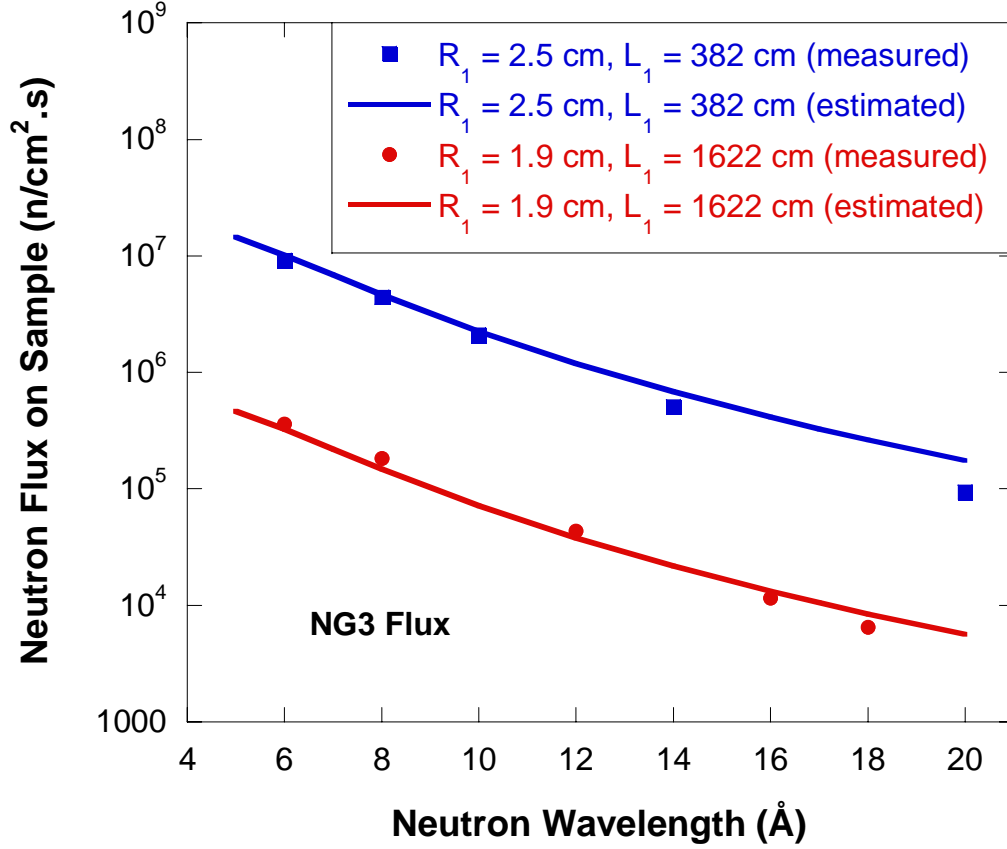
Figure 2: Measured neutron flux on sample with varying wavelength for the high flux configuration ($R_1 = 2.5$ cm, $L_1 = 3.82$ m) and the low flux configuration ($R_1 = 1.9$ cm, $L_1 = 16.22$ m). Estimates values are also plotted.

Note that the neutron current on sample (n/s) is obtained by multiplying the neutron flux by the area of the sample aperture A_2 ($= \pi R_2^2$). In our notation, that quantity is given by $\Phi(\lambda) = \dfrac{\varphi(\lambda)}{4\pi} \Delta\lambda\Delta\Omega$.

Considering a sample aperture of radius $R_2 = 0.635$ cm, the following neutron currents can be estimated:

$$\Phi(6\text{Å}) = \frac{\varphi(6\text{Å})}{4\pi} \Delta\lambda\Delta\Omega = 1.28*10^7 \text{ n/s for the high flux configuration.}$$

$$\Phi(6\text{Å}) = \frac{\varphi(6\text{Å})}{4\pi} \Delta\lambda\Delta\Omega = 4.10*10^5 \text{ n/s for the low flux configuration.}$$

These are reasonably high numbers for a SANS instrument (Cook et al, 2005).

5. NEUTRON BEAM MONITOR COUNT RATE

The neutron beam monitor count rate is measured on a regular basis for increasing wavelength. Measurements shown here were taken on the NG3 30 m SANS instrument at the NIST CNR before the optical filter was installed. The beam monitor is a low-efficiency fission counter. It detects neutrons through their absorption in a thin U-235 plate. The absorption cross section varies like "1/v" (v being the neutron velocity). It is proportional to the neutron wavelength λ, i.e., $\sigma_a(\lambda) = c\lambda$ where c is a constant.

The measured monitor count rate $m(\lambda)$ is compared to the following empirical expression:

$$m(\lambda) = \frac{2.25 * 10^7}{\lambda^3} \exp\left[-\left(\frac{7.37}{\lambda} \right)^2 \right]. \tag{8}$$

The multiplicative constant depends on the fission counter used. Note the characteristic λ-dependence. The tail drops out like $1/\lambda^3$. Recall that the cold source spectrum drops out like $1/\lambda^5$. Use of a velocity selector (with constant $\Delta\lambda/\lambda$) changes the tail of the transmitted spectrum to $1/\lambda^4$. Therefore, the tail of the corrected monitor count rate varies like $m(\lambda)/\sigma_a(\lambda) \sim 1/\lambda^3$. The wavelength dependence of the monitor count rate/wavelength and the neutron current density are the same. It is not clear as to why the constants in the exponential are different.

Neutron Beam Monitor

35
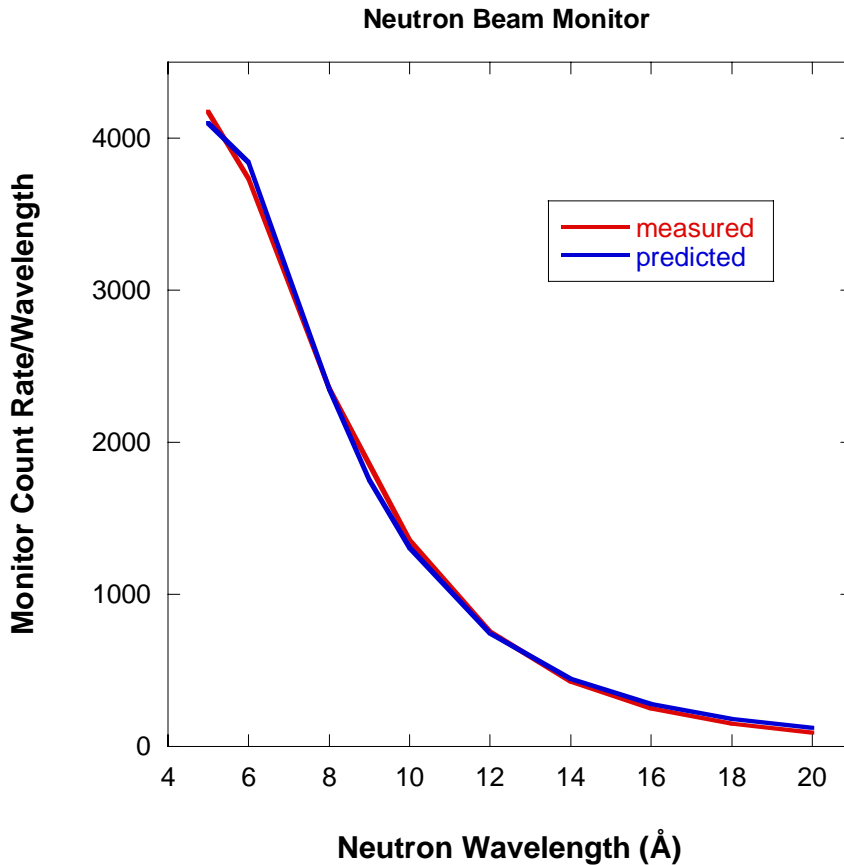
Figure 3: Variation of the neutron beam monitor count rate divided by the neutron wavelength with increasing wavelength.

REFERENCE

J.C. Cook, C.J. Glinka, and I.G. Schroder, "Performance of the vertical optical filter for the NG-3 30 m SANS instrument at the National Institute of Standards and Technology's Center for Neutron Research", Review of Scientific Instruments, <u>76</u>, no. 2, 25108-1-8, (2005).

QUESTIONS

1. What is the neutron current?
2. What is the neutron flux (or current density) at the sample?
3. What is the highest neutron flux on sample for 6 Å neutrons at the NG3 SANS instrument?
4. How do neutron fluxes compare with x-ray fluxes?
5. Is the neutron current crossing the sample aperture the same as the detector count rate?

ANSWERS

1. The neutron current is the number of neutrons per second.
2. The neutron flux at the sample is expressed in $n/cm^2.s$. It is independent of sample area.
3. The highest neutron flux on sample for 6 Å neutrons at the NG3 SANS instrument is around 10^7 $n/cm^2.s$. It is obtained for a high-Q high flux configuration.
4. Neutron fluxes are orders of magnitude lower than x-ray fluxes. Even fluxes for a rotating anode x-ray source are higher than the highest neutron source fluxes.
5. The neutron current crossing the sample aperture is not the same as the detector count rate because of loss due to attenuation in the scattering flight path, due to neutrons that are scattered outside of the detector solid angle and due to the detector absorption cross section and non-perfect detector efficiency.

Chapter 6 - **INTRODUCTION TO NEUTRON SCATTERING**

Neutron scattering is the technique of choice for condensed matter investigations in general because thermal/cold neutrons are a non-invasive probe; they do not change the investigated sample since they do not deposit energy into it.

1. CHARACTERISTICS OF NEUTRON SCATTERING

A few advantages of neutron scattering are included here.

-- Neutron scattering lengths vary "randomly" with atomic number and are independent of momentum transfer Q. This is used to advantage in deuterium labeling using the fact that the scattering lengths for hydrogen and deuterium are widely different (b_H = -3.739 $*10^{-13}$ cm and b_D = 6.671 $*10^{-13}$ cm respectively). The negative sign in front of b_H means that the scattered neutrons wavefunction is out of phase with respect to the incident neutrons wavefunction.

-- Neutrons interact through nuclear interactions. X-rays interact with matter through electromagnetic interactions with the electron cloud of atoms. Electron beams interact through electrostatic interactions. Light interacts with matter through the polarizability and is sensitive to fluctuations in the index of refraction. For this, neutrons have high penetration (low absorption) for most elements making neutron scattering a bulk probe. Sample environments can be designed with high Z material windows (aluminum, quartz, sapphire, etc) with little loss.

-- In neutron scattering, scattering nuclei are point particles whereas in x-ray scattering, atoms have sizes comparable to the wavelength of the probing radiation. In the very wide angle (diffraction) range, x-ray scattering contains scattering from the electron cloud, whereas neutron scattering does not. In the SANS range, this is not the case.

-- Neutrons have the right momentum transfer and right energy transfer for investigations of both structures and dynamics in condensed matter.

-- A wide range of wavelengths can be achieved by the use of cold sources. Probed size range covers from the near Angstrom sizes to the near micron sizes. One can reach even lower Q's using a double crystal monochromator (so called Bonse-Hart) USANS instrument.

-- Since neutron detection is through nuclear reactions (rather than direct ionization for example) the detection signal-to-noise ratio is high (almost 1 MeV energy released as kinetic energy of reaction products).
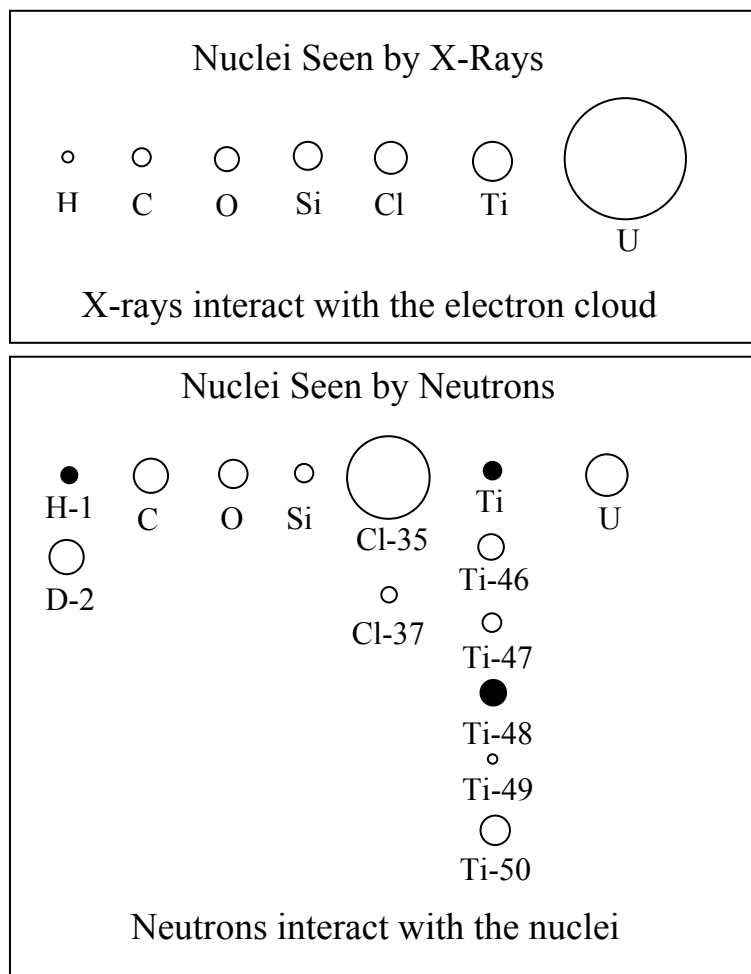
Figure 1: Neutrons are scattered from nuclei while x-rays are scattered from electrons. Scattering lengths for a few elements are compared. Negative neutron scattering lengths are represented by dark circles.

A few disadvantages of neutron scattering follow.

-- Neutron sources are very expensive to build and to maintain. It costs millions of US dollars annually to operate a nuclear research reactor and it costs that much in electrical bills alone to run a spallation neutron source. High cost (billions of dollars) was a major factor in the cancellation of the Advanced Neutron Source project in the mid 1990s.

-- Neutron sources are characterized by relatively low fluxes compared to x-ray sources (synchrotrons) and have limited use in investigations of rapid time dependent processes.

-- Relatively large amounts of samples are needed: typically 1 mm-thickness and 1 cm diameter samples are needed for SANS measurements. This is a difficulty when using expensive deuterated samples or precious (hard to make) biology specimens.

2. TYPES OF NEUTRON SCATTERING

There are four main types of neutron scattering.

(1) The simplest type consists in a measurement of the sample transmission. This measurement requires a monochromatic beam (or the time-of-flight method), some collimation and a simple neutron detector (end-window counter). Transmission measurements contain information about the sample content and the relative fractions of the various elements. For example, the relative ratio of carbon to hydrogen in crude oils (the so-called cracking ratio) could be measured accurately.

(2) Elastic neutron scattering consists in measuring the scattered intensity with varying scattering angle. This is a way of resolving the scattering variable $Q = (4\pi/\lambda)\sin(\theta/2)$ where λ is the neutron wavelength and θ is the scattering angle. This is performed by either step-scanning or using a position-sensitive detector. The main types of elastic scattering instruments are diffractometers (either for single-crystal, powder diffraction or for diffuse scattering from amorphous materials), reflectometers and SANS instruments. Diffractometers probe the high Q range ($Q > 0.5$ Å^{-1}) whereas reflectometers and SANS instrument cover the low-Q range ($Q < 0.5$ Å^{-1}). They all investigate sample structures either in crystalline of amorphous systems.

(3) Quasielastic/inelastic neutron scattering consists in monochromation, collimation, scattering from a sample, analysis of the neutron energies then detection. The extra step uses a crystal analyzer (or the time-of flight method) in order to resolve the energy transfer during scattering. In this case both $\vec{Q} = \vec{k}_s - \vec{k}_i$ and $E = E_s - E_i$ are resolved. Quasielastic scattering corresponds to energy transfers around zero, whereas inelastic scattering corresponds to finite energy transfers. The main types of quasielastic/inelastic spectrometers are the triple axis, the time-of-flight, and the backscattering spectrometers. These instruments cover the μeV to meV energy range. They investigate sample dynamics and structure. Inelastic instruments are used to investigate phonon, optic and other types of normal modes. Quasielastic instruments are used to investigate diffusive modes mostly.

(4) The spin-echo instrument is another type of quasielastic spectrometer. It is singled out here because it measures correlations in the time (not energy) domain. It uses polarized neutrons that are made to precess in the pre-sample flight path, get quasielastically scattered from the sample, then are made to precess in the other direction in the post-sample flight path. A neutron spin analyzer keeps track of the number of spin precessions. The difference in the number of spin precessions before and after the sample is proportional to the neutron velocity change during scattering and therefore to the energy transfer. Scanned Q ranges are between 0.01 Å^{-1} and 0.5 Å^{-1} and probed times are in the nanoseconds range. This instrument is useful for investigating diffusive motions in soft materials.

TRANSMISSION MEASUREMENT

DIFFRACTOMETER

QUASIELASTIC/INELASTIC SCATTERING

NEUTRON SPIN ECHO
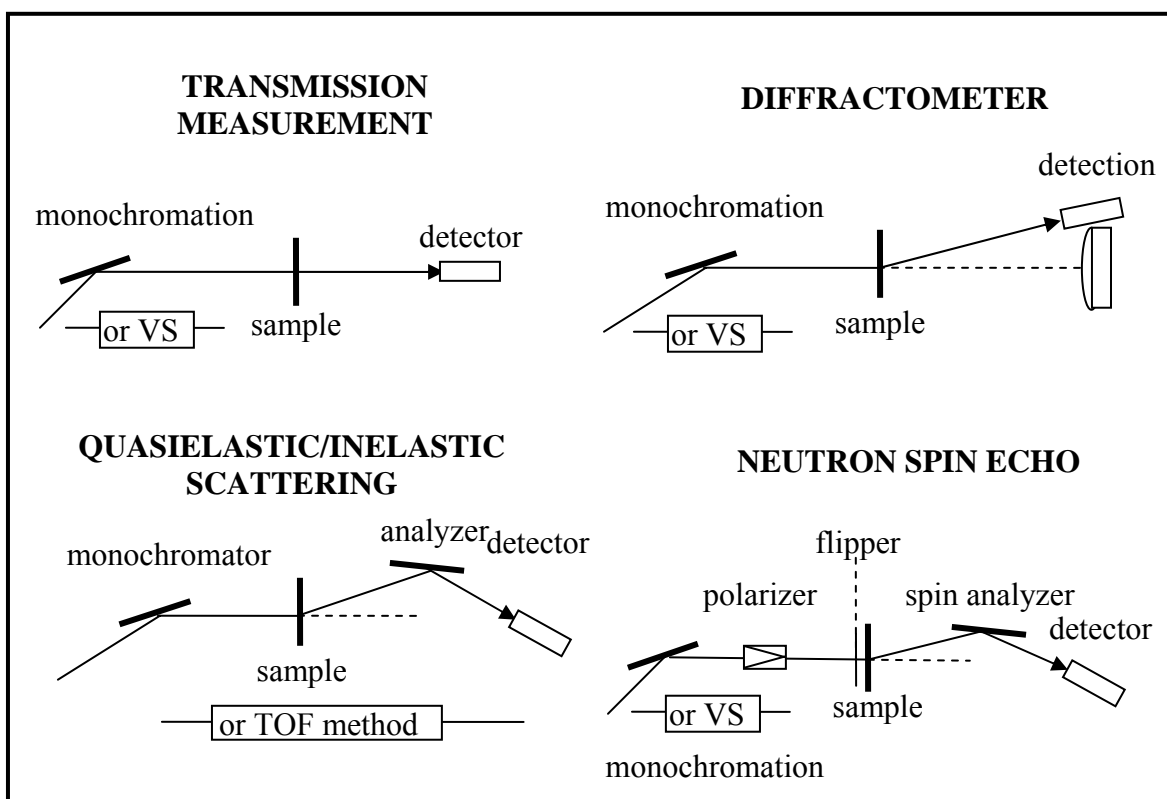
Figure 2: Schematic representation of the four types of neutron scattering methods.

3. DIFFRACTOMETER TYPES

The main types of diffractometers include (1) single-crystal and powder diffractometers, (2) diffuse and liquid scattering instruments, (3) small-angle neutron scattering instruments and (4) reflectometers. All of these diffractometers correspond to "double axis" diffraction, i.e., they are schematically represented by a monochromator (first axis) and diffraction from the sample at an angle θ (second axis). Types (1) and (2) probe the high Q scale $Q > 0.1$ Å^{-1} (i.e., small d-spacings $d < 60$ Å). The third and fourth type probe the lower Q scale 0.4 Å$^{-1} > Q > 0.001$ Å^{-1} (i.e., 16 Å $< d < 6000$ Å). The measurement window for SANS instruments and reflectometers covers from the near atomic sizes (near Å) to the near optical sizes (near μm). Type (1) measures purely crystalline samples whereas the other types are used mostly for amorphous systems. SANS however can measure both amorphous and crystalline samples. Types (1), (2) and (3) measure bulk samples whereas type (4) (reflectometers) measure surface structures only. Similar discussions can be found elsewhere (Price-Skold, 1986).

REFERENCES

D.L Price and K. Skold, "Introduction to Neutron Scattering" Methods of Experimental Physics 23A, 1 (1986)

"NIST Cold Neutron Research Facility and Instruments", a series of articles covering the entire issue, National Institute of Standards and Technology Journal of Research, <u>98</u>, Issue No 1 (1993).

QUESTIONS

1. Name a couple of advantages of neutron scattering.
2. Neutrons interact with what part of the atom?
3. Name a couple of disadvantages of neutron scattering.
4. Name the four types of neutron scattering instruments.
5. What type is the SANS instrument?

ANSWERS

1. Neutrons are very penetrating, they do not heat up or destroy the sample, deuterium labeling is unique, they have the right wavelengths (Angstroms) and kinetic energies (μeV to meV) to probe structures and dynamics of materials.
2. Neutrons interact with the nuclei.
3. Neutron sources are characterized by low flux compared to x-ray sources. Relatively large amounts of sample (gram amounts) are required for neutron scattering measurements.
4. The four types of neutron scattering instruments are: transmission, elastic, quasielastic/inelastic and neutron spin echo.
5. The SANS instrument is a "diffractometer" for diffuse elastic neutron scattering.

Elements of neutron scattering theory are described here. The scattering amplitude, scattering lengths and cross sections are introduced and discussed.

1. SOLUTION OF THE SCHRODINGER EQUATION

Neutron scattering theory involves quantum mechanical tools such as the solution of the Schrodinger equation even though the scattering problem is not a quantum mechanical problem (no bound states are involved). A simple solution of the Schrodinger equation involving perturbation theory is presented here. This is to so-called Born approximation method.
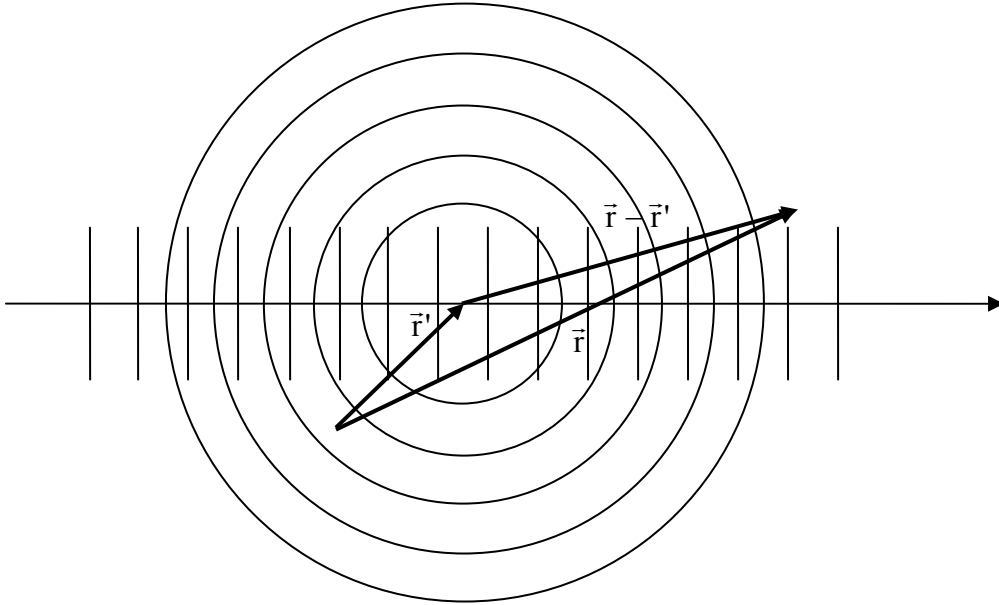
Figure 1: Incident plane wave and scattered spherical wave.

The Schrodinger equation is expressed as follows:

$$H_i \psi_i = E_i \psi_i \qquad (1)$$
$$H\psi = E\psi$$
$$H = H_i + V.$$

H is the full Hamiltonian operator, H_i is the incident neutron kinetic energy operator and V is the neutron-nucleus interaction potential. E_i and E are the eigenvalue energies for the incident neutron and for the neutron-nucleus interacting pair. Ψ_i and Ψ are the eigenfunctions for the same two systems.

$$H_i = \frac{p^2}{2m} = -\frac{\hbar^2}{2m}\nabla^2 \qquad (2)$$

$\vec{p} = i\hbar\vec{\nabla}$ is the momentum operator.

$$E_i = \frac{\hbar^2 k_i^2}{2m}.$$

E_i is the incident neutron kinetic energy and k_i is its incident wavenumber. Ψ_i is the solution of the homogeneous differential equation:

$$(H_i - E_i)\Psi_i(\vec{r}) = -\frac{\hbar^2}{2m}(\nabla^2 + k_i^2)\Psi_i(\vec{r}) = 0. \qquad (3)$$

The solution is an incident plane wave $\Psi_i(r) = \exp(i\vec{k}_i \cdot \vec{r})$ using vector notation. The full differential equation is written as:

$$-\frac{\hbar^2}{2m}(\nabla^2 + k^2)\Psi(\vec{r}) = V(\vec{r})\Psi(\vec{r}). \qquad (4)$$

Its solution is an integral equation is of the form:

$$\Psi(\vec{r}) = \Psi_i(\vec{r}) + \left(\frac{m}{2\pi\hbar^2}\right)\int d\vec{r}' G(\vec{r} - \vec{r}')V(\vec{r}')\Psi(\vec{r}') \qquad (5)$$

Here $G(\vec{r} - \vec{r}')$ is a Green's function satisfying the following differential equation:

$$(H - E)G(\vec{r}) = -\frac{\hbar^2}{2m}(\nabla^2 + k_s^2)G(\vec{r}) = \delta(\vec{r}) \qquad (6)$$

k_s is the scattered neutron wavenumber. Its solution is a spherical outgoing wave of the form:

$$G(\vec{r}) = \frac{\exp(ik_s r)}{r}. \qquad (7)$$

In order to verify this result, the following relations valid in spherical coordinates are used:

$$\nabla\left(\frac{1}{r}\right) = \frac{\partial}{\partial r}\left(r^2 \frac{1}{r}\right) = \frac{1}{r^2} \qquad (8)$$

$$\nabla^2\left(\frac{1}{r}\right) = \frac{1}{r^2}\left[\frac{\partial}{\partial r}r^2\left(\frac{\partial}{\partial r}\right)\right]\left(\frac{1}{r}\right) = \delta(r).$$

Therefore:

$$\Psi(\vec{r}) = \Psi_i(\vec{r}) + \left(\frac{m}{2\pi\hbar^2}\right) \int d\vec{r}' \frac{\exp(ik_s|\vec{r}-\vec{r}'|)}{|\vec{r}-\vec{r}'|} V(\vec{r}')\Psi(\vec{r}') \qquad (9)$$

Vector $\vec{r}'$ is within the sample and $\vec{r}$ is far from the sample so that $r \gg r'$ and therefore one can approximate $|\vec{r}-\vec{r}'| \cong r - \frac{\vec{r}.\vec{r}'}{r}$.

$$G(|\vec{r}-\vec{r}'|) = \frac{\exp(ik_s r)}{r}\exp\left(\frac{-ik_s\vec{r}.\vec{r}'}{r}\right) = \frac{\exp(ik_s r)}{r}\exp(-i\vec{k}_s.\vec{r}') . \qquad (10)$$

Here, the scattered neutron wavevector $\vec{k}_s$ has been defined as $\vec{k}_s = k_s\vec{r}/r$.

The general solution of the Schrodinger equation is an integral equation that can be solved iteratively through the expansion:

$$\Psi(\vec{r}) = \Psi_i(\vec{r}) + \left(\frac{m}{2\pi\hbar^2}\right)\int d\vec{r}' G(\vec{r}-\vec{r}')V(\vec{r}')\Psi_i(\vec{r}') +$$

$$\left(\frac{m}{2\pi\hbar^2}\right)^2 \int d\vec{r}' G(\vec{r}-\vec{r}')V(\vec{r}')\int d\vec{r}'' G(\vec{r}-\vec{r}'')\Psi_i(\vec{r}'') + ... \qquad (11)$$

Keeping only the first integral term corresponds to the first Born approximation which can be presented in the form:

$$\Psi(\vec{r}) = \Psi_i(\vec{r}) + \left(\frac{m}{2\pi\hbar^2}\right)\int d\vec{r}' G(\vec{r}-\vec{r}')V(\vec{r}')\Psi_i(\vec{r}') \qquad (12)$$

$$\Psi(\vec{r}) = \exp(i\vec{k}_i.\vec{r}) + \frac{\exp(ik_s r)}{r}\left(\frac{m}{2\pi\hbar^2}\right)\int d\vec{r}' \exp(-i\vec{k}_s.\vec{r}')V(\vec{r}')\exp(i\vec{k}_i.\vec{r}')$$

$$\Psi(\vec{r}) = \exp(i\vec{k}_i.\vec{r}) + \frac{\exp(ik_s r)}{r}f(\theta) .$$

The scattering amplitude $f(\theta)$ has been defined as:

$$f(\theta) = \left(\frac{m}{2\pi\hbar^2}\right)\int d\vec{r}' \exp(-i\vec{Q}.\vec{r}')V(\vec{r}) \qquad (13)$$

$\vec{Q} = \vec{k}_s - \vec{k}_i$ is the scattering vector. $f(\theta)$ is the Fourier transform of the interaction potential $V(r')$. $f(\theta)$ has been assumed to be independent of the azimuthal angle.

The first Born approximation applies to thermal/cold neutrons neutron scattering corresponding to "s wave" scattering (i.e., corresponding to a zero orbital angular quantum number). This includes all of neutron scattering except for neutron reflectivity whereby

higher order terms in the Born expansion have to be included. Neutron reflectometry involves refraction (not diffraction).

$\vec{Q}$ characterizes the probed length scale and its magnitude is given for elastic scattering in terms of the neutron wavelength λ and scattering angle θ as $Q = (4\pi/\lambda) \sin(\theta/2)$. For small angles (SANS), it is simply approximated by $Q = 2\pi\theta/\lambda$. Since Q is the Fourier variable (in reciprocal space) conjugate to scatterer positions (in direct space), investigating low-Q probes large length scales in direct space and vice versa.

In summary, the solution of the Schrodinger equation is an incident plane wave and a scattered spherical wave multiplied by the scattering amplitude.

2. SCATTERING CROSS SECTIONS

The microscopic differential scattering cross section is defined here. It represents the fraction of neutrons scattered into solid angle $d\Omega$ with a scattering angle θ.
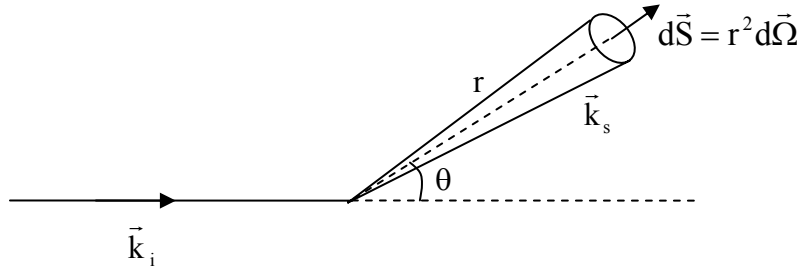
Figure 2: Representation of neutrons scattered with angle θ inside a solid angle $d\Omega$.

Consider incident neutrons of wavenumber k_i and scattered neutrons of wavenumber k_s. The incident neutron flux also called current density (neutrons/cm^2.s) is given by:

$$\vec{J}_i = \frac{i\hbar}{2m}\left(\Psi_i \vec{\nabla}\Psi_i{}^* - \Psi_i{}^* \vec{\nabla}\Psi_i\right). \qquad (14)$$

Here * represents the complex conjugate and $\Psi_i = \exp(i\vec{k}_i.\vec{r})$ is the incident plane wave. Performing the simple operation $\vec{\nabla}\Psi = i\vec{k}_i\Psi$, one obtains $\vec{J}_i = \hbar\vec{k}_i/m$. Similarly for the scattered neutron flux:

$$\vec{J}_s = \frac{i\hbar}{2m}\left(\chi\vec{\nabla}\chi{}^* - \chi{}^* \vec{\nabla}\chi\right). \qquad (15)$$

Where $\chi = \Psi - \Psi_i = \dfrac{\exp(ik_s r)}{r} f(\theta)$. Here also performing the differentiations one obtains:

$\vec{J}_s = \dfrac{\hbar \vec{k}_s}{m} \dfrac{f(\theta)}{r^2}$. The differential neutron scattering cross section is defined

$$d\sigma_s(\theta) = \vec{J}_s r^2 d\vec{S} = \dfrac{\hbar k_s}{m} |f(\theta)|^2 \, d\Omega \qquad (16)$$

This is the ratio of the neutron flux scattered in $d\Omega$ over the incident neutron flux. Within the first Born approximation (also called the Fermi Golden Rule):

$$\dfrac{d\sigma_s(\theta)}{d\Omega} = \dfrac{k_s}{k_i} |f(\theta)|^2 \qquad (17)$$

$$\dfrac{d\sigma_s(\theta)}{d\Omega} = \dfrac{k_s}{k_i} \left| \left(\dfrac{m}{2\pi\hbar^2} \right) \int dr' \exp(-i\vec{Q}.\vec{r}') V(\vec{r}') \right|^2 .$$

This cross section contains information about what inhomogeneities are scattering and how they are distributed in the sample. The microscopic scattering cross section is its integral over solid angles: $\sigma_s = \int \left(\dfrac{d\sigma_s}{d\Omega} \right) d\Omega$. Cross sections are given in barn units (1 barn = 10^{-24} cm^2).

Given the (atomic) number density N/V (number of scattering nuclei/cm^3) in a material, a macroscopic cross section is also defined as: $\Sigma_s = (N/V)\, \sigma_s$ (units of cm^{-1}). SANS data are often presented on an "absolute" macroscopic cross section scale independent of instrumental conditions and of sample volume. It is given by $d\Sigma_s/d\Omega = (N/V)\, d\sigma_s/d\Omega$.

3. THE BRA-KET NOTATION

The <bra|ket> approach is useful for simplifying notation. Consider the following definitions:

$$< \vec{r} \,|\, \vec{k}_i > = \exp(i\vec{k}_i.\vec{r}) \qquad (18)$$
$$< \vec{r} \,|\, \Psi > = \Psi(\vec{r})$$
$$< r \,|\, V = V(r)$$
$$< \vec{r} \,|\, G \,|\, \vec{r}') = G(\vec{r} - \vec{r}')$$
$$< \vec{r} \,|\, \vec{r}') = \delta(\vec{r} - \vec{r}') .$$

Define the following closure relations:

$$\int |\,\vec{r}'> d\vec{r}' < \vec{r}'| = 1$$

$$\int |\vec{k}> d\vec{k} <\vec{k}| = 1. \tag{19}$$

The integrations are over all direct $\vec{r}$ or reciprocal $\vec{k}$ space. The scattering amplitude is expressed as:

$$f(\theta) = \left(\frac{m}{2\pi\hbar^2}\right)\int d\vec{r}' \exp(-i\vec{Q}.\vec{r}')V(\vec{r}') \tag{20}$$

$$= \left(\frac{m}{2\pi\hbar^2}\right)\int d\vec{r}' \exp(-i\vec{k}_s.\vec{r}')\exp(i\vec{k}_i.\vec{r}')V(\vec{r}').$$

Using the <bra|ket> notation, $f(\theta)$ can be also manipulated to the form:

$$f(\theta) = \left(\frac{m}{2\pi\hbar^2}\right)<\vec{k}_s | V | \vec{k}_i >. \tag{21}$$

The scattering cross section is therefore given in terms of the transition probability $<\vec{k}_s | V | \vec{k}_i >$ as:

$$\frac{d\sigma_s(\theta)}{d\Omega} = \frac{k_s}{k_i}\left|<\vec{k}_s | \left(\frac{m}{2\pi\hbar^2}\right)V | \vec{k}_i >\right|^2. \tag{22}$$

This result ignores the effect of spin interactions and therefore does not apply to scattering from magnetic systems.

4. SIMPLE MODEL FOR NEUTRON SCATTERING LENGTHS

A simple argument is used here in order to appreciate the origin of the scattering length (Squires, 1978). Consider a neutron of thermal/cold incident energy E_i being elastically scattered from a nucleus displaying an attractive square well potential $-V_o$ (note that $V_o \gg E_i$). Recall the Schrodinger equation for this simplest potential.

$$\left[-\frac{\hbar^2}{2m}\nabla^2 + V(r)\right]\psi(r) = E\psi(r) \tag{23}$$

The Schrodinger equation can be solved in 2 regions (inside and outside of the well region).
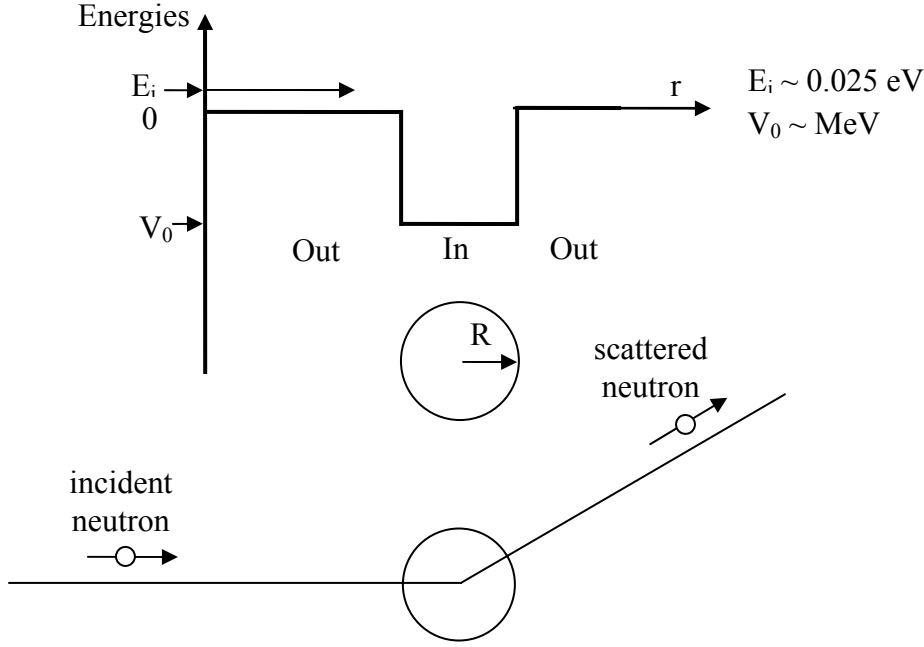
Figure 2: Neutron scattering from the quantum well of a nucleus.

Outside of the well region (i.e., for $r > R$) where $V(r) = 0$, the solution has the form:

$$\psi_s{}^{Out}(r) = \frac{\sin(k_i r)}{k_i r} - b \frac{\exp(ik_s r)}{r} \quad \text{(s-wave scattering)} \qquad (24)$$

Here b is the scattering length and for elastic scattering $k_s = k_i = \sqrt{2mE_i}/\hbar$. Note that in this case, the scattering amplitude is simply $f(\theta) = -b$.

Inside of the well ($r < R$) where $V(r) = -V_0$ the solution is of the form:

$$\psi_s{}^{In}(r) = A \frac{\sin(qR)}{qr} \quad \text{with } q = \sqrt{2m(E_i + V_0)}/\hbar. \qquad (25)$$

The continuity boundary conditions are applied at the surface ($r = R$):

$$\psi_s{}^{In}(r{=}R) = \psi_s{}^{Out}(r{=}R) \qquad (26)$$

$$\frac{d}{dr}[r\psi_s{}^{In}](r = R) = \frac{d}{dr}[r\psi_s{}^{Out}](r = R).$$

Here $k_s r = k_s r = \sqrt{2mE_i}\, r/\hbar \ll 1$ and therefore $\psi_s{}^{Out} \sim 1 - b/r$. Finally:

$$A \frac{\sin(qr)}{q} = R - b \qquad (27)$$
$$A \cos(qR) = 1.$$

In another form:

$$A = \frac{1}{\cos(qR)} \qquad (28)$$
$$\frac{b}{R} = 1 - \frac{\tan(qR)}{qR}.$$

The solution of this transcendental equation:

$$\frac{b}{R} = 1 - \frac{\tan(qR)}{qR} \qquad (29)$$

gives a first order estimate of the scattering length b as a function of the radius of the spherical nucleus R and the depth of the potential well V_0.
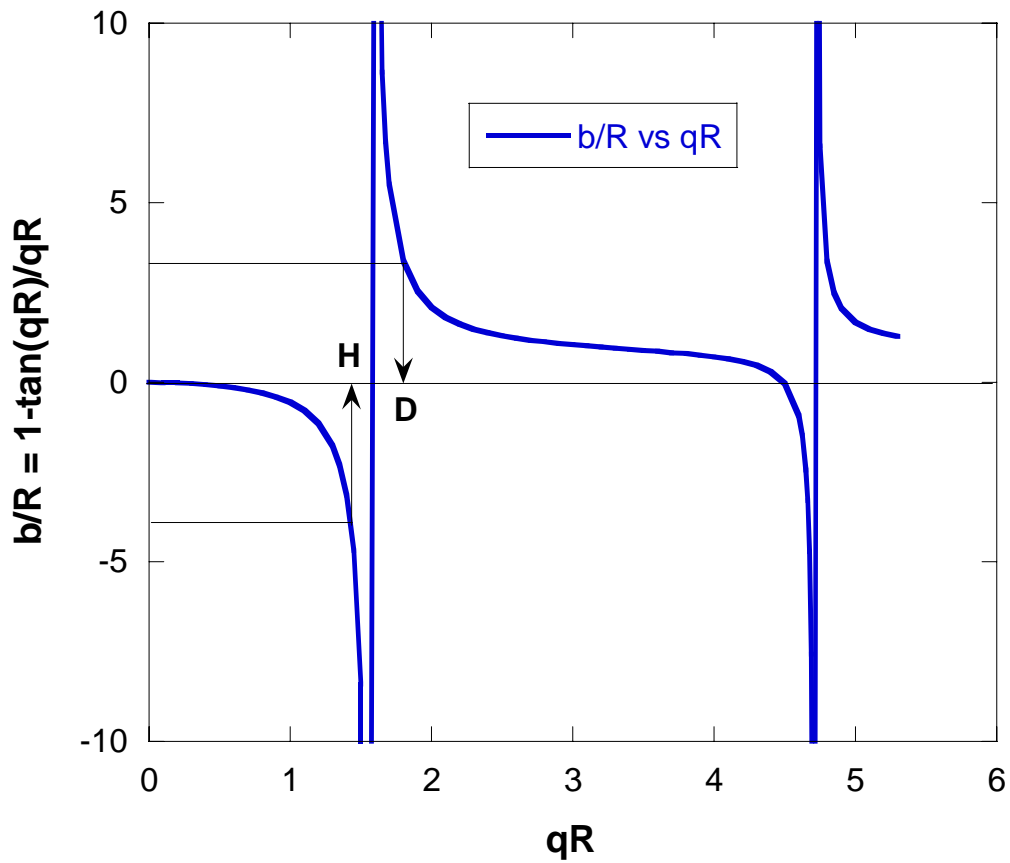
Figure 3: Solution of the Schrodinger equation subject to the boundary conditions.

Due to the steep variation of the solution to the above transcendental equation, adding only one nucleon (for example, going from H to D) gives a very large (seemingly random) variation in b. The scattering length can be negative like for H-1, Li-7, Ti-48, Ni-62, etc. The H and D nuclei have been added to the figure knowing their scattering lengths ($b_H = -0.374$ fm and $b_D = 6.671$ fm) and assuming $R_H = 1$ fm and $R_D = 2$ fm. The Fermi (1 fm = 10^{-13} cm) is a convenient unit for scattering lengths. The neutron-nucleus interaction potential can be estimated for the case of H as $V_0 = 30$ MeV. These are huge energies compared to the thermal neutron kinetic energy of 25 meV.

The scattering length itself can be complex if absorption is non negligible: $b = b_R - ib_I$. Neutron absorption is small for most organic materials. It has been neglected completely in the simple model discussed above.

Since no nucleus is completely free, bound scattering lengths should be used instead: $b_{bound} = b_{free} (A + 1)/A$, where A is the atomic number. Free and bound scattering lengths are substantially different only for low mass elements such as hydrogen.

5. MEASUREMENTS OF NEUTRON SCATTERING LENGTHS

Note that the index of refraction n is related to the material atomic density ρ (atoms/cm^3), the neutron scattering length b, and the neutron wavelength λ as:

$$n = 1 - \frac{\rho b}{2\pi} \lambda^2 . \qquad (30)$$

The scattering length b can be measured by measuring the index of refraction n using optical methods. Note that most materials have a negative index of refraction for neutrons and a positive index of refraction for light.

Neutron interferometry methods are another way of measuring scattering lengths.

REFERENCES

G.L. Squires, "Introduction to the Theory of Thermal Neutron Scattering" Dover Publications (1978).

QUESTIONS

1. What is the neutron scattering length of an element?
2. What is the scattering cross section of an element? How does it relate to the scattering length?
3. What is the differential scattering cross section?
4. What is the strength of typical neutron-nucleus interaction potentials? What is a typical neutron kinetic energy?

5. Write down the Schrodinger equation.
6. What is the first Born approximation? What type of neutron scattering is not well modeled by the first Born approximation?
7. What is a simple description of the solution of the Schrodinger equation in terms of waves?

ANSWERS

1. The neutron scattering length of an element represents the apparent "size" of this element during scattering.
2. The scattering cross section of an element is the apparent area that it offers during scattering. The scattering cross section σ is related to the scattering length b as $\sigma = 4\pi b^2$.
3. The differential scattering cross section is the cross section per unit solid angle $d\sigma/d\Omega$.
4. Typical neutron-nucleus interaction potentials are of order MeV. Typical neutron kinetic energies are of order meV (thermal neutron energy is 25 meV).

5. The Schrodinger equation is $[\frac{-\hbar^2}{2m} \nabla^2 + V(r)] \psi(r) = E \psi(r)$ where the first term is the kinetic energy, the second term is the potential energy, V(r) is the neutron-nucleus interaction potential, E is the so-called system energy and $\psi(r)$ is the so-called eigenfunction. This equation can also be written as $H\psi = E\psi$ where H is the system Hamiltonian.
6. The first Born approximation corresponds to keeping only the first term in the expansion solution of the Schrodinger equation. The first Born approximation does not model reflectivity well.
7. The solution of the Schrodinger equation corresponds to an incident plane wave and a scattered spherical wave.

Chapter 8 - ELASTIC AND QUASIELASTIC/
INELASTIC NEUTRON SCATTERING

Structures are investigated using elastic scattering instruments whereas dynamics are probed using quasielastic/inelastic scattering instruments.

1. DEFINITIONS

Defining the momentum and energy for the incident neutron as ($\vec{k}_i$, E_i) and for the scattered neutron as ($\vec{k}_s$, E_s), the momentum transfer (scattering vector) is $\vec{Q} = \vec{k}_s - \vec{k}_i$ and the energy transfer is $E = E_s - E_i$ during the scattering event. Elastic scattering occurs when there is no energy transfer $E = 0$ (zero peak position and peak width). Inelastic scattering occurs when there is a transfer of both momentum and energy. Qasielastic scattering is a form of inelastic scattering where the energy transfer peak is located around $E = 0$ (zero peak position but with a finite peak width). In practice, the peak width is always limited by the instrumental energy resolution function.
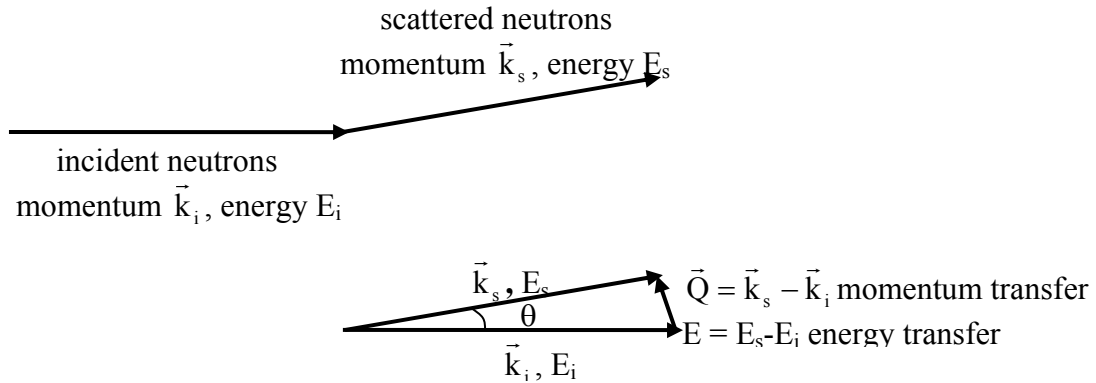
Figure 1: Schematic representation of the momentum and energy initial state ($\vec{k}_i$, E_i) and final state ($\vec{k}_s$, E_s).

2. SCATTERING SIZES AND ENERGY RANGES

The various elastic and quasielastic/inelastic neutron scattering instruments have specific window ranges in the (Q,E) space.
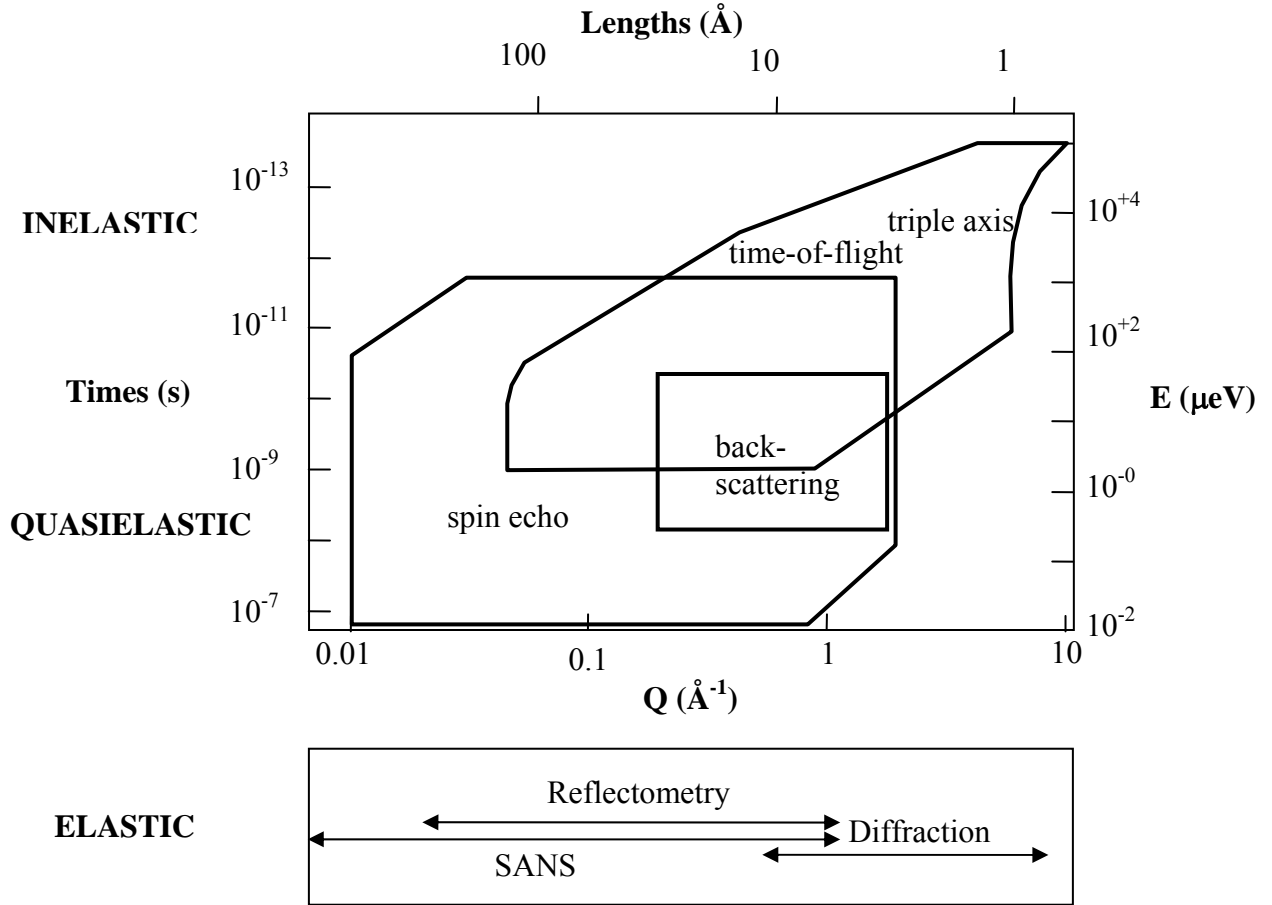
Figure 2: Schematic representation of the various elastic and quasielastic/inelastic neutron scattering instrument windows in (Q,E) space.

3. DIFFRACTION AND REFRACTION

Most neutron scattering methods operate in the "diffraction limit". They involve single scattering and avoid multiple scattering events. Neutron reflectometry on the other hand operates in the "refraction limit". It involves a large number of incremental scattering events that tend to steer the incident neutron beam until it is completely reflected. Describing reflection therefore involves a completely different theoretical basis than all other (single) scattering methods. The focus here will be on these methods that do not involve reflection. Within the first order perturbation theory, the so-called "master formula of neutron scattering" is derived next.

4. THE MASTER FORMULA OF NEUTRON SCATTERING

The single-scattering theory is based on the first Born approximation (the so-called Fermi Golden rule) describing s-wave scattering (Schiff, 1955; Bee, 1990). This corresponds to most forms of neutron scattering except for neutron reflectometry which requires higher

order terms in the Born expansion. Defining an initial state for the neutron-nucleus system as $|i> = |\vec{k}_i n_i>$ where $\vec{k}_i$ is the incident neutron momentum and n_i is the initial nuclear state and a scattered state as $|s> = |\vec{k}_s n_s>$, the double differential neutron scattering cross section can expressed as:

$$\frac{d^2\sigma}{dEd\Omega} = \frac{k_s}{k_i} |< s| \left(\frac{m}{2\pi\hbar^2}\right) V |i>|^2 \, \delta(E - E_s + E_i) \qquad (1)$$

$$= \left(\frac{m}{2\pi\hbar^2}\right)^2 \frac{k_s}{k_i} \sum_{n_i,n_s} P_{n_i} |< \vec{k}_s n_s | V(r) | \vec{k}_i n_i >|^2 \delta(E - E_s + E_i).$$

Here m is the neutron mass, and P_{n_i} is the probability of finding a scattering nucleus in initial state $|n_i>$. E_{n_i} and E_{n_s} are the energy states of the nucleus before and after scattering and $V(r)$ is the interaction potential. Averaging over initial states and summing up over final states has also been performed.

Since neutron-nucleus interactions are short ranged, the following Fermi pseudo-potential is used.

$$V(r) = -\left(\frac{2\pi\hbar^2}{m}\right) \sum_{j}^{N} b_j \delta(r - r_j). \qquad (2)$$

Here b_j is the scattering length for nucleus j and N is the number of scattering nuclei in the sample. The following closure relation is introduced:

$$\int | \vec{r} > d\vec{r} < \vec{r} | = 1. \qquad (3)$$

The <bra|ket> notation is used as follows:

$$< \vec{r} | \vec{k}_i > = \exp(i\vec{k}_i.\vec{r}) \qquad (4)$$
$$< \vec{k}_s | \vec{r} > = \exp(-i\vec{k}_s.\vec{r})$$

The transition matrix element is calculated as:

$$< \vec{k}_s | \left(\frac{m}{2\pi\hbar^2}\right) V | \vec{k}_i > = \sum_{j} b_j < \vec{k}_s | \vec{r} > \int \delta(\vec{r} - \vec{r}_j) d\vec{r} < \vec{r} | \vec{k}_i > \qquad (5)$$
$$= \sum_{j} b_j \exp(i\vec{Q}.\vec{r}_j)$$

Here $\vec{Q} = \vec{k}_s - \vec{k}_i$ and a property of the Dirac Delta function have been used. Moreover a special representation of the Delta function is used to express the following term as:

$$\delta(E - E_s + E_i) = \frac{2\pi}{\hbar} \int\limits_{-\infty}^{+\infty} dt \, \exp\left(\frac{-i(E - E_s + E_i)t}{\hbar}\right). \qquad (6)$$

Finally the Heisenberg operator helps represent time dependence as follows:

$$\vec{r}_j(t) = \exp\left(\frac{-iHt}{\hbar}\right)\vec{r}_j(0)\exp\left(\frac{iHt}{\hbar}\right). \qquad (7)$$

Here H is the scattering system Hamiltonian.

$$H\,|n_i> = E_i\,|n_i>, \; H\,|n_s> = E_s\,|n_s>. \qquad (8)$$

Putting all terms together, the cross section is expressed as follows:

$$\frac{d^2\sigma}{dEd\Omega} = \frac{k_s}{k_i}\sum_{n_i,n_s}P_{n_i}\int\limits_{-\infty}^{+\infty} dt \, \exp\left(\frac{iE}{\hbar}\right) < n_s \mid \sum_{j,l} b_j b_l \, \exp\left(i\vec{Q}.\vec{r}_j(0)\right)\exp\left(-i\vec{Q}.\vec{r}_l(t)\right)\mid n_i >$$

$$= \frac{k_s}{k_i}S(Q,E). \qquad (9)$$

This is the most general neutron scattering cross section within the first order perturbation theory. The dynamic structure factor S(Q,E) has been defined in terms of the scattering density n(Q,t) as follows:

$$n(Q,t) = \sum_{j=1}^{N} b_i \, \exp\left(i\vec{Q}.\vec{r}_j(t)\right) \qquad (10)$$

$$S(Q,E) = \frac{2\pi}{\hbar} \int\limits_{-\infty}^{+\infty} dt \, \exp\left(\frac{iE}{\hbar}\right) < n(-Q,0)n(Q,t) >. \qquad (11)$$

The averaging notation $\sum\limits_{n_i,n_s} P_{n_i} < n_s \mid ... \mid n_i >$ has also been simplified to $<...>$. The summations are over scattering nuclei. Note that at this level the scattering lengths are still included in n(Q,t) and in S(Q,E).

Note that the differential cross section $\dfrac{d\sigma(Q)}{d\Omega}$ used in elastic scattering is related to the double differential cross section $\dfrac{d^2\sigma(Q,E)}{dEd\Omega}$ used in quasielastic/inelastic scattering through an integral over energy transfers.

$$\frac{d\sigma(Q)}{d\Omega} = \int dE \, \frac{d^2\sigma(Q,E)}{dEd\Omega}. \qquad (12)$$

There are many definitions for S(Q,E) in the literature.

5. THE VARIOUS STRUCTURE FACTORS

Many textbooks discuss the various structure factors (Bacon, 1962; Marshall-Lovesey, 1971). The Fourier transform of S(Q,E) is in the time domain.

$$S(Q,t) = \int_{-\infty}^{+\infty} dE \exp\left(\frac{-iEt}{\hbar}\right) S(Q,E) \tag{13}$$

S(Q,t) is the time-dependent density-density correlation function also called time-dependent structure factor.

S(Q,E) is measured by most quasielastic/inelastic neutron scattering spectrometers such as the triple axis, the backscattering and the time-of-flight instruments. S(Q,t) is measured by the neutron spin echo instrument.

The initial value S(Q,t = 0) is the so-called static scattering factor S(Q). S(Q) is what diffractometers and SANS instruments measure. Note that S(Q) is also expressed as:

$$S(Q) = S(Q,t = 0) = \int S(Q,E)dE . \tag{14}$$

Elastic scattering does not really mean with energy transfers E = 0 (zero peak and zero width); it rather means integrated over all energy transfers (summing up over all energy modes).

S(Q) is the density-density correlation function.

$$S(Q) = < n(-Q)n(Q) > \tag{15}$$

It is related to the pair correlation function $g(\vec{r})$ through the space Fourier transform:

$$S(Q) = 1 + \overline{N} \int d\vec{r} \exp(i\vec{Q}.\vec{r})[g(\vec{r}) - 1]. \tag{16}$$

Here $\overline{N} = N/V$ is the particle number density. Note that some authors define S(Q) differently. Note also that the scattering lengths will be averaged for each scattering unit to form the contrast factor which will be multiplying S(Q).

REFERENCES

M. Bee, "Quasielastic Neutron Scattering", Adam Hilger (1990).

L.I. Schiff, "Quantum Mechanics", McGraw Hill (1955).

G.E. Bacon, "Neutron Diffraction", Oxford, Clarendon Press (1962).

W. Marshall and S.W. Lovesey, "Theory of Thermal Neutron Scattering", Clarendon Press, Oxford (1971).

QUESTIONS

1. What is the difference between quasielastic and inelastic scattering?

2. Define the terms in the following expression: $Q = \sqrt{k_i^2 + k_s^2 - 2k_i k_s \cos(\theta)}$.

3. What is "s-wave scattering"? What does it correspond to?
4. Can reflectometry data be described by the first Born approximation?
5. What is the Fermi pseudo-potential?
6. What is the differential cross section? How about the double differential cross section?
7. Write down the double differential cross section (the Master formula) for neutron scattering.

ANSWERS

1. Quasielastic scattering is characterized by energy transfer peaks centered at zero energy (with finite widths). Inelastic scattering is characterized by energy transfer peaks centered at finite energy (μev to meV).

2. k_i and k_s are the incident and scattered neutron momentums and θ is the scattering angle.

3. s-wave scattering corresponds to a zero angular orbital momentum ($l = 0$). It corresponds to single (not multiple) scattering.

4. Reflectometry involves refraction (not single diffraction). It cannot be described by first Born approximation. Higher order terms of the perturbation theory would have to be accounted for.

5. The Fermi pseudo-potential describes the short range neutron-nucleus interactions. It is formed of a series of Dirac Delta functions.

6. The differential cross section is $d\sigma/d\Omega$. The double differential cross section is $d^2\sigma/d\Omega dE$.

7. The double differential cross section is written as: $\dfrac{d^2\sigma}{dEd\Omega} = \dfrac{k_s}{k_i} S(Q,E)$. Here k_s and k_i are the scattering and incident neutron momentums and $S(Q,E)$ is the dynamic structure factor.

Chapter 9 - **COHERENT AND INCOHERENT NEUTRON SCATTERING**

Neutron scattering is characterized by coherent and incoherent contributions to scattering. Coherent scattering depends on Q and is therefore the part that contains information about scattering structures, whereas SANS incoherent scattering is featureless (Q independent) and contains information about the scattering materials density only. Here only elastic scattering is considered.

1. COHERENT AND INCOHERENT CROSS SECTIONS

The coherent and incoherent parts of the elastic scattering cross section are separated. Consider a set of N nuclei with scattering lengths b_i in the sample. The scattering cross section is given by:

$$\frac{d\sigma(\theta)}{d\Omega} = |f(\theta)|^2 = \left(\frac{m}{2\pi\hbar^2}\right)^2 |<\int d\vec{r}\exp(-i\vec{Q}.\vec{r})V(r)>|^2 . \qquad (1)$$

Here $f(\theta)$ is the scattering amplitude, $\vec{Q} = \vec{k}_s - \vec{k}_i$ is the scattering vector and V(r) is the Fermi pseudopotential describing neutron-nucleus interactions:

$$V(r) = -\left(\frac{2\pi\hbar^2}{m}\right)\sum_{i=1}^{N}b_i\delta(\vec{r} - \vec{r}_i) . \qquad (2)$$

Here $\vec{r}_i$ is the position and b_i the scattering length of nucleus i. Therefore, the differential scattering cross section is the sum of the various scattering phases from all of the nuclei in the sample properly weighed by their scattering lengths:

$$\frac{d\sigma(\theta)}{d\Omega} = \sum_{i=1}^{N}\sum_{j=1}^{N}b_ib_j < \exp\left(i\vec{Q}.(\vec{r}_i - \vec{r}_j)\right)> \qquad (3)$$

where <...> represents an "ensemble" average (i.e., average over scatterers' positions and orientations).

Consider an average over a "molecule" consisting of a number m of nuclei:

$$\{...\} = \frac{1}{m}\sum_{i=1}^{m}... \qquad (4)$$

This average could be over one monomeric unit for macromolecular systems or over all atoms in one molecule for a single component molecular system.

Define average and fluctuating parts for the scattering lengths $b_i = \{b\} + \delta b_i$ and positions $\vec{r}_i = \vec{R}_\alpha + \vec{S}_{\alpha i}$ as well as the following:

$\vec{R}_{\alpha i}$: position of the center-of-mass of molecule α

$\vec{S}_{\alpha i}$: relative position of scatterer i inside molecule α

m: number of nuclei per molecule

M: number of molecules in the sample (Note that N = mM).
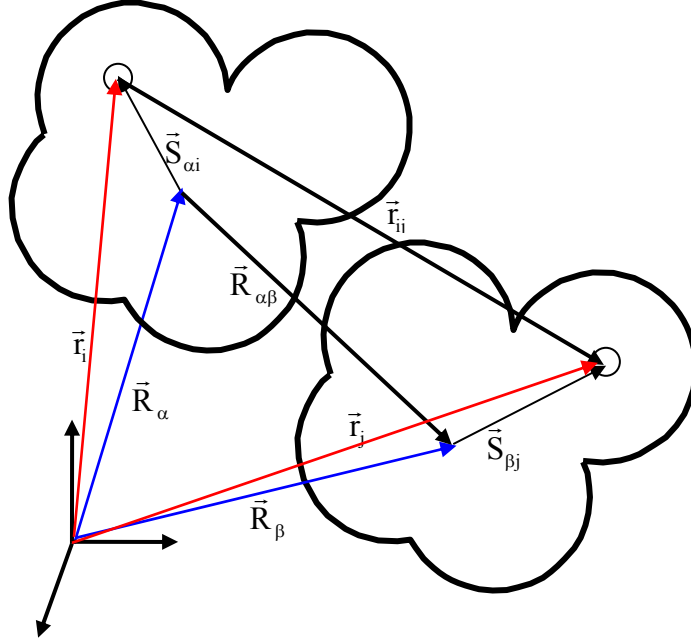
Figure 1: Parametrization for two scattering molecules.

The various terms of the scattering cross section can be separated as:

$$\frac{d\sigma(\theta)}{d\Omega} = \sum_{i,j}^{N} \left[\{b\} + \delta b_i\right]\left[\{b\} + \delta b_j\right] < \exp\!\left(i\vec{Q}.(\vec{r}_i - \vec{r}_j)\right) > \qquad (5)$$

$$\frac{d\sigma(\theta)}{d\Omega} = \{b\}^2 \sum_{i,j}^{N} < \exp\!\left(i\vec{Q}.\vec{r}_{ij}\right) > + \sum_{i,j}^{N} \delta b_i \delta b_j < \exp\!\left(i\vec{Q}.\vec{r}_{ij}\right) > + 2\{b\}\sum_{i,j}^{N} \delta b_i < \exp\!\left(i\vec{Q}.\vec{r}_{ij}\right) >$$

where $\vec{r}_{ij} = \vec{r}_i - \vec{r}_j$. If $\vec{r}_{ij}$ is approximated by $\vec{R}_{\alpha\beta}$ which is equivalent to $S_{\alpha i} << R_\alpha$ (all nuclei of one molecule are located very close to each other) the term:

$$\sum_{i}^{N} \delta b_i < \exp\!\left(i\vec{Q}.\vec{r}_{ij}\right) > \cong \left(\sum_{i}^{N} \delta b_i\right) < \exp\!\left(i\vec{Q}.\vec{R}_{\alpha\beta}\right) = 0 \qquad (6)$$

can be neglected. This is due to the definition of the center-of-mass $\{\delta b_i\} = \sum\limits_i^N \delta b_i = 0$.

The term $\sum\limits_{i,j}^N \delta b_i \delta b_j < \exp(i\vec{Q}.\vec{r}_{ij}) >$ contributes only when i=j. When $i \neq j$,

$$\sum\limits_{i,j}^N \delta b_i \delta b_j < \exp(i\vec{Q}.\vec{r}_{ij}) > \cong \left(\sum\limits_i^N \delta b_i\right)\left(\sum\limits_j^N \delta b_j\right) < \exp(i\vec{Q}.\vec{R}_{\alpha\beta}) >= 0$$

Therefore the scattering cross section can be written simply as the sum of two contributions:

$$\frac{d\sigma(\theta)}{d\Omega} = \{b\}^2 \sum\limits_{i,j}^N < \exp(i\vec{Q}.\vec{r}_{ij}) > + \sum\limits_{i,j}^N \delta b_i^{\ 2} \qquad\qquad (7)$$

$$= \left[\frac{d\sigma(\theta)}{d\Omega}\right]_{coh} + \left[\frac{d\sigma(\theta)}{d\Omega}\right]_{inc}.$$

The last term is the incoherent cross section for the whole sample:

$$\left[\frac{d\sigma(\theta)}{d\Omega}\right]_{inc} = \{\delta b^2\} = \{b^2\} - \{b\}^2. \qquad\qquad (8)$$

Note that these are cross sections per atom. Cross sections can also be defined per molecule instead as $m\dfrac{d\sigma(\theta)}{d\Omega}$ where m is the number of atoms per molecule.

Incoherent scattering has two contributions: one from spin incoherence and the other from isotopic and composition incoherence (also called disorder incoherence). These will be described in turn in the next sections.

2. SPIN INCOHERENCE

Nuclei with nonzero spin contribute to spin incoherence since neutron and nuclear spins could be either parallel or antiparallel during the scattering process. The neutron is a Fermion with spin 1/2 which couples to the nuclear spin I to give:

-- 2I + 2 states (for which the scattering length is noted b_+) corresponding to parallel neutron and nuclear spins, or
-- 2I states (for which the scattering length is noted b_-) corresponding to antiparallel neutron and nuclear spins.

There are 2(2I + 1) total states with the following weighing factors:

$$W_+ = \frac{(2I+2)}{2(2I+1)} = \frac{I+1}{2I+1} \text{ and } W_- = \frac{2I}{2(2I+1)} = \frac{I}{2I+1}. \qquad (9)$$

Note that $W_+ + W_- = 1$. In the case of the hydrogen nucleus ($I = 1/2$), W_+ corresponds to a triplet state and W_- corresponds to a singlet state.

	spin operators	eigenvalues	number of degenerate states

$I + 1/2$ → $I + 1/2$ $2(I+1/2)+1=2I+2$

$I - 1/2$ $2(I-1/2)+1=2I$
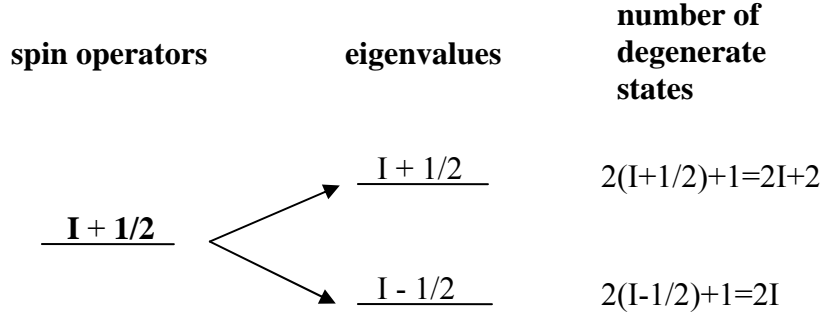
Figure 2: Representation of the neutron spin $\frac{1}{2}$ with its up and down values and the nuclear spin $\vec{I}$.

The averages over spin states are calculated for coherent and spin-incoherent scatterings as:

$$\{b\} = W_+ b_+ + W_- b_- = \frac{(I+1)b_+ + Ib_-}{2I+1} \qquad (10)$$

$$\{b^2\} = W_+ b_+^2 + W_- b_-^2 = \frac{(I+1)b_+^2 + Ib_-^2}{2I+1}.$$

Either the two scattering lengths b_+ and b_- or the other two scattering lengths b_c and b_i could be tabulated for each (isotope) element. It is the b_c and b_i scattering lengths that are tabulated most often. Tables are based on measurements made using thermal neutrons.

$$b_c = \{b\} = W_+ b_+ + W_- b_- \qquad (11)$$

$$b_i = \sqrt{\{b^2\} - \{b\}^2} = \sqrt{W_+ W_-}(b_+ - b_-).$$

For the scattering from hydrogen (pure H-1) nuclei:

$b_c = -3.7406$ fm, $b_i = 25.274$ fm, $\sigma_c = 1.7583$ barn, $\sigma_i = 80.27$ barn.

The corresponding microscopic cross sections are obtained as $\sigma_c = 4\pi b_c^2$ and $\sigma_i = 4\pi b_i^2$.

The b_+ and b_- scattering lengths can be calculated from b_c and b_i as follows:

$$b_+ = b_c + \sqrt{\frac{W_-}{W_+}}b_i = b_c + \sqrt{\frac{I}{I+1}}b_i \qquad (12)$$

$$b_- = b_c - \sqrt{\frac{W_+}{W_-}}b_i = b_c - \sqrt{\frac{I+1}{I}}b_i.$$

For hydrogen (I=1/2), b_+ = 10.851 fm and b_- = -47.517 fm. A spin-dependent scattering length is expressed in terms of the neutron and nuclear spin operators $\vec{s}$ and $\vec{I}$ as:

$$b_c + \frac{2\vec{s}.\vec{I}}{\sqrt{I(I+1)}}b_i. \qquad (13)$$

In order to separate out the coherent and incoherent components, three options present themselves. (1) Use of polarized neutrons along with polarization analysis. Polarization analysis is not easy to achieve due to the large divergence angle of the SANS scattered beam. (2) Aligning the nuclear spins along with using polarized neutrons. Aligning nuclear spins is extremely difficult and has not matured to be a viable alternative. Note that the field of magnetism involves aligning electron (not nuclear) spins. (3) Using deuterium labeling. Deuterium labeling is used routinely to minimize the incoherent signal from hydrogen atoms (deuterium has a low incoherent component).

3. COHERENT SCATTERING CROSS SECTION

The coherent scattering cross section is given by the integral of the differential cross section over solid angle:

$$\sigma_c = \int \frac{d\sigma_c}{d\Omega} d\Omega.$$

Consider the case of a generic molecule $A_m B_n$ made out of m atoms of element A and n atoms of element B. Define the number fractions $f_A = m/(m+n)$ and $f_B = n/(m+n)$ obeying $f_A + f_B = 1$. The coherent scattering cross section per atom for molecule $A_m B_n$ is given by:

$$\sigma_c(A_m B_n) = 4\pi < b >^2 = 4\pi(f_A b_A + f_B b_B)^2. \qquad (14)$$

Consider the case of water (H_2O) with b_H = -3.739 fm, b_O = 5.803 fm, f_H = 2/3 and f_O = 1/3 yielding $\sigma_c(H_2O) = 4\pi(-2*3.739/3 + 5.803/3)^2$ fm^2 = 0.039 barn. Note that b_H = -3.739 fm for hydrogen with natural abundance of H-1, H-2 (D), and H-3 (T), whereas b_H = -3.7406 fm for pure H-1. Recall that 1 barn = 10^{-24} cm^2 and 1 fm = 10^{-13} cm. This is the cross section per atom. The cross section per H_2O molecule is 3*0.039 = 0.117 barn.

Similarly for heavy water (D_2O) with b_D = 6.671 fm, one obtains $\sigma_c(D_2O)$ = 5.12 barn. The cross section per D_2O molecule is 3*5.12 = 15.35 barn.

4. INCOHERENT SCATTERING CROSS SECTION

Every element in the periodic table has a spin incoherence scattering cross section except if the nuclear spin is zero. Mixing isotopes and/or different elements contributes composition incoherence as well. Consider the $A_m B_n$ molecule again.

The spin incoherence cross section per atom for the $A_m B_n$ mixture is given by:

$$[\sigma_i(A_m B_n)]_{spin} = f_A \sigma_i(A) + f_B \sigma_i(B). \qquad (15)$$

The composition incoherence cross section per atom involves the following difference:

$$[\sigma_i(A_m B_n)]_{comp} = 4\pi(<b^2> - <b>^2). \qquad (16)$$

The two averages are $<b> = f_A b_A + f_B b_B$ and $<b^2> = f_A b_A^2 + f_B b_B^2$. Therefore:

$$[\sigma_i(A_m B_n)]_{comp} = 4\pi[f_A b_A^2 + f_B b_B^2 - (f_A b_A + f_B b_B)^2] \qquad (17)$$
$$= 4\pi[f_A f_B (b_A - b_B)^2].$$

Putting both contributions together, the incoherent cross section per atom is obtained as:

$$\sigma_i(A_m B_n) = f_A \sigma_i(A) + f_B \sigma_i(B) + 4\pi f_A f_B (b_A - b_B)^2. \qquad (18)$$

Note that the incoherent cross section per molecule is obtained by multiplying by the number of atoms per molecule (m+n).

Consider the case of water (H_2O):

$$\sigma_i(H_2O) = f_H \sigma_i(H) + f_O \sigma_i(O) + 4\pi f_H f_O (b_H - b_O)^2. \qquad (19)$$

Using $\sigma_i(H) = 80.27$ barn, $\sigma_i(O) = 0$ barn, $b_H = -3.739$ fm, $b_O = 5.803$ fm, $f_H = 2/3$ and $f_O = 1/3$, the following result is obtained $\sigma_i(H_2O) = 53.5 + 2.54 = 56.04$ barn. This is the cross section per atom. The cross section per H_2O molecule is $3*56.04 = 168.12$ barn.

Similarly for heavy water (D_2O). Using $\sigma_i(D) = 2.05$ barn and $b_D = 6.671$ fm, the following result is obtained $\sigma_i(D_2O) = 1.37 + 0.021 = 1.39$ barn. This is the cross section per atom. The cross section per D_2O molecule is $3*1.39 = 4.17$ barn.

Note that in both cases the spin incoherence cross section (first term in units of barn) dominates over the composition incoherence cross section (second term in units of fm^2).

5. TOTAL SCATTERING CROSS SECTION

The total scattering cross section is the sum of the coherent and incoherent contributions.

$$\sigma_s(A_m B_n) = \sigma_c(A_m B_n) + \sigma_i(A_m B_n) \qquad (20)$$

$$= 4\pi < b^2 > + f_A \sigma_i(A) + f_B \sigma_i(B)$$

$$= 4\pi[f_A b_A^2 + f_B b_B^2] + f_A \sigma_i(A) + f_B \sigma_i(B).$$

The first term $<b^2>$ contains both coherent and composition incoherence contributions and the other two terms contain the spin incoherence contribution.

For the cases of H_2O and D_2O, one obtains $\sigma_s(H_2O) = 56.08$ barn and $\sigma_s(D_2O) = 6.51$ barn respectively. These are the cross sections per atom. The cross sections per molecule are $3*56.08 = 168.24$ barn and $3*6.51 = 19.53$ barn.

6. SCATTERING LENGTH DENSITY

What is needed to calculate neutron contrast factors is the scattering length density (not the scattering length). The scattering length density is defined as the ratio of the scattering length per molecule and the molecular volume. Assuming an $A_m B_n$ molecule, the scattering length density is given by:

$$\left(\frac{b}{v}\right)_{AmBn} = \frac{(f_A b_A + f_B b_B)(m+n)}{v} = \frac{mb_A + nb_B}{v}. \qquad (21)$$

Here $mb_A + nb_B$ is the scattering length per molecule and v is the volume of molecule $A_m B_n$ comprising m atoms A and n atoms B.

The molecular volume v is given in terms of the density d and molar mass m for molecule $A_m B_n$ and Avogradro's number N_{av} ($N_{av} = 6*10^{23}$ /mol) as:

$$v = \frac{m}{N_{av}d}. \qquad (22)$$

For H_2O the density is $d = 1$ g/cm^3, the molar mass is $m = 18$ g/mol so that the molecular volume is $v = 3*10^{-23}$ cm^3 and $(b/v)_{H_2O} = -5.58*10^9$ cm$^{-2} = -5.58*10^{-7}$ Å^{-2}. For D_2O, $d = 1.11$ g/cm^3, $m = 20$ g/mol so that $v = 3*10^{-23}$ cm^3 and $(b/v)_{D_2O} = 6.38*10^{-10}$ cm$^{-2} = 6.38*10^{-6}$ Å^{-2}.

7. CONTRAST FACTORS

The scattering intensity is proportional to the contrast factor. Consider the simple case of scattering inhomogeneities consisting of A molecules in a background of B molecules (think

polymers, proteins or micelles in solution). The scattering length densities are (b_A/v_A) and (b_B/v_B). The contrast factor often referred to as $\Delta\rho^2$ is defined as:

$$\Delta\rho^2 = \left(\rho_A - \rho_B\right)^2 = \left(\frac{b_A}{v_A} - \frac{b_B}{v_B}\right)^2.$$

Scattering length densities can be changed through the deuteration process. Adjusting the relative amount of deuterated to non-deuterated solvent is called a contrast variation series and yields the zero contrast condition whereby the scattering length density of the mixed solvent matches that of the scattering inhomogeneities.

8. MACROSCOPIC SCATTERING CROSS SECTIONS

Keeping the same notation for molecule A_mB_n, the macroscopic scattering cross section Σ is the product of the microscopic cross section per molecule $\sigma(m+n)$ times the number of molecules per unit volume N/V. N is the total number of molecules and V is the total sample volume. For a sample comprising pure A_mB_n substance, $V/N = v$ is the molecular volume. This applies to coherent σ_c, incoherent σ_i or total scattering σ_s cross sections.

$$\Sigma_c = \left(\frac{N}{V}\right)\sigma_c(m+n) \qquad\qquad (23)$$

$$\Sigma_i = \left(\frac{N}{V}\right)\sigma_i(m+n)$$

$$\Sigma_s = \left(\frac{N}{V}\right)\sigma_s(m+n).$$

The number density of molecules is given in terms of the density d and molar mass m for molecule A_mB_n and Avogradro's number N_{av} as:

$$\left(\frac{N}{V}\right) = \frac{N_{av}d}{m}. \qquad\qquad (24)$$

For H_2O, the macroscopic scattering cross sections per molecule are

$$\Sigma_c(H_2O) = \frac{0.117*10^{-24}}{3*10^{-23}} = 3.9*10^{-3} \text{ cm}^{-1}$$

$$\Sigma_i(H_2O) = \frac{168.12*10^{-24}}{3*10^{-23}} = 5.6 \text{ cm}^{-1}$$

$$\Sigma_s(H_2O) = \frac{168.24*10^{-24}}{3*10^{-23}} = 5.6 \text{ cm}^{-1}.$$

For D_2O, the macroscopic scattering cross sections per molecule are

$$\Sigma_c(D_2O) = \frac{15.35*10^{-24}}{3*10^{-23}} = 0.512 \text{ cm}^{-1}$$

$$\Sigma_i(D_2O) = \frac{4.17*10^{-24}}{3*10^{-23}} = 0.139 \text{ cm}^{-1}$$

$$\Sigma_s(D_2O) = \frac{19.53*10^{-24}}{3*10^{-23}} = 0.651 \text{ cm}^{-1}.$$

The results for H_2O and D_2O are summarized next.

9. SUMMARY FOR H_2O AND D_2O

For the case of H_2O

Coherent cross section per atom $\sigma_c(H_2O) = 0.039$ barn.
Coherent cross section per H_2O molecule is $3*\sigma_c(H_2O) = 0.117$ barn.

Incoherent cross section per atom $\sigma_i(H_2O) = 53.51 + 2.54 = 56.04$ barn
Incoherent cross section per molecule is $3*\sigma_i(H_2O) = 168.12$ barn.

Total scattering cross section per atom $\sigma_s(H_2O) = 56.08$ barn
Total scattering cross section per molecule is $3*\sigma_s(H_2O) = 168.24$ barn

Molecular volume $v = 3*10^{-23}$ cm^3
Scattering length density $(b/v)_{H_2O} = -5.58*10^{-7}$ Å^{-2}

Macroscopic coherent cross section $\Sigma_c(H_2O) = 3.9*10^{-3}$ cm^{-1}
Macroscopic incoherent cross section $\Sigma_i(H_2O) = 5.604$ cm^{-1}
Macroscopic total cross section $\Sigma_s(H_2O) = 5.608$ cm^{-1}

Table 1: Scattering lengths and cross sections (per atom) for water. In order to obtain cross sections per molecule, one has to multiply by the number of atoms per molecule (i.e., by 3).

		Mixing Fraction	b Fermi	σ_c Barn	σ_i-spin Barn	σ_i-comp Barn	σ_i Barn	σ_s Barn
Hydrogen	H	2/3	-3.739	------	80.27	------	------	------
Oxygen	O	1/3	5.803	------	0	------	------	------
Water	H_2O	1	-0.558	0.039	53.51	2.54	56.04	56.08

For the case of D_2O

Coherent cross section per atom $\sigma_c(D_2O) = 5.12$ barn.
Coherent cross section per D_2O molecule is $3*\sigma_c(D_2O) = 15.35$ barn.

Incoherent cross section per atom $\sigma_i(D_2O) = 1.37 + 0.021 = 1.39$ barn
Incoherent cross section per molecule is $3*\sigma_i(D_2O) = 4.17$ barn.

Total scattering cross section per atom $\sigma_s(D_2O) = 6.51$ barn
Total scattering cross section per molecule is $3*\sigma_s(D_2O) = 19.53$ barn

Molecular volume $v = 3*10^{-23}$ cm^3
Scattering length density $(b/v)_{D_2O} = 6.38*10^{-6}$ Å^{-2}

Macroscopic coherent cross section $\Sigma_c(D_2O) = 0.512$ cm^{-1}
Macroscopic incoherent cross section $\Sigma_i(D_2O) = 0.139$ cm^{-1}
Macroscopic total cross section $\Sigma_s(D_2O) = 0.651$ cm^{-1}

Table 2: Scattering lengths and cross sections (per atom) for heavy water. In order to obtain cross sections per molecule, one has to multiply by the number of atoms per molecule (i.e., by 3).

		Mixing Fraction	b Fermi	σ_c Barn	σ_i-spin Barn	σ_i-comp Barn	σ_i Barn	σ_s Barn
Deuterium	D	2/3	6.671	------	2.05	------	------	------
Oxygen	O	1/3	5.803	------	0	------	------	------
Heavy Water	D$_2$O	1	6.382	5.118	1.367	0.0210	1.387	6.505

Two quantities are relevant to SANS measurements: the scattering length density that enters in the contrast factor and the macroscopic incoherent scattering cross section which appears as a constant (Q-independent) background. These two quantities are summarized for H$_2$O and D$_2$O.

Table 3: Calculated scattering length densities and macroscopic scattering cross sections (per molecule) for water and heavy water.

		v cm^3	b/v Å^{-2}	Σ_c cm^{-1}	Σ_i cm^{-1}	Σ_s cm^{-1}
Water	H$_2$O	$3*10^{-23}$	$-5.583*10^{-7}$	0.00392	5.608	5.612
Heavy Water	D$_2$O	$3*10^{-23}$	$6.382*10^{-6}$	0.512	0.139	0.651

The measured and calculated total cross section ($\Sigma_T = \Sigma_s + \Sigma_a$) for H$_2$O and D$_2$O are included in a table for thermal neutrons ($\lambda = 1.8$ Å). Note that the absorption cross sections are small. These were obtained from the Evaluated Nuclear Data File (ENDF) online database. This is the so-called "Barn Book".

Table 4: Measured and calculated macroscopic cross sections for H$_2$O and D$_2$O for thermal neutrons

	Σ_T Measured	Σ_T Calculated
H$_2$O	3.7 cm^{-1}	5.612 cm^{-1}

| D$_2$O | 0.49 cm^{-1} | 0.651 cm^{-1} |

The calculated and measured values are different for a number of reasons including the neglect of inelastic scattering effects.

10. GENERAL CASE

Consider the general case of a molecule $A_{n_A}B_{n_B}C_{n_C}$... containing n_A atoms of element A, etc. The total number of atoms per molecule is $n = n_A + n_B + n_C$... and the number fractions are $f_A = n_A/n$, etc.

The scattering length density is given by:

$$\left(\frac{b}{v}\right) = \frac{n_A b_A + n_B b_B + n_C b_C...}{v} \qquad (25)$$

Here v is the molecular volume and b_A, b_B, b_C... are the tabulated scattering lengths.

The macroscopic scattering cross section is given by:

$$\Sigma_i = \left(\frac{N}{V}\right)\left([\sigma_i]_{spin} + [\sigma_i]_{comp}\right) \qquad (26)$$

N is the number of molecules in the sample of volume V. The spin incoherence and composition incoherence microscopic cross sections per molecule are given by:

$$[\sigma_i]_{spin} = n[f_A \sigma_i(A) + f_B \sigma_i(B) + f_C \sigma_i(C)...] \qquad (27)$$

$$[\sigma_i]_{comp} = n[<b^2> - <b>^2] \qquad (28)$$

$$[\sigma_i]_{comp} = n\left[f_A b_A^2 + f_B b_B^2 + f_C b_C^2... - (f_A b_A + f_B b_B + f_C b_C...)^2\right]$$

$$[\sigma_i]_{comp} = n\left[f_A f_B (b_A - b_B)^2 + f_A f_C (b_A - b_C)^2 + f_B f_C (b_B - b_C)^2...\right]$$

The relation $f_A + f_B + f_C... = 1$ has been used. For pure substances, the molecules number density is $(N/V) = 1/v$ where v is the molecular volume given by:

$$v = \frac{m}{N_{av}d} \qquad (29)$$

m and d are the molecular mass and mass density and N_{av} is Avogadro's number.

11. TABULATED SCATTERING LENGTHS AND CROSS SECTIONS

The coherent and incoherent thermal neutron scattering lengths and cross sections are tabulated here for a few elements (Koester, 1991; Sears, 1992). That table also contains the absorption cross section σ_a for thermal neutrons (i.e., with a wavelength of $\lambda = 1.8$ Å or a kinetic energy of 0.025 eV). Neutron absorption is small for most elements except for boron, cadmium and gadolinium (that are used as neutron absorbers). The absorption cross section is related to the imaginary part b_a of the scattering length $b-ib_a$. Only neutron absorbing materials have an imaginary part. The absorption cross section is expressed as

$$\sigma_a = \frac{4\pi\{b_a\}}{k}$$ (30)

k is the incident neutrons wavenumber $k = mv/\hbar$ where $\hbar$ is Planck's constant, m is the neutron mass and v is the incident neutron speed. $\{b_a\}$ is the composition averaged absorption length. The absorption cross section varies like $\sim 1/v$ where v is the neutron speed. The macroscopic absorption cross section is given by $\Sigma_a = (N/V)\sigma_a = \sigma_a/V_{sp}$ where (N/V) is the number density and V_{sp} is the specific volume of the material.

Table 5: Coherent and incoherent thermal neutron scattering lengths (b_c and b_i) and cross sections (σ_c and σ_i) as well as absorption cross section (σ_{abs}) for some nuclei. Note that 1 fermi=10^{-13} cm and 1 barn=10^{-24} cm^2.

Element	b	σ_c	σ_i	σ_s	σ_a
	Fermi	Barn	Barn	Barn	Barn
H	-3.739	1.757	80.30	82.057	0.333
D	6.671	5.592	2.05	7.642	0.000
C	6.646	5.550	0.001	5.551	0.003
N	9.36	11.01	0.50	11.51	1.90
0	5.803	4.232	0.000	4.232	0.000
F	5.654	4.232	0.001	4.233	0.000
Na	3.63	1.66	1.62	3.28	0.530
Si	4.149	2.163	0.004	2.167	0.171
P	5.13	3.307	0.005	3.312	0.172
S	2.847	1.017	0.007	1.024	0.53
Cl	9.577	11.526	5.3	16.826	33.5

The coherent scattering length for a mixture involves the mean and the incoherent scattering length involves the standard deviation. If one considers a fictitious sample comprising a few low-Z elements in equal amounts, then the deviation from the incoherent scattering length would be the deviation from the average of the scattering lengths plotted *vs* Z.
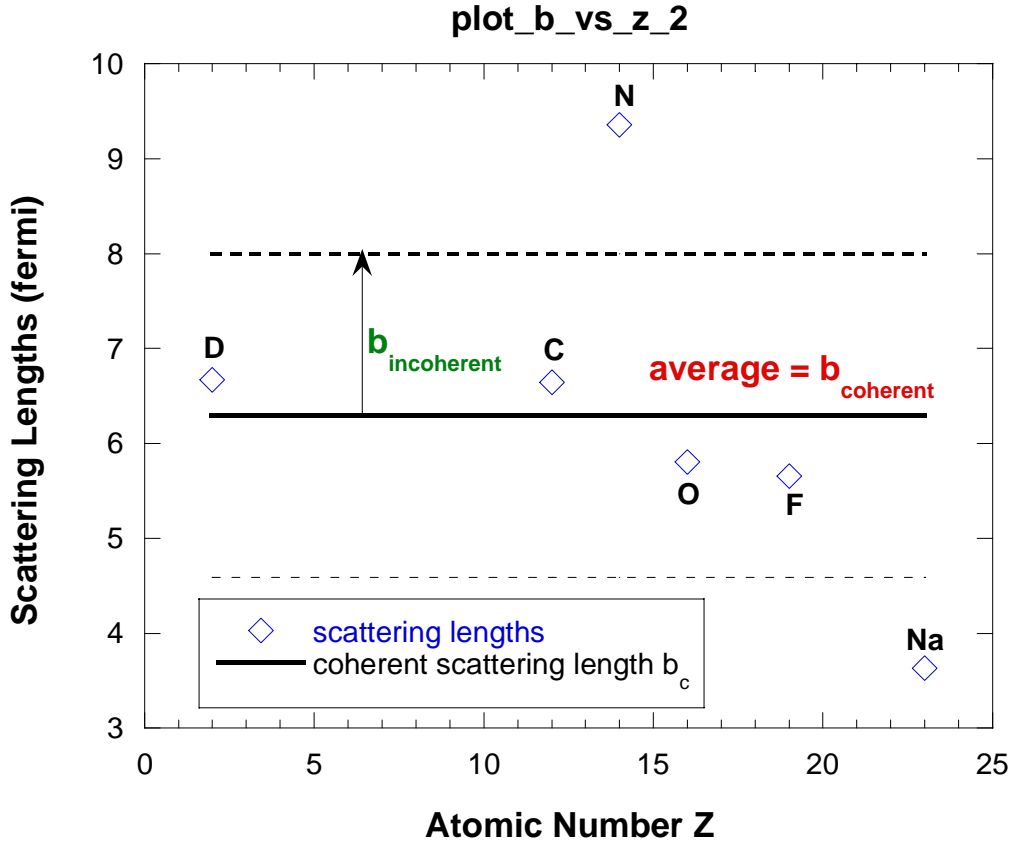
Figure 3: Variation of the scattering length for a few low-Z elements.

12. NEUTRON TRANSMISSION

Neutrons incident on a sample have three choices: they either cross it without interaction, get scattered or get absorbed. Neutron absorption is small for most materials. The neutron transmission of a flat slab sample (appropriate for SANS measurements) of thickness d and total macroscopic cross section:

$$\Sigma_t = \Sigma_s + \Sigma_a = \Sigma_c + \Sigma_i + \Sigma_a \tag{31}$$

is given by:

$$T = \exp(-\Sigma_t d) . \tag{32}$$

Here d is the sample thickness. The transmission is measured as the ratio of the direct beam intensity with and without the sample. Transmission gets lower for longer neutron wavelengths.

13. MEASURED MACROSCOPIC CROSS SECTION FOR WATER

Water scatters mostly incoherently and is characterized by a flat (Q-independent) SANS signal. Water is used as a secondary absolute intensity standard since its macroscopic scattering cross section is well known. The SANS measured cross section corresponds to $\Sigma_T/4\pi$. These were obtained from the Evaluated Nuclear Data File (ENDF) online database.
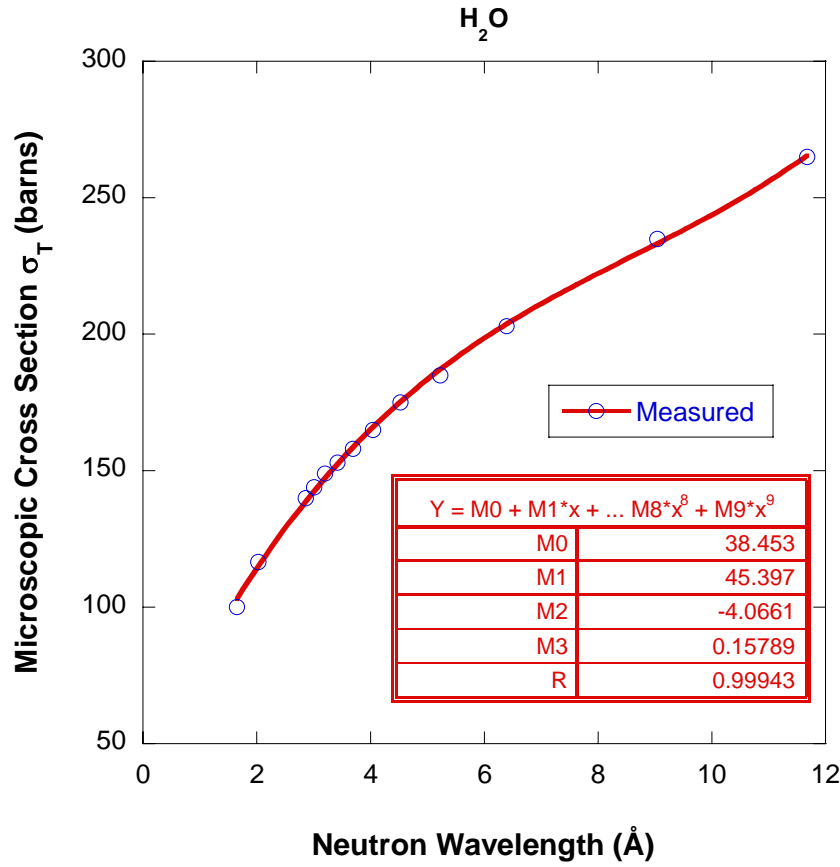
Figure 4: Variation of the microscopic cross section σ_T for H_2O with neutron wavelength.
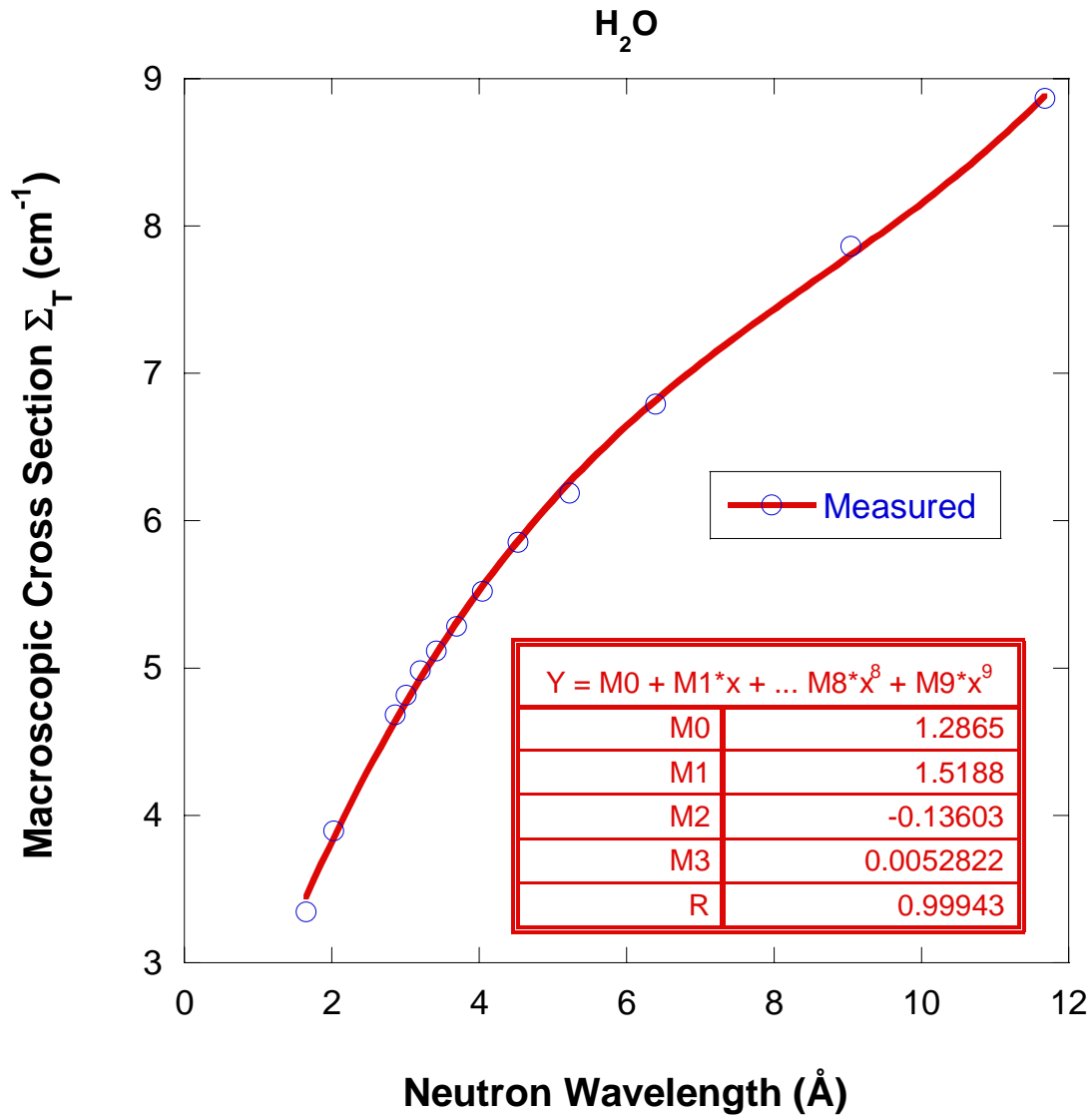
Figure 5: Variation of the macroscopic cross section Σ_T for H_2O. Note that the cross section measured by SANS corresponds to $\Sigma_T/4\pi$.

REFERENCES

L. Koester, H. Rauch, and E. Seymann, "Neutron Scattering Lengths: a Survey of Experimental Data and Methods", Atomic Data and Nuclear Data Tables 49, 65 (1991)

V.F. Sears, Neutron Scattering Lengths and Cross Sections", Neutron News 3, 26-37 (1992).

The Barn Book, Evaluated Nuclear Data File online database is found at the following web address http://www.nndc.bnl.gov/exfor7/endf00.htm.

QUESTIONS

1. Neutrons are scattered by what part of the atom?
2. Are higher fluxes achieved in research reactors (neutron sources) or in synchrotron x-ray sources?
3. Is deuteration always needed for neutron scattering?
4. What is the origin of the name for neutron cross sections (barn)?
5. Work out the relative composition of an H_2O/D_2O mixture that would have zero average coherent cross section (so called semi-transparent mixture).
6. Comparing the coherent scattering cross sections for a deuterated polymer in hydrogenated solvent and a hydrogenated polymer in deuterated solvent, which one has the highest signal-to-noise ratio for dilute solutions?
7. Why does carbon have a negligible incoherent scattering cross section?
8. What is the meaning of a negative scattering length?
9. Work out the scattering contrast for a mixture of your choice (or of your own research interest).
10. Calculate the incoherent microscopic scattering cross section per molecule for H_2O.
11. Define the neutron transmission for a SANS sample. Does it depend on neutron wavelength?

ANSWERS

1. Neutrons are scattered by the nuclei.
2. Synchrotron x-ray sources have much higher fluxes than neutron sources.
3. Deuteration is not always needed for neutron scattering. Many systems are characterized by "natural contrasts". Deuteration is however necessary to enhance the contrast of specific structures.
4. The word barn was first used by Fermi in 1942 when initial measurements came up with estimates for the size of neutron-nuclear cross sections. These estimates were larger than expected (as large as a barn!). 1 barn = 10^{-24} cm^2. 1 fm^2 = 10^{-26} cm^2 was expected.
5. The scattering length density for H_2O (density = 1 g/cm^3) is $-5.6*10^{-7}$ Å^{-2}. The scattering length density for D_2O (density = 1.111 g/cm^3) is $6.39*10^{-6}$ Å^{-2}. The H_2O/D_2O mixture that would give zero scattering length density corresponds to 92 % H_2O and 8 % D_2O.
6. The contrast factor is the same for the two systems: deuterated polymer in hydrogen solvent and hydrogenated polymer in a deuterated solvent (this is the so-called Babinet principle). However, for dilute polymer solutions the level of incoherent scattering background is lower when the solvent is deuterated. The signal to noise (contrast factor/incoherent background level) is higher when deuterated solvent and hydrogenated polymer is used.
7. Carbon has a negligible incoherent scattering cross section because it has zero spin and therefore no spin-incoherence.
8. A negative scattering length (such as in the case of H) means that the phase of the eigenfunction (solution of the Schrodinger equation) is shifted by 180 $^\circ$ during the scattering process.

9. Consider the polymer solution comprising poly(ethylene oxide) or hPEO in d-water or D_2O. The following calculates the scattering lengths b, scattering length densities b/v and then the contrast factor. The specific volume v is needed in each case.

hPEO: C_2H_4O, $b_{hPEO} = 4.139*10^{-13}$ cm, $v_{hPEO} = 38.94$ cm^3/mol

d-water: D_2O, $b_{D2O} = 19.14*10^{-13}$ cm, $v_{D2O} = 18$ cm^3/mol

Contrast Factor: $(b_{hPEO}/V_{hPEO} - b_{D_2O}/v_{D_2O})^2 N_{av} = 5.498*10^{-3}$ mol/cm^4, N_{av} is Avogadro's number.

10. Use the standard expression for the cross section per atom $\sigma_{incoh}(H_2O) = 4\pi f_H f_O(b_H-b_O)^2 + f_H\sigma_{incoh}(H) + f_O\sigma_{incoh}(O)$ where $b_H = -3.739$ fm and $b_O = 5.803$ fm are the coherent scattering lengths for H and O, $\sigma_{incoh}(H) = 80.27$ barn and $\sigma_{incoh}(O) = 0$ barn are the spin-incoherent scattering cross sections and $f_H = 2/3$ and $f_O = 1/3$ are the relative number fractions. Note that 1 fm $= 10^{-13}$ cm and 1 barn $= 10^{-24}$ cm^2. The result for the cross section per atom is $\sigma_{incoh}(H_2O) = 56$ barn. The cross section per molecule is $3\sigma_{incoh}(H_2O) = 168$ barn.

11. The SANS transmission from a flat sample of thickness d and total microscopic scattering cross section Σ_t is given by $T = exp(-\Sigma_T d)$. Transmission decreases with increasing neutron wavelength.

Chapter 10 - **THE SANS TECHNIQUE**

1. RECIPROCAL SPACE

Small-Angle Neutron Scattering (SANS) is a technique of choice for the characterization of structures in the nanoscale size range (Hammouda, 1995). This covers structures from the near Angstrom sizes to the near micrometer sizes. How small are the small angles? They are typically from 0.2 $^{\circ}$ to 20 $^{\circ}$ and cover two orders of magnitude in two steps. A low-Q configuration covers the first order of magnitude (0.2 $^{\circ}$ to 2 $^{\circ}$) and a high-Q configuration covers the second one (2 $^{\circ}$ to 20 $^{\circ}$). The scattering variable is defined as $Q = (4\pi/\lambda) \sin(\theta/2)$ where λ is the neutron wavelength and θ is the scattering angle. Within the small-angle approximation, Q simplifies to $Q = 2\pi\theta/\lambda$. The SANS scattering variable Q range is typically from 0.001 Å^{-1} to 0.45 Å^{-1}. This corresponds to d-spacings from 6,300 Å down to 14 Å.

Scattering measurements are performed in the Fourier (also called reciprocal) space, not real space like microscopy. For this, scattering data have to be either inverted back to real space or fitted to models describing structures in reciprocal space. Scattering methods measure correlation functions. These are not the Fourier transform of the density of inhomogeneities within the sample. They are the density-density correlation functions instead. It should be noted that because of this, the "phase" information is completely lost. It is not possible to reconstruct a complete image of the sample structure by scattering from one sample. Trying to recover phase information is complicated and involves measuring a series of samples with identical structures but different contrasts.

2. COMPARING SANS TO OTHER TECHNIQUES

The advantage of SANS over other small-angle scattering methods (such as small-angle x-ray or light scattering) is the deuteration method. This consists in using deuterium labeled components in the sample in order to enhance their contrast. This is reminiscent of contrast variation in microscopy whereby the level of light incident upon a sample is varied using a diaphragm. SANS can measure either naturally occurring contrasts or artificial contrasts introduced through deuteration. Labeling is difficult to achieve with x-rays (SAXS) since this involves heavy atom labels that change the sample drastically. SANS can measure density fluctuations and composition (or concentration) fluctuations. SAXS can measure only density fluctuation. The deuteration method allows this bonus.

SANS is disadvantaged over SAXS by the intrinsically low flux of neutron sources (nuclear reactors or spallation sources using cold source moderators) compared to the orders of magnitude higher fluxes for x-ray sources (rotating anode or synchrotrons). Neutron scattering in general is sensitive to fluctuations in the density of nuclei in the sample. X-ray scattering is sensitive to inhomogeneities in electron densities whereas light scattering is sensitive to fluctuations in polarizability (refraction index).

Microscopy has the advantage that data are acquired in direct (real) space whereas scattering methods (such as SANS) measure in reciprocal space. Electron microscopy (EM) and SANS

are complementary methods. EM is applied on very thin samples only, it cannot measure samples at different concentrations and temperatures directly, and the observed images are a 2D projection. SANS can do all these things but cannot produce an image in real space.

SANS data analysis is performed at many levels. The initial level consists of "follow the trends" type of approach using standard plot methods. The next level uses nonlinear least squares fits to realistic models. The final trend makes use of sophisticated ab-initio or "shape reconstruction" methods in order to obtain insight into the structure and morphology within the investigated sample. Oftentimes, it takes independent information obtained from other methods of characterization to obtain a thorough understanding of SANS data because "most SANS data look alike". SANS is not known for abundance in scattering peaks (unlike single-crystal diffraction, Nuclear Magnetic Resonance, Infra-Red spectroscopy, etc) but enough features (i.e., "clues") are available. Available models describe scattering from compact shape objects in dilute or concentrated systems as well as "non-particulate" scattering such as in the case of gel-like or porous media. SANS has been used for single-phase as well as multi-phase systems. Phase transitions have been investigated as well as the thermodynamics of demixing.
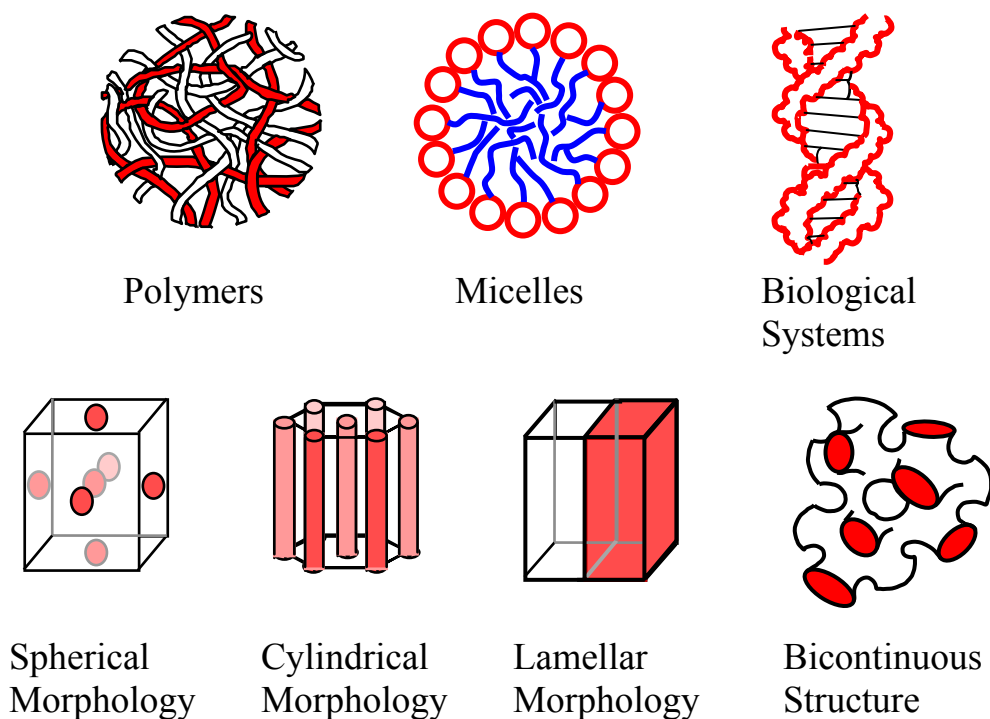
Figure 1: Various classes of samples and morphologies investigated by SANS.

3. THE SANS TECHNIQUE

SANS involves the basic four steps used in all scattering techniques: monochromation, collimation, scattering and detection. Monochromation is performed mostly using a velocity

selector. Collimation is preformed through the use of two apertures (a source aperture and a sample aperture) placed far (meters) apart. Scattering is performed from either liquid or solid samples. Detection is performed using a neutron area detector inside an evacuated scattering vessel. The large collimation and scattering lengths make SANS instruments very large (typically 30 m long) compared to other scattering instruments.
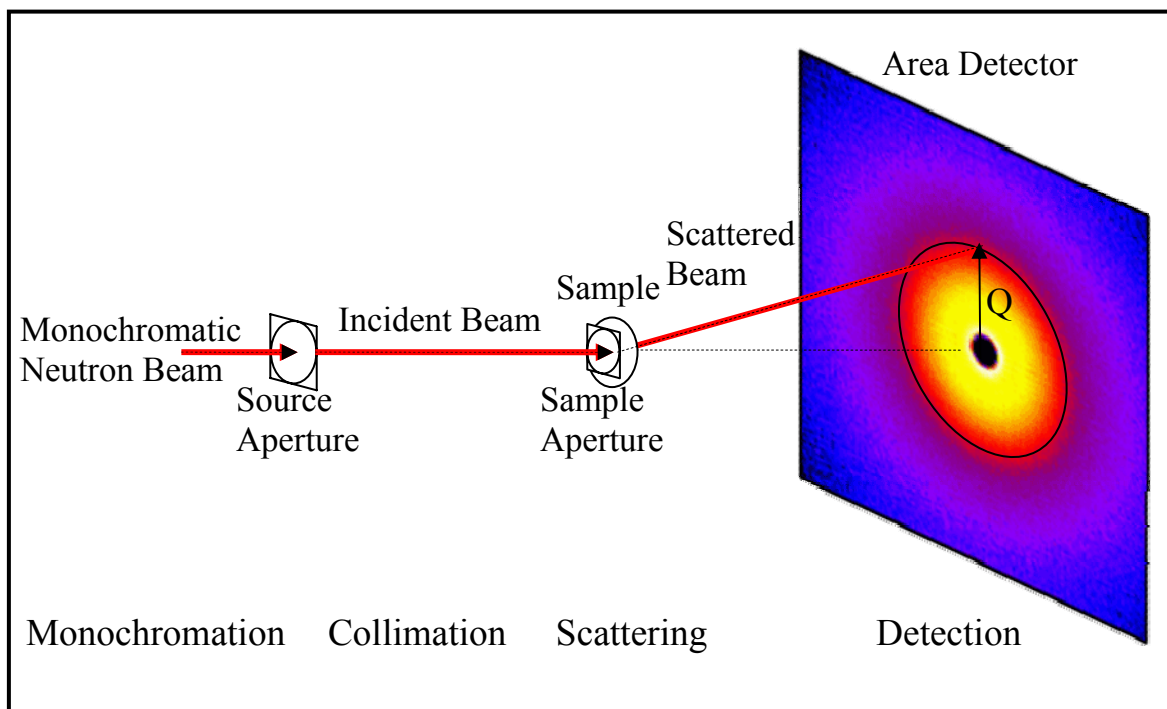
Figure 2: This figure represents the schematics of the SANS technique. It is not to scale with vertical sizes are in centimeters whereas horizontal distances are in meters.

The SANS technique has been an effective characterization method in many area of research including Polymers, Complex Fluids, Biology, and Magnetism. Other Materials Science and Condensed Matter areas also benefited from SANS. SANS instruments have been essential components for any neutron scattering facility for almost three decades. They provide the main justification for the growth and are highly oversubscribed. New sample environments have given new momentum to the technique. These include in-situ shear cells, flow cells and rheometers, pressure cells, electromagnets and superconducting magnets, vapor pressure cells, humidity cells, in-situ reaction cells, etc. New advances in electronics, data handling methods and computers have made SANS a sophisticated "user friendly" characterization method for the non-experts and for "routine" characterization as well as cutting edge research.

4. THE MEASURED MACROSCOPIC SCATTERING CROSS SECTION

Consider a simple scattering system consisting of globular (think spherical) inhomogeneities in a matrix (think solvent). If this system is assumed to be incompressible, the SANS

coherent macroscopic scattering cross section (scattering intensity in an absolute scale) can be modeled as:

$$\frac{d\Sigma_c(Q)}{d\Omega} = \left(\frac{N}{V}\right) V_P^2 \Delta\rho^2 P(Q) S_I(Q). \tag{1}$$

(N/V) is the number density of particles, V_P is the particle volume, $\Delta\rho^2$ is the contrast factor, $P(Q)$ is the single particle and $S_I(Q)$ is the inter-particle scattering factors. Note that $P(Q)$ and $S_I(Q)$ are normalized as follows: $P(Q\rightarrow 0) = 1$, $P(Q\rightarrow\infty) = 0$ and $S_I(Q\rightarrow\infty) = 1$. $S_I(Q)$ has a peak corresponding to the average particle inter-distance (the so-called coordination shell) in the case of "concentrated" system where the particle inter-distance is of the same order as the particle size. The inter-distance is much larger than the particle size for "dilute" system.

The incoherent scattering cross section $d\Sigma_i/d\Omega = \Sigma_i/4\pi$ is a constant (Q-independent) background to be added to the coherent scattering level. Its contribution is mostly from hydrogen scattering in the sample.

5. NEUTRON CONTRAST CONDITIONS

Consider a scattering system made of spheres in a solvent background. The following figures consider four types of contrast conditions (finite contrast, zero contrast for two component systems and multiple contrasts and the scattering length density match condition for three component systems). The scattering length density match condition corresponds to zero contrast factor for the blue spheres.
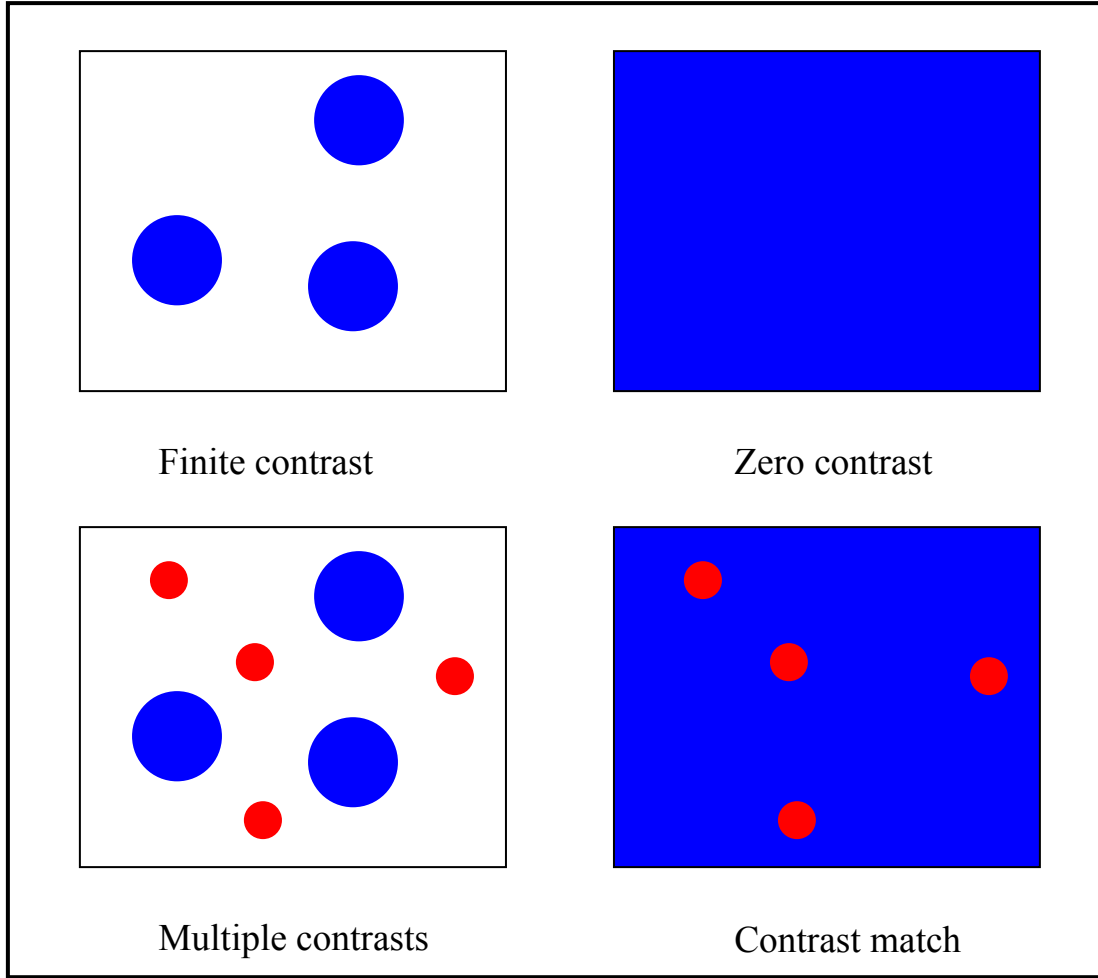
Figure 3: Various contrast conditions.

6. THE PHASE PROBLEM

The so-called "phase problem" affects all scattering methods because measurements are performed in reciprocal (Fourier) space. In order to explain the issue, let us consider the simple case of a scattering medium (think solvent) of scattering length density ρ_g (think "grey" color), and two set of structures, one comprised of "white" spheres of scattering length density ρ_w and one comprised of "black" spheres of scattering length density ρ_b. Assume that the white and black spheres are identical except for their scattering length densities (i.e., "color" as appearing to neutrons) that are opposite. Also assume that the white spheres are hydrogenated ($\rho_w < \rho_g$) and the black spheres are deuterated ($\rho_b > \rho_g$). Microscopy is sensitive to the following differences $\rho_w-\rho_g <0$ and $\rho_b-\rho_g >0$ whereas scattering methods are sensitive to the following "contrast factors" $(\rho_w-\rho_g)^2 > 0$ and $(\rho_b-\rho_g)^2 >0$. Both are positive and therefore appear the same. In order to defeat the phase problem, a second sample is necessary where the scattering length density of the solvent matches that of the black spheres for example ($\rho_g = \rho_b$). In this case the black spheres will be invisible and the white spheres will be distinguished.

| Microscopy | Scattering - Same Sample | Scattering - Second Sample |
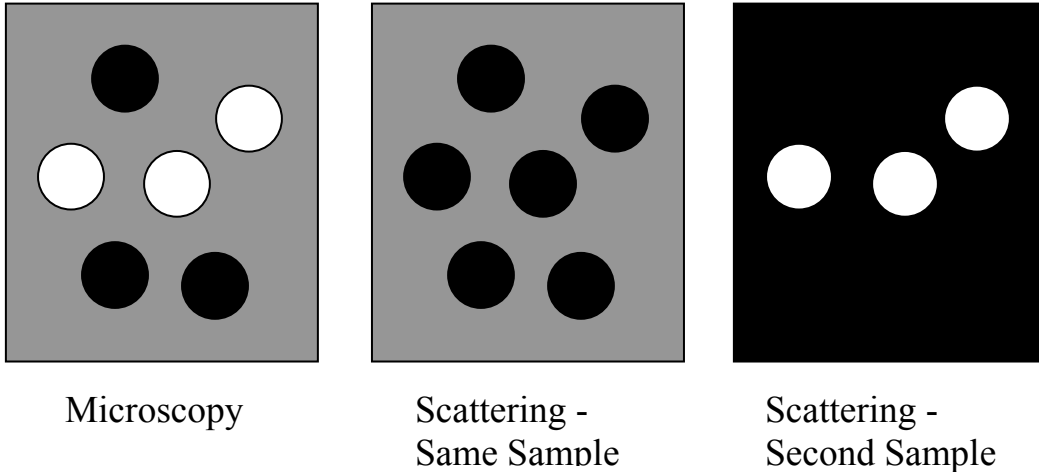
Figure 4: Microscopy sees the white spheres and the black spheres as distinct. Scattering with one sample sees the black balls and the white spheres as similar. A second sample (where the scattering length density of the solvent matches that of the black spheres) shows the white spheres.

This is an oversimplified view of the more complex phase problem. The central aspect of the phase problem comes from the square in the $P(Q) = F^2(Q)$ factor instead. Consider the case of scattering from a sphere of radius R for which $F(QR) = 3j_1(QR)/QR$ where $j_1(QR)$ is the spherical Bessel function given by $j_1(QR) = \sin(QR)/(QR)^2 - \cos(QR)/QR$. In order to obtain the variation of $F(QR)$ from $P(QR)$, one needs more information in order to reconstruct the negative values of $F(QR)$. Here also scattering from one sample does not suffice.
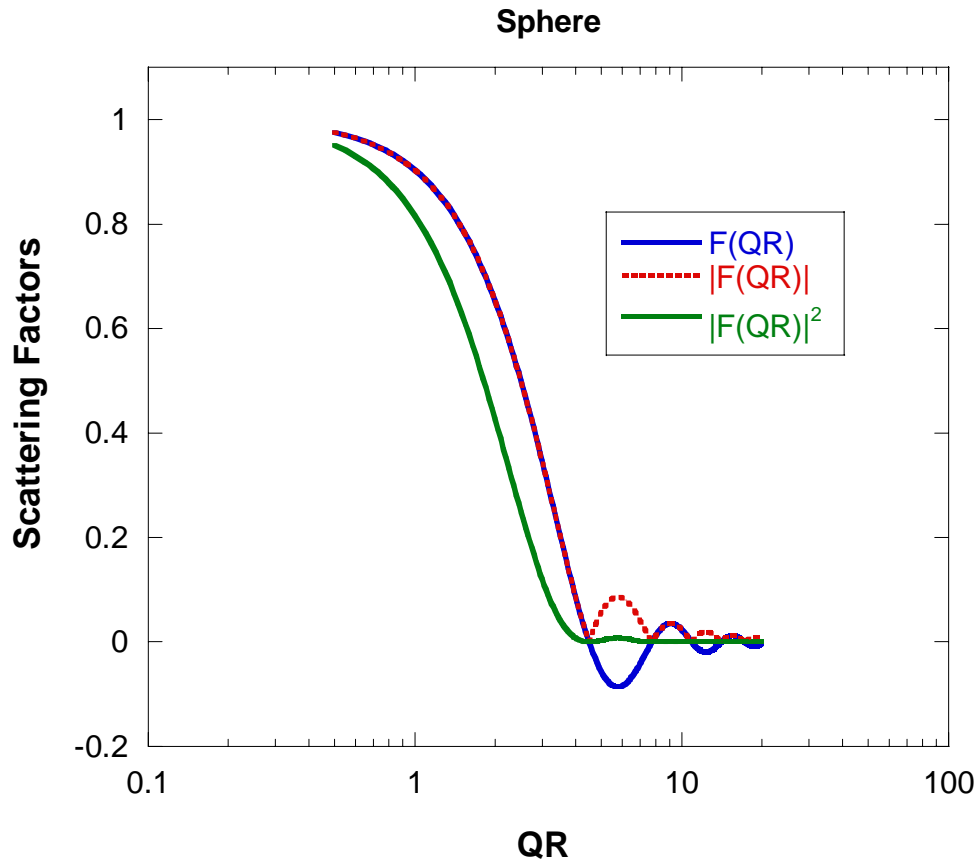
Sphere

Figure 5: Comparison of the three scattering factors for a sphere $F(QR)$, $|F(QR)|$ and $P(QR) = |F(QR)|^2$.

The phase problem is resolved for x-ray single crystal diffraction by including heavy atoms in the structure and in neutron reflectometry and SANS by preparing samples with the same structures but different deuteration schemes.

REFERENCE

B. Hammouda, "SANS from Polymers Tutorial", NIST Center for Neutron Research Report (1995)

QUESTIONS

1. What is reciprocal space?
2. What is the phase problem? How to go around it?
3. What are the four basic steps involved in the SANS instrument?
4. What is the range of scattering angles used in SANS?
5. What are typical sample environments for in-situ SANS measurements?
6. What are the major SANS research areas?

7. Why are SANS instruments bigger than SAXS instruments?

ANSWERS

1. Reciprocal space is the Fourier transform space.
2. The phase problem is due to the fact the scattering contrast factors involve the square of the difference in the scattering length densities so that differences that are opposite in sign show the same contrast. The phase problem is resolved by preparing more than one sample with different deuteration strategies.
3. The four basic steps are monochromation, collimation, scattering and detection.
4. SANS uses scattering angles between 0.2° and 20° in two steps.
5. In-situ SANS environments include: shear cells/rheometers, pressure cells, electromagnets/superconducting magnets, humidity cells, etc.
6. SANS research areas include: polymers, complex fluids, biology, magnetism, materials science, etc.
7. SANS instruments are bigger than SAXS instruments because of the inherently lower flux neutron sources. Neutron current on sample is increased for SANS instruments by making larger samples. Larger samples imply longer SANS instruments in order to cover the same Q range.

Chapter 11 - **THE SANS INSTRUMENT**

The first SANS instruments utilizing long flight paths, long wavelength neutrons from a reactor cold source and position sensitive detectors were developed over 35 years ago. Small angle neutron scattering instruments should really be called low-Q instruments. Q is the scattering variable which is expressed in terms of the neutron wavelength λ and low scattering angle θ as $Q = 2\pi\theta/\lambda$. Low Q can be realized either through the use of small angles or long wavelengths (or both). In order to obtain small angles, good collimation and a good resolution area detector are needed. Good collimation is achieved through the use of long neutron flight paths before and after the sample. SANS instruments on continuous neutron sources use velocity selectors to select a slice of the (often cold) neutron spectrum while time-of-flight SANS instruments use a wide slice of the spectral distribution with careful timing between the source chopper and the detector to separate out the various wavelength frames. In this last case (TOF instruments) the maximum length of an instrument is determined by the pulse frequency so as to avoid frame overlap (whereby the fastest neutrons of one pulse would catch up with the slowest neutrons of the previous pulse).

1. CONTINUOUS SANS INSTRUMENT COMPONENTS

A brief description of the main components of reactor-based SANS instruments follows. This description covers the main features found on the NG3 30 m SANS instrument at the NIST Center for Neutron Research (Hammouda et al, 1993; Glinka et al, 1998).

-- Cold neutrons are transported through total internal reflection at glancing angles inside neutron guides. These transmit neutrons from the cold source to the entrance of scattering instruments with little loss (1 % per meter). Neutron guides are coated with natural Ni or Ni-58 which has a wider critical angle for reflection. This critical angle increases linearly with neutron wavelength thereby allowing more cold neutrons to reach the SANS instrument. Note that supermirrors (characterized by even higher critical angles) are not used due to the tight collimation requirement of SANS instruments; neutrons that experience too many reflections never make it through the tight SANS collimation.

-- Beam filters (for example Be for neutrons and Bi for gammas) are used to clean up the beam from unwanted epithermal neutrons and gamma rays. Gammas are stopped by high-Z materials such as Bi. Be transmits neutrons with wavelengths > 4 Å. Note that if a curved guide is used, no crystal filter is needed because there is no direct line-of-sight from the reactor core (no gammas in the beam). Curved guides transmit only wavelengths above a cutoff value (no epithermal neutrons in the beam). Typical crystal filter thickness is between 15 cm and 20 cm. For better efficiency, filters are cooled down to liquid nitrogen temperature (77 K = -196 ^{o}C).

-- Optical filters are devices that stir a neutron beam away from the direct line-of-sight and replace crystal filters. They consist of tapered neutron guides that transmit only neutrons that are reflected. They have the advantage of gains in flux over crystal filters at long wavelengths.
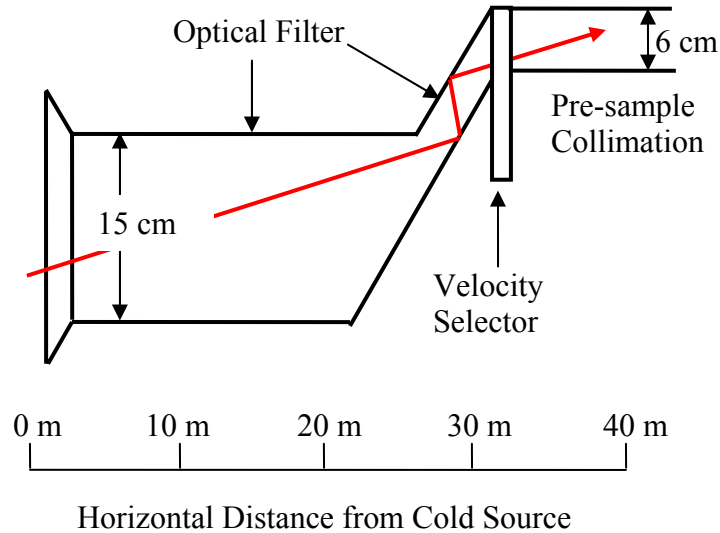
Figure 1: Schematic side view representation of an optical filter used on the NG3 SANS instrument at the NIST CNR facility. The reflecting guide surfaces are made out of Ni and Ni-58. Since there was no room horizontally, the neutron beam is steered vertically. This figure is not to scale.

-- A velocity selector yields a monochromatic beam (with wavelengths λ between 4 Å and 20 Å and wavelength spreads $\Delta\lambda/\lambda$ between 10 % and 30 %). Some SANS instruments that need sharp wavelength resolution use crystal monochromators (with wide mosaic spreads to give $\Delta\lambda/\lambda < 10$ %) instead. Since $\Delta\lambda/\lambda$ is constant, the neutron spectrum transmitted by the velocity selector falls off as $1/\lambda^4$ (instead of the $1/\lambda^5$ coming from the moderator produced Maxwellian distribution).
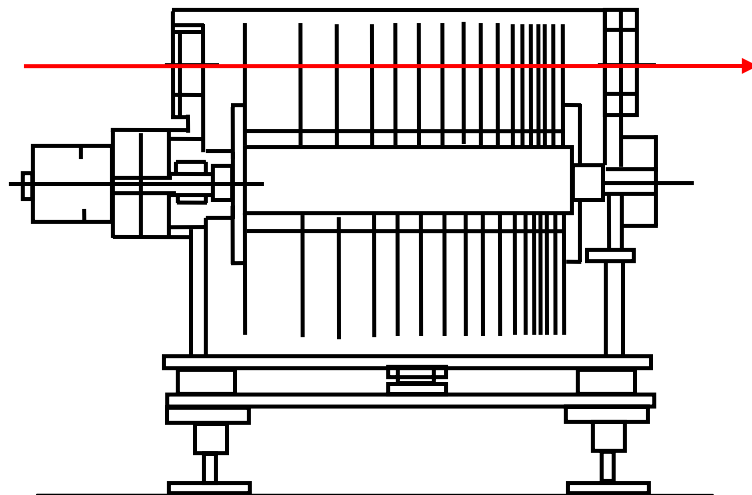
Figure 2: Schematic representation of a multi-disk velocity selector. A white neutron is incident from the left and a monochromated beam is transmitted toward the right. Changing the rotation speed changes the neutron wavelength. Tilting the selector horizontally changes the wavelength spread. Magnetic coupling is used to drive the selector rotation to high rotation speed. Temperature and vibration sensors insure reliable operation.

-- The collimation usually consists of a set of circular (source and sample) apertures that converge onto the detector. An evacuated pre-sample flight path contains the beam collimation system. Typical adjustable flight path distances are from 1 m to 20 m depending on resolution and intensity considerations. Inside the pre-sample flight path, more neutron guides (with reflecting inner surfaces) are included in parallel with the collimation system for easy insertion into the beam. This allows a useful way to adjust the desired flux on sample along with the desired instrumental resolution by varying the effective source-to-sample distance. A normal configuration consists of a certain number of guides inserted into the neutron beam, followed by a source aperture right after, then a series of empty beam positions up to the sample aperture located inside the sample chamber.
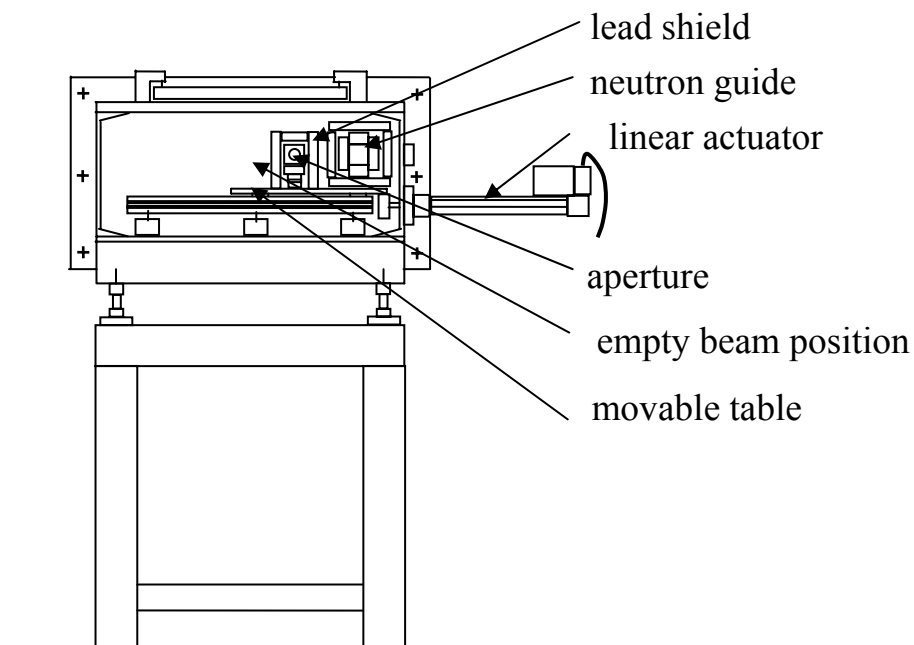
Figure 3: Cross section of a pre-sample flight path box showing an aperture, a neutron guide and an empty beam position that can be inserted in the beam using an actuator and a movable translation table.

-- A sample chamber usually contains a translation frame that can hold many samples (measured in sequence). Heating and cooling of samples (-10 $^{\circ}$C to 200 $^{\circ}$C) as well as other sample environments (cryostats, electromagnets, ovens, shearing devices, etc) are often accommodated. The oversized sample environments are mounted on a 22" diameter Huber sample table instead. This sample table can be rotated around a vertical axis and translated in and out of the neutron beam. This translation is useful for moving the in-situ Couette shear

cell (for example) from the radial position to the tangential position. All of these motions are computer controlled.
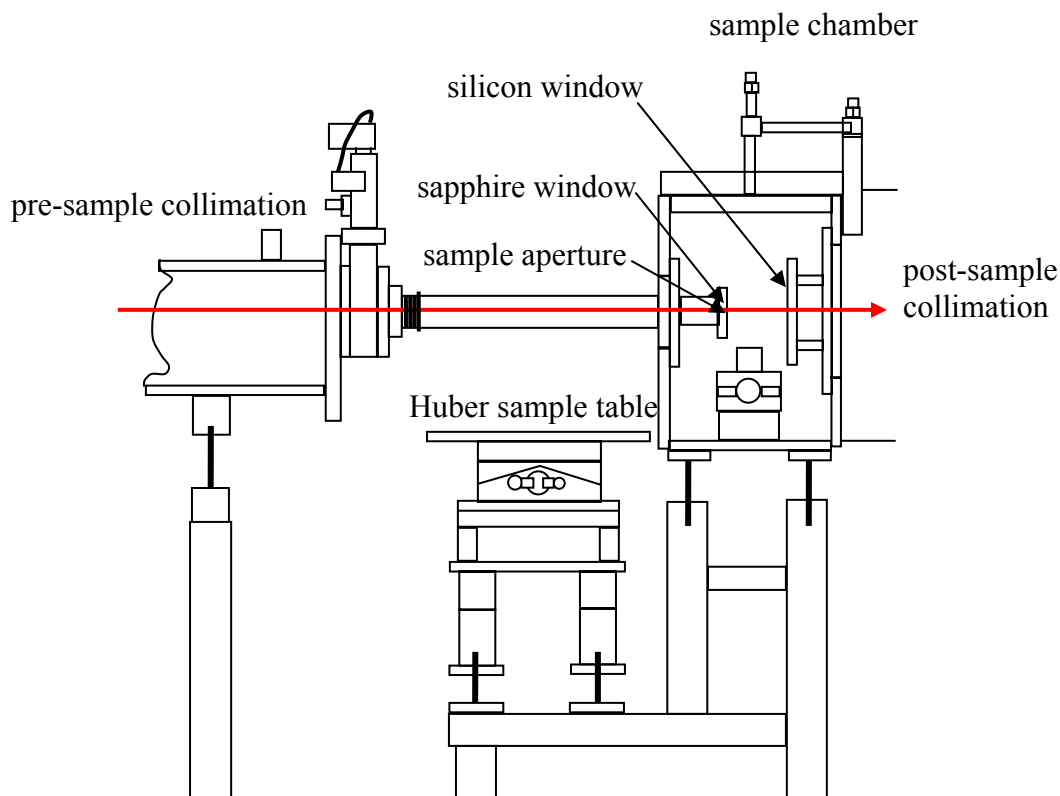
Figure 4: Schematic drawing of the sample area showing the sample chamber on the right and a sample table for oversized environments on the left. Two gate valves are used to isolate the evacuated areas (pre-sample and post-sample flight path) when pumping down or evacuating the sample chamber. This softens the shock on the brittle neutron windows during such rapid pressure surges.

-- A set of three main neutron windows are used: (1) One at the entrance to the pre-sample flight path. This window is before the source aperture and can be made out of quartz. (2) A second window just before the sample. This window is between the two defining apertures and could therefore produce unwanted diffuse scattering. It is often made out of sapphire (more expensive than quartz but with better neutron transmission). Sapphire is transparent thereby allowing a laser beam parallel to the neutron beam through for rapid sample holder alignment. The laser itself is installed on one of the collimation boxes and produces a beam that gets reflected (90 $^{\circ}$) by a silicon mirror placed at 45 $^{\circ}$ from the beam axis. The silicon wafer reflects the laser beam but is transparent to neutrons. (3) A wide silicon window is used at the entrance to the scattering vessel (just after the sample). Silicon has the best neutron transmission and is the best window material when optical transparency is not required. These windows are between 3 mm and 6 mm thick.

-- Precise alignment of sample blocks with respect to the sample aperture is performed using a "neutron camera". A double exposure picture is taken with and without the sample

aperture. A neutron camera is a regular flat camera outfitted with a scintillation plate (using material such as Li-6).

-- The post sample flight path is usually an evacuated cylindrical tube (to avoid scattering from nitrogen in air) that permits the translation of an area detector along rails in order to change to sample-to-detector distance. The vacuum level is kept at less than 100 mT. In order to evacuate such a large volume, a large capacity vacuum pump and a roots blower are used.

-- The area detector is often a gas detector with 0.5 cm to 1 cm resolution and typically 128*128 cells. The detection electronics chain starts with preamplifiers on the back of the detector and comprises amplifiers, coincidence and timing units, plus encoding modules and a means of histogramming the data and mapping them onto computer memory. In order to avoid extensive use of vacuum feedthroughs, high count rate area detector designs incorporates most electronics modules (amplification, coincidence, encoding, etc) inside an electronics chamber located on the back of the detector. In this design, flexible hoses are, however, needed to ventilate the electronics and to carry the high voltage and powering cables in and the encoded signal out.
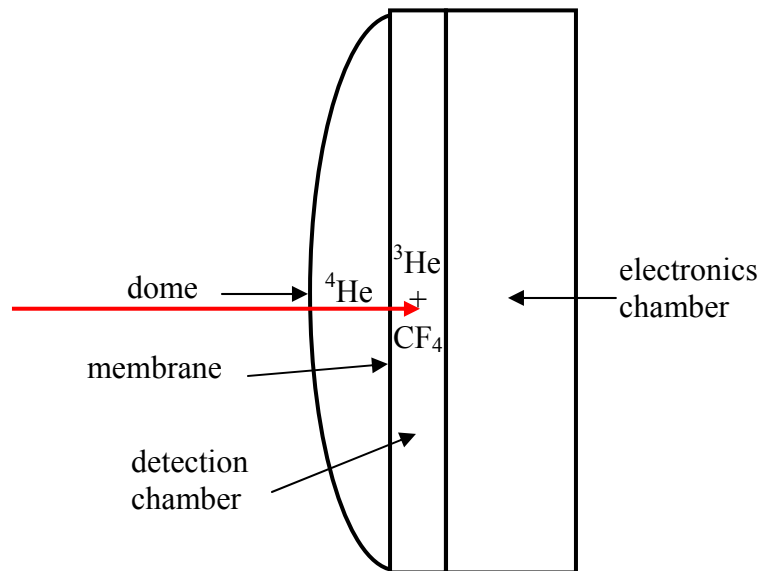
Figure 5: Schematic representation of a neutron area detector.

-- Detector protection is performed in two ways: (1) through an analog monitoring of the total count rate and (2) through software monitoring of each detector cell count rate. If either the total detector count rate or a preset number of cells overflow, the data acquisition system pauses, the next attenuator is moved in and data acquisition is restarted. Typical presets are 50,000 cps for the total detector count rate and 100 cps for 10 cells.

-- A set of beam stops is used to prevent the unattenuated main beam from reaching the detector and therefore damaging it due to overexposure. Use of glass seeded with Li-6 as

neutron absorber avoids the gamma-ray background obtained with Cd, B or Gd containing materials. For easy alignment, motion of the beam stops should be independent of that of the area detector.

-- Between the velocity selector and the pre-sample collimation system, a low-efficiency fission chamber detector is used to monitor the neutron beam during data acquisition.

-- Just before the pre-sample collimation flight path a set of calibrated attenuators are used to attenuate the neutron beam. This system consists of a slab of plexiglass milled stepwise so as to provide attenuators of varying thickness. The insertion of this attenuator set is computer controlled. For example, if the area detector count rate is above a preset ceiling, the thinnest attenuator is moved into the beam by the data acquisition software. If this does not attenuate the beam enough, the next attenuator in thickness is moved in, etc. Another option for an attenuator system is to use neutron absorbing material (such as cadmium) plates with holes milled into them. The density of holes determines the attenuation factor.

-- Gamma radiation produced by neutron capture in various neutron absorbing materials (Cd, Gd, B) is stopped using high-Z shielding materials (Fe, Pb, concrete). Shields surround the velocity selector (especially the front disk that gets most of the dose) and beam defining apertures. The scattering vessel is also shielded in order to minimize background radiation from reaching the detector.

-- The pre-sample and post-sample flight paths are often made out of non magnetic metals (like aluminum or non-magnetic steel) in order to allow use of polarized neutrons.

-- A neutron polarizer consists of a Fe/Si coating on 1 mm thick silicon plates aligned to form a V inside a copper-coated neutron guide. This polarizing cavity is 1.2 m long and polarizes a $4*5$ cm^2 neutron beam for a wavelength between 5 Å and 15 Å. Immediately following the polarizing cavity is a flat coil π spin flipper for reversing the direction of polarization. Permanent magnets maintain a 500 gauss vertical field to magnetize the supermirror coating and a 50 gauss field from the supermirror to the sample area to maintain neutron polarization.

-- In order to avoid diffuse scattering from the beam defining apertures, these are tapered (5$^{\text{o}}$ taper angle is enough) and made out of material like boron nitrite or lithiated glass with the smaller inner edge made out of cadmium. This keeps the beam sharp and gamma radiation emitted to a minimum.

-- Data acquisition is computer controlled within menu-driven screen management environments and on-line imaging of the data is usually available. Encoded 2D data are received from the area detector electronics, binned into histogramming memories, then regularly displayed and saved. The data acquisition software interface also controls the various peripheral functions such as controlling the various motors, the sample heating/cooling protocols, and handshaking with the various other stand-alone sample environments (shear cells, pressure cells, etc).

-- There are many figures of merit used to judge the performance of SANS instruments. These include: instrumental resolution, minimum scattering variable (Q_{min}), flux on sample, dynamic Q range and background level.
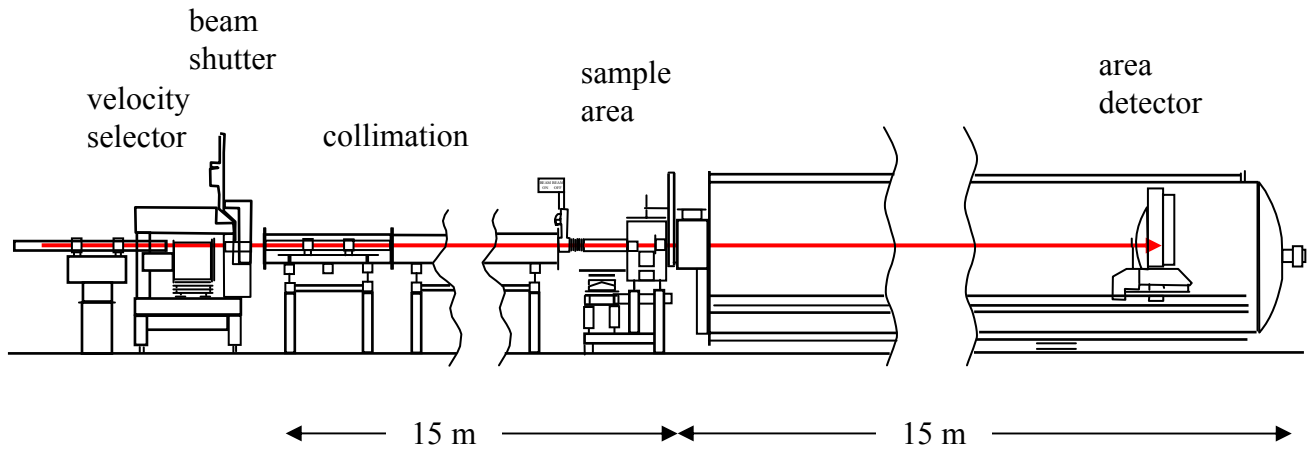
Figure 6: Schematics of a 30m SANS instrument at NIST.

Figure 7: Photograph of the NG3 30 m SANS instrument. The picture was taken from the cat walk just before the velocity selector shield.

Table 1: 30 m NIST-SANS Instruments Characteristics.

Source:	neutron guide (NG3), 6 * 6 cm^2
Monochromator:	mechanical velocity selector with variable speed and pitch
Wavelength Range:	variable from 5 Å to 20 Å
Wavelength Resol.:	10 to 30 % for $\Delta\lambda/\lambda$ (FWHM)
Source-to-Sample Dist.:	3.5 to 15 m in 1.5 m steps via insertion of neutron guides
Sample-to-Detector Dist.:	1.3 to 13.2 m continuously variable for NG3
Collimation:	circular pinhole collimation
Sample Size:	0.5 to 2.5 cm diameter
Q-range:	0.001 to 0.6 Å^{-1}
Size Regime:	10 to 6000 Å
Detector:	64 * 64 cm^2 He-3 position-sensitive proportional counter (0.5 cm^2 resolution)

Table 2: Short list of ancillary equipment used on SANS.

Ancillary Equipment:	- Automatic multi-specimen sample changer with temperature control from -10 to 200 $^{\circ}$C. - Electromagnet (0 to 9 Tesla). - Couette flow shearing cell, plate/plate shear cell, in-situ rheometer. - Cryostats and closed cycle refrigerators (1 K to 300 K). - Oven for in-situ use (300 K to 1800 K). - Pressure cell (0 to 1*10^8 Pa, 25 $^{\circ}$C to 160 $^{\circ}$C).

2. TIME-OF-FLIGHT SANS INSTRUMENT COMPONENTS

In order to avoid frame overlap, time-of-flight SANS instruments tend to be shorter at typical pulsed sources. TOF SANS instruments comprise some of the main features described above (collimation, sample chamber, flight paths, area detector, etc) as well as some specific features described here:

-- A source chopper is used to define the starting neutron pulse.

-- The area detector is synchronized to the source chopper so that a number of wavelength frames (for example 128) are recorded for each pulse. No monochromator is necessary with the time-of-flight method.

-- A supermirror bender can be used to remove short wavelengths and let the instrument get out of the direct line of sight from the source. Note that curved guides have a cutoff wavelength below which neutrons are not transmitted. This bender replaces the crystal filter.

-- High wavelengths (say above 14 Å) have to be eliminated in order to avoid frame overlap. This can be done by gating the detector or through the use of frame overlap mirrors. Reflecting mirrors are set at a slight angle (1°) from the beam direction so as to reflect only long wavelength neutrons (note that the reflection critical angle varies linearly with wavelength).

-- Prompt gamma rays emitted during the spallation reaction are eliminated by paralyzing the detection system for the first microsecond after each pulse.

Because of the wide wavelength range used in time-of-flight instruments, materials that display a Bragg cutoff (such as sapphire windows) cannot be used. Data reduction becomes more complex with time-of-light instruments since most corrections (transmission, monitor normalization, detector efficiency, linearity, uniformity, etc) become wavelength dependent. Time-of-flight instruments have the advantage, on the other hand, of measuring a wide Q range at once. Also the large number of wavelength frames can be kept separate therefore yielding very high wavelength resolution ($\Delta\lambda/\lambda < 1$ %) which is useful for highly ordered scattering structures (characterized by sharp peaks).

3. SAMPLE ENVIRONMENTS

Typical sample thickness for SANS measurements is of order of 1 mm for hydrogenated samples and 2 mm for deuterated samples. Liquid samples (polymer solutions, microemulsions) are often contained in quartz or demountable cells into which syringes can be inserted. Solid polymer samples are usually melt-pressed above their softening temperature, then confined in special cells between quartz windows.

Flexibility of design for some instruments allows the use of typical size samples under temperature control or bulky sample environments. Temperature is easily varied between ambient temperature and 200 ^{o}C using heating cartridges or between -10 ^{o}C and room temperature using a circulating bath. Other sample environment equipment such as low-temperature cryostats (4 to 350 K) and electromagnets (1-10 Teslas) are sometime made available to users. Various shear cells (Couette, plate-and-plate, in-situ rheometers, etc) help probe "soft" materials at the molecular level in order to better understand their rheology. Pressure cells are also finding wide use for investigations of compressibility effects on the thermodynamics of phase separation as well as on structure and morphology.

4. SANS MEASUREMENTS

SANS measurements using cold neutrons take from a few minutes to a few hours depending on the scattering sample, the neutron source and the instrument configuration used. The process starts by sample preparation, loading into cells and measurement of the sample thickness.

A reasonable instrument configuration is chosen at first by setting a low wavelength and varying the sample-to-detector distance so as to optimize the desired Q-range. If the maximum available sample-to-detector distance of that instrument is reached, wavelength is then increased. Choice of the source-to-sample distance, wavelength spread, and aperture sizes are dictated by the desired instrumental resolution (sharp scattering features require good resolution) and flux on sample. Scattered intensity is proportional to many factors that have to be optimized. Transmission measurements are required as well. In order to avoid complicated multiple scattering corrections, sample transmissions are kept high (> 60 %). Many experiments require a wide Q range covering two orders of magnitude (from $Q = 0.003 \text{ Å}^{-1}$ to $Q = 0.3 \text{ Å}^{-1}$). This range is obtained over two instrument configurations. In order to improve counting statistics, a third configuration is often used. The use of focusing lenses lowers the minimum Q down to slightly below $Q = 0.001 \text{ Å}^{-1}$.

A complete set of data involves measurements from the sample, from an incoherent (usually nondeuterated) scatterer that yields a flat (Q-independent) signal, from the empty cell and blocked beam and from a calibrated (absolute standard) sample. The beam flux measurement method (measurement of the direct beam transmission) can be used to replace the absolute standard measurement.

SANS data are corrected, rescaled to give a macroscopic cross section (units of cm^{-1}) then averaged (circularly for isotropic scattering or sector-wise for anisotropic scattering). Reduced data are finally plotted using standard linear plots (Guinier, Zimm, Kratky, etc) in order to extract qualitative trends for sample characteristics (radius of gyration, correlation length, persistence length, etc) or fitted to models for more detailed data analysis.

5. SANS INSTRUMENTS IN THE WORLD

Since the first SANS instrument went into operation at the Institut Laue Langevin (Grenoble, France) in the mid-1970s, many more SANS instruments have been built. Every neutron scattering facility has at least one such instrument. The SANS technique has managed to keep a steady growth and a high level of user subscription. A web site keeps a SANS instruments directory in the world (http://www.ill.fr/lss/SANS_WD/sansdir.html).

REFERENCES

B. Hammouda, S. Krueger and C. Glinka, "Small Angle Neutron Scattering at the National Institute of Standards and Technology", NIST Journal of Research 98, 31-46 (1993).

C.J. Glinka, J.G. Barker, B. Hammouda, S. Krueger, J. Moyer and W. Orts, "The 30m SANS Instruments at NIST", J. Appl. Cryst. <u>31</u>, 430-445 (1998).

K. Ibel, "World Directory of SANS Instruments", available online at the address
http://www.ill.fr/lss/SANS_WD/sansdir.html

QUESTIONS

1. Why are small-angle neutron scattering instruments bigger than small-angle x-ray scattering instruments?
2. Why are crystal monochromators not used (instead of velocity selectors) in SANS instruments?
3. Could one perform SANS measurements without using an area detector?
4. What is the useful range of cold neutron wavelengths?
5. When is it necessary to use wide wavelength spread $\Delta\lambda/\lambda$?
6. Find out how does a velocity selector work?
7. How does a He-3 area detector work?
8. What is the cost of building a SANS instrument?
9. Name some materials used for neutron windows.
10. Do cold neutrons destroy samples?
11. Why are time-of-flight SANS instruments short?

ANSWERS

1. Neutron fluxes are lower than x-ray fluxes. SANS samples are made bigger than SAXS samples in order to enhance the neutron current on sample. Bigger samples require larger flight paths in order to cover the same Q range.
2. Crystal monochromators are characterized by narrower wavelength spreads than velocity selectors and therefore lower neutron currents. Moreover the use of a crystal monochromator would require the pivoting of the entire SANS instrument around the monochromator axis in order to change the neutron wavelength because they operate in reflection geometry. Velocity selectors operate in transmission geometry.
3. SANS measurements can be performed using an end-window or a 1D position-sensitive detector. Count rate would however be prohibitively low.
4. Cold neutron wavelength range from 4 Å to 20 Å. The range used is effectively from 5 Å to 12 Å. Longer wavelengths are characterized by low fluxes.
5. SANS uses wide wavelength spread in order to increase the neutron current on sample.
6. Velocity selectors rotate at a specific speed for every neutron wavelength. The helical selector slot lets neutrons of the right speed through. Those that are either too slow or too fast are absorbed and never get transmitted.
7. He-3 absorbs a neutron to give two charged particles: a proton (H-1) and a triton (H-3). These two charges create an electron detection cloud that drifts towards the anode (at high voltage) and therefore get sensed by the cathodes.
8. A SANS instrument costs as much as its level of sophistication. A deluxe model costs over $ 1 million.

9. Neutron windows have to be very transparent to neutrons. Silicon is the most transparent but is opaque to visible light. Sapphire is less transparent to neutrons, very transparent to visible light but rather expensive. Quartz is like sapphire but less expensive. In practice, sapphire is used for windows before the sample. They can transmit neutrons as well as let a laser beam through for sample alignment purposes. After the sample, silicon windows are used.

10. Cold neutrons do not destroy most samples. Unlike x-rays they do not heat them up. Samples containing elements that can be activated by neutrons (such as Fe for example) have to be handled differently. Most SANS samples (polymers, complex fluids and biology) contain organic molecules that do not get activated (C, H, D, O, N, etc).

11. Time-of flight SANS instruments are made short in order to avoid frame overlap (when the fast neutrons of one pulse catch up with the slow neutrons of the previous pulse).

Chapter 12 - **VELOCITY SELECTORS AND**
TIME-OF-FLIGHT MEASUREMENTS

Characteristics of velocity selectors and time-of-flight measurement of the neutron wavelength distribution are described. Monochromation is a necessary step for SANS instruments that do not use the time-of-flight method. Continuous SANS instruments use velocity selectors instead of crystal monochromators. The basic concept for velocity selectors is to allow neutrons to travel in a rotating helical path. Neutrons that are either too fast or too slow get absorbed. Only neutrons with the right velocities are transmitted thereby transforming a white incident neutron beam into a monochromated distribution with mean wavelength λ and wavelength spread (FWHM) $\Delta\lambda$. Velocity selectors are either of the solid drum type (with helical slot) or of the multidisk type.
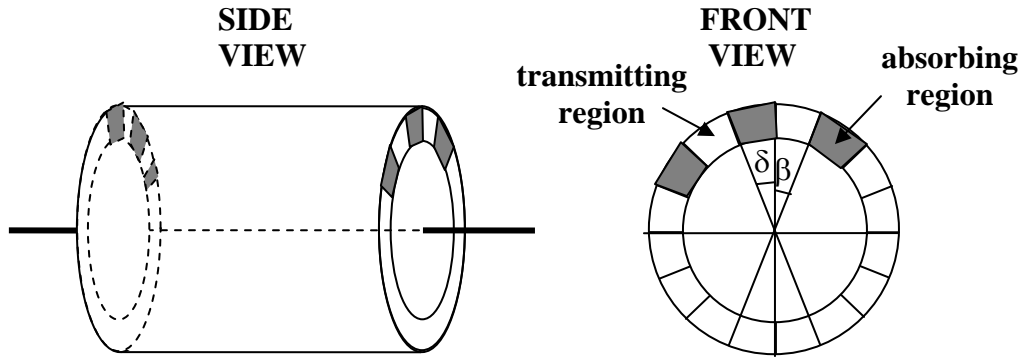
Figure 1: Schematics of a velocity selector explicitly showing three absorbing sectors and two transmitting windows between them.

1. VELOCITY SELECTORS CHARACTERISTICS

Velocity selectors rotate at constant frequency ω which is varied to change the transmitted neutron wavelength λ. A typical selector has an overall length L (length of the rotating "drum") and a radius R (between the selector rotation axis and the neutron window). The helical path is characterized by a pitch angle α. This is the angle by which the selector rotates while neutrons cross its length L.

Equating the time it takes for neutrons to travel that distance L to the time it takes the selector to rotate the angle α gives a relationship between the neutron wavelength λ and the rotation speed ω.

$$\lambda = \frac{\alpha h}{Lm\omega}. \tag{1}$$

Here h is Planck's constant, and m is the neutron mass. This relationship is expressed in more convenient units as:

$$\lambda[\text{Å}] = 6.59 * 10^5 \frac{\alpha[\text{deg}]}{\omega[\text{rpm}]L[\text{mm}]}. \tag{2}$$

Here, the selector rotation frequency ω is given in rpm (rotations per minute).

The selector transmission is proportional to the uncovered area of the input face. Two angles are defined. β is the angle subtending the transmitting window and δ is the angle corresponding to the absorbing region between two transmitting windows. The selector transmission is expressed as the following ratio:

$$T = \frac{\beta}{\beta + \delta}. \tag{3}$$

The wavelength spread $\Delta\lambda$ is defined as the FWHM of the selector output distribution. The selector resolution (relative wavelength spread) is simply expressed as the ratio of the two relevant angles.

$$\frac{\Delta\lambda}{\lambda} = \frac{\beta}{\alpha}. \tag{4}$$

Note that $\Delta\lambda$ is independent of λ so that the incoming λ^{-5} wavelength distribution from the neutron source becomes $\lambda^{-5}\frac{\Delta\lambda}{\lambda} \sim \lambda^{-4}\Delta\lambda$ after the selector. The transmitted wavelength distribution is of the triangular form with slightly rounded angles (as will be described later).

To decrease the wavelength resolution, one can either (1) decrease the transmitting window angle β, or (2) increase the pitch angle α at the design stage. The first possibility is limited by the accompanying loss in selector neutron transmission. The second possibility comes with an increase in rotation speed in order to reach the same wavelength. In order to keep the same rotation speed, both the pitch angle α and the selector length L could be varied proportionately.

In order to change the wavelength spread on a selector, the selector axis is tilted (in the horizontal plane) by an angle ν relative to the beam axis thereby modifying the effective pitch angle as:

$$\alpha_{\text{eff}} = \alpha + \frac{\nu L}{R}. \tag{5}$$

Tilting modifies both the wavelength spread $\Delta\lambda$ and the neutron wavelength λ.
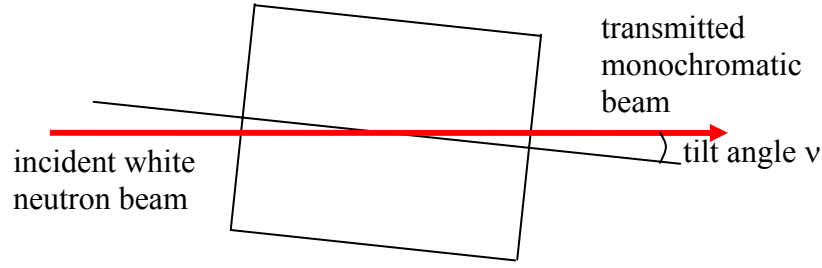
Figure 2: Schematic top view of a velocity selector showing the horizontal tilt angle ν.

2. TYPICAL VELOCITY SELECTOR

The following parameters correspond to a velocity selector used on a 30 m SANS instrument at the NIST Center for Neutron Research (Hammouda, 1992). It is a multi-disk unit of Hungarian type design.

Selector length L = 42 cm.
Radius to the middle of the window R = 17.5 cm.
Helix rotation angle $\alpha = 17^o$.
Open window aperture angle $\beta = 2.25^o$.
Absorbing region between windows $\delta = 0.75^o$.
Number of disks n = 22.

These design parameters yield the following predicted selector characteristics.

Neutron transmission T = 0.75.
Wavelength $\lambda[\text{Å}] = 2.669*10^4/\omega[\text{rpm}]$.
Relative wavelength spread $\Delta\lambda/\lambda = 0.132$ for a tilt angle of ν = 0.
Effect of tilt angle ν on the helix angle $\alpha_{eff} = 17^o + 2.4\ \nu$.
Therefore $\left(\dfrac{\Delta\lambda}{\lambda}\right) = \dfrac{2.25^o}{17^o + 2.4\ \nu}$.

These are theoretical numbers predicted based on design parameters. Measured characteristics using the time-of-flight method are described in the following section.

3. VELOCITY SELECTOR CALIBRATION BY TIME-OF-FLIGHT

The time-of-flight (TOF) method consists in chopping the neutron beam (using a rotating chopper) and gating a neutron detector with the time-zero chopper pulse. All neutrons cross the chopper at the same time despite their spread in velocities. As neutrons travel beyond the chopper, they spread out with faster neutrons arriving to the detector first. The neutron pulse is sharp at the chopper level and becomes spread out at the detector level.

Here the time-of-flight method is used to characterize the wavelength distribution coming out of the velocity selector described earlier. The setup consists of a neutron disk-chopper followed by two pencil detectors installed close to the SANS instrument sample area. The pencil detectors have a diameter of 1.27 cm. The second pencil detector is used for redundancy and in order to obtain an exact measurement of the SANS sample-to-detector distance. The two pencil detectors are located 0.5 m apart and the distance between the second pencil detector and the area detector is 3 m. The chopper has a neutron slit 1 mm wide and 1.27 cm tall. A fixed slit aperture of the same size is located just ahead of the chopper in order to define the neutron beam. The chopper rotation is synchronized with the neutron detectors data acquisition system through the time-zero pulse.
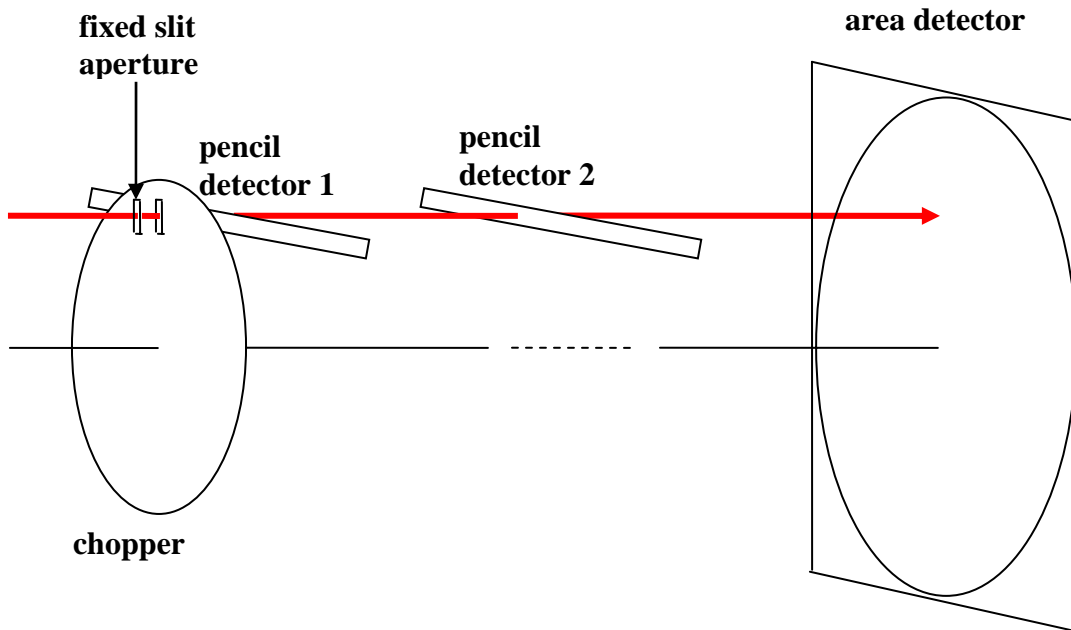
Figure 3: Schematic representation of the time-of-flight setup comprising a chopper, two pencil detectors and the area detector. The fixed slit aperture is located just before the chopper.

A multi-channel scaler electronic unit was used to record the neutron pulses from the neutron detectors using the gated signal from the chopper. A typical spectrum corresponding to a wavelength around 6 Å, a source-to-chopper distance of 14.27 m, a detector 1-to-detector 2 distance of 0.5 m and a pencil detector 2-to-area detector distance of 3 m is shown below.
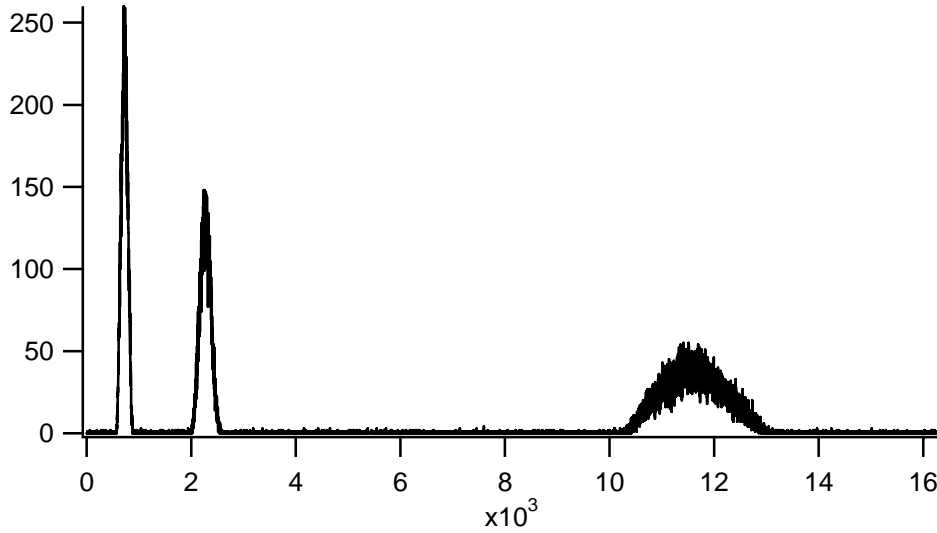
Figure 4: Neutron spectrum obtained by time-of-flight. The first two peaks were recorded by the two pencil detectors and the third peak was recorded by the SANS area detector. The horizontal axis is in time channel numbers (0.5 μsec/channel) and the vertical axis is in neutron counts. The chopper frequency was set to 113 Hz.

Fits of the various peaks to Gaussian shapes were performed in order to obtain peak positions and standard deviations. Peak positions yielded flight times (and therefore wavelengths) and standard deviations yielded wavelength spreads.

Wavelength Measurement

Knowing the distances between any two detectors, the neutron wavelength is proportional to the measured flight time between them and inversely proportional to the inter-distance between them.

$$\lambda[\text{Å}] = \frac{3.956 * 10^3}{v[\text{m/sec}]} \qquad (6)$$

v[m/sec] = inter-distance[m]/flight time[sec].

The velocity selector rotation speed was varied and the neutron wavelength is measured in each case. Using different detector pairs gave the same result.
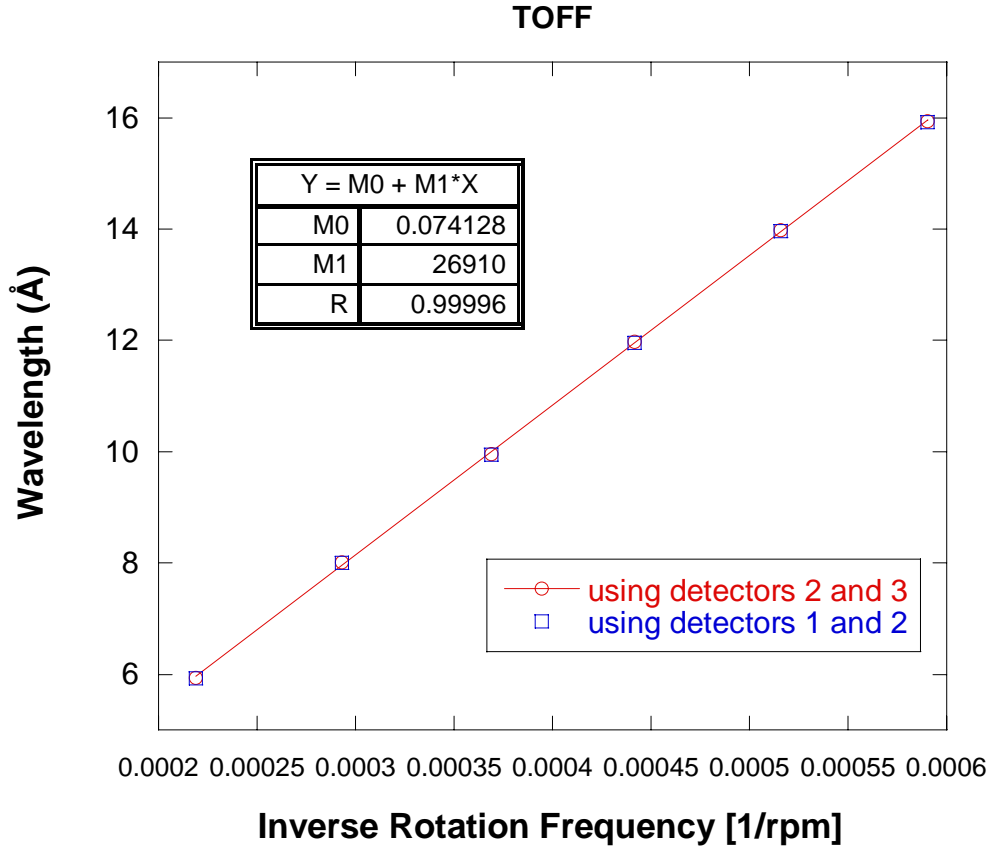
Figure 5: Variation of the measured wavelength with inverse velocity selector rotation frequency.

A linear fit to the $\lambda[\text{Å}]$ with $1/\omega[\text{rpm}]$ gives the following measured relationship:

$$\lambda[\text{Å}] = 0.0741 + 2.691 * 10^4 / \omega[\text{rpm}]. \qquad (7)$$

The measured slope of $2.691 * 10^4$ agrees with the predicted one of $2.669 * 10^4$ reported earlier.

Variation of the neutron wavelength with inverse rotation frequency is plotted for three tilt angles.

Time of Flight Calibration
NG3 SANS Instrument
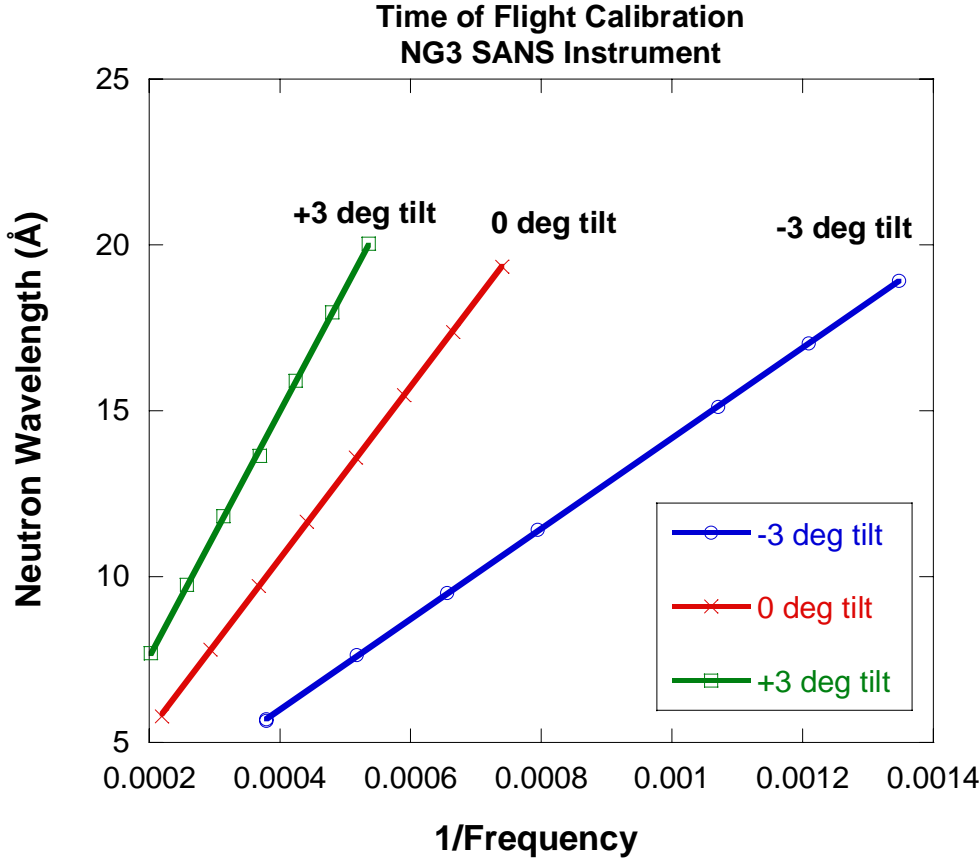
Figure 6: Variation of the measured wavelength with inverse frequency for three tilt angles.

Wavelength Spread Measurement

Gaussian fits to the measured spectra gave average flight times t_1, t_2 and t_3 and standard deviations σ_1, σ_2 and σ_3 for the peaks corresponding to detectors 1, 2 and 3 (recall that 1 and 2 are pencil detectors and 3 is the area detector). The relative wavelength spread obtained from detectors 1 and 3 is obtained as:

$$\left(\frac{\Delta\lambda}{\lambda}\right)_{1,3} = 2.355 \frac{\sqrt{\sigma_3^2 - \sigma_1^2}}{(t_3 - t_1)} \sqrt{\frac{L_3 - L_1}{L_3 + L_1}} \, . \tag{8}$$

Subtracting σ_1^2 insures that smearing contributions from the chopper's finite size slit (1 mm wide) and from the pencil detector's finite width (1.27 cm diameter) are removed. The factor $2.355 = 2(2\ln2)^{1/2}$ is used to convert the standard deviation of the Gaussian shaped distribution σ into a full-width at half maximum (FWHM); $\Delta\lambda = 2(2\ln2)^{1/2}\sigma_\lambda$.

The last term $\sqrt{\dfrac{L_3 - L_1}{L_3 + L_1}}$ is obtained through the following argument. The variance of the pulse time at a distance L_3 from the chopper is given by:

$$\sigma_t^2(L_3) = L_3^2 \sigma_\tau^2 + \sigma_t^2(0). \tag{9}$$

Here $\sigma_t(0)$ is the standard deviation at the chopper position and σ_τ is the standard deviation of the time-of-flight distribution. Applying this relation to two positions L_1 and L_3, one obtains the following relation:

$$\left(\frac{\sigma_\lambda}{\lambda}\right) = \left(\frac{\sigma_\tau}{\tau}\right) = \frac{\sqrt{\sigma_3^2 - \sigma_1^2}}{(t_3 - t_1)} \sqrt{\frac{L_3 - L_1}{L_3 + L_1}}. \tag{10}$$

In practice $L_1 \ll L_3$ so that the last term (square root) becomes unity.

Varying the velocity selector tilt angle decreases the relative wavelength spread.
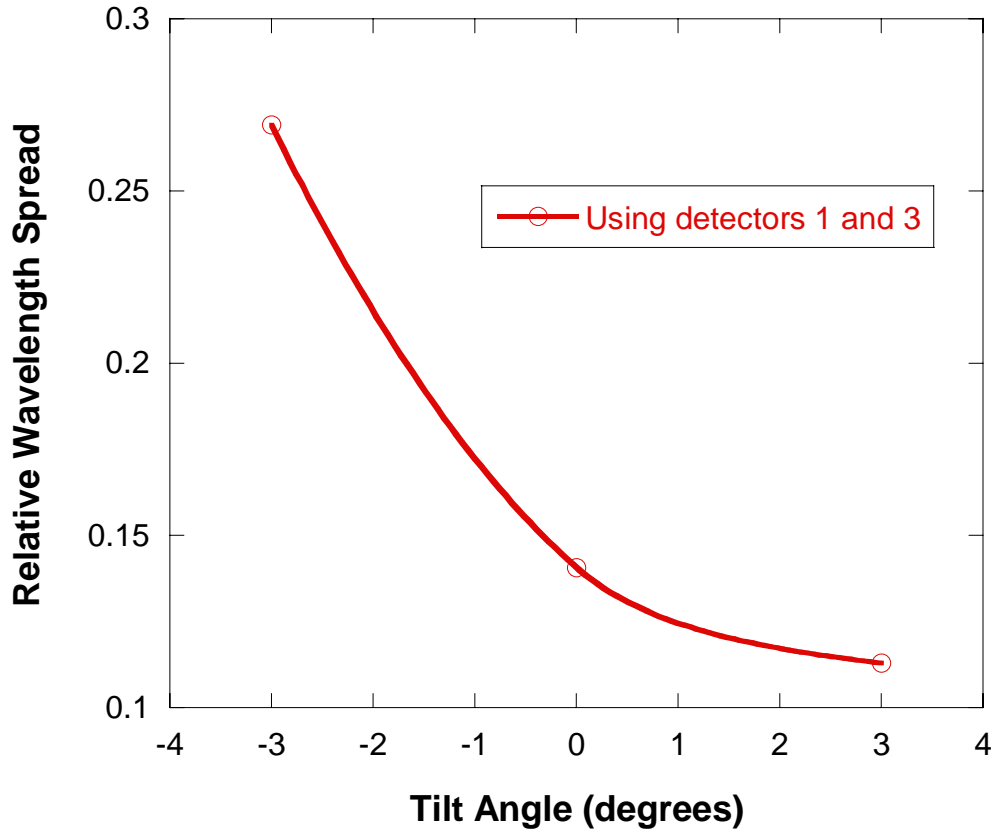
Figure 7: Variation of the measured relative wavelength spread with increasing selector tilt angle.

The measured relative wavelength spreads ($\Delta\lambda/\lambda$) corresponding to the three measured tilt angles (-3°, 0° and $+3^\circ$) are 0.269, 0.141 and 0.113.

The measured inverse of the relative wavelength spread gives the following linear variation with the tilt angle ν.

$$\left(\frac{\lambda}{\Delta\lambda}\right) = 6.55 + 0.85\nu \ . \tag{11}$$

This variation is far from the predicted value of

$$\left(\frac{\lambda}{\Delta\lambda}\right) = 7.55 + 1.07\nu. \tag{12}$$

The wavelength spread is a very sensitive measurement to make. This is due to many factors: the assumption of Gaussian shape (for fitting purposes), smearing due to the defining slit's finite width, smearing due to the detectors finite detection depth, etc… For example, the pencil detectors are 1.27 cm in diameter and the area detector has a detection depth of 2.54 cm. Measured wavelength spreads are expected to be larger than predicted ones.

Wavelength Distribution Profile
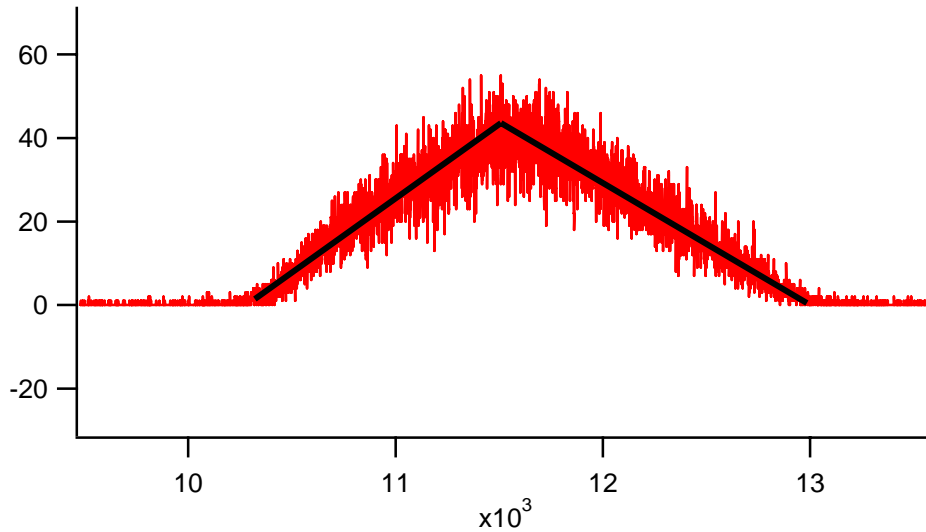
Figure 8: Wavelength distribution peak measured using the area detector with a wavelength around 6 A, a source-to-chopper distance of 14.27 m (corresponding to 1 pre-sample collimation guide inserted), and a pencil detector 2-to-area detector distance of 3 m. This distribution is characterized by a triangular shape.
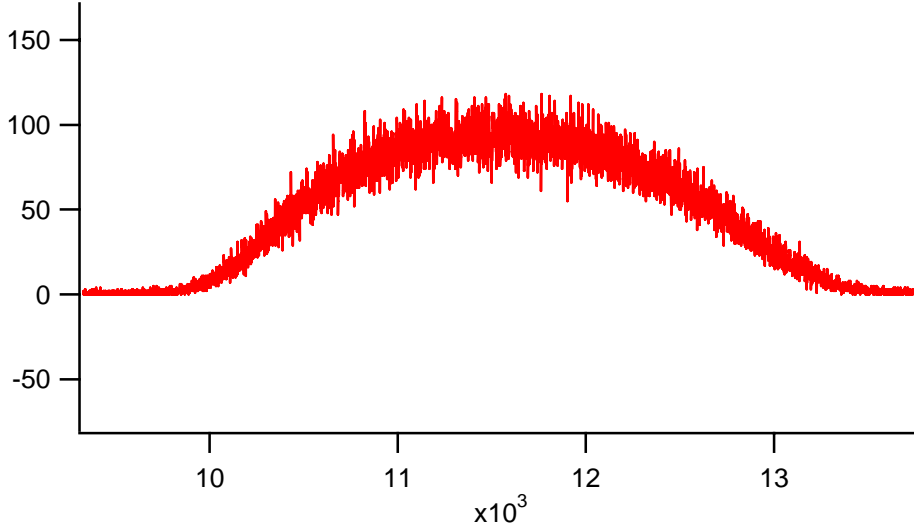
Figure 9: Wavelength distribution peak measured using the area detector with a wavelength around 6 A, a source-to-chopper distance of 3.38 m (corresponding to 8 pre-sample collimation guides inserted), and a pencil detector 2-to-area detector distance of 3 m. This distribution is characterized by a rounded Gaussian shape.

The source-to-chopper distance is varied by inserting neutron guides into the SANS instrument's pre-sample flight path. The monochromated neutron beam is therefore reflected (by the guides surface) before reaching the chopper. The first case shown corresponds to 1 guide inserted (source-to-chopper distance of 14.27 m) whereas the second case shown corresponds to 8 guides inserted (source-to-chopper distance of 3.42 m). The fist case is characterized by a triangular wavelength distribution whereas the second case is characterized by a rounded up Gaussian distribution (due to time-of-flight smearing). Inserted neutron guides introduce smearing to the wavelength distribution because they smear the flight time distribution.

Assuming a triangular wavelength distribution, the second moment is expressed as:

$$< \lambda^2 > = < \lambda >^2 \left[1 + \frac{1}{6} \left(\frac{\Delta \lambda}{< \lambda >} \right)^2 \right]. \tag{13}$$

Assuming a Gaussian wavelength distribution, this quantity is expressed as:

$$< \lambda^2 > = < \lambda >^2 \left[1 + \left(\frac{\sigma_\lambda}{< \lambda >} \right)^2 \right]. \tag{14}$$

Here σ_λ^2 is the variance of the Gaussian distribution defined as $\sigma_\lambda^2 = <\lambda^2> - <\lambda>^2$. Recall that the FWHM of a Gaussian distribution defined as $\Delta \lambda$ is given by $\Delta \lambda = 2(2\ln 2)^{1/2} \sigma_\lambda = 2.355 \sigma_\lambda$. In this case:

$$< \lambda^2 > = < \lambda >^2 \left[1 + \frac{1}{2.355^2} \left(\frac{\Delta\lambda}{<\lambda>} \right)^2 \right].$$ (15)

In order to simplify the notation, ($\Delta\lambda/<\lambda>$) is often represented by ($\Delta\lambda/\lambda$).

Discussion

Wavelength calibration can be performed by either measuring a sample with a well-defined SANS peak or by the time-of flight method. The measured neutron wavelength agrees with prediction whereas it is hard to precisely predict the wavelength spread. Many time-smearing (or pulse-broadening) factors contribute to the uncertainty in wavelength spread. For example, increasing the chopper frequency decreases this time smearing. Time-of-flight calibration measurements are better performed with a high chopper frequency even if peaks corresponding to consecutive time frames overlap. It is easier to unravel what peak corresponds to what time frame than introduce a systematic uncertainty due to changing chopper frequency.

The finite depth of the detector volume in area detectors introduces more pulse broadening. Moreover, increasing the neutron wavelength decreases the sample-to-detector distance measurably (by as much as 1.27 cm equivalent to the active depth up to the anode plane in the area detector) because slower neutrons are stopped closer to the entrance side of the detection volume. This is due to the "1/v"-dependence of the neutron absorption cross-section in He-3.

Inserting neutron guides between the velocity selector and the sample (done to reduce the SANS source-to-sample distance) rounds off the edges of the neutron spectral distribution from a triangular shape to a Gaussian shape. This increases the wavelength spread.

Such "second order effect" corrections could include (1) slight variation of the wavelength spread with wavelength and with number of guides in the incident pre-sample flight path collimation, and (2) slight variation of the sample-to-detector distance with wavelength.

Some of the issues discussed here are essential in understanding the resolution of time-of-flight (TOF) SANS instruments located at pulsed neutron sources.

The Graphite Bragg Diffraction Edge

In order to independently check the wavelength calibration, it is nice to use other methods. The Bragg edge method is reliable. The Bragg law $\lambda = 2d \sin(\theta/2)$ relates the neutron wavelength λ, the d-spacing in the crystal d, and the scattering angle θ. The Bragg edge occurs when the incident neutrons are parallel to the crystal lattice planes. This is obtained when $\theta/2 = 0^o$ or 180°. There is a drop in diffraction intensity at that condition (neutrons are transmitted through and not diffracted). Note that the scattering angle is defined as θ in SANS terminology (not as 2θ as done in some diffraction books).

Polycrystalline graphite is characterized by a Bragg diffraction edge at 6.708 Å. Placing a graphite block in the neutron beam along with the time-of-flight setup gives an independent check of the wavelength calibration. A pencil detector and the area detector are used in the time-of-flight setup. The spectrum shown in the figure corresponds to a neutron wavelength around 6.7 Å, a source-to-chopper distance of 5.42 m, and a pencil detector-to-area detector distance of 6 m. Here only one pencil detector and the area detector are used. A chopper frequency of 70 Hz and a dwell time of 1 μsec were used. The first sharp peak corresponds to the pencil detector located just after the chopper. The broad peak corresponds to the area detector and shows the graphite edge. The second narrow peak corresponds to the next neutron pulse on the pencil detector.
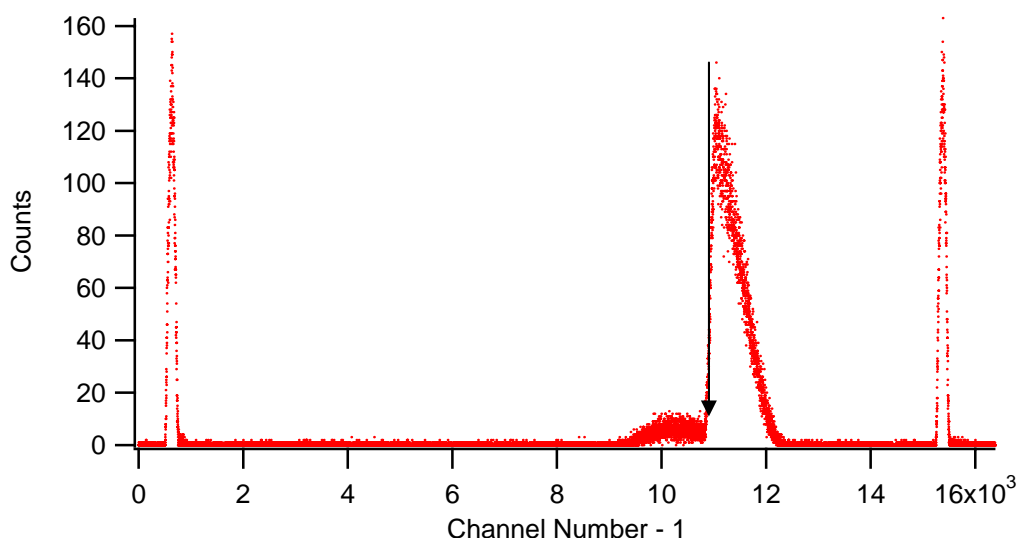
Figure 10: Time-of flight spectrum using a pencil detector and the area detector and placing a (4 cm thick) polycrystalline graphite block just after the pencil detector. Graphite is characterized by a sharp Bragg diffraction edge at 6.708 Å (located by the arrow).

4. OTHER WAVELENGTH CALIBRATION METHODS

There are other methods to calibrate the neutron wavelength based mostly on scattering samples that are characterized by Bragg peaks in the SANS range. Here Silver Behenate and Kangaroo tail tendon are discussed briefly.

Silver Behenate

Silver Behenate is characterized by a sharp Bragg ring with a d-spacing of 58.38 Å. It is useful for a "quick" wavelength check. It cannot, however, be used to determine the wavelength spread.
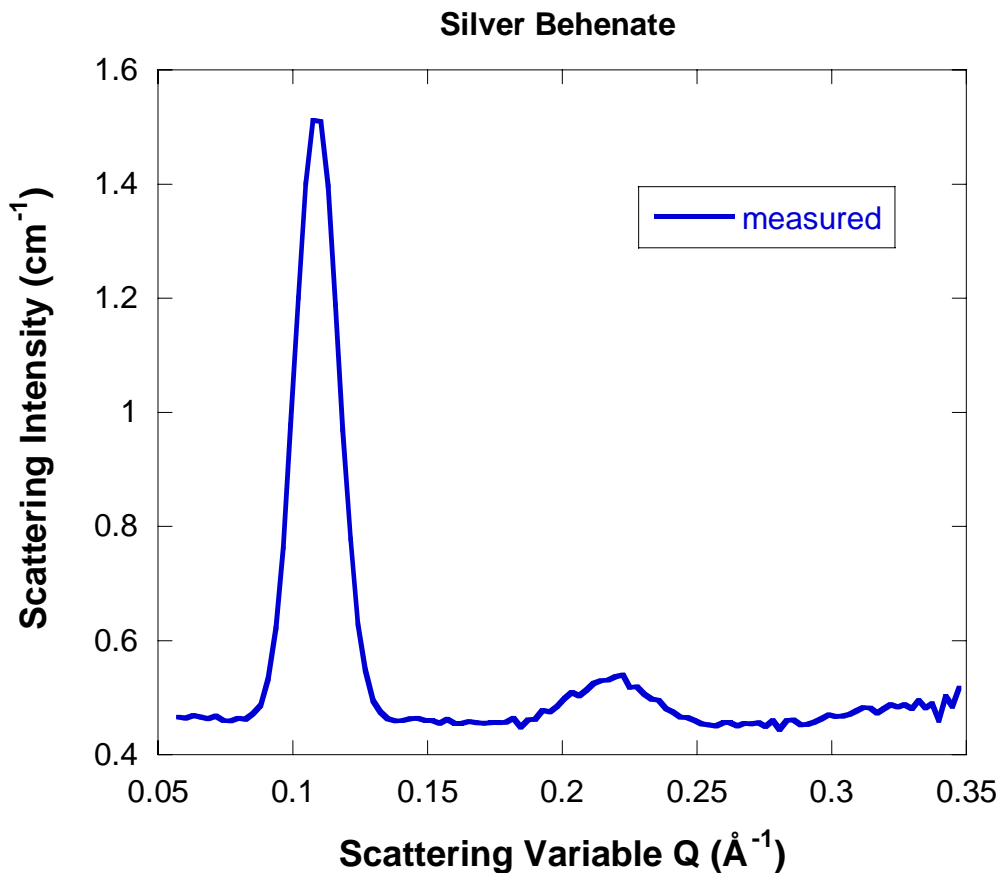
Silver Behenate

Figure 11: SANS spectrum from Silver Behenate showing a sharp first peak at Q = 0.01076 Å^{-1} (d-spacing of 58.38 Å).

Kangaroo Tail Tendon

Kangaroo tail tendon is characterized by a regular periodic structure along the fiber with a d-spacing of 667 Å. SANS scattering from Kangaroo tail tendon in D_2O is anisotropic. Sector averaging along the Bragg spots shows many order reflections. The first peak is strong, the second reflection is extinct and the third peak is well defined even with typical SANS smearing ($\Delta\lambda/\lambda = 0.13$).
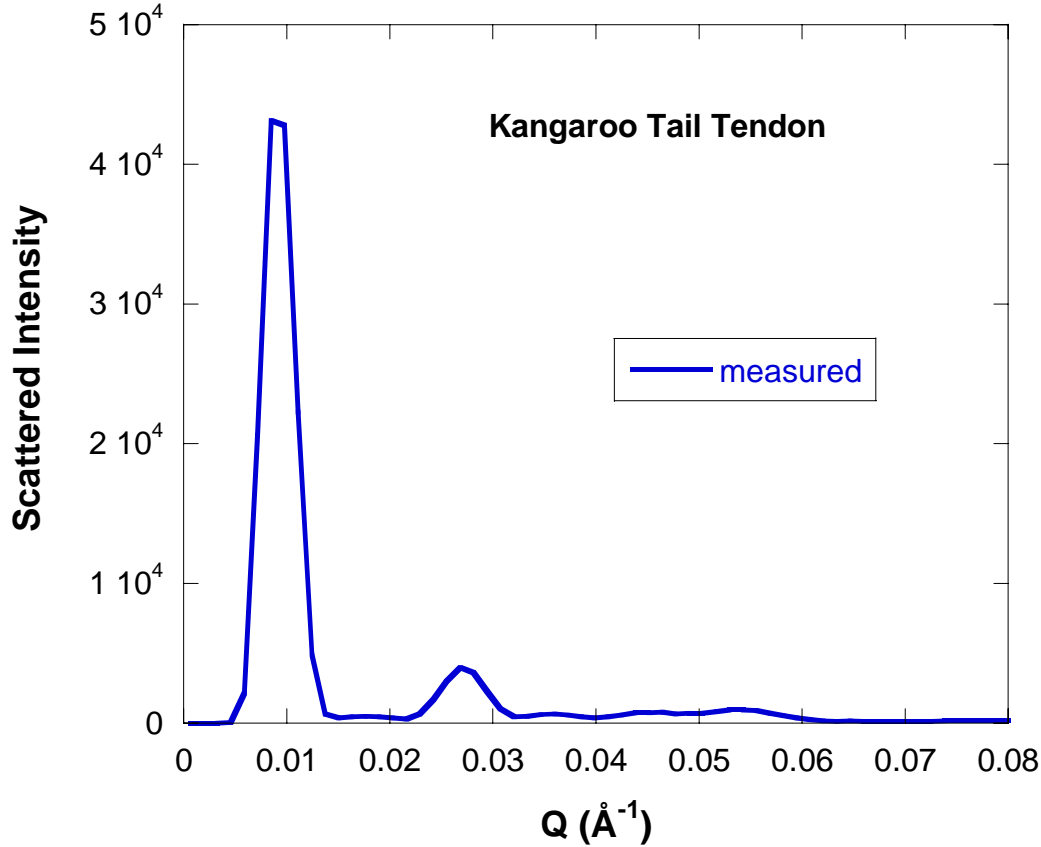
Figure 12: SANS spectrum from Kangaroo tail tendon characterized by a first sharp peak at $Q = 0.00942$ Å^{-1} corresponding to a d-spacing of 667 Å. The third order peak is also strong.

5. DISCUSSION

Monochromation is an essential step for SANS as well as other diffraction methods. Instruments located at pulsed neutron sources use the time-of-flight method. Continuous beam instruments use either velocity selectors or crystal monochromators. Velocity selectors are preferred because monochromation occurs without change in the incident beam direction. When using crystal monochromators, the entire SANS instrument has to be rotated horizontally around the crystal monochromator axis in order to change neutron wavelength. This is a prohibiting factor in guide halls where experimental space between close together guides is at a premium. An advantage of crystal monochromators is the tight wavelength spread due to the typically small mosaic spread of crystals. That spread can be widened by using superlayers of slightly misaligned crystals. Velocity selectors commonly cover a wide wavelength spread (from $\Delta\lambda/\lambda = 10$ % to 30 %). Crystal monochromations cover the lower scale (from $\Delta\lambda/\lambda = 0.1$ % to 5 %). The use of two velocity selectors in parallel (for either low or wide $\Delta\lambda/\lambda$) would be a nice option for both low-resolution and high-resolution SANS measurements.

REFERENCE

L. Rosta, Physica, "Multi-Disk Neutron Velocity Selectors", B156-157, 615-618 (1989).

B. Hammouda, "Multidisk Neutron Velocity Selectors", Nuclear Instruments and Methods in Physics Research A321, 275-283 (1992).

QUESTIONS

1. How does a velocity selector work?
2. How does a crystal monochromator work?
3. What is the main feature of a SANS instrument that uses a crystal monochromator?
4. Does the velocity selector transmission vary with neutron wavelength?
5. Does the predicted wavelength spread vary with neutron wavelength?
6. What is the wavelength dependence of the neutron spectrum before and after the velocity selector?
7. What is the purpose of tilting a velocity selector to an angle with respect to the neutron beam? What is the range of effective tilt angles?
8. How would you measure the transmission of a velocity selector?
9. What are the main pieces of equipment necessary to perform time-of-flight measurements?
10. What samples are characterized by sharp peaks in the SANS range and could be used for cold neutron wavelength calibration?
11. The standard deviation of a Gaussian distribution σ can be related to its full-width at half maximum (FWHM) by $FWHM = 2(2\ln2)^{1/2}\sigma$. Derive this factor.
12. Velocity selectors transform the neutron wavelength distribution from Maxwellian tail to a triangular distribution. Why is that?
13. Assuming a triangular wavelength distribution outputted by a velocity selector calculate the variance $\sigma_\lambda^2 = <\lambda^2> - <\lambda>^2$.
14. What causes a Bragg diffraction edge? Bragg diffraction edges occur at what wavelengths for graphite and for beryllium?
15. Find out possible suppliers of velocity selectors. What are the essential characteristics to provide that the supplier requires.
16. Find out possible suppliers of neutron choppers, pencil detectors and multi-channel scalers.

ANSWERS

1. A velocity selector works by letting through only neutrons of the right speed.
2. A crystal monochromator uses the Bragg law of diffraction. It works by scattering neutrons of a certain wavelength into a specific scattering angle.
3. A SANS instrument that uses a crystal monochromator has to pivot around the vertical monochromator axis in order to change the neutron wavelength.
4. The predicted velocity selector transmission does not vary with wavelength.
5. The predicted wavelength spread does not vary with wavelength.

6. The tail of the Maxwellian neutron spectrum from the cold source varies like $1/\lambda^5$ whereas after the velocity selector the spectrum varies like $1/\lambda^4$ where λ is the neutron wavelength.

7. Velocity selectors are tilted horizontally in order to vary the wavelength spread. Tilt angles vary between -3 $^\circ$ to +3 $^\circ$.

8. The transmission of a velocity selector could be measured similarly to the transmission of any SANS sample, by using a second selector operating at the same wavelength at the sample location. Transmission is the ratio of the detector counts with the selector in over that with the selector out.

9. Time-of-flight measurements can be performed using a chopper, two detectors positioned a known distance apart and a multi-channel scaler gated with the time zero from the chopper.

10. Examples of samples that are characterized by sharp peaks in the SANS range include: Silver Behenate, phase separated copolymers, fibers like collagen from a Kangaroo tail tendon, highly packed silica or latex particles.

11. Consider a Gaussian function $P(\lambda) = (1/2\pi\sigma^2)^{1/2} \exp(-\lambda^2/2\sigma^2)$ where σ is the standard deviation. Setting $P(\lambda) = \frac{1}{2}$, two solutions can be found for $\lambda = \pm \sqrt{2\ln(2)}\ \sigma$. This yields a band FWHM $= \Delta\lambda = 2\sqrt{2\ln(2)}\ \sigma = 2.355\sigma$.

12. The output of a velocity selector is a triangular wavelength distribution because of the geometry of neutron trajectories through the selector windows.

13. Consider an isosceles triangular distribution of FWHM $\Delta\lambda$ (and base $2\Delta\lambda$) and centered at a wavelength λ_0. The left side of the triangle is given by $F(\lambda) = (\lambda-\lambda_0)/\Delta\lambda + 1$. The right side of the triangle is given by $F(\lambda) = (-\lambda+\lambda_0)/\Delta\lambda + 1$. The variance $\sigma_\lambda^2 = <\lambda^2>-<\lambda>^2$ involves the following integrations $\sigma_\lambda^2 = <\lambda^2>-<\lambda>^2 =$

$$\frac{\int\limits_{\lambda_0-\Delta\lambda}^{\lambda_0} d\lambda\lambda^2\left(\frac{\lambda-\lambda_0}{\Delta\lambda}+1\right) + \int\limits_{\lambda_0-\Delta\lambda}^{\lambda_0} d\lambda\lambda^2\left(\frac{-\lambda+\lambda_0}{\Delta\lambda}+1\right)}{\Delta\lambda} = \frac{1}{6}(\Delta\lambda)^2.$$

14. A Bragg diffraction edge occurs when the incident neutrons are parallel to the crystal lattice planes and the crystal is probed edgewise. Bragg diffraction edges for graphite and beryllium occur at neutron wavelengths of 6.708 Å and 4.05 Å respectively.

15. Possible suppers of velocity selectors are the KFKI Hungarian and the Dornier German companies.

16. There are many suppliers of choppers and a wide range in prices. For multi-channel scaler suppliers, the name Ortec comes to mind. Neutron pencil detectors are sold by Reuter Stokes and by Lehnard Neutron Detector (LND). Both are companies based in the USA.

Chapter 13 - **NEUTRON AREA DETECTORS**

1. NEUTRON DETECTOR BASICS

Two-dimensional area detectors are essential components for SANS instruments. The position sensitive detection is achieved in one of two ways. (1) Delay line detectors sense the position of the detection event through the time delay at both ends of each cathode. Only two winding cathodes wires (one for X and one for Y positioning) are used. (2) The other (and most used) detection scheme uses the coincidence method whereby only X and Y events that arrive in time coincidence are counted. This last method uses 128 wires for X and 128 wires for Y cathodes and can handle higher count rates.

Most neutron area detectors use ^{3}He as the detection gas that undergoes the following nuclear reaction:

$$^1n_0 + {}^3He_2 \rightarrow {}^1H_1 + {}^3H_1 + 765 \text{ keV} \qquad\qquad (1)$$
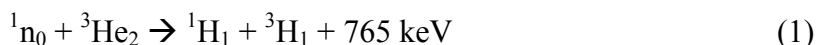
The reaction products consist of two charged particles: a proton ($^1H_1$) and a triton ($^3H_1$) released in opposite directions with a combined kinetic energy of 765 keV. This kinetic energy is dissipated by ionization of the proportional counting gas (CF_4 mostly). Since the incident neutron kinetic energy is very small (1/40 eV for thermal neutrons), thermal neutron detectors cannot measure neutron energies; they can measure only detected neutron positions. The released charged particles are attracted by the anode plane high voltage and liberate electrons. These are accelerated towards the anodes and therefore create a detection cloud through secondary ionization (charge multiplication). The two cathode planes (for detection in X and Y) are located on both sides of the anode and are kept at a low bias voltage in order to increase detection behind the cathodes. The detection cloud which is created close to the anode induces a charge on the closest cathodes (through capacitive coupling) which can be sensed by the charge sensitive preamplifiers. An X-Y coincidence pair is then selected and processed as real event.

The two main suppliers of neutron area detectors are CERCA (Grenoble, France) and ORDELA (Oak Ridge, Tennessee, USA). Both types of area detectors use the coincidence method. The NIST Center for Neutron Research SANS group has experience with both detector types.

2. NEUTRON AREA DETECTOR SPECIFICS

The ^{3}He/CF_4 gas mixture is kept at high pressure (2.4 Bars = 243 kPa) inside the detection chamber. An additional detector "dome" chamber filled with neutron transparent ^{4}He is added in front of the detection chamber in order to equilibrate pressure on both sides of the entrance window. This helps avoid the use of thick detector entrance windows that would attenuate the scattered neutrons beam. The detector localization gap (distance between the two cathodes) is 1.5 cm and the total detection gap is 2.5 cm.

In the CERCA detector, both anode and cathode wires are made out of a CuBe alloy. Each cathode consists of a band of nine narrowly spaced stretched wires; the bands themselves are spaced 1 cm apart (center-to-center). The ORDELA detector comprises one wire per cathode.

The active detection area of typical neutron area detectors is 64 cm*64 cm with a spatial resolution of either 1 cm*1 cm for the CERCA detector or 0.5 cm*0.5 cm for the ORDELA unit. The detector efficiency is high (around 75 %) for typical neutron wavelengths (around λ = 6 Å). Count rates of order $5*10^4$ counts per second over the whole detector are achieved.
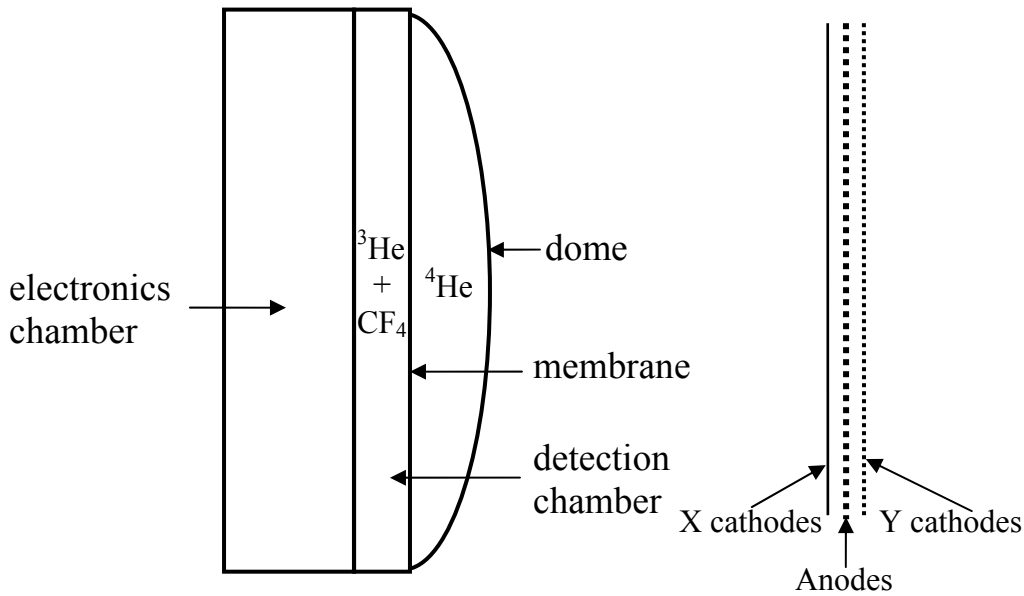
Figure 1: Schematic representation of a neutron area detector. This figure is not to scale. The detection chamber is 2.5 cm wide and 64 cm high.

Because the detector operates inside an evacuated chamber, and in order to avoid using a large number of vacuum feed-throughs for the cathode signals, all of the signal processing is performed using electronics that are mounted on the back of the detector. The detection electronics chain comprises amplification of the analog signals for each cathode wire, monitoring of X-Y coincidences and encoding to produce a digital signal which is sent out to the data acquisition system.

3. NEUTRON MEASUREMENTS

Measurements of the performance of area detectors have been conducted on both CERCA and ORDELA type detectors. Results for one or the other type are described in each of the following sections. All measurements were made using a monochromatic neutron beam.

Pulse Height Spectrum

The pulse height spectrum is measured using a multi-channel analyzer (MCA). A figure shows the pulse height spectrum of the anode plane measured on a CERCA detector at a high voltage of 2550 V. A narrow neutron peak with a resolution of about 16 % (FWHM divided by the average peak position) is observed. This main peak corresponds to the 765 keV energy released as kinetic energy during neutron capture by ^{3}He. That energy is split into 191 keV for the triton ^{3}H and 574 keV for the proton ^{1}H. When the detection reaction occurs close to the detector wall, one of the products (either the proton or the triton) ends up absorbed in the wall while the other one deposits its kinetic energy in the stop gas. This "wall effect" is manifested by two more peaks and the long plateau region. The triton peak can be observed at 191 keV but the proton peak has merged with the main neutron peak and cannot be resolved. The low pulse height noise is due mainly to low energy electrons that are knocked off by gamma rays that are absorbed in the detector walls. The main neutron peak at 765 keV corresponds to both proton and triton being absorbed in the detection gas.
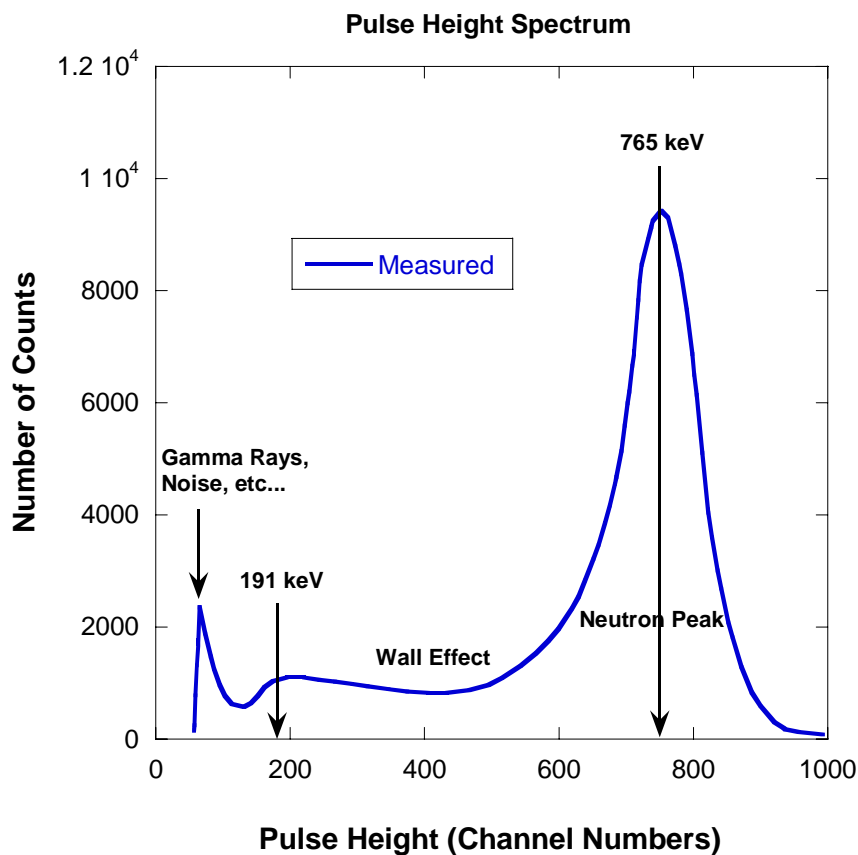
Figure 2: The anode pulse height spectrum for a CERCA detector showing a sharp neutron detection peak and low noise. The horizontal scale is in arbitrary MCA channel numbers and represents the pulse heights (measured in mV to represent the absorbed energies in keV).

Gas Multiplication Factor

Using the variation of the anode pulse height for increasing detector high voltage yields the gas multiplication curve and the gas multiplication factor which represents the number of charges produced by the detection of one neutron. Figure 3 shows measurements made on the CERCA detector. In order to express this variation in an absolute scale, an electronics pulse equivalent to the absorption of one neutron (i.e., the creation of a charge of 0.0035 pC) is injected into the anode plane. Measuring the amplified output of this signal on the cathodes and comparing it to that output during "normal" detector operation yields a gas multiplication factor of 117 at a high voltage setting of 2700 V.
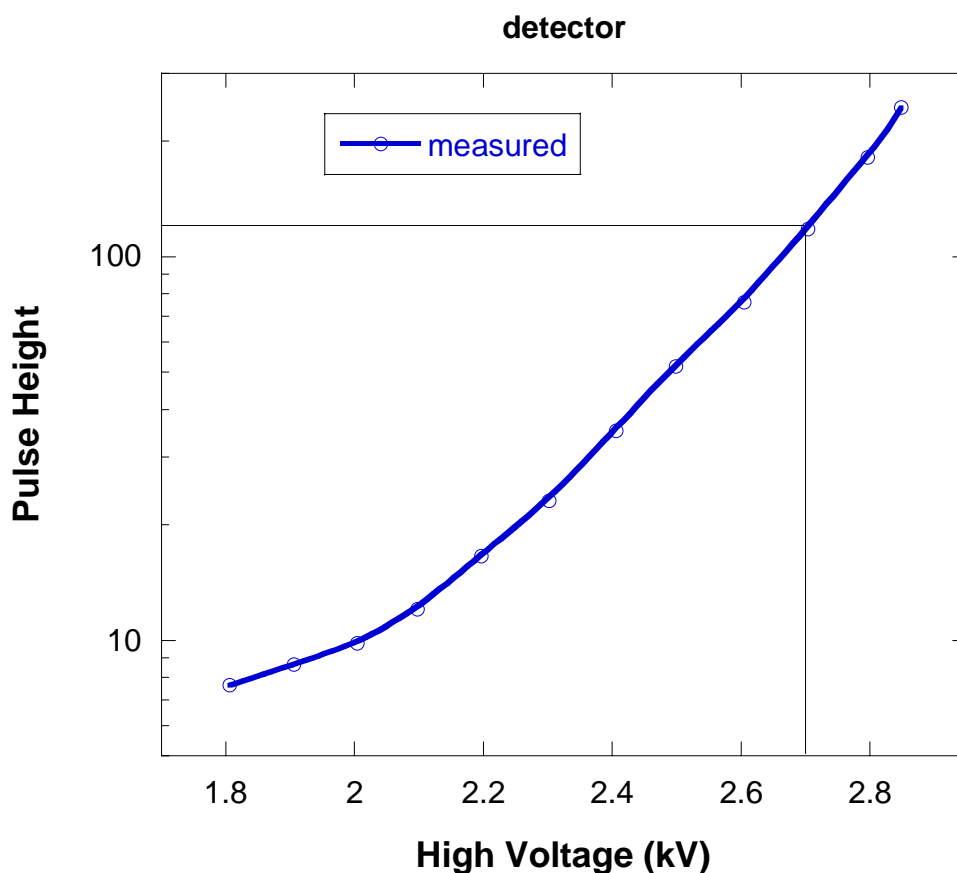
detector

Figure 3: Variation of the gas multiplication factor with high voltage.

Amplifier Gain and Threshold

The detection electronics chain comprises a preamplifier then an amplifier for each cathode. The preamplifier plays the role of impedance matching mostly. The amplifier gain and lower level discrimination (LLD) settings must produce "healthy" amplified analog signals around 1 V in height.

Gain adjustments on the cathode amplifiers are made using a square wave signal (20 mV amplitude) injected into the anode plane and equalizing the output signals from the various cathodes. Final adjustments are made in a normal operation condition using a uniform scatterer such as (1 mm thick) plexiglass or water characterized by mostly incoherent (Q-independent) scattering.

Setting of the LLD also called "threshold" is described here for the CERCA detector. At the chosen high voltage setting of 2700 V, the LLD value is estimated by measuring the total detection count rate on the cathodes for increasing values of the LLD as shown in Figure 4. At low LLD settings, the electronics system is paralyzed by the processing of low amplitude noise, while at high LLD values, the count rate decreases due to the loss of neutrons detection events; this gives a reliable operating LLD around 275 mV.
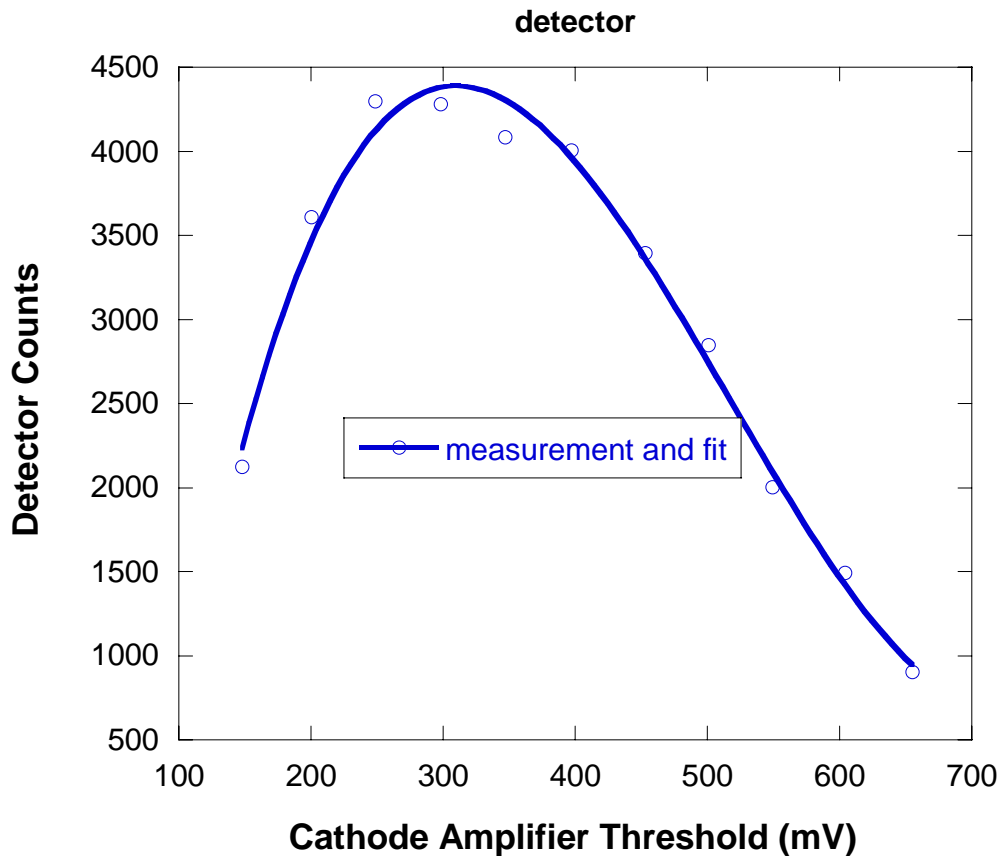
detector

Figure 4: Setting of the cathode amplifier LLD (threshold) level. Optimal level is around the peak.

The Detector Proportional Region

Neutron detectors are "proportional" counters because the total amount of charge created remains proportional to the amount of charge liberated in the original neutron detection event. The neutron detector proportional counting region is mapped out by monitoring increases in detector count rate for increasing high voltage. A convenient operating high

voltage is chosen in the proportional region and well below the "plateau" region as shown in a figure for a CERCA detector.
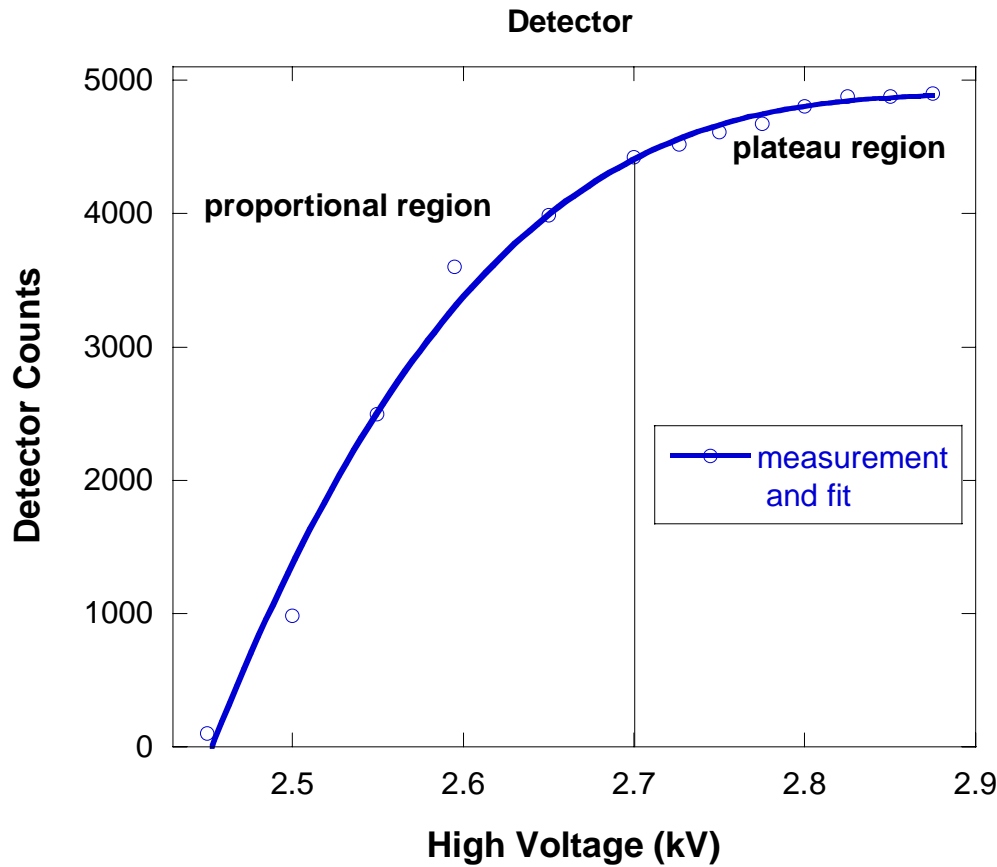
Detector

Figure 5: Determination of a convenient operating high voltage in the proportional region.

Spatial Resolution

Position sensitive detectors are characterized by their spatial resolution. The spatial resolution for a CERCA detector is determined as follows. Using a narrow (1 mm*2.54 cm) vertical slit to define a neutron beam, a scan of the detector response along the X cathodes is made by recording the count rates of individual cathodes when the detector is moved stepwise perpendicular to the neutron beam. Counts for two adjacent cathodes are shown in a figure. The detector spatial resolution is confirmed to be 1 cm and the counting efficiency is seen to remain reasonably constant within each detection band. This is seen by summing up counts for the two adjacent cathodes.
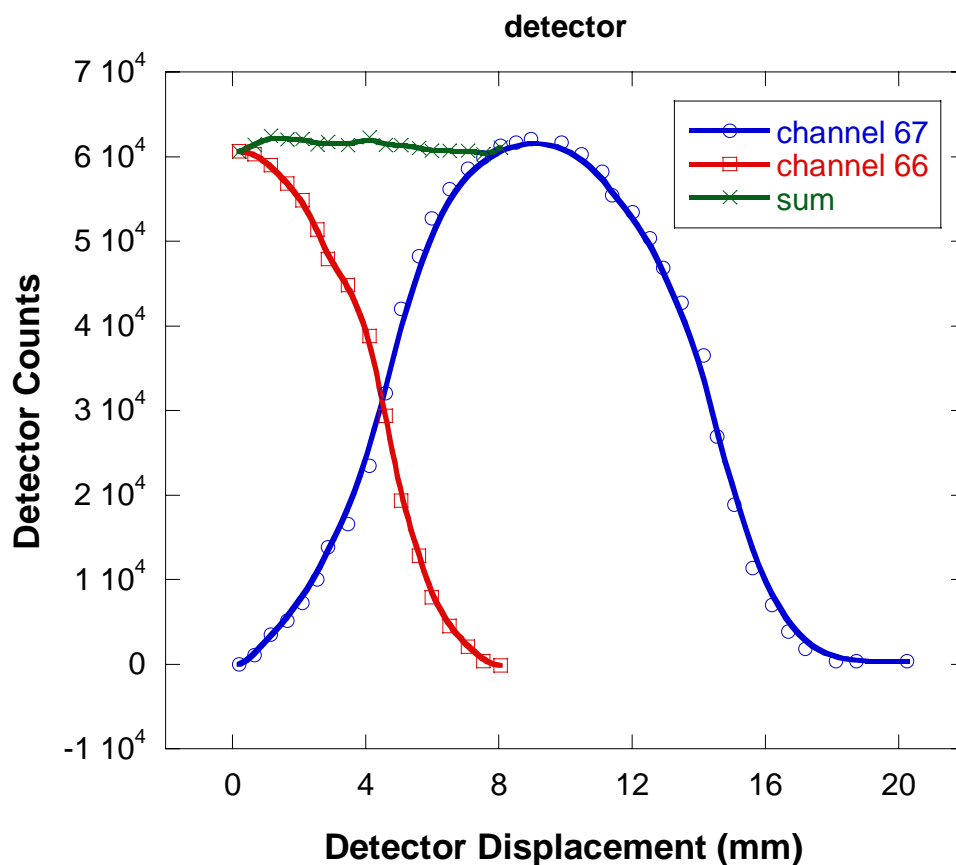
Figure 6: Determination of the detector spatial resolution.

Detector Efficiency

The detector absolute efficiency is measured using another (pencil) detector of known efficiency. The high gas pressure in the pencil detector gives it a very high efficiency at all wavelengths making it nearly "black". The detector efficiency was measured for an ORDELA detector and shown here. The ^{3}He neutron absorption cross section increases with wavelength ("1/v" absorber). This combined with various losses gives the observed variation.

Detector Efficiency Measurement
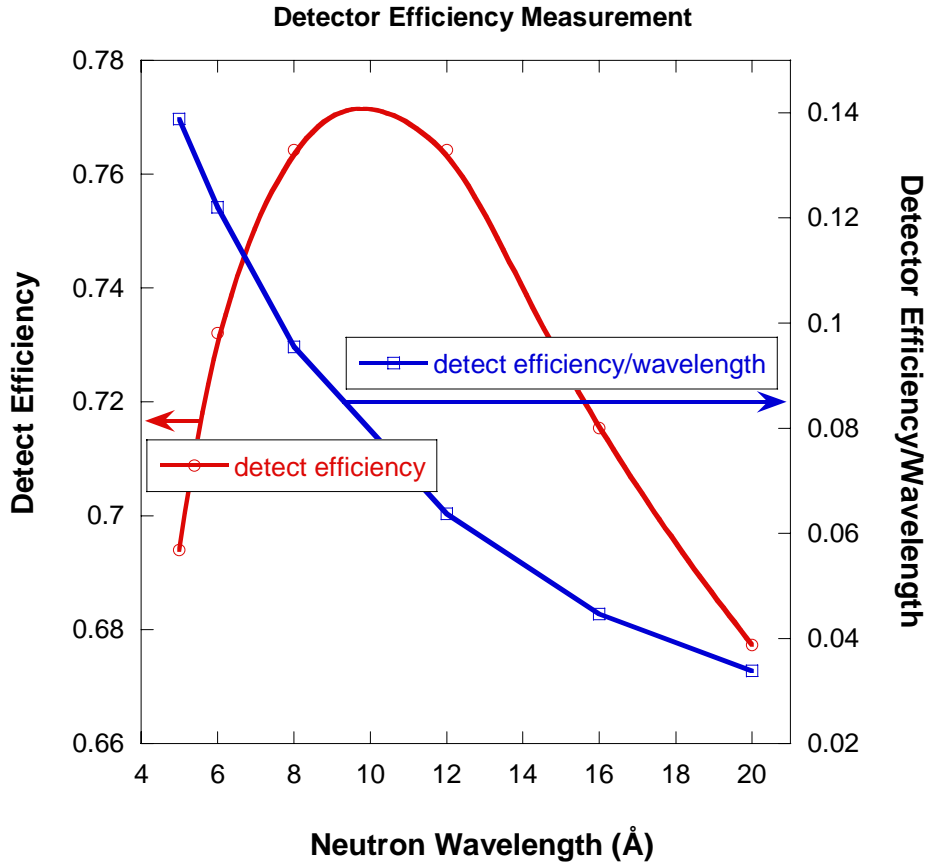
Figure 7: Variation of the detector efficiency (left axis) with increasing wavelength. Performing the "1/v" absorber correction involves dividing by the neutron wavelength (right axis).

Estimation of Dead Time

Dead time is inherent in most detection systems. Defining the "true" neutron current as N_T, the "measured" count rate as N_M and the detection rate time constant as τ, the following can be calculated. The fraction of total time for which the detector is dead is $N_T\tau$, and the rate at which true events are lost is $N_M N_T\tau$. That rate of loss is also given by $N_T - N_M$ so that:

$$N_T - N_M = N_M N_T \tau \qquad (2)$$

This assumes "nonparalysable" systems whereby the detection system does not get paralysed by detected events. It keeps counting during signal processing. The true current rate is therefore estimated as:

$$N_T = \frac{N_M}{1 - N_M \tau} \ . \qquad (3)$$

Consider two measurements made with two different source apertures. These correspond to N_{T1} and N_{T2} and N_{M1} and N_{M2}. The ratio $R_T = N_{T1}/N_{T2}$ can be expressed in terms of the ratio $R_M = N_{M1}/N_{M2}$ as follows.

$$R_T = R_M \frac{1 - N_{M2}\tau}{1 - N_{M1}\tau}. \qquad (4)$$

Or:

$$R_M = R_T + \tau N_{M1}(1-R_T). \qquad (5)$$

Plotting R_M *vs* N_{M1} would yield a linear behavior with intercept R_T and slope $m = \tau(1-R_T)$. The dead time τ can therefore be obtained from $\tau = m/(1-R_T)$.

In order to implement this procedure, the following measurement method is followed for an ORDELA detector. A set of two beam defining (sample) apertures of 1.27 cm and "effective" 2.27 cm diameters are used in turn. The neutron current crossing each of them is measured for different attenuation conditions. Different thickness plexiglass pieces are used to attenuate the neutron beam. The neutron currents are measured as count rates on the detector. An isotropic scatterer (thick piece of plexiglass) is used to "diffuse" the neutron beam therefore broadening the neutron spot on the detector. Plotting the ratio of the count rates for the two apertures with increasing count rate (for the 1.27 cm aperture) yields a linear behavior as shown in a figure. The intercept R_T is of course close to the ratio of aperture areas $R_T = (1.27/2.27)^2 = 0.313$ and the slope is around $m = 3.535*10^{-6}$ sec giving an estimated dead time of $\tau = m/(1-R_T) = 5.16$ μsec. This is the dead time for the combined detector, detection electronics chain and data acquisition system.
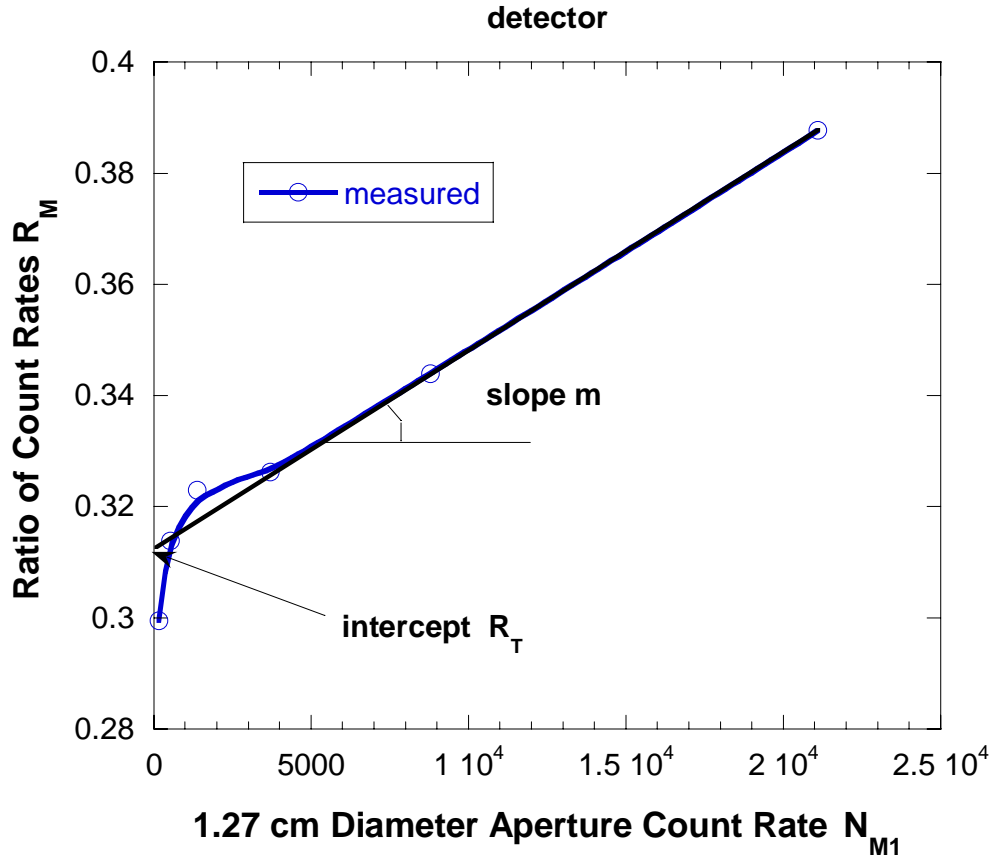
detector

Figure 7: The dead time is estimated as $\tau = m/(1-R_T)$ where m is the slope and R_T is the intercept on the linear part of the measured curve.

Using the estimated dead time of $\tau = 5.16$ μsec, detector losses can be estimated when count rates are increased. The relative (percent) loss factor is given by:

$$L = \frac{N_T - N_M}{N_T} = \frac{N_T \tau}{1 + N_T \tau} \qquad (6)$$
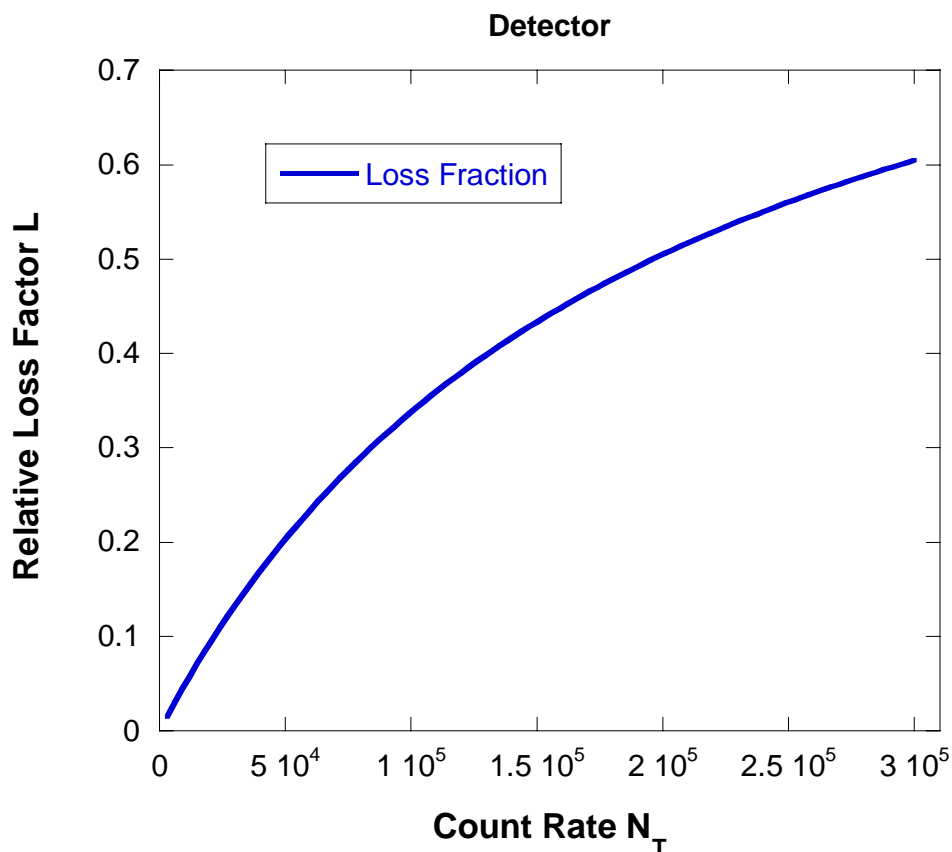
Figure 8: Percent loss factor as a function of count rate for a dead time of 5.16 μsec.

Table 1 gives estimates of dead time losses for increasing count rate.

Table 1: Estimation of dead time losses.

Count Rate N_T (counts per second)	Percent Loss Factor $L = (N_T - N_M)/N_T$
10,000 cps	4.85 %
30,000 cps	13.3 %
60,000 cps	23.4 %
90,000 cps	31.5 %

Detector Reliability

Using an intense localized neutron beam (> 10,000 cps), close inspection of the full 2D detector image shows whether miscoding "ghost" features are observed. These appear as faint spot "shadows" of the main neutron spot. Such shadows have been observed for both types of detector systems but are less severe in the ORDELA system. They are however not a problem since neutron area detectors operate in a less harsh neutron current condition.

4. OTHER NEUTRON DETECTORS

There are many types of other neutron detectors. Old type Boron (BF_3) neutron detectors are hardly ever used anymore due to safety considerations (the BF_3 gas is highly toxic). They have been replaced by He-3 detectors. Neutron scintillators use a converting plate made of a neutron absorbing material (mostly Gd_2O_3) that emits gammas upon neutron absorption. The gamma rays are then detected as any other photons would through the use of photomultipliers. Neutron scintillators are very sensitive to gamma ray background.

Fission chambers are used as neutron beam monitors. They use a thin plate of fissile material (mostly ^{235}U) that releases two highly energetic fission fragments upon fission reaction with a total kinetic energy of 2 MeV. Fission chambers have very low efficiency (of order 10^{-4}) but large signal to noise ratios due to the high degree of ionization generated in the gas.

Note that the absorption cross section in neutron detectors varies inversely with neutron speed (1/v absorber) or linearly with neutron wavelength $\sigma_a(\lambda)$. Assuming a flat detection volume of thickness d and an atomic density ρ (number of absorbing atoms per cm^3), the detector efficiency is estimated as 1-T where T is the transmission through the detection volume and is given as $T = \exp[-\rho.\sigma_a(\lambda).d]$.

Table 2: Comparing a few characteristics for three types of neutron detectors. The B-10 and the He-3 types are proportional counters. The Li-6 type is a scintillator.

Detector Type	B-10(n,α)Li-7	He-3(n,p)T-3	Li-6(n,α)T-3
Energy of Reaction	2.79 MeV	0.76 MeV	4.78 MeV
Charged Particles Energies	α = 1.77 MeV Li = 1.01 MeV	p = 0.57 MeV T = 0.19 MeV	T = 2.73 MeV α = 2.05 MeV
Particles Range	α = 3 mm Li = 2 mm	p = 30 mm T = 6 mm	T = 0.04 mm α = 0.007 mm
Emitted Gammas	0.48 MeV	None	None
Typical Thickness	5 mm	20 mm	2 mm
Atomic Density	$0.053*10^{20}$ cm^{-3}	$0.81*10^{20}$ cm^{-3}	$173*10^{20}$ cm^{-3}
Absorption Cross Section at 5 Å	10,67 Barn	14,83 Barn	2,62 Barn
Efficiency at 5 Å	3 %	80 %	100 %

REFERENCES

G. Knoll, "Radiation Detection and Measurement", John Wiley & Sons Inc. (1979).

P. Convert and J.B. Forsyth, "Position Sensitive Detection of Thermal Neutrons", Academic Press (1983).

L.H. Schwartz and J.B. Cohen, "Diffraction from Materials". Springer Verlag (1987).

G Marx, B. Hammouda, N. Thillosen, J. Jacobe, J.G. Barker and C. Glinka, "An ILL_Type Area Detector for SANS", private communication (1993).

QUESTIONS

1. What are the two main gases used to detect neutrons? Which one is the most used nowadays?
2. What are the reaction products when a neutron gets absorbed by a ^{3}He nucleus? How much energy is released during that nuclear reaction?
3. Why is ^{3}He referred to as a "1/v" absorber?
4. What is the pulse height spectrum of a detector? How is it measured?
5. What is the "wall effect" feature in a pulse height spectrum? What is the "neutron peak"?
6. What are the two basic ways of performing position sensing in position-sensitive neutron detectors?
7. How does the coincidence method of detection work?
8. What is the basic difference between a gas detector and a scintillator?
9. What is a fission chamber? How does it operate? What is it used for?
10. What are the two typical sizes of neutron area detectors used on SANS instruments? What is the typical detector spatial resolution?
11. Name four measurement tests for characterizing neutron area detectors?
12. How is the proportional detection region test performed? How is the multiplication gain factor test performed?
13. What is the gas multiplication factor?
14. How is the area neutron detector efficiency test performed?
15. How is the detector and electronics dead time test performed?
16. How is the spatial resolution test performed for neutron area detectors?
17. How to choose an operational threshold setting for an amplifier?
18. What is the percent loss for a non-paralysable detector system with 5.16 μsec dead time and 10,000 cps neutron current?
19. Why are the analog electronics modules mounted right on the back of area detectors used on SANS instruments?
20. What are the two major suppliers of neutron area detectors for SANS instruments?
21. Find out a possible supplier of multi-channel analyzers (MCAs)?

ANSWERS

1. Neutron detectors use either BF_4 or ^{3}He. BF_4 is no longer used because if is highly toxic.
2. The detection nuclear reaction in ^{3}He detectors is: $^1n_0 + {}^3He_2 \rightarrow {}^1H_1 + {}^3H_1 + 765$ keV.
3. ^{3}He is referred to as a "1/v" absorber because its absorption cross section varies like 1/v (v being the neutron velocity or speed). This absorption cross section increases with neutron wavelength.

4. The pulse height spectrum of a detector is the distribution of electronics signal amplitudes outputted by the detector electronics. It is measured using a multi-channel analyzer (MCA).

5. The wall effect represents nuclear reaction products (either proton or triton) hitting the detector wall. The neutron peak corresponds to both reaction products being entirely absorbed in the gas (no wall effect).

6. Position sensing is done either through the delay line method or the time coincidence method.

7. The coincidence method registers a real detected event when an X and a Y cathode signals arrive in coincidence (i.e., within a specified time window).

8. A gas detector uses a neutron absorbing gas (either BF_4 or ^3He) whereas a scintillator uses a neutron-absorbing solid (^6LiF or Gd_2O_3).

9. A fission chamber is a very low efficiency neutron detector. It uses fissionable material (^{235}U mostly) to detect neutrons. An energy of 2 MeV is released as kinetic energy for the fission fragments. Fission counters are used as neutron beam monitors.

10. Neutron area detectors used on SANS instruments are either 64 cm*64 cm or 1 m*1 m in area. The spatial resolution is either 1 cm* 1 cm or 0.5 cm*0.5 cm.

11. The various tests performed to characterize neutron area detectors are: pulse height spectrum, multiplication factor, amplifier gain and threshold settings, gas proportional region, spatial resolution, detector efficiency, detector and electronics dead time.

12. The gas proportional region is determined by increasing the HV and recording the number of detector counts (see Figure 5).

13. The gas multiplication factor represents the number of electrons released from the absorption of one neutron.

14. The area detector efficiency is measured using another 100 % efficiency pencil detector.

15. The dead time is measured using two different apertures and varying the count rate each time by inserting attenuators in the beam. The dead time is given by $\tau = m/(1-R_T)$ where m is the slope and R_T the intercept of the ratio of counts (for the two apertures) *vs* count rate.

16. The spatial resolution test is performed by stepping the area detector laterally (perpendicular) to a neutron beam defined through a thin vertical slit.

17. The threshold (also called lower level discriminator or LLD) level for an amplifier is chosen as that setting that gives the maximum number of neutron counts.

18. Eq (6) gives the formula and Table 1 gives the answer of L = 4.85 % loss for a dead time of 5.16 μsec and 10,000 cps neutron current.

19. Analog electronics modules are mounted right on the back of area detectors used on SANS instruments so that a minimum number of wires have to cross vacuum. The wires transmit detection signals to the data acquisition system (DAC) outside of the detector vessel (which is evacuated).

20. The two major suppliers of area detectors for SANS instruments are CERCA (Grenoble, France) and ORDELA (Oak Ridge, Tennessee, USA).

21. The company Canberra is a possible suppier of MCAs. A Google search with "multi channel analyzer suppliers" comes up with dozens of other possible suppliers.

Chapter 14 - **SAMPLE ENVIRONMENTS**

A number of sample environments are available for SANS measurements. These consist in standard cells and cell holders that can be heated (up to 300 ^{o}C) using heating cartridges or cooled (down to 0 ^{o}C) using circulating baths. Between 0 ^{o}C and 10 ^{o}C, the sample chamber must be evacuated and/or filled with inert gas (nitrogen or helium) in order to avoid condensation on the cooling block. A host of special sample environments are also available at the NIST CNR. These include in-situ pressure cells, in-situ (Couette or plate/plate) shear cells as well as a rheometer, electromagnets (up to 2 Teslas), a superconducting magnet (9 Teslas), low temperature closed cycle helium refrigerators for temperatures down to 5 K, and a furnace for temperatures up to 450 ^{o}C. Only a few highly used pieces of equipment are described here.

1. STANDARD SAMPLE CELLS

SANS measurements involve a variety of different cells. The first type is the standard off-the-shelf "banjo cell" owing to its characteristic shape. This type is used for photon scattering as well and has quartz windows (transparent to both neutrons and light). Their diameter is 2 cm and a gap with a sample thickness of either 1 mm or 2 mm corresponding to a sample volume of 0.3 ml or 0.6 ml respectively. This type of cell is appropriate for liquid samples that can be handled using a syringe.

The second type of cell used for SANS has grown out of successive iterations at the NIST CNR. It is of the demountable type with titanium body and quartz windows. An inner spacer ring of thickness either 1 mm or 2 mm is part of the cell body and sets the sample gap. The sample thickness is uniform between the two quartz windows. Sealing is performed through back up o-rings and tightening retainers on each side. This type of cell can handle liquids, gels, wafers and powders. Gel and powder samples are loaded from one side after tightening the retainer piece on the other side. Slightly larger volumes than for banjo cells are required.
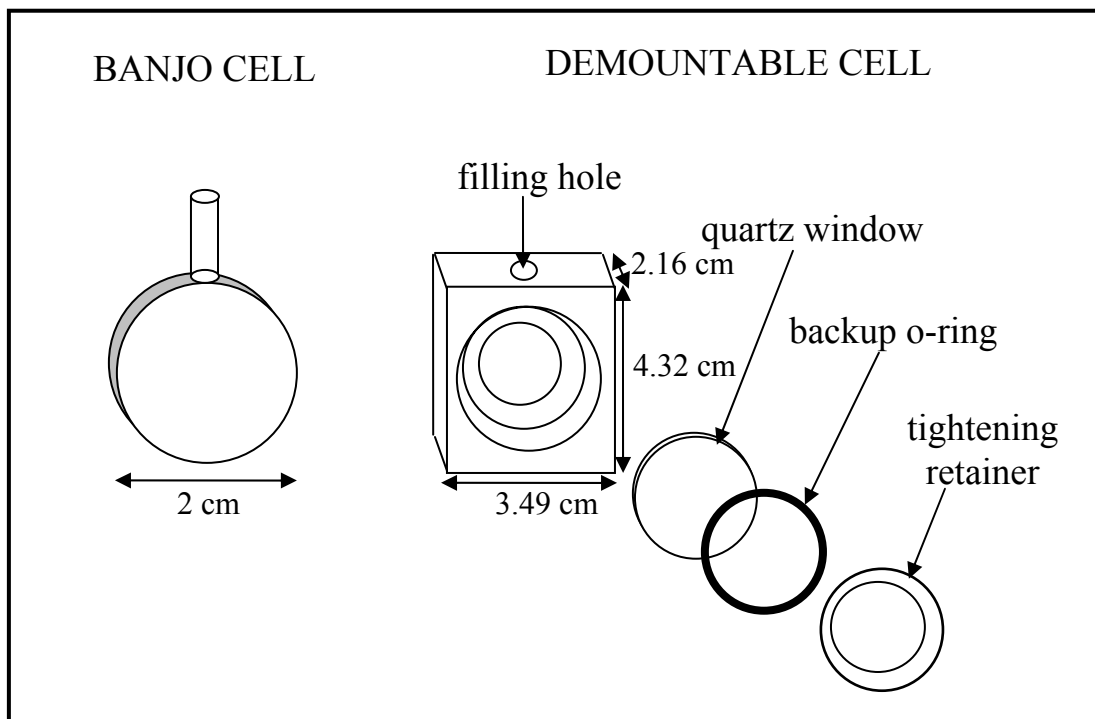
Figure 1: Sample holder cells used for SANS at the NIST CNR.

2. HEATING AND COOLING BLOCKS

A 7-position heating block made out of aluminum is used for temperature control. It uses two pieces of bakelite at the base to thermally decouple the main heated block from the other pieces in the sample chamber. This heating block controls temperature between ambient and 300 $^{\circ}$C with a precision of less than 1 $^{\circ}$C. The actual sample temperature lags slightly behind the block temperature. A resistance temperature detector (RTD) is used to monitor the block temperature.
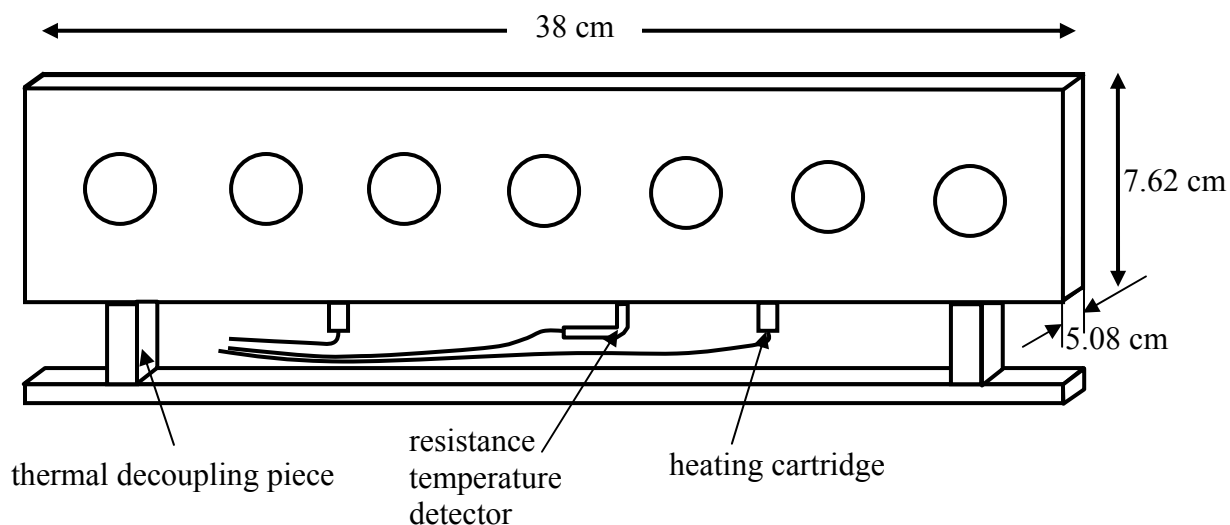
Figure 2: A 7-position heating block using heating cartridges and an RTD to monitor the temperature.

A similar (10-position) block uses flow of coolant instead (50 % water and 50 % antifreeze) to cool samples down to 0 $^{\circ}$C. The heating range for that block is limited to 90 $^{\circ}$C. Another heating/cooling block uses silicon oil to reach an even wider temperature range (up to 150 $^{\circ}$C).

3. THE PRESSURE CELL

Two generations of pressure cells for in-situ SANS measurements were designed to handle polymer samples. The polymer wafer is first melt pressed inside a metal ring to set a uniform thickness (of 1 mm). This produces a homogeneous clear sample. The right amount of sample (0.3 ml) is used in order to fill the available volume. This wafer is then transferred to the middle of a confining o-ring. The "encapsulated" o-ring (flexible rubber for the inside and Teflon coating for the outside) transmits pressure from the pressurizing fluid (water in this case) to the sample. The sample is also confined between two sapphire windows with a 1 mm gap between them. The cell body is made out of Iconel metal (75 % nickel, 15 % chromium) which is good for its high corrosion resistance and tensile strength at high temperatures. The pressure cell is surrounded by a heating jacket using heating cartridges for temperatures from ambient to 160 $^{\circ}$C. Another (cooling) jacket uses a circulating fluid to reach down to 10 $^{\circ}$C. The second generation pressure cell can handle up to 3 kbar pressures.

The pressurizing system consists of a pressure pump, two remotely controlled valves, high pressure tubing, two gauges, etc. The pump and the two valves are computer controlled and use a feedback signal from the digital gauge. The pressuring system and the main SANS data acquisition system follow a handshake protocol through a two bits process ("acknowledge" and "release" lines). When using a liquid sample, a separator is inserted between the pump

and the pressure cell. This consists of a cylindrical tube with a piston inside to separate out the pressurizing fluid from the liquid sample.
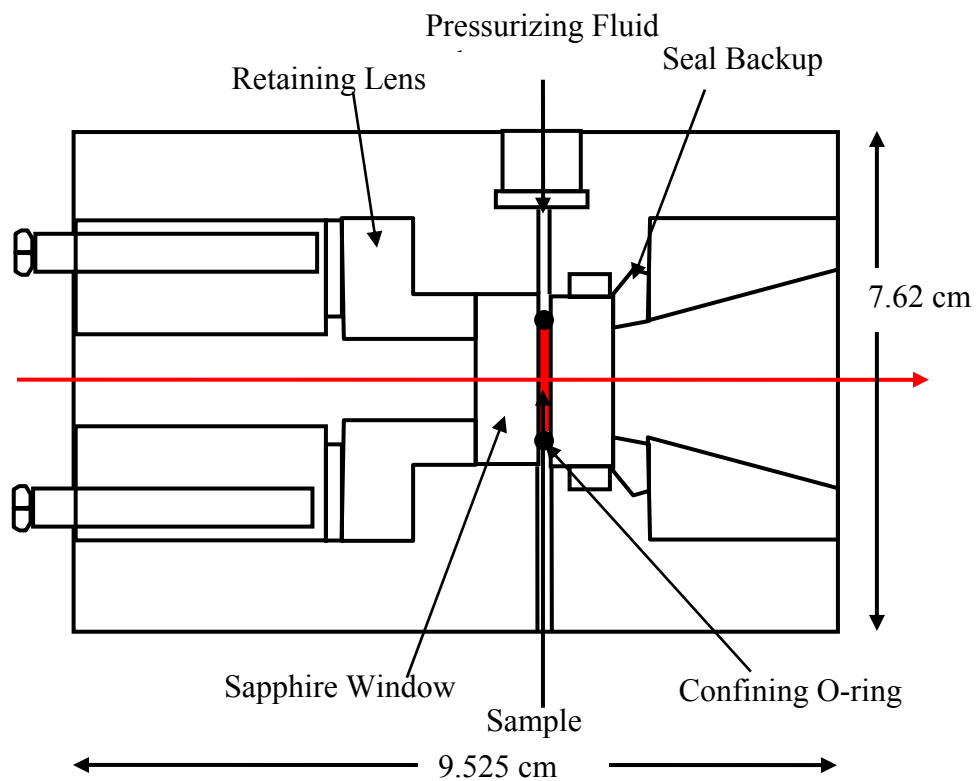

Figure 3: The first generation pressure cell for in-situ pressure measurements.
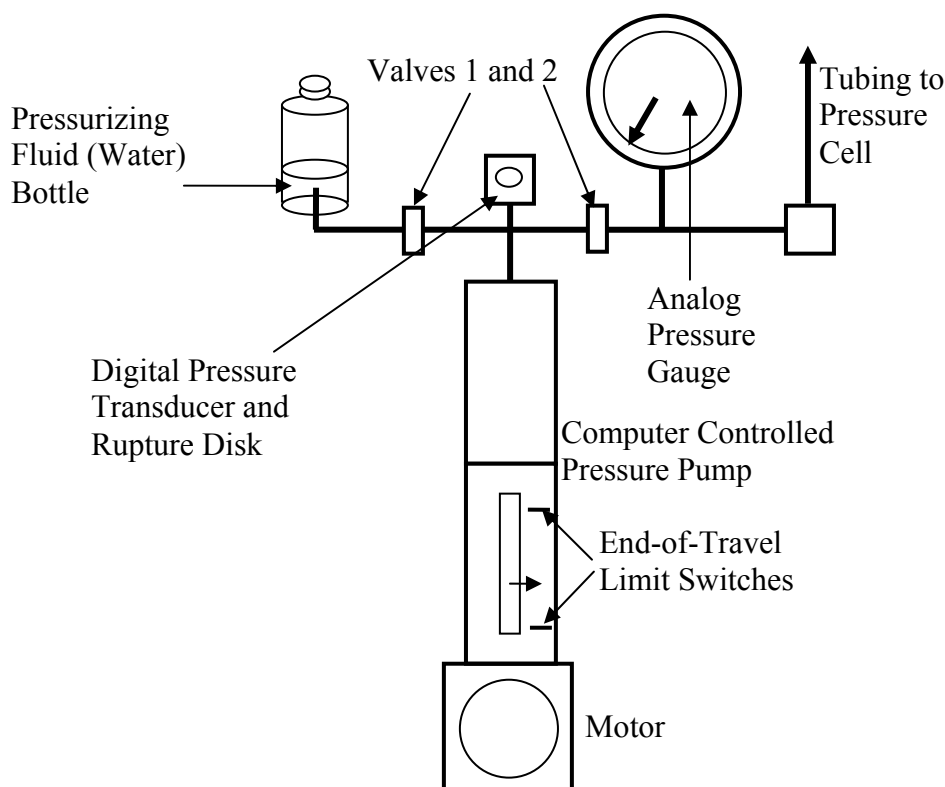
Figure 4: Schematic representation of the pressure cell system including the computer controlled pump and valves, the pressure transducer, the main gauge, and the various high pressure tubing. Note that the pressurizing fluid bottle is standing vertical (out of the page).

4. THE COUETTE SHEAR CELL

The Couette shear cell used for in-situ SANS measurements is a simple device for aligning samples. It consists of a stator which is lowered into a rotor cup to shear liquid samples within the 0.5 mm gap. Note that the neutron beam crosses the gap twice. The stator and the rotor are made out of quartz. The rotor base is made out of a material called Invar which has a thermal expansion coefficient similar to quartz. A set of x-y translation Verniers allows the precise alignment of the stator with respect to the rotor. The rotor cup takes about 12 ml. When the stator is lowered, the fluid sample level rises (in the gap between the stator and rotor) until it covers the neutron beam level.

The shear cell is used in one of two main geometries: (1) the radial mode whereby the 1.27 cm diameter neutron beam goes through the middle of the cell and (2) the tangential mode whereby a vertical slit (1.27 cm*0.3 mm) defines the neutron beam incident tangential to the cell.

This shear cell has been used for easily flowing liquids as well as for highly viscous fluids. Temperature control is performed using a circulating fluid. Coolant circulates inside the stator without getting in the neutron beam. Cell temperature can be controlled from 10 ^{o}C up

to 90 °C. The shear cell is used in either the steady shear mode or the reciprocating shear (or jiggle) mode. Shear rates up to 5,000 Hz for are possible.
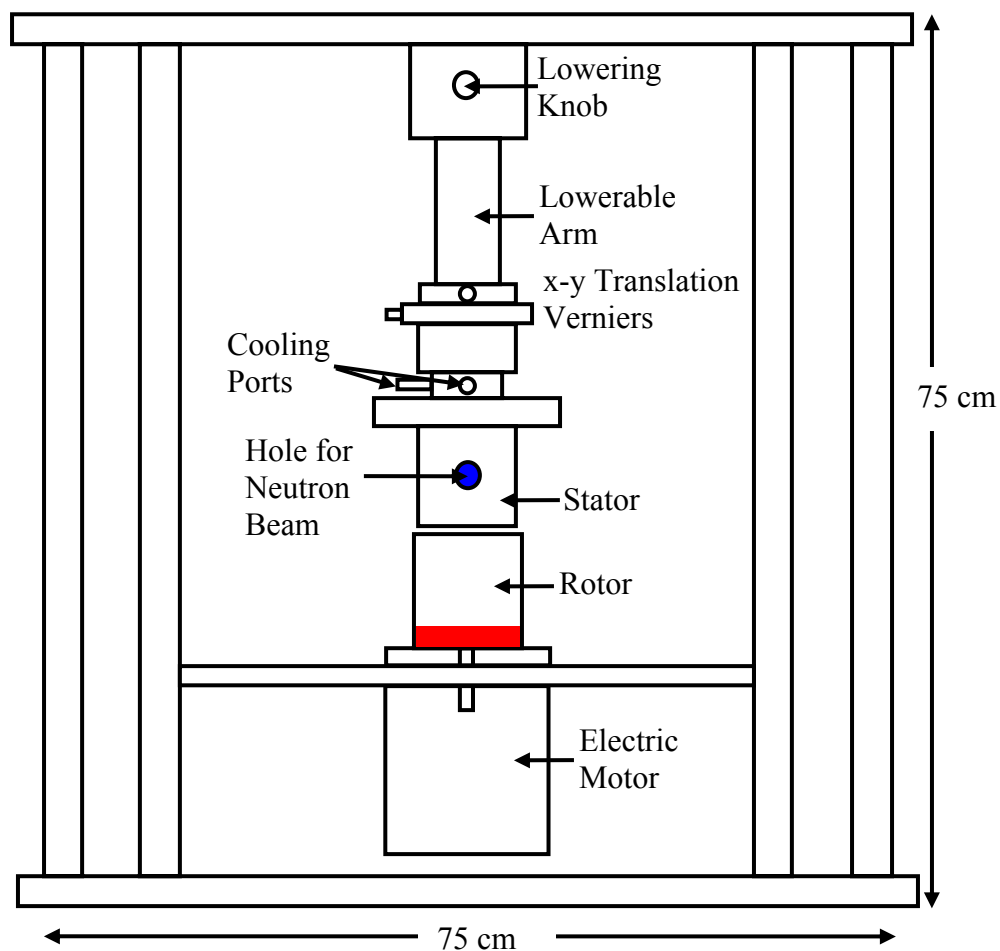
Figure 5: Schematic representation of the Couette shear cell setup with the stator in the raised position.
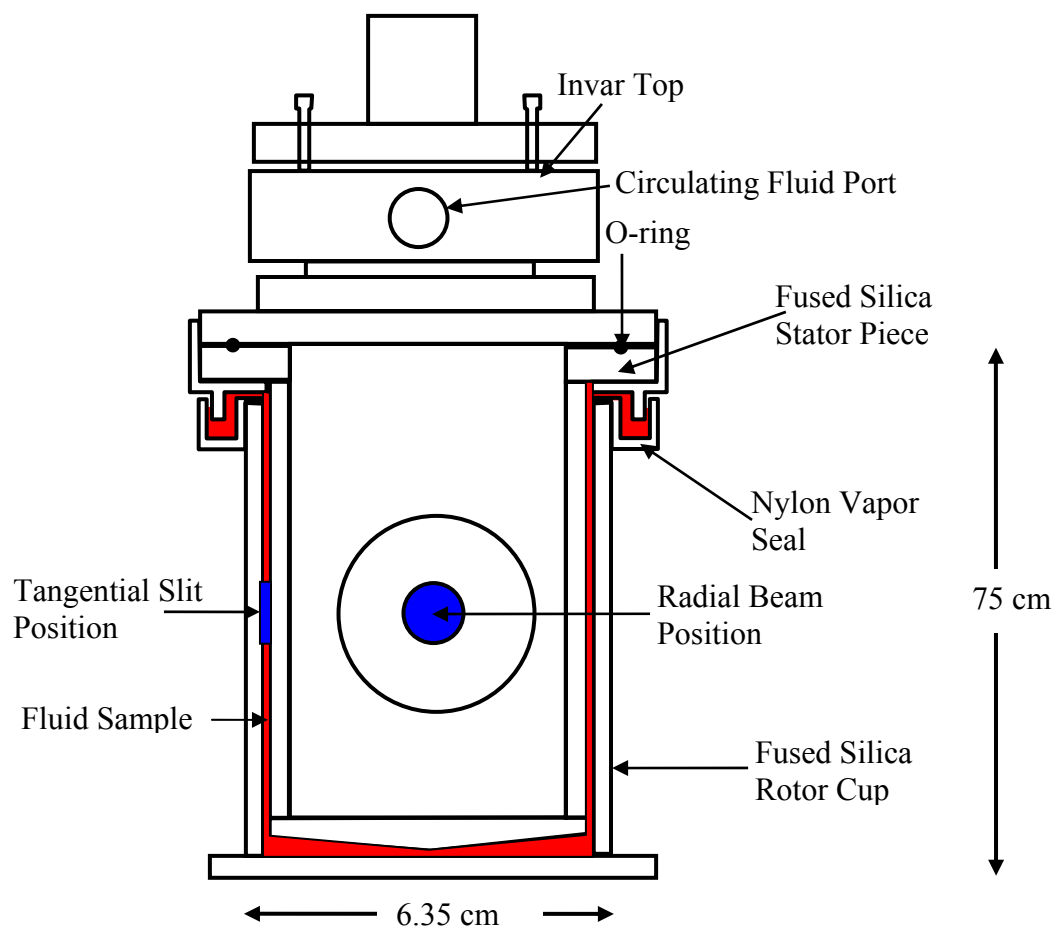
Figure 6: Schematics of the rotor and stator for the in-situ Couette shear cell. The neutron beam is perpendicular to the plane of this drawing.

5. THE PLATE/PLATE SHEAR CELL

A plate/plate shear cell is available at the NIST CNR for in-situ SANS measurements. This device was designed for investigations of oriented block copolymers. It consists of two arms; one fixed and one moving. The sample is melt pressed into a special (1 mm thick) holding cell which is mounted between the two arms. The fixed arm holding the sample is tightened in order to squeeze the sample between the two arms. The translation screw transforms the rotational motion (from the motor) into a translational motion (up and down). Two limit switches limit the travel range and therefore the strain. A strain of 100 % is obtained for a 1 mm travel.
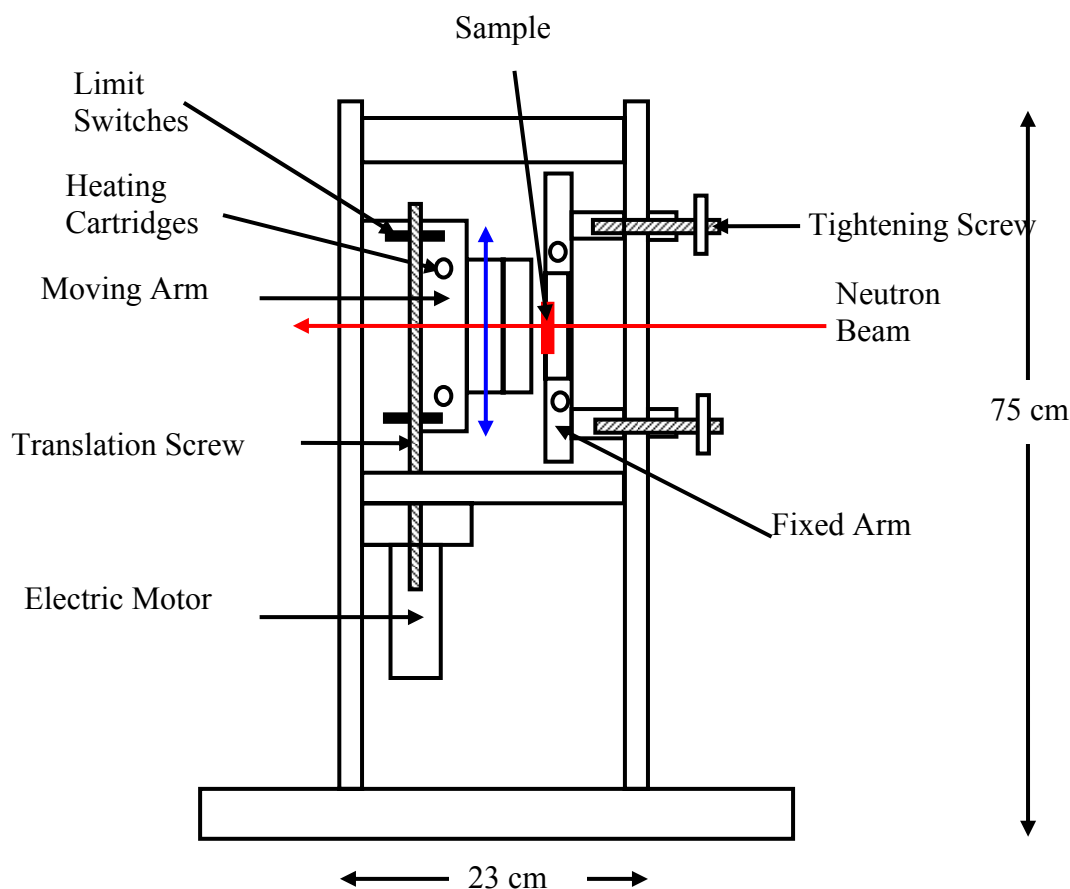
Figure 7: Schematics of the in-situ plate/plate shear cell.

6. OTHER SAMPLE ENVIRONMENTS

Other sample environments are available for in-situ SANS measurements at the NCNR. These include a rheometer for in-situ rheology. The shear cells described above can orient samples but cannot measure torque. The rheometer is a standard piece of equipment that was modified to allow a neutron beam to be incident on the sample. A standard rheometer has been modified for in-situ SANS measurements. The main modification consisted in raising the sample cup from its standard location (inside a temperature bath) to a higher (more accessible) location in the neutron path. Temperature control is performed through air circulation.

Other pieces of equipment include electro-magnets (up to 2 Teslas) and a superconducting magnet (up to 9 Teslas). A humidity chamber and a vapor cell allow sample humidity and vapor control. Other cells are available.

REFERENCES

G. Straty, "The NIST SANS in-situ Couette Shear Cell", Internal Report (1993)

B. Hammouda and S. Kline, "The NIST SANS in-situ Pressure Cell", Internal Reports (1995, 1998).

QUESTIONS

1. Why are quartz windows used with sample cells?
2. What is the maximum reachable temperature for the heating block? What is the temperature range for the cooling block?
3. What are the units for ambient pressure?
4. Why doesn't water boil above 100 ^{o}C inside the pressure cell?
5. What is the characteristic of most SANS data with in-situ shear?

ANSWERS

1. Quartz windows are fairly transparent to neutrons and to light. Moreover quartz is less expensive than sapphire.
2. The heating block can reach up to 300 ^{o}C. The cooling block uses 50 % water and 50 % ethylene glycol (antifreeze) and can reach from 0 ^{o}C to 90 ^{o}C. The range between 0 ^{o}C and 10 ^{o}C is above the dew point (where water condensation occurs on windows). This range should be used only in inert (either nitrogen or helium) atmosphere to avoid water condensation.
3. Ambient pressure corresponds to 14.7 psi = 1 atm = 1 Bar. This is equivalent to 760 mm of mercury or 760 torr and converts to 101,325 Pa in SI units.
4. Water does not boil above 100 ^{o}C inside the pressure cell because a positive pressure (at least 100 psi) is always maintained.
5. Most SANS data with in-situ shear are characterized by anisotropic scattering with oriented contour maps.

Part D – SANS RESOLUTION AND DATA SMEARING

Chapter 15. The SANS Instrumental Resolution
      15.1 The Resolution Function
      15.2 Variance of the Q Resolution
      15.3 SANS Resolution Variance
      15.4 Minimum Q
      15.5 Measured SANS Resolution
      15.6 Discussion
      References
      Questions
      Answers

Chapter 16. Neutron Focusing Lenses
      16.1 Focusing Lenses' Basic Equations
      16.2 Resolution with Focusing Lenses
      16.3 Minimum Q with Focusing Lenses
      16.4 Measured SANS Resolution
      16.5 Lens Transmission
      References
      Questions
      Answers

Chapter 17. Gravity Correcting Prisms
      17.1 Neutron Trajectory
      17.2 The Prism Deflection Angle
      17.3 Contribution to the Q Resolution
      17.4 Contribution to Q_{min}
      17.5 Measurements with Gravity Correcting Prisms
      17.6 Prisms Transmission
      17.7 Discussion
      References
      Questions
      Answers

Chapter 18. Neutron Beam Current
      18.1 Variation of Beam Current with Spot Size
      18.2 Variation of Beam Current with Q_{min}
      References
      Questions
      Answers

Chapter 19. The Smearing Effect
      19.1 The Resolution Function
      19.2 The Resolution Correction
      19.3 Iso-Intensity Contour Maps with Gravity Effect
      19.4 Numerical Application
      19.5 Smearing For Hard Spheres

Chapter 15 - **THE SANS INSTRUMENTAL RESOLUTION**

Instrumental smearing affects SANS data. In order to analyze smeared SANS data, either de-smearing of the data or smearing of the fitting model function is required. The second approach is more common because it is a direct method. Smearing corrections use the instrumental resolution function.

1. THE RESOLUTION FUNCTION

Instrumental smearing is represented by the following 1D convolution smearing integral (suitable for radially averaged data):

$$\frac{d\Sigma(Q)}{d\Omega} = \int_0^{+\infty} Q' dQ' P_{1D}(Q') \frac{d\Sigma(Q-Q')}{d\Omega}. \tag{1}$$

Here Q is the scattering variable, $\frac{d\Sigma(Q)}{d\Omega}$ is the scattering cross section and the 1D resolution function is defined as a Gaussian function:

$$P_{1D}(Q') = \left(\frac{1}{2\pi\sigma_{Q'}^2}\right)^{1/2} \exp\left[-\frac{Q'^2}{2\sigma_{Q'}^2}\right]. \tag{2}$$

The Q standard deviation σ_Q is a measure of the neutron beam spot on the detector (Q = 0). It is also a measure of the instrumental part of the width of scattering peaks from samples (Q $\neq$ 0). σ_Q is related to the spatial standard deviation (i.e., standard deviation of the neutron beam spot at the detector) σ_r by $\sigma_Q = (2\pi/\lambda L_2)\sigma_r$, where L_2 is the sample-to-detector distance.

2. VARIANCE OF THE Q RESOLUTION

Scattering measurements are made in reciprocal (Fourier transform) space where the magnitude of the scattering vector is given by:

$$Q = \frac{4\pi}{\lambda}\sin\left(\frac{\theta}{2}\right). \tag{3}$$

Here λ is the neutron wavelength and θ is the scattering angle. At small angles, Q is approximated by: $Q = 2\pi\theta/\lambda$.

In order to express σ_Q, differentiate Q on both sides:

$$dQ = \frac{2\pi}{\lambda}d\theta - \frac{2\pi}{\lambda^2}\theta d\lambda. \tag{4}$$

Take the square:

$$(dQ)^2 = \left(\frac{2\pi}{\lambda}\right)^2 (d\theta)^2 + \left(\frac{2\pi}{\lambda^2}\right)^2 \theta^2 (d\lambda)^2 - 2\frac{(2\pi)^2}{\lambda^3}\theta(d\theta)(d\lambda). \quad (5)$$

Then perform the statistical averages:

$$< (dQ)^2 >= \left(\frac{2\pi}{\lambda}\right)^2 < (d\theta)^2 > + \frac{(2\pi)^2}{\lambda^4}\theta^2 < (d\lambda)^2 > -2\frac{(2\pi)^2}{\lambda^3} < \theta(d\theta)(d\lambda) > \quad (6)$$

Note that $< \theta(d\theta)(d\lambda) >=< \theta(d\theta) >< (d\lambda) >$ because the scattering angle θ and the wavelength λ are uncorrelated. Moreover $< (d\lambda) >=< (\lambda - < \lambda >) >=< \lambda > - < \lambda >= 0$. This cancels out the last term.

Define the different variances:

$$\begin{aligned}
\sigma_Q{}^2 &= <(dQ)^2>=<Q^2>-<Q>^2, \\
\sigma_\theta{}^2 &= <(d\theta)^2>=<\theta^2>-<\theta>^2, \\
\sigma_\lambda{}^2 &= <(d\lambda)^2>=<\lambda^2>-<\lambda>^2
\end{aligned} \qquad (7)$$

The SANS resolution variance has two contributions:

$$\sigma_Q{}^2 = [\sigma_Q{}^2]_{geo} + [\sigma_Q{}^2]_{wav} = \frac{4\pi^2}{\lambda^2}\sigma_\theta{}^2 + Q^2\frac{\sigma_\lambda{}^2}{\lambda^2} \qquad (8)$$

These correspond to the "geometry" part (first term) and to the "wavelength spread" part (second term) of the Q resolution variance.

3. SANS RESOLUTION VARIANCE

The main parts of the resolution variance $\sigma_Q{}^2$ are derived for a SANS instrument with circular apertures (Mildner-Carpenter, 1984; Mildner et al, 2005).

Geometry Contribution to the Q Resolution

Consider the geometry contribution to the Q resolution variance:

$$\sigma_\theta{}^2 = \frac{\sigma_r{}^2}{L_2{}^2} \qquad (9)$$

L_2 is the sample-to-detector distance. The variance for the radially averaged data corresponds to 1D. The 1D case of σ_x^2 (in the horizontal x direction) is considered first.
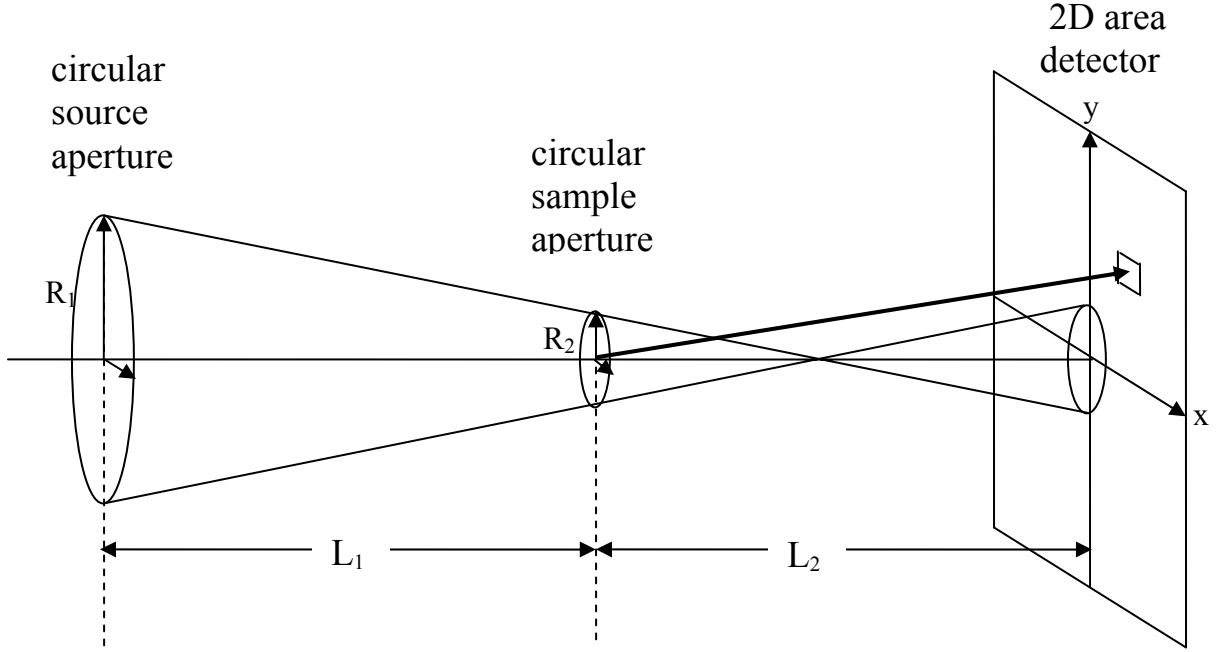
Figure 1: Typical SANS geometry with circular source and sample apertures and 2D area detector. This figure is not to scale. The horizontal scale is in meters whereas the vertical scale is in centimeters. Aperture sizes have been drawn out of scale compared to the size of the area detector.

Consider a uniform neutron distribution within the source and sample apertures. The horizontal contribution can be written:

$$\sigma_x^2 = \left(\frac{L_2}{L_1}\right)^2 < x^2 >_1 + \left(\frac{L_1 + L_2}{L_1}\right)^2 < x^2 >_2 + < x^2 >_3. \quad (10)$$

L_1 is the source-to-sample distance, L_2 is the sample-to-detector distance, $<x^2>_1$ is the averaging over the source aperture, $<x^2>_2$ is the averaging over the sample aperture and $<x^2>_3$ is the averaging over a detector cell. R_1 and R_2 define the source and sample aperture radii respectively. In order to see the origin of the (L_2/L_1) scaling factor, consider the case where $R_2 = 0$. Then the spot at the detector would be similar to the source aperture size scaled by (L_2/L_1). Similarly, in order to see the origin of the $(L_1+L_2)/L_1$ scaling factor, consider the case of $R_1 = 0$. The spot would be similar to the sample aperture size scaled by $(L_1+L_2)/L_1$.
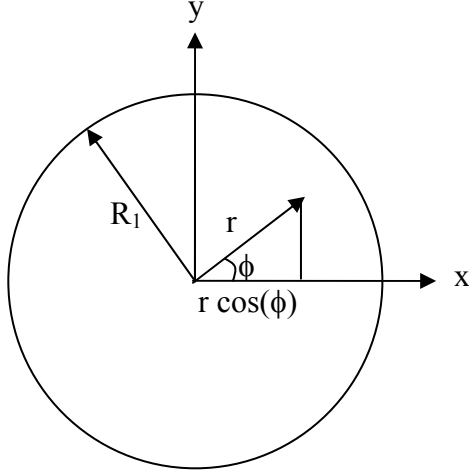
Figure 2: Geometry of the circular source aperture.

The various averages can be readily calculated:

$$< x^2 >_1 = \frac{\int_0^{2\pi}\int_0^{R_1} r^2\cos^2(\phi)r\,dr\,d\phi}{\int_0^{2\pi}\int_0^{R_1} r\,dr\,d\phi} = \frac{\int_0^{R_1} r^3\,dr\int_0^{2\pi}\cos^2(\phi)d\phi}{\int_0^{R_1} r\,dr\int_0^{2\pi} d\phi} = \frac{R_1^2}{4}. \quad (11)$$

Similarly $<x^2>_2 = \dfrac{R_2^2}{4}$. Averaging over the square (or rectangular) detector cell of sides Δx_3 and Δy_3 follows.

$$< x^2 >_3 = \frac{\int_{-\Delta x_3/2}^{\Delta x_3/2} dx\, x^2}{\int_{-\Delta x_3/2}^{\Delta x_3/2} dx} = \frac{\Delta x_3^2}{12} = \frac{1}{3}\left(\frac{\Delta x_3}{2}\right)^2. \quad (12)$$

Therefore:

$$\sigma_x^2 = \left(\frac{L_2}{L_1}\right)^2\frac{R_1^2}{4} + \left(\frac{L_1+L_2}{L_1}\right)^2\frac{R_2^2}{4} + \frac{\Delta x_3^2}{12}. \quad (13)$$

Similarly for the vertical part (assuming no effect of gravity on the neutron trajectory):

$$\sigma_y^2 = \left(\frac{L_2}{L_1}\right)^2\frac{R_1^2}{4} + \left(\frac{L_1+L_2}{L_1}\right)^2\frac{R_2^2}{4} + \frac{\Delta y_3^2}{12}. \quad (14)$$

So that:

$$\left[\sigma_{Qx}{}^2\right]_{geo} = \left(\frac{2\pi}{\lambda}\right)^2 \frac{\sigma_x{}^2}{L_2{}^2}.$$ (15)

$$\left[\sigma_{Qy}{}^2\right]_{geo} = \left(\frac{2\pi}{\lambda}\right)^2 \frac{\sigma_y{}^2}{L_2{}^2}.$$

This is the first part of the Q resolution variance.

Wavelength Spread Contribution to the Q Resolution

The neutron wavelength is assumed to obey a triangular distribution peaked around λ and of full-width at half maximum $\Delta\lambda$.
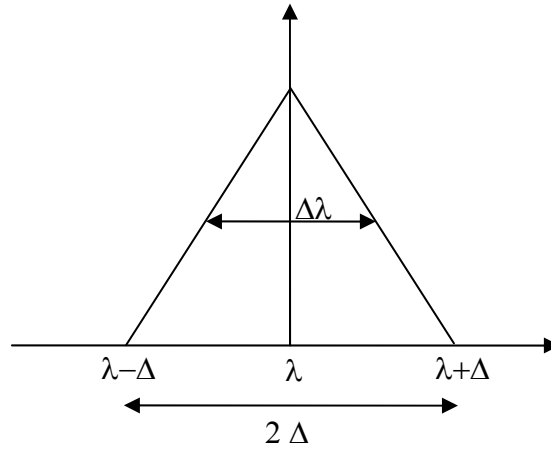
Figure 3: Triangular wavelength distribution.

This is a typical distribution outputted by a velocity selector. For simplicity of notation, the same symbol λ is used to denote both the wavelength variable λ and the average wavelength $<\lambda>$. The average over this wavelength distribution can be readily calculated as:

$$< \lambda^2 > = \lambda^2 \left[1 + \frac{1}{6}\left(\frac{\Delta\lambda}{\lambda}\right)^2\right].$$ (16)

Note that if we had assumed a square (also called "box") wavelength distribution, the factor of 1/6 would be replaced by 1/12.

The wavelength variance is therefore:

$$\frac{\sigma_{\lambda}^{2}}{\lambda^{2}} = \frac{\left(<\lambda^{2}> - <\lambda>^{2}\right)}{\lambda^{2}} = \frac{1}{6}\left(\frac{\Delta\lambda}{\lambda}\right)^{2}. \tag{17}$$

The wavelength spread contribution to the Q resolution variance is therefore as follows:

$$\left[\sigma_{Qx}^{2}\right]_{wav} = Q_{x}^{2}\frac{1}{6}\left(\frac{\Delta\lambda}{\lambda}\right)^{2} \tag{18}$$

$$\left[\sigma_{Qy}^{2}\right]_{wav} = Q_{y}^{2}\frac{1}{6}\left(\frac{\Delta\lambda}{\lambda}\right)^{2}$$

This is the second part of the Q resolution variance.

Neutron Trajectories

Gravity affects neutron trajectories. Consider neutrons of wavelength λ and wavelength spread $\Delta\lambda$ incident on the source aperture. The initial neutron velocity is v_0 with components v_{0y} and v_{0z} along the vertical and horizontal directions.
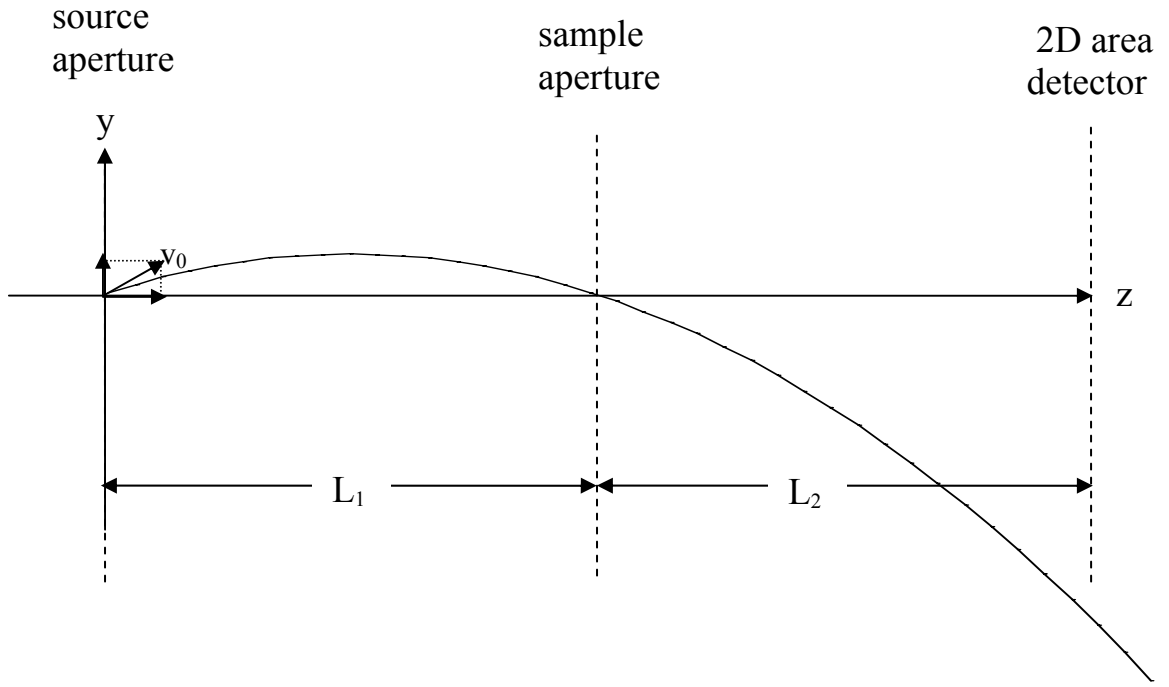
Figure 4: Parabolic neutron trajectory under gravity effect. Neutrons must cross the source and sample apertures. This figure is not to scale.

Under the effect of gravity, neutrons follow the following trajectories:

$$z = v_{0z} t \qquad\qquad (19)$$

$$y = -\frac{1}{2} g t^2 + v_{0y} t .$$

Here g is the gravity constant (g = 9.81 m/s^2) and t is time. Neutrons are assumed to be at the horizontal axis origin at time zero. In order to obtain the neutron trajectories equation, the time variable is eliminated using the fact that neutrons must cross the source and sample apertures; i.e., the condition y = 0 for z = 0 and for z = L$_1$. This gives:

$$L_1 = v_{0z} t \qquad\Rightarrow\qquad t = \frac{L_1}{v_{0z}} \qquad\qquad (20)$$

$$0 = -\frac{1}{2} g t^2 + v_{0y} t \qquad\Rightarrow\qquad v_{0y} = \frac{1}{2} g \frac{L_1}{v_{0z}} .$$

The horizontal neutron speed v_{0z} is related to the neutron wavelength λ by:

$$v_{0z} = \frac{h}{m\lambda} . \qquad\qquad (21)$$

Here also, h is Planck's constant and m is the neutron mass. At any other position along the neutron path (other than z = 0 and z = L_1), the parabolic variation followed is:

$$y(z) = -\frac{1}{2} g \left(\frac{m\lambda}{h} \right)^2 (z^2 - zL_1) = -B\lambda^2 (z^2 - zL_1) \qquad (22)$$

where:

$$B = \frac{gm^2}{2h^2}. \qquad (23)$$

The neutron fall trajectory is characterized by a parabolic variation with respect to z and with respect to λ.

For z = L_1+L_2, neutrons fall by the distance y(L_1+L_2) = -B λ^2 L_2(L_1+L_2) with respect to the initial position y_0.

Effect of Gravity on the Q Resolution

Gravity affects the fall of the neutron and therefore the resolution in the y direction. Neutron trajectories follow a parabola:

$$y = y_0 - A\lambda^2 \quad \text{with} \quad A = BL_2(L_1 + L_2) \quad \text{and} \quad B = \frac{gm^2}{2h^2}. \qquad (24)$$

g is the gravitation constant (g = 9.81 m/s^2), m is the neutron mass and h is Plank's constant (h/m=3995 Å.m/s). A= 3.073*10^{-7} L_2(L_1+L_2) given in units of m/Å^2 where L_1 and L_2 are the source-to-sample and sample-to-detector distances given in meters.

The gravity contribution to the Q_y variance is given by:

$$\left[\sigma_{Qy}{}^2 \right]_{grav} = \left(\frac{2\pi}{\lambda} \right)^2 \frac{[\sigma_y{}^2]_{grav}}{L_2{}^2} \qquad (25)$$

$$\left[\sigma_y{}^2 \right]_{grav} = <(y-y_0)^2> - <(y-y_0)>^2 = A^2(<\lambda^4> - <\lambda^2>^2).$$

The two averages over the triangular wavelength distribution are performed as follows:

$$<\lambda^2> = \lambda^2 \left[1 + \frac{1}{6} \left(\frac{\Delta\lambda}{\lambda} \right)^2 \right] \qquad (26)$$

$$< \lambda^4 >= \lambda^4 \left[1 + \left(\frac{\Delta\lambda}{\lambda} \right)^2 + \frac{1}{15} \left(\frac{\Delta\lambda}{\lambda} \right)^4 \right].$$

Therefore:

$$< \lambda^4 > - < \lambda^2 >^2 \cong \lambda^4 \frac{2}{3} \left(\frac{\Delta\lambda}{\lambda} \right)^2. \tag{27}$$

So that:

$$\left[\sigma_y^2 \right]_{grav} = A^2 \lambda^4 \frac{2}{3} \left(\frac{\Delta\lambda}{\lambda} \right)^2. \tag{28}$$

and finally:

$$\left[\sigma_{Qy}^2 \right]_{grav} = \left(\frac{2\pi}{L_2} \right)^2 A^2 \lambda^2 \frac{2}{3} \left(\frac{\Delta\lambda}{\lambda} \right)^2. \tag{29}$$

This term is added in quadrature with the other two contributions (geometry and wavelength spread) to the Q resolution variance σ_Q^2.

Summary of the Q Resolution

Putting the geometry contribution, the wavelength spread contribution and the gravity contribution together yields:

$$\sigma_{Qx}^2 = \left(\frac{2\pi}{\lambda L_2} \right)^2 \left[\left(\frac{L_2}{L_1} \right)^2 \frac{R_1^2}{4} + \left(\frac{L_1 + L_2}{L_1} \right) \frac{R_2^2}{4} + \frac{1}{3} \left(\frac{\Delta x_3}{2} \right)^2 \right] + Q_x^2 \frac{1}{6} \left(\frac{\Delta\lambda}{\lambda} \right)^2 \tag{30}$$

$$\sigma_{Qy}^2 = \left(\frac{2\pi}{\lambda L_2} \right)^2 \left[\left(\frac{L_2}{L_1} \right)^2 \frac{R_1^2}{4} + \left(\frac{L_1 + L_2}{L_1} \right) \frac{R_2^2}{4} + \frac{1}{3} \left(\frac{\Delta y_3}{2} \right)^2 + A^2 \lambda^4 \frac{2}{3} \left(\frac{\Delta\lambda}{\lambda} \right)^2 \right] + Q_y^2 \frac{1}{6} \left(\frac{\Delta\lambda}{\lambda} \right)^2$$

$$A = L_2 (L_1 + L_2) \frac{gm^2}{2h^2}$$

where:

R₁: source aperture radius
R_1: source aperture radius
R_2: sample aperture radius
Δx_3 and Δy_3: sides of the detector cell
L_1: source-to-sample distance

L_2: sample-to-detector distance
$\Delta\lambda$: wavelength spread, FWHM of triangular distribution function
g: gravity constant
m: neutron mass
h: Planck's constant.

This result was obtained assuming a uniform neutron distribution within the apertures and a triangular wavelength distribution.

4. MINIMUM Q

A figure of merit for SANS instruments is the minimum value of tha scattering variable Q (also called Q_{min}) that can be reached for a given configuration. This value is imposed by the neutron spot size on the area detector and dictates the size of the beam-stop to be used. In order to minimize the spot size, one has to minimize the "umbra" and "penumbra" of the neutron beam.
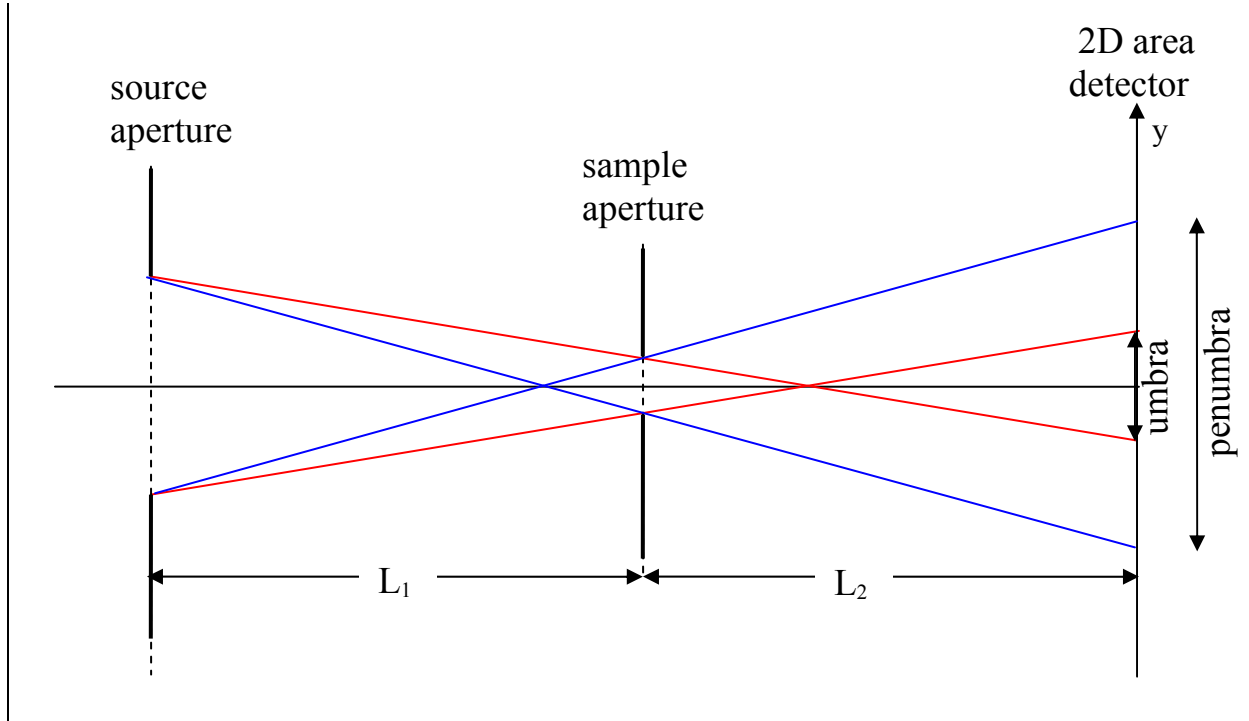

Figure 5: Converging collimation geometry to minimize spot size. This figure is not to scale. The penumbra is the maximum spot size to be blocked by the beam-stop.

Given the standard SANS geometry, the extent of the penumbra in the horizontal direction is given by:

$$X_{min} = \frac{L_2}{L_1}R_1 + \frac{L_1 + L_2}{L_1}R_2 + \frac{\Delta x_3}{2}. \qquad (31)$$

And the minimum Q in the horizontal direction is therefore $Q^X_{min} = (2\pi/\lambda)(X_{min}/L_2)$.

In the vertical direction, the effect of gravity plays a role. The upper edge of the penumbra moves down by $A(\lambda-\Delta\lambda)^2$ because it corresponds to faster neutrons with wavelength $\lambda-\Delta\lambda$. The lower edge of the penumbra drops down by more; i.e., by $A(\lambda+\Delta\lambda)^2$ because it corresponds to slower neutrons with wavelength $\lambda+\Delta\lambda$. This results in a distorted beam spot at the detector. To first order in wavelength spread, one obtains:

$$Y_{min} = \frac{L_2}{L_1}R_1 + \frac{L_1+L_2}{L_1}R_2 + \frac{\Delta y_3}{2} + 2A\lambda^2\left(\frac{\Delta\lambda}{\lambda}\right). \qquad (32)$$

Note that Q_{min} is determined by the spot size in the vertical direction where the beam is the broadest $Q_{min} = Q^Y_{min} = (2\pi/\lambda)(Y_{min}/L_2)$.

$$Q_{min} = \left(\frac{2\pi}{\lambda L_2}\right)\left(\frac{L_2}{L_1}R_1 + \frac{L_1+L_2}{L_1}R_2 + \frac{\Delta y_3}{2} + 2A\lambda^2\left(\frac{\Delta\lambda}{\lambda}\right)\right). \qquad (33)$$
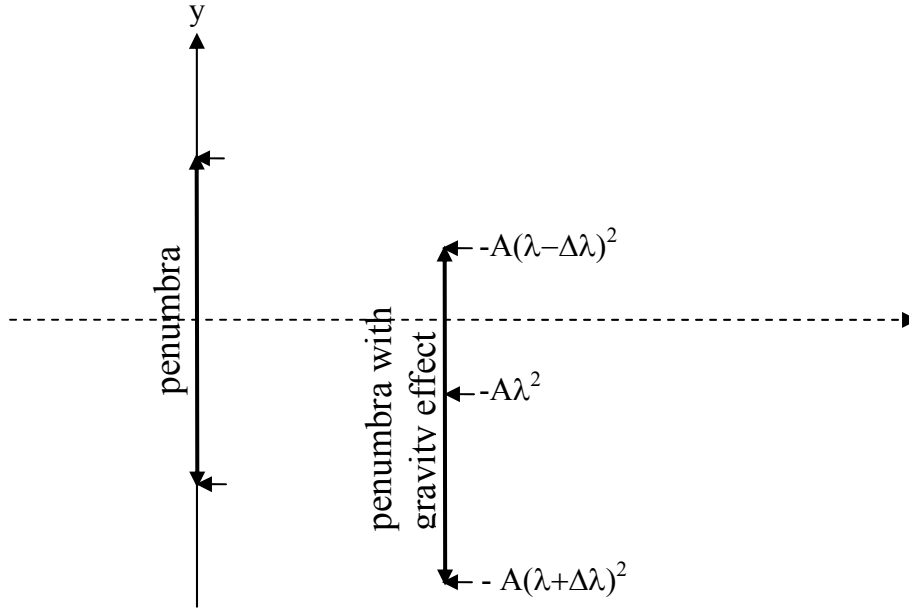
Figure 6: Neutron spot on the detector. The effect of gravity is to drop both the upper edge and the lower edge of the penumbra. The lower edge drops more resulting in distorted iso-intensity contours.

5. MEASURED SANS RESOLUTION

Specific Instrument Configuration

Consider the following low-Q instrument configuration.

$L_1 = 16.14$ m
$L_2 = 13.19$ m
$R_1 = 0.715$ cm
$R_2 = 0.635$ cm
$\Delta x_3 = \Delta y_3 = 0.5$ cm
$\dfrac{\Delta \lambda}{\lambda} = 0.13.$

This gives a gravity fall parameter of $A = 0.01189$ cm/Å^2. This configuration does not strictly obey the "cone rule" whereby the beam spot umbra at the detector is minimized.

Assuming a neutron wavelength of $\lambda = 6$ Å, the variance σ_Q^2 has the following Q dependence:

$$\sigma_Q^2 = 5.55 * 10^{-7} + 0.0028 Q^2 (\text{Å}^{-2}). \qquad (34)$$

The minimum scattering variable is:

$$Q_{min} = 0.0017 \text{Å}^{-1}. \qquad (35)$$

Gravity effects are small for 6 Å neutrons. Neutrons fall by only 0.428 cm.

The focus here will be on empty beam measurement (i.e., with no sample in the beam). This corresponds to the resolution limit of $Q = 0$.
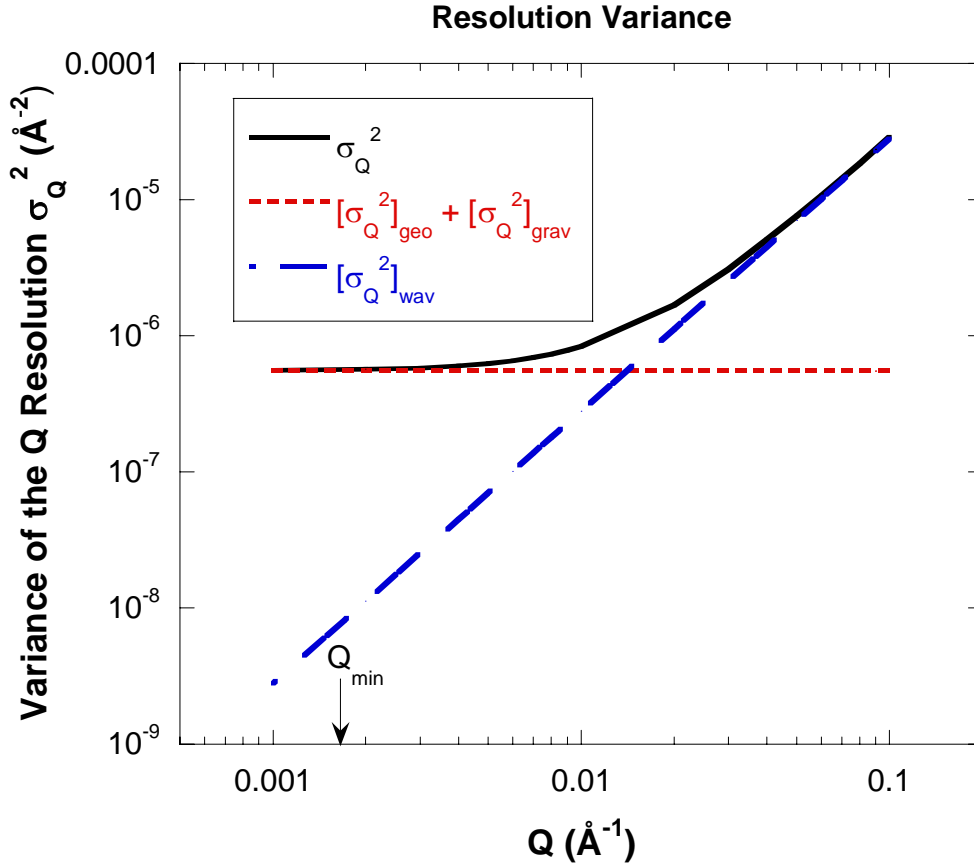
Figure 7: Variation of σ_Q^2 with Q plotted on a log-log scale. The main contributions (geometry, wavelength spread and gravity effect) are added in quadrature.

Empty Beam Measurements

Empty beam measurements were made using the above instrument configuration and varying the neutron wavelength.

Predicted and measured resolution characteristics are compared in a series of figures. First, the position of the beam spot on the detector is plotted for increasing wavelength.
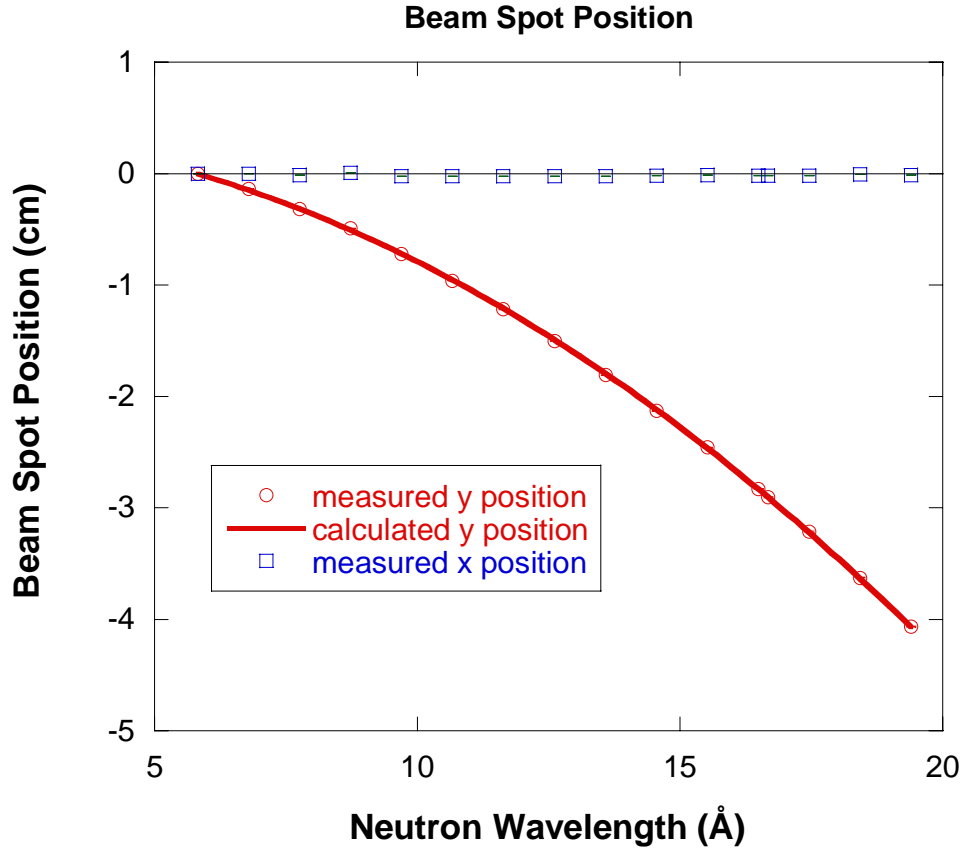
Beam Spot Position

Figure 8: Variation of the horizontal and vertical neutron beam spot positions with wavelength.

Next, the standard deviations σ_x and σ_y of the neutron spot size are plotted with increasing neutron wavelength. The measured values were obtained by performing non-linear least-squares fits to a Gaussian function in the x and in the y directions. Fits were performed on cuts through the beam spot center, both horizontally and vertically. Data recorded by two adjacent detector cells (normal to the cut) were added in each case in order to improve statistics. A scaling factor of $\sqrt{1.45} = 1.2$ was used to scale the measured data. This scaling factor gave good agreement between the measured and calculated values for σ_x. The same scaling factor was used for σ_y.

This necessary scaling factor of 1.2 is probably related to the procedure used to obtain measured beam spot widths. (1) Slice cuts were performed in the horizontal and vertical directions. (2) Gaussian fits were performed on these slices even though the beam profile is known to be close to a trapezoidal (not Gaussian) shape. (3) Lastly, the measured beam spots were so small (covering only a few detector cells) that Gaussian fits were performed with four to eight points only.
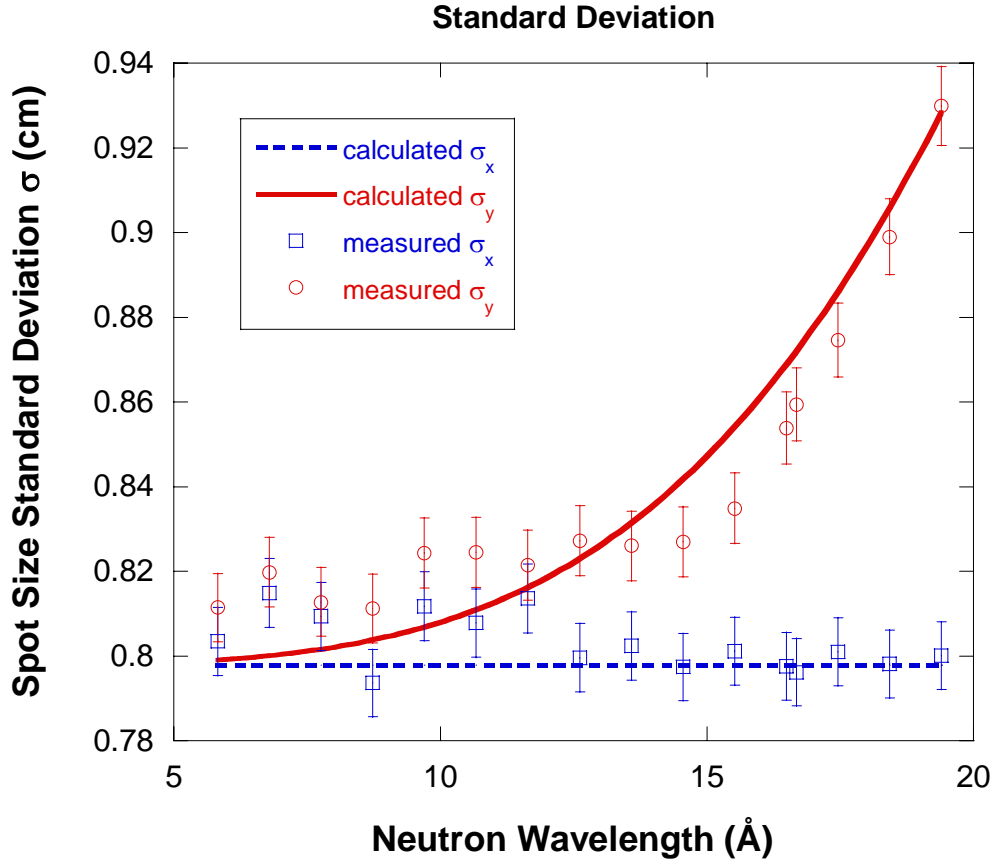
Figure 9: Variation of the measured and calculated neutron beam spot size standard deviations σ_x and σ_y with increasing wavelength.

The minimum spot sizes X_{min} and Y_{min} were obtained experimentally as the values where the intensity (of the horizontal or vertical cuts across the beam spot) goes to zero. This method is conservative and overestimates the measured values for X_{min}. It is not precise, yielding poor agreement between measured and calculated values. Our calculated values neglect for instance diffuse scattering from the beam defining sample aperture and from the pre-sample and post-sample neutron windows. Such scattering tends to broaden the neutron beam. At long wavelengths the gravity effect broadens the neutron spot in the vertical direction with the extra difference Y_{min}-X_{min} given by the term $2A\lambda^2(\Delta\lambda/\lambda)$.
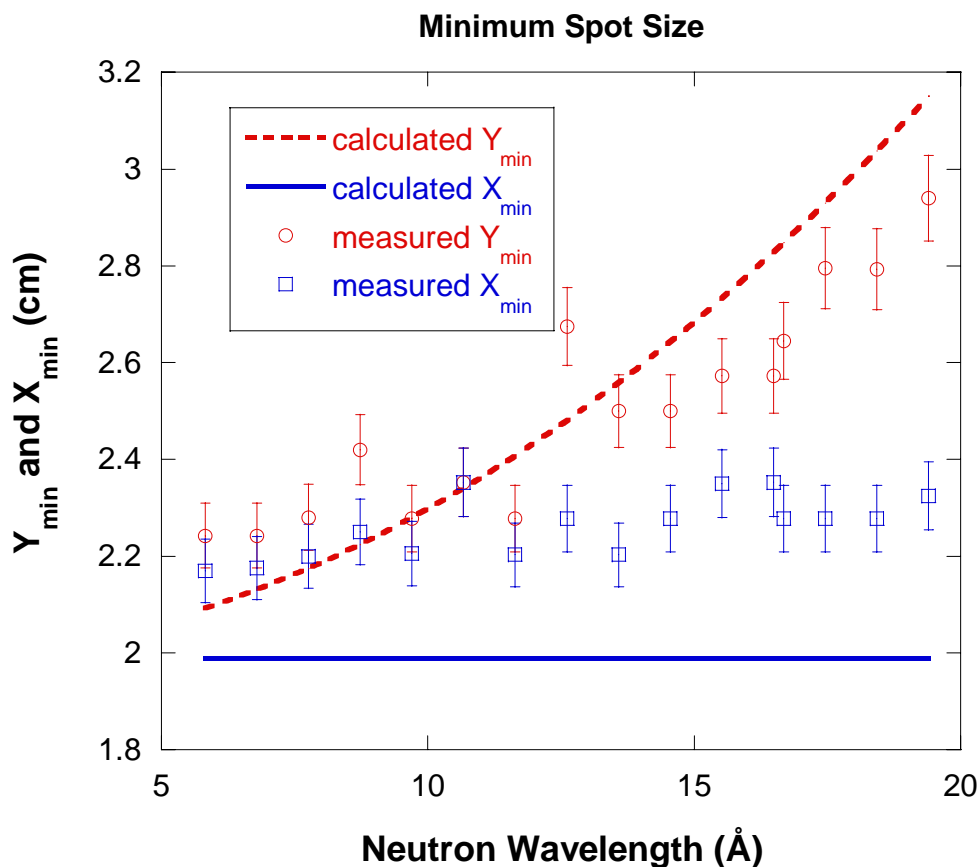
Figure 10: Variation of the neutron beam spot sizes in the horizontal and vertical directions with increasing wavelength.

6. DISCUSSION

The choice of a SANS instrument configuration is always a compromise between high intensity and good resolution. The instrumental resolution is the main source of data smearing. Estimation of the SANS resolution is an integral part of the data reduction process. Reduced SANS data include not only the scattering variable Q and the scattered intensity I(Q), but also the resolution standard deviation σ_Q. σ_Q is needed to smear models before fitting to the data.

Corrections for smearing due to gravity are never made because they are small and deemed to be complex manipulations of the 2D data. The effect of gravity smearing is small except at long neutron wavelengths. Fortunately, the wide majority of experiments maximize flux by using low wavelengths (5 Å or 6 Å).

REFERENCES

D.F.R. Mildner, J.M. Carpenter, "Optimization of the Experimental Resolution for SAS", J. Appl. Cryst. <u>17</u>, 249-256 (1984).

D.F.R. Mildner, B. Hammouda, and S.R. Kline, "A Refractive Focusing Lens System for SANS", J. Appl. Cryst. <u>38</u>, 979-987 (2005).

QUESTIONS

1. What is the relationship between the standard deviation and the variance of a peaked function?
2. What function best describes the wavelength distribution function?
3. What is the shape of the penumbra of the neutron beam spot on the detector?
4. Given a Gaussian function, what is the relationship between its FWHM and its standard deviation σ?
5. Calculate the following average $<\lambda^2>$ over a triangular wavelength distribution. Calculate $<\lambda^2>$ over a Gaussian wavelength distribution of standard deviation σ_λ.
6. What are the various contributions to the SANS instrumental resolution?
7. The gravity effect is worse at what wavelength range?
8. What is the shape of the neutron beam spot on the detector for long wavelengths?
9. Cold neutrons of 20 Å wavelength fall by how much over a distance of 30 m?
10. Name the main "figures of merit" for a SANS instrument.
11. How would you obtain a lower Q_{min}?

ANSWERS

1. The variance σ_Q^2 is the square of the standard deviation σ_Q.
2. The wavelength distribution is best described by a triangular function.
3. The neutron beam spot on the detector has a shape close to trapezoidal.
4. For a Gaussian distribution, the following relationship holds FWHM $= 2\sqrt{2\ln(2)}\ \sigma$. In order to derive this relation, consider a Gaussian function $P(x) = (1/2\pi\sigma^2)^{1/2}\ \exp(-x^2/2\sigma^2)$ with standard deviation σ. Setting $P(x) = \frac{1}{2}$, two solutions can be found for $x = \pm\sqrt{2\ln(2)}\ \sigma$. This yields a band FWHM $= 2\sqrt{2\ln(2)}\ \sigma = 2.355\sigma$.
5. The integrations are simple. Only the results are given.

$$<\lambda^2> = \lambda^2\left[1 + \frac{1}{6}\left(\frac{\Delta\lambda}{\lambda}\right)^2\right] \text{ for triangular distribution of FWHM } \Delta\lambda.$$

$$<\lambda^2> = \lambda^2\left[1 + \left(\frac{\sigma_\lambda}{\lambda}\right)^2\right] \text{ for Gaussian distribution of standard deviation } \sigma_\lambda.$$

6. The SANS instrumental resolution contains contributions from (1) "geometry" (source, sample aperture and detector cell sizes and source, sample and detector inter-distances), (2)

from "wavelength spread" and (3) from "gravity" effect. Remember that $[\sigma_Q^2]_{geo} \sim$ constant, $[\sigma_Q^2]_{wav} \sim Q^2(\Delta\lambda/\lambda)^2$ and $[\sigma_Q^2]_{grav} \sim \lambda^4(\Delta\lambda/\lambda)^2$.

7. The effect of gravity is worse for longer wavelengths.

8. Neutrons fall more at the bottom of the neutron beam than at the top. For this reason, beam spot iso-intensity contour maps are weakly elliptical (weakly oval actually).

9. Cold neutrons of 20 Å wavelength fall by about 4 cm over a distance of 30 m (see Figure 8).

10. Typical figures of merit for SANS instrument include: resolution σ_Q, Q_{min}, flux-on-sample, Q-range (called ΔQ) and background level.

11. A lower Q_{min} could be obtained by increasing the sample-to-detector distance. When this distance is at its maximum, then one could increase the neutron wavelength. The reason for this is that the beam intensity (1) decreases as sample-to-detector distance square but (2) it decreases as neutron wavelength to the fourth power.

Neutron lenses are used to focus neutron beams. They increase intensity on the sample and shrink the neutron spot size on the detector therefore reducing the minimum Q. The effects of focusing lenses on SANS resolution are discussed.

1. FOCUSING LENSES' BASIC EQUATIONS

The focusing lenses' basic equations are described here (Mildner et al, 2005; Hammouda-Mildner, 2007). The focal length for a set of N lenses of radius of curvature R and index of refraction n is given by:

$$f = \frac{R}{2N(1-n)}.$$ (1)

The index of refraction n is related to the material atomic density ρ, neutron scattering length b_c, and neutron wavelength λ as:

$$n = 1 - \frac{\rho b_c}{2\pi}\lambda^2.$$ (2)

The focal length is also related to the source-to-lenses distance L_1 and lenses-to-focal point distance L_2 as:

$$\frac{1}{f} = \frac{1}{L_1} + \frac{1}{L_2}.$$ (3)

Combining the above two equations gives a relationship between the number N of lenses used and the neutron wavelength λ for an optimized instrument configuration where the detector is located at the focal spot.

$$\frac{\pi}{\rho b_c}\frac{R}{N\lambda^2} = \frac{L_1 L_2}{L_1 + L_2}.$$ (4)
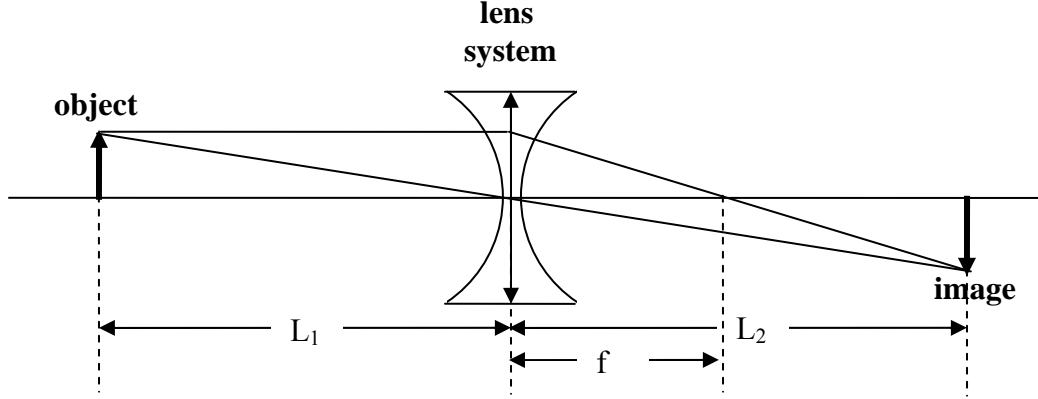
Figure 1: Schematic representation of a focusing lens system showing an object (the neutron source aperture) and its image (on the detector plane). L_1 and L_2 are the source-to-sample and sample-to-detector distances and f is the focal length. In practice, neutron focusing devices comprise many lenses used together.

For MgF_2 lenses the factor, one has:

$$\rho b_c / \pi = 1.632 * 10^{-6} \, \text{Å}^{-2}$$

so that:

$$\frac{N\lambda^2}{R}\left(\frac{L_1 L_2}{L_1 + L_2}\right) = \frac{\pi}{\rho b_c} = 6.13 * 10^5 \, \text{Å}^2 . \qquad (5)$$

Consider lenses of radius of curvature R = 2.5 cm and height H = 2.5 cm that are thin at the center (1 mm thickness) in order to keep neutron transmission high. Source-to-sample and sample-to-detector distances corresponding to the following SANS instrument configuration (L_1 = 16.14 m, L_2 = 13.19 m) give a focal length of

$$f = \left(\frac{L_1 L_2}{L_1 + L_2}\right) = 726 \, \text{cm} \qquad (6)$$

This gives $N\lambda^2 = 2111 \, \text{Å}^2$. The use of 7 consecutive lenses (N = 7) focuses neutrons of wavelength λ = 17.36 Å with a focal distance of 726 cm. The use of 30 consecutive lenses focuses neutrons of wavelength λ = 8.39 Å down to the same focal spot. The use of 14 consecutive lenses corresponds to a focusing wavelength λ = 12.20 Å.

For MgF_2, the index of refraction is:

$$n = 1 - 0.816 * 10^{-6} \lambda^2 . \qquad (7)$$

Note that the index of refraction of MgF_2 for neutrons is less than unity so that concave lenses focus neutrons whereas convex lenses defocus them. This is opposite to basic optics for light whereby the index of refraction is greater than unity.

2. RESOLUTION WITH FOCUSING LENSES

Consider a neutron beam with a triangular wavelength distribution and a focusing lens system optimized for the main wavelength λ_0 in that distribution. The main focal length is noted f_0 and corresponds to object-to-lens and lens-to-image distances of L_1 and L_2 respectively. Moreover consider another wavelength λ within the same distribution and its corresponding focal length f. The object-to-lens and lens-to-image distances are L_1 and L_4 respectively for this wavelength.

$$\frac{1}{f_0} = \frac{1}{L_1} + \frac{1}{L_2} = \frac{2N}{R}\frac{\rho b_c}{2\pi}\lambda_0^2 .$$ (8)

$$\frac{1}{f} = \frac{1}{L_1} + \frac{1}{L_4} = \frac{2N}{R}\frac{\rho b_c}{2\pi}\lambda^2 .$$
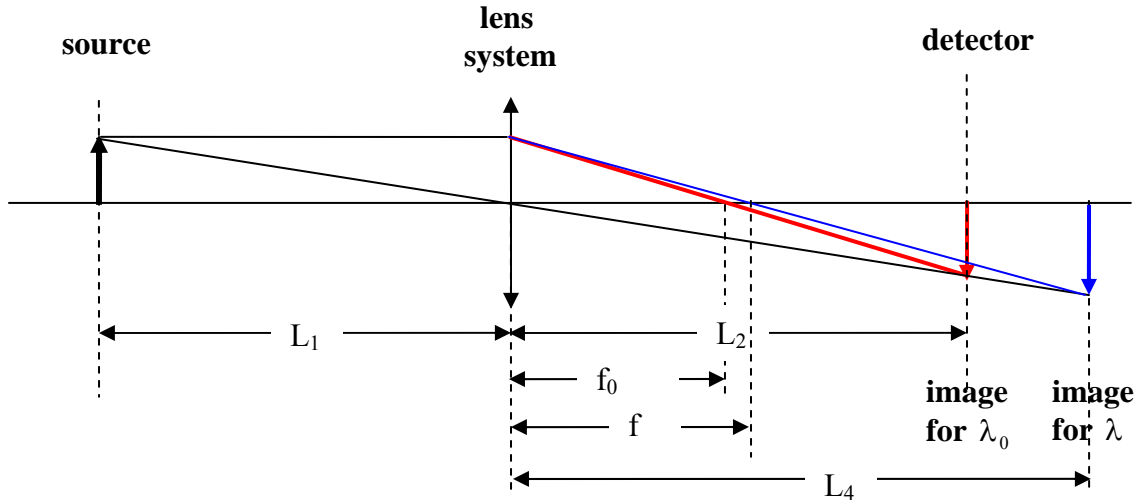
Figure 2: SANS focusing system showing the main image of the neutron source corresponding to the main neutron wavelength λ_0 and another image corresponding to another wavelength λ.

In order to calculate the resolution with the lens system, the "geometry" contribution contains three terms: one that corresponds to the image of the source aperture; another that corresponds to the sample aperture and a term that corresponds to averaging over a detector cell.
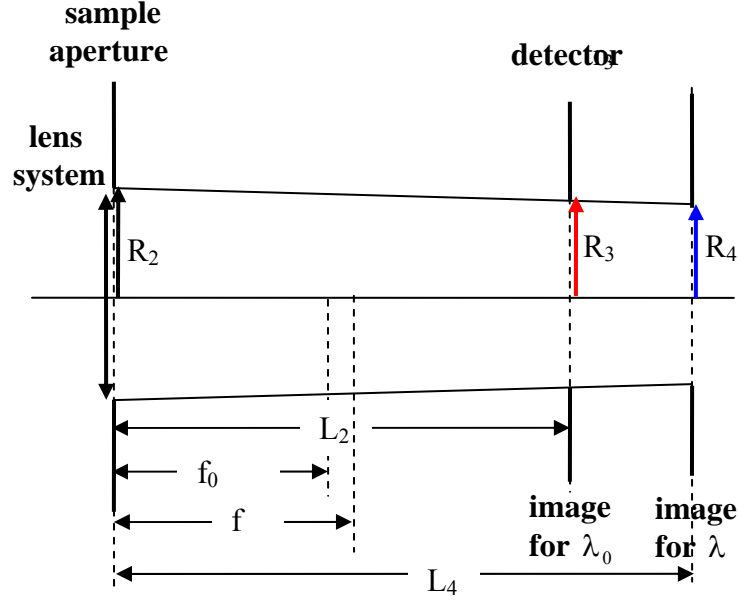
Figure 3: Schematic representation of the three main vertical planes containing the sample aperture, the area detector (source aperture image for λ_0) and the source aperture image for another wavelength λ.

Projection of the "geometry" part of the spatial resolution onto the detector plane in the horizontal direction is expressed as σ_x^2:

$$\left[\sigma_x^2\right]_{geo} = \left(\frac{L_2}{L_4}\right)^2 \frac{R_4^2}{4} + \left(\frac{L_4 - L_2}{L_4}\right)^2 \frac{R_2^2}{4} + \frac{1}{3}\left(\frac{\Delta x_3}{2}\right)^2. \tag{9}$$

Here R_4 is the radius of the image of the source aperture for the focal length f at wavelength λ. In order to see how the two scale factors were derived, consider the case $R_2 = 0$ for which $R_3 = \frac{L_2}{L_4} R_4$, then the case of $R_4 = 0$ for which $R_3 = \left(\frac{L_4 - L_2}{L_4}\right) R_2$. Δx_3 is the detector cell horizontal size. The image of the source aperture is given by $R_4 = \frac{L_4}{L_1} R_1$.

From the focusing equations, one obtains:

$$\frac{1}{f_0} - \frac{1}{f} = \frac{1}{L_2} - \frac{1}{L_4} = \frac{L_4 - L_2}{L_2 L_4} = \frac{1}{f_0}\left(1 - \left(\frac{\lambda}{\lambda_0}\right)^2\right). \tag{10}$$

Therefore:

160

$$\left[\sigma_x{}^2\right]_{geo} = \left(\frac{L_2}{L_1}\right)^2 \frac{R_1{}^2}{4} + \left(\frac{L_1 + L_2}{L_1}\right)\left(1 - \left(\frac{\lambda}{\lambda_0}\right)^2\right)^2 \frac{R_2{}^2}{4} + \frac{\Delta x_3{}^2}{12}. \qquad (11)$$

This is the result valid for any wavelength λ. Around the focal wavelength λ_0, the averaging

over the triangular wavelength distribution yields for the square term $\left(1 - \left(\frac{\lambda}{\lambda_0}\right)^2\right)^2$ the

result $\frac{2}{3}\left(\frac{\Delta\lambda}{\lambda}\right)^2$. Even though the subscript on λ_0 is dropped, it should be remembered that these results are valid only for the focusing wavelength.

Finally:

$$\left[\sigma_y{}^2\right]_{geo} = \left(\frac{L_2}{L_1}\right)^2 \frac{R_1{}^2}{4} + \left(\frac{L_1 + L_2}{L_1}\right)\frac{2}{3}\left(\frac{\Delta\lambda}{\lambda}\right)^2 \frac{R_2{}^2}{4} + \frac{\Delta x_3{}^2}{12}. \qquad (12)$$

The spatial resolution in the vertical direction $\sigma_y{}^2$ involves the same terms as $\sigma_x{}^2$ along with contributions due to the gravity effect.

Neutrons follow a parabolic trajectory:

$$y(z) = y_0 - A\lambda^2 \qquad \text{where } A = L_2(L_1 + L_2)\frac{gm^2}{2h^2}. \qquad (13)$$

The effect of gravity and wavelength spread contribute terms of the following form to $\sigma_y{}^2$:

$$\left[\sigma_{Qy}{}^2\right]_{grav} = <y(z)^2> - <y(z)>^2 = A^2[<\lambda^2> - \lambda^2] = A^2\lambda^4 \frac{2}{3}\left(\frac{\Delta\lambda}{\lambda}\right)^2. \qquad (14)$$

$$\left[\sigma_{Qy}{}^2\right]_{wav} = Q^2 \frac{1}{6}\left(\frac{\Delta\lambda}{\lambda}\right)^2.$$

In summary, the Q resolution is then obtained as:

$$\sigma_{Qy}{}^2 = \left[\sigma_{Qy}{}^2\right]_{geo} + \left[\sigma_{Qy}{}^2\right]_{wav} + \left[\sigma_{Qy}{}^2\right]_{grav} \qquad (15)$$

$$\sigma_{Qx}{}^2 = \left(\frac{2\pi}{\lambda L_2}\right)^2\left[\left(\frac{L_2}{L_1}\right)^2 \frac{R_1{}^2}{4} + \left(\frac{L_1 + L_2}{L_1}\right)\frac{2}{3}\left(\frac{\Delta\lambda}{\lambda}\right)^2 \frac{R_2{}^2}{4} + \frac{1}{3}\left(\frac{\Delta x_3}{2}\right)^2\right] + Q_x{}^2 \frac{1}{6}\left(\frac{\Delta\lambda}{\lambda}\right)^2$$

$$\sigma_{Qy}^{2} = \left(\frac{2\pi}{\lambda L_2}\right)^2\left[\left(\frac{L_2}{L_1}\right)^2\frac{R_1^{\,2}}{4}+\left(\frac{L_1+L_2}{L_1}\right)^2\frac{2}{3}\left(\frac{\Delta\lambda}{\lambda}\right)^2\frac{R_2^{\,2}}{4}+\frac{1}{3}\left(\frac{\Delta y_3}{2}\right)^2+A^2\lambda^4\frac{2}{3}\left(\frac{\Delta\lambda}{\lambda}\right)^2\right]+Q_y^{\,2}\frac{1}{6}\left(\frac{\Delta\lambda}{\lambda}\right)^2$$

Using focusing lenses modifies the "sample" term only (second term proportional to $R_2^{\,2}$). This term becomes much smaller with lenses. When lenses are used, the source aperture R_2 can be made larger without much resolution penalty.

3. MINIMUM Q WITH FOCUSING LENSES

The minimum reachable value of Q starts at the edge of the beam spot. The geometry of focusing lenses is characterized by an umbra only (with no penumbra). The neutron beam spot at the detector is therefore characterized by a box (not a trapezoidal) profile. A simple optics argument gives for the edge of the beam umbra in the horizontal and vertical directions for each wavelength λ the following:

$$X_{min}(\lambda) = \frac{L_2}{L_1}R_1+\left(\frac{L_1+L_2}{L_1}\right)\left|1-\left(\frac{\lambda}{\lambda_0}\right)^2\right|R_2+\frac{\Delta x_3}{2} \qquad (16)$$

$$Y_{min}(\lambda) = \frac{L_2}{L_1}R_1+\left(\frac{L_1+L_2}{L_1}\right)\left|1-\left(\frac{\lambda}{\lambda_0}\right)^2\right|R_2+\frac{\Delta y_3}{2}+2A\lambda^2\left(\frac{\Delta\lambda}{\lambda}\right).$$

The last term in $Y_{min}(\lambda)$ is due to gravity effect. Now the minimum achievable spot sizes are obtained by considering the part of the spot due to a wavelength spread $\Delta\lambda$.

$$X_{min}(\lambda) = \frac{L_2}{L_1}R_1+\left(\frac{L_1+L_2}{L_1}\right)\left|\left(1-\left(\frac{\lambda_0+\Delta\lambda}{\lambda_0}\right)^2\right)-\left(1-\left(\frac{\lambda_0}{\lambda_0}\right)^2\right)\right|R_2+\frac{\Delta x_3}{2}. \qquad (17)$$

The magnitude part reduces to:

$$\left|\left(1-\left(\frac{\lambda_0+\Delta\lambda}{\lambda_0}\right)^2\right)-\left(1-\left(\frac{\lambda_0}{\lambda_0}\right)^2\right)\right| \cong 2\left(\frac{\Delta\lambda}{\lambda}\right). \qquad (18)$$

Now that the wavelength averaging has been performed, the 0 subscript in λ_0 is dropped for simplicity. The horizontal and vertical beam spot sizes are:

$$X_{min} = \frac{L_2}{L_1}R_1+\frac{L_1+L_2}{L_1}2\left(\frac{\Delta\lambda}{\lambda}\right)R_2+\frac{\Delta x_3}{2} \qquad (19)$$

$$Y_{min} = \frac{L_2}{L_1}R_1+\frac{L_1+L_2}{L_1}2\left(\frac{\Delta\lambda}{\lambda}\right)R_2+\frac{\Delta y_3}{2}+2A\lambda^2\left(\frac{\Delta\lambda}{\lambda}\right).$$

162

The corresponding values of the minimum Q are:

$$Q_{min}{}^{X} = \frac{2\pi}{\lambda}\frac{X_{min}}{L_2}$$

$$Q_{min}{}^{Y} = \frac{2\pi}{\lambda}\frac{Y_{min}}{L_2}$$

(20)

4. MEASURED SANS RESOLUTION

Specific Instrument Configuration

Consider the following instrument configuration:

$L_1 = 16.14$ m
$L_2 = 13.19$ m
$R_1 = 0.715$ cm
$R_2 = 0.635$ cm
$\Delta x_3 = \Delta y_3 = 0.5$ cm
$\frac{\Delta\lambda}{\lambda} = 0.13.$

(21)

This gives $A = 0.01189$ cm/ Å^2.

Measurements with Focusing Lenses

Neutron optics measurements were made using a set of 7 consecutive biconcave MgF_2 lenses (described earlier) inserted in the beam just before the sample aperture. This set corresponds to a focal wavelength λ_0 around 17.36 Å.

The measured position of the neutron beam spot on the detector agrees with predictions.

With Neutron Lenses
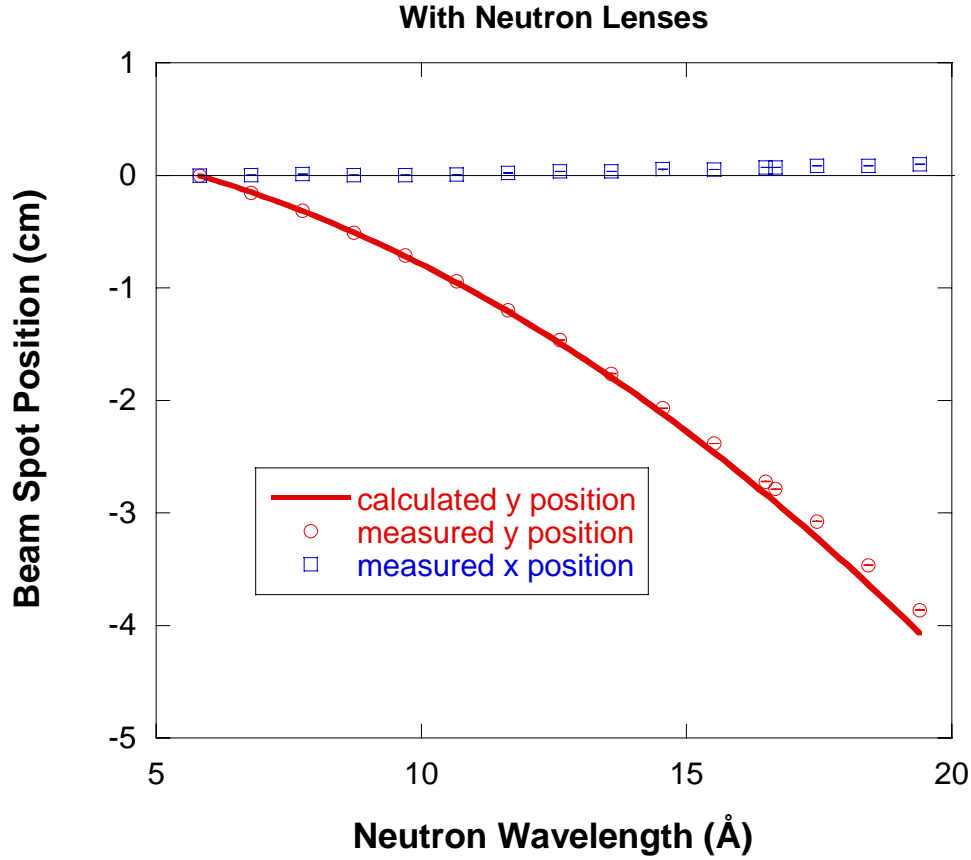
Figure 4: Variation of the neutron beam spot positions with wavelength.

The beam spot resolution has strong (parabolic) wavelength dependence both in the x and in the y directions. The minimum resolution in the horizontal direction corresponds to a focal wavelength λ_0. The minimum in the x direction ($\lambda_0 = 17.2$ Å) is taken to be the focal wavelength for our focusing arrangement since the x direction is independent of gravity effects. A procedure of using slice cuts across the beam spot was used to obtain these plotted results (including the $\sqrt{1.45}$ scaling discussed in a previous chapter). The calculated trends agree with the measured ones.
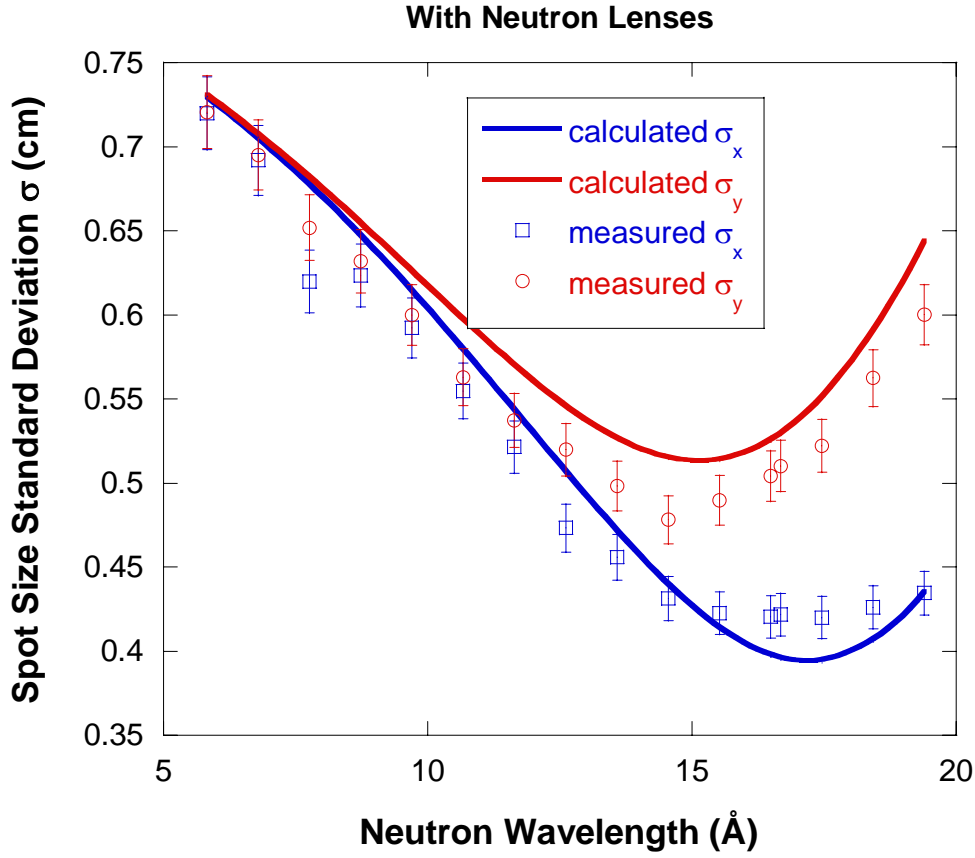
Figure 5: Variation of the spot size standard deviation with wavelength in the horizontal and vertical directions.

Variation of the minimum spot sizes as a function of increasing wavelength is characterized by a minimum around $\lambda_0 = 17.2$ Å. The measured values have been chosen conservatively and are found to be overestimates that are higher than the calculated values.
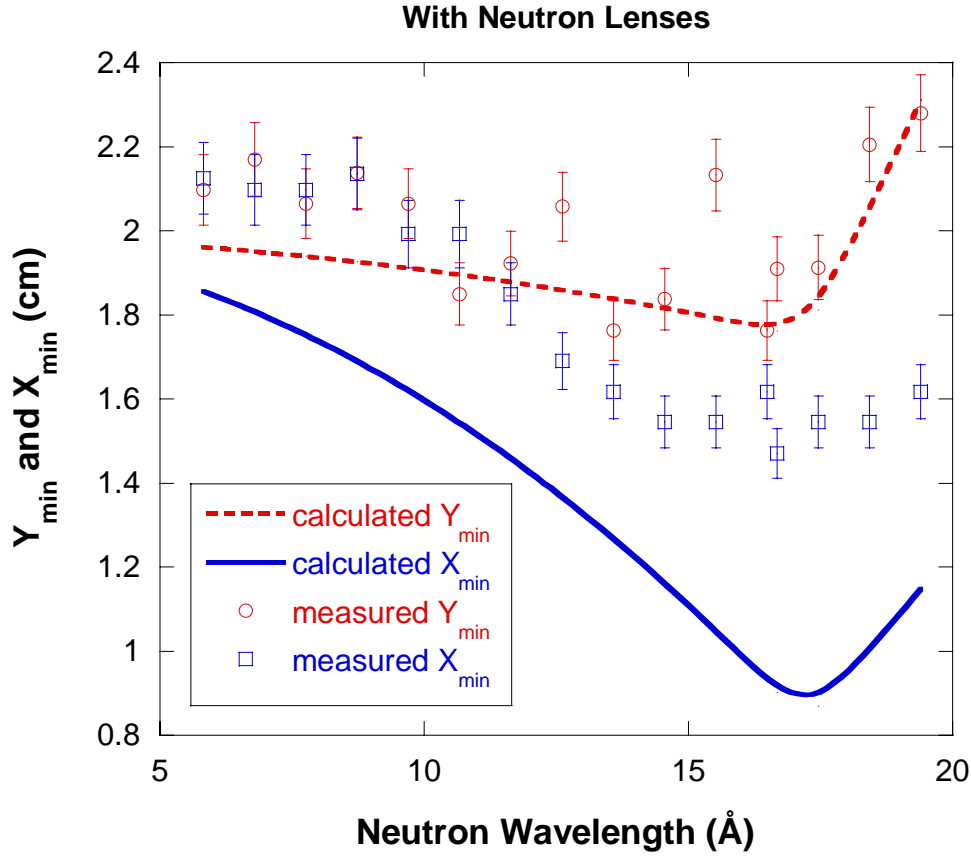
Figure 6: Variation of the minimum spot sizes with increasing wavelength.

Discussion

The use of converging lenses has the advantage of allowing the opening up of the sample aperture (i.e., increasing R_2) without penalty in resolution. This happens because the penumbra is minimized when lenses are used. The main effect is increased neutron current on sample.

Refractive lenses are characterized by chromatic aberrations that show up as a dependence of both the variance σ_x^2 and X_{min} on $(\Delta\lambda/\lambda)$. In order to reduce these chromatic aberrations, $(\Delta\lambda/\lambda)$ could be made smaller; which would result in a penalty in neutron current on sample. Focusing devices that use reflection (rather then refraction) optics (such as elliptical or torroidal mirrors) are not hampered by such chromatic aberrations.

5. LENS TRANSMISSION

The transmission of a set of 7 concave spherical lenses is calculated and compared to transmission measurements. Consider a lens of spherical radius R and thickness 2h at the center and assume that the beam defining aperture has a radius of B.
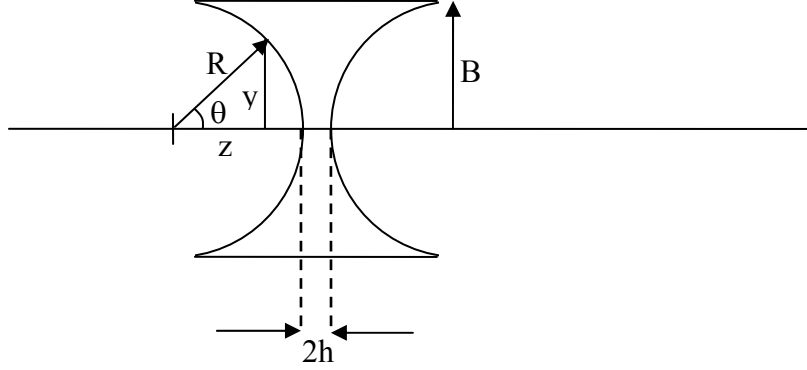
Figure 7: Schematics of the lens geometry.

The transmission of one focusing lens averaged over the beam aperture is given by:

$$T_1 = \frac{1}{\pi B^2} \int_0^B dy \, 2\pi y \exp[-2\Sigma_t (h + R - z)] \qquad (22)$$

Here y is the vertical coordinate, z is the horizontal coordinate obeying $z = \sqrt{R^2 - y^2}$ and Σ_t is the macroscopic cross section for MgF_2. Note that Σ_t varies with neutron wavelength as Σ_t = 0.000513 λ where λ is in Å and Σ_t in mm^{-1}. This variation was measured using a uniform thickness slab of MgF_2.

Performing the simple integration, one obtains:

$$T_1 = \frac{\exp[-2\Sigma_t (h + R)]}{2(\Sigma_t B)^2} \left\{ \left[1 - 2\Sigma_t \sqrt{R^2 - B^2} \right] \exp\left[2\Sigma t \sqrt{R^2 - B^2} \right] - (1 - 2\Sigma_t R) \exp[2\Sigma_t R] \right\}$$

(23)

The transmission of a set of 7 focusing lenses is given by $T_7 = T_1^7$.

The calculated and measured transmissions for the 7-lens system are compared for increasing neutron wavelength.
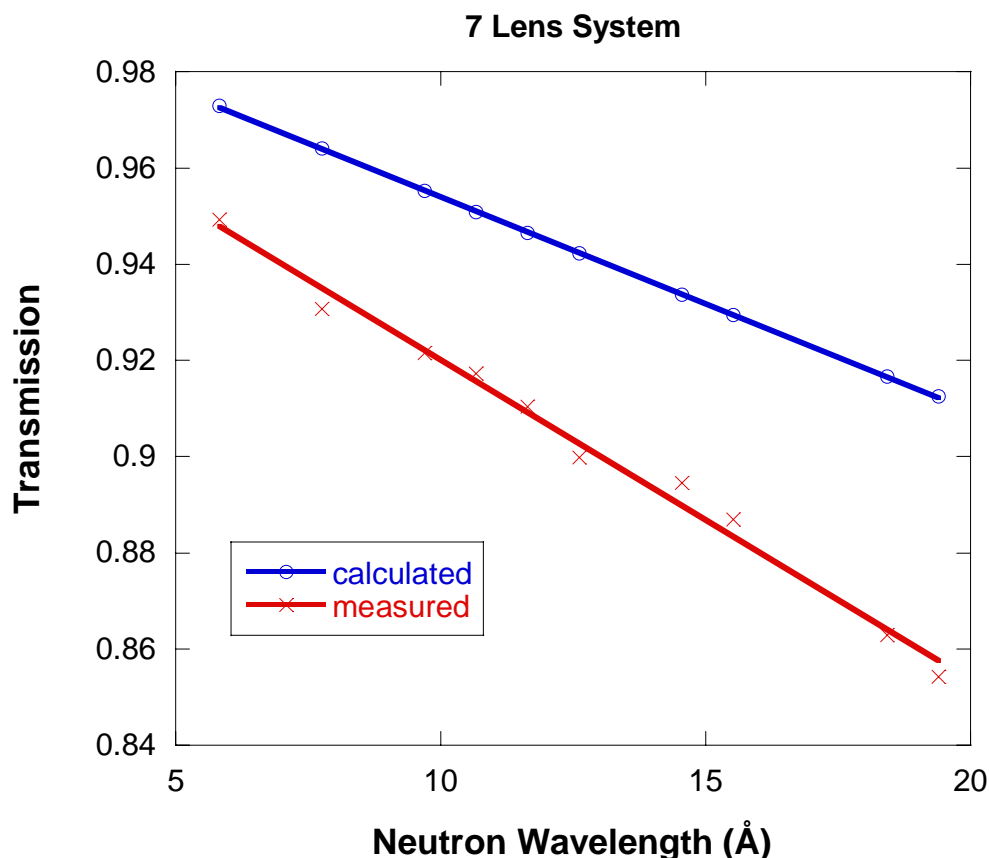
7 Lens System

Figure 8: Calculated and measured neutron transmissions for a 7-lens system.

The calculated and measured transmissions agree only partially.

REFERENCES

D.F.R. Mildner, B. Hammouda, and S.R. Kline, "A Refractive Focusing Lens System for SANS", J. Appl. Cryst. 38, 979-987 (2005).

B. Hammouda and D.F.R. Mildner, "SANS Resolution with Refractive Optics", J. Appl. Cryst. 40, 250-259 (2007).

QUESTIONS

1. What is the main difference between focusing lenses for neutrons and focusing lenses for light?
2. Name a typical neutron focusing lens material.
3. When using neutron focusing lenses, what term of the instrumental resolution variance is modified? What is the advantage of this?
4. What are chromatic aberrations?

5. Do reflective optical devices suffer from chromatic aberrations? Name a refractive optics focusing device.

6. Given the transmission T_1 of one focusing lens, calculate the transmission T_7 of a 7-lens system.

7. Using many lens systems, could one build a neutron microscope?

8. What is the two main figures of merit for making a good refractive material to be used for making neutron lenses?

ANSWERS

1. Focusing lenses for neutrons are concave. Focusing lenses for light are convex. This is due to the fact that the index of refraction for neutrons is negative while that for light is positive for most typical focusing materials.

3. MgF_2 is a commonly used neutron focusing lens material.

4. The use of focusing lenses modifies the "sample aperture" term of the resolution variance. This term becomes much smaller even for larger source apertures. The advantage is a larger neutron current on sample.

4. Chromatic aberrations correspond to the de-focusing effect for different wavelengths. The position of the source aperture image changes with wavelength.

5. There are no chromatic aberrations with refractive optics. Torroidal or elliptical mirrors are typical refractive optics focusing devices.

6. The transmission of a 7-lens system is given by $T_7 = T_1{}^7$ where T_1 is the transmission of one lens.

7. If one had lenses before and lenses after the sample, one could obtain magnification using a neutron beam. Chromatic aberrations, the required long flight paths and coarse area detector resolution give only modest magnification and a fuzzy picture.

8. The two figures of merit for making good refractive materials for making neutron lenses are as follows. (1) High density ρ and high coherent scattering length b_c in order to make the index of refraction n as small as possible. Recall that $1 - n = \dfrac{\rho b_c}{2\pi}\lambda^2$. Making 1-n large (i.e., n small) reduces the focal distance f since $f = \dfrac{R}{2N(1-n)}$ where R is the lens radius and N is the number of lenses. (2) One would want to minimize the incoherent and absorption scattering cross sections Σ_i and Σ_a in order to minimize background and maximize lens transmission.

Chapter 17 - **GRAVITY CORRECTRING PRISMS**

Prisms are used to deflect the neutron beam upward therefore correcting for neutron fall due to gravity at long wavelengths. Prisms contribution to SANS resolution and Q_{min} are discussed here (Hammouda-Mildner, 2007).

1. NEUTRON TRAJECTORY

The parabolic neutron trajectory equation in the pre-sample collimation follows.

$$y(z) = B\lambda^2 z(L_1 - z) \qquad\qquad 0 \leq z \leq L_1 \qquad\qquad (1)$$

With:

$$B = \frac{gm^2}{2h^2} = 3.073*10^{-9}\,cm^{-1}Å^{-2}. \qquad\qquad (2)$$

The z-direction is along the neutron beam and the y axis is in the vertical direction. L_1 is the source-to-sample distance. The vertical component of the neutron trajectory slope $y'(z)$ is therefore:

$$y'(z) = B\lambda^2(L_1 - 2z) \qquad\qquad 0 \leq z \leq L_1 \qquad\qquad (3)$$
$$y'(L_1) = -B\lambda^2 L_1 \qquad\qquad z = L_1.$$

This neutron trajectory holds between the sample and detector. The addition of a prism changes the neutron trajectory by introducing an upward deflection.
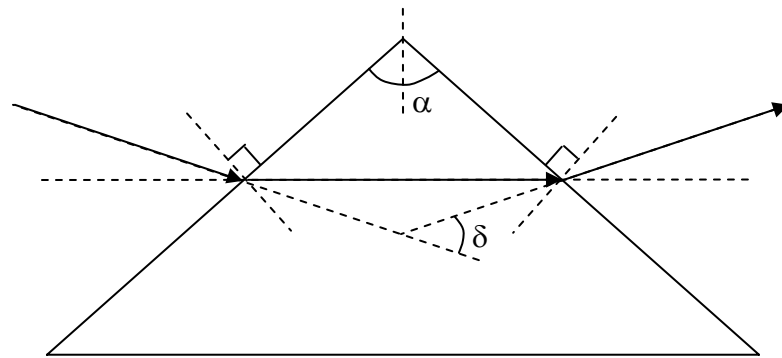

Figure 1: Schematics of a prism showing the deflected neutron trajectory in the simple case of minimum deviation.

The slope of the neutron trajectory is changed to

$$y'(L_1) = -B\lambda^2 L_1 + \delta \qquad\qquad z = L_1. \qquad\qquad (4)$$

The neutron trajectory is therefore changed between the sample and detector to the following form:

$$y(z) = -B\lambda^2 (z - L_1)^2 + [-B\lambda^2 L_1 + \delta](z - L_1) \qquad L_1 \le z \le L_1 + L_2. \qquad (5)$$
$$y(L_1 + L_2) = -B\lambda^2 L_2 (L_1 + L_2) + \delta L_2 \qquad\qquad z = L_1 + L_2.$$

The use of a prism with deflection angle $\delta = B\lambda^2(L_1+L_2)$ would correct for the gravity effect exactly.

2. THE PRISM DEFLECTION ANGLE

The "prism equation" (case of minimum deflection where the refracted beam is parallel to the prism base) relates the deflection angle δ, the prism angle α and the index of refraction n as:

$$n = \frac{\sin\left(\dfrac{\alpha - \delta}{2}\right)}{\sin\left(\dfrac{\alpha}{2}\right)}. \qquad\qquad (6)$$

The deflection angle is expressed as:

$$\delta = \alpha - 2\sin^{-1}\left[n\sin\left(\frac{\alpha}{2}\right)\right]. \qquad\qquad (7)$$

The wavelength dependence of the deflection angle enters through the index of refraction.

$$n = 1 - \frac{\rho b_c}{2\pi}\lambda^2. \qquad\qquad (8)$$

For MgF$_2$ prisms, $\rho b_c/\pi = 1.632*10^{-6}$ Å^{-2} so that n = 1-0.816*10$^{-6}\lambda^2$ (where λ is the neutron wavelength in Å).

In the small deviation angle approximation, one can expand the prism formula with $\delta \ll \alpha$ to obtain:

$$\delta(\lambda) \cong \left(\frac{\rho b_c}{\pi}\right)\tan\left(\frac{\alpha}{2}\right)\lambda^2 = C\lambda^2. \qquad\qquad (9)$$

This is an easier (approximate) expression to use in order to obtain analytical results.

3. CONTRIBUTION TO THE Q RESOLUTION

The Q resolution at the detector (where $z = L_1+L_2$) involves the spatial variance $\sigma_y{}^2$.

$$\sigma_y{}^2 = \left[\sigma_y{}^2\right]_{geo} + <y(L_1+L_2)^2> - <y(L_1+L_2)>^2 \qquad (10)$$

$$y(L_1+L_2) = -B\lambda^2 L_2(L_1+L_2) + \delta(\lambda)L_2. \qquad z = L_1+L_2$$

With the deviation angle given by $\delta(\lambda) = C\lambda^2$, where C depends on the prism material and apex angle the following result is obtained.

$$\sigma_y{}^2 = \left[\sigma_y{}^2\right]_{geo} + [A - L_2 C]^2 [<\lambda^4> - <\lambda^2>^2]. \qquad (11)$$

Here the gravity variable $A = BL_2(L_1+L_2)$ has been used.

Assuming a triangular wavelength distribution, the wavelength averages are calculated as follows:

$$[<\lambda^4> - <\lambda^2>^2] = \lambda^4 \frac{2}{3}\left(\frac{\Delta\lambda}{\lambda}\right)^2. \qquad (12)$$

Therefore:

$$\sigma_y{}^2 = \left[\sigma_y{}^2\right]_{geo} + [A - L_2 C]^2 \lambda^4 \frac{2}{3}\left(\frac{\Delta\lambda}{\lambda}\right)^2 \qquad (13)$$

This is the variance of the neutron spot spatial resolution at the detector in the vertical direction. By analogy, the case without prisms is obtained for $C = 0$. The familiar "geometry" contribution is given in terms of the source aperture radius R_1, sample aperture radius R_2 and detector cell size Δy_3.

$$\left[\sigma_y{}^2\right]_{geo} = \left(\frac{L_2}{L_1}\right)^2 \frac{R_1{}^2}{4} + \left(\frac{L_1+L_2}{L_1}\right)^2 \frac{R_2{}^2}{4} + \frac{\Delta y_3{}^2}{12} \qquad (14)$$

Since most often $\Delta x_3 = \Delta y_3$, $[\sigma_x{}^2]_{geo} = [\sigma_y{}^2]_{geo}$. The standard deviation of the Q resolution σ_{Qy} is related to the spatial standard deviation σ_y as $\sigma_{Qy} = \left(\frac{2\pi}{\lambda L_2}\right)\sigma_y$.

4. CONTRIBUTION TO Q_{MIN}

Q_{min} has contributions from geometry, gravity effect and the addition of a prism.

$$Y_{min} = [Y_{min}]_{geo} + |A - L_2 C| \frac{[(\lambda + \Delta\lambda)^2 - (\lambda - \Delta\lambda)^2]}{2}. \qquad (15)$$

The wavelength term can be expressed (to first order) as:

$$\frac{[(\lambda + \Delta\lambda)^2 - (\lambda - \Delta\lambda)^2]}{2} \cong 2\lambda^2 \left(\frac{\Delta\lambda}{\lambda}\right) \qquad (16)$$

Therefore:

$$Y_{min} = \frac{L_2}{L_1} R_1 + \frac{L_1 + L_2}{L_1} R_2 + \frac{\Delta y_3}{2} + |A - L_2 C| 2\lambda^2 \left(\frac{\Delta\lambda}{\lambda}\right). \qquad (17)$$

Note that the same factor $|A - L_2 C|$ enters in the resolution variance σ_y^2 and in Y_{min}. Q_{ymin} is obtained by multiplying Y_{min} by the factor $(2\pi/\lambda L_2)$.

5. MEASUREMENTS WITH GRAVITY CORRECTING PRISMS

A prism cassette containing a row of five prisms is used for neutron optics measurements. Each prism is made out of single-crystal MgF_2 and has a base of 3 cmx3 cm and a height of 0.5 cm. In order to correct fully for the effect of gravity, between one and two prism cassettes would have to be used. Here only one cassette is used for the sake of simplicity.
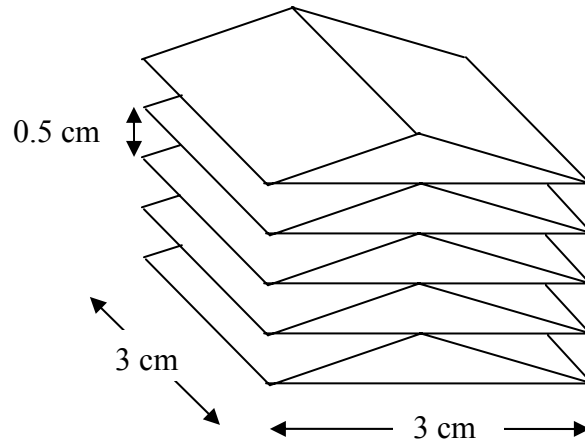
Figure 2: Representation of the prism cassette containing a row of 5 MgF_2 prisms.

The prism angle is equal to $\alpha = 2\tan^{-1}(1.5/0.5) = 143.13^{\circ}$. The prism variable is $C = 4.896*10^{-6}$ Å^{-2} yielding an estimate for the factor $L_2C = 6.458*10^{-3}$ cm.Å^{-2} and for the factor $|A - L_2C| = 0.00543$ cm/Å^2.

A set of neutron optics measurements have been performed using the following instrument configuration:

$$L_1 = 16.14 \text{ m} \tag{18}$$
$$L_2 = 13.19 \text{ m}$$
$$R_1 = 0.715 \text{ cm}$$
$$R_2 = 0.635 \text{ cm}$$
$$\Delta x_3 = \Delta y_3 = 0.5 \text{ cm}$$
$$\frac{\Delta\lambda}{\lambda} = 0.13.$$

This gives $A = 0.01189$ cm/ Å^2.

The vertical position of the neutron beam varies with the neutron wavelength l following the parabola:

$$y(L_1 + L_2) = (-A + L_2C)\lambda^2 \qquad z = L_1 + L_2 \tag{19}$$

When no prisms are used ($C = 0$), neutrons fall due to gravity. When prisms are used, falling neutrons are deflected upward. This is plotted as a function of wavelength and compared to the measured values. The value corresponding to $\lambda = 6$ Å has been subtracted in each case for simplicity.
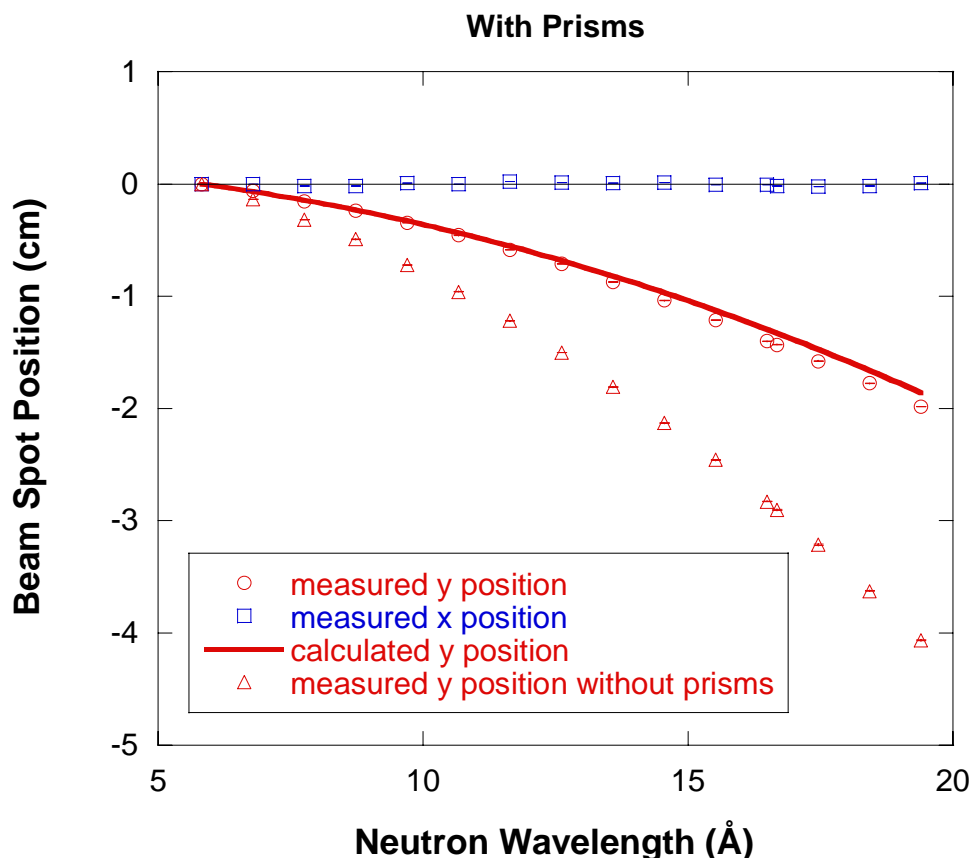
With Prisms

Figure 3: Variation of the neutron beam spot positions with wavelength. Statistical error bars are smaller than the plotting symbols.

The variance of the neutron beam spot at the detector has also been measured in each case and compared to the calculated value. A figure shows the square root of the difference in the variances of the beam spot in the orthogonal directions as a function of wavelength. The measured values are obtained using the same procedure described before (taking horizontal and vertical slice cuts across the neutron beam spot). The prediction for the case without prisms is also shown. The measured values are seen to be systematically higher than the calculated ones. This is believed to be caused principally by neutrons leaking between the apex and the base of adjacent prisms.

With Prisms
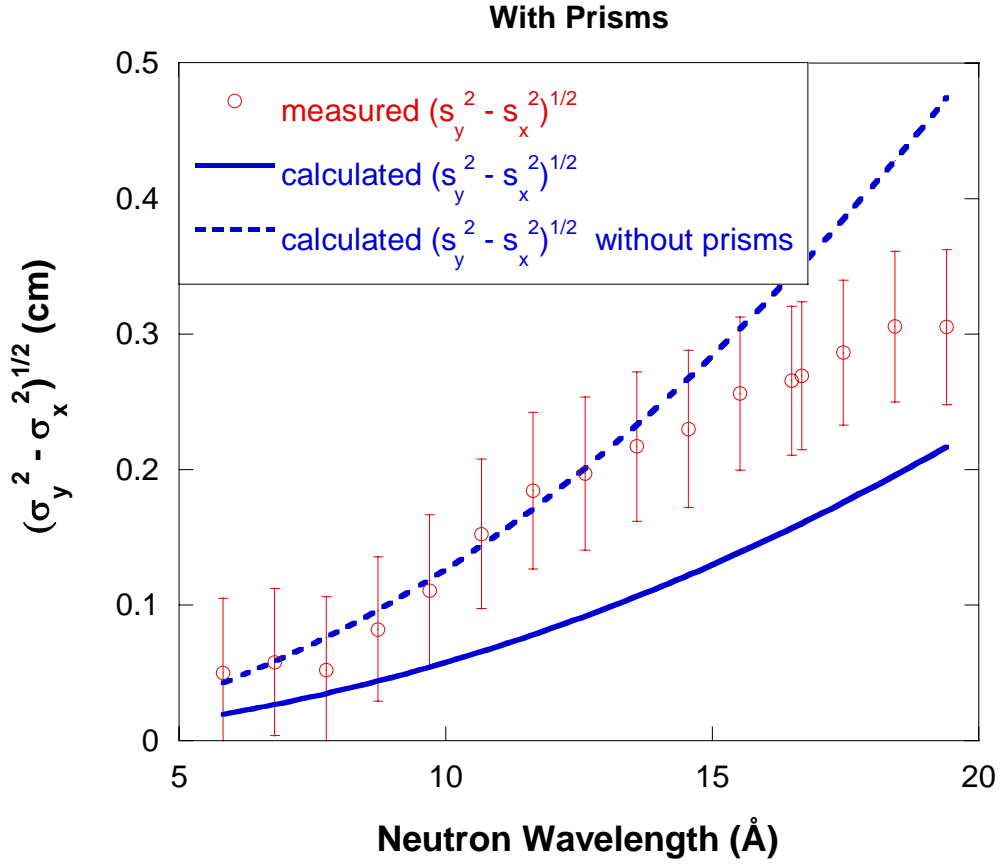
Figure 4: Variation of the variance of the neutron spot at the detector with wavelength. Statistical error bars have been included. Discrepancy between measured and calculated values is likely due to neutron leakage between adjacent prisms.

6. PRISMS TRANSMISSION

Consider a prism system containing a row of prisms of width W and height H and assume a beam defining aperture of radius B.

Figure 5: Transmission through one row of prisms.

The transmission through one row of prisms using a source aperture of diameter $2R_2$ can be calculated as follows.

$$T = \frac{\int_0^{2B} dy \, \exp[-\Sigma_t 2z]}{2B} \tag{20}$$

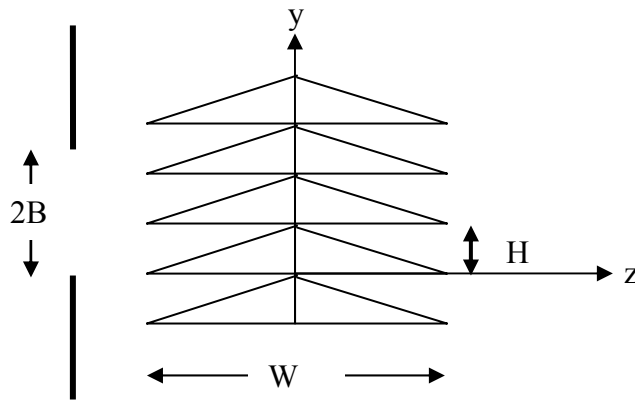Here 2z is the path across a prism at a height y. For $0 \leq y \leq H$, it is $2z = (H-y)W/H$. The integration is performed for y covering each prism. When 2B is not a multiple of H, the result is:

$$T = \frac{[2 - 3\exp(-\Sigma_t W) + \exp(-3\Sigma_t W + \Sigma_t 2BW/H)]}{\Sigma_t 2BW/H} \tag{21}$$

Note that this expression is for the transmission of one row of prisms. When 2B is a multiple of H, T is given simply by T_m:

$$T_m = \frac{[1 - \exp(-\Sigma_t W)]}{\Sigma_t W} \tag{22}$$

This result assumes that the beam defining aperture is rectangular. The total cross section for MgF_2 is estimated empirically as Σ_t (cm^{-1}) = 0.00513 λ (Å). A transmission measurement of the cassette containing two rows of prisms has been made using a sample aperture of 2B = 1.27 cm and a neutron wavelength of λ = 17.2 Å. The measured transmission was found to be T = 0.70 while the predicted transmission is T = 0.75. This result is not reliable due to the neutron streaming in-between the prisms..

7. DISCUSSION

Prisms correct for the neutron fall by deflecting the direct neutron beam back up. They also correct for the anisotropy of the neutron beam spot on the detector. Gravity deforms this spot to an oval shape. Prisms correct this shape back to a circular shape. Analytical expressions for the spatial resolution have been presented. Neutron beam optics measurements using a prism cassette have been made. Good agreement was found between calculated and measured beam spot positions. However, no good agreement was found for the instrumental resolution variance due to neutron leakage between adjacent prisms.

REFERENCE

B. Hammouda and D.F.R. Mildner, "SANS Resolution with Refractive Optics", J. Appl. Cryst. <u>40</u>, 250-259 (2007).

QUESTIONS

1. What is the advantage of using prisms in neutron optics?
2. Prisms refract incident white light into what?
3. The use of gravity correcting prisms affects what part of the instrumental resolution variance?
4. What is the wavelength dependence of the prism deflection angle?
5. What is the prisms minimum deviation approximation?
6. Could a prism system be used for all neutron wavelengths?

ANSWERS

1. Prisms correct for gravity effects. At long wavelengths the effect of neutron fall (due to gravity) is to lower the neutron beam spot and deform it into an oval shape. The use of prisms kicks the neutron spot back up and corrects it back to a circular shape.
2. Prisms refract incident white light into the rainbow spectrum.
3. The use of gravity correcting prisms affects the wavelength spread part of the instrumental resolution variance.
4. The prism deflection angle varies like the square of the wavelength.
5. The prism's minimum deviation approximation corresponds to the case where the refracted beam (inside the prism) is parallel to the prism's base.
6. Since the gravity correction factor $(A-L_2C)$ is independent of neutron wavelength λ, the same prism system can be used to correct for gravity at all wavelengths.

Chapter 18 - NEUTRON BEAM CURRENT

1. VARIATION OF DETECTOR COUNT RATE WITH SPOT SIZE

One important figure of merit relevant to the performance of SANS instruments is the neutron beam current on sample (i.e., number of neutrons per second reaching the sample aperture) as measured by the area detector; this is related to the total detector count rate summed up over the beam spot (Hammouda-Mildner, 2007). Since the detector is a "1/v" absorber, the beam current is proportional to the count rate/wavelength.

Using the same notation as before, consider the following SANS instrument configuration.

$$L_1 = 16.14 \text{ m} \qquad\qquad\qquad\qquad\qquad (1)$$
$$L_2 = 13.19 \text{ m}$$
$$R_1 = 0.715 \text{ cm}$$
$$R_2 = 0.635 \text{ cm}$$
$$\Delta x_3 = \Delta y_3 = 0.5 \text{ cm}$$
$$\frac{\Delta\lambda}{\lambda} = 0.13.$$

Total detector count rates are included here for the 3 cases considered previously: empty beam configuration, the use of focusing lenses and the use of gravity correcting prisms. A figure summarizes the variation of the total detector count rate with the minimum neutron spot size (in the vertical direction) Y_{min} for each case. Note that Y_{min} (not X_{min}) is what determines Q_{min}. The beam current depends on the ratio $(R_1 R_2 / L_1)^2$ which was the same in all three cases, and also on the neutron source spectrum. Each point corresponds to a different neutron wavelength (from 6 Å to 20 Å). No corrections have been made to account for the area detector efficiency ("1/v" absorber) or dead time losses. These effects are strongly wavelength dependent and are outside of the scope of the present discussion. The main observation is that increasing the neutron wavelength increases Y_{min} (i.e., broadens the neutron beam) for regular SANS optics but decreases Y_{min} when focusing lenses are used. Using prisms corrects for the beam broadening with increasing wavelength.

Using neutron lenses lowers Y_{min} substantially without too much loss in neutron current whereas using prisms is accompanied by neutron losses because of the prisms' low neutron transmission and due to the ineffective first generation prisms system used here. The lowest Y_{min} obtained with the lenses (at 17.2 Å neutrons) has low detector count rate (1,252 counts per second). Note that the sample aperture radius R_2 can be increased considerably without degrading the overall resolution. The use of lenses with a large sample area can enable a great increase in count rate on sample, with small penalty on resolution. The prisms used here correct only partially for the effect of gravity. If we had used prisms that correct "exactly" for the gravity effect, the prisms curve in the figure would have been vertical and shown no wavelength dependence.

All Cases
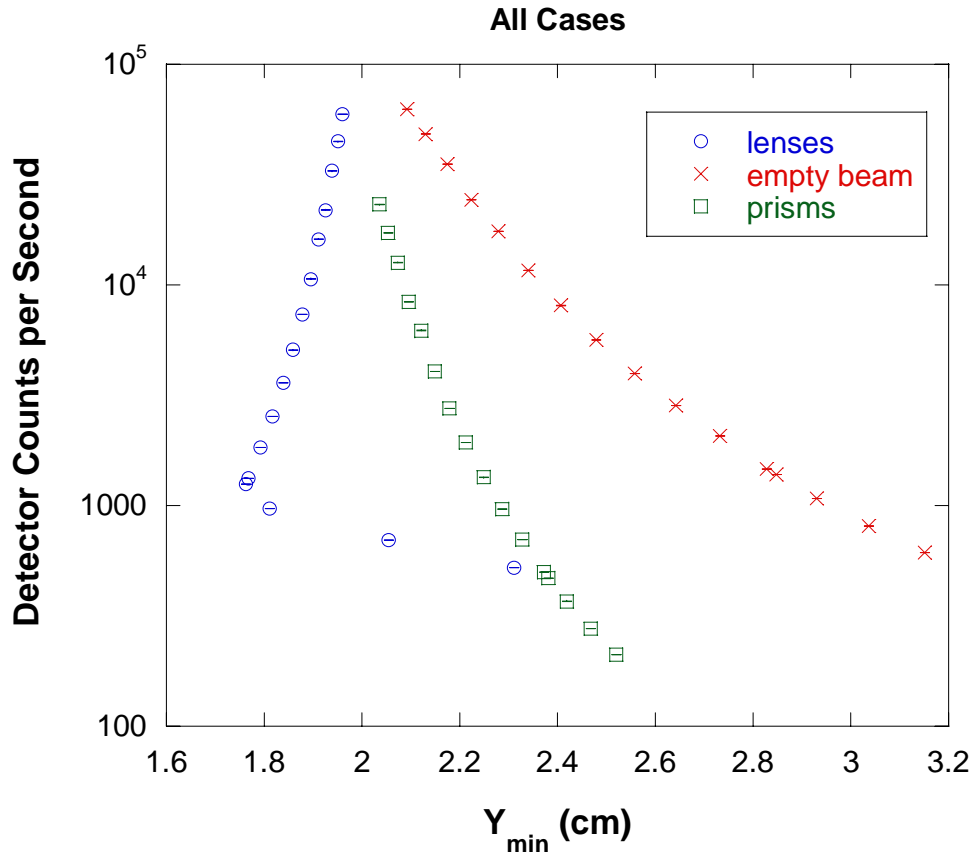
Figure 1: Variation of the total detector counts rate within the neutron spot with the extent of the beam size in the vertical direction Y_{min}. The 3 curves correspond to the 3 cases: (1) empty beam, (2) with lenses and (3) with prisms. Each data point corresponds to a different neutron wavelength.

2. VARIATION OF DETECTOR COUNT RATE WITH Q_{min}

Another slightly modified plot uses $Q^Y_{min} = (2\pi Y_{min})/(\lambda L_2)$ instead for the horizontal axis. Here λ is the neutron wavelength, L_2 is the sample-to-detector distance, Y_{min} is the vertical size of the neutron spot on the detector. The detector count rate is seen to drop quickly for lower Q_{min}. A log-log plot shows no simple power law behavior between the detector count rate and Q_{min}.
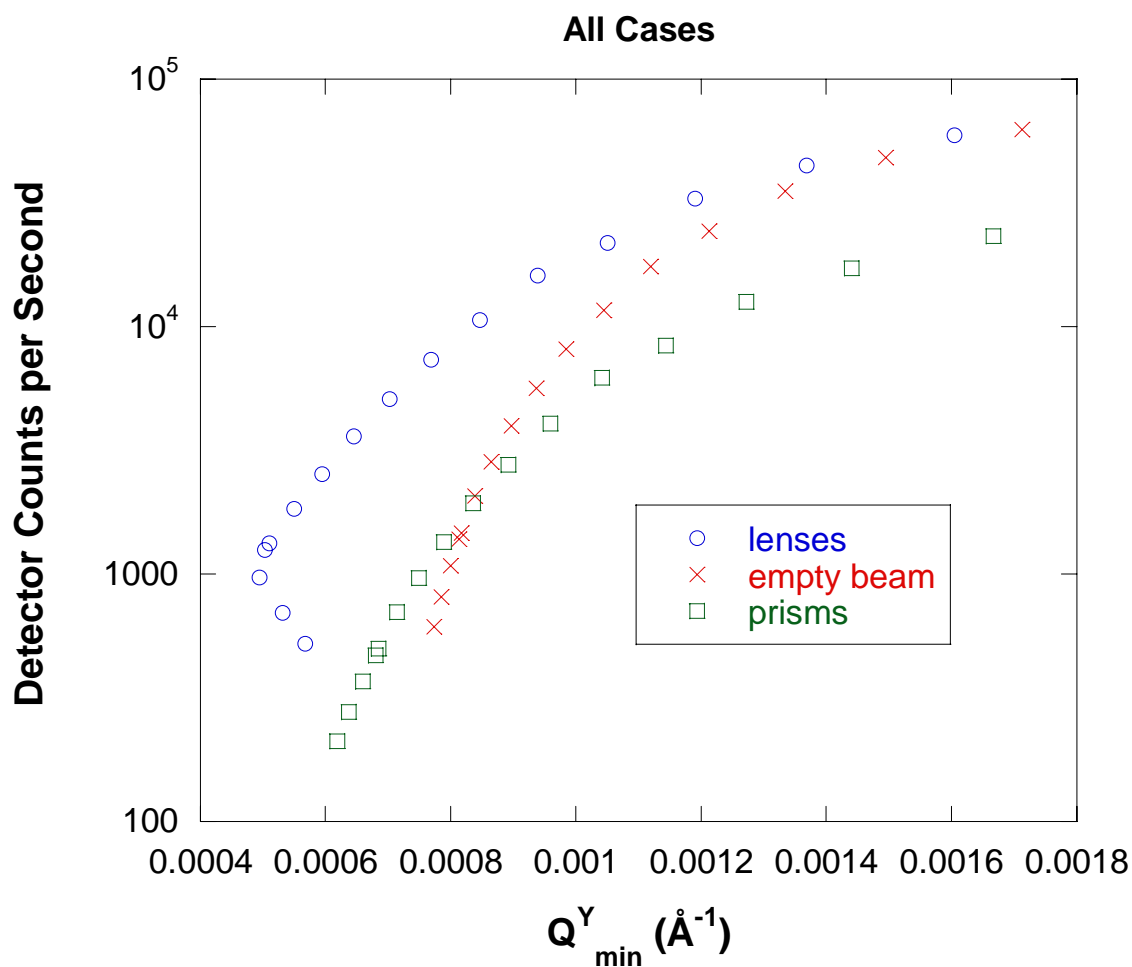
Figure 2: Variation of the detector count rate with Q^Y_{min} for the same 3 cases.

REFERENCE

B. Hammouda and D.F.R. Mildner, "SANS Resolution with Refractive Optics", J. Appl. Cryst. <u>40</u>, 250-259 (2007).

QUESTIONS

1. What is the neutron flux? What is the neutron beam current?
2. Why does the neutron beam spot on the detector broaden in the vertical direction when the wavelength is increased?
3. Why is there a minimum in the variation of the neutron beam current with neutron wavelength when a focusing lens system is used?

ANSWERS

1. The neutron flux is the number of neutrons per cm^2 per second. The neutron beam current is the number of neutrons per second. The neutron flux is also called the current density.
2. The neutron beam spot on the detector broadens in the vertical direction when the wavelength is increase due to the larger gravity effect. The neutron fall increases with wavelength square.
3. When a specific focusing lens system is used, there is a specific "focusing" wavelength whereby the source image occurs exactly at the detector position. This corresponds to the smallest focal spot on the detector.

In analyzing SANS data, smearing of the model function used is necessary before performing nonlinear least-squares fits. The smearing procedure involves a convolution integral between the resolution function and the scattering cross section for the scattering model.

1. THE RESOLUTION FUNCTION

Consider a 1D Gaussian resolution function (Barker-Pedersen, 1995):

$$P_{1D}(Q_x) = \left(\frac{1}{2\pi\sigma_{Q_x}^2} \right)^{1/2} \exp\left[-\frac{Q_x^2}{2\sigma_{Q_x}^2} \right] \tag{1}$$

This distribution is normalized to 1. $\int_{-\infty}^{+\infty} dQ_x P_{1D}(Q_x) = 1$.

In order to show this normalization, make a variable change to $X = Q_x^2$ so that $dX = 2Q_x dQ_x$ and the normalization integral becomes as follows.

$$\int_{-\infty}^{+\infty} dQ_x P_{1D}(Q_x) = 2\int_0^{+\infty} dQ_x P_{1D}(Q_x) = 2\int_0^{+\infty} dX \frac{1}{2\sqrt{X}} \left(\frac{1}{2\pi\sigma_{Q_x}^2} \right)^{1/2} \exp\left[-\frac{X}{2\sigma_{Q_x}^2} \right]. \tag{2}$$

The following integral is used:

$$\int_0^{+\infty} dX \frac{1}{\sqrt{X}} \exp[-aX] = \sqrt{\frac{\pi}{a}} \text{ (for a>0)} \tag{3}$$

This verifies that the $P_{1D}(Q_x)$ distribution is normalized. The Q_y distribution is similar.

Consider a 2D Gaussian resolution function:

$$P_{2D}(Q) = P_{1D}(Q_x)P_{1D}(Q_y) \tag{4}$$

$$= \left(\frac{1}{2\pi\sigma_{Q_x}^2} \right)^{\frac{1}{2}} \left(\frac{1}{2\pi\sigma_{Q_y}^2} \right)^{\frac{1}{2}} \exp\left[-\frac{Q_x^2}{2\sigma_{Q_x}^2} - \frac{Q_y^2}{2\sigma_{Q_y}^2} \right].$$

This distribution is also normalized to 1.

$$\int\limits_0^{+\infty} QdQ \int\limits_0^{2\pi} d\phi P_{2D}(Q) = 1 \tag{5}$$

In order to show this, make a variable change to $R = Q^2$ and $dR = 2QdQ$ and the normalization integral becomes as follows.

$$\int\limits_0^{+\infty} QdQ \int\limits_0^{2\pi} d\phi P_{2D}(Q) = \frac{1}{2} \int\limits_0^{+\infty} dR \left(\frac{1}{\pi\sigma_Q^2}\right) \exp\left[\frac{-R}{\sigma_Q^2}\right](2\pi) = \left[-\exp\left(-\frac{\infty}{\sigma_Q^2}\right) + \exp\left(-\frac{0}{\sigma_Q^2}\right)\right] = 1.$$
$$\tag{6}$$

2. THE RESOLUTION CORRECTION

The smeared 1D cross section corresponds to radially averaged SANS data and is given by the following integral (using polar corrdinates):

$$\frac{d\Sigma(Q)}{d\Omega} = \int\limits_0^{+\infty} Q'dQ' P_{1D}(Q')\frac{d\Sigma(Q-Q')}{d\Omega} =$$

$$= \int\limits_{-\infty}^{+\infty} dQ' \left(\frac{1}{2\pi\sigma_{Q'}^2}\right)^{1/2} \exp\left[-\frac{Q'^2}{2\sigma_{Q'}^2}\right]\frac{d\Sigma(Q-Q')}{d\Omega}. \tag{7}$$

The smeared 2D cross section integral corresponds to 2D SANS data and is given by the following expression:

$$\frac{d\Sigma(Q_x,Q_y)}{d\Omega} = \int\limits_{-\infty}^{+\infty} dQ'_x\, P_{1D}(Q'_x) \int\limits_{-\infty}^{+\infty} dQ'_y\, P_{1D}(Q'_y)\frac{d\Sigma(Q_x - Q'_x, Q_y - Q'_y)}{d\Omega}$$
$$\tag{8}$$

Note that (Q_x, Q_y) are in Cartesian coordinates. In cases where radial averaging of the data is not possible, the σ_{Qx}^2 and σ_{Qy}^2 variances are needed. Note that the variance $\sigma_Q^2 = \sigma_{Qx}^2 + \sigma_{Qy}^2$ is never used.
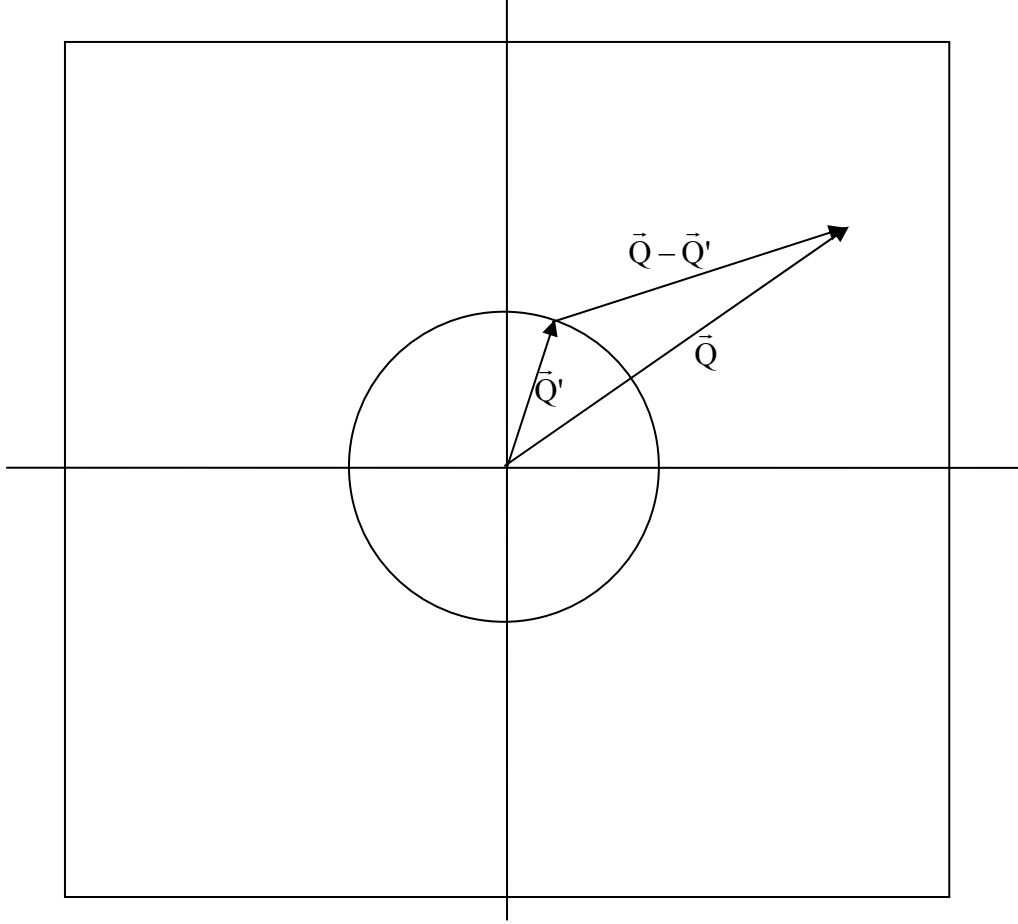
Figure 1: Parametrization in the detector plane.

3. ISO-INTENSITY CONTOUR MAPS WITH GRAVITY EFFECT

Gravity effect on the neutron trajectory distorts the iso-intensity contour maps from concentric circles to concentric oval shapes. The following parametric equation describes an elliptical shape:

$$\frac{x^2}{a^2} + \frac{y^2}{(a+b)^2} = 1. \tag{9}$$

Here a is the minor (horizontal) axis and a+b is the major (vertical) axis of the elliptical shape. If we consider different major axes for the top and bottom parts, an oval shape is obtained.

$$b = A(2\overline{\lambda}\Delta\lambda - \mathrm{sign}(y)\Delta\lambda^2). \tag{10}$$

The top and bottom parts have been represented using the sign function. The x and y coordinates can be expressed as:

$$x = r(\phi)\cos(\phi) \qquad\qquad (11)$$
$$y = r(\phi)\sin(\phi).$$

ϕ is the azimuthal angle for binning in the detector plane. Combining these equations, one obtains the following parametric equation:

$$r^2(\phi) = \frac{1}{\dfrac{\cos^2\phi}{a^2} + \dfrac{\sin^2\phi}{(a+b)^2}}. \qquad\qquad (12)$$

This represents the equal-Q contours for the constant-Q binning. Note that the gravity contribution is constant (independent of Q) so that the contours are oval at very low Q, become elliptical at intermediate Q then become circular at high Q.

4. NUMERICAL APPLICATION

Consider the following realistic case:

$$\begin{aligned}
&L_1 = 16.14 \text{ m} \qquad\qquad\qquad (13)\\
&L_2 = 13.19 \text{ m}\\
&\overline{\lambda} = 18 \text{ Å}\\
&\frac{\Delta\lambda}{\lambda} = 0.13\\
&A = 0.01189 \text{ cm/Å}^2
\end{aligned}$$

This gives

$$\lambda_{min} = 15.66 \text{ Å}, \ \lambda_{max} = 20.34 \text{ Å}.$$

Assuming $y_0 = 0$, the following results are obtained:

$$\begin{aligned}
&y_{min} = 2.916 \text{ cm}, \ y_{max} = 4.919 \text{ cm}\\
&\overline{y} = 3.852 \text{ cm}, \ <y> = 3.863 \text{ cm}\\
&\Delta y_{top} = y_{max} - \overline{y} = 1.0667 \text{ cm}\\
&\Delta y_{bot} = \overline{y} - y_{min} = 0.9365 \text{ cm}
\end{aligned}$$

Here $\overline{y}$ is the spot height corresponding to the mean wavelength $\overline{\lambda}$ and $<y>$ is the height of the beam center. Note that for any practical purpose $\overline{y} = <y>$ and the difference $\Delta y_{top} - \Delta y_{bot} = 0.130 \text{ cm}$ is so small that the oval shapes are really elliptical.

The beam standard deviation in the vertical direction is estimated to be $\sigma_y = 0.409$ cm using both the numerical integration over y and the analytical averaging over λ (formula given above).

Contour Plot
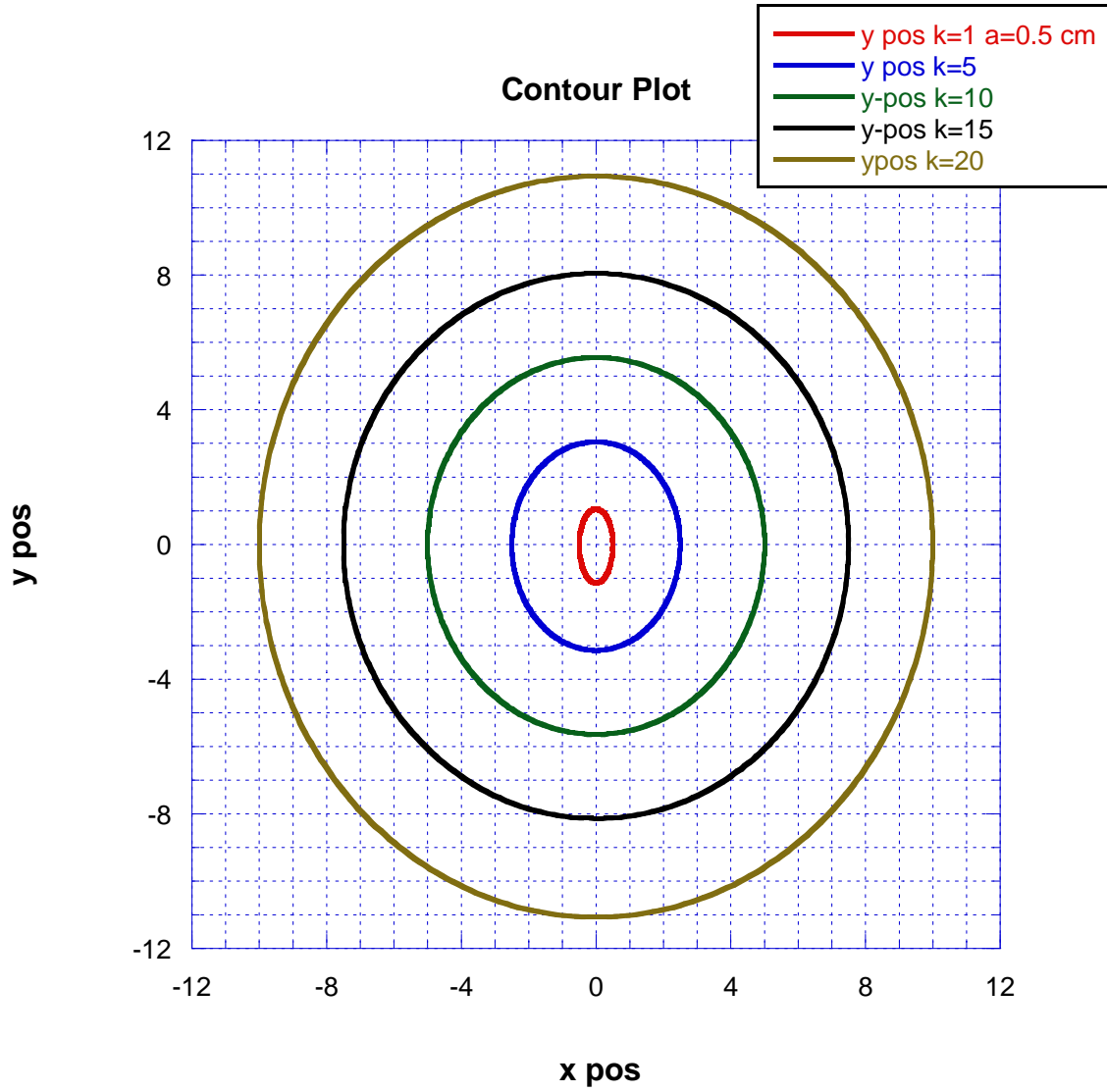
Figure 2: Iso-intensity contour map when neutrons are under the influence of gravity; i.e., at long wavelength ($\lambda = 18$ Å) and typical wavelength spread ($\frac{\Delta\lambda}{\lambda} = 13$ %). Contours corresponding to a = 0.5 cm and k = 1, 5, 10, 15 and 20 are shown. The x and y axes are in channel numbers (each detector channel corresponds to 0.5 cm).

5. SMEARING FOR HARD SPHERES

Consider idealized scattering from hard spheres and compare it to the smeared case. The form factor for a hard sphere of radius R = 50 Å is given by the following function:

$$P(Q) = \left[\left(\frac{3}{QR} \right) \left(\frac{\sin(QR)}{(QR)^2} - \frac{\cos(QR)}{QR} \right) \right]^2 \qquad (14)$$

Consider the following high-Q configuration:

$R_1 = 2.5$ cm $\qquad\qquad\qquad\qquad\qquad\qquad\qquad (15)$
$R_2 = 0.5$ cm
$\Delta x_3 = \Delta y_3 = 0.5$ cm
$L_1 = 1.5$ m
$L_2 = 1.5$ m
$\lambda = 6$ Å
$\dfrac{\Delta\lambda}{\lambda} = 15$ %.

The direct beam spatial resolution on the detector plane is:

$\sigma_x^2 = 1.83$ cm^2 $\qquad\qquad\qquad\qquad\qquad\qquad (16)$
$\sigma_y^2 = 1.83$ cm^2.

The variance of the Q resolution is:

$$\sigma_{Qx}^2 = 8.94 * 10^{-5} + 0.0037\, Q_x^2 \text{ (in units of Å}^{-2}) \qquad (17)$$
$$\sigma_{Qy}^2 = 8.94 * 10^{-5} + 0.0037\, Q_y^2 \text{ (in units of Å}^{-2}) .$$

The wavelength spread contribution dominates for this high-Q configuration. The gravity contribution is negligible for the 6 Å wavelength.

For this high-Q configuration,

$$Q_{min}^{X} = Q_{min}^{Y} = 0.028 \text{ Å}^{-1}. \qquad (18)$$

Figure 3: Plot of the structure factor for a sphere of radius R = 50 Å before and after smearing produced by the high-Q configuration.

Figure 4: Variation of the standard deviation of the Q resolution *vs* Q.

Consider the following low-Q instrument configuration and spheres of radius R = 500 Å.

$$R_1 = 2.5 \text{ cm} \tag{19}$$
$$R_2 = 0.5 \text{ cm}$$
$$\Delta x_3 = \Delta y_3 = 0.5 \text{ cm}$$
$$L_1 = 15 \text{ m}$$
$$L_2 = 15 \text{ m}$$
$$\lambda = 12 \text{ Å}$$
$$\frac{\Delta\lambda}{\lambda} = 15 \text{ %}.$$

Therefore:

$$A = 0.0138 \text{ cm/Å}^2 \tag{20}$$
$$\sigma_x^2 = 1.83 \text{ cm}^2$$
$$\sigma_y^2 = 1.83 \text{ cm}^2$$

So that:

$$\sigma_{Qx}^2 = 2.23*10^{-7} + 0.0037\,Q_x^2 \text{ (in units of Å}^{-2}) \tag{21}$$
$$\sigma_{Qx}^2 = 2.31*10^{-7} + 0.0037\,Q_y^2 \text{ (in units of Å}^{-2}).$$

The first term is slightly different for σ_{Qx} and σ_{Qy} because of the small gravity contribution. For this configuration the geometry part dominates at low-Q, the wavelength-spread part contributes at higher Q, and the gravity term is small.

For this low-Q configuration,

$$Q_{min}^{X} = 0.0014 \text{ Å}^{-1},$$
$$Q_{min}^{Y} = 0.0016 \text{ Å}^{-1}. \tag{22}$$
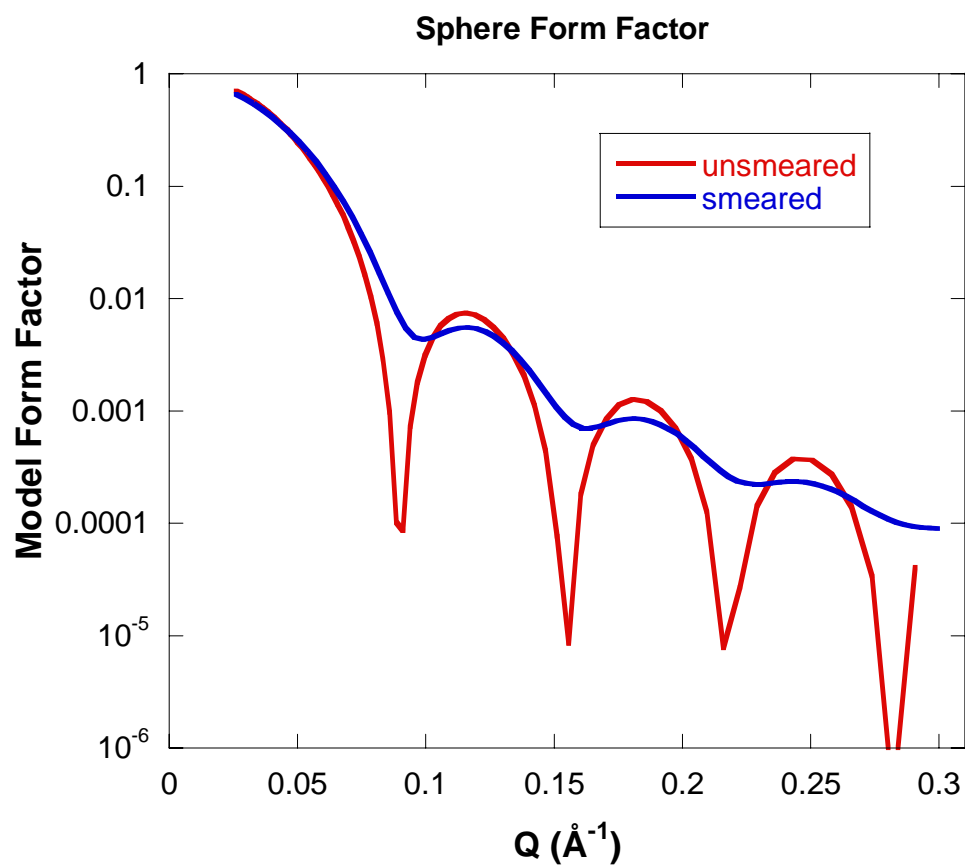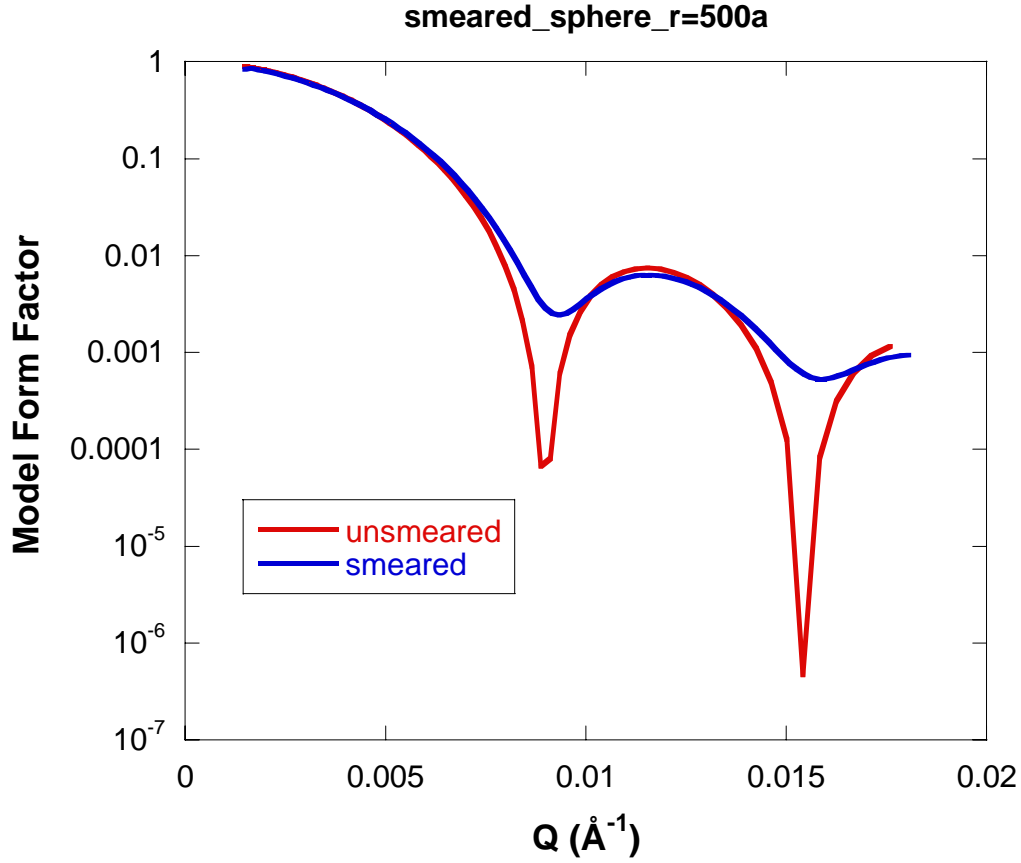

Figure 5: Plot of the structure factor for a sphere of radius R = 500 Å before and after smearing produced by the low-Q configuration.
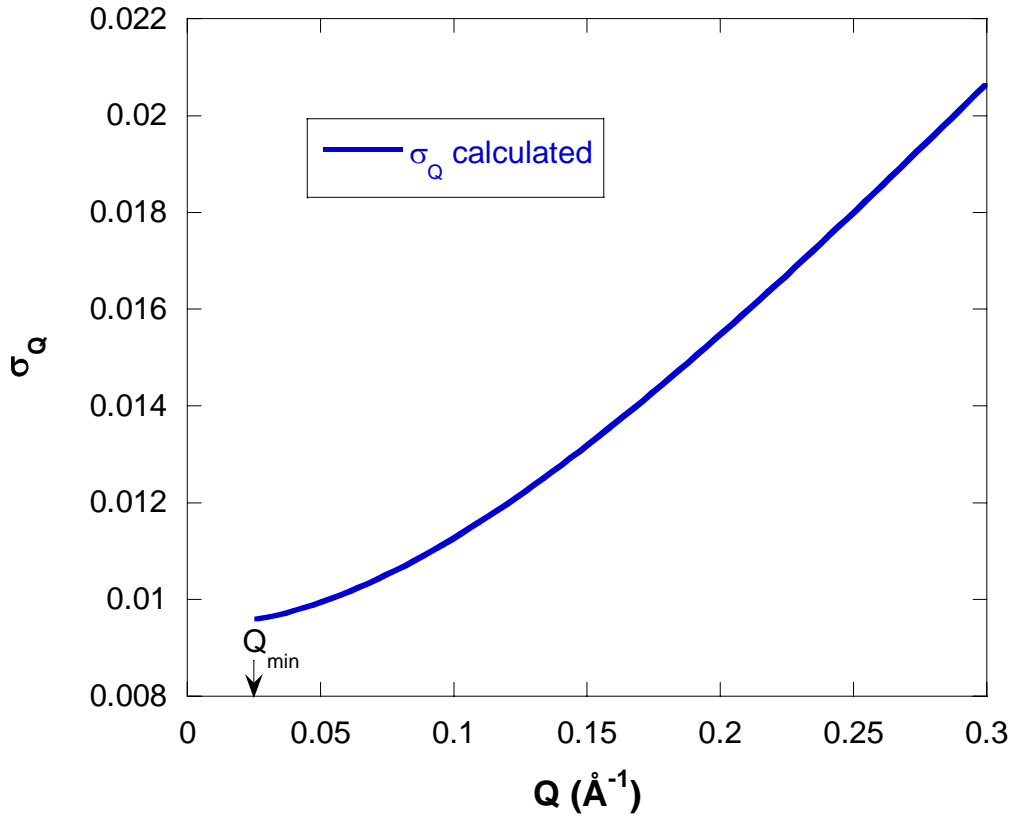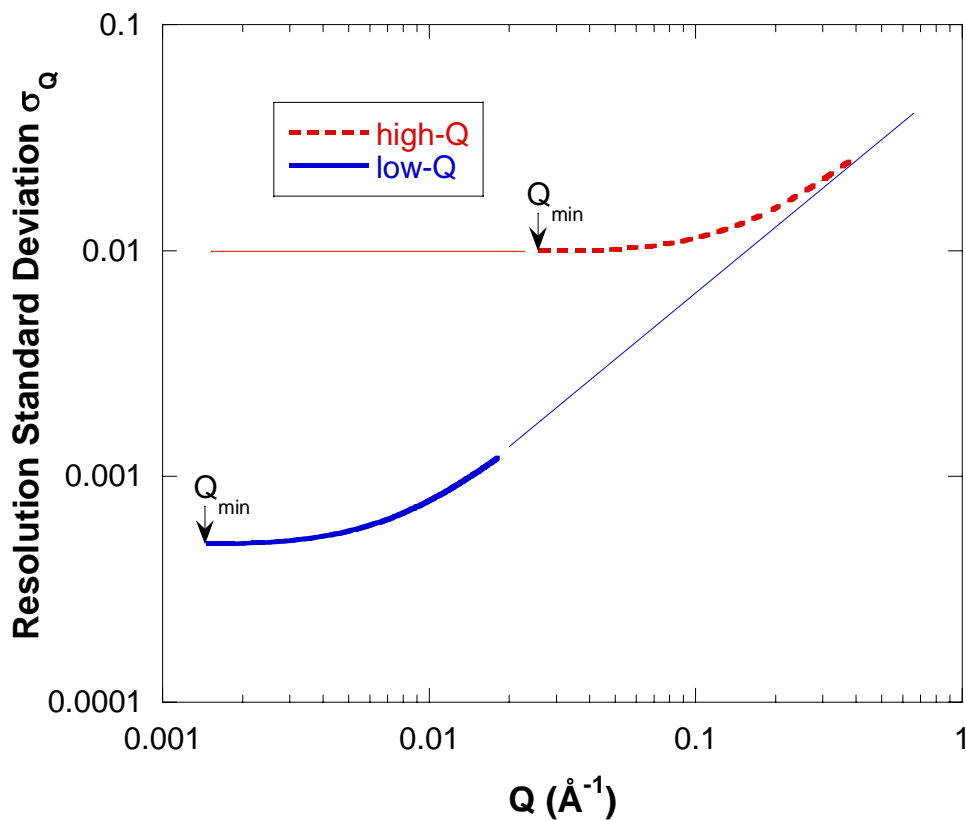
Figure 6: Plot of the standard deviation of the Q resolution for both the low-Q and the high-Q configurations. The values of Q_{min} are also indicated.

6. SANS FROM SILICA PARTICLES

SANS data have been taken from a dilute solution of monodisperse silica particles in D_2O (volume fraction of 0.1 %) and fit to the sphere model. Fit results gave a sphere radius of R = 563.51 ± 0.45 Å. SANS data were taken using a low-Q instrument configuration.
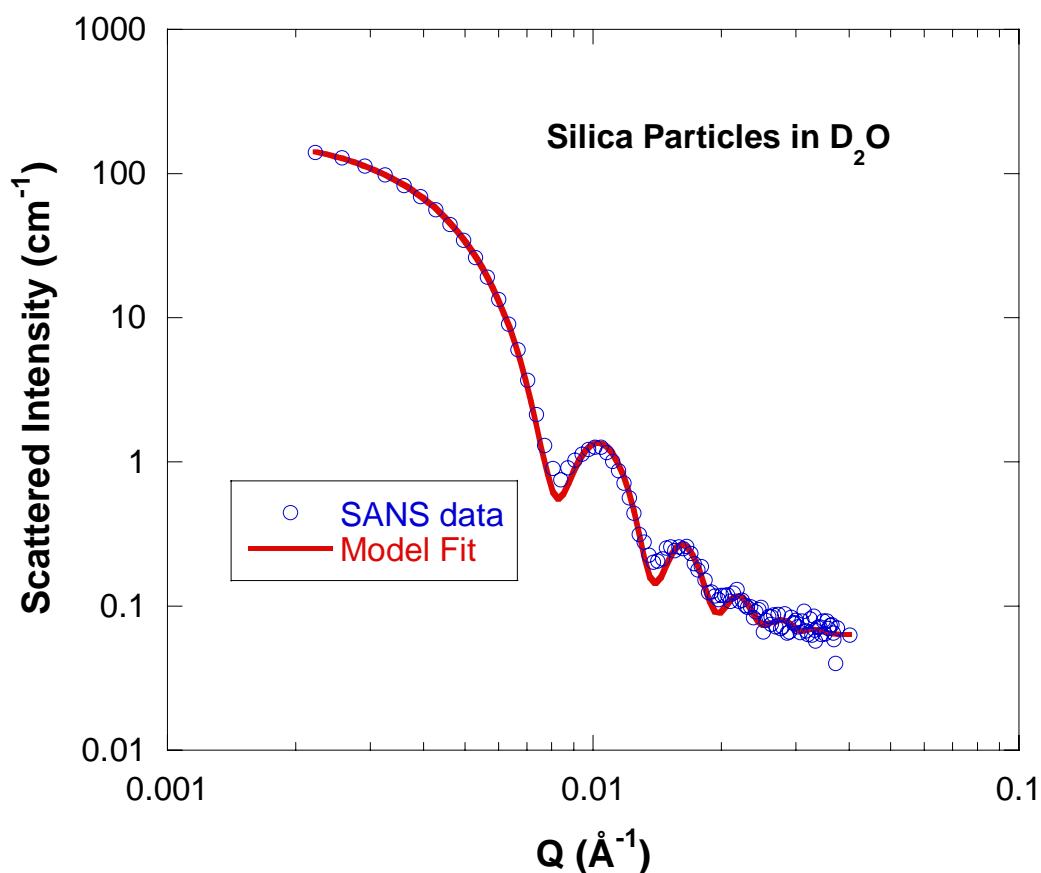
Figure 7: SANS data from a dilute solution of monodisperse silica particles in D_2O along with the fit to the sphere model.

REFERENCE

J.G. Barker, and J.S. Pedersen, "Instrumental Smearing Effects in Radially Symmetric SANS by Numerical and Analytical Methods", J. Appl. Cryst. <u>28</u>, 105-114 (1995).

QUESTIONS

1. What are the two ways of accounting for instrumental resolution?
2. Is it OK to perform a 1D smearing convolution integral on 2D SANS data?
3. What is the effect of instrumental smearing on the radius of gyration obtained from a Guinier fit?
4. What are the two ways of correcting for the effect of gravity?

ANSWERS

1. Instrumental resolution is included either (1) by smearing of the model used to fit the data or (2) by desmearing the data through an iterative process. Method (1) is the most reliable and the most used. Method (2) does not work well when sharp peaks appear in the data.
2. It is OK to perform a 1D smearing convolution integral if the 2D SANS data are azimuthally symmetric (scattering is isotropic).
3. Instrumental resolution tends to broaden peaks. The Guinier region is the tail of a peak at $Q = 0$. Broadening implies a lower slope and therefore a lower radius of gyration. The smeared radius of gyration is lower than the real value.
4. Gravity correction can be made (1) through a software method by defining constant-Q elliptical bins or (2) through a hardware method using gravity-correcting prisms.

Part E – **SANS DATA CORRECTIONS AND DATA REDUCTION**

Chapter 20 - **SANS DATA CORRECTIONS**

The 2D SANS data undergo a number of corrections during the data reduction process. Some of these corrections are described here (Berk-Glinka, 1985; Krueger-Hammouda, 1993).

1. THE SOLID ANGLE CORRECTION

The scattering geometry is represented by an Ewald sphere in general terms. For SANS, scattering angles are small and the detector is planar. This brings about a solid angle correction performed early on in the data reduction process.

The corrected macroscopic scattering cross section is related to the measured one by:

$$\left(\frac{d\Sigma}{d\Omega'}\right)_{corrected} = \left(\frac{d\Sigma}{d\Omega}\right)_{measured} \frac{d\Omega}{d\Omega'} . \tag{1}$$

The ratio of the two (corrected and measured) solid angles is expressed as:

$$\frac{d\Omega}{d\Omega'} = \frac{A}{r^2} \frac{r'^2}{A'} = \frac{A}{A'} \frac{r'^2}{r^2} . \tag{2}$$

Here A and A' are the solid angle base areas on the sphere and on the detector plane respectively and r and r' are the magnitudes of the vectors subtending these bases. These ratios can be calculated by inspecting the scattering geometry involved. The bottom part of the figure (which is a projection onto the vertical scattering plane) shows that

$$\frac{r'^2}{r^2} = \cos^2(\theta) \text{ and } \frac{A}{A'} = \cos(\theta). \tag{3}$$

Therefore, the solid angle correction factor is:

$$\frac{d\Omega}{d\Omega'} = \cos^3(\theta). \tag{4}$$

This correction is performed as the first manipulation of the 2D data.
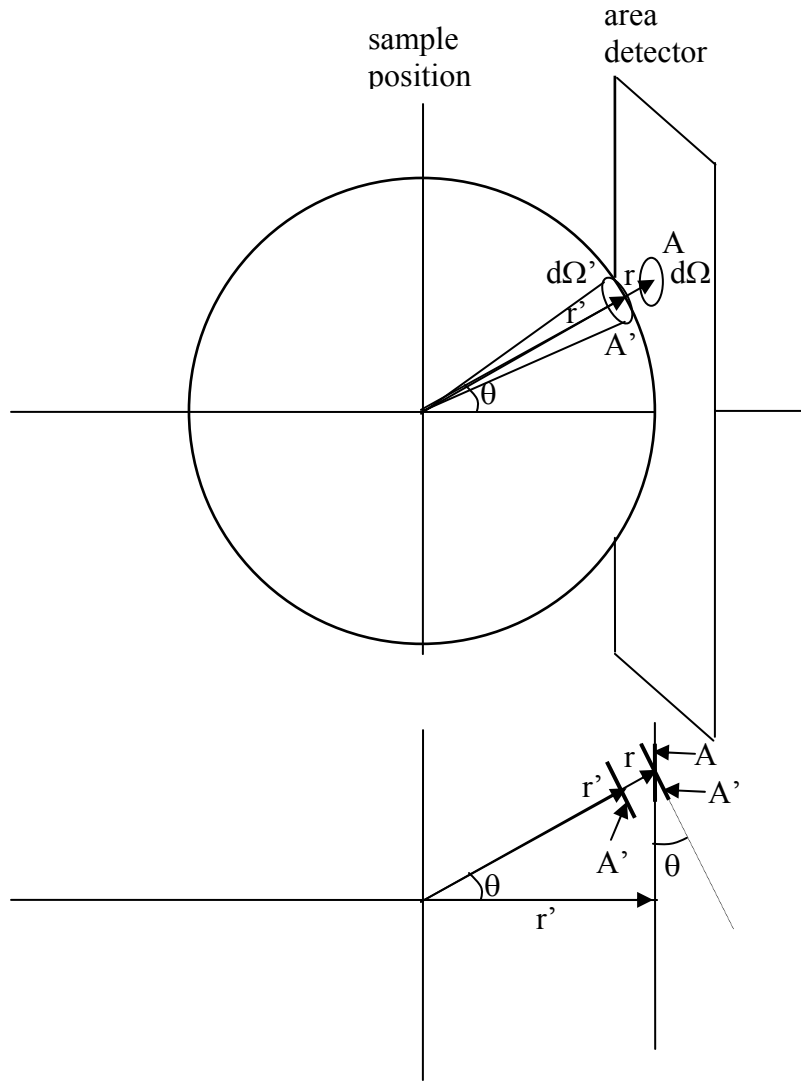
Figure 1: Schematic representation of the scattering geometry. The bottom part represents a projection onto the vertical scattering plane. The scales are grossly exaggerated. The horizontal scale is of order meters while the vertical scale is of order centimeters.

2. THE JACOBIAN CORRECTION

Some SANS instruments use neutron area detector that use the delay line method. This method uses only two detection (anode) wires that wind their way horizontally for y and vertically for x. The advantage of this method is that it uses only 4 signals (2 for x and 2 for y) from the detector. The time difference between the two x signals determines the position

of the detection event. One disadvantage is the low count rate saturation level.
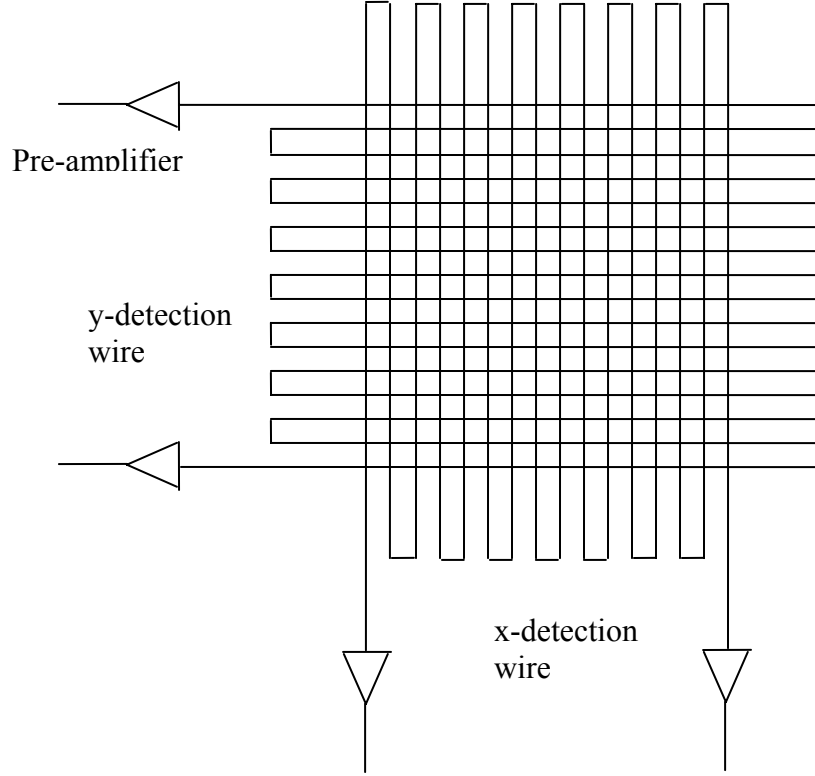
Figure 2: Schematic representation of a delay line detector showing only 16 wires. A more realistic detector contains 64 wires for x and 64 wires for y.

This type of area detector introduces a systematic distortion of the detection event coordinates due to the nonlinearity of the process. The coordinate of a detected event x in channel number space corresponds to a coordinate x' in real position space. This nonlinear mapping corresponds to the transformation:

$$x' = B \tan(x/B). \tag{5}$$

Here B is the nonlinearity detector constant in x. The x-dependence of the scattering cross section $d\Sigma(x)/d\Omega$ obeys the following conservation relation:

$$\frac{d\Sigma(x)}{d\Omega} dx = \frac{d\Sigma(x')}{d\Omega} dx'. \tag{6}$$

The cross section in real position space is therefore given by:

$$\frac{d\Sigma(x')}{d\Omega} = \frac{d\Sigma(x)}{d\Omega} \cos^2\left(\frac{x}{B}\right). \tag{7}$$

Here the Jacobian of the (x,x') transformation has been obtained from the following derivative:

$$\frac{dx}{dx'} = \cos^2\left(\frac{x}{B}\right).$$ (8)

This correction is made on the 2D SANS data. The detector nonlinearity constants B for x and C for y are measured using the cadmium mask method. This method consists in using a large cadmium mask with equally spaced holes right in front of the detector. The measured (distorted) positions and the equally spaced (known) positions are then used to obtain the nonlinearity constants.

In practice, most SANS instruments nowadays use area detectors that are based on the coincidence method with grids of wires for x and y positioning. These detector types are not hampered by the described distortion and therefore do not require any Jacobian correction.

3. ABSOLUTE INTENSITY

SANS data are rescaled to form a macroscopic scattering cross section (units of cm^{-1}). This rescaling involves a measurement from the scattering sample $I_s(Q)$ and a measurement from the empty beam transmission $I_0(\lambda)$ which is the incident neutron beam current. Here λ is the neutron wavelength. The measured SANS scattered intensity can be expressed as:

$$I_s(Q) = I_0(\lambda)\ T(\lambda)\ d\ \frac{d\Sigma(Q)}{d\Omega}\ \Delta\Omega.$$ (9)

$I_0(\lambda)$ is given by:

$$I_0(\lambda) = \phi(\lambda)\ A_2\ \varepsilon(\lambda)\ t.$$ (10)

Here:

$\phi(\lambda)$ is the neutron flux on sample,
A_2 is the illuminated sample area,
$T(\lambda)$ is the sample transmission,
d is the sample thickness,
$d\Sigma(Q)/d\Omega$ is the macroscopic scattering cross section,
$\Delta\Omega$ is the solid angle that subtends a detector cell,
$\varepsilon(\lambda)$ is the detector efficiency for the neutron wavelength used
t is the effective counting time normalized to a fixed number of monitor counts
(10^8 cps).

$I_s(Q)$ is the number of neutrons detected in a unit detector cell in time t. The scattering cross section can be measured as the ratio:

$$\frac{d\Sigma(Q)}{d\Omega} = \frac{I_s(Q)}{I_0(\lambda)Td\Delta\Omega}.$$ (11)

199

$I_0(\lambda)$ is measured as an empty beam transmission run and $I_s(Q)$ is the usual SANS scattering run. This absolute intensity rescaling is performed on the 2D SANS data.

Note that when the small-angle approximation is not valid, there are angular corrections to the detector efficiency $\varepsilon(\lambda,\theta)$ and to the sample transmission $T(\lambda,\theta)$ (here θ is the scattering angle). Correction to the detector efficiency is taken care of by measuring the sensitivity correction sample (either water or plexiglass) placed in the same stringent angular condition as the sample.

For finite scattering angles, the transmission angular correction involves the following integral:

$$\int_0^d dz\, \exp(-\Sigma_T z)\frac{d\Sigma(Q)}{d\Omega}\exp\left(-\Sigma_T\frac{(d-z)}{\cos(\theta)}\right) \tag{12}$$

$$\cong \frac{d\Sigma(Q)}{d\Omega}\exp\left(-\Sigma_T\frac{d}{\cos(\theta)}\right)\int_0^d dz\,\exp(-\Sigma_T z)\exp\left(\Sigma_T\frac{z}{\cos(\theta)}\right).$$

Some of the angular correction to the transmission is containing in the second term and is due to the longer neutron path inside the sample at large scattering angles. The remaining correction is taken into account by the integral. The following result is obtained:

$$\frac{d\Sigma(Q)}{d\Omega}Td\frac{(1-T^a)}{(\Sigma_T d)a}. \tag{13}$$

Here $T=\exp(-\Sigma_T d)$ is the regular sample transmission given in terms of the macroscopic (total) scattering cross section Σ_T and $a=\left(\dfrac{1}{\cos(\theta)}-1\right)$ is the angular correction factor. This angular correction is performed at the stage of radially averaging the SANS data.
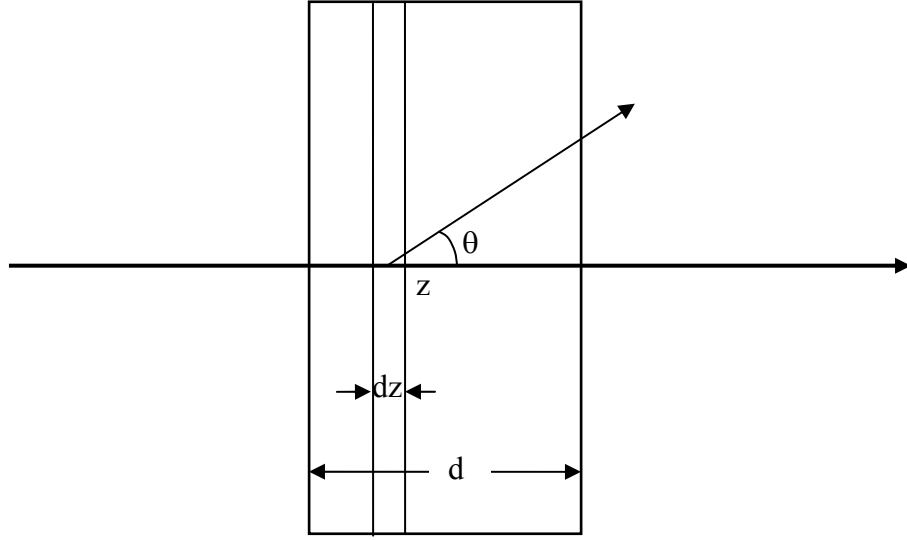
Figure 3: Geometry of the angular dependence of the sample transmission when the scattering angle is not small.

4. DEAD TIME CORRECTION

Processing of the detector signal takes a finite amount of time. The neutron area detector time response constant τ was measured and found to be between 3 and 5 μsec. The "measured" count rate N_M and the "true" count rate N_T are related by the following relation:

$$N_T = \frac{N_M}{1 - N_M \tau} . \qquad (14)$$

This assume a non-paralyzable detector response; i.e., that the detector keeps on counting even when it is processing signals.

This dead time detector correction could be performed at any stage of the data reduction process (Brulet et al, 2007). It depends solely on the total detector count rate N_M.

5. INCOHERENT SCATTERING SAMPLE

In order to subtract incoherent scattering from hydrogen (mostly), an incoherent scattering sample is often prepared and measured for each sample measured. The incoherent scattering sample contains the same number density of hydrogen atoms. It could consist of a mixture of H_2O and D_2O that would reproduce the level of flat (mostly incoherent) SANS scattering from aqueous solutions. It could also consist of pure hydrogenated polymers that would reproduce the incoherent level in mixtures of deuterated and non-deuterated polymer blends. Subtraction of the scattering from the incoherent scattering sample is best performed on the 2D data just in case there is anisotropy in the data. Actually, some prefer to consider the incoherent scattering run as their "empty" run; it replaces the empty cell run. Another

alternative is to estimate the incoherent scattering level though nonlinear least squares fitting methods.

REFERENCES

N. Berk and C. Glinka, "Data Reduction and Imaging System Manual", NIST Center for Neutron Research (1985).

S. Krueger and B. Hammouda "SANS Data Acquisition Manual" and "NIST Center for Neutron Research Data Reduction Manual", NIST Center for Neutron Research (1993, 2000).

A. Brulet, D. Lairez, A. Lapp, and J.P. Cotton, "Improvement of Data Treatment in SANS", J. Appl. Cryst. <u>40</u>, 165-177 (2007).

QUESTIONS

1. What is the origin of the solid angle correction?
2. What is the absolute scattering cross section?
3. Why is the scaling to an absolute cross section necessary?
4. What is the difference between a delay line detector and a coincidence detector?
5. Why is it important to perform the various corrections on the 2D data (before radial averaging).

ANSWERS

1. The solid angle correction is due to the fact that scattering occurs on the Ewald sphere whereas SANS area detectors are flat.
2. The absolute cross section is the macroscopic scattering cross section $d\Sigma(Q)/d\Omega$ (units of cm^{-1}). It is related to the microscopic scattering cross section $d\sigma(Q)/d\Omega$ (units of barns) by the number density of the scattering objects (N/V).
3. When the SANS data are reduced to an absolute cross section, the number density of the scattering objects can be obtained. For example, if the scattering objects are aggregates, one could obtain the number of molecules per aggregate.
4. A delay line detector uses one wire for x and one wire for y detection. These wires wind their way to form a grid.
5. It is important to perform the various corrections on the 2D data (before radial averaging) so as to preserve any scattering anisotropy in the data.

Chapter 21 - **SANS DATA REDUCTION**

The SANS data reduction procedures used at the NIST Center for neutron research are described here after a brief summary of the data acquisition process (Krueger-Hammouda, 1993; Kline, 2006).

1. INSTRUMENT CONFIGURATIONS

Every SANS experiment begins with the choice of one (or more) instrument configurations to be measured. Decisions are made based on the characteristic features of the investigated system (characteristic sizes and scattering level). A program is used to "simulate" configurations by choosing a neutron wavelength and wavelength spread, source and sample aperture sizes, source-to-sample and sample-to-detector distances. The Q range, neutron beam current and beamstop size are obtained for each configuration.

The following high-Q configuration was obtained from the SASCALC program for the NG3 SANS instrument.

Input:
  Neutron Wavelength: $\lambda = 6.0$ Å
  Wavelength spread: $\Delta\lambda/\lambda = 0.15$ (FWHM)
  Detector Offset: 25 cm
  Source aperture diameter: $D_1 = 5.0$ cm
  Sample Aperture diameter: $D_2 = 1.27$ cm
  Source aperture to sample aperture distance: $L_1 = 537$ cm
  Sample-to-detector distance: $L_2 = 133$ cm

Output:
  Total $Q_{min} = 0.0179$ A^{-1}
  Total $Q_{max} = 0.4742$ A^{-1}, Horizontal $Q_{max} = 0.4211$ A^{-1}, Vertical $Q_{max} = 0.2467$ A^{-1}
  Beam diameter: 2.39 cm, Beamstop diameter: 2.54 cm, Umbra/Penumbra: 0.414
  Attenuator transmission: 0.0003 (Attenuator number 8 for transmission runs.)
  Neutron beam current at the sample: $7.5543*10^5$ counts/sec

2. SANS DATA ACQUISITION

The data acquisition software package consists of a set of menus and tables within a graphical user interface. The main menu contains "single run" and "multiple runs" modes as well as a "manual operations" mode. This last mode contains all aspects of hardware control.

Typically two to three configurations are chosen and saved as templates at the beginning of every new set of measurements (i.e., for every new user group). A set of SANS measurements includes scattering runs and transmission runs from every sample as well as

from the empty cell. Transmission runs are performed by attenuating the beam and moving the beamstop out. Note that the transmission measurements depend on neutron wavelength but are independent of collimation parameters. When the same wavelength is chosen for the low-Q and the high-Q configurations, only one transmission run is needed. A scattering run is taken for the beam blocked background measurement. The neutron beam is blocked using a neutron absorber (lithiated compounds are preferred because they do not produce gammas).

Every run is taken for a fixed amount of time. The total measurement time is divided into a number of prefactors. This allows the recording of the beam monitor and total detector counts for each prefactor. A change of the total detector counts points to changes occurring in the sample. A change in the beam monitor counts points to changes in the neutron source. A transmission run is also taken from the empty beam for every instrument configuration. This run measures the neutron beam current and is used to scale the scattering intensity to an absolute cross section (unit of cm^{-1}). This run replaces the use of a secondary standard sample. Scattering from a flat hydrogen-containing scatterer (such as water or plexiglass) is taken on a regular basis by the instrument staff and made available to users to correct for slight difference in detector cell efficiency. The data acquisition sequence is programmed into a series of runs that are performed automatically. Stepping among the samples as well as varying sample environment conditions (such as temperature) are also programmed. Real time imaging of the data is helpful in monitoring the data acquisition process.

The SANS data files are in the binary format. The data header (256 bytes) contains all instrumental parameters along with sample information (label, thickness, etc). The main data part consists of 16,384 values (= 14-bit) comprising data from 128*128 detector cells. Historically, binary SANS data have been compressed to keep file sizes small.

3. THE SANS DATA CORRECTION STEPS

Calculation of the various sample (and empty cell) transmissions is performed. SANS raw data files are loaded into "work files" and normalized to a fixed (= 10^8) number of monitor counts. The empty cell and blocked beam runs are subtracted and rescaled following a specific recipe:

$$I_s(Q) = \frac{\left(I_{s+c}(Q) - I_b\right)}{T_{s+c}} - \frac{\left(I_c(Q) - I_b\right)}{T_c}. \tag{1}$$

$I_{s+c}(Q)$ is the scattering run from the sample + cell, $I_c(Q)$ is the scattering from the empty cell, I_b is the scattering with beam blocked, T_{s+c} is the transmission for the sample inside the cell and T_c is the empty cell transmission. Note that $T_{s+c} = T_s.T_c$.

Using the neutron beam counts (empty beam transmission) $I_0(\lambda)$, the scattering intensity is scaled to an absolute cross section (units of cm^{-1}) as:

$$\frac{d\Sigma(Q)}{d\Omega} = \frac{I_s(Q)}{I_0(\lambda)Td\Delta\Omega}. \tag{2}$$

T, d and ΔΩ are the sample transmission and thickness and the solid angle subtending one detector cell. SANS data in peripheral detector cells and those close to the beamstop are masked in order to keep only the reliable data. Then the 2D corrected and scaled data are radially averaged to produce 1D data. Circular binning is the norm for isotropic scattering. Sector or rectangular averaging is used for scattering with anisotropic features.
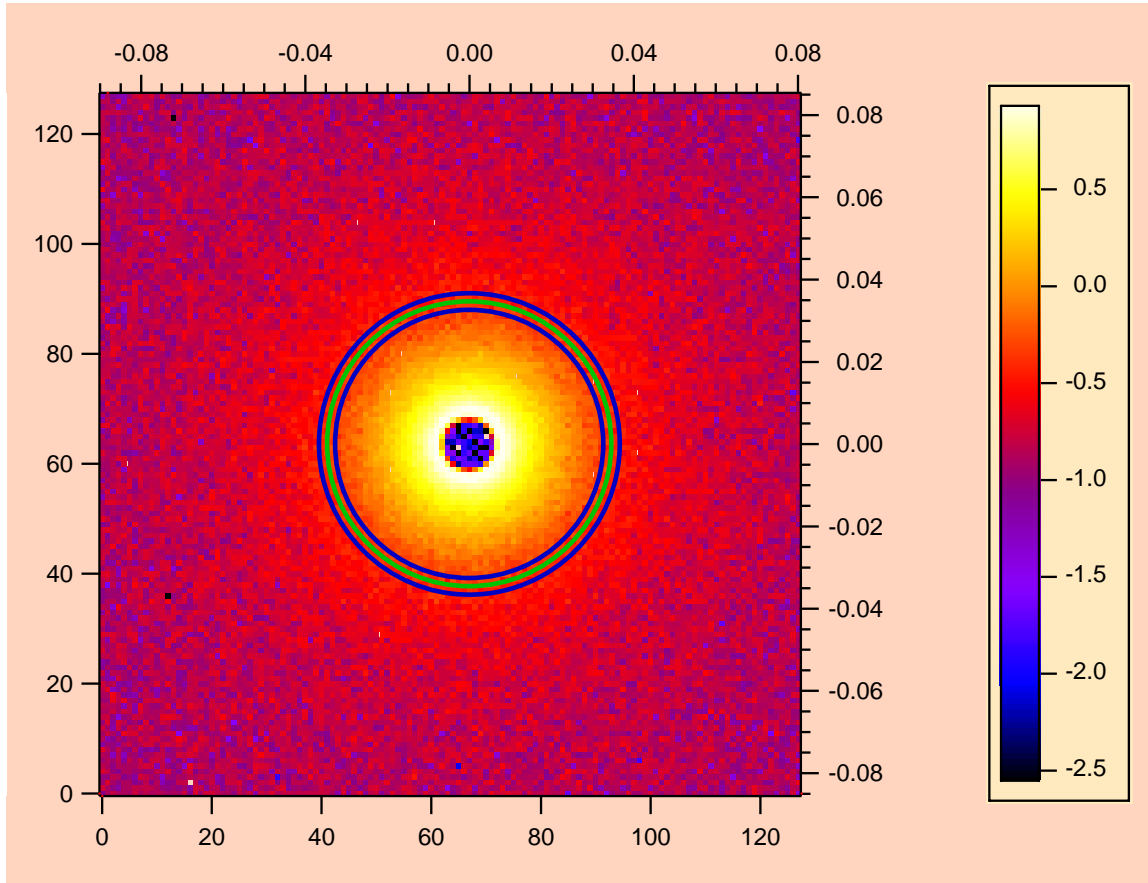
Figure 1: Typical SANS data image. Radial averaging consists in forming circular bins in which data are summed up.
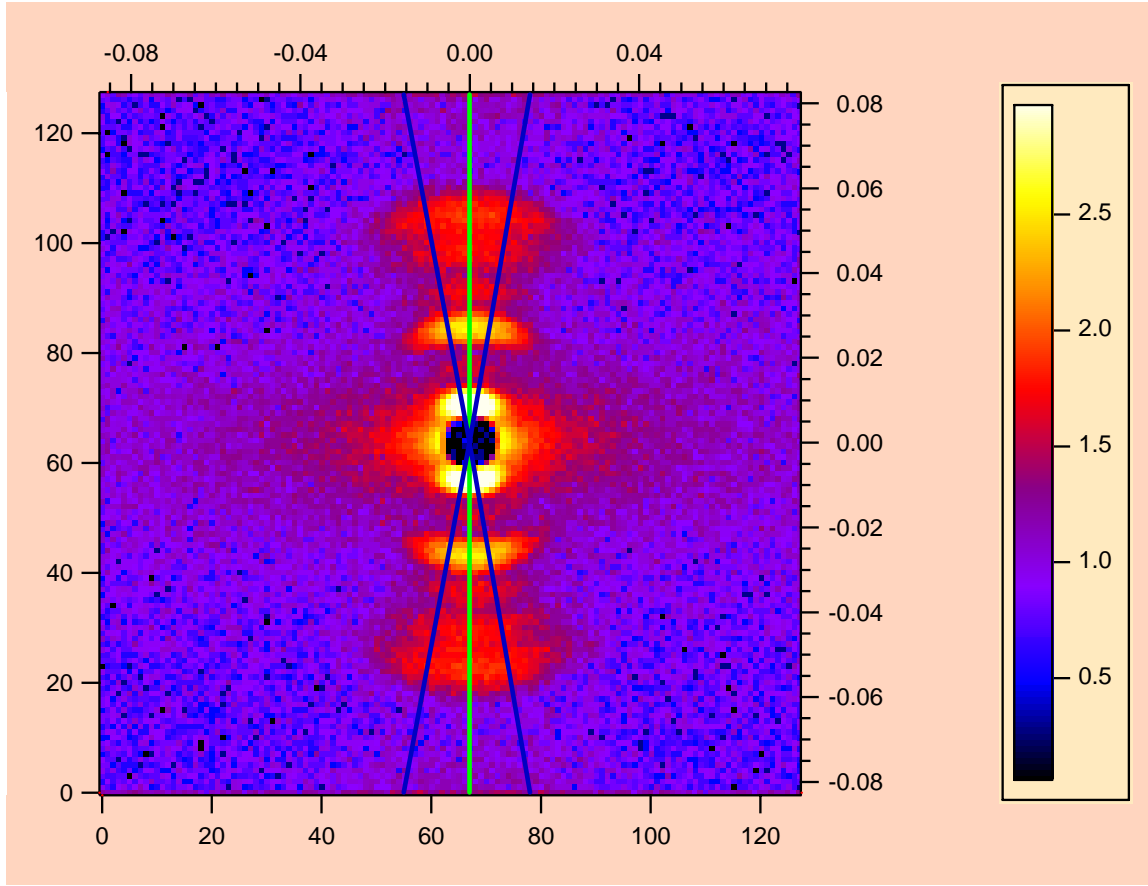
Figure 2: Typical SANS data from an anisotropic scatterer (collagen from kangaroo tail tendon). Sector averaging is performed on this asymmetric data.

The radially averaged data format contains the following columns:

$$Q, d\Sigma(Q)/d\Omega, \sigma_I, <Q>, \sigma_Q, BS \qquad (3)$$

σ_I is the statistical uncertainty on the scattering intensity, $<Q>$ is the average Q over the neutron beam spot, σ_Q is the standard deviation of the Q resolution function, and BS is the beam shadowing factor which is equal to zero for cells under the beamstop and to one for cells far from it.

The last step in the data reduction process consists in merging data taken from the two (or three) instrument configurations together into one combined data file.

4. TYPICAL REDUCED SANS DATA

Typical SANS data taken from 4 % poly(ethylene oxide) of molecular weight $M_w = 42,900$ g/mol in deuterated ethanol are shown. First data taken using a high-Q configuration data are shown.
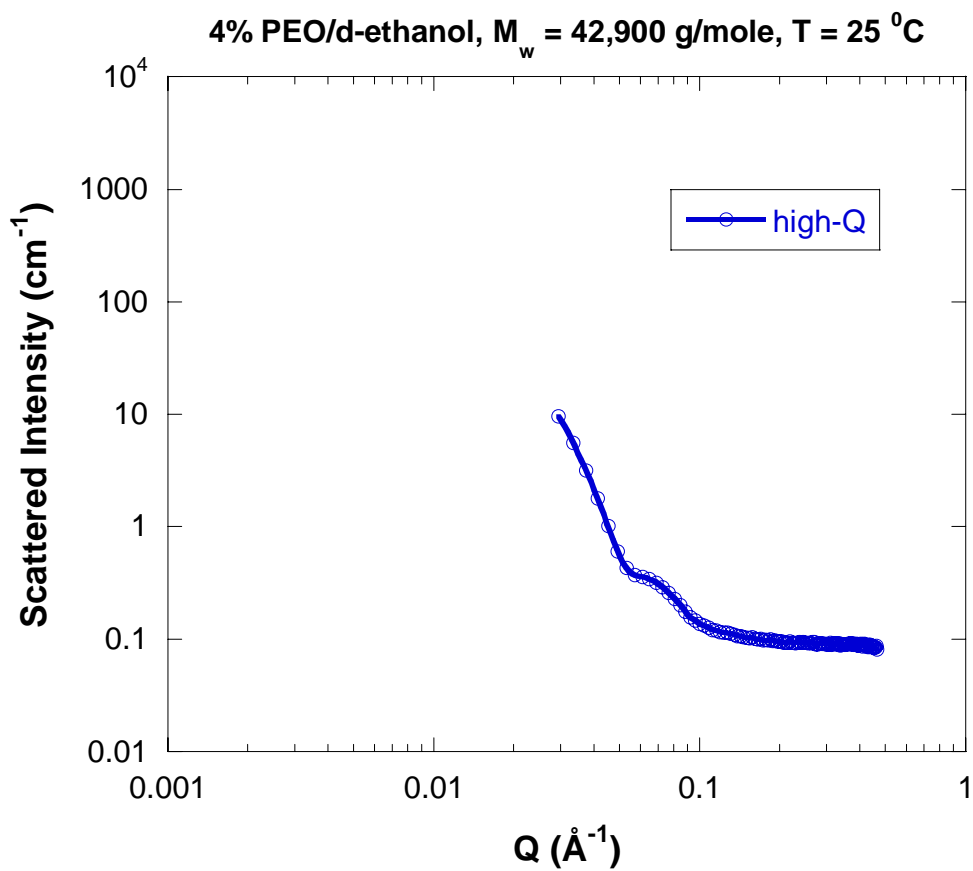
Figure 1: Reduced SANS data taken with a high-Q resolution configuration.

Then data taken using both a low-Q and a high-Q configuration are plotted together.
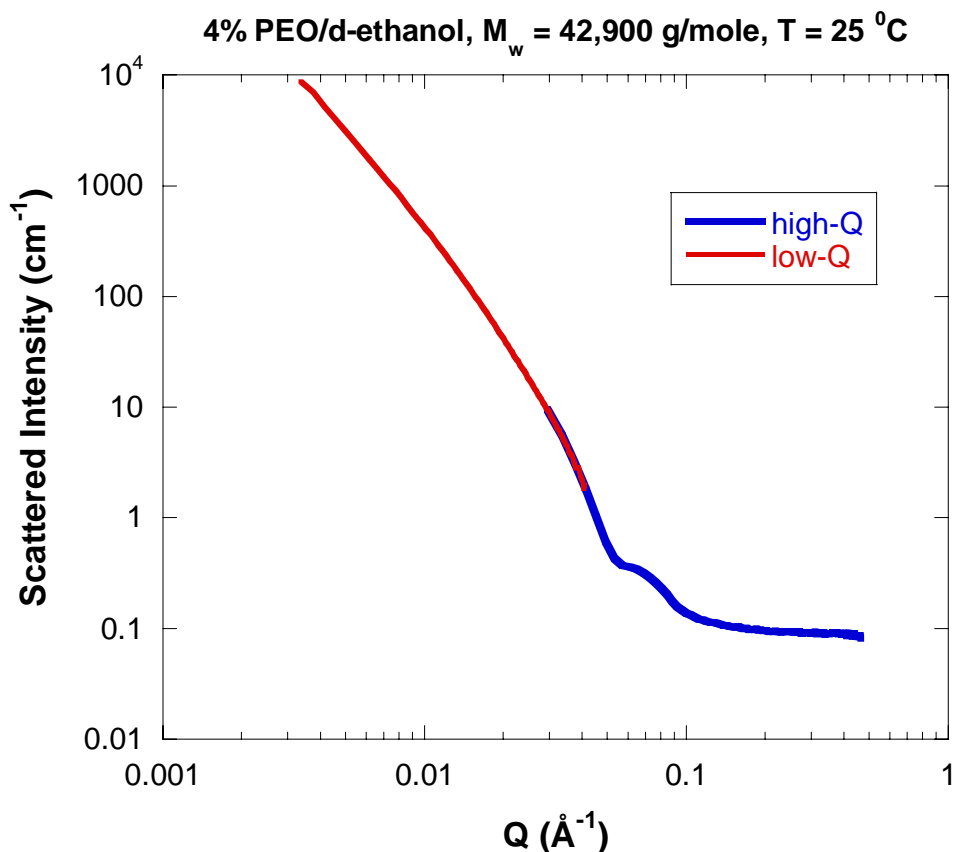
Figure 2: Reduced SANS data taken with a low-Q and the high-Q resolution configurations spliced together.

This figure shows scattering from a large structure (at low-Q) and local crystalline ordering (at high-Q).

REFERENCES

S. Krueger and B. Hammouda "SANS Data Acquisition Manual" and "SANS Data Reduction Manual", NIST Center for Neutron Research (1993, 2000).

S. Kline, "Reduction and analysis of SANS and USANS data using IGOR Pro", J. Appl. Cryst. 39, 895-900 (2006).

QUESTIONS

1. What are the required runs for a complete set of SANS measurements?
2. What are the main steps in the SANS data reduction process?
3. Is there any information about the instrumental resolution in the averaged 1D data file?
4. What type of radial averaging is required for anisotropic scattering?
5. What produces the blocked beam background?

ANSWERS

1. In order to obtain a complete set of SANS measurements the required runs are: transmission and scattering from the sample, transmission and scattering from the empty cell, scattering run from the blocked beam, transmission run from the empty beam and the detector sensitivity run from plexiglass.

2. The data reduction process involves the following steps: calculating the various transmissions, subtracting the empty cell and blocked beam, rescaling the 2D data to an absolute cross section, masking the unwanted detector cells, and radially averaging to obtain 1D data. Merging ("sorting") of data from multiple configurations is also performed.

3. The averaged 1D data file contains the standard deviation of the Q resolution function σ_Q in the 5th data column.

4. Anisotropic scattering yields asymmetric (oriented) 2D data. It requires either sector or rectangular averaging.

5. The blocked beam background is produced by electronics noise on the detector and stray neutrons outside of the neutron beam collimation.

Part F – **SIMPLE SANS DATA INTERPRETATION**

Chapter 22. Standard Plots

Chapter 23. Empirical Models

Chapter 24. Representative SANS Data

Chapter 25. SANS Data from Oriented Samples

Chapter 22 - **STANDARD PLOTS**

The first tool used to understand SANS data consists of a set of standard plots that yield results right after data reduction. These are linear plots of functions of the scattered intensity I(Q) plotted against functions of the scattering variable Q. Note that the absolute intensity I(Q) is a short hand notation for the macroscopic scattering cross section $d\Sigma(Q)/d\Omega$.

1. THE GUINIER PLOT

The Guinier plot involves plotting $Ln[I(Q)]$ *vs* Q^2 (Ln refers to natural logarithm) in order to obtain the slope $R_g^2/3$ (R_g is the radius of gyration of the scattering objects). The expansion is as follows:

$$I(Q) = I_0 \exp\left(-\frac{Q^2 R_g^2}{3}\right) \tag{1}$$

$$Ln[I(Q)] = Ln[I_0] - \frac{Q^2 R_g^2}{3}.$$

The radius of gyration represents the effective size of the scattering "particle" whether it is a polymer chain, part of a protein, a micelle, or a domain in a multiphase system. The usefulness of this plot stems from the fact that the obtained particle "size" R_g is independent of the absolute intensity I_0 and of any model. Instrumental smearing as well as polydispersity and multiple scattering appear to decrease the effective R_g. Inter-particle effects also contribute to R_g except at the infinite dilution limit (case of an isolated particle).

Consider the Guinier plot for a solution of pluronics P85 in D_2O. Pluronics are triblock copolymers of poly(ethylene oxide)-poly(propylene oxide)-poly(ethylene oxide), i.e., PEO-PPO-PEO. At low temperature both PEO and PPO dissolve in water so that SANS observes isolated polymer chains. This is the case for 20 ^{o}C. The radius of gyration obtained from the Guinier plot gives an estimate of polymer chain dimension. A Guinier plot is shown for 10 % (g/g) P85 in D_2O measured at 20 ^{o}C.
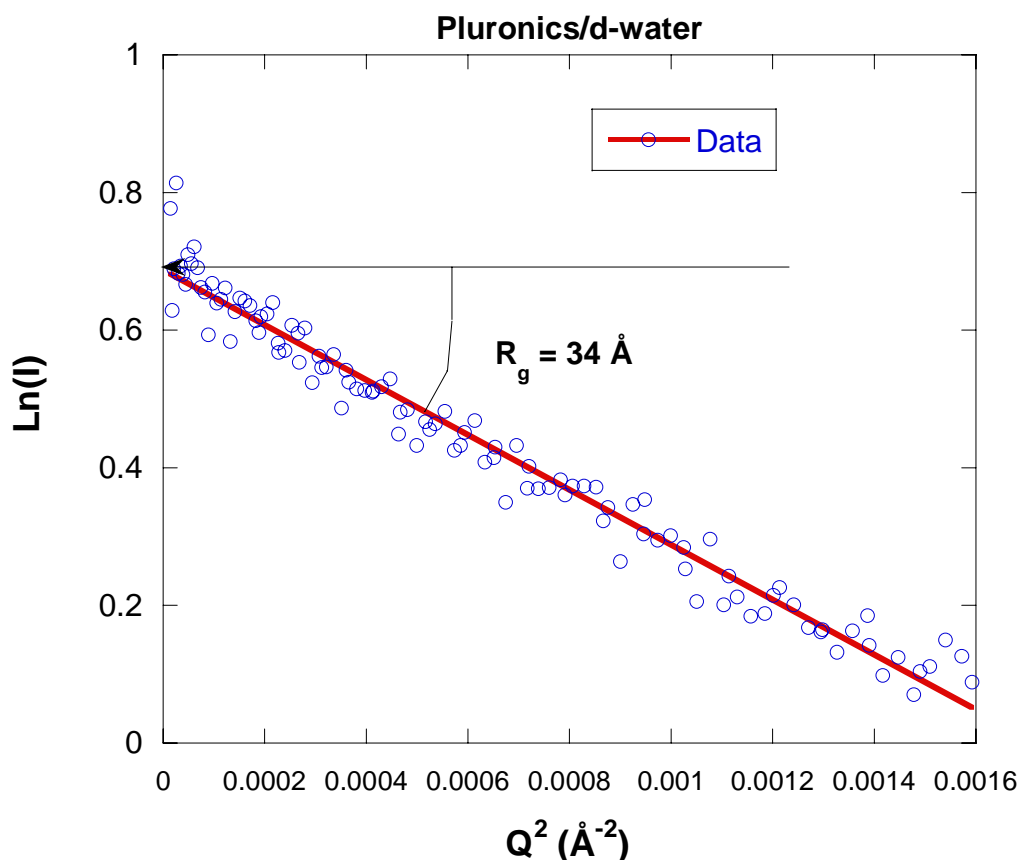
Figure 1: Guinier plot for SANS data taken from 10 % (g/g) P85 pluronics in D_2O at 20 °C. The slope of the Guiner plot is $R_g^2/3$.

Note that at higher temperatures, PPO does not dissolve in water so that P85 forms micelles with PPO forming the core and PEO forming an outside shell. An inter-particle peak forms and the Guinier plot can no longer be used. Other methods used to analyze such SANS data will be described later.

Another example of a Guinier plot is for SANS data from a solution of PAMAM dendrimers formed of seven generations and dissolved in D_2O. The dendrimer fraction (g/g) is varied in the dilute solution range. No acid or salt has been added. The apparent radius of gyration is seen to decrease with dendrimer fraction.

Dendrimer/d-water
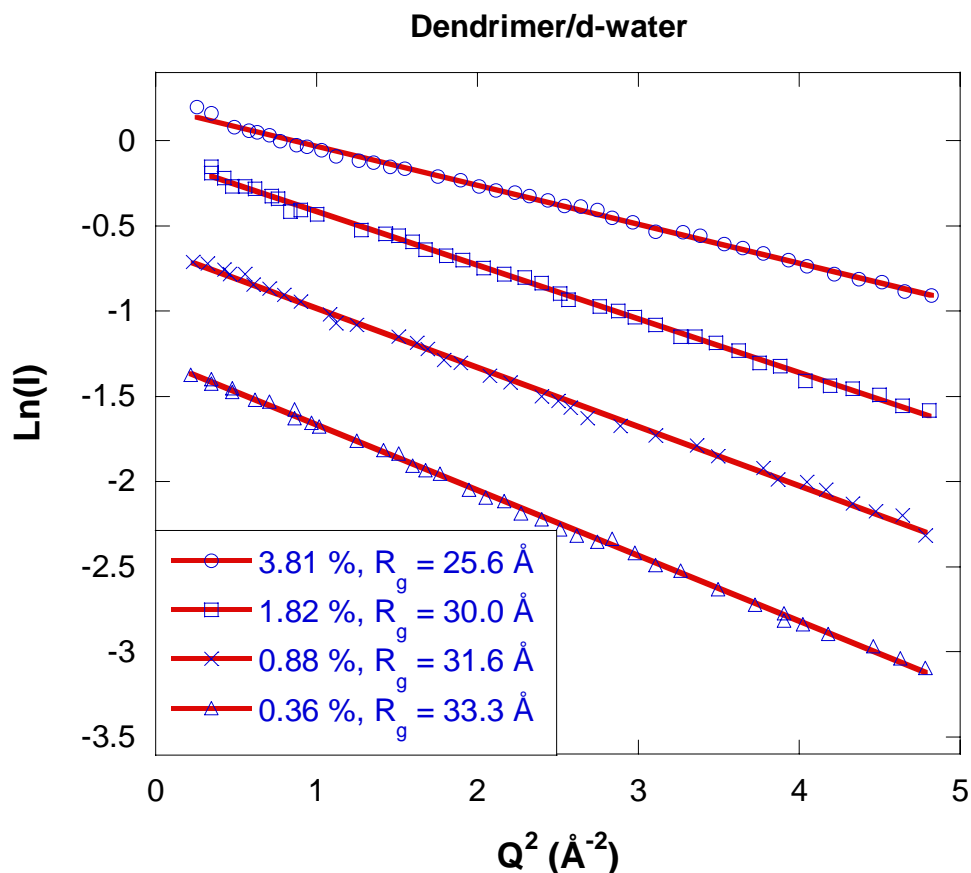
Figure 2: Guinier plot for SANS data taken from seventh-generation PAMAM dendrimers in D_2O. The dendrimer fraction is varied.

The range of a Guinier plot corresponds to $QR_g < \sqrt{3}$. This is obtained when the probed range $(2\pi/Q)$ is larger than the particle size.
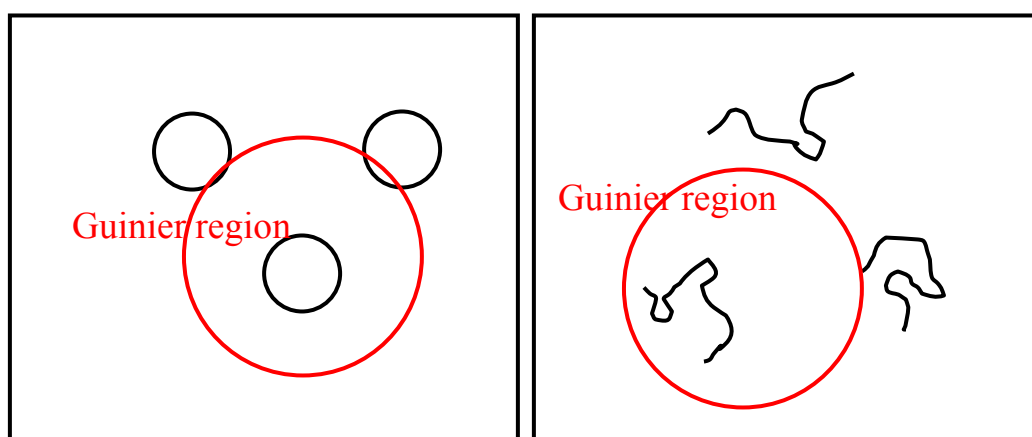
Figure 3: Scattering particles are smaller than the probed range in the Guinier region shown for isolated particles and for single polymer coils.

2. THE POROD LAW

Consider the case of an infinitely dilute solution of spheres of radius R and smooth surfaces. The scattering intensity is given by:

$$I(Q) = \left(\frac{N}{V}\right) \Delta\rho^2 V_P^2 F^2(QR) . \qquad (2)$$

The standard characteristic parameters have been defined as: (N/V) is the spheres number density, $\Delta\rho^2$ is the contrast factor, V_P is the sphere volume and F(QR) is the single-sphere form factor amplitude given as follows:

$$F(QR) = \frac{3j_1(QR)}{QR} = \frac{3}{QR}\left(\frac{\sin(QR)}{(QR)^2} - \frac{\cos(QR)}{QR}\right) . \qquad (3)$$

Note that the single-sphere form factor $P(QR) = F^2(QR)$ is also defined as:

$$P(QR) = \int d^3r \exp[i\vec{Q}.\vec{r}] \, P(r) = \frac{1}{V_P}\int_0^\infty dr 4\pi r^2 \frac{\sin(Qr)}{Qr}\gamma(r) . \qquad (4)$$

Here the pair correlation function $P(\vec{r})$ has been defined. The pair correlation function $P(\vec{r})$ is the probability of finding a scatterer at a vector distance $\vec{r}$ inside the sphere knowing that there is another scatterer at the origin. $\gamma(r)$ is the equivalent 1D probability distribution defined radially. Consider a sphere of radius R and a scatterer located at a radial distance r' from the sphere origin. Draw another sphere of radius r. $\gamma(r)$ represents the relative fraction of area of the second sphere located inside the large sphere integrated over all possible locations. Defining that relative fraction as p(r,r'), the following two cases can be considered:

$$p(r,r') = 1 \qquad\qquad R\text{-}r > r' \qquad (5)$$

$$p(r,r') = \frac{1}{2} + \frac{1}{4}\left[\frac{R^2 - r^2 - r'^2}{rr'}\right] \qquad R\text{-}r \leq r' .$$

The radial pair correlation function for a sphere is therefore (Stein et al, 1963):

$$\gamma(r) = \frac{\int_0^{R_A} dr' 4\pi r'^2 \, p(r,r')}{\int_0^{R_A} dr' 4\pi r'^2} = 1 - \frac{3}{4}\left(\frac{r}{R}\right) + \frac{1}{16}\left(\frac{r}{R}\right)^3 . \qquad (6)$$
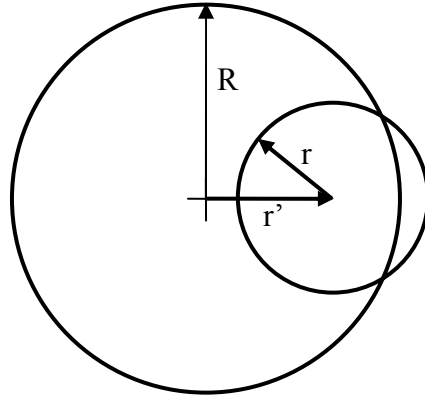
Figure 4: Representation of the geometry used to calculate the radial pair correlation function for a sphere.

The pair correlation function $\gamma(r)$ is the 3D Fourier transform of the single particle scattering factor $P(Q)$. The 1D sine Fourier transform of $P(Q)$ is $r\gamma(r)$.
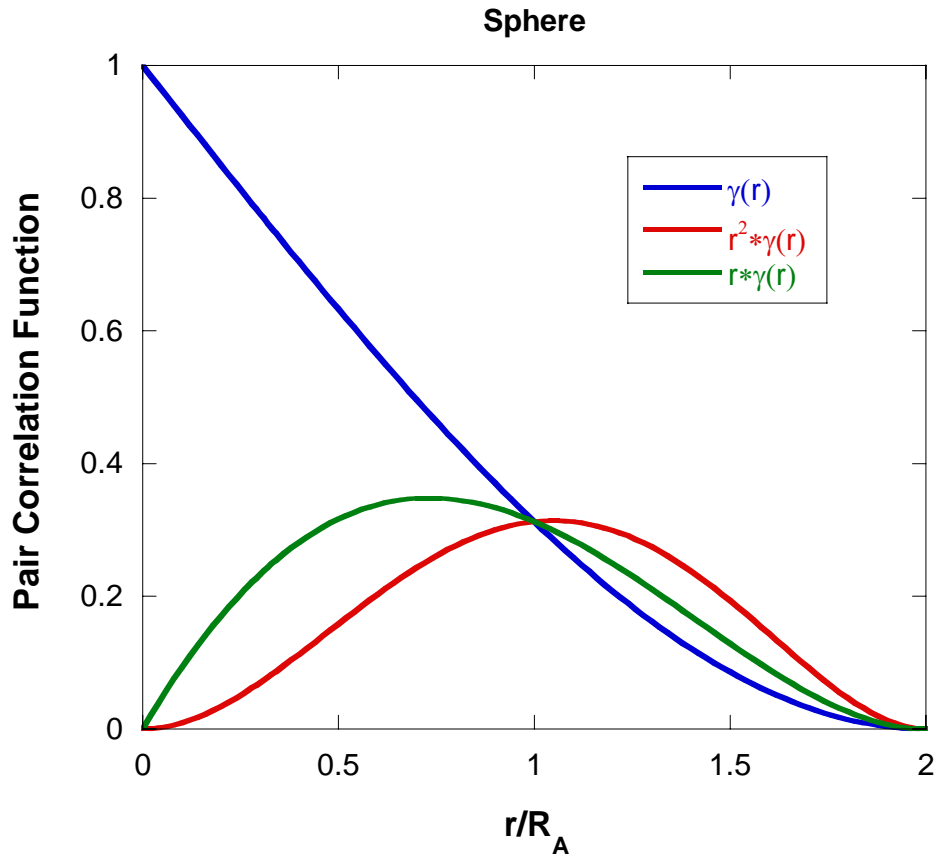
Figure 5: Plot of the pair correlation function $\gamma(r)$, of $r^2\gamma(r)$ and of $r\gamma(r)$.

Using this form, $P(QR)$ can be expressed as follows:

$$P(QR) = \frac{1}{V_P} \int_0^\infty dr 4\pi r^2 \frac{\sin(Qr)}{Qr} \left[1 - \frac{3}{4}\left(\frac{r}{R}\right) + \frac{1}{16}\left(\frac{r}{R}\right)^3 \right]. \qquad (7)$$

Note that this is the well known form factor for a sphere $P(QR) = [3j_1(QR)/QR]^2$ introduced earlier. The interest here is in the high-Q expansion. The highest order in this expansion is obtained by integrating by parts three times:

$$P(QR) \sim -\frac{4\pi}{V_P}\frac{2\gamma'(0)}{Q^4} = \frac{S_P}{V_P R^2}\frac{3}{2Q^4 R} = \frac{3}{2R^3}\left(\frac{S_P}{V_P}\right)\frac{1}{Q^4}. \qquad (8)$$

(S_P/V_P) is the surface to volume ratio. This is the so-called Porod law.

The scattering intensity can simply be expressed as $I(Q) = A/Q^4 + B$ where B is the constant (mostly incoherent) scattering background.

3. THE POROD PLOT

The Porod region corresponds to a probed range smaller than the scattering objects so that the scattering radiation is probing the local structure. The Porod plot $Log(I)$ vs $Log(Q)$ (Log is base-10 logarithm) yields information about the so-called "fractal dimension" of the scattering objects. At high-Q, one can approximate:

$$I(Q) = \frac{A}{Q^n} + B \quad \text{or} \quad Log[I(Q) - B] = Log(A) - nLog(Q). \qquad (9)$$

A Porod slope $n = 1$ is obtained for scattering from rigid rods; a slope $n = 4$ represents a smooth surface for the scattering particle; whereas a slope n between 3 and 4 characterizes rough interfaces of fractal dimension D with $n = 6-D$. This is called a surface fractal.

Moreover, in the case of polymer coils, the Porod slope n is related to the excluded volume parameter ν as its inverse $n = 1/\nu$. A slope $n = 2$ is a signature of Gaussian chains in a dilute environment, a slope $n = 5/3$ is for fully swollen coils and a slope $n = 3$ is for collapsed polymer coils. A slope between 2 and 3 is for "mass fractals" such as branched systems (gels) or networks.

An example of a Porod plot is shown for SANS data from a 4 % (g/g) solution of salmon DNA in d-ethyelene glycol) at a temperature of 50 $^\circ$C. At this temperature, the helical structure has melted into coil conformation.1 M NaCl salt has been added in order to screen charge interactions. The slope of the Porod plot of $n = 1.76$ is close to the value $n = 5/3 = 1.667$ which is a signature for fully swollen coils.
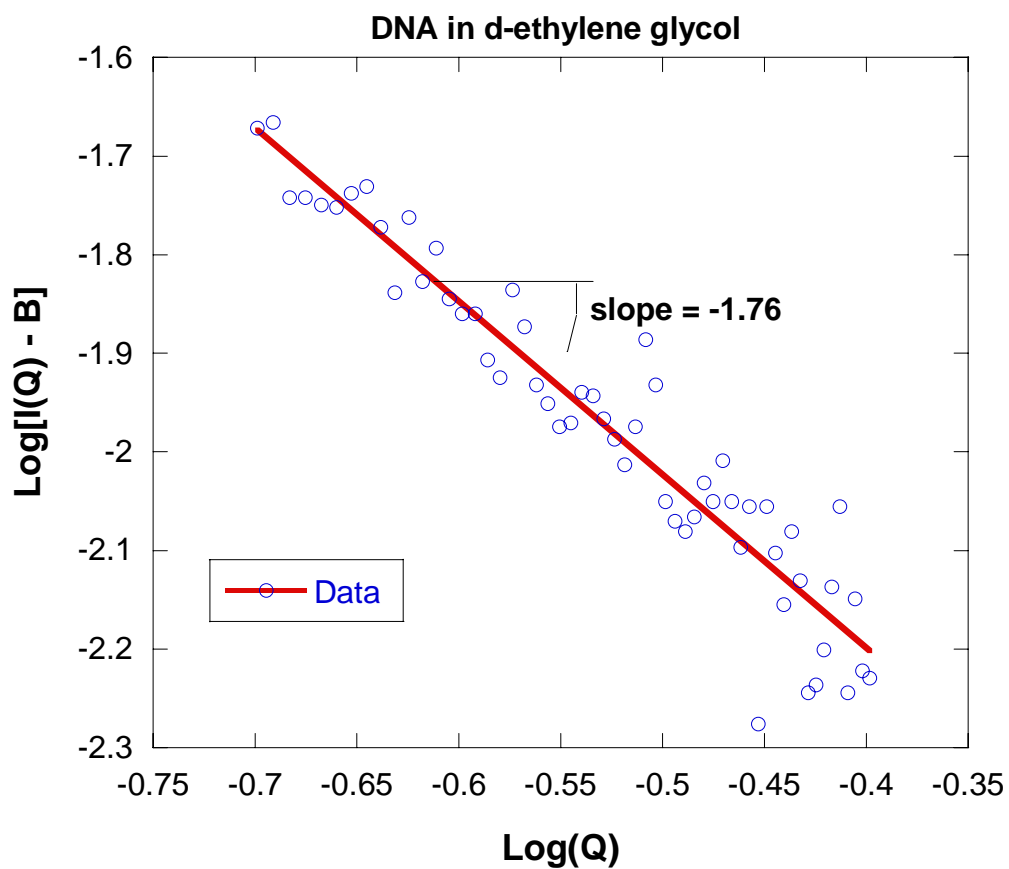
Figure 6: Porod plot for SANS data taken from 4 % (g/g) DNA coils in D_2O at 50 ^{o}C (above the helix-to-coil transition temperature). 0.1 M NaCl was added to screen change interactions.
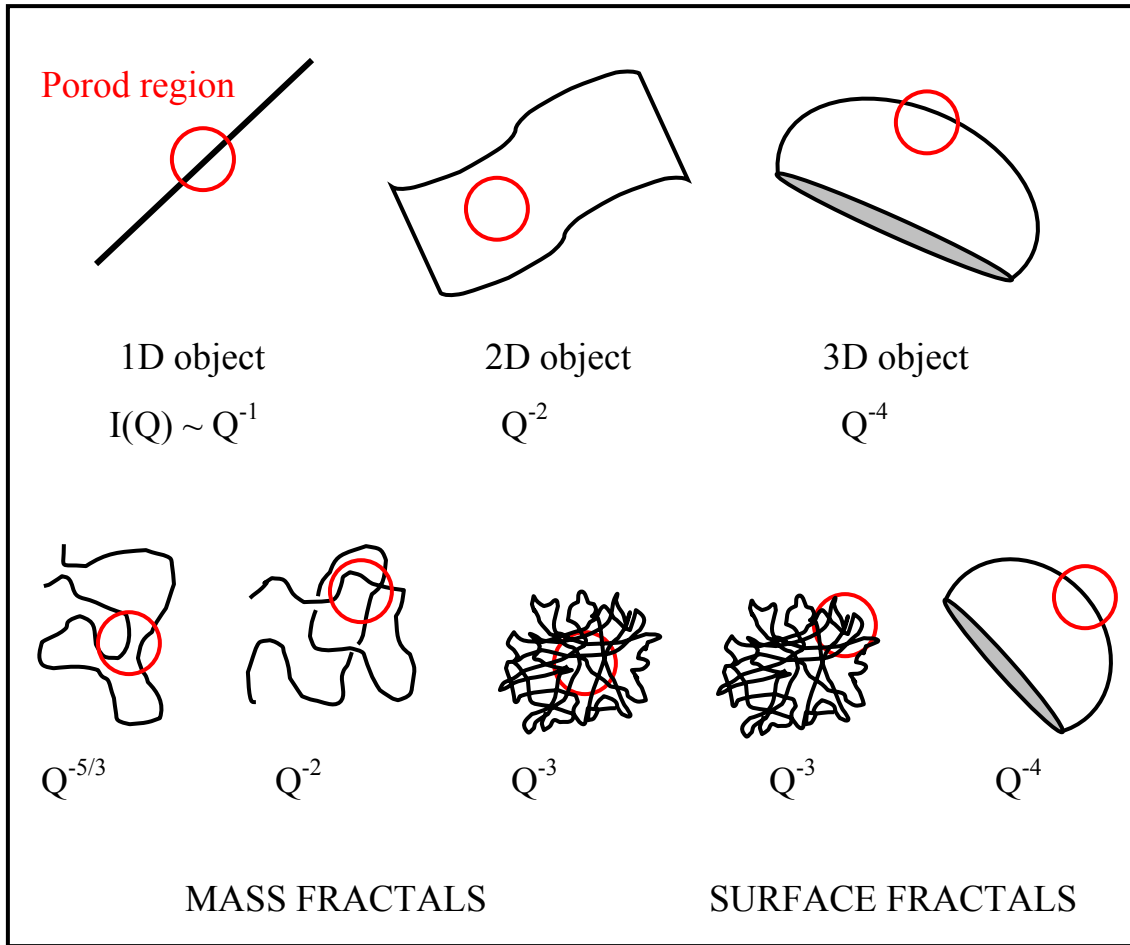
Figure 7: Assortment of Porod law behaviors for different shape objects.

4. THE ZIMM PLOT

Another well known plot is the Zimm plot (1/I vs Q^2) which found wide use in light scattering from dilute polymer solutions where extrapolation to zero Q and zero concentration yields the molecular weight, the radius of gyration and the second virial coefficient. The Zimm plot is also useful in polymer blends (in the single-phase region) where the slope is proportional to the correlation length, which is proportional to the Flory-Huggins interaction parameter (incompressible RPA model) to be described later.

Assume a Lorentzian form for the Q-dependence of the scattering intensity:

$$I(Q) = \frac{I_0}{1 + Q^2 \xi^2} . \qquad (10)$$

Here ξ is the correlation length. A plot of $1/I(Q)$ *vs* Q^2 yields $1/I_0$ as intercept and ξ^2/I_0 as slope. The correlation length is obtained as $\xi = (\text{slope/intercept})^{1/2}$. In the low-Q region, one can also expand:

$$I(Q) = \frac{I_0}{1 + \frac{Q^2 R_g^2}{3}} = I_0 \left(1 - \frac{Q^2 R_g^2}{3} + ... \right). \tag{11}$$

Therefore yielding $\xi = R_g / \sqrt{3}$ for low-Q. The Zimm plot applies, however, beyond the low-Q region. In the high-Q region where $Q^2 \xi^2 < 1$, one can approximate:

$$\frac{1}{I(Q)} = \frac{Q^2 \xi^2}{I_0}. \tag{12}$$

In this region, the single polymer chain structure factor behaves as $2/Q^2 R_g^2$ (high-Q expansion of the Debye function) so that $\xi = R_g / \sqrt{2}$ is identified for high-Q. In the case of polymer solutions with excluded volume interactions, the high-Q expansion is, instead:

$$I(Q) = I_0 \frac{2}{(QR_g)^{1/\nu}}. \tag{13}$$

Here ν is the excluded volume exponent ($\nu = 3/5$ for fully swollen chains, $\nu = 1/2$ for theta chains and $\nu = 1/3$ for collapsed chains).

Low-Q departure from linear behavior of the Zimm plot is a signature of non-homogeneity in the sample or of chain-branching. A negative value of the intercept I_0 (obtained through extrapolation) is a sign of phase separation.

An example of a Zimm plot is shown for SANS data taken from a blend mixture of poly(ethyl butylene) and deuterated poly(methyl butylene); i.e., hPEB/dPMB. The molecular weights for hPEB/dPMB are $M_w = 40,100$ g/mol and 88,400 g/mol respectively. The volume fraction of the represented sample corresponds to 57 % hPEB. This blend mixture was measured at a temperature of 10 $^\circ$C. The Zimm plot is linear pointing to Gaussian chains. The slope yields an apparent radius of gyration which depends on the polymer/polymer interaction parameter. These issues will be described in detail when the Random Phase Approximation (RPA) model is introduced.
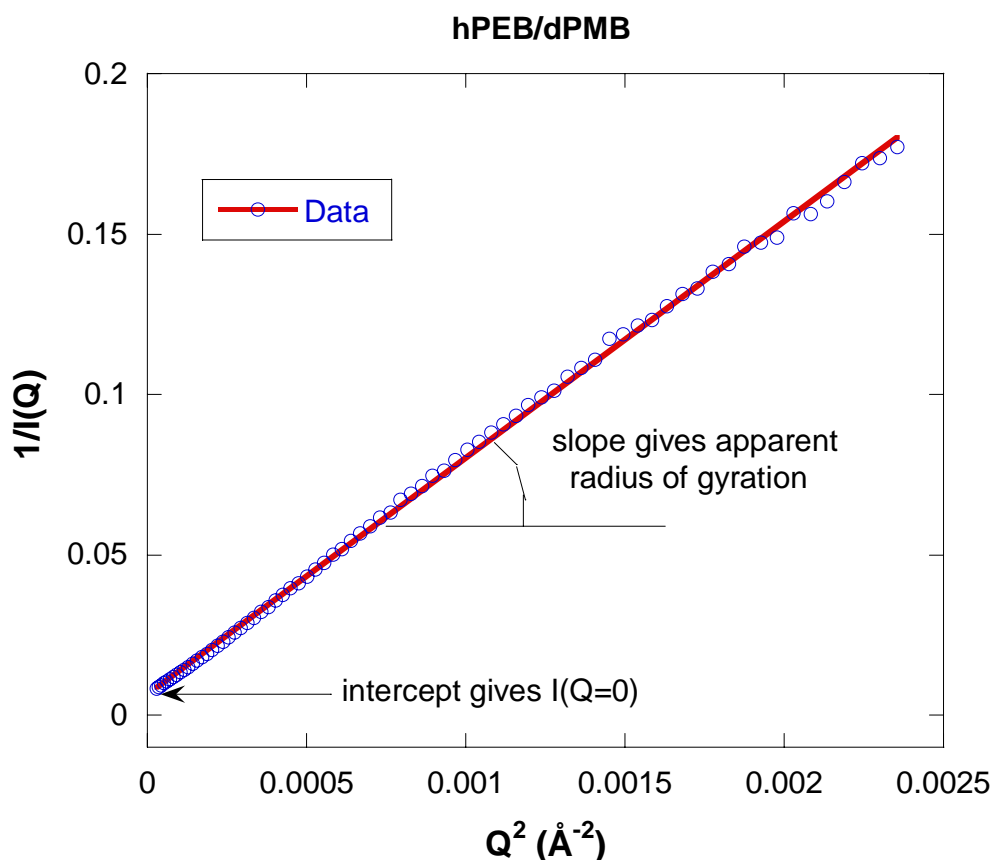
Figure 8: Zimm plot for a polymer blend mixture of hPEB and dPMB with $M_w = 40,100$ g/mol, and 88,400 g/mol respectively. The hPEB fraction is 57 % (g/g) and the measurement temperature is 10 ^{o}C (single-phase region).

A more detailed Zimm plot is for SANS data from a polymer blend mixture of deuterated polystyrene and poly(vinyl methyl ether); i.e., dPS/PVME (Briber et al, 1994). Four dilute dPS volume fractions were measured at a temperature of 140 ^{o}C. The dPS/PVME blend system is characterized by a Lower Critical Spinodal temperature (LCST) and 140 ^{o}C corresponds to the single-phase region. Extrapolation to zero volume fraction yields a slope and intercept which give the degree of polymerization for polystyrene and the radius of gyration respectively.

dPS/PVME
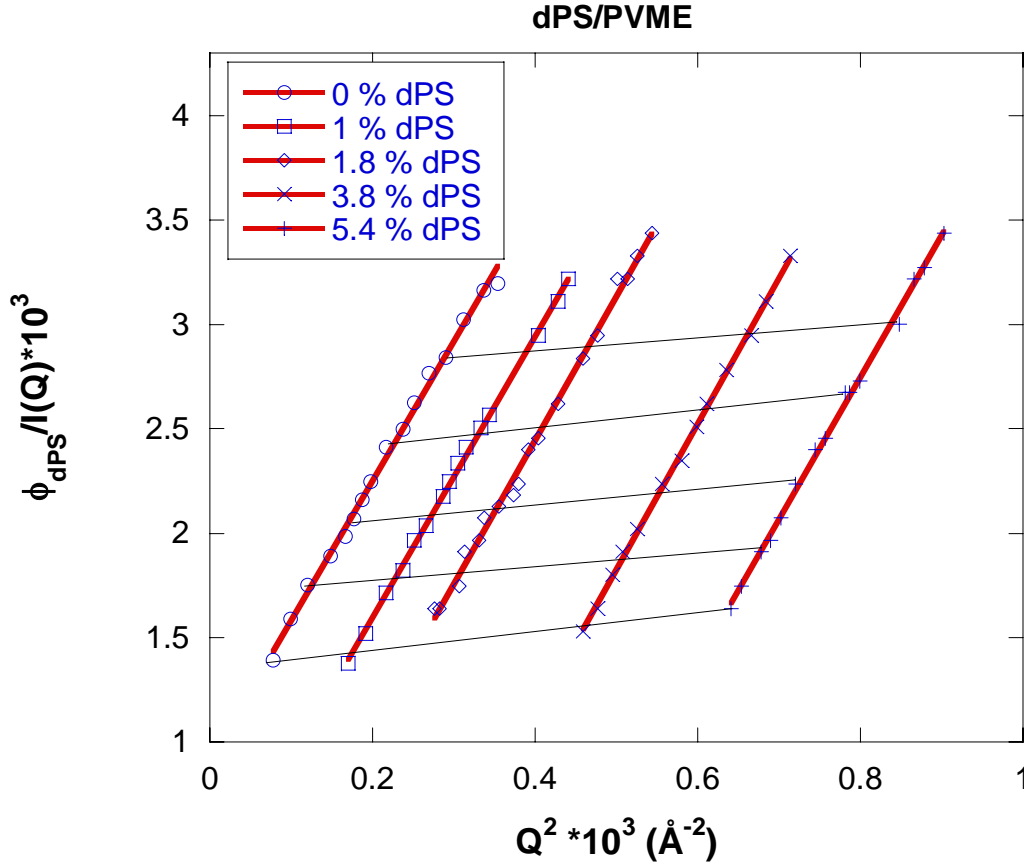
Figure 9: Zimm plot for a deuterated polystyrene/polyvinylmethylether blend (M_w = $1.88*10^5$ g/mol and $3.98*10^5$ g/mol respectively) mixture for four dilute polystyrene volume fractions of ϕ_{dPS} = 1 %, 1.8 %, 3.8 % and 5.4 % at a temperature of 140 ^{o}C.

5. THE KRATKY PLOT

Kratky plots emphasize deviation from the high-Q behavior of the scattering intensity I(Q). For polymer chains, the Kratky plot (Q^2I(Q) *vs* Q) emphasizes the Gaussian chain nature or departure from it. Since the structure factor for Gaussian chains varies like I(Q) ~ $1/Q^2$ at high-Q, this plot tends to a horizontal asymptote. Inter-chain contributions affect only the constant multiplying this term and not the $1/Q^2$ scaling behavior. Deviation from a horizontal asymptotic behavior indicates a non-Gaussian characteristic for the scattering chains.

For instance for rigid rods, this plot would go to a linearly increasing asymptote Q^2I = A + BQ because the form factor for a rod varies like I(Q) ~ 1/Q at high Q and one has to use a more suitable Kratky plot for a rod (QI *vs* Q) in order to recover the horizontal asymptote. In order to illustrate this in simple terms, three functions that die out differently at high Q are considered. These three cases are (1) for rigid rods where I(x) = I_0/(1+x), (2) for Gaussian chains where I(x) = I_0/(1+x^2), and (3) for branched systems (or mass fractals) where I(x) = I_0/(1+x^3). Here x is the dimensionless variable x = Qξ where ξ is a characteristic length

(radius of gyration or correlation length). These functions reproduce the proper low x and high x limits.
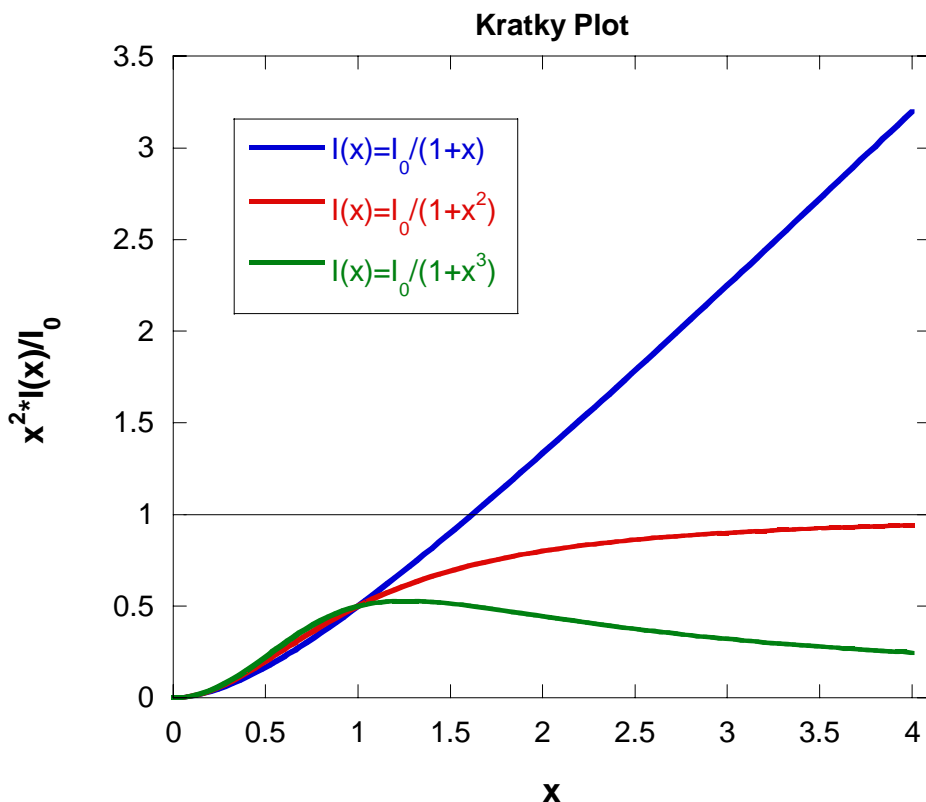
Kratky Plot

Figure 10: Symbolic representation of the Kratky plot for the three cases of a rigid rod, a Gaussian chain and a mass fractal.

Gaussian chains tend to the Kratky plot limit of 1. Stiff chains (for example rigid rods) increase linearly at high x and branched systems (mass fractals) reach a maximum then decrease as $1/x$ at high x.

An example of a Kratky plot is shown for SANS data taken from an isotopic blend mixture of deuterated polystyrene with non-deuterated polystyrene, i.e., dPS/hPS with $M_w = 174,000$ g/mol and 195,000 g/mol respectively at 50 % fraction (g/g) and measured at ambient temperature. This plot represents the Gaussian nature of polymer chains in isotopic blends and tends to the asymptote of 1 at high Q.

dPS/hPS
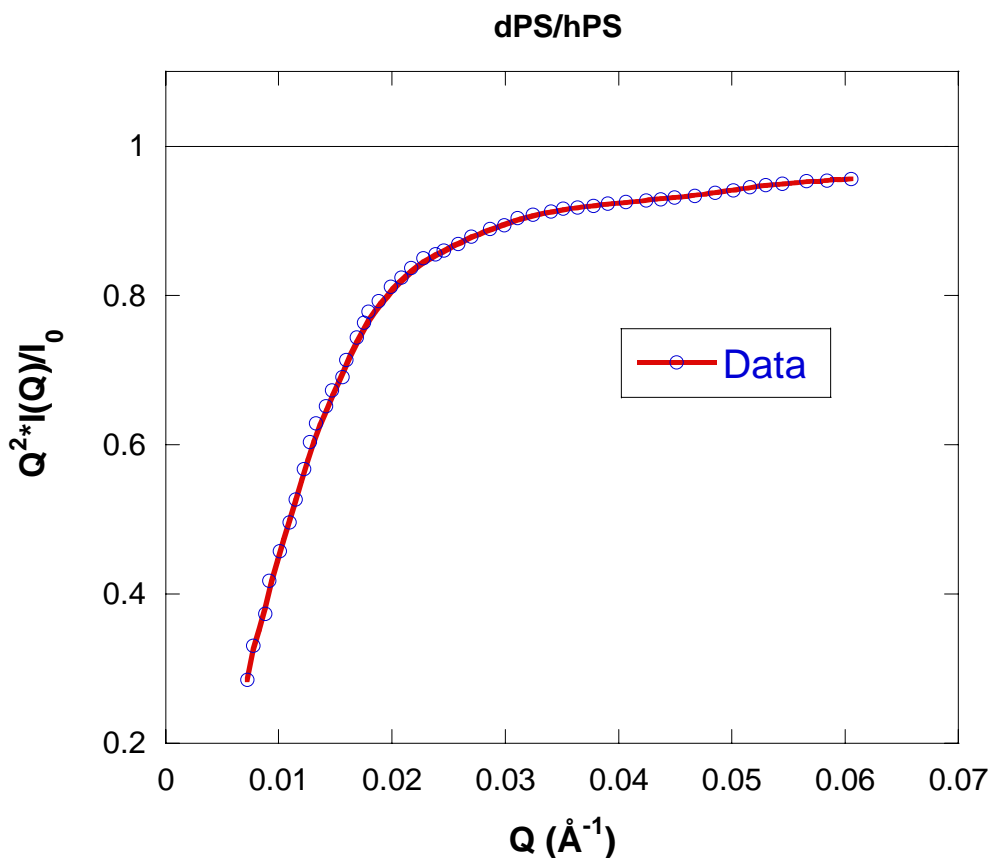
Figure 11: Kratky plot for an isotopic blend mixture of dPS and hPS with M_w = 174,000 g/mol and 195,000 g/mol, 50 % fraction (g/g) measured at ambient temperature. The line is a smoothing fit as a guide to the eye.

Another Kratky plot is shown for a seventh generation PAMAM dendrimer in D_2O. SANS data were taken from a series of dilute solutions and extrapolated to the infinite dilution limit (Hammouda, 1992). Measurements were taken at ambient temperature. This plot represents the branched character of this scattering system. It has not been rescaled at high Q.
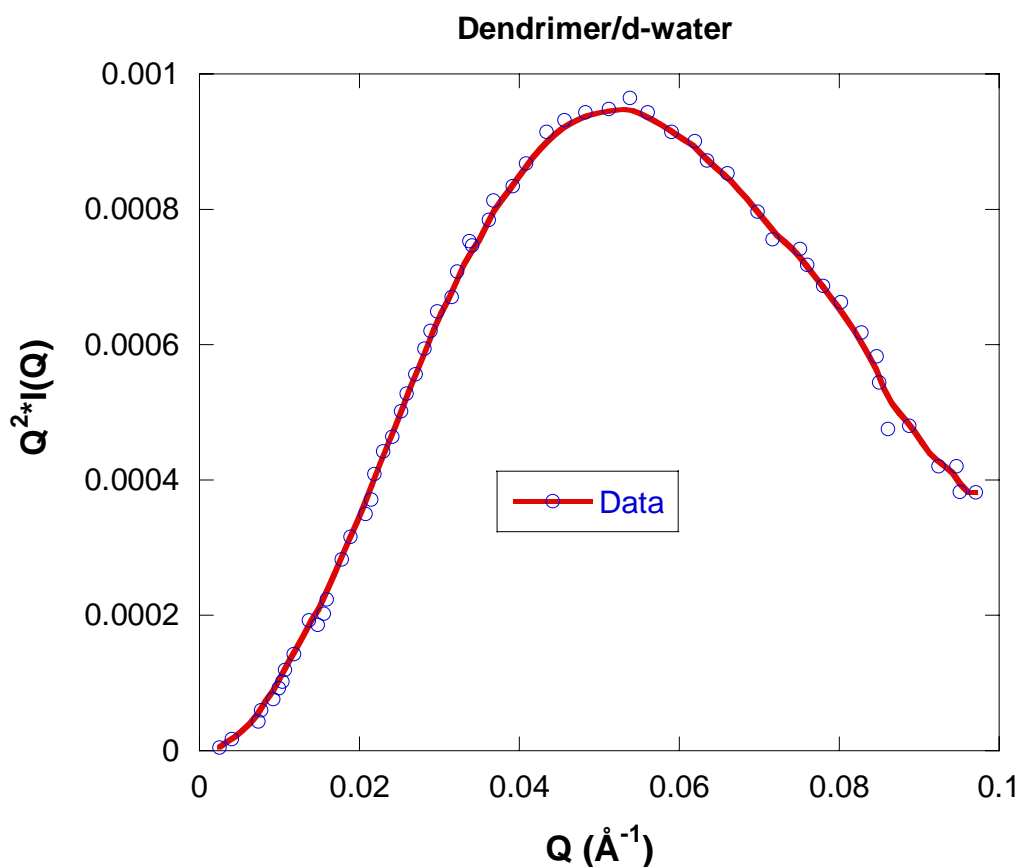
Figure 12: Kratky plot for seventh generation PAMAM dendrimer solution in D_2O extrapolated to the infinite dilution limit (zero concentration). The Katky plot reaches a maximum then tends to a constant level at high Q.

The manner in which the asymptote of a Kratky plot is reached yields information about chain branching. For instance, in a plot of Q^2I vs $1/Q^2$ ($Q^2I = A + B/Q^2$) the intercept B is related to the crosslink density in branched gels and networks (Benoit et al, 1993).

REFERENCES

R.S. Stein, P.R. Wilson and S.N. Stidham, "Scattering of Light by Heterogeneous Spheres", J. Applied Physics 34, 46-50 (1963)

B. Hammouda, "Structure Factor for Dendrimer Polymer Gels', J. Polym. Sci., Polym. Phys. Ed., 30, 1387-1390 (1992)

R.M. Briber, B.J. Bauer and B. Hammouda, "SANS from Polymer Blends in the Dilute Concentration Limit", J. Chem. Phys. 101, 2592-2599 (1994)

H. Benoit, J.F. Joanny, G. Hadziioannou and B. Hammouda, Macromolecules 26, 5790 (1993)

QUESTIONS

1. What is a Guinier Plot? What can be obtained from it? What can be obtained from the intercept?
2. Do scattering inhomogeneities have to be spherical for a radius of gyration to be defined and measured through a Guinier plot?
3. What information could be obtained using a Porod plot for smooth interfaces?
4. How does polydispersity and instrumental smearing affect the Guinier plot and the Porod plot?
5. Consider the pair correlation function for a sphere of radius R_A, given by:

$$\gamma(r) = 1 - \frac{3}{4}\left(\frac{r}{R}\right) + \frac{1}{16}\left(\frac{r}{R_A}\right)^3$$. Explain the limit g(r=2R_A) = 0.

6. A Zimm plot is linear for what scattering objects?
7. What information can be obtained from a Kratky plot?

ANSWERS

1. A Guinier plot is a plot of Ln(I) *vs* Q^2. The radius of gyration (R_g) can be obtained from the slope of a Guinier plot (slope = $Rg^2/3$). The intercept of a Guinier plot is I(0) which can yield the aggregation number which is the number of basic scattering units per scattering "particle". A scattering unit could be a monomer and a scattering particle could be a polymer.
2. The Guinier plot Ln(I) *vs* Q^2 measure a radius of gyration from any shape objects. These do not have to be globular.
3. The Porod plot Log(I) *vs* Log(Q) for scattering objects with smooth interfaces yields an exponent from the slope and a surface-to-volume ratio from the intercept.
4. Polydispersity and instrumental smearing yield broader forward scattering peaks and therefore a lower radius of gyration from the Guinier plot. These, however, do not affect the Porod exponent which remains unchanged.
5. Consider a scatterer inside a sphere of radius R_A and draw another sphere of radius r. Choosing the first scatterer on the surface of the sphere and choosing a second sphere of radius $r = R_A$ covers the maximum correlation range of $2R_A$. Beyond that range, scatterers are not correlated.
6. A Zimm plot 1/Log(I) *vs* Q^2 is linear for Gaussian polymer coils.
7. A Kratky plot Log(Q^2I) *vs* Q saturates to a constant level at high-Q for flexible polymer coils but increase linearly for rigid rods. The break between the constant and the linear behaviors yields an estimate of the persistence length.

Chapter 23 - **EMPIRICAL MODELS**

Standard plots give the first order interpretation of SANS data. Precise models give a more detailed approach at obtaining results. Precise molecular models are however not always available or too complex to use. An intermediate approach consists in using empirical models that reproduce the main trends observed in the SANS data. Some of these models are described here.

1. THE CORRELATION LENGTH MODEL

Oftentimes when the scattering intensity I(Q) is a decreasing function with Q, it is modeled using the following functional form:

$$I(Q) = \frac{C}{1 + (Q\xi)^m} + B. \hspace{3cm} (1)$$

Here C and B are (Q-independent) constants obtained for $I(Q\xi \to 0) = C + B$ and $I(Q\xi \to \infty) = B$, ξ is a correlation length and m is a Porod exponent. Note that when m = 2, this functional form becomes the familiar Lorentzian function. The Fourier transform of a Lorentzian function corresponds to correlations dying out as exp(-r/ξ)/r. The correlation length ξ is large for systems that are highly correlated like polymers and gels. For example, ξ is equal to the entanglement distance for a semi-dilute polymer solution and it is equal to the end-to-end distance for very dilute polymers.

A figure shows SANS data from 4 % (g/g) solution of poly(ethylene oxide) or PEO for short of M_w = 41,500 g/mol in D_2O at a temperature of 20 ^oC (Hammouda et al, 2004). Fit to the correlation length model gave the following parameters: C = 0.52 cm^{-1}, ξ = 17.47 Å, m = 1.93 and B = 0.069 cm^{-1}. The fit is good except for the very low-Q points where statistics are poor. The correlation length ξ gives a good estimate of the average entanglement length for this semi-dilute polymer solution. The Porod exponent m points to a "mass fractal" for dissolved polymer chains close to the theta condition. The fractal exponent for chains in a good solvent is m = 5/3 and that for chains in theta condition is m = 2. The theta condition is defined when monomer-solvent, monomer-monomer and solvent-solvent molecular interactions are comparable.

Poly(ethylene oxide)/d-water
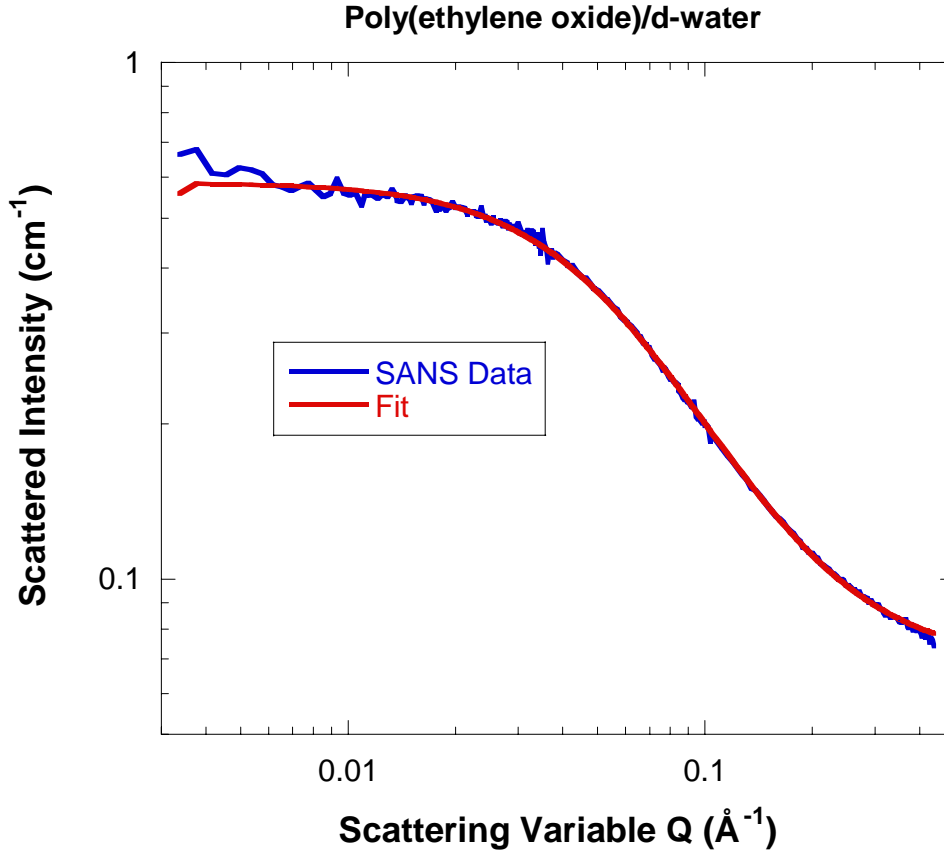
Figure 1: SANS data from 4 % solution of PEO (M_w = 41,500 g/mol) in D_2O at 20 ^{o}C temperature and fit to the correlation length model.

2. THE BROAD PEAK MODEL

Many SANS spectra are characterized by a broad peak even though they are from amorphous soft materials. The d-spacing corresponding to the broad peak is a characteristic distance between the scattering inhomogeneities (such as in lamellar, cylindrical, or spherical morphologies or for bicontinuous structures). The following simple functional form reproduces the broad peak feature:

$$I(Q) = \frac{C}{1 + \left(|Q - Q_0| \, \xi \right)^m} + B .$$ (2)

Here the peak position is related to the d-spacing as $Q_0 = 2\pi/d_0$. Soft systems that show a SANS peak include copolymers, polyelectrolytes, multiphase systems, layered structures, etc.

A figure shows SANS data from 4 % poly(lysine) polyelectrolyte solution in D_2O at 25 ^{o}C temperature. Poly(lysine) is a poly(amino acid). Fit to the broad peak model gave the following parameters: C = 0.075 cm^{-1}, ξ = 13.10 Å, Q_0 = 0.099 Å^{-1}, m = 1.05 and B = 0.064

227

cm^{-1}. Here again, the fit is good except for the low-Q points where statistics are poor. The d-spacing is $d_0 = 2\pi/Q_0 = 63.47$ Å. This is an average inter-distance between charged polyelectrolyte domains.

Poly(lysine)/d-water
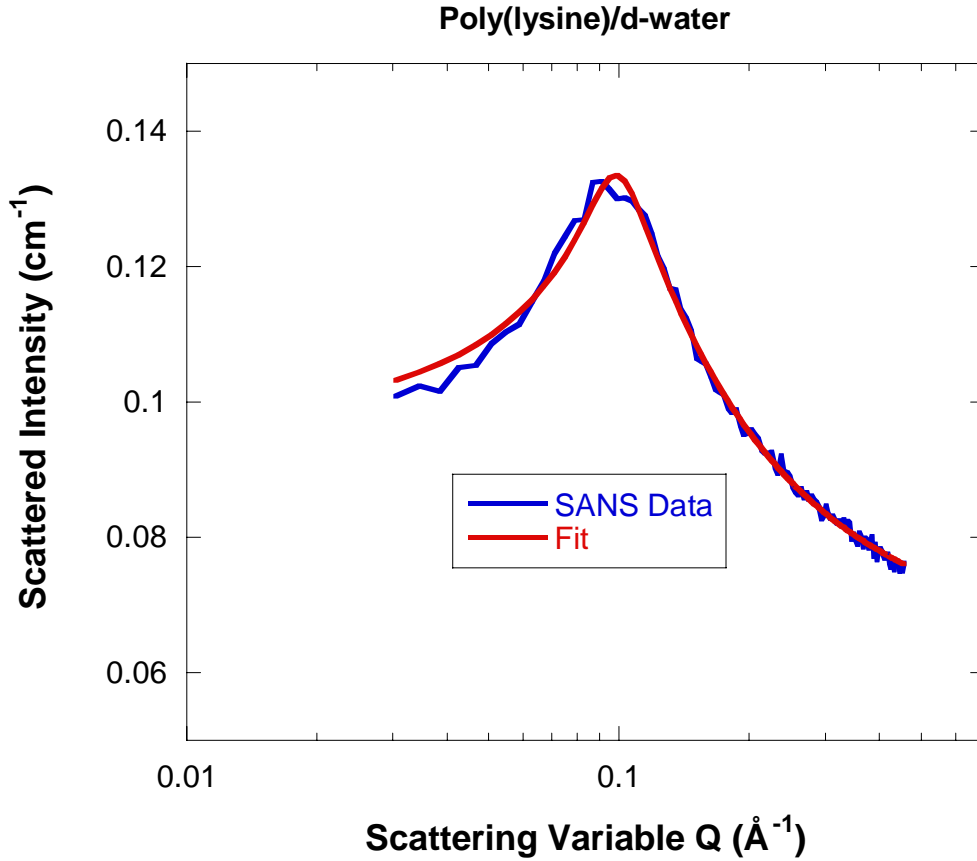
Figure 2: SANS data from 4 % poly(lysine) poly(amino acid) solution in D$_2$O at 25 ^{o}C temperature and fit to the broad peak model.

3. THE TEUBNER-STREY MODEL

The Teubner-Strey model (Teubner-Strey, 1987) was originally introduced to represent the structure of micellar systems. These are characterized by a peak representing inter-micellar interactions. This model assumes a pair correlation function of the form:

$$\gamma(r) = \frac{d}{2\pi r} \exp\left(-\frac{r}{\xi}\right) \sin\left(\frac{2\pi r}{d}\right). \tag{3}$$

Here ξ is a correlation length (length beyond which correlations die out) and d is a d-spacing (characteristic of a domain size or periodicity). The functional form for the scattering intensity (Fourier transform) follows:

$$I(Q) = \left(\frac{8\pi}{\xi}\right)\left(\frac{c_2 V \Delta\rho^2}{a_2 + c_1 Q^2 + c_2 Q^4}\right) + B. \tag{4}$$

V is the scattering volume and $\Delta\rho^2$ is the contrast factor. The various parameters a_2, c_1 and c_2 are fitting parameters and B is the Q-independent coherent scattering background. The correlation length ξ and the d-spacing d are expressed as:

$$\xi = \frac{1}{\sqrt{\frac{1}{2}\sqrt{\frac{a_2}{c_2}} + \frac{1}{4}\frac{c_1}{c_2}}} \tag{5}$$

$$d = \frac{2\pi}{\sqrt{\frac{1}{2}\sqrt{\frac{a_2}{c_2}} - \frac{1}{4}\frac{c_1}{c_2}}}.$$

Consider SANS data from 10 % P85 Pluronic (triblock copolymer of PEO-PPO-PEO) measured in D_2O at 60 °C (temperature for which the micelles are well formed). Fits of the SANS data to the Teubner-Strey model yields the following fitting results.

$$\begin{aligned} a_2 &= 0.038 \\ c_1 &= -51.23 \\ c_2 &= 24{,}929 \\ B &= 0.118. \end{aligned} \tag{6}$$

Note that for the functional form to produce a peak, parameter c_1 has to be negative. These parameters give the following value for the two characteristic lengths:

$$\begin{aligned} \xi &= 96 \text{ Å} \\ d &= 186.6 \text{ Å}. \end{aligned} \tag{7}$$
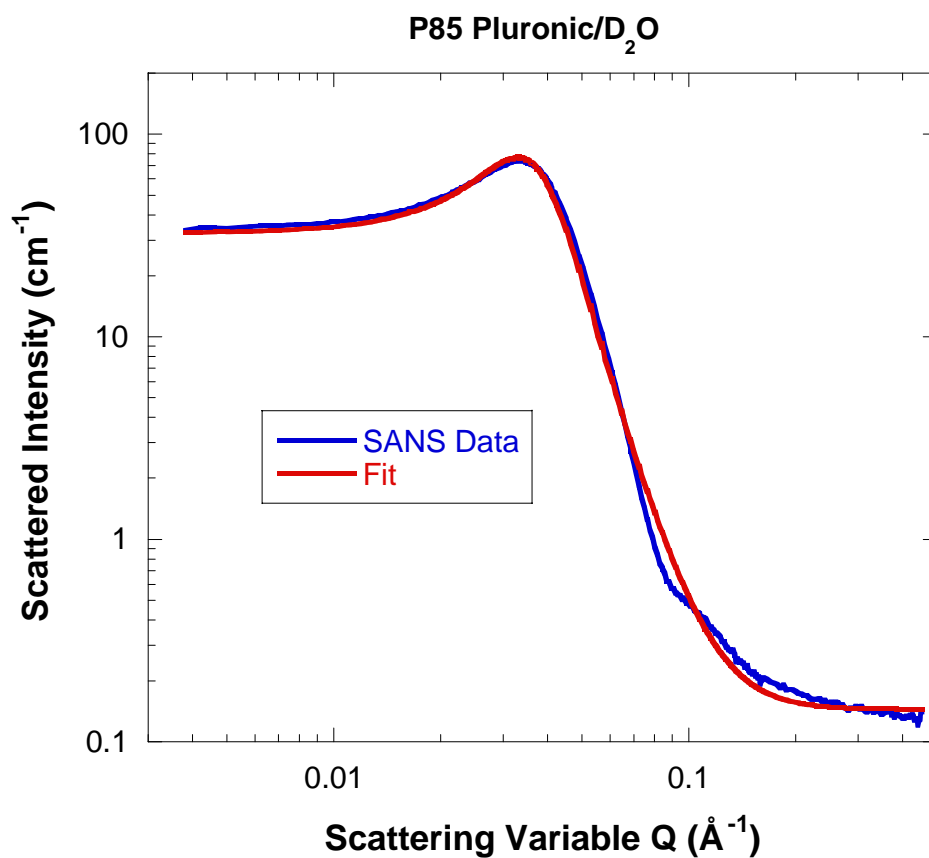
P85 Pluronic/D$_2$O

Figure 3: SANS data from 10 % P85 Pluronic in D$_2$O at 60 ^{o}C plotted along with the fit to the Teubner-Strey model.
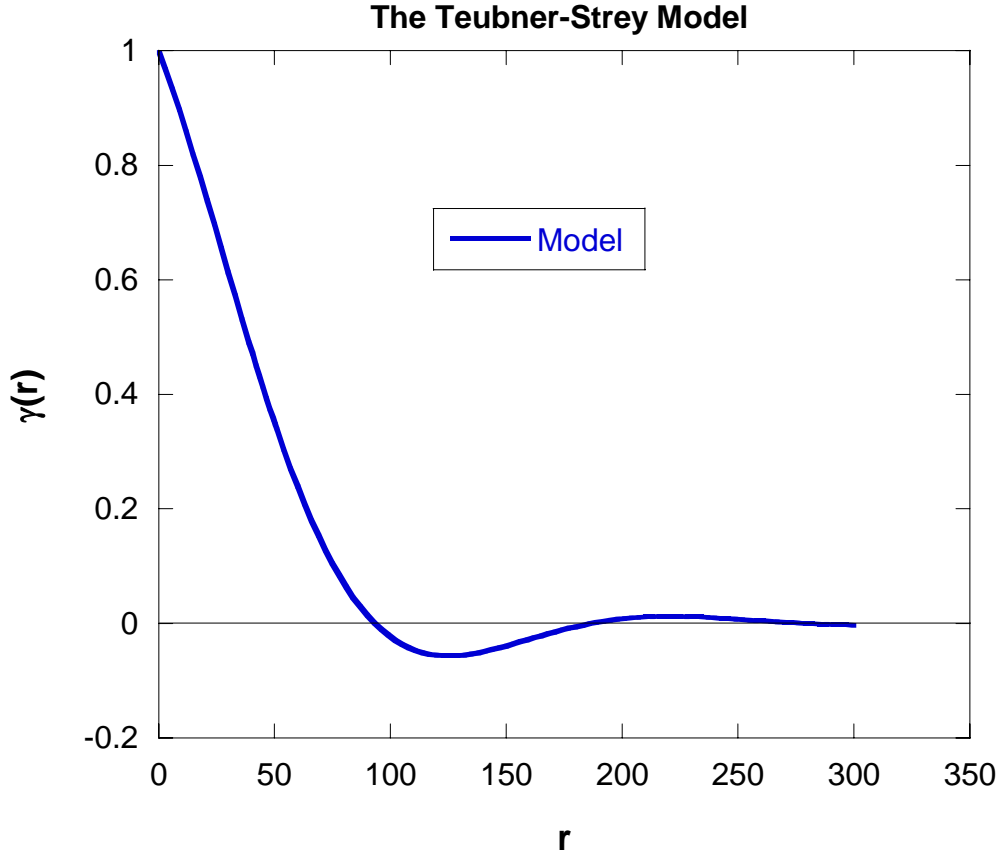
Figure 4: The pair correlation function γ(r) for the Teubner-Strey model.

Note that a peaked behavior in I(Q) results in a pair correlation function γ(r) going negative then positive. This is referred to as the "correlation hole" effect. This happens in block copolymers, in polyelectrolytes and in concentrated systems.

The Teubner-Strey model applies to concentrated solutions of particles (spheres, cylinders, etc) and to the bicontinuous structure. It does not do well for lamellar systems and for other highly ordered morphologies (for example, ordered diblock copolymers). It misses the higher order oscillations completely. Moreover, the Teubner-Strey model was developed for water/oil/surfactant ternary mixtures in the micelle-formation region. Using it for polymer/copolymer mixtures requires some adjustments.

4. THE BEAUCAGE MODEL

The Beaucage model (Beaucage, 1995) applies to systems with different levels of hierarchical organization. These are characterized by scattering data with more than one Guinier and Porod regions. The functional form for the one-level case follows.

$$I(Q) = G \exp\left[\frac{-Q^2 Rg^2}{3}\right] + \frac{C[erf(QRg/\sqrt{6})]^{3m}}{Q^m} + B. \qquad (8)$$

G is the forward scattering intensity (sometime referred to as I_0), R_g is the radius of gyration, C is scaling constant, m is the Porod exponent and B is the usual constant background at high-Q. Note that relationship:

$$C = \frac{G_m}{R_g{}^m \Gamma(m)}.$$

(9)

$\Gamma(m)$ is the Gamma function. In the two-level case, the functional form becomes:

$$I(Q) = G_1 \exp\left[\frac{-Q^2 Rg_1{}^2}{3}\right] + \frac{C_1 [erf(QRg_1 / \sqrt{6})]^{3m_1}}{Q^{m_1}}$$

$$+ G_2 \exp\left[\frac{-Q^2 Rg_2{}^2}{3}\right] + \frac{C_2 [erf(QRg_2 / \sqrt{6})]^{3m_2}}{Q^{m_2}}.$$

(10)

Consider SANS data taken from a 4 % poly(ethylene oxide) solution (M_w = 41,800 g/mol) in D_2O taken at 25 °C. The SANS signal is characterized by a low-Q clustering part and a high-Q solvation part. Only the tail of the low-Q feature is observed. Fits to the two-level Beaucage model gives the following fitting parameters:

$G_1 = 13.53$ (11)
$R_{g1} = 725.95$
$C_1 = 3.0928*10^{-5}$
$m_1 = 1.91$
$G_2 = 0.53$
$R_{g2} = 25.99$
$C_2 = 0.0014$
$m_2 = 2.14$
$B = 0.091$.

The values of G_1 and Rg_1 are not reliable since no Guiner region is observed at low-Q. The Porod exponents for the low-Q clustering and the high-Q solvation regions point to a mass fractal.

Poy(ethylene oxide)/d-water
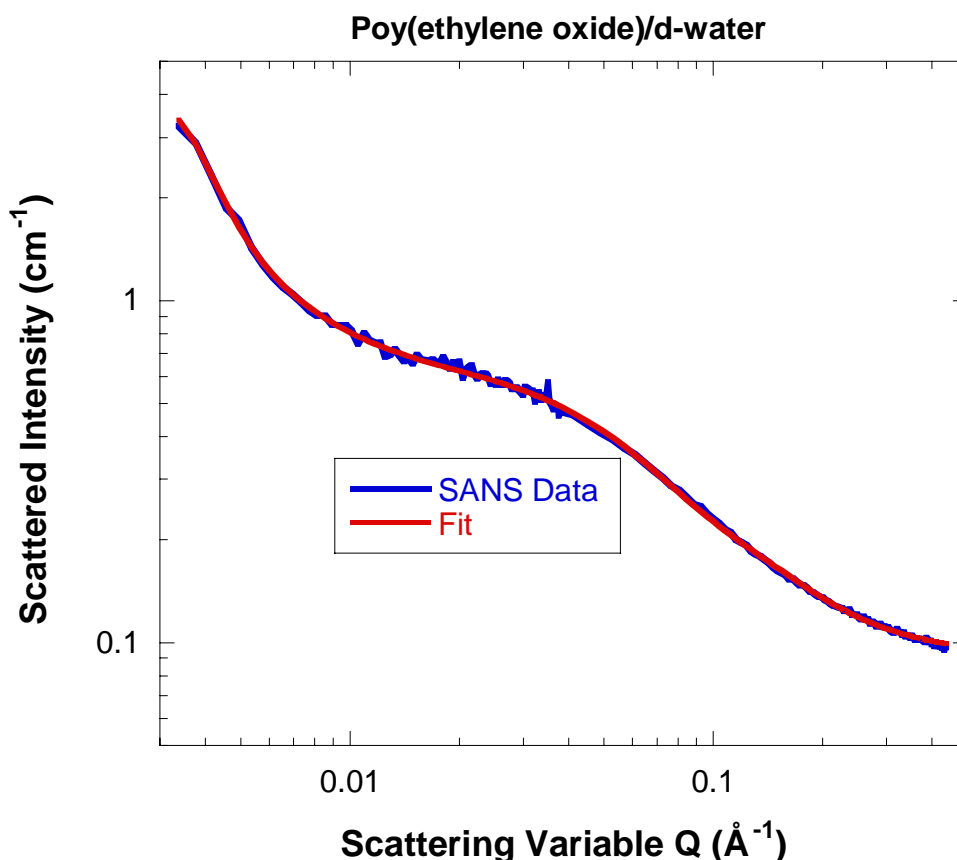
Figure 5: Plot of the SANS data from 4 % PEO solution (M_w = 41,800 g/mol) in D_2O at 25 ^oC along with fit to the two-level Beaucage model.

REFERENCES

B. Hammouda, D. Ho and S. Kline, "Insight into Clustering in Poly(ethylene oxide) Solutions", Macromolecules 37, 6932-6937 (2004)

M. Teubner and R. Strey, "Origin of the Scattering Peak in Microemulsions", J. Chem. Phys. 87, 3195-3200 (1987)

G. Beaucage, "Approximations Leading to a Unified Exponential/Power Law Approach to Small-Angle Scattering", J. Appl. Cryst., 28, 717-728 (1995).

QUESTIONS

1. What are the three main methods to analyze SANS data?
2. What is referred to as the Ornstein Zernike functional form? What parameter can be obtained from a fit to that form?
3. What is the meaning of a peak in SANS data (at Q_0 for example)?
4. What type of scattering does the Teubner-Strey model apply to?

5. What are the main parameters for the Beaucage model? In what scattering range does it apply?

ANSWERS

1. The three main ways to analyze SANS data are: (1) standard plots (linear plots of functions of I(Q) *vs* functions of Q), (2) non-linear least squares fits to reasonable models including empirical models and (3) molecularly realistic complex methods for particle shape reconstruction and molecular simulation.

2. The Ornstein-Zernike functional form is a Lorentzian. A correlation length can be obtained.

3. A peak in SANS data (at Q_0) means that there is a structure with a characteristic repeat distance $d = 2\pi/Q_0$.

4. The Teubner-Strey model applies to scattering data with a peak and that decay as $1/Q^4$ at high Q. These are concentrated systems with inter-particle separation distance comparable to particle size or to bicontinuous structures.

5. Data fitting to the Beaucage model yields an intercept I_0, a radius of gyration R_g, a Porod exponent m and a surface to volume ratio for the scattering object.

SANS data come in many trends and shapes. Most data sets show a forward scattering peak. Some show a peaked behavior at finite Q. Only a few show a multitude of peaks. The SANS technique is not abundant in peaks like other characterization methods. Representative SANS data are presented here.

1. INCREASING FLUCTUATIONS

Increase in SANS intensity is a signature of an increase in density or composition fluctuations. This is observed for systems undergoing phase transition, aggregation or crystallization. SANS is a good monitor of phase separation.

A figure summarizes SANS data taken from a phase separating polymer solution as temperature is increased (Hammouda et al, 2002). The polymer solution is made of 4 % poly(ethylene oxide) of M_w = 41,800 g/mol in d-water. This high-Q signal represents solvent-polymer interactions (though hydrogen bonding in this case). As temperature is increased, hydrogen bonding breaks leading to the onset of a lower critical solution temperature. The upturn at low Q is due to a clustering effect characterizing most water-soluble systems.

Poly(ethylene oxide)/d-water

85 °C
65 °C
50 °C
37.5 °C
25 °C
10 °C
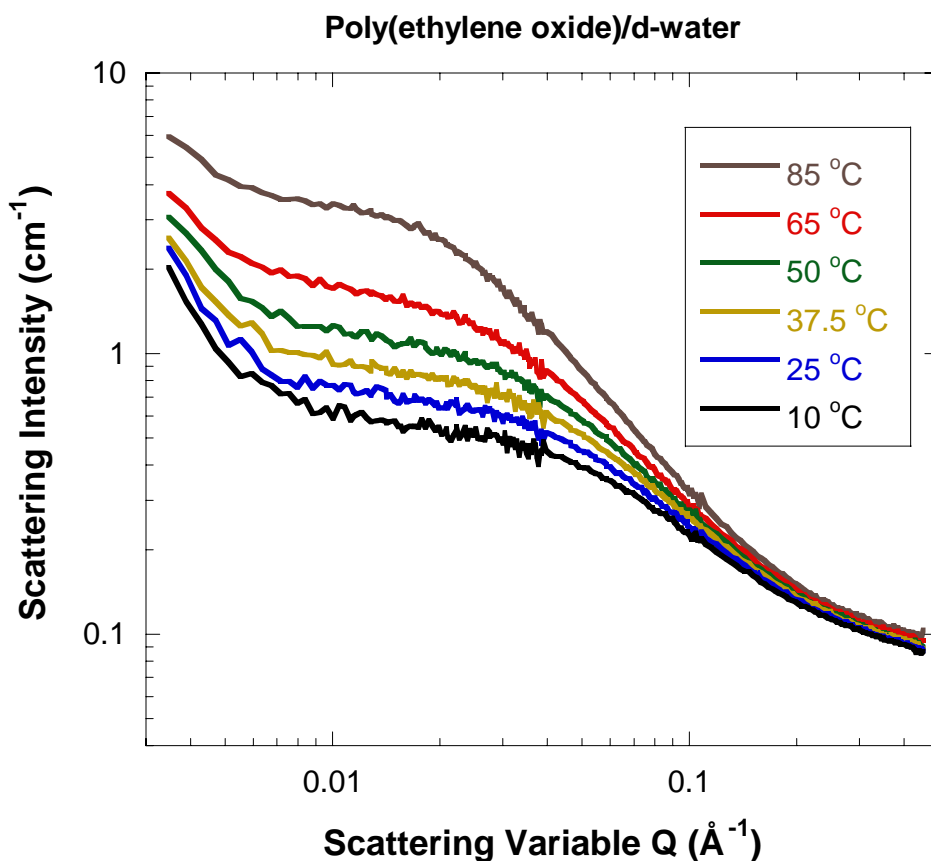
Figure 1: SANS data taken from a 4 % poly(ethylene oxide) solution in d-water. The polymer molecular weight is $M_w = 41,800$ g/mol.

2. ORDERED STRUCTURES

A class of SANS spectra is characterized by a sharp peak. The peak is either due to a well-defined repeat distance (in lamellar systems for example) or due to the correlation hole.
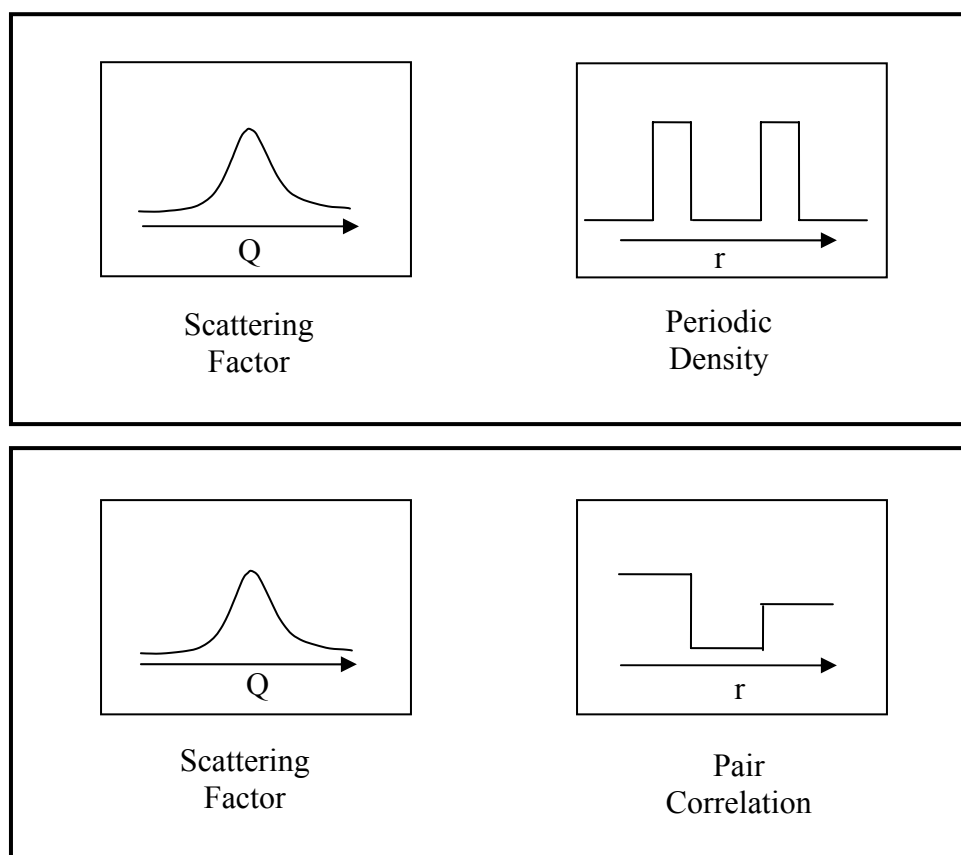
Figure 2: Representation of the two cases that can give a SANS peak.

SANS data from a polystyrene-polyisoprene diblock copolymer are included. The SANS peak is due to the correlation hole. At low-temperatures, the morphology formed is highly ordered (lamellar).

Polystyrene-Polyisoprene Diblock Copolymer
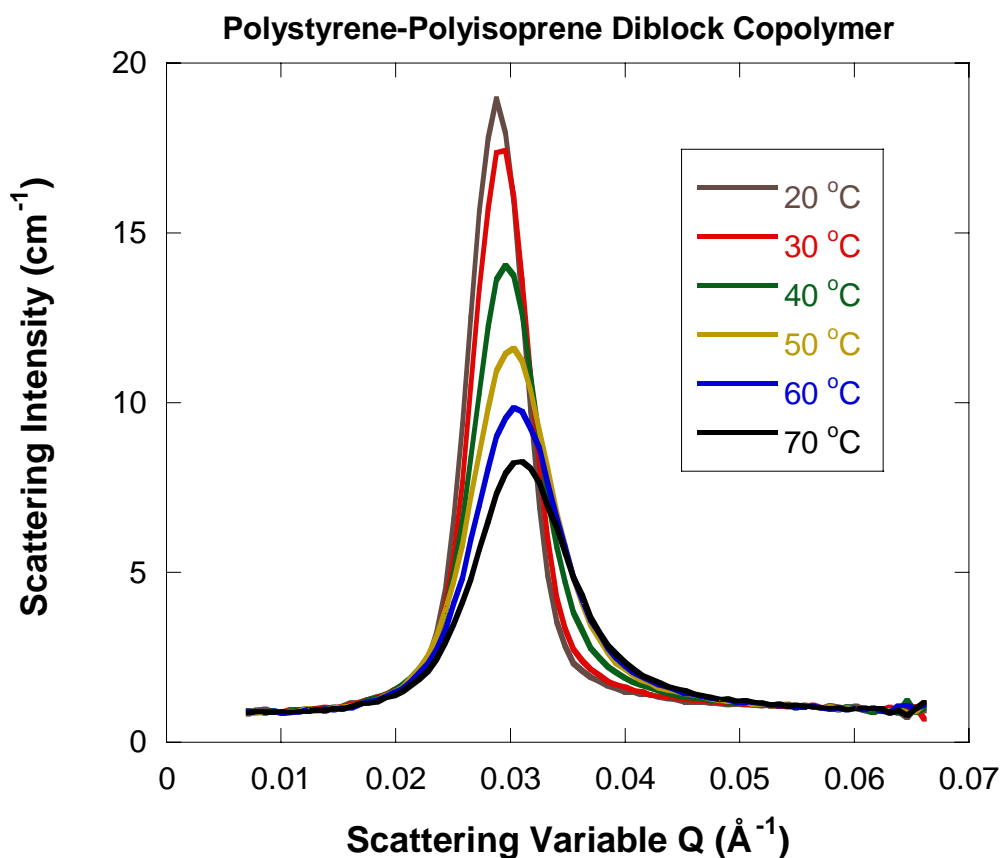
Figure 3: SANS data from a polystyrene-polyisoprene diblock copolymer solution in DOP solvent.

3. CONCENTRATED SYSTEMS

Another class of SANS spectra is when an inter-particle peak is formed. This is the case where the inter-particle spacing is comparable to the particle size and is characteristic of "concentrated" systems. The case of a 25 % pluronics (PEO-PPO-PEO triblock copolymer) micelles in d-water is included. Micelles form above ambient temperature due to the hydrophobic nature of PPO.

P85/d-water
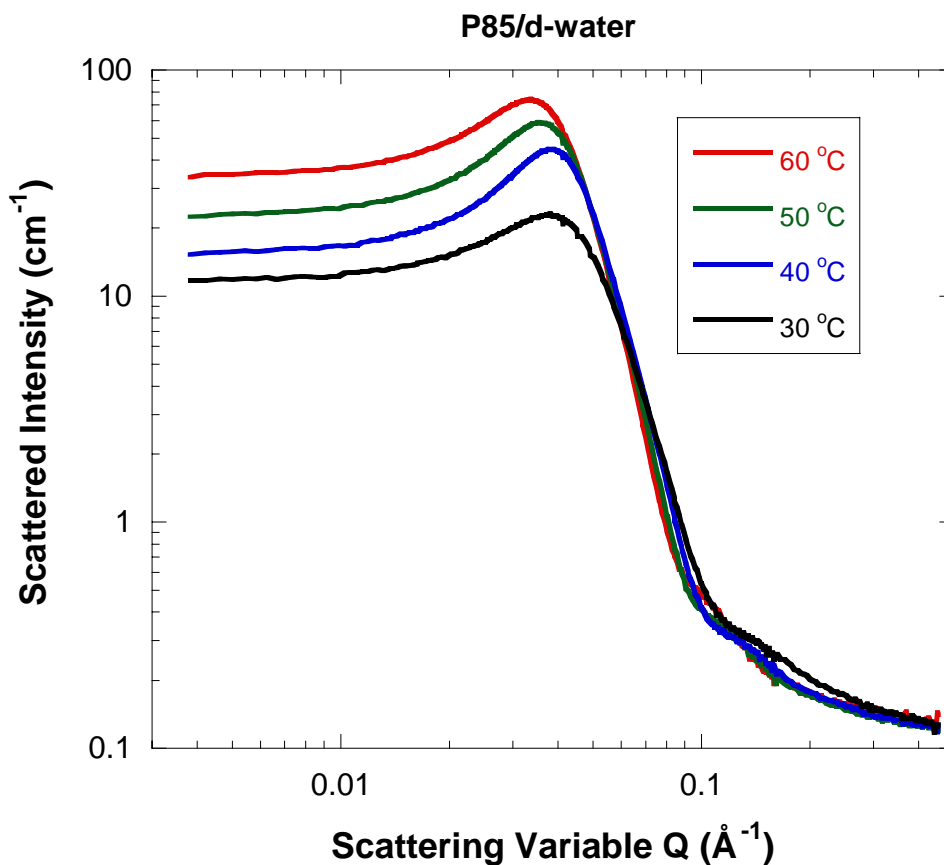
Figure 4: SANS data from P85 pluronics micelles. The inter-particle interaction peak is clearly observed.

4. DILUTE SOLUTION OF MONODISPERSE PARTICLES

The case of dilute solutions is characterized by scattering from "isolated" particles. A 0.1 % solution of silica particles in d-water is included here. The higher order peaks are a signature of monodispersity and are limited by instrumental resolution. The fitted sphere radius is R = 563 Å.
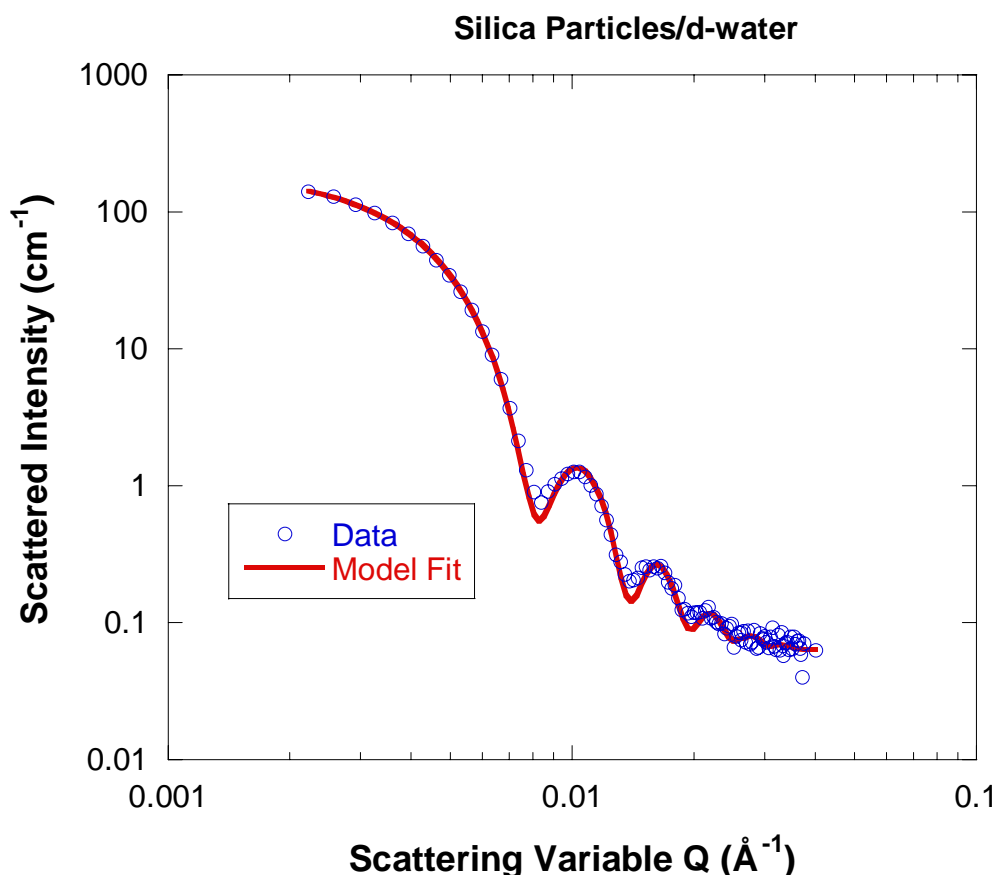
Figure 5: SANS data from a dilute solution of silica particles (0.1 % mass fraction) in d-water and fit to sphere model. The fitted sphere radius is R = 563 Å.

REFERENCES

B. Hammouda, D. Ho and S. Kline, "Neutron Scattering from Associating PEO Systems", Macromolecules <u>35</u>, 8578-8585 (2002)

QUESTIONS

1. Why does scattering increase when a phase transition line is approached?
2. What is the "correlation hole" effect in block copolymers?
3. Why does the block copolymer peak broaden when the mixed-phase region is entered?
4. Why are SANS data from concentrated systems characterized by a peak?
5. What is the origin of the higher order peaks observed in SANS data from monodisperse dilute solution of particles.

ANSWERS

1. The approach to phase transition conditions is accompanied by composition fluctuations. Likewise molecules attract each other whereas unlike molecules repel each other.

2. Copolymers are formed of blocks that are covalently bonded. Consider, say, a diblock A-B. Around each A block, there is a region where another A block cannot reside because of crowding from B blocks. This region empty of A block is referred to as a "correlation hole" effect.

3. The mixed phase (also called disordered phase) region is obtained by dissolving the macrodomain morphology formed in the ordered phase. The SANS peak in the ordered phase is sharp due to the characteristic (lamellar, cylindrical or spherical) morphology. The SANS peak in the disordered phase is due to the correlation hole effect.

4. SANS data from concentrated systems are characterized by a peak because the inter-particle d-spacing becomes comparable to the size of the particles. The SANS peak position characterizes the nearest neighbor inter-distance. It is due to the inter-particle structure factor $S_I(Q)$.

5. The single-particle scattering factor for a single spherical particle is given by the spherical Bessel function $P(Q) = [3j_1(QR)/QR]^2$ where R is the sphere radius and $j_1(X) = \sin(X)/X^2 - \cos(X)/X$. This is an oscillatory function with many higher order peaks.

Scattering from oriented samples is rich in peaks and anisotropic features as observed on the 2D detector. A series of these "interesting" spectra is included here in order to sample the wide variety of possibilities.

1. ORIENTED FIBERS

Collagen from a kangaroo tail tendon is characterized by a fiber-like structure with structure (along the oriented fibers) with repeat spacing of 667 Å.
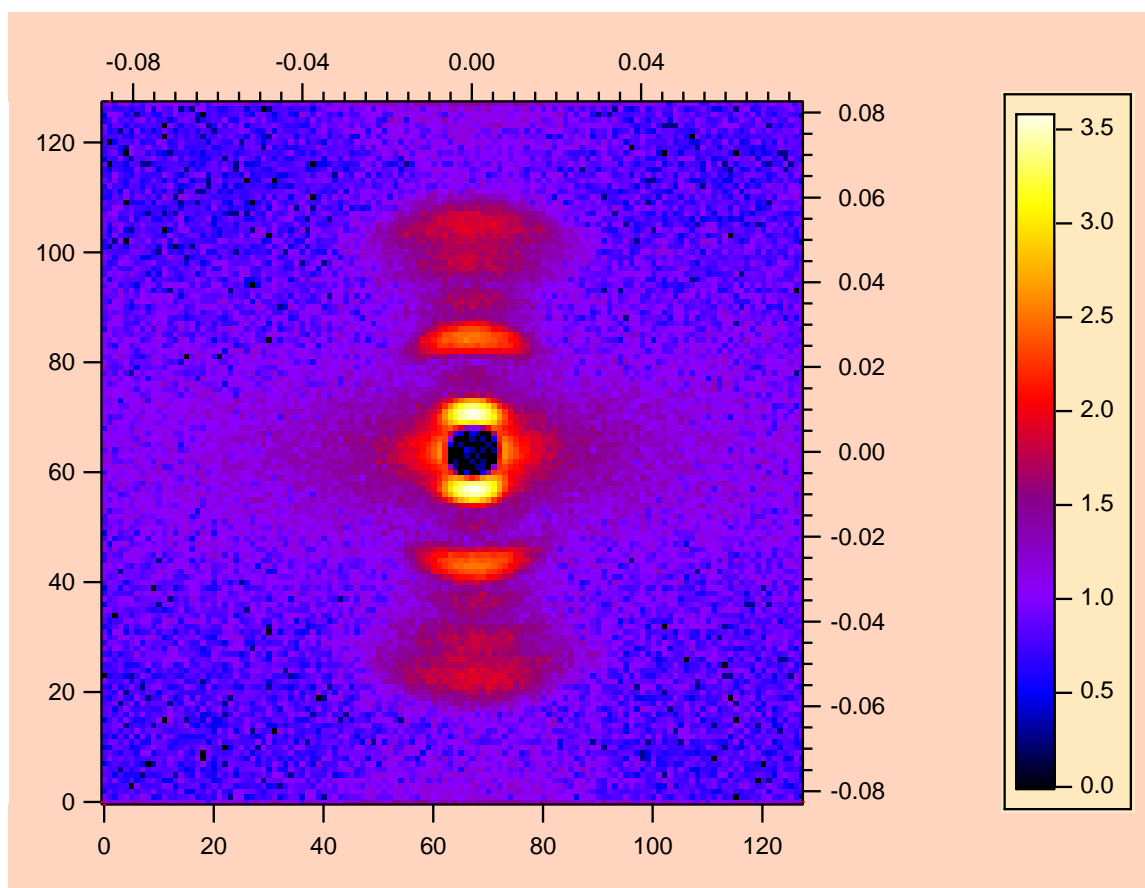
Figure 1: Scattering pattern from highly ordered biopolymer (collagen from a kangaroo tail tendon) showing the strong first and third reflection peaks as well as weak higher order reflection peaks; the second reflection peak is not allowed. The ordered structure is along the fibers and has a d-spacing of 667 Å.

2. SINGLE NANOCRYSTAL

Anisotropic SANS data from P85 pluronics micelles sheared in a Couette shear cell are included. The characteristic hexagonal peak pattern (six fold symmetry) points to a cubic structure formed by the spherical micelles for 25 % mass fraction P85 in D2O solutions. P85 is a triblock copolymer of poly(propylene) which is hydrophobic in the middle of the molecule and poly(ethylene oxide) which is hydrophilic on the outside of the molecule (PEO-PPO-PEO). P85 micelles are well formed at ambient temperature. Shearing helps the packing of the spherical micelles into a face centered cubic structure (Slawecki et al, 1998).
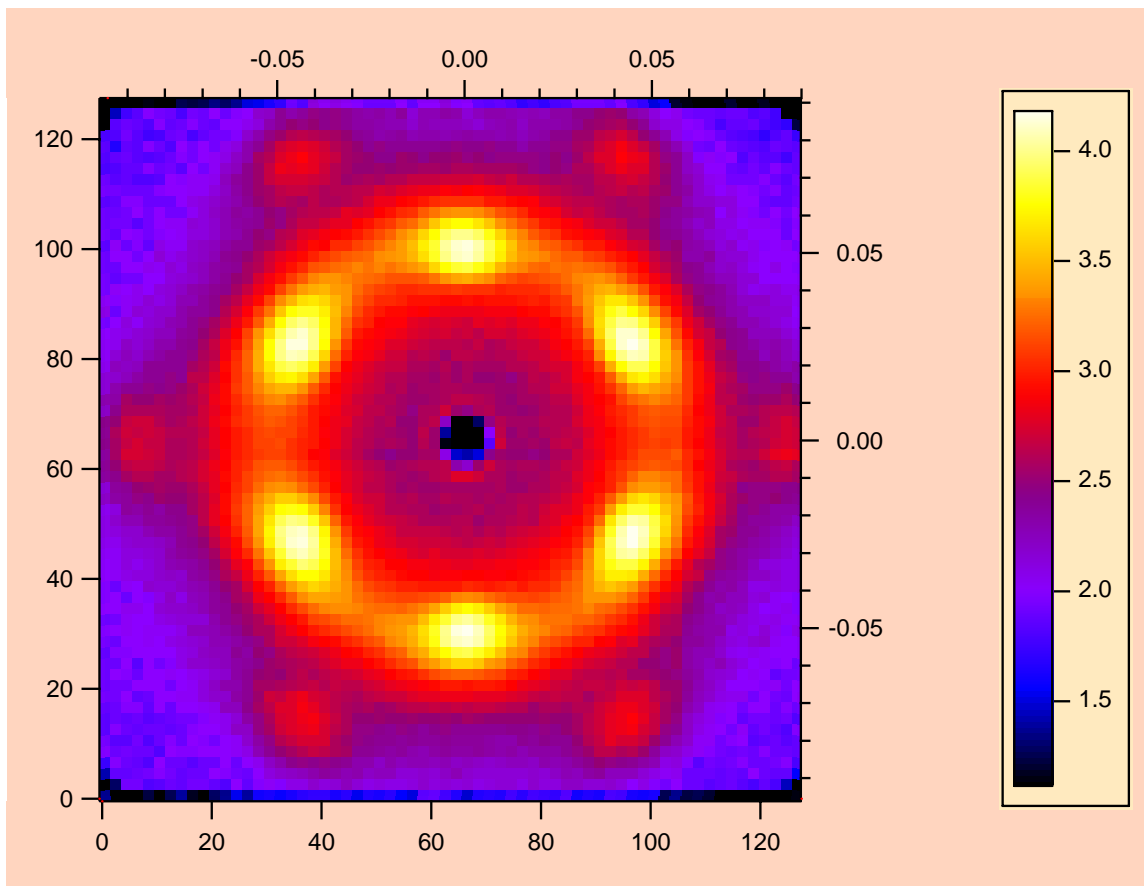
Figure 2: SANS data from 25 % P85 Pluronic (PEO-PPO-PEO triblock copolymer) in D2O under Couette shear (5 Hz frequency) at 40 $^{oC.}$ The micelles form a cubic "single crystal" structure.

3. MULTILAYER VESICLES

Multilayer vesicles are formed by mixing AOT surfactant with a brine/D2O solution. A brine solution contains more than 100 g/l sodium chloride salt. Shearing the multilayer vesicles in an in-situ Couette shear cell shows orientation along the shearing direction (i.e., horizontally). The sheared structure resembles a horizontally elongated "onion skin" structure. Two weaker spots along the equatorial axis show weak orientation of the vesicle layers parallel to the shearing cell walls as well. This SANS image was obtained with

oscillatory (i.e., reciprocating) shear and with the neutron beam incident tangentially to the shear cell through a vertical beam defining slit (Bergenholtz-Wagner, 1996).
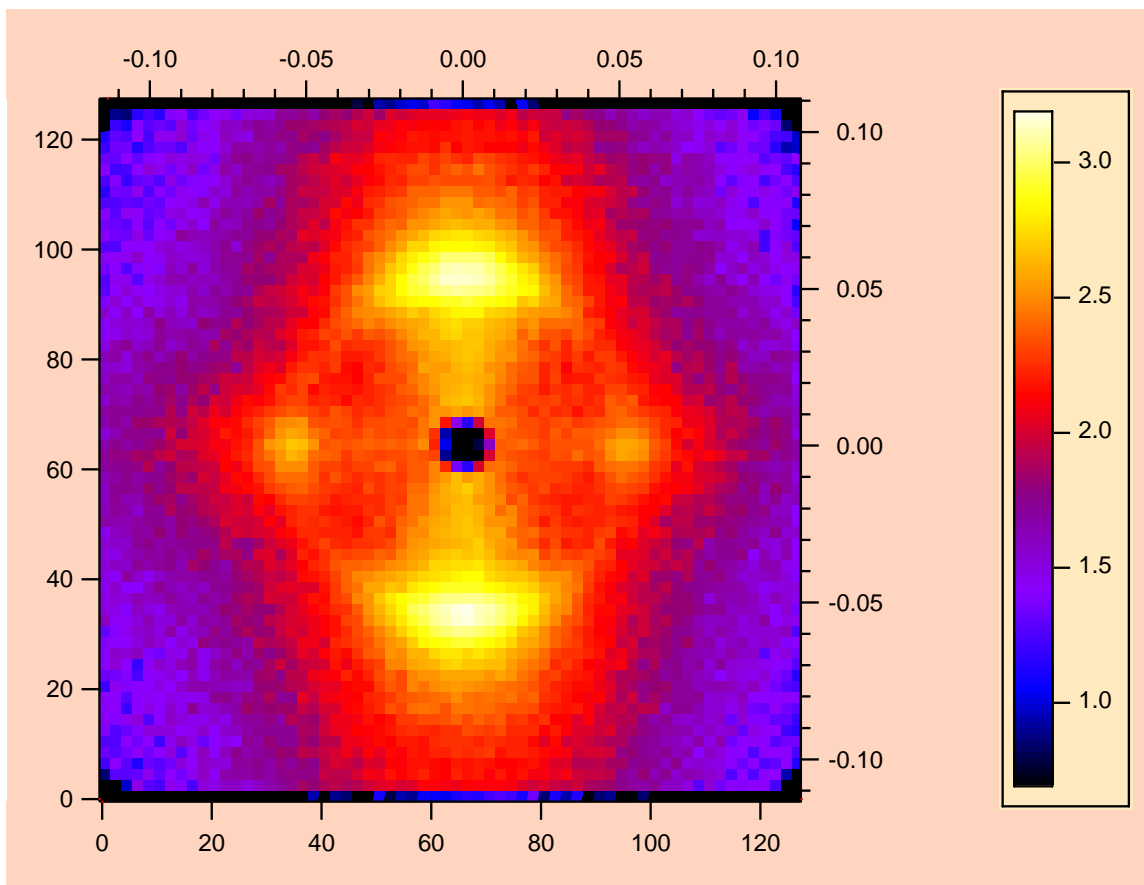
Figure 3: SANS data from multilayer vesicles formed of AOT in brine/d-water solution under oscillatory Couette shear. This view corresponds to a configuration where the neutron beam is incident tangentially to the shear cell.

4. ORIENTED MEMBRANE

Highly oriented samples containing supramolecular peptide assemblies imbedded in multilayer membranes have been investigated. Samples were prepared in the form of orientated multilayers that were held between several parallel quartz plates. Deuterated water fills the inter-layer space for enhanced neutron contrast. Peptides form inter-layer "pores" that can be clearly observed. Temperature and relative humidity were controlled during SANS data acquisition. Fully hydrated samples show no inter-layer correlation. Dehydrated samples show strong such correlation that shows up as rich anisotropy in the SANS pattern characteristic of "single crystal" structure. The shown data set was taken from magainin peptide in dimyristoyl phosphatidylcholine (DMPC) bilayers at the peptide-to-lipid ratio of 1 to 30. In order to sample both the in-plane and the out-of-plane structure, the oriented membrane was tilted with respect to the neutron beam (Yang et al, 1998).
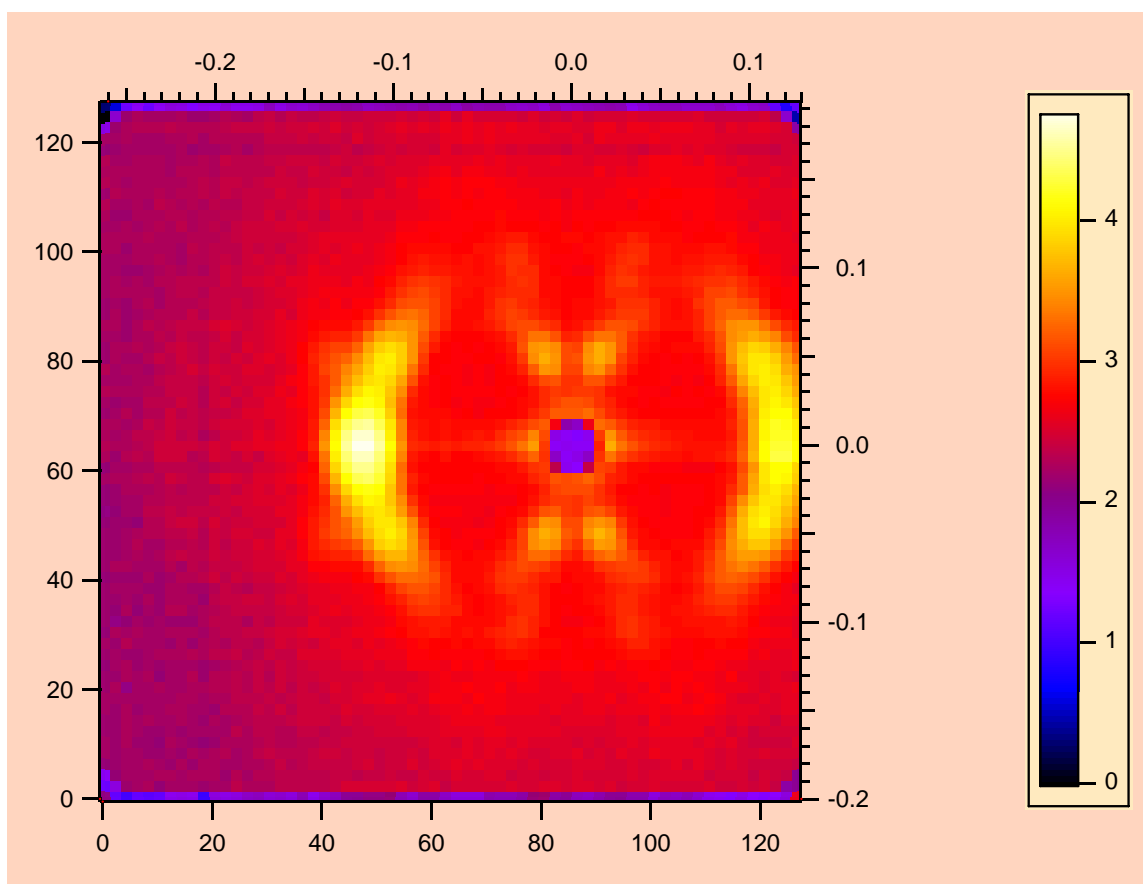
Figure 4: SANS data from oriented DMPC/DMPG membranes containing magainin peptides in DMPC bilayers and D2O. The sample was oriented at 60 ^{o} to the neutron beam in order to observe structures both parallel and perpendicular to the membrane surface.

5. MAGNETIC MATERIAL

SANS from a single-crystal of NdBa2Cu3O7 (high Tc superconductor) at 100 K is shown. Since this sample is twinned (i.e., is formed of two orthogonally orientation crystals), the nuclear scattering overwhelms the magnetic scattering. Crystal boundaries occur when two crystals intergrow with a highly symmetrical interface, often with one crystal being the mirror image of the other; atoms are shared by the two crystals at regular intervals. De-twinning of the crystal is necessary in order to reduce the nuclear scattering thereby enhancing the magnetic scattering component (Lynn et al, 1989).

244
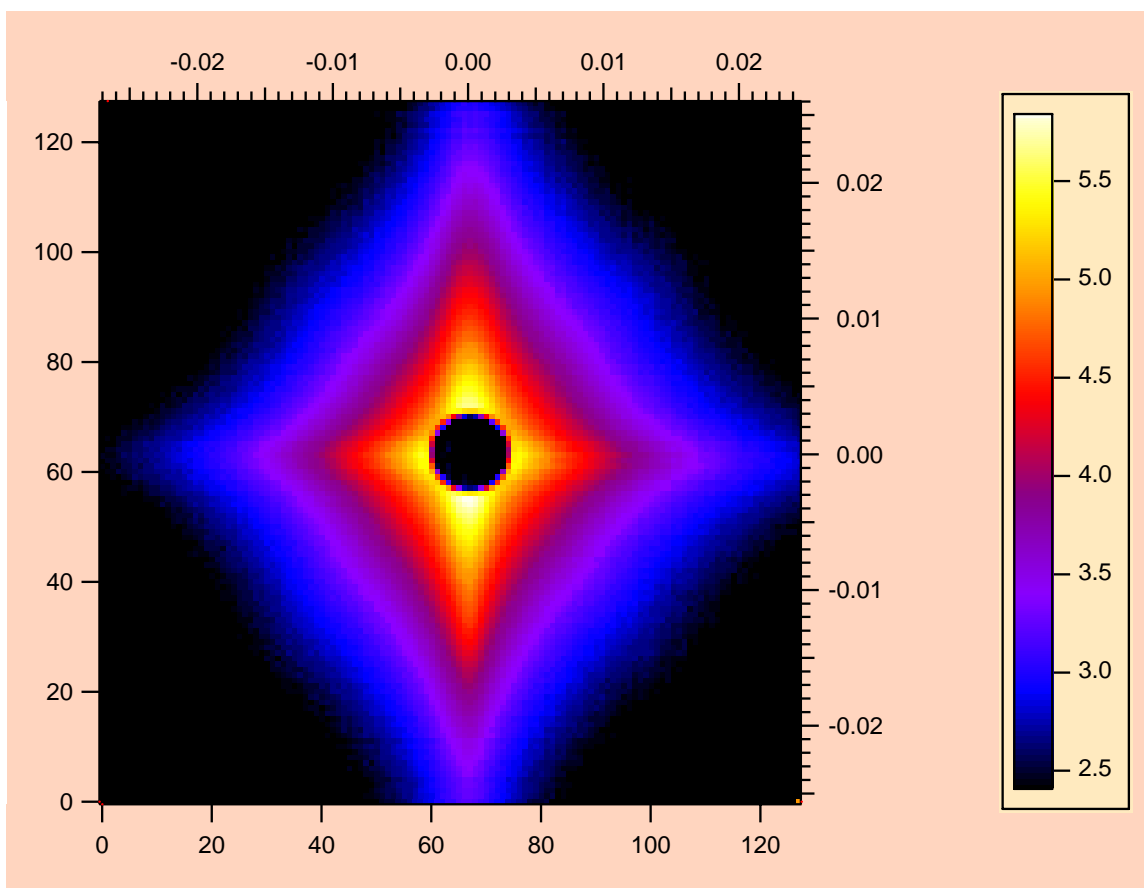
Figure 5: SANS data from the high Tc superconducting NdBa2Cu3O7 cuprate at 100 K. Most of the scattering is due to the nuclear structure. The oriented structures characterizing the two crystals forming the twinned crystal are orthogonal (i.e, have orthorhombic symmetry) yielding the cross-like SANS patterns.

REFERENCES

T. Slawecki, C. Glinka and B. Hammouda, "Shear-Induced Micellar Crystal Structures in an Aqueous Triblock Copolymer Solution", Phys Rev E 58, R4084-4086 (1998)

J Bergenholtz and N.J Wagner, "Formation of AOT/Brine Multilamellar Vesicles", Langmuir 12, 3122-3126 (1996)

L. Yang, T.A. Harroun, W.T. Heller, T.M. Weiss and H.W. Huang, "Neutron Off-Plane Scattering of Aligned Membranes, Method of Measurement", Biophysical Journal 75, 641-645 (1998).

J.W. Lynn, T.W. Clinton, W.H. Li, R.W. Erwin, J.Z. Liu, K. Vandervoort, R.N. Shelton and P. Klavins, "2D and 3D Magnetic Ordering of Er in ErBa2Cu3O7", Phys. Rev. Lett. 63, 2606-2609 (1989)

QUESTIONS

1. If a sample is oriented along the vertical direction, is the most likely axis of symmetry of the iso-intensity contour maps in the vertical or horizontal direction? Is this always the case? What is the exception?
2. When scattering contains bright peaks, why are peaks at high Q broader than peaks at low Q?
3. Thinks whether you could learn more about a sample of your research interests by aligning it (either though shear, rubbery stretch, or by applying a magnetic field).

ANSWERS

1. If a sample is oriented along the vertical direction, the most likely axis of symmetry of the iso-intensity contour maps is in the horizontal direction. The direct space and the reciprocal space are conjugate and therefore give orthogonal asymmetry. This applies in most cases. The known exception is the case of the "butterfly" pattern whereby the asymmetry in the scattering plane and the direct space plane are along the same direction.
2. Bright spots in the 2D SANS image are usually broader at high Q due to the increase of the instrumental resolution with Q. Recall that the variance of the resolution function has two contributions: (1) one due to geometry which is independent of Q and (2) one that varies like the square of the relative wavelength spread ($\tilde{\ }$)2 .
3. SANS data from aligned samples always contains more information than from randomly oriented samples. If the SANS image contains spots, the d-spacing in the two orthogonal directions could be different pointing to anisotropic structures. Bright spots turn into scattering rings when the sample orientation is random.

Part G – **SANS DATA MODELING**

Chapter 26 - **RADIUS OF GYRATION CALCULATIONS**

The radius of gyration is a measure of the size of an object of arbitrary shape. It can be obtained directly from the Guinier plot [ln(I(Q)] *vs* Q^2] for SANS data. The radius of gyration squared R_g^2 is the second moment in 3D.

1. SIMPLE SHAPES

First consider some simple shape objects.
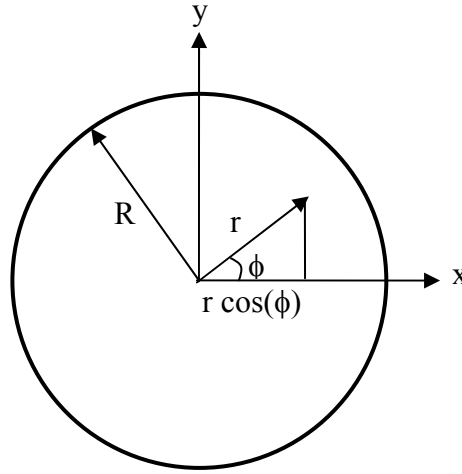
Figure 1: Representation of the polar coordinate system for a disk.

For an infinitely thin disk of radius R, R_g^2 is given by the following integral using polar coordinates.

$$R_{gx}^2 = \frac{\int\limits_0^{2\pi}\int\limits_0^{R_1} r^2\cos^2(\phi)rdrd\phi}{\int\limits_0^{2\pi}\int\limits_0^{R_1} rdrd\phi} = \frac{\int\limits_0^{R_1} r^3dr \int\limits_0^{2\pi}\cos^2(\phi)d\phi}{\int\limits_0^{R_1} rdr \int\limits_0^{2\pi} d\phi} = \frac{R^2}{4}. \qquad (1)$$

Similarly for $R_{gy}^2 = \dfrac{R^2}{4}$. For an infinitely thin disk $R_g^2 = R_{gx}^2 + R_{gy}^2 = \dfrac{R^2}{2}$.
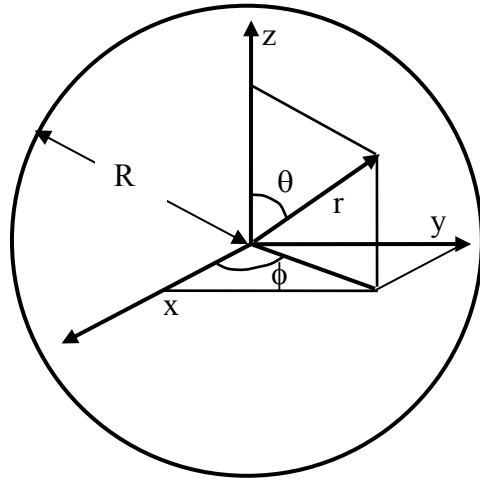
Figure 2: Representation of the spherical coordinate system for a sphere.

In the case of a full sphere, the integration is performed with spherical coordinates.

$$R_g^2 = \frac{\int\limits_0^\pi \sin(\theta)d\theta \int\limits_0^R r^2 dr \, r^2}{\int\limits_0^\pi \sin(\theta)d\theta \int\limits_0^R r^2 dr} = \frac{3R^2}{5}. \tag{2}$$

The radius of gyration (squared) for the spherical shell of radii R_1 and R_2 is given by:

$$R_g^2 = \frac{3}{4\pi(R_2^3 - R_1^3)} \int\limits_{R_1}^{R_2} 4\pi r^4 dr \tag{3}$$

$$= \frac{3}{5}\frac{(R_2^5 - R_1^5)}{(R_2^3 - R_1^3)}.$$
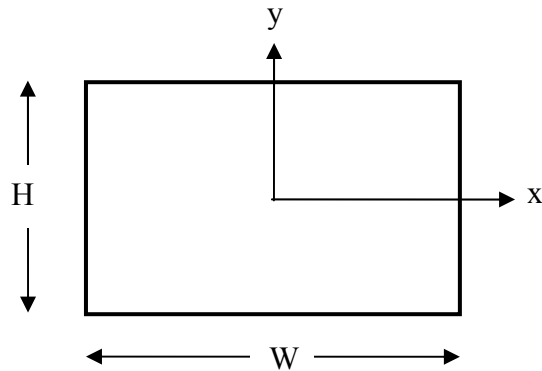
Figure 3: Representation of the Cartesian coordinate system for a rectangular plate.

For an infinitely thin rectangular object of sides W and H, the integration is performed in Cartesian coordinates.

$$R_{gx}^2 = \frac{\int_{-W/2}^{W/2} dx\, x^2}{\int_{-W/2}^{W/2} dx} = \frac{1}{3}\left(\frac{W}{2}\right)^2. \tag{4}$$

Similarly for $R_{gy}^2 = \frac{1}{3}\left(\frac{H}{2}\right)^2$. The sum gives $R_g^2 = \frac{1}{3}\left[\left(\frac{W}{2}\right)^2 + \left(\frac{H}{2}\right)^2\right]$.

Note that the moment of inertia I for a plate of width W, height H and mass M is also given by the second moment.

$$I = I_{xx} + I_{yy} = \frac{M}{3}\left[\left(\frac{W}{2}\right)^2 + \left(\frac{H}{2}\right)^2\right]. \tag{5}$$

2. CIRCULAR ROD AND RECTANGULAR BEAM

Circular Rod
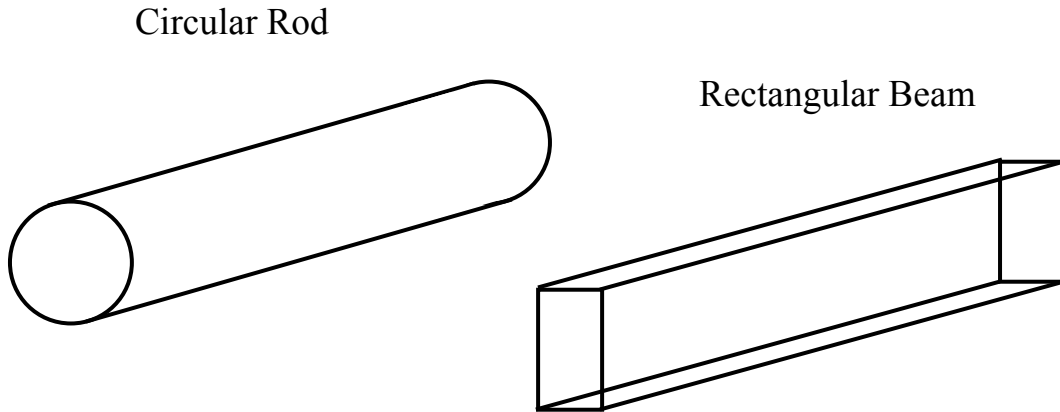
Rectangular Beam

Figure 4: Representation of the cylindrical rod and rectangular beam.

The radius of gyration for a cylindrical rod of length L and radius R is given by:

$$R_g^2 = \frac{R^2}{2} + \frac{1}{3}\left(\frac{L}{2}\right)^2 = \frac{R^2}{2} + \frac{L^2}{12}. \tag{6}$$

The radius of gyration for a rectangular beam of width W, height H and length L is given by:

$$R_g^2 = \frac{1}{3}\left[\left(\frac{W}{2}\right)^2 + \left(\frac{H}{2}\right)^2 + \left(\frac{L}{2}\right)^2\right].$$ (7)

This formula holds for a straight "ribbon" where W<H<<L.

The value of R_g^2 for a cylindrical rod with radius R = 10 (diameter D = 20) and length L = 10 is R_g^2 = 58.3. This value is to be compared with the case of a rectangular beam with sides W = L = 20 and length L = 10 for which R_g^2 = 75.

3. COMMENTS

The radius of gyration squared can be calculated for other more complicated shapes as the second moment for each of the symmetry direction.

Note that R_{gx}^2 for a horizontal strip is the same as that for the whole square plate $R_{gx}^2 = \frac{1}{3}\left(\frac{W}{2}\right)^2$. R_{gx}^2 is independent of the height of the object. Of course R_{gy}^2 depends of the height but not on the width.
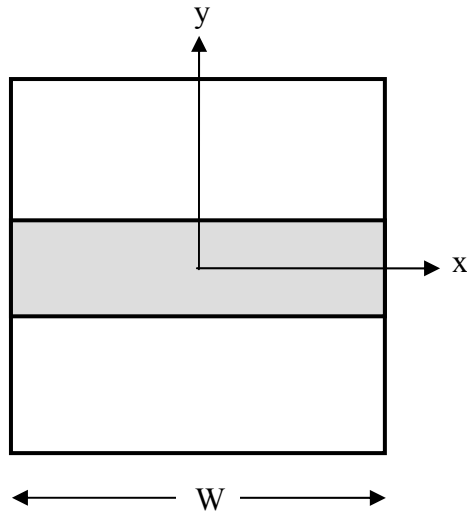
Figure 5: Case of a horizontal flat strip.
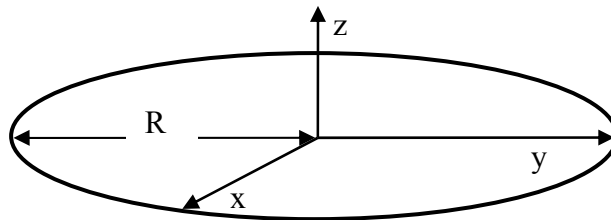
Figure 6: Case of a circular ring.

The radius of gyration for an infinitely thin circular ring of radius R is $R_{gz}^2 = R^2$. This is obtained by spinning the ring in the horizontal plane (around the z-axis). Note that it is the same value for an infinitely thin spherical shell of radius R.

4. TWISTED RIBBON

The radius of gyration for rigid twisted shape objects are worked out here. Consider the simple case of a rigid helical wire, then the case of a rigid twisted ribbon with finite size thickness.

Helical Wire

Consider a very thin helically twisted wire aligned along the vertical z axis. Choose the origin of the Cartesian coordinate system at the center-of mass of the twisted wire. The helix has a radius R and a height L so that $-L/2 \leq z \leq L/2$. The parametric equation of the helix is:

$$X = R \cos(\phi) \quad\quad\quad\quad\quad\quad (8)$$
$$Y = R \sin(\phi)$$
$$Z = p\phi/2\pi.$$

Where p is the helix pitch and ϕ is the azimuthal angle in the horizontal plane. The wire position along the helix is represented by the vector $\vec{r}(\phi)$. Note that by definition of the center-of-mass, the average of this vector is null, $<\vec{r}(\phi)> = 0$.
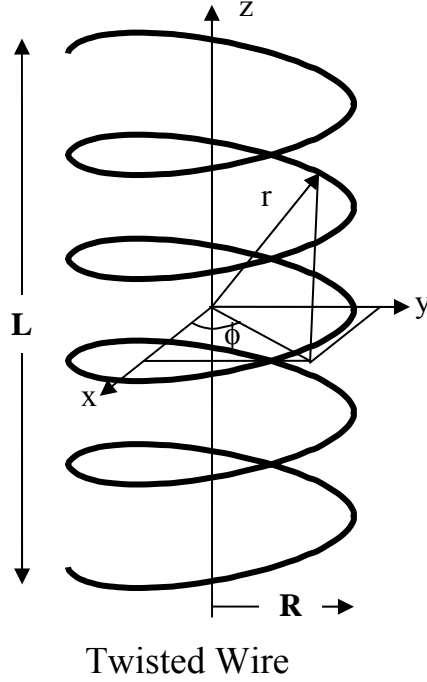
Twisted Wire

Figure 7: Schematic representation of the twisted wire.

The radius of gyration (squared) $R_g{}^2$ is defined as follows:

$$R_g{}^2 = <r^2(\phi)> = \frac{\int d\phi \, r^2(\phi)}{\int d\phi} \, .$$

(9)

Here $r^2(\phi) = X^2 + Y^2 + Z^2 = R^2 + (p\phi/2\pi)^2$. The azimuthal angle ϕ varies in the range: $-\pi L/p \leq \phi \leq \pi L/p$.

The ϕ integration is readily performed to give:

$$R_g{}^2 = R^2 + \frac{1}{3}\left(\frac{L}{2}\right)^2 .$$

(10)

Note that this is the same result as for a cylindrical shell of radius R and height L. This is not surprising since a cylinder could be built by a number of twisted wires stacked vertically.

Thin Twisted Ribbon

The case of a thin twisted helical ribbon of width W can be worked out similarly using a two-variable parametric notation $r^2(\phi,z)$ where ϕ is the azimuthal angle and z is the vertical ribbon width with $-W/2 \leq z \leq W/2$.
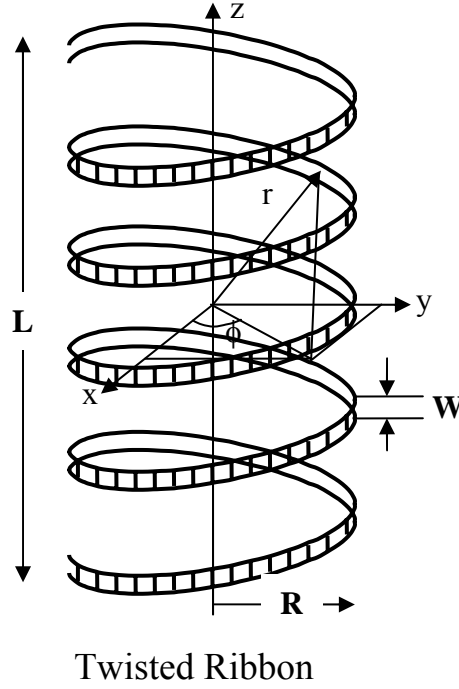
Twisted Ribbon

Figure 8: Schematic representation of the thin twisted ribbon.

Here, the variable Z is replaced by Z+z. The radius of gyration (squared) is therefore given by:

$$R_g^2 = <r^2(\phi,z)> = \frac{\int d\phi \int dz\, r^2(\phi,z)}{\int d\phi \int dz} \qquad (11)$$

$r^2(\phi,z)$ is now given by $r^2(\phi,z) = R^2 + \left(\dfrac{p\phi}{2\pi} + z\right)^2$. The integrations can here also be readily performed to give:

$$R_g^2 = R^2 + \frac{1}{3}\left(\frac{L}{2}\right)^2 + \frac{1}{3}\left(\frac{W}{2}\right)^2. \qquad (12)$$

These involve contributions from $<Z^2>$ and $<z^2>$. The cross term gives no contribution because it involves the null average $<z> = 0$.

Thick Twisted Ribbon

For the case of a twisted ribbon of horizontal thickness T, the variable R is replaced by R+ρ where $-T/2 \leq \rho \leq T$.

255
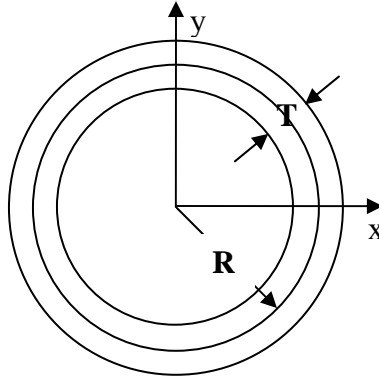
Thick Twisted Ribbon
Top View

Figure 9: Top view of a thick twisted ribbon.

The calculation of the second moment proceeds as before:

$$X = \rho \cos(\phi) \qquad (13)$$
$$Y = \rho \sin(\phi)$$
$$Z = p\phi/2\pi.$$

Here ρ is the polar coordinate variable in the horizontal plane with limits: $R-T/2 \le \rho \le R+T/2$. In this case $r^2(Z,z,\rho) = \rho^2 + (Z+z)^2$ where z is the same parameter as before. $R_g^2 = <\rho^2> + <(Z+z)^2>$ involves two averages. The first average is:

$$<\rho^2> = \frac{\int_0^{2\pi} d\phi \int_{R-T/2}^{R+T/2} \rho d\rho\, \rho^2}{\int_0^{2\pi} d\phi \int_{R-T/2}^{R+T/2} \rho d\rho} = \frac{\frac{1}{4}\left[\left(R+\frac{T}{2}\right)^4 - \left(R-\frac{T}{2}\right)^4\right]}{\frac{1}{2}\left[\left(R+\frac{T}{2}\right)^2 - \left(R-\frac{T}{2}\right)^2\right]} = R^2 + \left(\frac{T}{2}\right)^2.$$

$$(14)$$

The final result involving both (horizontal and vertical) averages is:

$$R_g^2 = R^2 + \left(\frac{T}{2}\right)^2 + \frac{1}{3}\left(\frac{L}{2}\right)^2 + \frac{1}{3}\left(\frac{W}{2}\right)^2. \qquad (15)$$

Note that all terms add up in quadrature since all cross terms (first moments) average to zero.

5. GAUSSIAN POLYMER COIL

The radius of gyration (squared) for a polymer coil is defined as:

$$R_g^2 = \frac{1}{n}\sum_i^n <S_i^2>. \tag{16}$$

S_i refers to the position of monomer i with respect to the center-of-mass of the polymer coil and n is the total number of monomers per coil. The inter-distance vector between two monomers within the same macromolecule is defined as $\vec{S}_{ij} = \vec{S}_i - \vec{S}_j$. Consider the following relation:

$$\sum_{i,j}^n \vec{S}_{ij}^2 = n\sum_i^n \vec{S}_i^2 + n\sum_j^n \vec{S}_j^2 - 2\sum_{i,j}^n \vec{S}_i.\vec{S}_j. \tag{17}$$

The last summation is null $\sum_{i,j}^n \vec{S}_i.\vec{S}_j = \sum_i^n \vec{S}_i.\sum_j^n \vec{S}_j = 0$ since by definition of the center-of-

mass $\sum_i^n \vec{S}_i = 0$. The radius of gyration (squared) is therefore simplified as:

$$R_g^2 = \frac{1}{2n^2}\sum_{i,j}^n <S_{ij}^2> = \frac{1}{2n^2}\sum_{i,j}^n <r_{ij}^2>. \tag{18}$$

The vectorial notation has been dropped for simplicity.
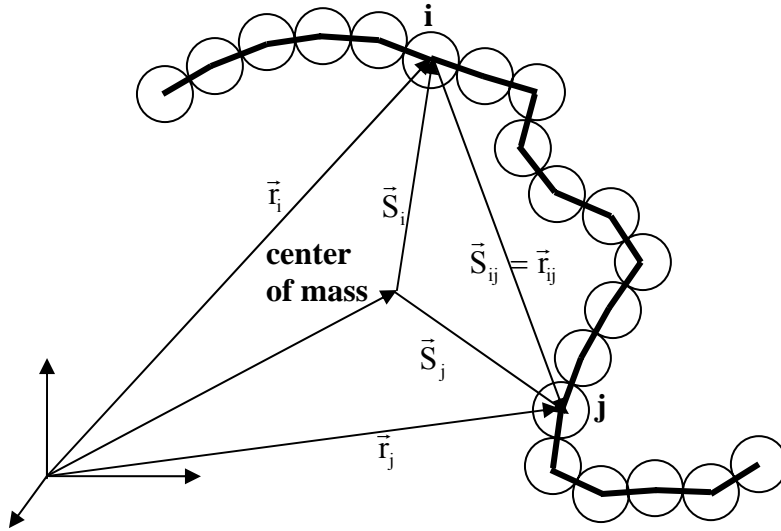
Figure 10: Schematic representation of a Gaussian coil showing monomers i and j and their inter-distance r_{ij}. Note that $\vec{S}_{ij} = \vec{r}_{ij}$ in the notation used.

$$<S_{ij}^2> = a^2|i\text{-}j|. \tag{19}$$

Here a is the statistical segment length, and $<...>$ is an average over monomers. The following formulae for the summation of arithmetic progressions are used:

$$\sum_{k=1}^{n} k = \frac{n(n+1)}{2} \tag{20}$$

$$\sum_{k=1}^{n} k^2 = \frac{n(n+1)(2n+1)}{6}.$$

The radius of gyration squared becomes:

$$R_g^{\,2} = \frac{a^2}{2n^2} \sum_{i,j}^{n} |i-j| = \frac{a^2}{n} \sum_{k}^{n} (1-\frac{k}{n})k \tag{21}$$

$$= \frac{a^2}{6} \frac{(n^2-1)}{n} \cong \frac{a^2 n}{6} \quad \text{for } n \gg 1.$$

Note that taking the $n \gg 1$ limit early on allows us to replace the summations by integrations. Using the variable $x = k/n$, one obtains:

$$R_g^{\,2} = a^2 n \int_0^1 dx (1-x)x = a^2 n \left(\frac{1}{2} - \frac{1}{3} \right) = \frac{a^2 n}{6}. \tag{22}$$

Similarly, the end-to-end distance squared $R_{1n}^{\,2}$ for a Gaussian polymer coil is given by:

$$R_{1n}^{\,2} = a^2 n \quad \text{for } n \gg 1. \tag{23}$$

These results are for Gaussian coils that follow random walk statistics (Flory, 1969).

6. THE EXCLUDED VOLUME PARAMETER APPROACH

The Flory mean field theory of polymer solutions describes chain statistics as a random walk process along chain segments. For Gaussian chain statistics, the monomer-monomer inter-distance is proportional to the number of steps:

$$<S_{ij}^{\,2}> = a^2 |i\text{-}j|^{2v}. \tag{24}$$

Here a is the statistical segment length, v is the excluded volume parameter, S_{ij} represents an inter-segment distance and $<\ldots>$ is an average over monomers. The radius of gyration squared for Gaussian chains is expressed as:

$$R_g^{\,2} = \frac{1}{2n^2} \sum_{i,j}^{n} <S_{ij}^{\,2}> = \frac{a^2}{2n^2} \sum_{i,j}^{n} |i-j|^{2v} \tag{25}$$

$$= \frac{a^2}{n} \sum_{k}^{n} (1-\frac{k}{n}) k^{2v} = \frac{a^2}{(2v+1)(2v+2)} n^{2v}.$$

i and j are a pair of monomers and n is the number of chain segments per chain. Three cases are relevant:

(1) Self-avoiding walk corresponds to swollen chains with $\nu = 3/5$, for which $R_g^2 = \frac{25}{176} a^2 n^{6/5}$.

(2) Pure random walk corresponds to chains in theta conditions (where solvent-solvent, monomer-monomer and solvent-monomer interactions are equivalent) with $\nu = \frac{1}{2}$, for which $R_g^2 = \frac{1}{6} a^2 n$.

(3) Self attracting walk corresponds to collapsed chains with $\nu = 1/3$, for which $R_g^2 = \frac{9}{40} a^2 n^{2/3}$.

Note that the renormalization group estimate of the excluded volume parameter for the fully swollen chain is $\nu = 0.588$ (instead of the 0.6 mean field value).

Note also that the radius of gyration for a thin rigid rod can be recovered from this excluded volume approach by setting $\nu = 1$ and defining the rod length as $L = na$.

$$R_g^2 = \frac{a^2}{(2\nu+1)(2\nu+2)} n^{2\nu} = \frac{a^2 n^2}{12} = \frac{L^2}{12}. \qquad (26)$$

This is the same result derived earlier for a thin rod.

REFERENCES

http://en.wikipedia.org/wiki/List_of_moments_of_inertia

P.J. Flory, "Statistical Mechanics of Chain Molecules", Interscience Publishers (1969)

QUESTIONS

1. How is the radius of gyration measured by SANS?
2. How is the center-of-mass of an object defined?
3. Why is the radius of gyration squared for an object related to the moment of inertia for that object?
4. Calculate R_g^2 for a full sphere of radius R. Calculate R_g^2 for a thin spherical shell of radius R.
5. What is the value of R_g^2 for a Gaussian coil of segment length a and degree of polymerization n? How about the end-to-end distance?
6. What is the radius of gyration squared for a rod of length L and radius R?

ANSWERS

1. The radius of gyration is measured by performing a Guinier plot on SANS data. The slope of the linear variation of $\ln[I(Q)]$ *vs* Q^2 is $R_g^2/3$.

2. The center-of-mass of an object is defined as the spot where the first moment is zero.

3. The radius of gyration squared and the moment of inertia for that object are both expressed in terms of the second moment.

4. R_g^2 for a full sphere of radius R is given by:

$$R_g^2 = \left(\int_0^\pi \sin(\theta)d\theta \int_0^R r^2 dr r^2\right) / \left(\int_0^\pi \sin(\theta)d\theta \int_0^R r^2 dr\right) = \frac{3R^2}{5}. \quad R_g^2 \text{ for a thin spherical shell is simply}$$

given by: $R_g^2 = R^2$.

5. For a Gaussian coil of segment length a and degree of polymerization n, one can calculate the radius of gyration squared as $R_g^2 = a^2 n / 6$ and the end-to-end distance squared as $R_{1n}^2 = a^2 n$.

6. The radius of gyration squared for a rod of length L and radius R is given by:

$$R_g^2 = R^2 + \frac{1}{3}\left(\frac{L}{2}\right)^2.$$

Chapter 27 – SINGLE PARTICLE FORM FACTORS

1. DEFINITION OF SCATTERING FACTORS

Consider a scattering object consisting of n scatterers occupying a volume V. The scattering density and its Fourier transform are defined as:

$$n(r) = \sum_{i=1}^{n} \delta(\vec{r} - \vec{r}_i) \tag{1}$$

$$n(Q) = \sum_{i=1}^{n} \exp[i\vec{Q}.\vec{r}_i].$$

Note that these quantities vary randomly with position $\vec{r}$ and scattering vector $\vec{Q}$. The average density being constant ($<n(r)> = \bar{n} = n/V$), a fluctuating density and its Fourier transform are defined as:

$$\Delta n(r) = \sum_{i}^{n} \delta(\vec{r} - \vec{r}_i) - \bar{n} \tag{2}$$

$$\Delta n(Q) = \sum_{i}^{n} \exp[i\vec{Q}.\vec{r}_i] - (2\pi)^3 \bar{n}\delta(\vec{Q}).$$

Here $\delta(\vec{Q})$ is the Dirac Delta function which does not contribute except at $\vec{Q} = \vec{0}$ (along the very forward scattering direction) which is experimentally irrelevant. The static form factor for the scattering "particles" is defined as the density-density correlation function summed up (or integrated) over the particle volume:

$$P(Q) = \frac{<n(-Q)n(Q)>}{n^2} = \frac{1}{n^2} \sum_{i,j}^{n} < \exp[i\vec{Q}.(\vec{r}_i - \vec{r}_j)] > \tag{3}$$

$$= \int dr \int dr' \frac{<n(r)n(r')>}{n^2} \exp[i\vec{Q}.(\vec{r} - \vec{r}')].$$

The form factor of various shape objects are worked out next (Guinier-Fournet, 1955; Glatter-Kratky, 1982; Hammouda, 1995; Higgins-Benoit, 1994; Roe, 2000).

2. FORM FACTOR FOR A UNIFORM SPHERE

Consider a sphere of radius R and uniform density (this could be a spherical domain in a microphase separated block copolymer or a latex particle in a colloidal suspension). The single particle form factor P(Q) involves integrations over the volume V of the sphere (in spherical coordinates):

$$P(Q) = \frac{< n(-Q)n(Q) >}{n^2} = \int dr \int dr' \frac{< n(r)n(r') >}{n^2} \exp[i\vec{Q}.(\vec{r} - \vec{r}')]. \quad (4)$$

Since the scattering elements are not correlated, the average of the product $<n(r)n(r')>$ is equal to the product of the averages $<n(r)><n(r')>$ and therefore:

$$P(Q) = | F(Q) |^2. \quad (5)$$

Here the amplitude of the form factor $F(Q)$ has been defined as:

$$F(Q) = \int dr \frac{< n(r) >}{n} \exp[-i\vec{Q}.\vec{r}]. \quad (6)$$

For uniform density, the average over configurations $<n(r)>$ becomes trivial:

$$< n(r) >= \frac{n}{V} = \bar{n} \qquad \text{if } r \leq R \qquad (7)$$
$$< n(r) >= 0. \qquad \text{if } r > R$$

Therefore:

$$F(Q) = \frac{3}{4\pi R^3} \int_0^R r^2 dr \int_{-1}^1 d\mu \exp[iQr\mu] \int_0^{2\pi} d\phi \quad (8)$$

$$= \frac{3}{R^3} \int_0^R r^2 dr \frac{\sin(Qr)}{Qr} = \frac{3j_1(QR)}{QR}. \quad (9)$$

Here the spherical Bessel function $j_1(x)$ has been defined as:

$$j_1(x) = \frac{\sin(x)}{x^2} - \frac{\cos(x)}{x} = \sqrt{\frac{\pi}{2x}} J_{3/2}(x). \quad (10)$$

The spherical Bessel function $j_1(x)$ is related to the cylindrical Bessel function $J_{3/2}(x)$ as shown. It is also related to $j_0(x)$ as follows:

$$j_1(x) = -\frac{d}{dx}[j_0(x)] \text{ and } j_0(x) = \frac{\sin(x)}{x}. \quad (11)$$

The form factor for the sphere is therefore:

$$P(Q) = \left[\frac{3j_1(QR)}{QR} \right]^2 = \left[\frac{3}{QR} \left(\frac{\sin(QR)}{(QR)^2} - \frac{\cos(QR)}{QR} \right) \right]^2. \quad (12)$$

Note the following normalization $P(Q \to 0) = 1$ and recall the calculation of the radius of gyration squared for a uniform density sphere of radius R as $R_g^2 = 3R^2/5$.

The low-Q Guinier expansion follows:

$$P(Q) \to \left[1 - \frac{(QR)^2}{10} + \frac{(QR)^4}{280} \right]^2 \cong 1 - \frac{Q^2 R^2}{5} + \frac{3}{175}(QR)^4 \quad (13)$$

$$= 1 - \frac{Q^2 R_g^2}{3} + \frac{Q^4 R_g^4}{21} \qquad \text{for } Q^2 R_g^2 < 1$$
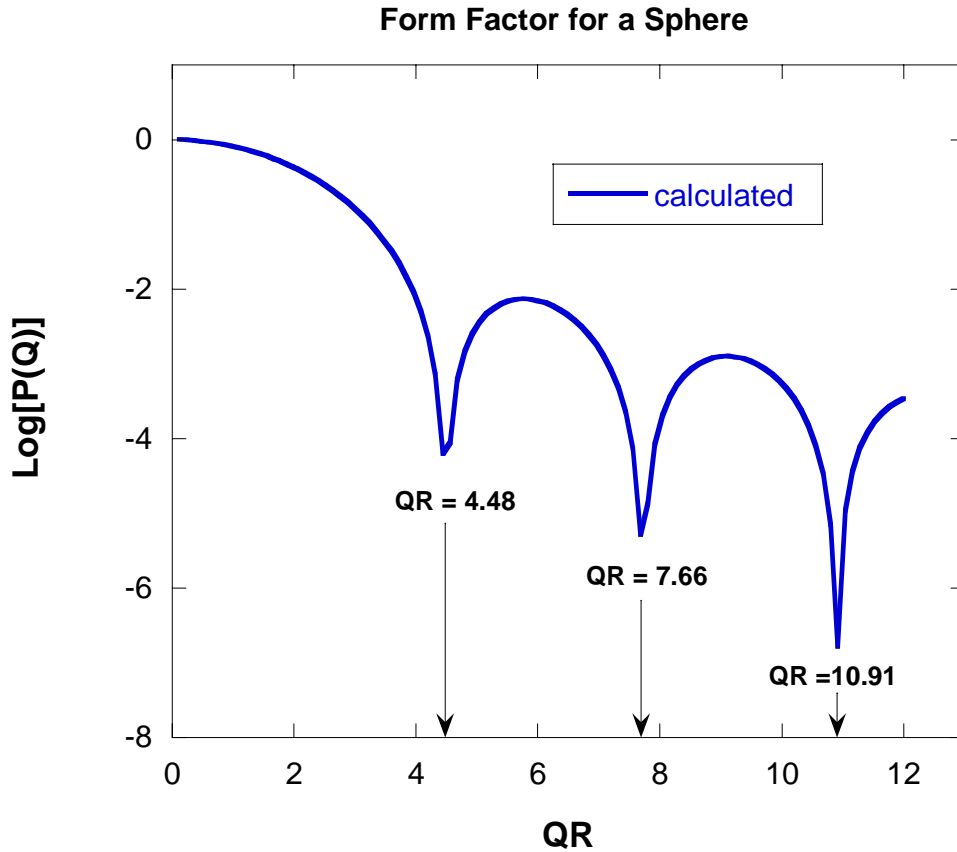
Figure 1: Plot of Log[P(Q)] *vs* QR for a uniform sphere showing many order oscillations.

3. SPHERICAL CORE-SHELL

Consider a sphere with an inner core and an outer shell. Three regions can be defined corresponding to the inner core, the outer shell and the solvent. Three cases are considered where (1) the shell is visible (with matched core and solvent scattering lengths), (2) the core and shell scattering length densities are matched and (3) the core is visible (with matched shell and solvent scattering length densities).

Note that the "correlation hole" peak is enhanced in case 1 for which the shell is visible whereas the core is not (i.e., it is matched to the solvent). Polydispersity ($\sigma/R = 0.3$) has been included in order to damp higher order oscillations. This level of polydispersity was enough to damp oscillations for case 3 but not enough for case 2.
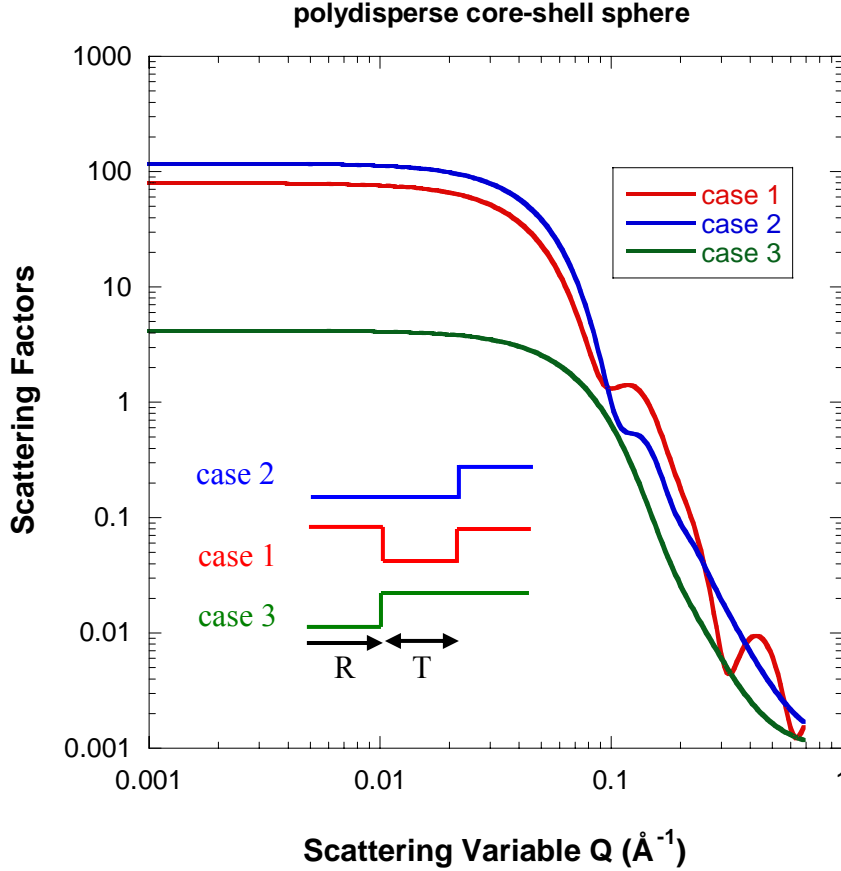
Figure 2: Scattering factors for a core-shell sphere of inner radius $R = 20$ Å and radial shell thickness $T = 20$ Å. Case 1 corresponds to the core scattering length density matched to the solvent. Case 2 corresponds to matched scattering length densities for the core and shell. Case 3 corresponds to the shell scattering length density matched to the solvent. The vertical scale is arbitrary and a constant background value of 0.001 has been added.

4. FORM FACTORS FOR OTHER SPHEROID SHAPES

Following the same procedure, the form factor for a spherical shell between radii R_1 and R_2 (and hollow for $r<R_1$) can be calculated as follows:

$$F(Q) = \frac{3}{4\pi(R_2^{\ 3} - R_1^{\ 3})} \int_{R_1}^{R_2} r^2 dr \int_{-1}^{+1} d\mu \exp[iQr\mu] \int_0^{2\pi} d\phi \qquad (14)$$

264

$$= \frac{1}{(R_2{}^3 - R_1{}^3)} \left[\left(\frac{3 j_1(QR_2)}{QR_2} \right) R_2{}^3 - \left(\frac{3 j_1(QR_1)}{QR_1} \right) R_1{}^3 \right].$$

For an ellipsoid of half axes a, b, c oriented so that its axes make angles α, β, θ with the $\vec{Q}$ direction, an effective radius R_e is defined as:

$$R_e{}^2 = a^2 \cos^2(\alpha) + b^2 \cos^2(\beta) + c^2 \cos^2(\theta). \tag{15}$$

The form factor amplitude is the same as the one for a sphere of radius R_e:

$$F(Q,\mu) = \frac{3 j_1(QR_e)}{QR_e}. \tag{16}$$

The form factor (for a randomly oriented sample) is an average over all possible orientations of the ellipsoid.:

$$P(Q) = \frac{1}{2} \int_{-1}^{+1} d\mu \, | F(Q,\mu) |^2 . \tag{17}$$

$\mu = \cos(\theta)$ and θ is the angle between the major axis of the ellipsoid and the $\vec{Q}$ direction. It is straightforward to extend these results to an ellipsoidal shell.

5. FORM FACTORS FOR CYLINDRICAL SHAPES

The form factor amplitude F(Q) for a uniform cylinder (rod) of radius R and length L oriented at an angle γ from the $\vec{Q}$ direction is the product of a longitudinal (z along the rod) and a transverse ($\perp$ perpendicular to the rod) contributions in cylindrical coordinates:

$$F(Q,\mu) = F_z(Q,\mu) F_\perp(Q,\mu) \tag{18}$$

$$F_z(Q,\mu) = \frac{1}{L} \int_{-L/2}^{L/2} dz \exp[iQ\mu z] = \frac{\sin(Q\mu L/2)}{Q\mu L/2}$$

$$F_\perp(Q,\mu) = \frac{1}{\pi R^2} \int_0^R d\rho\rho \int_0^{2\pi} d\phi \exp[iQ\sqrt{1-\mu^2} \cos(\phi)\rho].$$

Here $\mu = \cos(\theta)$ and θ is the inclination angle. The following definition of the cylindrical Bessel function is used:

$$J_0(z) = \frac{1}{\pi} \int_0^\pi d\phi \, \exp[iz \cos(\phi)].$$ (19)

One obtains:

$$F_\perp(Q,\mu) = \frac{2}{R^2} \int_0^R d\rho \rho J_0(Q\sqrt{1-\mu^2}\rho).$$ (20)

An integration variable change to $t = \rho/R$ is made and the following integral is used:

$$\int_0^1 t \, dt J_0(at) = \frac{1}{a} J_1(a).$$ (21)

The following result is obtained:

$$F_\perp(Q,\mu) = \frac{2J_1(Q\sqrt{1-\mu^2}R)}{Q\sqrt{1-\mu^2}R}.$$ (22)

The final result for the form factor amplitude for an oriented rod is:

$$F(Q,\mu) = \left[\frac{\sin(Q\mu L/2)}{Q\mu L/2}\right]\left[\frac{2J_1(Q\sqrt{1-\mu^2}R)}{Q\sqrt{1-\mu^2}R}\right].$$ (23)

The form factor for a randomly oriented rod is therefore given by the following orientation average:

$$P(Q) = \frac{1}{2} \int_{-1}^1 d\mu \, | F(Q,\mu) |^2.$$ (24)

In order to model the scattering from very dilute solutions of rods, the last integral (over θ) is performed numerically.
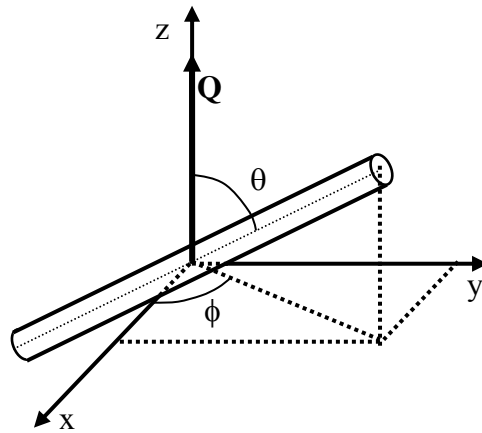
Figure 3: Geometry of the uniform rod.
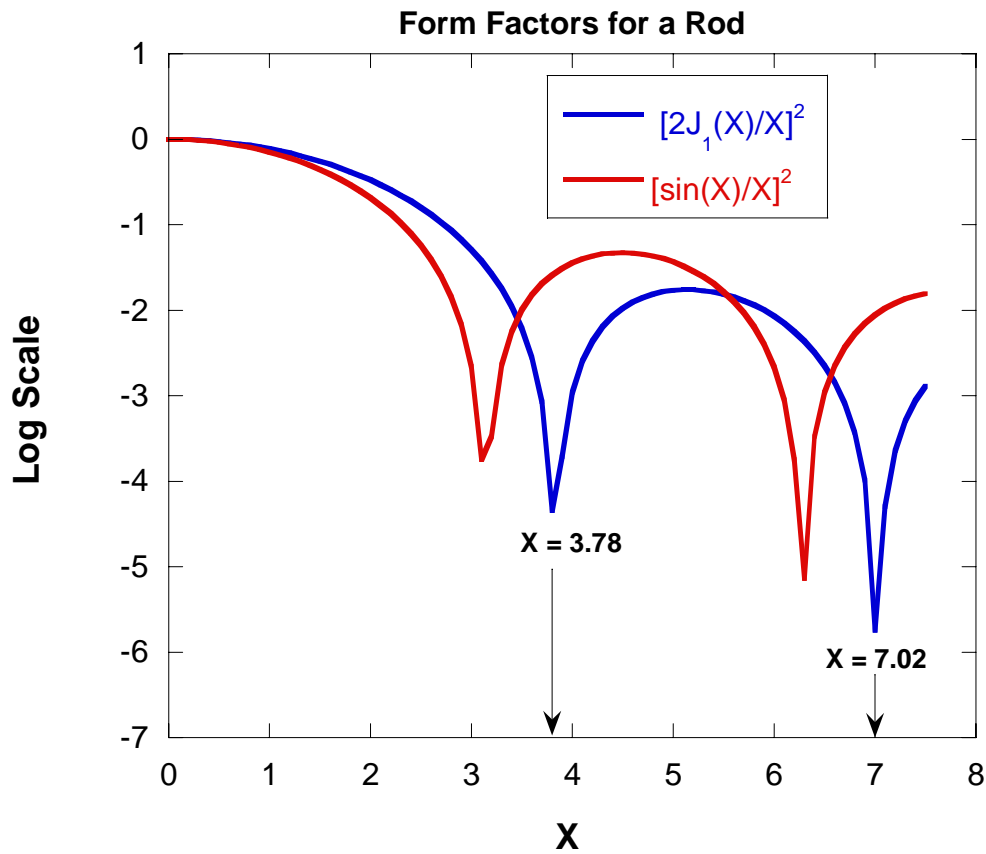
Figure 4: Plots of the two functions $[2J_1(X)/X]^2$ and $[\sin(X)/X]^2$ that give the variations of the form factor perpendicular and parallel to the rod axis respectively.

Cylinder with R = 20 Å, L = 400 Å
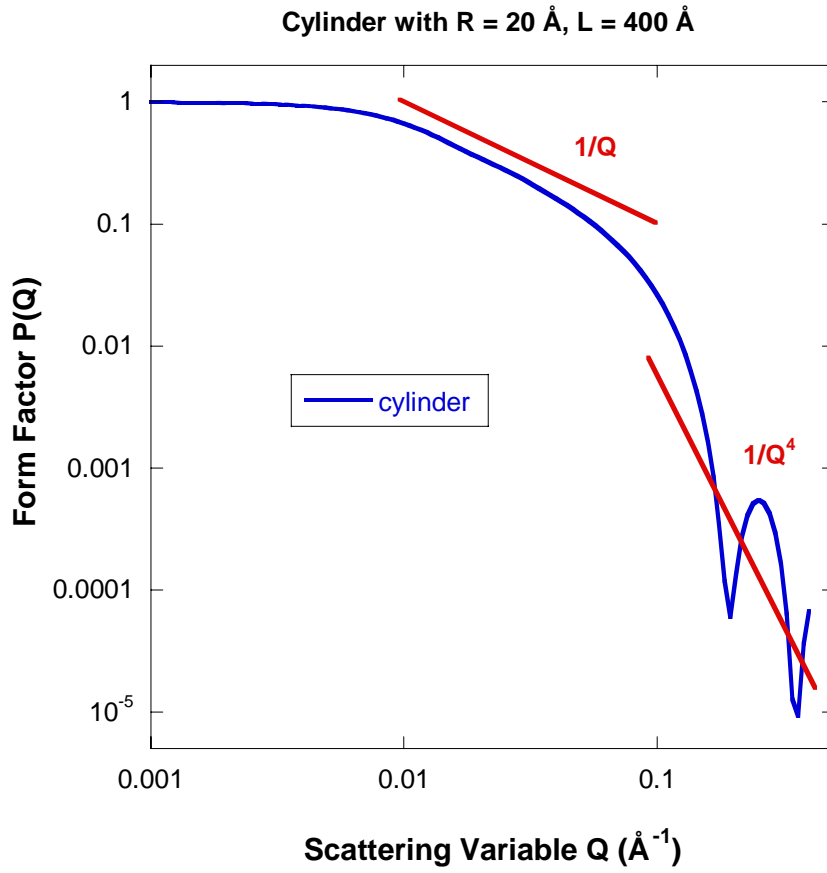
Figure 5: Form factor P(Q) for a cylinder with radius R = 20 Å and length L = 400 Å.

Note that the result for a disk of thickness L applies also to a randomly oriented rod of length L.

For a disk of radius R and negligible thickness, the $L \rightarrow 0$ limit in the general result is taken so that:

$$F_\perp(Q,\mu) = \frac{1}{\pi R^2} \int_0^R d\rho\,\rho \int_0^{2\pi} d\phi \exp[iQ\sqrt{1-\mu^2}\cos(\phi)\rho] \qquad (25)$$

$$= \frac{2J_1(Q\sqrt{1-\mu^2}R)}{Q\sqrt{1-\mu^2}R}.$$

Averaging over orientations is performed as follows:

$$P(Q) = \frac{1}{2} \int_{-1}^{1} d\mu \left[\frac{2J_1(Q\sqrt{1-\mu^2}R)}{Q\sqrt{1-\mu^2}R} \right]^2 \qquad (26)$$

$$= \frac{2}{(QR)^2}\left[1 - \frac{J_1(2QR)}{QR}\right].$$

To obtain the form factor for an infinitely thin rod of length L, we take the $R \to 0$ limit instead, and obtain:

$$P(Q) = \frac{1}{2}\int_{-1}^{1} d\mu \left[\frac{\sin(Q\mu L/2)}{Q\mu L/2}\right]^2. \tag{27}$$

Integrate by part once to obtain:

$$P(Q) = \frac{1}{2}\left\{\left[-\frac{\sin^2(QL\mu/2)}{(QL/2)^2\mu}\right]_{\mu=-1}^{\mu=1} + \int_{-1}^{+1} d\mu \frac{2\sin(QL\mu/2)\cos(QL\mu/2)}{(QL\mu/2)}\right\} \tag{28}$$

$$= \left(\frac{2}{QL}\right)Si(QL) - \frac{\sin^2(QL/2)}{(QL/2)^2}.$$

Si(x) is the sine integral function defined as:

$$Si(x) = \int_0^x du \frac{\sin(u)}{u}. \tag{29}$$

6. FORM FACTOR FOR A PARALLELEPIPED

Consider a uniform density rectangular parallelepiped of sides a, b, c. In Cartesian coordinates, the form factor amplitude can be split into the product of three parts that depend on the three coordinates respectively:

$$F(Q) = \frac{1}{abc}\left[\int_{-a/2}^{a/2} dx \exp[iQ_x x]\right]\left[\int_{-b/2}^{b/2} dy \exp[iQ_y y]\right]\left[\int_{-c/2}^{c/2} dz \exp[iQ_z z]\right] \tag{30}$$

$$= \left[\frac{\sin(Q_x a/2)}{(Q_x a/2)}\right]\left[\frac{\sin(Q_y b/2)}{(Q_y b/2)}\right]\left[\frac{\sin(Q_z c/2)}{(Q_z c/2)}\right].$$

The form factor is, here also, an average over orientations:

$$P(Q) = \frac{1}{2}\int_{-1}^{1} d\mu \, | F(Q,\mu) |^2. \tag{31}$$

$\mu = \cos(\theta)$ and θ is the orientation angle between $\vec{Q}$ and one of the symmetry axes of the parallelepiped.

7. TWISTED RIBBON FORM FACTOR

The parametrization of the twisted ribbon was described in an earlier section when calculating the radius of gyration. Consider a helically twisted ribbon aligned along the vertical z axis with a helical radius R, height L, width W and ribbon thickness T. Define the helix pitch p and the azimuthal angle ϕ in the horizontal plane. Define also the polar coordinate variable in the horizontal plane ρ and the vertical variable z. The parametric position along the ribbon is given by:

$$r(\phi, z, \rho) = \sqrt{\rho^2 + \left(\frac{p\phi}{2\pi} + z\right)^2} .$$ (32)

The single twisted ribbon form factor amplitude is given by:

$$F(Q, \mu) = \frac{\int d\phi \int dz \int \rho d\rho \left[\frac{\sin[Qr(\phi, z, \rho)\mu]}{Qr(\phi, z, \rho)\mu}\right]}{\int d\phi \int dz \int \rho d\rho} .$$ (33)

All three integration can be performed numerically using the following limits: $-\pi L/p \leq \phi \leq \pi L/p$, $-W/2 \leq z \leq W/2$ and $R-T/2 \leq \rho \leq R+T/2$.

Here also, the form factor is given by an average over orientations:

$$P(Q) = \frac{1}{2} \int_{-1}^{1} d\mu \, | F(Q, \mu) |^2 .$$ (34)

$\mu = \cos(\theta)$ and θ is the orientation angle between $\vec{Q}$ and the vertical axis of the ribbon.

8. PAIR CORRELATION FUNCTIONS

The form factor P(Q) is the Fourier transform of the probability distribution function $P(\vec{r})$:

$$P(Q) = \int d\vec{r} \exp(i\vec{Q}.\vec{r}) P(\vec{r}) .$$ (35)

Given an infinitesimal scattering volume chosen randomly inside the considered "particle", $P(\vec{r})$ represents the probability of finding another scatterer within the particle a distance $\vec{r}$ away. Usually, a one-dimensional probability distribution p(r) (also referred to as "distance distribution function") is defined instead:

270

$$P(Q) = \frac{1}{R} \int_0^R dr \frac{\sin(Qr)}{Qr} p(r). \tag{36}$$

p(r) is available for some of the common shape objects. For a sphere of radius R:

$$p(r) = 12\left(\frac{r}{2R}\right)^2 \left(1 - \frac{r}{2R}\right)^2 \left(2 + \frac{r}{2R}\right) \tag{37}$$

$$= 3\left(\frac{r}{R}\right)^2 \left(1 - \frac{3}{4}\frac{r}{R} + \frac{1}{16}\left(\frac{r}{R}\right)^3\right).$$

Note the other definition $p(r) = 3(r/R)^2 \gamma(r)$ where $\gamma(r)$ is the radial pair correlation function given by $\gamma(r) = \left(1 - \frac{3}{4}\frac{r}{R} + \frac{1}{16}\left(\frac{r}{R}\right)^3\right)$.

For a disk of radius R, the distance distribution function is given by:

$$p(r) = \frac{8}{\pi}\frac{r}{R}\left[\arccos\left(\frac{r}{2R}\right) - \frac{r}{2R}\sqrt{1 - \left(\frac{r}{2R}\right)^2}\right]. \tag{38}$$

For an infinitely thin rod of length L, the integration is performed from 0 to L and the normalization constant is 1/L so that:

$$p(r) = 2\left(1 - \frac{r}{L}\right). \tag{39}$$

Note that the probability distribution function $P(\vec{r})$ is better known when defined for the "inter-particle" structure factor $S_I(Q)$ and is often referred to as pair correlation function $g(\vec{r}) = VP(\vec{r})$ (where V is the sample volume):

$$S_I(Q) = \frac{1}{V} \int d\vec{r} \exp(i\vec{Q}.\vec{r})[g(\vec{r}) - 1]. \tag{40}$$

Here the following constant term:

$$\int d\vec{r} \exp(i\vec{Q}.\vec{r}) = (2\pi)^3 \delta(\vec{Q}) \tag{41}$$

has been subtracted to $g(\vec{r})$. This term has no contribution except in the (experimentally irrelevant) forward scattering direction (for which $\vec{Q} = \vec{0}$).

REFERENCES

A. Guinier, and G. Fournet, "Small-Angle Scattering of X-Rays", John Wiley and Sons, New York, (1955).

O Glatter and O Kratky, "Small Angle X-Ray Scattering", Academic Press (1982).

B. Hammouda, "SANS from Polymers Tutorial", NIST Center for Neutron Research Report (1995)

R.J. Roe, "Methods of X-Ray and Neutron Scattering in Polymer Science", Oxford University Press, New York, (2000).

QUESTIONS

1. What is the relationship between the form factor P(Q) and its amplitude F(Q) for the case of a uniform sphere? How about the case of a Gaussian polymer coil?
2. What is the form factor for a uniform sphere of radius R?
3. What is the form factor for a disk of radius R with its axis of rotation oriented parallel to the $\vec{Q}$ direction?
4. What is the form factor for a disklike lamella of thickness L with its normal axis oriented parallel to the $\vec{Q}$ direction?

5. What is the form factor for a cylinder R and length L oriented parallel to the $\vec{Q}$ direction?
6. How is the averaging over random orientations performed for the calculation of the form factor?
7. Write down the radial pair correlation function $\gamma(r)$ for a uniform sphere of radius R. $\gamma(r)$ is

defined through the following 1D Fourier transform: $P(Q) = \dfrac{1}{V} \int\limits_0^R dr 4\pi r^2 \dfrac{\sin(Qr)}{Qr} \gamma(r)$.

8. What are the various parts that are used to calculate the SANS macroscopic scattering cross section for a solution of compact scatterers?
9. What is the Porod exponent for an infinitely thin rod of length L?
10. Define the spherical Bessel function of first order $j_1(x)$. What is $J_1(x)$?

ANSWERS

1. For a uniform sphere $P(Q) = |F(Q)|^2$. For a Gaussian coil, there is no uniform density and the form factor amplitude cannot be defined.
2. The form factor for a uniform sphere is given as $P(Q) = [3j_1(QR)/QR]^2$ where $j_1(QR)$ is the spherical Bessel function.
3. The form factor for a disk of radius R with its axis of rotation oriented parallel to the $\vec{Q}$ direction is given by $P(Q) = [\sin(QR)/QR]^2$.

4. The form factor for a disklike lamella of thickness L with its normal axis oriented parallel to the $\vec{Q}$ direction is given by $P(Q) = [2J_1(QL/QL]^2$ where $J_1(QL)$ is the cylindrical Bessel function.

5. The form factor for a cylinder of radius R and length L oriented parallel to the $\vec{Q}$ direction is given by $P(Q) = [\sin(QR)/QR]^2 [2J_1(QL/QL]^2$.

6. The form factor for a randomly oriented object with its symmetry axis along the z-direction is calculated as $P(Q) = (1/2)\int_{-1}^{1} d\mu P(Q,\mu)$ where $P(Q,\mu)$ is the form factor for the object oriented at an angle θ from the $\vec{Q}$ direction ($\mu = \cos(\theta)$).

7. The radial pair correlation function for a uniform sphere of radius R is given as

$$\gamma(r) = \left(1 - \frac{3}{4}\frac{r}{R} + \frac{1}{16}\left(\frac{r}{R}\right)^3\right).$$

8. The SANS macroscopic scattering cross section for a solution of compact scatterers is the product of (1) the contrast factor, (2) the number density of scatterers, (3) the scatterer's volume squared, (4) the form factor and (4) the structure factor.

9. Since $P(Q)$ for an infinitely thin rod of length L is given by

$$P(Q) = \frac{1}{2}\int_{-1}^{1} d\mu \left[\frac{2J_1(Q\sqrt{1-\mu^2}R)}{Q\sqrt{1-\mu^2}R}\right]^2 \text{, one would think that the Porod law gives } P(Q) \to 1/Q^2.$$

However after orientational averaging, one obtains the following

$$P(Q) = \left(\frac{2}{QL}\right)Si(QL) - \frac{\sin^2(QL/2)}{(QL/2)^2} \text{, so that } P(Q) \to 1/Q.$$

10. The spherical Bessel function of first order is given by $j_1(x) = \frac{\sin(x)}{x^2} - \frac{\cos(x)}{x}$. $J_1(x)$ is the cylindrical Bessel function.

1. THE DEBYE FUNCTION FOR GAUSSIAN CHAINS

Polymer coils in theta solvents or in the melt state follow Gaussian chain statistics whereby the inter-monomer distance r_{ij} is given by the following Gaussian distribution function:

$$P(r_{ij}) = \left(\frac{3}{2\pi < r_{ij}^2 >} \right)^{3/2} \exp\left[-\frac{3r_{ij}^2}{2 < r_{ij}^2 >} \right]. \tag{1}$$

Here $<r_{ij}^2>$ is the variance given in terms of the statistical segment length a as:

$$< r_{ij}^2 >= a^2 |i - j|. \tag{2}$$

The single-chain form factor is given by:

$$P(Q) = \frac{1}{n^2} \sum_{i,j}^{n} < \exp[i\vec{Q}.\vec{r}_{ij}] > \tag{3}$$

$$= \frac{1}{n^2} \sum_{i,j}^{n} \int d\vec{r}_{ij} P(r_{ij}) \exp\left[i\vec{Q}.\vec{r}_{ij} \right]$$

$$= \frac{1}{n^2} \sum_{i,j}^{n} \exp\left[-\frac{Q^2 < r_{ij}^2 >}{6} \right]$$

$$= \frac{1}{n^2} \sum_{i,j}^{n} \exp\left[-\frac{Q^2 a^2 |i - j|}{6} \right].$$

The following property of the Gaussian distribution has been used:

$$< \exp[iQ_x x_{ij}] >= \exp\left[-\frac{Q_x^2 < x_{ij}^2 >}{2} \right] = \exp\left[-\frac{Q_x^2 < r_{ij}^2 >}{6} \right] \tag{4}$$

$$< \exp[i\vec{Q}.\vec{r}_{ij}] >= \exp\left[-\frac{Q^2 < r_{ij}^2 >}{6} \right].$$

The general identity is used:

$$\sum_{i,j}^{n} F(|i-j|) = n + 2\sum_{k=1}^{n}(n-k)F(k). \tag{5}$$

Assuming that the number of chain segments n is large (n>>1), one obtains the Debye function (Debye, 1947):

$$P(Q) = \frac{1}{n^2}\left\{ n + 2\sum_{k=1}^{n}(n-k)\exp\left[-\frac{Q^2 a^2 k}{6} \right] \right\} \tag{6}$$

$$P(Q) = \frac{2}{Q^4 R_g^4}\left[\exp(-Q^2 R_g^2) - 1 + Q^2 R_g^2 \right].$$

The radius of gyration is given by $R_g = \sqrt{a^2 n / 6}$.

Small-Q and high-Q expansions of the Debye function are:

$$P(QR_g \ll 1) = 1 - \frac{Q^2 R_g^2}{3} \tag{7}$$

$$P(QR_g \gg 1) = \frac{2}{Q^2 R_g^2}.$$

Two approximations are included here for the Debye function:

$$P(Q) = \frac{1}{\left(1 + \dfrac{Q^2 R_g^2}{3} \right)} \tag{8}$$

$$P(Q) = \frac{1}{\left(1 + \dfrac{Q^2 R_g^2}{2} \right)}.$$

The first form agrees better at low-Q and the second form agrees better at high Q.
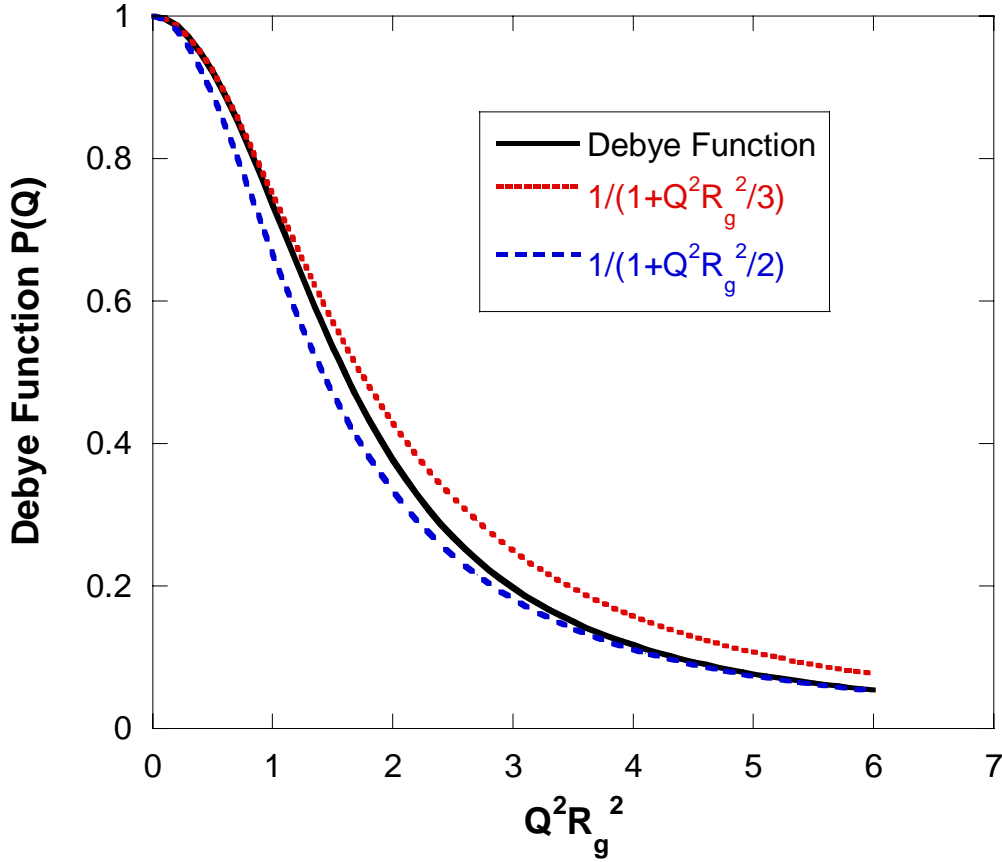
Figure 5: Variation of the Debye function P(Q) along with two approximations that bracket its variation. The form $1/\left(1 + Q^2 R_g^2 / 3\right)$ is a good approximation at low-Q and the form $1/\left(1 + Q^2 R_g^2 / 2\right)$ is a good approximation at high-Q.

Polymer chains are not characterized by uniform density. The form factor (Debye function) is not a square and cannot therefore be expressed as a square of the amplitudes.

2. SINGLE-CHAIN FORM FACTOR FOR GAUSSIAN CHAINS

Consider a flexible polymer coil where each monomer pair located a distance $\vec{r}_{ij}$ apart obeys the Gaussian distribution:

$$P(\vec{r}_{ij}) = \left(\frac{3}{2\pi < r_{ij}^2 >}\right)^{3/2} \exp\left[-\frac{3 r_{ij}^2}{2 < r_{ij}^2 >}\right]. \qquad (9)$$

The average of the segment inter-distances squares is kept in the general form:

$$< r_{ij}^2 >= a^2 \, |i - j|^{2\nu} . \qquad (10)$$

v is the excluded volume parameter. Note that $\vec{S}_{ij} = \vec{r}_{ij}$ in the notation used where $\vec{r}_{ij}$ is in the laboratory reference frame and $\vec{S}_{ij}$ is in the center-of-mass reference frame. Within this approach, the single-chain structure factor is expressed as:

$$P(Q) = \frac{1}{n^2} \sum_{i,j}^{n} < \exp[i\vec{Q}.\vec{r}_{ij}] > \qquad (11)$$

$$= \frac{1}{n^2} \sum_{i,j}^{n} \int d\vec{r}_{ij} P(r_{ij}) \exp\left[i\vec{Q}.\vec{r}_{ij}\right]$$

$$= \frac{1}{n^2} \sum_{i,j}^{n} \exp\left[-\frac{Q^2 a^2}{6} |i-j|^{2v}\right].$$

Note that the monomer pair is always correlated through chain connectivity so that the simplifying approximation $P(Q) = |F(Q)|^2$ (which is made for uniform density objects) is not valid for polymers. The typical manipulations (as in the case of the Debye function described previously) are performed.

Assuming that the number of chain segments n is large (n >> 1), one obtains:

$$P(Q) = \frac{1}{n^2} 2 \sum_{k=1}^{n} (n-k) \exp\left[-\frac{Q^2 a^2}{6} k^{2v}\right]. \qquad (12)$$

Going to the continuous limit (n >> 1):

$$P(Q) = 2 \int_0^1 dx\,(1-x) \exp\left[-\frac{Q^2 a^2}{6} n^{2v} x^{2v}\right]. \qquad (13)$$

This integral is "almost" analytical and can be expressed in terms of the incomplete gamma function:

$$\gamma(d, U) = \int_0^U dt \exp(-t) t^{d-1}. \qquad (14)$$

The result is:

$$P(Q) = \frac{1}{vU^{1/2v}} \gamma(\frac{1}{2v}, U) - \frac{1}{vU^{1/v}} \gamma(\frac{1}{v}, U). \qquad (15)$$

The modified variable is $U = \dfrac{Q^2 a^2 n^{2v}}{6}$.

The high-Q limit of this form is given by:

$$P(Q \to \infty) = \frac{1}{\nu U^{1/2\nu}} \Gamma(\frac{1}{2\nu}) - \frac{1}{\nu U^{1/\nu}} \Gamma(\frac{1}{\nu}).$$ (16)

Here $\Gamma(x) = \gamma(x, \infty)$ is the gamma function. The asymptotic limit is dominated by the $\frac{1}{\nu U^{1/2\nu}} \Gamma(\frac{1}{2\nu})$ term which varies like $U^{-1/2\nu} \sim Q^{-1/\nu}$.

Polymer chains follow Gaussian statistics in polymer solutions: they are swollen in good solvents, are thermally relaxed in "theta" solvents and partially precipitate in poor solvents. The familiar Debye function is recovered when $\nu = \frac{1}{2}$.

3. OTHER POLYMER CHAIN ARCHITECTURES

Many polymer chain architectures exist: "stars" consist of many equal size branches connected to a central core, "combs" consist of side branches grafted onto a main chain, "rings" consist of looped chains, "gels" consist of highly branched structures that are grown outwardly (dendrimers are the most regular gels), "networks" consist of crosslinked systems that contain a large number of inter-connected structures, etc. These various polymer systems are made in the homopolymer form (all monomers are chemically identical) or copolymer form (each chain portion consists of blocks of monomers that are chemically different). Single-chain structure factors for such architectures have been worked out and are summarized elsewhere (Burchard, 1983; Hammouda, 1993; Higgins-Benoit, 1994). Basic elements are included here.

In the same spirit used to derive the form factor for an isolated polymer chain (Debye function):

$$P(Q) = \frac{2}{Q^4 R_g^4} \left[\exp(-Q^2 R_g^2) - 1 + Q^2 R_g^2 \right].$$ (17)

one can also derive the form factor amplitude for a polymer chain anchored at one end. In this case:

$$F(Q) = \frac{1}{n} \sum_i^n \exp\left[-\frac{Q^2 a^2 |i-1|}{6} \right]$$ (18)

$$= \frac{1 - \exp\left[-Q^2 R_g^2 \right]}{Q^2 R_g^2}.$$

Similarly, a propagation factor can be defined (involving no summation):

$$E(Q) = \exp[-Q^2 R_g{}^2].$$
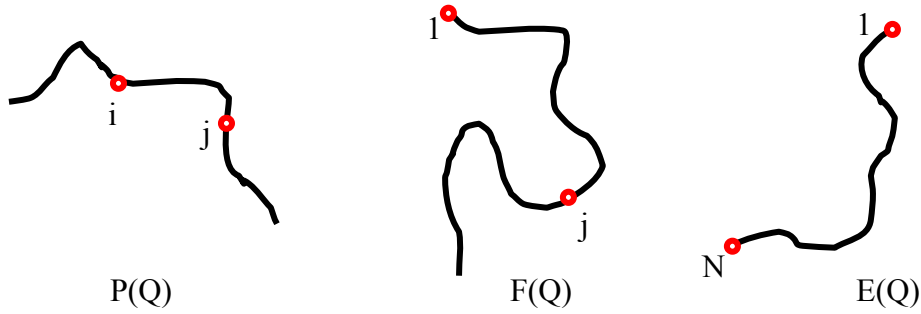
Figure 6: Schematic representation of the summation variables for the various scattering factors for Gaussian polymer chains.

The three scattering factors E(Q), F(Q), and P(Q) can be used to work out the form factors for many polymer architectures.

Consider the simple case of a diblock copolymer A-B consisting of two blocks with N_A-N_B segments. The various partial form factors follow:

$$P(Q) = n_A{}^2 P_{AA}(Q) + n_B{}^2 P_{BB}(Q) + 2n_A n_B P_{AB}(Q) \qquad (19)$$

$$P_{AB}(Q) = F_A(Q)F_B(Q).$$

Consider now an A-B-C triblock copolymer with n_A-n_B-n_C segments. The form factor involves many terms:

$$P(Q) = n_A{}^2 P_{AA}(Q) + n_B{}^2 P_{BB}(Q) + n_C{}^2 P_{CC}(Q) \qquad (20)$$
$$+ 2n_A n_B P_{AB}(Q) + 2n_B n_C P_{BC}(Q) + 2n_A n_C P_{AC}(Q)$$

$$P_{AB}(Q) = F_A(Q)F_B(Q)$$

$$P_{BC}(Q) = F_B(Q)F_C(Q)$$

$$P_{AC}(Q) = F_A(Q)E_B(Q)F_C(Q).$$

The scattering lengths have been omitted for convenience. They have all been assumed to be equal. In order to calculate the SANS scattering cross section, one would have to include the contrast factors, the segment volumes, the polymer macromolecules number densities, and the inter-polymer structure factors.

Other more complex architectures can be handled this way.

Star Polymer   Comb Polymer   Dendrimer
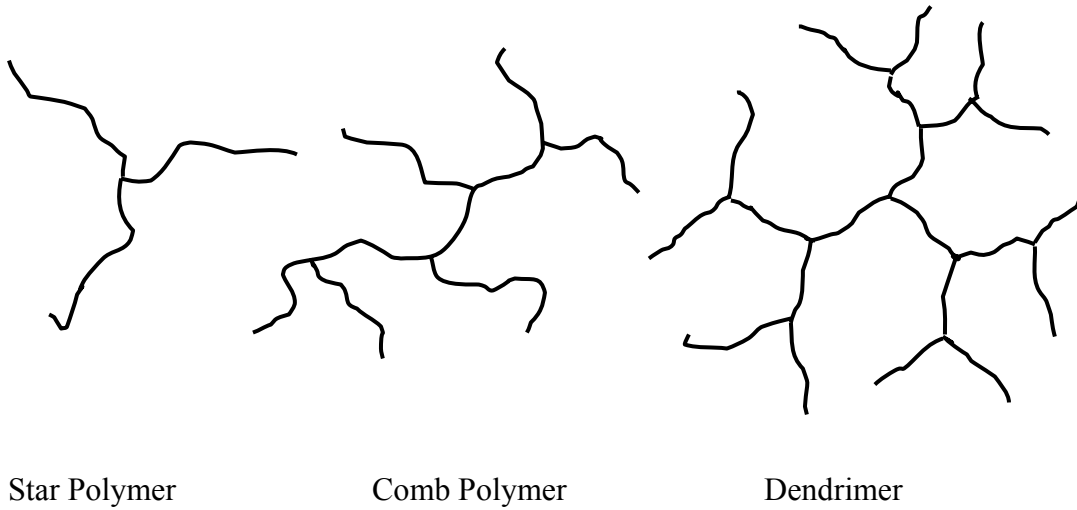
Figure 7: Various possible polymer architectures exist.

4. STAR POLYMER ARCHITECTURE

The simplest case of polymer chain branching is the star polymer which is considered here.
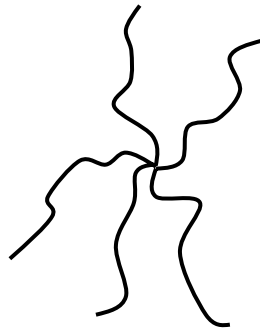
Figure 8: Representation of a star polymer with 5 branches.

The form factor for a star polymer containing n_b branches and n statistical segments per branch is given by:

$$P(Q) = \frac{1}{n_b^2 n^2}\left(n_b n^2 P(n) + n_b(n_b - 1)n^2 F^2(n)\right). \qquad (21)$$

P(n) is the form factor for a chain with n segments (Debye function) and F(n) is the form factor amplitude. Consider the following relationship:

$$(2n)^2 P(2n) = 2n^2 P(n) + 2n^2 F^2(n). \qquad (22)$$

Therefore:

$$P(Q) = \frac{1}{n_b}\left(2P(2n) + (n_b - 2)F^2(n)\right). \tag{23}$$

This is the result for the form factor for a Gaussian polymer star. More complicated architectures (comb, dendrimers, arborescent structures, etc) can be handled this way.

5. POLYMER RINGS

The form factor for a polymer ring can be calculated using a multivariate Gaussian distribution approach. For a Gaussian polymer ring, P(Q) can be calculated as follows:

$$P(Q) = \frac{1}{n^2}\sum_{i,j}^{n}\exp\left[-\frac{Q^2 <r_{ij}^2>}{6}\right]. \tag{24}$$

In order to evaluate $<r_{ij}^2>$, construct the ring from a linear chain which is then closed.
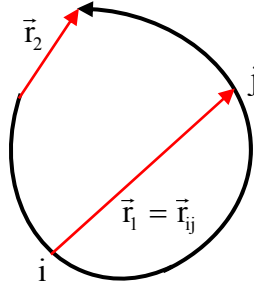
Figure 9: A polymer ring can be constructed by closing a linear chain.

A bivariate Gaussian distribution is defined as:

$$P(\vec{r}_1, \vec{r}_2) = \left(\frac{3}{2\pi a^2}\right)^3 \frac{1}{\Delta}\exp\left(-\frac{3}{2a^2}\sum_{\mu,\nu}^{2}\vec{r}_\mu . D_{\mu\nu} . \vec{r}_\nu\right). \tag{25}$$

Here $\vec{r}_1 = \vec{r}_{ij}$, Δ is the determinant of the correlation matrix $\underline{\underline{C}}$, $\underline{\underline{D}}$ is the inverse ($\underline{\underline{D}} = \underline{\underline{C}}^{-1}$) and the 4 elements of $\underline{\underline{C}}$ are given by: $C_{\mu\nu} = <\vec{r}_\mu . \vec{r}_\nu> / a^2$ with $\{\mu,\nu=1,2\}$. The ring closing is formed by setting $\vec{r}_2 = 0$. This leaves a univariate Gaussian distribution:

$$P(\vec{r}_1) = \frac{P(\vec{r}_1, 0)}{\int d\vec{r}_1 P(\vec{r}_1, 0)} \tag{26}$$

$$= \left(\frac{3}{2\pi a^2}\right)^{\frac{3}{2}} D_{11}^{\frac{3}{2}} \exp\left(-\frac{3}{2a^2} D_{11} \vec{r}_1^{\;2}\right).$$

The average mean square distance between 2 monomers i and j that belong to the blocks of length n is therefore given by:

$$\frac{< r_{ij}^{\;2} >}{a^2} = \frac{1}{D_{11}}. \tag{27}$$

More specifically in this case:

$$C_{11} = \frac{< r_1^{\;2} >}{a^2} = (j-i) \tag{28}$$

$$C_{22} = \frac{< r_2^{\;2} >}{a^2} = n.$$

So that:

$$D_{11} = \frac{n}{|i-j|\,(n-|i-j|)} \tag{29}$$

$$< r_{ij}^{\;2} >= a^2 \,|i-j|\left(1-\frac{|i-j|}{n}\right).$$

The form factor for the polymer ring is therefore:

$$P(Q) = \frac{1}{n^2} \sum_{i,j}^{n} \exp\left[-\frac{Q^2 a^2 \,|i-j|}{6}\left(1-\frac{|i-j|}{n}\right)\right] \tag{30}$$

$$= \frac{1}{n^2}\left\{n + 2n\sum_{k=1}^{n}\left(1-\frac{k}{n}\right)\exp\left[-\frac{Q^2 a^2 k}{6}\left(1-\frac{k}{n}\right)\right]\right\}.$$

The first term is dropped for $n \gg 1$. In order to simplify this equation, we take the continuous chain limit (whereby $Q^2 a^2/6 \ll 1$ and $n \gg 1$ but keeping $Q^2 a^2 n/6$ finite) and change the summations into integrations:

$$P(Q) = 2\int_0^1 ds(1-s)\exp\left[-\frac{Q^2 a^2 n}{6}s(1-s)\right]. \tag{31}$$

We notice the following identity:

$$2\int_0^1 ds(1-s)\exp\left[-\frac{Q^2a^2n}{6}s(1-s)\right] = \int_0^1 ds\exp\left[-\frac{Q^2a^2n}{6}s(1-s)\right]. \qquad (32)$$

Therefore:

$$P(Q) = \int_0^1 ds\exp\left[-\frac{Q^2a^2n}{6}s(1-s)\right]. \qquad (33)$$

After integration variable changes and a few manipulations, one obtains the final result:

$$P(Q) = \frac{D(U)}{U}. \qquad (34)$$

Here $D(U)$ is Dawson's integral:

$$D(U) = \exp\left(-U^2\right)\int_0^U dt\exp\left(t^2\right). \qquad (35)$$

The variable U is given by $U = \sqrt{Q^2a^2n/6}/2 = QR_g/2$.

The method described here for a single ring can be generalized to calculate more complex structures containing looping features.

6. MORE COMPLEX RING-CONTAINING ARCHITECTURES

Another case involving correlations between 2 blocks (n monomers each) separated by 3 linear chain portions (n_1, n_2 and n_3 monomers respectively) that are joined at the extremities of the 2 blocks is considered here. This structure can be constructed using a long linear chain (with $2n+n_1+n_2+n_3$ monomers) that includes 2 crosslinks (corresponding to $\vec{r}_2 = 0$ and $\vec{r}_3 = 0$). All segment lengths are assumed to be equal to a for simplicity.
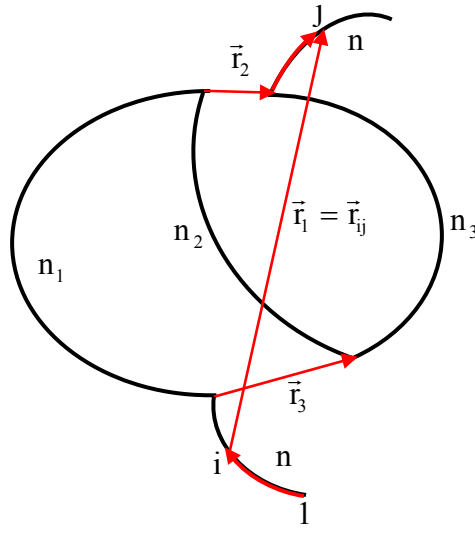
Figure 10: Correlations between two (outer) blocks for a particular polymer chain architecture.

A trivariate Gaussian distribution describing this structure is given by:

$$P(\vec{r}_1, \vec{r}_2, \vec{r}_3) = \left(\frac{3}{2\pi a^2}\right)^{\frac{9}{2}} \frac{1}{\Delta^{\frac{3}{2}}} \exp\left(-\frac{3}{2a^2} \sum_{\mu,\nu}^{3} \vec{r}_\mu . D_{\mu\nu} . \vec{r}_\nu\right). \tag{36}$$

Here also $\vec{r}_1 = \vec{r}_{ij}$ and $\underline{C}$ has 9 elements. The two crosslinks are formed by setting $\vec{r}_2 = \vec{r}_3 = 0$ leading to $P(\vec{r}_1)$.

In this case:

$$\begin{aligned}
C_{11} &= (n-i+j+n_1+n_2+n_3) \\
C_{12} &= C_{21} = (n_2+n_3) \\
C_{13} &= C_{31} = (n_1+n_2) \\
C_{22} &= (n_2+n_3) \\
C_{23} &= C_{32} = n_2 \\
C_{33} &= (n_1+n_2).
\end{aligned} \tag{37}$$

Therefore:

$$< r_{ij}^2 > = a^2 \left[\frac{(-i+j+n)(n_1 n_2 + n_1 n_3 + n_2 n_3) + n_1 n_2 n_3}{n_1 n_2 + n_1 n_3 + n_2 n_3}\right]. \tag{38}$$

The partial structure factor describing correlations between the two outer blocks is given by:

284

$$P(Q) = \frac{1}{n^2} \sum_{i,j}^{n} \exp\left(-\frac{Q^2 <r_{ij}^2>}{6}\right) \tag{39}$$

which can be written simply as:

$$P(Q) = \exp\left[-\frac{Q^2 a^2}{6}\left(\frac{1}{n_1} + \frac{1}{n_2} + \frac{1}{n_3}\right)\right] \frac{\left[1 - \exp\left(-Q^2 a^2 n/6\right)\right]^2}{\left[Q^2 a^2 n/6\right]^2}. \tag{40}$$

In summary, this method consists in forming the correlation diagram using one single chain and choosing judiciously the location of crosslinks. All elements of the correlation matrix $\underline{\underline{C}}$ need to be calculated so that the first element (recall that $\vec{r}_1 = \vec{r}_{ij}$) of its inverse, $D_{11} = \Delta_{11}/\Delta$ (where Δ_{11} is the cofactor of element C_{11} and Δ is the determinant of $\underline{\underline{C}}$) is obtained therefore yielding $<r_{ij}^2>/a^2 = \Delta/\Delta_{11}$. This procedure is useful for the calculation of correlations needed in the modeling of more complicated architectures ("olympic rings", regular networks, etc).

REFERENCES

P. Debye, J. Phys. Colloid. Chem. 51, 18 (1947)

W. Burchard, "Static and Dynamic Light Scattering from Branched Polymers and Biopolymers", Advances in Polymer Science 48, 1 (1983)

B. Hammouda, "SANS from Homogeneous polymer Mixtures: A Unified Overview", Advances in Polymer Science 106, 87 (1993).

J.S. Higgins and H. Benoit, "Polymers and Neutron Scattering", Oxford (1994).

QUESTIONS

1. What is the form factor for a Gaussian polymer coil of radius of gyration R_g?
2. Calculate the form factor $P_{AC}(Q)$ between the two outer blocks for a triblock copolymer A-B-C.
3. What is the form factor for a Gaussian polymer ring?
4. Calculate the radius of gyration for a Gaussian ring polymer.

ANSWERS

1. The form factor for a Gaussian polymer coil is given by the Debye function
$P(Q) = 2\left[\exp\left(-Q^2 R_g^2\right) - 1 + Q^2 R_g^2\right]/Q^4 R_g^4$ where R_g is the radius of gyration.

2. The form factor $P_{AC}(Q)$ between the two outer blocks for a triblock copolymer A-B-C is

given by $P_{AC}(Q) = \dfrac{1 - \exp\left[-Q^2 R_{gA}^{\ 2}\right]}{Q^2 R_{gA}^{\ 2}} \dfrac{\exp\left[-Q^2 R_{gB}^{\ 2}\right]}{Q^2 R_{gB}^{\ 2}} \dfrac{1 - \exp\left[-Q^2 R_{gC}^{\ 2}\right]}{Q^2 R_{gC}^{\ 2}}$ where R_g's are the

radii of gyration of the blocks.

3. The form factor for a Gaussian polymer ring is given by $P(Q) = \left\{\exp\left(-U^2\right)/U\right\}\displaystyle\int_0^U dt\,\exp\left(t^2\right)$

where $U = R_g/2$.

4. The radius of gyration squared for a Gaussian ring polymer is given by:

$$R_g^{\ 2} = na^2 \int_0^1 ds\, s(1-s)^2 = na^2 \int_0^1 ds\,(s - 2s^2 + s^3) = na^2 \left[\frac{s^2}{2} - 2\frac{s^3}{3} + \frac{s^4}{4}\right]_0^1 = \frac{na^2}{12} = \frac{1}{2}\frac{na^2}{6}.$$

Recall that for a linear polymer $R_g^{\ 2} = \dfrac{na^2}{6}$. Here n is the degree of polymerization and a is

the statistical segment length.

Chapter 29 - **EFFECT OF POLYDISPERSITY**

Most scattering systems are characterized by a size distribution regardless of their shapes and sizes. Polydispersity is discussed briefly here by introducing the main polydispersity size distributions used in the literature and presenting averages over these distributions for a few quantities relevant to SANS measurements.

1. SCATTERING FROM A MONODISPERSE SYSTEM

Consider the following scattering cross section for an infinitely dilute solution of monodisperse particles (think spheres) containing N particles of radius R.

$$\frac{d\Sigma(Q)}{d\Omega} = \left(\frac{N}{V}\right)\Delta\rho^2 V_P^2 P(QR) = \left(\frac{N}{V}\right)\Delta\rho^2 \left(\frac{4\pi}{3}\right)^2 R^6 P(QR) \quad (1a)$$

$$= \frac{\phi}{V_P}\Delta\rho^2 V_P^2 P(QR) = \phi\Delta\rho^2 \left(\frac{4\pi}{3}\right)R^3 P(QR). \quad (1b)$$

ϕ is the particles' volume fraction ($\phi = NV_P/V$), $\Delta\rho^2$ is the contrast factor, V is the sample volume, V_P is the particle volume and $P(Q) = |F(Q)|^2$ is the form factor of the scattering particles.

The forward scattering cross section is obtained for $Q = 0$; i.e., for $P(QR) = 1$. The radius of gyration (also called Guinier radius) is given by the low-Q expansion:

$$P(QR) \cong 1 - \frac{Q^2 R_g^2}{3} = 1 - \frac{Q^2 R^2}{5}. \quad (2)$$

2. EFFECT OF POLYDISPERSITY

Consider polydisperse size particles with distribution f(R) which is normalized as $\int_0^\infty dRf(R) = 1$. The polydispersity averaged cross section can have one of two forms:

$$\left\{\frac{d\Sigma(Q)}{d\Omega}\right\} = \left(\frac{N}{V}\right)\Delta\rho^2 \left(\frac{4\pi}{3}\right)^2 \int_0^\infty dRf(R)R^6 P(QR) \quad (3a)$$

$$\left\{\frac{d\Sigma(Q)}{d\Omega}\right\} = \phi\Delta\rho^2 \left(\frac{4\pi}{3}\right)\int_0^\infty dRf(R)R^3 P(QR). \quad (3b)$$

These two forms apply depending on whether the number density (N/V) or the volume fraction ϕ is independent of polydispersity.

The first formula is used in the literature (Kotlarchyk-Chen, 1983; Walter et al, 1985).

The low-Q Guinier expansion for $P(QR) = 1 - Q^2 R^2/5$ yields either one of the two following cases:

$$\left\{\frac{d\Sigma(Q)}{d\Omega}\right\} = \left\{\frac{d\Sigma(Q=0)}{d\Omega}\right\}\left[1 - Q^2 \left\{R_g^{\,2}\right\}/3\right] = \left(\frac{N}{V}\right)\Delta\rho^2\left(\frac{4\pi}{3}\right)^2 \int_0^{\infty} dR f(R)R^6\left[1 - \frac{Q^2 R^2}{5}\right]$$

(4a)

$$\left\{\frac{d\Sigma(Q=0)}{d\Omega}\right\} = \left(\frac{N}{V}\right)\Delta\rho^2\left(\frac{4\pi}{3}\right)^2 \left\{R^6\right\}$$

$$\left\{R_g^{\,2}\right\} = \frac{3}{5}\frac{\left\{R^8\right\}}{\left\{R^6\right\}}$$

$$\left\{\frac{d\Sigma(Q)}{d\Omega}\right\} = \left\{\frac{d\Sigma(Q=0)}{d\Omega}\right\}\left[1 - Q^2 \left\{R_g^{\,2}\right\}/3\right] = \phi\Delta\rho^2\left(\frac{4\pi}{3}\right)\int_0^{\infty} dR f(R)R^3\left[1 - \frac{Q^2 R^2}{5}\right]$$

(4b)

$$\left\{\frac{d\Sigma(Q=0)}{d\Omega}\right\} = \phi\Delta\rho^2\left(\frac{4\pi}{3}\right)\left\{R^3\right\}$$

$$\left\{R_g^{\,2}\right\} = \frac{3}{5}\frac{\left\{R^5\right\}}{\left\{R^3\right\}}.$$

Note that these results do not apply only to spherical particles.

3. THE GAUSSIAN POLYDISPERSITY DISTRIBUTION

The Gaussian polydispersity distribution is given by:

$$f(R) = \frac{1}{\sigma\sqrt{2\pi}} \exp\left[-\frac{(R - R_{av})^2}{2\sigma^2}\right].$$

(5)

σ is the standard deviation and R_{av} is the average radius (R_{av}=<R>). Their ratio is defined as $p = \sigma/R_{av}$.

The Nth moment is given by:

$$\left\{R^N\right\} = R_{av}^{\,N}(1 + A_2 p^2 + 3 A_4 p^4 + 3*5 A_6 p^6 + ...)$$

(6)

The following coefficients have been used:

$$A_2 = \frac{N(N-1)}{2} \tag{7}$$

$$A_4 = \frac{N(N-1)(N-2)(N-3)}{4!} = \frac{N!}{(N-4)!\,4!}$$

$$A_6 = \frac{N!}{(N-6)!\,4!}.$$

N! represents "N factorial" given by N! = N(N-1)(N-2)…3.2.1. The A_{2k} are the even coefficients of the Nth-nomial expansion:

$$(1+R)^N = 1 + A_1 R + A_2 R^2 + \dots A_N R^N \tag{8}$$

$$A_k = \frac{N(N-1)(N-2)\dots(N-k+1)}{k!} = \frac{N!}{(N-k)!\,k!}.$$

The average scattering particle volume is given by:

$$\{V_P\} = \frac{4\pi}{3}\{R^3\} = \frac{4\pi}{3} R_{av}{}^3 \left(1 + 3p^2\right). \tag{9}$$

The low Q (Guinier) expansion involves the following averages:

$$\{R^3\} = R_{av}{}^3 \left(1 + 3p^2\right) \tag{10}$$

$$\{R^5\} = R_{av}{}^5 \left(1 + 10p^2 + 15p^4\right)$$

$$\{R^6\} = R_{av}{}^6 \left(1 + 15p^2 + 45p^4 + 15p^6\right)$$

$$\{R^8\} = R_{av}{}^8 \left(1 + 28p^2 + 210p^4 + 420p^6 + 105p^8\right).$$

4. THE LOG-NORMAL POLYDISPERSITY DISTRIBUTION

The Log-Normal polydispersity distribution is identical to the Gaussian distribution but with the variable ln(R) instead or R. It is sometime used to describe bicontinuous (non-particulate) structures and is given by:

$$f(R) = \frac{1}{\sigma R \sqrt{2\pi}} \exp\left[-\frac{(\ln(R)-\mu)^2}{2\sigma^2}\right]. \tag{11}$$

$\mu = \ln(R_{med})$ and R_{med} is the median radius. The various relevant averages are as follows:

$$\{R^N\} = \exp\left(N\mu + \frac{N^2\sigma^2}{2}\right) \qquad (12)$$

$$\{R\} = \exp\left(\mu + \frac{1}{2}\sigma^2\right)$$

$$\{V\} = \frac{4\pi}{3}\{R^3\} = \frac{4\pi}{3}\exp\left(3\mu + \frac{9}{2}\sigma^2\right)$$

$$R_{peak} = \exp\left(\mu - \sigma^2\right).$$

The low Q (Guinier) expansion involves the following averages:

$$\{R^3\} = \exp\left(3\mu + \frac{9}{2}\sigma^2\right) \qquad (13)$$

$$\{R^5\} = \exp\left(5\mu + \frac{25}{2}\sigma^2\right)$$

$$\{R^6\} = \exp\left(6\mu + \frac{36}{2}\sigma^2\right)$$

$$\{R^8\} = \exp\left(8\mu + \frac{64}{2}\sigma^2\right).$$

5. THE SCHULZ POLYDISPERSITY DISTRIBUTION

The Schulz polydispersity distribution (Schulz, 1939) was introduced to describe the molecular weight distribution of synthetic polymers. It is given by:

$$f(R) = (z+1)^{z+1} x^z \frac{\exp[-(z+1)x]}{R_{av}\Gamma(z+1)} \qquad \text{for } z > -1 \qquad (14)$$

R_{av} is the average radius and x is the scaled variable $x = R/R_{av}$, p is given by the ratio of the standard deviation σ to the average radius as $p = \sigma/R_{av}$ and $z = 1/p^2 - 1$ is the width parameter. $\Gamma(z+1)$ is the Gamma function. Note that $\Gamma(z+1) = z\Gamma(z) = z!$ (factorial z). The Schulz distribution tends to the Gaussian distribution at large z (i.e., for the highly monodisperse case).

The various relevant averages are calculated through the Nth moment:

$$\{R^N\} = \int_0^\infty dR \, R^N f(R) \tag{15}$$

$$= \int_0^\infty dR \, R^N (z+1)^{z+1} \left(\frac{R}{R_{av}}\right)^z \frac{\exp[-(z+1)R/R_{av}]}{R_{av}\Gamma(z+1)}$$

$$= \int_0^\infty dR (z+1)^{z+1} \frac{R^{z+N}}{R_{av}^z} \frac{\exp[-(z+1)R/R_{av}]}{R_{av}\Gamma(z+1)}$$

Integrate by parts once:

$$\{R^N\} = \frac{(z+N)}{(z+1)} R_{av} \int_0^\infty dR (z+1)^{z+1} \frac{R^{z+N-1}}{R_{av}^z} \frac{\exp[-(z+1)R/R_{av}]}{R_{av}\Gamma(z+1)} \tag{16}$$

It is noted that $\left[R.\exp\{-(z+1)R/Rav\}\right]_0^\infty = 0$. Integrate by parts N times to obtain the final result:

$$\{R^N\} = \frac{(z+N)!}{(z+1)^N} R_{av} \int_0^\infty dR (z+1)^{z+1} \frac{R^{z+N-1}}{R_{av}^z} \frac{\exp[-(z+1)R/R_{av}]}{R_{av}\Gamma(z+1)} \tag{17}$$

$$\{R^N\} = \frac{R_{av}^N}{(z+1)^N} \frac{(z+N)!}{z!}.$$

This can be used to obtain:

$$\{V\} = \frac{4\pi}{3}\{R^3\} = \frac{4\pi}{3} R_{av}^3 \frac{(z+3)(z+2)}{(z+1)^2}.$$

The low Q (Guinier) expansion involves the following averages:

$$\{R^3\} = R_{av}^3 \frac{(z+3)(z+2)}{(z+1)^2} \tag{18}$$

$$\{R^5\} = R_{av}^5 \frac{(z+5)!}{(z+1)^5 z!}$$

$$\{R^6\} = R_{av}^6 \frac{(z+6)!}{(z+1)^6 z!}$$

$$\left\{R^8\right\} = R_{av}^{\ 8} \frac{(z+8)!}{(z+1)^8 \, z!} \; .$$

These averages are used to calculate $\left\{\dfrac{d\Sigma(Q=0)}{d\Omega}\right\}$ and $\left\{R_g^{\ 2}\right\}$.

A figure compares the Gaussian and the Schulz polydispersity distributions.
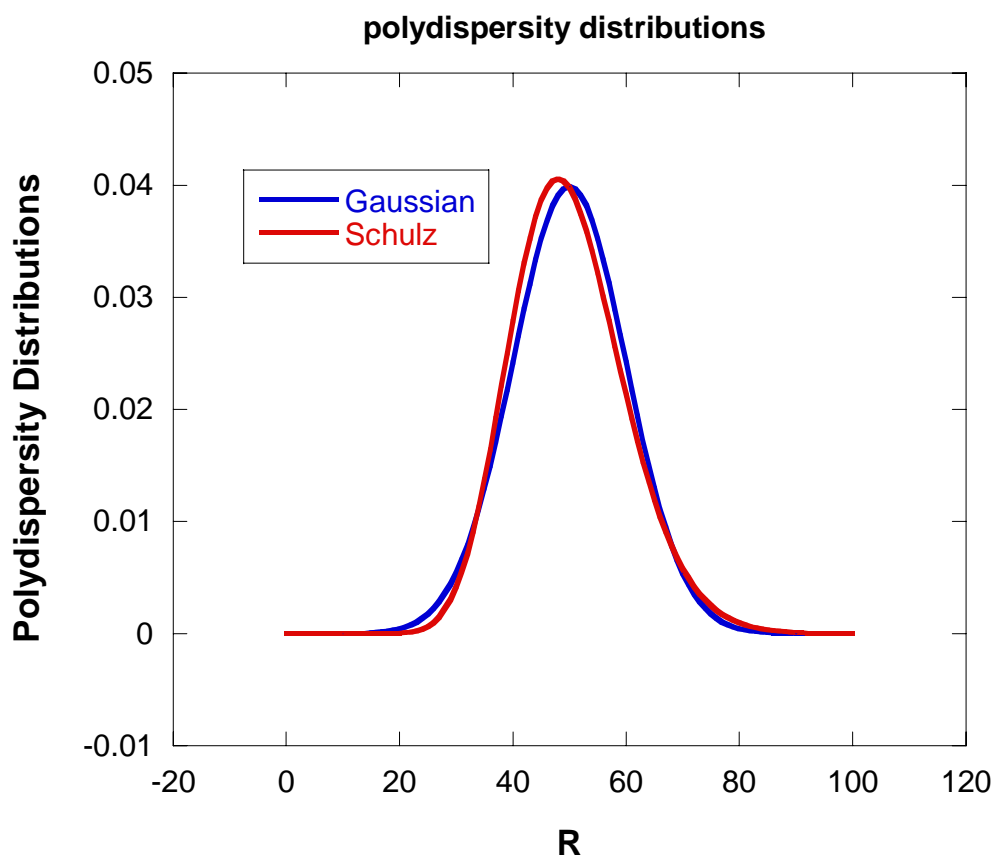
Figure 1: Comparison of the Gaussian and Schulz polydispersity distributions for R_{av} = 50 Å and σ = 10 Å. The Schulz distribution is skewed toward larger sizes (it goes over the Gaussian distribution R around 80 Å).

REFERENCES

G.V. Schulz, Z. Phys. Chem. 43, 25-46 (1939).

M. Kotlarchyk and S.H. Chen, J. Chem. Phys. 79, 2461-2459 (1983).

G. Walter, R. Kranold, T. Gerber, J. Baldrian and M. Steinhart, "Particle-Size Distribution from Small-Angle X-Ray-Scattering Data", J. of Appl. Cryst. 18, 205-213 (1985)

QUESTIONS

1. What is the effect of polydispersity on SANS data?
2. Which of the polydispersity distributions is used for polymers?
3. Calculate <R> using any distribution.
4. Calculate <R^3> using the Schulz distribution.
5. How to calculate the polydispersity averaged scattering cross section for a dilute system?

ANSWERS

1. Polydispersity has the same effect as instrumental smearing. It tends to broaden peaks and fill in valleys.
2. The Schulz distribution is the best choice for describing polydispersity effects in polymers. It yields compact analytical results for characteristic chain properties (radius of gyration and form factor).
3. <R> = R_{av} by definition regardless of the distribution used.

4. For the Schulz distribution $< R^3 >= R_{av}^3 \frac{(z+3)(z+2)}{(z+1)^2}$. In order to demonstrate this,

integrate by parts three times.
5. The polydispersity averaged scattering cross section for a dilute system is calculated

through the following integration: $\left\{ \frac{d\Sigma(Q)}{d\Omega} \right\} = \left(\frac{N}{V} \right) \Delta\rho^2 \left(\frac{4\pi}{3} \right)^2 \int_0^\infty dRf(R)R^6 P(QR)$.

Chapter 30 - SCATTERING FROM DILUTE POLYDISPERSE SYSTEMS

As the next step towards calculating the scattering cross section for realistic systems, we introduce the case of non-interacting systems. A good example for this could be a non-interacting (think infinitely dilute) solution of spheres or a non-interacting solution of polymer coils. Consider the simple monodisperse cases first then introduce the effect of polydispersity.

1. INIFINITELY DILUTE SOLUTION OF MONODISPERSE SPHERES

The macroscopic scattering cross section for a solution of non-interacting monodisperse spheres (of radius R) contains the spheres number density (N/V), the contract factor $\Delta\rho^2$, the particle volume squared $\left(\frac{4\pi}{3}R^3\right)^2$ and the single-particle form factor $P(QR)$ given by:

$$P(QR) = \left[\frac{3j_1(QR)}{(QR)}\right]^2 = \left[\frac{3[\sin(QR)-(QR)\cos(QR)]}{(QR)^3}\right]^2. \quad (1)$$

Putting these terms together, one obtains:

$$\frac{d\Sigma(Q)}{d\Omega} = \left(\frac{N}{V}\right)\Delta\rho^2\left(\frac{4\pi}{3}R^3\right)^2\left[\frac{3j_1(QR)}{(QR)}\right]^2. \quad (2)$$

Note that this cross section has units of cm^{-1} and that the single-particle form factor is normalized to unity, i.e., P(QR=0) = 1. This result is for non-interacting spheres only (in the so-called infinite dilute limit). The effect of polydispersity is included next.

2. INFINITELY DILUTE SOLUTION OF POLYDISPERSE SPHERES

Consider a solution of non-interacting polydisperse spheres (or radius R) and include polydispersity to the sphere size by choosing the Schulz distribution for the sphere radius with R_{av} as the mean radius and σ as the standard deviation. Defining the polydispersity parameter $z = \frac{R_{av}}{\sigma}-1$, the macroscopic cross section becomes:

$$\frac{d\Sigma(Q)}{d\Omega} = \left(\frac{N_A}{V}\right)\Delta\rho^2\int_0^\infty dRf(R)\left(\frac{4\pi}{3}R^3\right)^2\left[\frac{3j_1(QR)}{QR}\right]^2 \quad (3)$$

where:

$$f(R) = (z+1)^{z+1} \left(\frac{R}{R_{av}} \right)^z \frac{1}{R_{av}\Gamma(z+1)} \exp\left[-(z+1)\frac{R}{R_{av}} \right] \text{ for } z > -1 \quad (4)$$

Therefore:

$$\frac{d\Sigma(Q)}{d\Omega} = \left(\frac{N_A}{V} \right) \Delta\rho^2 \left(\frac{4\pi}{3} \right)^2 3^2 *$$

$$\left(\frac{1}{Q^6} \right) \int_0^\infty dR (z+1)^{z+1} \left(\frac{R}{R_{av}} \right)^z \frac{1}{R_{av}\Gamma(z+1)} \exp\left[-(z+1)\frac{R}{R_{av}} \right] \left[\sin(QR) - (QR)\cos(QR) \right]^2 .$$

$$(5)$$

This long formula could not fit in one line. The integral in the second line involves Laplace transforms of trigonometric functions multiplied by powers of the variable R. The integration steps are too tedious to report here. The final result is (Bartlett-Ottewill, 1992):

$$\frac{d\Sigma(Q)}{d\Omega} = \left(\frac{N}{V} \right) \Delta\rho^2 \left(\frac{4\pi}{3} \right)^2 3^2 *$$

$$\left[\frac{1}{2} + \frac{1}{2}\frac{(z+2)}{(z+1)}(QR)^2 - \frac{1}{2}\left[G(2QR) \right]^{\frac{(z+1)}{2}} \cos[(z+1)F(2QR)] \right.$$

$$- (QR)\left[G(2QR) \right]^{\frac{(z+2)}{2}} \sin[(z+2)F(2QR)]$$

$$\left. + \frac{1}{2}(QR)^2 \frac{(z+2)}{(z+1)}\left[G(2QR) \right]^{\frac{(z+3)}{2}} \cos[(z+3)F(2QR)] \right]. \quad (6)$$

The following functions have been defined:

$$G(2QR) = \frac{(z+1)^2}{(z+1)^2 + (2QR)^2} \quad (7)$$

$$F(2QR) = \tan^{-1}\left(\frac{2QR}{(z+1)} \right)$$

Tan^{-1} is the inverse trigonometric function sometime referred to as Arctan. This result is for a solution of non-interacting polydisperse spheres.

3. DILUTE SOLUTION OF NON-INTERACTING MONODISPERSE POLYMER COILS

The macroscopic scattering cross section for a solution of non-interacting polymer coils (of radius of gyration R_g) contains the coils number density (N/V), the contract factor $\Delta\rho^2$, the coils volume squared $(nv)^2$ where n is the degree of polymerization (number of monomers per coil) and the single-particle form factor

$$P(QR_g) = 2\left[\frac{\exp[-Q^2 R_g^2]-1+Q^2 R_g^2}{(Q^2 R_g^2)^2}\right]. \qquad (8)$$

$P(QR_g)$ is also referred to as the Debye function. Note that in this case, the single-coil form factor cannot be written as a square like in the spheres case. Putting all terms together gives:

$$\frac{d\Sigma(Q)}{d\Omega} = \left(\frac{N}{V}\Delta\rho^2\right)(nv)^2\, 2\left[\frac{\exp[-Q^2 R_g^2]-1+Q^2 R_g^2}{(Q^2 R_g^2)^2}\right]. \qquad (9)$$

Defining the polymer volume fraction as $\phi = Nnv/V$, this result can also be written as:

$$\frac{d\Sigma(Q)}{d\Omega} = \Delta\rho^2\, n\, v\, \phi\, P(QR_g) \qquad (10)$$

This non-interacting coils result applies to very dilute solutions only. Concentration effects will be considered by including inter-coil structure factors.

4. DILUTE SOLUTION OF NON-INTERTACTING POLYDISPERSE COILS

Consider polydisperse coils that follow the Schulz distribution f(n) with average number of monomers per coil (degree of polymerization) n = <n> and standard deviation $\sigma = \sqrt{\{n^2\}-\{n\}^2}$. The polydispersity variable z is related to σ and to the degree of polydispersity $\left(\frac{\{n^2\}}{\{n\}^2}-1\right)$ as:

$$\frac{1}{z+1} = \left(\frac{\sigma}{n}\right)^2 = \frac{\{n^2\}}{\{n\}^2}-1. \qquad (11)$$

The scattering cross section for a solution of non-interacting coils is given by:

$$\frac{d\Sigma(Q)}{d\Omega} = \left(\frac{N}{V}\right)\Delta\rho^2\, v^2\int_0^\infty dn f(n)n^2\, 2\left[\frac{\exp[-\alpha n]-1+\alpha n}{(\alpha n)^2}\right]. \qquad (12)$$

296

Another scattering variable is introduced as $\alpha = Q^2 a^2/6$ (a being the statistical segment length). The polydispersity integral can be performed to obtain the cross section for polydisperse coils (in the infinite dilution limit):

$$\frac{d\Sigma(Q)}{d\Omega} = \left(\frac{N}{V}\right)\Delta\rho^2 v^2 \cdot \frac{2}{\alpha^2}\left[\left(1+\alpha\frac{n}{(z+1)}\right)^{-(z+1)} - 1 + \alpha n\right] \qquad (13)$$

n is related to the number average molecular weight as:

$$M_n = m\{n\} = mn \qquad (14)$$

m is the molar mass of one monomer. The weight average molecular weight is defined as:

$$M_w = m\frac{\{n^2\}}{\{n\}} = mn\frac{z+2}{z+1}. \qquad (15)$$

The degree of polydispersity is expressed as:

$$\frac{M_w}{M_n} - 1 = \frac{\{n^2\}}{\{n\}^2} - 1 = \frac{1}{z+1}. \qquad (16)$$

The results derived in this section apply to polydisperse non-interacting coils (Aragon-Pecora, 1976; Higgins-Benoit, 1996).

REFERENCES

S.R. Aragon and R. Pecora, "Theory of Dynamic Light Scattering from Polydisperse Systems", J. Chem. Phys. 64, 2395-2404 (1976).

P. Bartlett and R.H. Ottewill, "A Neutron Scattering Study of the Structure of a Bimodal Colloidal Crystal", J. Chem. Phys. 96, 3306-3318 (1992).

J.S. Higgins, and H.C. Benoit, "Polymers and Neutron Scattering", Oxford Science Publications (1996).

QUESTIONS

1. Write down the scattering cross section for a dilute polydisperse solution of spheres. There is no need performing the integral.
2. Write down the scattering cross section for a dilute polydisperse solution of polymer coils using the Schulz distribution.
3. Write down the degree of polydispersity for polymers using the Schulz distribution.

ANSWERS

1. The scattering cross section for a dilute polydisperse solution of spheres is given by the following integral $\dfrac{d\Sigma(Q)}{d\Omega} = \left(\dfrac{N_A}{V}\right)\Delta\rho^2 \int\limits_0^\infty dRf(R)\left(\dfrac{4\pi}{3}R^3\right)^2\left[\dfrac{3j_1(QR)}{QR}\right]^2$.

2. The scattering cross section for a dilute polydisperse solution of polymer coils is given by the following integral $\dfrac{d\Sigma(Q)}{d\Omega} = \left(\dfrac{N}{V}\right)\Delta\rho^2 v^2.\dfrac{2}{\alpha^2}\left[\left(1+\alpha\dfrac{n}{(z+1)}\right)^{-(z+1)} -1+\alpha n\right]$ where $\alpha =$ $Q^2a^2/6$ and standard notation has been used.

3. Using the Schulz distribution, the degree of polydispersity is given by $\dfrac{M_W}{M_n} -1 = \dfrac{\{n^2\}}{\{n\}^2} -1$.

298

Chapter 31 – STRUCTURE FACTORS FOR POLYMER SYSTEMS

Up to now, this tutorial has focused on infinitely dilute systems only. Such systems are non-interacting and require solely the calculation of the form factor P(Q) for isolated particles. More concentrated (or interacting) systems require the calculation of the structure factor S(Q). Structure factors for fully interacting polymer systems are considered here. These apply to semi-dilute and concentrated polymer solutions and polymer blend mixtures in the homogeneous phase.

1. SCATTERING FROM INCOMPRESSIBLE SYSTEMS

Consider a system consisting of N "particles" of scattering length b_P occupying the sample volume V. The following would still hold if the word "polymers" were substituted for the word "particles". The scattering cross section is proportional to the density-density correlation function as follows:

$$\frac{d\Sigma(Q)}{d\Omega} = b_P{}^2 \frac{1}{V} \sum_{i,j}^{N} < \exp\left(i\vec{Q}.\vec{r}_{ij}\right) >= b_P{}^2 \frac{1}{V} < n_P(-Q)n_P(Q) > . \qquad (1)$$

Here $n_P(Q)$ is the fluctuation particle density in Fourier space. The cross section for particles in solution is given by:

$$\frac{d\Sigma(Q)}{d\Omega} = b_P{}^2 \frac{1}{V} < n_P(-Q)n_P(Q) > + b_S{}^2 \frac{1}{V} < n_S(-Q)n_S(Q) >$$

$$+ 2b_P b_S \frac{1}{V} < n_P(-Q)n_S(Q) > . \qquad (2)$$

The subscripts P and S stand for particle and solvent respectively. For the sake of convenience, the following scattering factors are defined:

$$S_{PP}(Q) = \frac{v_P{}^2}{V} < n_P(-Q)n_P(Q) > \qquad (3)$$

$$S_{SS}(Q) = \frac{v_S{}^2}{V} < n_S(-Q)n_S(Q) >$$

$$S_{PS}(Q) = \frac{v_P v_S}{V} < n_P(-Q)n_S(Q) > .$$

The specific volumes v_P and v_S and scattering length densities $\rho_P = b_P/v_P$ and $\rho_S = b_S/v_S$ are defined for the polymer and the solvent respectively. To clarify, v_P is the

monomer volume and v_S is the volume of the solvent molecule. The scattering cross section becomes:

$$\frac{d\Sigma(Q)}{d\Omega} = \rho_P{}^2 S_{PP}(Q) + \rho_S{}^2 S_{SS}(Q) + 2\rho_P\rho_S S_{PS}(Q). \qquad (4)$$

Most scattering systems are incompressible. It is often convenient to make the following incompressibility assumption:

$$v_P n_P(Q) + v_S n_S(Q) = 0. \qquad (5)$$

This introduces the following simplification:

$$v_P{}^2 < n_P(-Q)n_P(Q) > = v_S{}^2 < n_S(-Q)n_S(Q) > \qquad (6)$$

$$= -v_P v_S < n_P(-Q)n_S(Q) >.$$

In other words:

$$S_{PP}(Q) = S_{SS}(Q) = -S_{PS}(Q) = -S_{SP}(Q) \qquad (7)$$

This simplifies the cross section to the following form:

$$\frac{d\Sigma(Q)}{d\Omega} = (\rho_P - \rho_S)^2 S_{PP}(Q) = \Delta\rho^2 S_{PP}(Q). \qquad (8)$$

This is reasonable since the contrast factor $\Delta\rho^2$ is always calculated relative to a "background" scattering length density value. Here the solvent's scattering length density is taken to be that reference value.

2. INTER-PARTICLE INTERACTIONS

Consider a system consisting of N polymers of contrast factor $\Delta\rho^2$ occupying volume V. Each polymer comprises n monomers of volume v each so that the polymer volume is $v_P = nv$. Let us separate out the intra-polymer and the inter-polymer terms in the scattering cross section as follows:

$$\frac{d\Sigma(Q)}{d\Omega} = \Delta\rho^2 \frac{v^2}{V} \left[\sum_{\alpha=\beta}^{N} \sum_{i,j}^{n} < \exp\left(i\vec{Q}.\vec{r}_{\alpha i\beta j}\right) > + \sum_{\alpha\neq\beta}^{N} \sum_{i,j}^{n} < \exp\left(i\vec{Q}.\vec{r}_{\alpha i\beta j}\right) > \right]. \quad (9)$$

The indices α and β run over the polymer chains and the indices i and j run over the monomers in a specific polymer chain. Consider a pair of polymer coils (called 1 and 2) and sum over all pairs.

$$\frac{d\Sigma(Q)}{d\Omega} = \Delta\rho^2 \frac{v^2}{V}\left[N\sum_{i,j}^{n} < \exp\!\left(i\vec{Q}.\vec{r}_{1i1j}\right)> + N(N-1)\sum_{i,j} < \exp\!\left(i\vec{Q}.\vec{r}_{1i2j}\right)>\right]. \qquad (10)$$

Note that this formalism holds if the word "particles" were to be substituted for the word "polymers" assuming (of course) that the particles have internal structure (think monomers).
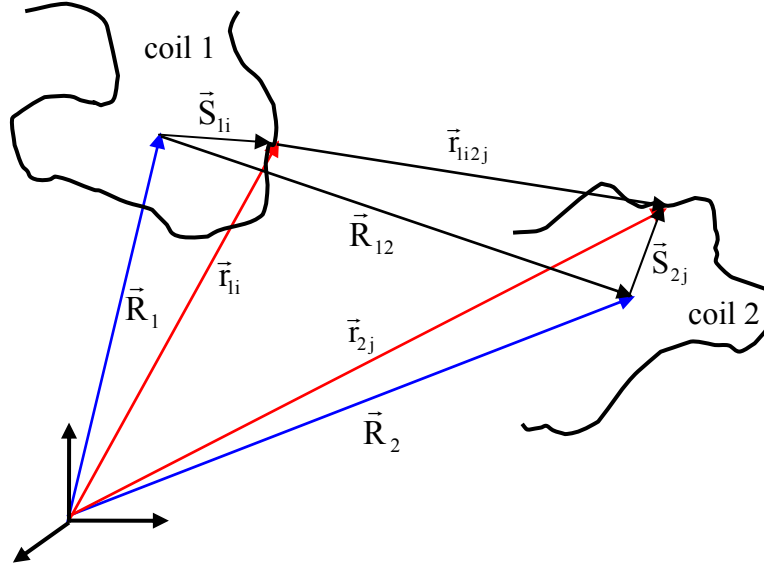
Figure 1: Schematic representation of the coordinate system showing a pair of scatterers that belong to two different polymer coils.

The inter-distance between the scattering pair $\vec{r}_{1i2j}$ can be expressed as $\vec{r}_{1i2j} = -\vec{S}_{1i} + \vec{S}_{2j} + \vec{R}_{12}$ and the inter-particle average can be split into the following parts:

$$< \exp\!\left(i\vec{Q}.\vec{r}_{1i2j}\right)> = < \exp\!\left(-i\vec{Q}.\vec{S}_{1i}\right)>< \exp\!\left(i\vec{Q}.\vec{S}_{2j}\right)>< \exp\!\left(i\vec{Q}.\vec{R}_{12}\right)>. \qquad (11)$$

The first two averages are within single particles and the third average is across particles. The summations become:

$$\sum_{i,j}^{n} < \exp\!\left(i\vec{Q}.\vec{S}_{1i2j}\right)> = < \exp\!\left(i\vec{Q}.\vec{R}_{12}\right)> \sum_{i}^{n} < \exp\!\left(-i\vec{Q}.\vec{S}_{1i}\right)> \sum_{j}^{n} < \exp\!\left(i\vec{Q}.\vec{S}_{2j}\right)>. \qquad (12)$$

The form factor amplitude is defined as:

$$F(Q) = \frac{1}{n}\sum_{i}^{n} < \exp\!\left(i\vec{Q}.\vec{S}_{1i}\right)> = \frac{1}{n}\sum_{j}^{n} < \exp\!\left(i\vec{Q}.\vec{S}_{2j}\right)>. \qquad (13)$$

The single-particle form factor itself is defined as:

$$P(Q) = \frac{1}{n^2} \sum_{i,j}^{n} < \exp\left(i\vec{Q}.\vec{S}_{1i1j}\right) > . \tag{14}$$

For uniform density particles, the following relation holds $P(Q) = | F(Q) |^2$. This is not true, however, for non-uniform density object such as polymer coils.

An inter-particle structure factor is defined as:

$$S_I(Q) = \frac{1}{N} \sum_{\alpha,\beta}^{N} < \exp\left(i\vec{Q}.\vec{R}_{\alpha\beta}\right) > . \tag{15}$$

The cross section can therefore be written as follows:

$$\frac{d\Sigma(Q)}{d\Omega} = \Delta\rho^2 \frac{v^2 n^2 N}{V} \left[P(Q) + | F(Q) |^2 \left(S_I(Q) - 1\right)\right]. \tag{16}$$

Note that the statistical average $< \exp\left(i\vec{Q}.\vec{r}_{1i2j}\right) >$ involves integration over the following probability distribution $P(\vec{r}_{1i}, \vec{r}_{2j}, \vec{R}_{12})$ which can be split to show a conditional probability $P(\vec{r}_{1i}, \vec{r}_{2j}, \vec{R}_{12}) = P(\vec{r}_{1i}, \vec{r}_{2j} | \vec{R}_{12})P(\vec{R}_{12})$. For compact scatterers which do not interfere with each other's rotation $P(\vec{r}_{1i}, \vec{r}_{2j} | \vec{R}_{12})$ is independent of $\vec{R}_{12}$. $P(\vec{R}_{12})$ is the probability of finding the centers of mass of polymer coils 1 and 2 a distance $\vec{R}_{12}$ apart.

$$S_I(Q) = N < \exp\left(i\vec{Q}.\vec{R}_{12}\right) >= \frac{N}{V} \int d\vec{R}_{12} P(\vec{R}_{12}) \exp\left(i\vec{Q}.\vec{R}_{12}\right). \tag{17}$$

The cross section for systems in this case is given by:

$$\frac{d\Sigma(Q)}{d\Omega} = \Delta\rho^2 \frac{v^2 n^2 N}{V} P(Q) \left[1 + \frac{| F(Q) |^2}{P(Q)} \left(S_I(Q) - 1\right)\right]. \tag{18}$$

This result applies to systems with non-spherical symmetry and non-uniform density such as polymers. Polymer are, however, so highly entangled that an inter-chain structure factor $S_I(Q)$ is meaningless except for dilute solutions whereby polymer coils do not overlap. Inter-chain interactions for polymer systems are better handled using other methods described below.

Uniform density scatterers (such as particles) are characterized by $P(Q) = | F(Q) |^2$, so that:

$$\frac{d\Sigma(Q)}{d\Omega} = \Delta\rho^2 \frac{v^2 n^2 N}{V} P(Q)S_I(Q). \tag{19}$$

Defining a particles' volume fraction as $\phi = Nnv/V$, the following result is obtained:

$$\frac{d\Sigma(Q)}{d\Omega} = \Delta\rho^2 S(Q) \qquad (20)$$

$$S(Q) = n\phi v P(Q) S_I(Q).$$

This is a well-known result. It is included here even-though it does not apply to polymer systems so that the derivation does not have to be repeated when covering scattering from particulate systems later. Note that the scattering factor S(Q) and the inter-particle structure factors $S_I(Q)$ should not be confused; S(Q) has the dimension of a volume whereas $S_I(Q)$ is dimensionless.

3. THE PAIR CORRELATION FUNCTION

Recall the definition for the inter-particle structure factor for a pair of particles (named 1 and 2):

$$S_I(Q) = N < \exp\left(i\vec{Q}.\vec{R}_{12}\right) >= \frac{1}{N} \sum_{\alpha,\beta}^{N} < \exp\left(i\vec{Q}.\vec{R}_{\varepsilon\beta}\right) > \qquad (21)$$

$$= \frac{1}{NV} \sum_{\alpha,\beta}^{N} \int d^3 R_{\alpha\beta} \exp\left(i\vec{Q}.\vec{R}_{\alpha\beta}\right) P(\vec{R}_{\alpha\beta}).$$

$P(\vec{R}_{\alpha\beta})$ is the probability of finding particle β in volume $d^3R_{\alpha\beta}$ a distance $\vec{R}_{\alpha\beta}$ away given that particle α at the origin. When the self term (α = β) is omitted, this result becomes:

$$S_I(Q) - 1 = \frac{1}{NV} \sum_{\alpha\neq\beta}^{N} \int d^3\vec{R}_{\varepsilon\beta} \exp\left(i\vec{Q}.\vec{R}_{\alpha\beta}\right) P(\vec{R}_{\alpha\beta}) \qquad (22)$$

$$= \frac{N}{V} \int d^3\vec{R}_{12} \exp\left(i\vec{Q}.\vec{R}_{12}\right) P(\vec{R}_{12}).$$

The probability $P(\vec{R}_{12})$ is referred to as the pair correlation function and is often called $g(\vec{R}_{12})$. Removing the forward scattering term yields the following well known result:

$$S_I(Q) - 1 = \frac{N}{V} \int d^3\vec{R}_{12} \exp\left(i\vec{Q}.\vec{R}_{12}\right)\left[g(\vec{R}_{12}) - 1\right] + (2\pi)^3 \delta(Q). \quad (23)$$

The last term (containing the Dirac Delta function) is irrelevant and can be neglected. This last equation shows that $S_I(Q) - 1$ and $g(\vec{R}_{12}) - 1$ are a Fourier transform pair. Note that $g(\vec{R}_{12})$ peaks at the first nearest-neighbor shell and goes asymptotically to unity at large distances. The total correlation function is introduced as $h(\vec{R}_{12}) = g(\vec{R}_{12}) - 1$.

4. POLYMER SOLUTIONS

In the case of polymer solutions, the Zimm single-contact approximation (Zimm, 1946; Zimm, 1948) is a simple way of expressing the inter-polymer structure factor. Within that approximation, the first order term in a "concentration" expansion is as follows:

$$\sum_{i,j}^{n} < \exp\left(i\vec{Q}.\vec{r}_{1i2j}\right) > = -\frac{v_{ex}}{V}\left(\frac{v^2}{V}n^2 P(Q)\right)^2 + ... \qquad (24)$$

v_{ex} is a dimensionless factor representing interactions. The cross section becomes an expansion:

$$\frac{d\Sigma(Q)}{d\Omega} = \Delta\rho^2\left[S_0(Q) - \frac{v_{ex}}{V}(S_0(Q))^2 + ...\right]. \qquad (25)$$

This expansion can be resumed as follows $1 - x + x^2 ... = 1/(1+x)$ to yield:

$$\frac{d\Sigma(Q)}{d\Omega} = \Delta\rho^2 \frac{S_0(Q)}{1 + \frac{v_{ex}}{V}S_0(Q)}. \qquad (26)$$

The bare structure factor for non-interacting polymers has been defined as:

$$S_0(Q) = \frac{Nn^2 v^2}{V}P(Q) = n\phi v P(Q). \qquad (27)$$

Resuming the series extends the single-contact approximation's applicability range to a wide concentration regime. The single-contact approximation applies best to semi-dilute solutions.

Included Interactions

Excluded Interactions
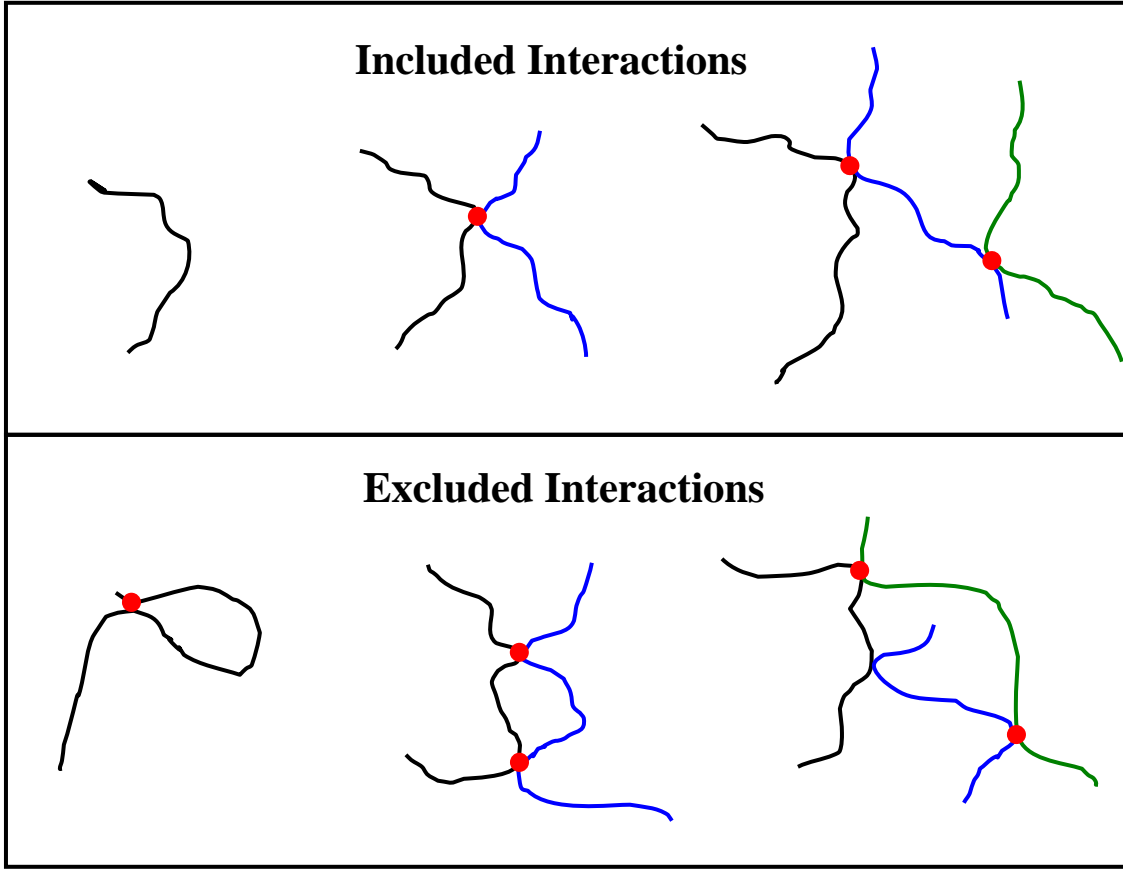
Figure 2: Typical interactions that are included and those that are excluded within the single-contact approximation.

5. THE ZERO CONTRAST METHOD

The zero contrast (or scattering length density match) method also called the high concentration method for polymer systems consists of using a mixture of deuterated and non-deuterated polymers and deuterated and non-deuterated solvents in order to isolate the single-chain form factor; i.e., in order to cancel out the inter-chain interaction terms. The scattering cross section for a polymer solution containing both deuterated and non-deuterated polymers is given by:

$$\frac{d\Sigma(Q)}{d\Omega} = \Delta\rho_D{}^2 S_{DD}(Q) + \Delta\rho_H{}^2 S_{HH}(Q) + 2\Delta\rho_D\Delta\rho_H S_{DD}(Q)S_{HH}(Q). \quad (28)$$

The scattering length density differences between the deuterated (or hydrogenated) polymer and the solvent are:

$$\Delta\rho_D = (\rho_D - \rho_S) = \left(\frac{b_D}{v_D} - \frac{b_S}{v_S}\right) \quad (29)$$

$$\Delta\rho_H = (\rho_H - \rho_S) = \left(\frac{b_H}{v_H} - \frac{b_S}{v_S}\right).$$

The various partial scattering factors are split into single-chain parts and inter-chain parts as follows:

$$S_{DD}(Q) = n_D\phi_D v_D\left[P^S_D(Q) + \phi_D P^I_{DD}(Q)\right] \tag{30}$$

$$S_{HH}(Q) = n_H\phi_H v_H\left[P^S_H(Q) + \phi_H P^I_{HH}(Q)\right]$$

$$S_{HD}(Q) = \sqrt{n_H\phi_H v_H}\sqrt{n_D\phi_D v_D}\sqrt{\phi_H\phi_D}P^I_{HD}(Q).$$

Note that the inter-chain structure factors could be negative depending on volume fraction. Assume that deuterated and hydrogenated polymers have the same degree of polymerization ($n_D = n_H = n_P$), and the same specific volume ($v_D = v_H = v_P$), and define the polymer volume fraction as $\phi_P = \phi_D + \phi_H$. The contrast match method consists in varying the relative deuterated to hydrogenated volume fraction but keeping the total polymer volume fraction constant.

Define the following average of the square and square of the average polymer contrast factors:

$$\left\{\Delta B_P^2\right\} = \left[\Delta\rho_D^2\frac{\phi_D}{\phi_P} + \Delta\rho_H^2\frac{\phi_H}{\phi_P}\right] \tag{31}$$

$$\left\{\Delta B_P\right\}^2 = \left[\Delta\rho_D\frac{\phi_D}{\phi_P} + \Delta\rho_H\frac{\phi_H}{\phi_P}\right]^2.$$

The scattering cross section becomes:

$$\frac{d\Sigma(Q)}{d\Omega} = \left\{\Delta B_P^2\right\}n_P\phi_P v_P P_S(Q) + \left\{\Delta B_P\right\}^2 n_P\phi_P v_P P_I(Q)$$

$$= \left(\left\{\Delta B_P^2\right\} - \left\{\Delta B_P\right\}^2\right)n_P\phi_P v_P P_S(Q) + \left\{\Delta B_P\right\}^2 n_P\phi_P v_P P_T(Q). \tag{32}$$

The following definition has been used:

$$P_T(Q) = P_S(Q) + \phi_P P_I(Q). \tag{33}$$

Note the following simplifications:

$$\left\{\Delta B_P^2\right\} - \left\{\Delta B_P\right\}^2 = (\rho_D - \rho_H)^2\frac{\phi_D\phi_H}{\phi_P^2}. \tag{34}$$

$$\{\Delta B_P\} = \Delta\rho_D \frac{\phi_D}{\phi_P} + \Delta\rho_H \frac{\phi_H}{\phi_P} = \rho_D \frac{\phi_D}{\phi_P} + \rho_H \frac{\phi_H}{\phi_P} - \rho_S.$$

The final result follows:

$$\frac{d\Sigma(Q)}{d\Omega} = \left(\rho_D - \rho_H\right)^2 \frac{\phi_D\phi_H}{\phi_P^2} n_P \phi_P v_P P_S(Q) + \left(\rho_D \frac{\phi_D}{\phi_P} + \rho_H \frac{\phi_H}{\phi_P} - \rho_S\right)^2 n_P \phi_P v_P P_T(Q) . \quad (35)$$

Setting the second contrast factor (between the polymer and the solvent) to zero cancels the second term containing $P_T(Q)$ leaving only the first term containing the single-chain form factor $P_S(Q)$. This zero contrast condition is therefore:

$$\rho_D \frac{\phi_D}{\phi_P} + \rho_H \frac{\phi_H}{\phi_P} = \rho_S . \quad (36)$$

Note that in general in order to achieve this condition, the solvent must also consist of mixtures of deuterated and non-deuterated solvents. Defining the following four indices DP, HP, DS, and HS for deuterated polymer, non-deuterated (hydrogenated) polymer, deuterated solvent and non-deuterated solvent, the contrast match condition becomes in the general case:

$$\rho_{DP} \frac{\phi_{DP}}{\phi_P} + \rho_{HP} \frac{\phi_{HP}}{\phi_P} = \rho_{DS} \frac{\phi_{DS}}{\phi_S} + \rho_{HS} \frac{\phi_{HS}}{\phi_S} . \quad (37)$$

Note that $\phi_{DP} + \phi_{HP} = \phi_P$, $\phi_{DS} + \phi_{HS} = \phi_P$ and $\phi_P + \phi_S = 1$.

6. THE RANDOM PHASE APPROXIMATION

The random phase approximation (de Gennes, 1979, Akcasu-Tombakoglu, 1990; Hammouda, 1993; Higgins-Benoit, 1994) is a simple mean-field approach used to calculate the linear response of a homogeneous polymer mixture following a thermodynamic fluctuation. Consider a binary mixture consisting of a mixture of polymers 1 and 2 with fluctuating densities $n_1(Q)$ and $n_2(Q)$. The interaction potentials between monomers 1 and 2 are W_{11}, W_{12}, W_{21} and W_{22}. Assume an external perturbation represented by potentials U_1 and U_2 and a constraint u that helps apply the incompressibility assumption. The parameter u can be though of as a Lagrange multiplier in an optimization problem with constraints. The constraint here is the incompressibility condition. The linear response equations follow:

$$v_1 n_1(Q) = -S^0_{11}(Q)\left[\frac{U_1 + u + W_{11}v_1 n_1(Q) + W_{12}v_2 n_2(Q)}{k_B T}\right] \quad (38a)$$

$$v_2 n_2(Q) = -S^0{}_{22}(Q)\left[\frac{U_2 + u + W_{21}v_1 n_1(Q) + W_{22}v_2 n_2(Q)}{k_B T}\right] \quad (38b)$$

$$v_1 n_1(Q) + v_2 n_2(Q) = 0. \quad (38c)$$

The last equation represents the incompressibility constraint. The non-interacting or "bare" structure factors $S^0{}_{11}(Q)$ and $S^0{}_{22}(Q)$ have been defined. These equations have assumed that no copolymers are present in the homogeneous mixture; i.e., that $S^0{}_{12}(Q) = S^0{}_{21}(Q) = 0$.

In order to solve the set of linear equations, we extract the perturbing potential u from the second equation and substitute it into the first equation to obtain:

$$v_1 n_1(Q) = -S^0{}_{11}(Q)\left[\frac{U_1 - U_2}{k_B T} + v_{11}(Q)n_1(Q)\right]. \quad (39)$$

This applies along with the following equation representing the response of the fully interacting system:

$$v_1 n_1(Q) = -S_{11}(Q)\left[\frac{U_1 - U_2}{k_B T}\right]. \quad (40)$$

The factor $v_{11}(Q)$ and the Flory-Huggins interaction parameter χ_{12} are defined as:

$$v_{11}(Q) = \frac{1}{S^0{}_{22}(Q)} - \frac{2\chi_{12}}{v_0} \quad (41)$$

$$\chi_{12} = \frac{W_{12}}{k_B T} - \left(\frac{W_{11} + W_{22}}{2k_B T}\right).$$

Here v_0 is a reference volume (often taken to be $v_0 = \sqrt{v_1 v_2}$).

The RPA result for a homogeneous binary blend mixture follows:

$$\frac{1}{S_{11}(Q)} = \frac{1}{S_{11}{}^0(Q)} + \frac{1}{S_{22}{}^0(Q)} - \frac{2\chi_{12}}{v_0} \quad (42)$$

$$S_{11}{}^0(Q) = n_1 \phi_1 v_1 P_1(Q).$$

$$P_1(Q) = \frac{2}{Q^4 R_{g1}{}^4}\left[\exp(-Q^2 R_{g1}{}^2) - 1 + Q^2 R_{g1}{}^2\right]$$

R_{g1} is the radius of gyration. The incompressibility assumption yields the simplifying relations:

$$S_{11}(Q) = S_{22}(Q) = -S_{12}(Q) = S(Q) .$$

(43)

The scattering cross section is given by:

$$\frac{d\Sigma(Q)}{d\Omega} = (\rho_1 - \rho_2)^2 S(Q)$$

(44)

$$\frac{(\rho_1 - \rho_2)^2}{\dfrac{d\Sigma(Q)}{d\Omega}} = \frac{1}{S_{11}{}^0(Q)} + \frac{1}{S_{22}{}^0(Q)} - \frac{2\chi_{12}}{v_0} .$$

This is the so-called de Gennes formula representing the scattering cross section for polymer blends in the single-phase (mixed phase) region. This is based on the Random Phase Approximation that applies for long degree of polymerizations ($n_1 \gg 1$ and $n_2 \gg 2$) and far from the phase boundary condition. This approach does not apply inside the demixed phase region.

This formalism also applies to polymer solutions by replacing one of the polymers (say component 2) by solvent; i.e., by setting $n_2 = 1$ and $P_2(Q) = 1$. In the case of polymer solutions, the excluded volume effect is included in the polymer form factor $P_1(Q)$.

The phase separation condition is achieved when the scattering intensity "blows up"; i.e., in the limit $S_{11}(Q = 0) \to \infty$. This is achieved for

$$S^0{}_{11}(0) + S^0{}_{22}(0) - \frac{2\chi_{12}}{v_0} S^0{}_{11}(0)S^0{}_{22}(0) = 0 .$$

(45)

This is the so-called spinodal condition. Note that with the simplifying assumptions that $n_1 = n_2 = n$, $v_1 = v_2 = v_0$ and $\phi_1 = \phi_2 = 0.5$, the spinodal condition for polymer blends simplifies to $\chi_{12}n = 2$.

7. THE ISOTHERMAL COMPRESSIBILITY FACTOR

Most mixed polymer systems have finite compressibility. The isothermal compressibility can be measured from the scattering cross section in the thermodynamic limit (i.e., for $Q = 0$). In this limit, the scattering cross section is expressed simply as:

$$\frac{d\Sigma(0)}{d\Omega} = \Delta\rho^2 \, k_B T \, \chi_T .$$

(46)

Here k_BT is the temperature in energy units and χ_T is the isothermal (or osmotic) compressibility which is defined as:

$$\chi_T = -\frac{1}{V}\left(\frac{\partial V}{\partial P}\right)_T . \tag{47}$$

Extrapolating scattering data to $Q = 0$ is a way of measuring χ_T. The cross section $d\Sigma(0)/d\Omega$ can be calculated using one of the models described above.

REFERENCES

B. Zimm, "Application of the Methods of Molecular Distribution to Solutions of Large Molecules", J. Chem. Phys. 14, 164 (1946); and B. Zimm, "The Scattering of Light and the Radial Distribution Function of High Polymer Solutions", J. Chem. Phys. 16, 1093 (1948).

P.G. de Gennes, "Scaling Concepts in Polymer Physics", Cornell University Press, New York (1979).

A.Z. Akcasu and M. Tombakoglu, "Dynamics of Copolymer and Homopolymer Mixtures in Bulk and in Solution via the Random Phase Approximation", Macromolecules 23, 607-612 (1990)

B. Hammouda, "SANS from Homogeneous polymer Mixtures: A Unified Overview", Advances in Polymer Science 106, 87 (1993).

J.S. Higgins and H. Benoit, "Polymers and Neutron Scattering", Oxford (1994).

QUESTIONS

1. What is the primary effect of the incompressibility assumption on the scattering cross section?
2. If an incompressible polymer solution is characterized by one (independent) structure factor, how many structure factors describe the equivalent compressible solution?
3. What is the Zimm single-contact approximation?
4. Does the inter-chain structure factor (with excluded volume) for dilute polymer solution tend to increase or decrease the scattering intensity at low-Q?
5. What is the use of the zero contrast condition in concentrated polymer systems? What is the procedure to follow?
6. The Random Phase Approximation applies in what conditions?
7. What is the origin of monomer/monomer interactions in polymer mixtures?
8. Are polymer chains in mixed polymer blends characterized by excluded volume; i.e., are they swollen?
9. What is the pair correlation function g(r)?

ANSWERS

1. The primary effect of the incompressibility assumption is to simplify the scattering cross section from its full form $\frac{d\Sigma(Q)}{d\Omega} = \rho_P^{\ 2}S_{PP}(Q) + \rho_S^{\ 2}S_{SS}(Q) + 2\rho_P\rho_S S_{PS}(Q)$ (where P and S represent the polymer and the solvent respectively) to its simplified form $\frac{d\Sigma(Q)}{d\Omega} = (\rho_P - \rho_S)^2 S_{PP}(Q) = \Delta\rho^2 S_{PP}(Q)$. This is due to the incompressibility condition relating the various partial structure factors $S_{PP}(Q) = S_{SS}(Q) = -S_{PS}(Q) = -S_{SP}(Q)$.

2. An incompressible polymer solution is characterized by one structure factor $S_{PP}(Q)$. The equivalent compressible polymer solution is described by three structure factors: $S_{PP}(Q)$, $S_{SS}(Q)$ and $S_{PS}(Q)$.

3. The Zimm single-contact approximation assumes that inter-chain interactions occur only through single contacts or chains of single contacts. Double contacts within the same chain or between two different chains or higher order contacts are not included.

4. The inter-chain structure factor (with excluded volume) for dilute solutions decreases the scattering intensity at low-Q. Recall the negative sign in Zimm's single-contact approximation formula: $\frac{d\Sigma(Q)}{d\Omega} = \Delta\rho^2 \left[S_0(Q) - \frac{v_{ex}}{V}(S_0(Q))^2 + ... \right]$.

5. The contrast match method is a way to extract single-chain properties (such as the radius of gyration) from concentrated polymer systems. This method consists in using a mixture of deuterated and non-deuterated polymers and deuterated and non-deuterated solvents in the zero average contrast condition. This involves changing the deuterated to non-deuterated polymer fraction but keeping the total polymer fraction constant.

6. The Random Phase Approximation applies for high molecular weight polymers in the single-phase (mixed phase) region. It does not apply in the demixed phase region.

7. Monomers interact with each other and with organic solvent molecules due to Van der Waals interactions mostly. Hydrogen bonding dominates in water-soluble polymers.

8. Polymer coils follow random walk statistics in mixed polymer blends. They are not swollen like in polymer solutions. Their form factor is the well-known Debye function.

9. The pair correlation function g(r) is the probability of finding a scatterer at a radial distance r from another scatterer at the origin.

Chapter 32 - **STRUCTURE FACTORS FOR PARTICULATE SYSTEMS**

Scattering factors from nanostructures consisting primarily of particles (think spheres) in a background medium (think solvent) are described here in the case of non-dilute systems. The Ornstein-Zernike approach is a suitable way to describe inter-particle contributions.

1. THE ORNSTEIN-ZERNIKE EQUATION

The radial distribution function for a pair of scattering particles with no internal structure separated by a distance r is called g(r). It is the probability of finding a scatterer at radial distance r provided that there is a scatterer at the origin. g(r) is related to the inter-particle interaction potential U(r) as follows:

$$g(r) = \exp[-U(r)/k_B T] . \tag{1}$$

Since the potential of mean-force U(r) contains contributions from many-body interactions, it is expanded in terms of binary (w_{ij}), ternary (w_{ijk}), and higher order interactions:

$$U(r) = \sum_{i,j} w_{ij}(r) + \sum_{i,j,k} w_{ijk}(r) + ... \tag{2}$$

Note that g(r) is zero for short distance since two particles cannot occupy the same space and is equal to one for large distance since at far enough distance, the particle can be located for sure.

Direct interactions between the interacting particles pair are represented by the direct correlation function c(r) whereas interactions through other particles are represented by the total correlation function h(r) = g(r) -1.
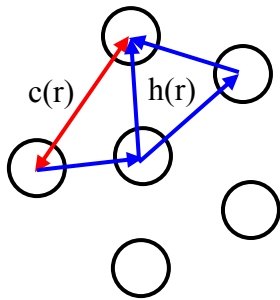
Figure 1: Direct and indirect inter-particle interactions.

The Ornstein-Zernike integral equation (Ornstein-Zernike, 1918; Hansen-McDonald, 1986) is a relation between the direct correlation function c(r) and the total correlation function h(r).

$$h(\vec{r}) = c(\vec{r}) + \overline{N}\int d\vec{r}\,'c(\vec{r}-\vec{r}\,')h(\vec{r}\,') . \qquad (3)$$

$\overline{N} = N/V$ is the particle number density.

In the Fourier variable space, this equation reads:

$$H(Q) = C(Q) + \overline{N}\,C(Q)\,H(Q) . \qquad (4)$$

The inter-particle structure factor is defined as:

$$S_I(Q) = 1 + \overline{N}\,H(Q) = \frac{1}{1-\overline{N}C(Q)} . \qquad (5)$$

Note that the Ornstein-Zernike equation contains two unknowns (h(r) and c(r)). It can be solved only if another (so called "closure") relation is added. Many of these closure relations have been introduced (hypernetted chains, Born-Green, Percus-Yevick, Mean Spherical Approximation, etc). Using one such closure relation, numerical solutions of the Ornstein-Zernike equation yield realistic inter-particle structure factors. The last two closure relations (Percus-Yevick and Mean Spherical Approximation) are discussed here because they permit simple analytical solutions to the integral equation.

Three inter-particle interaction potential are included. The hard sphere potential is used with the Percus-Yevick closure relation and the screened Coulomb potential is used with the Mean Spherical Approximation.
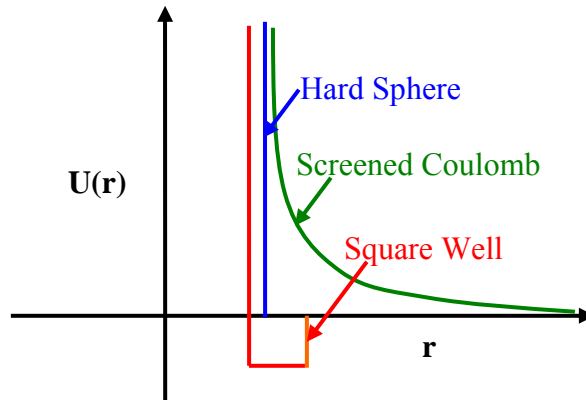
Figure 2: Representation of the various inter-particle interaction potentials.

2. THE PERCUS-YEVICK APPROXIMATION

The Percus-Yevick approximation (Percus-Yevick, 1958) uses the following closure relation in order to solve the Ornstein-Zernike integral equation:

$$c(r) = g(r)\left[1 - \exp\left(-\frac{w(r)}{k_B T}\right)\right]. \tag{6}$$

Assume the following hard sphere interaction potential between particles:

$$w(r) = 0 \qquad \text{for } r > D \tag{7}$$
$$w(r) = \infty \qquad \text{for } r < D.$$

Here D is the sphere diameter. Solution to the Ornstein-Zernike equation is analytical:

$$c(r) = 0 \qquad \text{for } r > D \tag{8}$$
$$c(r) = -\lambda_1 - 6\phi\lambda_2 \frac{r}{D} - \frac{\phi}{2}\lambda_1 \frac{r^3}{D^3} \qquad \text{for } r < D.$$

The following parameters have been defined:

$$\lambda_1 = \frac{(1 + 2\phi)^2}{(1 - \phi)^4} \tag{9}$$

$$\lambda_2 = \frac{-(1 + \phi/2)^2}{(1 - \phi)^4}.$$

ϕ is the particles volume fraction ($\phi = \pi \bar{N} D^3 / 6$), $\bar{N}$ is the density of scattering particles and D is the "effective" particle diameter.

The Fourier transform of the direct correlation function can be calculated as:

$$\bar{N}C(Q) = -24\phi\left\{\lambda_1\left[\frac{\sin(QD) - (QD)\cos(QD)}{(QD)^3}\right] - 6\phi\lambda_2\left[\frac{(QD)^2\cos(QD) - 2(QD)\sin(QD) - 2\cos(QD) + 2}{(QD)^4}\right]\right.$$

$$\left. -\phi\frac{\lambda_2}{2}\left[\frac{(QD)^4\cos(QD) - 4(QD)^3\sin(QD) - 12(QD)^2\cos(QD) + 24(QD)\sin(QD) + 24\cos(QD) - 24}{(QD)^6}\right]\right\}$$

$$(10)$$

The structure factor for a liquid of structureless particles is given by:

$$S_I(Q) = \frac{1}{1 - \overline{N}C(Q)} \qquad (11)$$

Percus Yevick Model
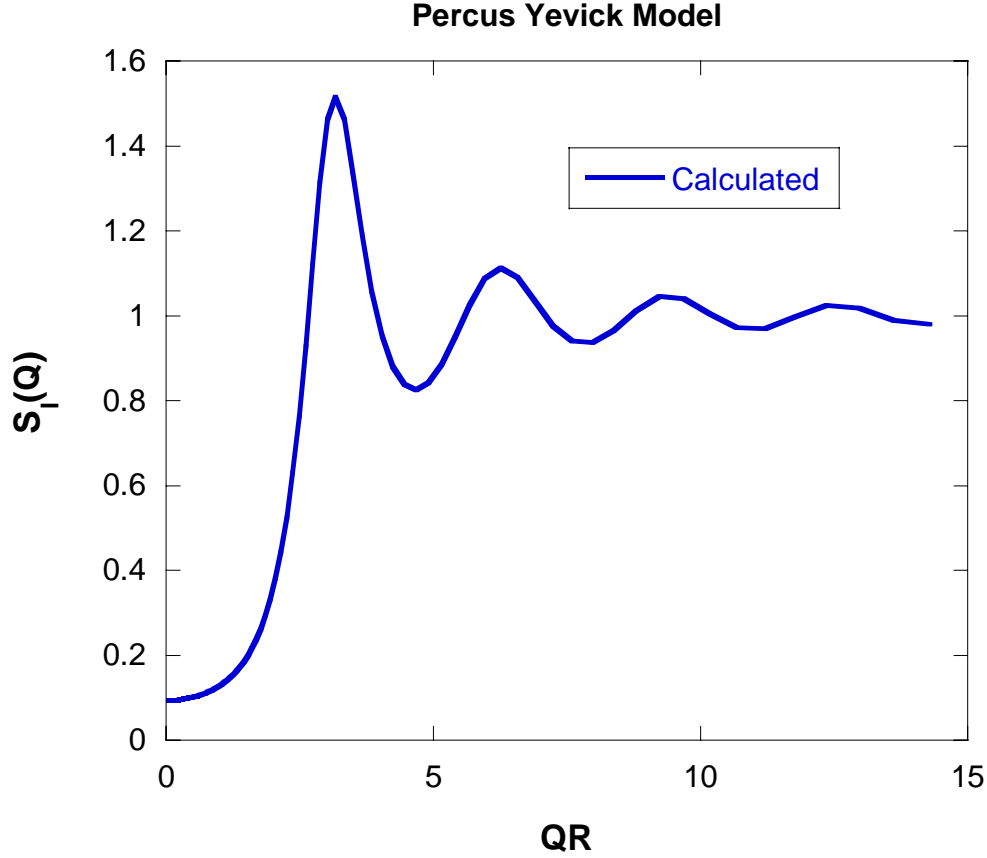
Figure 3: Inter-particle structure factor $S_I(QR)$ *vs* QR prediction from the Percus-Yevick model (with hard sphere potential) for $\phi = 0.30$. Note that the sphere radius is $R = D/2$.

The scattering cross section involves the product of the form factor and the structure factor:

$$\frac{d\Sigma(Q)}{d\Omega} = \Delta\rho^2 \phi V_P P(Q) S_I(Q) . \qquad (12)$$

Here $\Delta\rho^2$ is the contrast factor, ϕ is the volume fraction and V_P is the particle volume ($V_P = 4\pi R^3/3$).Note that in this simple "hard sphere" interaction potential model, the sphere diameter that enters in the form factor is taken to be the same as the hard sphere radius used in the structure factor.

Percus Yevick Model
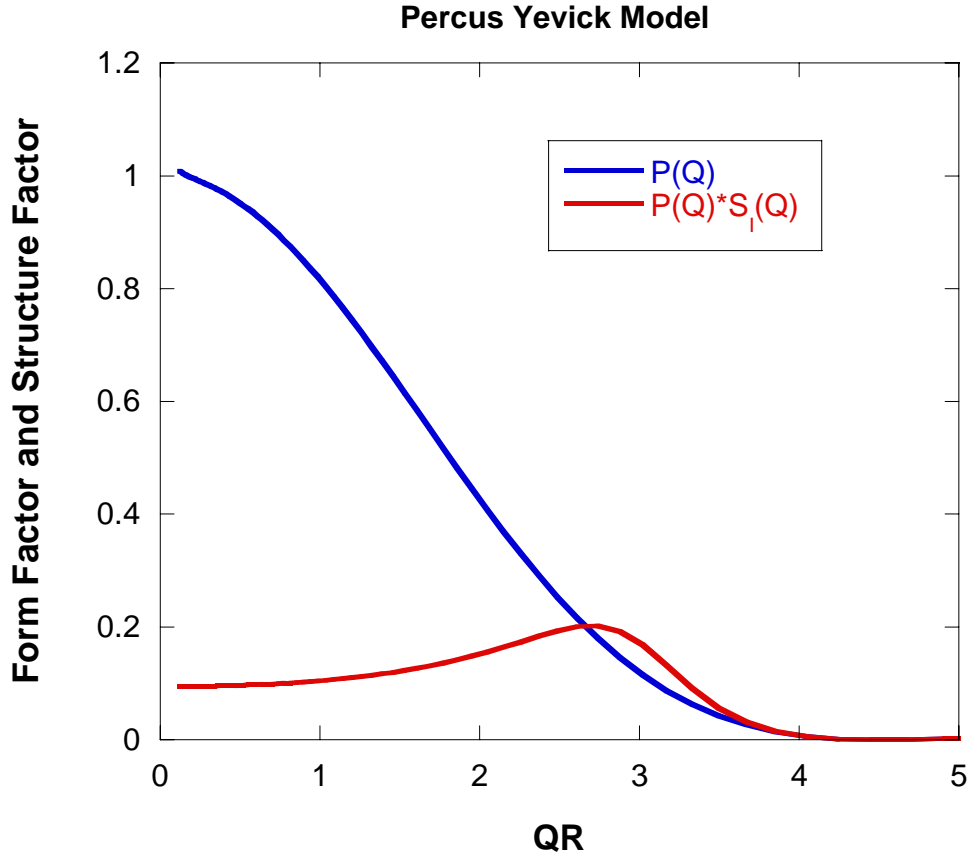
Figure 4: Form factor P(Q) for isolated spheres (infinite dilution limit), and product $P(Q)S_I(Q)$ for a solution of spheres with a volume fraction of $\phi = 0.30$. The Percus-Yevick model (hard sphere potential) has been used to model the inter-particle structure factor $S_I(Q)$.

3. THE MEAN SPHERICAL APPROXIMATION

When Coulomb interactions are present another closure relation to the OZ equation is applied; the Mean Spherical Approximation (Hayter-Penfold, 1981). Consider a scattering system consisting of macroions (charged positive), counter ions (charged negative) and solvent. The Coulomb interaction potential is defined as:

$$U(r) = \pi\varepsilon_0\varepsilon D^2\psi_0^2 \frac{\exp(-\kappa(r-D))}{r} \text{ for } r > D. \tag{13}$$

The macroion surface interaction potential is given by:

$$\psi_0 = \frac{z_m}{\pi\varepsilon_0\varepsilon(2 + \kappa D)}. \tag{14}$$

The following parameters have been defined:

ε_0: Permittivity of free vacuum

ε: Dielectric constant

D: Macroion diameter

κ : Debye-Huckel inverse screening length

z_m: Macroion electric charge (number of electrons).

The Debye-Huckel screening parameter (inverse length) is expressed as follows:

$$\kappa^2 = \frac{e^2}{k_B T} z_m \overline{N} \tag{15}$$

Here e is the electron charge, $z_m e$ is the macroion charge, $\overline{N}$ is the macroion number density (number per unit volume) and $k_B T$ is the sample temperature in absolute units.

Dimensionless parameters are defined:

$$x = \frac{r}{D}, \ k = \kappa D, \ K = QD \ \text{and} \ \beta = \frac{1}{k_B T}. \tag{16}$$

Along with the following contact potential (for r = 2D) as:

$$\gamma \exp(-k) = \beta \pi \varepsilon_0 \varepsilon \psi_0^2. \tag{17}$$

The Mean Spherical Approximation (MSA) closure relation to the Ornstein-Zernike equation is given by:

$$c(r) = -\beta U(r) \qquad \text{for } r > D \tag{18}$$
$$h(r) = -1 \qquad \text{for } r < D.$$

Note that the limiting case for which $\gamma \to 0$ or $k \to \infty$ yields the Percus-Yevick result.

The MSA closure is used to solve for c(r):

$$c(r) = A + Bx + \frac{1}{2}\phi A x^3 + \frac{C \sinh(kx)}{x} + \frac{F(\cosh(kx)-1)}{x} \qquad \text{for x<1}$$
$$c(r) = -\gamma \frac{\exp(-kx)}{x} \qquad \text{for x>1.} \tag{19}$$

The structure factor is obtained as:

$$S_I(Q) = \frac{1}{1 - \overline{N}C(Q)} \tag{20}$$

With:

$$\frac{\overline{N}C(Q)}{24\phi} = \frac{A(\sin(K) - K\cos(K))}{K^3} + \frac{B\left[\left(\frac{2}{K^2} - 1\right)K\cos(K) + 2\sin(K) - \frac{2}{K}\right]}{K^3}$$

$$+ \frac{\phi A\left[\frac{24}{K^3} + 4\left(1 - \frac{6}{K^2}\right)\sin(K) - \left(1 - \frac{12}{K^2} + \frac{24}{K^4}\right)K\cos(K)\right]}{2K^3}$$

$$+ \frac{C(k\cosh(k)\sin(K) - K\sinh(k)\cos(K))}{K(K^2 + k^2)}$$

$$+ \frac{F[k\sinh(k)\sin(K) - K(\cosh(k)\cos(K) - 1)]}{K(K^2 + k^2)}$$

$$+ \frac{F(\cos(K) - 1)}{K^2} - \frac{\gamma\exp(-k)(k\sin(K) + K\cos(K))}{K(K^2 + k^2)}. \qquad (21)$$

The macroion volume fraction $\phi = \pi\overline{N}D^3/6$ has been expressed in terms of the macroion number density $\overline{N}$. The forward scattering limit is given by $S_I(0) = -1/A$.

Note that expressions for the constants A, B, C, and F are too lengthy to reproduce here. They can be found in the original publication (Hayter-Penfold, 1981). F is the solution of a 4th power polynomial equation.
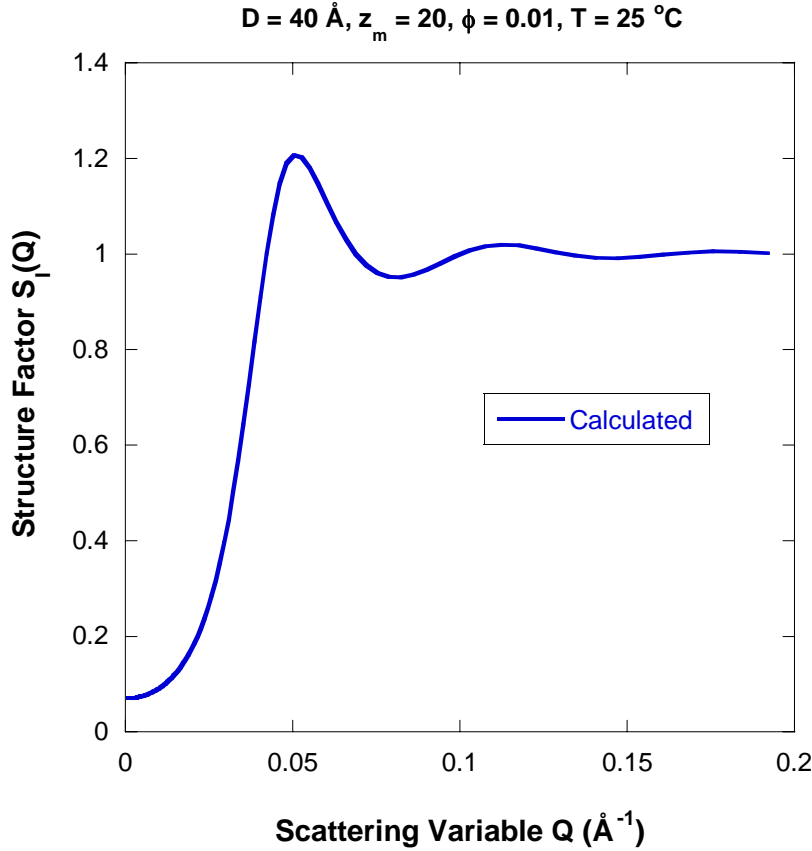
Figure 5: Variation of the structure factor $S_I(Q)$ obtained from the MSA for a spherical macroion diameter of $D = 40$ Å, macroion charge of $z_m = 20$ electrons, a volume fraction of $\phi = 0.01$ and at $T = 25\ ^\circ C$. The dielectric constant $\varepsilon = 78$ for D_2O at $25\ ^\circ C$.

4. THE RANDOM PHASE APPROXIMATION

Consider now particles with internal structure or polymers made out of spherical monomeric units. Note that spheres are assumed to fill the particles or replace the monomers in polymers. The Random Phase Approximation (RPA) provides another closure relation used to solve the OZ equation. The RPA assumes that $c(r) = -w(r)/k_BT$. Note that within the RPA, different notation is used for interaction potentials. By convention, these are called $w(r)$ for polymers and $U(r)$ for particulate systems.

The intra-particle contributions are included in the Ornstein-Zernike equation as follows (in Fourier space):

$$H(Q) = S_0(Q)C(Q)S_0(Q) + S_0(Q)C(Q)\overline{N}H(Q). \qquad (22)$$

Along with the RPA closure relation:

$$\overline{NC}(Q) = -\frac{W(Q)}{k_B T} .$$ (23)

This closure is reminiscent of the MSA closure relation for $r > \sigma$. Note the following relations for particles with internal structure (or polymers with spherical monomers):

$$S_I(Q) = \frac{1}{1 - S_0(Q)\overline{NC}(Q)}$$ (24)

$$S(Q) = S_0(Q)S_I(Q) = \frac{S_0(Q)}{1 - S_0(Q)\overline{NC}(Q)}$$

It follows that:

$$S^{-1}(Q) = S_0^{-1}(Q) + \frac{W(Q)}{k_B T} .$$ (25)

This is the Random Phase Approximation result obtained for compressible polymer mixtures. The scattering cross section is given by:

$$\frac{d\Sigma(Q)}{d\Omega} = \Delta\rho^2 S(Q) .$$ (26)

Note that this approach can be extended to the multi-component case by changing the various structure factors to matrices.

Note that the mean field approximation does not model the local interactions properly for inter-particle inter-distances smaller than particle sizes since packing effects on thermodynamics and phase separation are neglected. For this reason, the g(r) obtained from such a mean field approach does not show realistic oscillations for the neighboring coordination shells. The appeal of this approach, however, is that it gives simple analytical results.

REFERENCES

J.P. Hansen and I.R. McDonald, "Theory of Simple Liquids" Academic Press, London (1986)

L.S. Ornstein and F. Zernike, Phys. Z. <u>19</u>, 134 (1918)

J.K. Percus, G.J. Yevick, "Analysis of Classical Statistical Mechanics by Means of Collective Coordinates", Phys. Rev. <u>110</u> 1 (1958).

J.H. Hayter and J. Penfold, "An Analytic Structure Factor for Macroion Solutions", Molecular Physics 42, 109-118 (1981)

QUESTIONS

1. Does a numerical solution of the Ornstein-Zernike integral equation (with a realistic closure relation) describe local packing adequately? How about a mean field analytical solution (using the mean spherical approximation)?
2. Can the scattering cross section for a concentrated solution of particles (colloidal suspension for example) be described as the product of a single-particle and an inter-particle structure factors?
3. Name the closure relation that yields an analytical solution to the OZ integral equation in the case of hard sphere interaction potential.
4. What approach gives the most realistic solution of the Ornstein-Zernike equation?
5. What is the Mean Spherical Approximation (so called MSA)? What systems are well described by the MSA?
6. Are the Random Phase Approximation (used to describe polymer systems) and the Ornstein-Zernike equation (used to describe particulate systems) related at all?

ANSWERS

1. A numerical solution of the Ornstein-Zernike integral equation along with a realistic closure relation describes local packing well. A mean field analytical solution is too simplistic and yields correct over all trends but incorrect local packing information.
2. The scattering cross section for a concentrated solution of particles can be described as the product of a single-particle and an inter-particle structure factors provided that the particles are not elongated.
3. The Percus-Yevick closure relation yields a simple analytical solution to the OZ integral equation for the hard sphere interaction potential.
4. A numerical solution of the Ornstein-Zernike equation along with one of the closure relations gives more realistic results than highly approximated analytical solutions.
5. The Mean Spherical Approximation (MSA) is a closure relation used to solve the Ornstein-Zernike equation. Charged systems are well described by the MSA since Coulomb interactions are included. The MSA yields analytical (albeit lengthy) results.
6. The Random Phase Approximation (used to describe polymer systems) is a mean-field closure relation to the Ornstein-Zernike equation. The RPA closure is a simplified form of the MSA closure.

Chapter 33 - **SCATTERING FROM FRACTAL SYSTEMS**

Consider a system of interacting particles in a medium. The particles could have fractal (rough) surfaces or they could form a mass fractal structure through clustering. In general terms, the scattering cross section is given by:

$$\frac{d\Sigma(Q)}{d\Omega} = \overline{N}\Delta\rho^2 V_P{}^2 P(Q)S_I(Q)$$

(1)

$\overline{N} = (N/V)$ is the particle number density, VP is the particle volume, P(Q) is the form factor and SI(Q) is the structure factor. The two types of fractal behavior (mass fractal and surface fractal) have been investigated (Bale-Schmidt, 1984; Teixeira, 1988) and will be discussed in turn.

1. MASS FRACTAL

A mass fractal is a structure containing branching and crosslinking to form a 3D network.
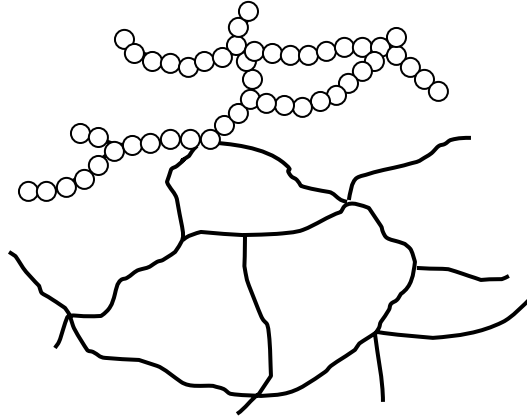
Figure 1: Schematic representation of a mass fractal structure containing branching points and crosslinks. This structure is made out of monomeric units or small particles that are clustered.

The inter-particle structure factor is given by:

$$S_I(Q) = 1 + 4\pi\overline{N}\int_0^\infty dr\ r^2 [g(r) - 1]\frac{\sin(Qr)}{Qr}$$

(2)

Here g(r) is the pair correlation function. It is the probability of finding another scatterer at position $\vec{r}$ given that there is a scatterer at the origin. Defining a mass fractal dimension D, g(r) can be modeled as follows:

$$\overline{N}[g(r) - 1] = \frac{D}{4\pi r_0^{\,D}} r^{D-3} \exp\left(-\frac{r}{\xi}\right).$$ (3)

The parameter ξ is a "correlation length" beyond which correlations die out. Performing the Fourier transform, one obtains:

$$S_1(Q) = 1 + \frac{1}{(Qr_0)^D} \frac{D\Gamma(D-1)}{\left[1 + 1/(Q^2\xi^2)\right]^{(D-1)/2}} \sin\left[(D-1)\tan^{-1}(Q\xi)\right].$$ (4)

The small-Q limit simplifies to:

$$S(Q \to 0) = \Gamma(D+1)\left(\frac{\xi}{r_0}\right)^D \left\{1 - \frac{D(D+1)}{6} Q^2\xi^2\right\}.$$ (5)

This gives an estimate of the radius of gyration for a mass fractal as:

$$R_g^{\,2} = \frac{D(D+1)\xi^2}{2}.$$ (6)

The mass fractal dimension D varies between 2 and 3 depending on the structure density.

Note that if the mass fractal is formed of a network of spheres with uniform density and smooth surface, P(Q) is modeled by the usual form factor for a sphere. The case of particles with a fractal surface is considered next.

2. SURFACE FRACTAL

Consider a particle with fractal (rough) surface of fractal dimension Ds between 3 and 4.
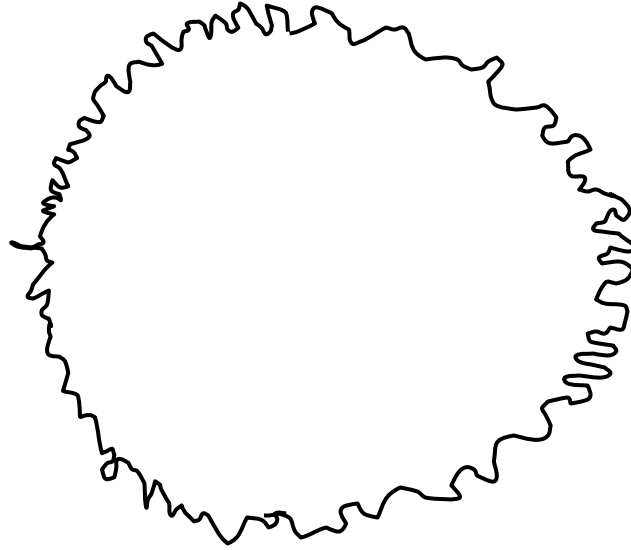
Figure 2: Schematic representation of a surface fractal structure of intermediate roughness.

The Porod law can be generalized to fractal surfaces through the following scaling for the surface:

$$S_P \sim \left(\frac{r}{R}\right)^{D_s}$$

(7)

The form factor for the particle with fractal surface becomes at high-Q:

$$V_P^2 P(Q) \sim \pi S_P \Gamma(5 - D_s) \sin\left[\frac{\pi(D_s - 1)}{2}\right] \frac{1}{Q^{6-D_s}}$$

(8)

A Porod plot (Log[I(Q)] *vs* Q) yields a slope of -6+Ds. A surface fractal dimension Ds = 2 corresponds to a smooth surface which, for high-Q, gives:

$$P(Q) \sim \frac{3}{2R^3} \frac{S_P}{V_P} \frac{1}{Q^4}$$

(9)

SP and VP are the particle surface and volume. This is the well known Porod law for smooth surfaces.

3. FRACTAL POROD EXPONENTS

A figure summarizes the various fractal Porod law exponents for mass fractal systems such as polymer chains and networks and for fractal surfaces.
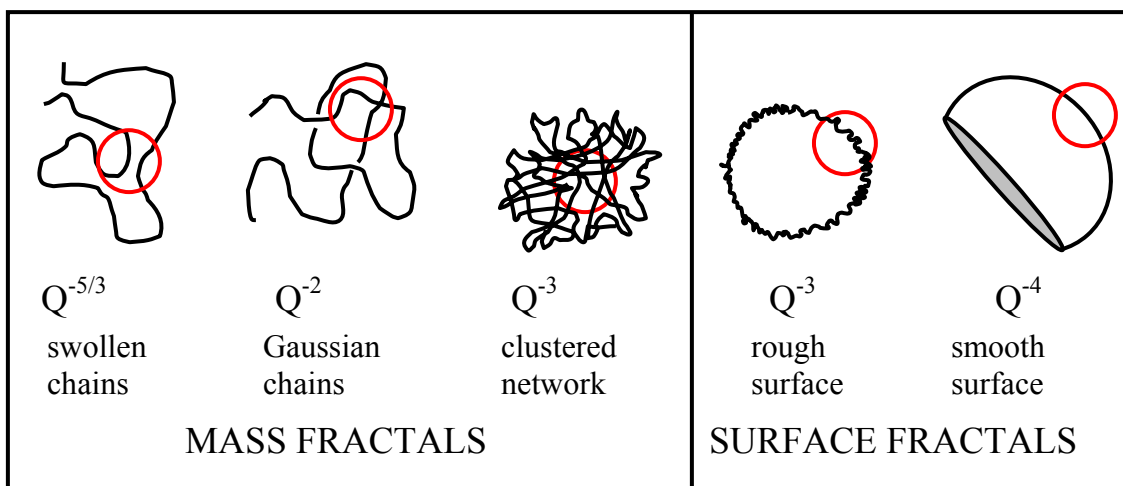
Figure 3: Assortment of fractal Porod exponents.

REFERENCES

H.D. Bale and P.W. Schmidt, "Small-Angle X-Ray-Scattering Investigation of Submicroscopic Porosity with Fractal Properties", Phys. Rev. Lett. <u>53,</u> 596-599 (1984)

J. Teixeira, "Small-Angle Scattering by Fractal Systems", J. Appl. Cryst. <u>21,</u> 781-785 (1988)

QUESTIONS

1. What is the Porod exponent for scattering from a fully swollen polymer coil?
2. What is the Porod exponent for scattering from a very rough surface? How about from a smooth surface?
3. What is the range of mass fractal Porod exponents for scattering from a clustered network?

ANSWERS

1. The Porod exponent for scattering from a fully swollen polymer coil is 5/3.
2. The Porod exponent for scattering from a very rough surface is 3. For a smooth surface, the Porod exponent is 4.
3. Scattering from a clustered network has a range of mass fractal Porod exponents between 2 and 3.

Chapter 34 – THE MULTI-COMPONENT
RANDOM PHASE APPROXIMATION

1. COMPRESSIBLE POLYMER MIXTURE

Consider a homogeneous mixture consisting of m polymer components. Components are homopolymers, blocks in copolymers or solvents. Within the Random Phase Approximation formalism (De Gennes, 1979; Benmouna et al, 1987; Akcasu-Tombakoglu, 1990) for compressible mixtures, the scattering cross section for this system is expressed in general terms as follows:

$$\frac{d\Sigma(Q)}{d\Omega} = \underline{\rho}^T . \underline{\underline{S}}(Q) . \underline{\rho} \ . \tag{1}$$

Here $\underline{\underline{S}}(Q)$ is an m*m matrix and $\underline{\rho}$ is a column vector containing the m scattering length densities. $\underline{\rho}^T$ is the "transpose" row vector. The fully interacting scattering factors $\underline{\underline{S}}(Q)$ are expressed in terms of the non-interacting (so called "bare") scattering factors $\underline{\underline{S_0}}(Q)$ and inter-monomer interaction potentials $\underline{\underline{W}}$ as follows:

$$\underline{\underline{S}}^{-1}(Q) = \underline{\underline{S_0}}^{-1}(Q) + \frac{\underline{\underline{W}}}{k_B T} \ . \tag{2}$$

This equation can easily be derived using the linear response approach without the incompressibility constraint. The incompressibility condition simplifies things as described next.

2. INCOMPRESSIBLE POLYMER MIXTURE

Now consider one of the m polymer components as the "background" component. This can be a homopolymer or a solvent. It cannot be a block that belongs to a copolymer. Imposing the incompressibility condition eliminates the background component. This leaves (m-1) explicit components. Even though this formalism is general, it is described here explicitly for four components (m = 4). The Random Phase Approximation formalism for incompressible mixtures yields the following macroscopic scattering cross section:

$$\frac{d\Sigma(Q)}{d\Omega} = \underline{\Delta\rho}^T . \underline{\underline{S}}(Q) . \underline{\Delta\rho} \tag{3}$$

$$= \Delta\rho_1{}^2 S_{11}(Q) + \Delta\rho_2{}^2 S_{22}(Q) + \Delta\rho_3{}^2 S_{33}(Q) + 2\Delta\rho_1\Delta\rho_2 S_{12}(Q) + 2\Delta\rho_1\Delta\rho_3 S_{13}(Q) + 2\Delta\rho_2\Delta\rho_3 S_{23}(Q)$$

In this general RPA formalism (Akcasu-Tombakoglu, 1990; Hammouda, 1993) $\underline{\underline{S}}(Q)$ is an $(m-1)*(m-1)$ matrix and $\underline{\Delta\rho}$ is an $(m-1)$ column vector for the scattering length density differences (the scattering length density of the background component is subtracted for each component). The new general relation follows:

$$\underline{\underline{S}}^{-1}(Q) = \underline{\underline{S_0}}^{-1}(Q) + \underline{\underline{v}}(Q) \tag{4}$$

$$\underline{\underline{S}}(Q) = \left(\underline{\underline{1}} + \underline{\underline{S_0}}(Q).\underline{\underline{v}}(Q)\right)^{-1}\underline{\underline{S_0}}(Q).$$

The "bare" scattering factor $\underline{\underline{S_0}}(Q)$ is a diagonal matrix for homopolymer polymer blends and solutions. Mixtures containing copolymers contain off-diagonal elements.

$$S_0(Q) = \begin{bmatrix} S^0_{11}(Q) & S^0_{12}(Q) & S^0_{13}(Q) \\ S^0_{21}(Q) & S^0_{22}(Q) & S^0_{23}(Q) \\ S^0_{31}(Q) & S^0_{32}(Q) & S^0_{33}(Q) \end{bmatrix}. \tag{5}$$

The interaction matrix is expressed in terms of the bare structure factor for the background component and the various Flory-Huggins interaction parameters.

$$v_{ii}(Q) = \frac{1}{S^0_{44}(Q)} - 2\frac{\chi_{i4}}{v_0} \quad \text{for } i = 1,2,3 \tag{6}$$

$$v_{ij}(Q) = \frac{1}{S^0_{44}(Q)} + \frac{\chi_{ij}}{v_0} - \frac{\chi_{i4}}{v_0} - \frac{\chi_{j4}}{v_0} \quad \text{for } i,j = 1,2,3.$$

The various scattering length densities for the various components are given by:

$$\Delta\rho_i = \rho_i - \rho_4 \quad \text{for } i = 1,2,3. \tag{7}$$

The incompressibility assumption in this case becomes:

$$v_1 n_1(Q) + v_2 n_2(Q) + v_3 n_3(Q) + v_4 n_4(Q) = 0. \tag{8}$$

$$S_{11}(Q) = < v_1 n_1(-Q).v_1 n_1(Q) > = -S_{12}(Q) - S_{13}(Q) - S_{14}(Q).$$

Note that the spinodal condition is obtained for

$$\text{Det}\left(\underline{\underline{1}} + \underline{\underline{S_0}}(0).\underline{\underline{v}}(0)\right) = 0. \tag{9}$$

Here $\underline{\underline{1}}$ is the identity matrix and $\text{Det}(...)$ denotes the determinant of a matrix.

3. THE SINGLE-CHAIN FORM FACTORS

The various single-chain form factors for homopolymers and block copolymers are expressed as follows:

$$S^0_{ii}(Q) = n_i \phi_i v_i P_i(Q) \tag{10}$$

$$S^0_{ij}(Q) = \sqrt{n_i \phi_i v_i n_j \phi_j v_j} \, P_{ij}(Q)$$

$$P_i(Q) = \frac{2}{Q^4 R_{gi}^4} \left[\exp(-Q^2 R_{gi}^2) - 1 + Q^2 R_{gi}^2 \right]$$

$$P_{ij}(Q) = F_i(Q) E_k(Q) F_j(Q) = \left(\frac{1 - \exp\left(-Q^2 R_{gi}^2\right)}{Q^2 R_{gi}^2} \right) \left(\exp(-Q^2 R_{gk}^2) \right) \left(\frac{1 - \exp\left(-Q^2 R_{gj}^2\right)}{Q^2 R_{gj}^2} \right).$$

For Gaussian chains, the radii of gyration are given in terms of the degree of polymerization n_i, and statistical segment lengths a_i as follows:

$$R_{gi}^2 = \frac{n_i a_i^2}{6}. \tag{11}$$

The last expression is better explained through examples. This is done next. Consider examples of block copolymer sequences.
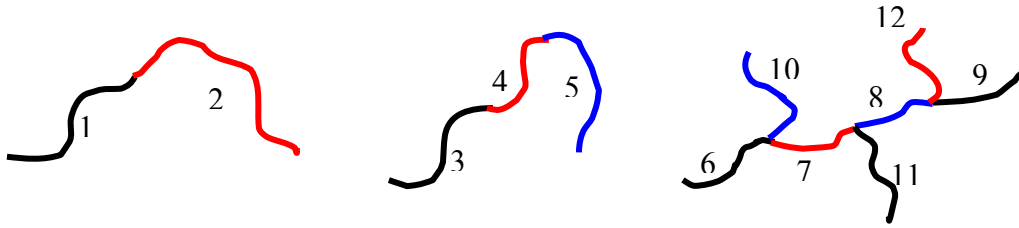
Figure 1: Examples of block copolymer sequences.

$F(Q)$ is used for the two blocks under consideration and $E(Q)$ is used for the blocks in-between. Some inter-block form factors are given here:

$$P_{12}(Q) = F_1(Q) F_2(Q) \tag{12}$$
$$P_{35}(Q) = F_3(Q) E_4(Q) F_5(Q)$$
$$P_{69}(Q) = F_6(Q) E_7(Q) E_8(Q) F_9(Q).$$

These results are valid for Gaussian chains following a random walk (theta condition). For fully swollen chains, the excluded volume parameter approach could be used.

4. BINARY HOMOPOLYMER BLEND MIXTURE

The simplest case to consider is that of a binary blend mixture of two homopolymers (components 1 and 2). In this case, component 2 is taken to be the background component. The results are:

$$S^0_{11}(Q) = n_1 \phi_1 v_1 P_1(Q) \tag{13}$$

$$v_{11}(Q) = \frac{1}{S^0_{22}(Q)} - 2\frac{\chi_{12}}{v_0}$$

$$\frac{1}{S_{11}(Q)} = \frac{1}{S^0_{11}(Q)} + v_{11}(Q)$$

$$S_{11}(Q) = \frac{S^0_{11}(Q)}{1 + v_{11}(Q)S^0_{11}(Q)}.$$

This is the so-called de Gennes formula (De Gennes, 1979) used to describe binary polymer blends in the mixed-phase region.

5. TERNARY HOMOPOLYMER BLEND MIXTURE

The case of a ternary homopolymer mixture is worked out similarly. Component 3 is taken to be the background component. The results are:

$$S^0_{11}(Q) = n_1 \phi_1 v_1 P_1(Q) \tag{14}$$
$$S^0_{22}(Q) = n_2 \phi_2 v_2 P_2(Q)$$
$$S^0_{33}(Q) = n_3 \phi_3 v_3 P_3(Q)$$

$$v_{11}(Q) = \frac{1}{S^0_{33}(Q)} - 2\frac{\chi_{13}}{v_0} \tag{15}$$

$$v_{22}(Q) = \frac{1}{S^0_{33}(Q)} - 2\frac{\chi_{23}}{v_0}$$

$$v_{12}(Q) = \frac{1}{S^0_{33}(Q)} + \frac{\chi_{12}}{v_0} - \frac{\chi_{13}}{v_0} - \frac{\chi_{23}}{v_0}$$

The partial structure factors for the fully interacting mixture are as follow:

$$S_{11}(Q) = \frac{S^0{}_{11}(Q)\left(1 + v_{22}S^0{}_{22}(Q)\right)}{\left(1 + v_{11}S^0{}_{11}(Q)\right)\left(1 + v_{22}S^0{}_{22}(Q)\right) - v_{12}{}^2 S^0{}_{11}(Q)S^0{}_{22}(Q)} \qquad (16)$$

$$S_{22}(Q) = \frac{S^0{}_{22}(Q)\left(1 + v_{11}S^0{}_{11}(Q)\right)}{\left(1 + v_{11}S^0{}_{11}(Q)\right)\left(1 + v_{22}S^0{}_{22}(Q)\right) - v_{12}{}^2 S^0{}_{11}(Q)S^0{}_{22}(Q)}$$

$$S_{12}(Q) = \frac{- S^0{}_{11}(Q) v_{12} S^0{}_{22}(Q)}{\left(1 + v_{11}S^0{}_{11}(Q)\right)\left(1 + v_{22}S^0{}_{22}(Q)\right) - v_{12}{}^2 S^0{}_{11}(Q)S^0{}_{22}(Q)}$$

Recall that the cross section for an incompressible ternary blend mixture is given by (Benmouna et al, 1987; Akcasu-Tombakoglu, 1990):

$$\frac{d\Sigma(Q)}{d\Omega} = \Delta\rho_1{}^2 S_{11}(Q) + \Delta\rho_2{}^2 S_{22}(Q) + 2\Delta\rho_1\Delta\rho_2 S_{12}(Q). \qquad (17)$$

This case applies to a ternary polymer mixture in the homogeneous phase region.

6. BLEND MIXTURE OF A COPOLYMER AND A HOMOPOLYMER

The case of a homopolymer and a copolymer mixture is also readily obtained from the RPA formalism. In this case, the background component is taken to be the homopolymer (component 3). The diblock is formed of components 1-2. The results follow.

$$S_{11}(Q) = \frac{S^0{}_{11}\left(1 + v_{21}S^0{}_{12} + v_{22}S^0{}_{22}\right) - S^0{}_{12}\left(v_{21}S^0{}_{11} + v_{22}S^0{}_{21}\right)}{\left(1 + v_{11}S^0{}_{11} + v_{12}S^0{}_{21}\right)\left(1 + v_{21}S^0{}_{12} + v_{22}S^0{}_{22}\right) - \left(v_{11}S^0{}_{12} + v_{12}S^0{}_{22}\right)\left(v_{21}S^0{}_{11} + v_{22}S^0{}_{21}\right)}$$

$$(18)$$

$$S_{22}(Q) = \frac{S^0{}_{22}\left(1 + v_{12}S^0{}_{21} + v_{11}S^0{}_{11}\right) - S^0{}_{21}\left(v_{12}S^0{}_{22} + v_{11}S^0{}_{12}\right)}{\left(1 + v_{11}S^0{}_{11} + v_{12}S^0{}_{21}\right)\left(1 + v_{21}S^0{}_{12} + v_{22}S^0{}_{22}\right) - \left(v_{11}S^0{}_{12} + v_{12}S^0{}_{22}\right)\left(v_{21}S^0{}_{11} + v_{22}S^0{}_{21}\right)}$$

$$S_{12}(Q) = \frac{- S^0{}_{11}\left(v_{11}S^0{}_{12} + v_{12}S^0{}_{22}\right) + S^0{}_{12}\left(1 + v_{11}S^0{}_{11} + v_{12}S^0{}_{21}\right)}{\left(1 + v_{11}S^0{}_{11} + v_{12}S^0{}_{21}\right)\left(1 + v_{21}S^0{}_{12} + v_{22}S^0{}_{22}\right) - \left(v_{11}S^0{}_{12} + v_{12}S^0{}_{22}\right)\left(v_{21}S^0{}_{11} + v_{22}S^0{}_{21}\right)}$$

The (Q) dependence has been dropped to lighten the notation.

7. THE DIBLOCK COPOLYMER CASE

The RPA result for polymer mixtures containing only copolymers (no homopolymers or solvent) is more complex and will not be included here. It has, however, been worked out explicitly using a matrix notation and assuming one of the blocks as the background component. The result for the simple case of a diblock copolymer is included here.

$$S_{11}(Q) = \frac{S^0{}_{11}(Q)S^0{}_{22}(Q) - S^0{}_{12}(Q)S^0{}_{21}(Q)}{\left[S^0{}_{11}(Q) + S^0{}_{22}(Q) + 2S^0{}_{12}(Q)\right] - \dfrac{2\chi_{12}}{v_0}\left[S^{0\,11}(Q)S^0{}_{22}(Q) - S^0{}_{12}(Q)S^0{}_{21}(Q)\right]} \,. \quad (19)$$

This is the so-called Leibler formula (Leibler, 1980). This formula can be derived using the linear response approach. Note that the binary blend case is recovered by setting the bare structure factor cross term $S^0{}_{12}(Q) = 0$.

8. THE TRIBLOCK COPOLYMER CASE

Consider a triblock copolymer in solution. In our terminology, this is a four "component" case with the triblock as components 1-2-3 and the solvent as component 4. Block 1 is connected to block 2 which is connected to block 3. Block 1 is not connected to block 3. Consider component 4 as the "background" component and apply the multi-component RPA formula:

$$S_0(Q) = \begin{bmatrix} S^0{}_{11}(Q) & S^0{}_{12}(Q) & 0 \\ S^0{}_{21}(Q) & S^0{}_{22}(Q) & S^0{}_{23}(Q) \\ 0 & S^0{}_{32}(Q) & S^0{}_{33}(Q) \end{bmatrix}. \quad (20)$$

In order to work out the various elements $S_{ij}(Q)$, 3*3 matrix inversion and matrix multiplication are needed. The result is too lengthy to reproduce here. The derivation is, however, straightforward (Akcasu et al, 1993).

9. DISCUSSION

The RPA approach described here can handle more complex polymer mixtures containing complex architectures and blockiness (Hammouda, 1993). It amounts to inverting and multiplying larger matrices. The effect of chain stiffness has also been included in limited cases. Mixtures of flexible and stiff polymer chains are characterized by the spinodal condition as well as by the isotropic-to-nematic phase transition (Hammouda, 1993).

It should be emphasized, however, that this mean-field approach applies strictly in the mixed-phase region (not too close to the phase boundary line). Non-mean field corrections have been worked out. These are, however, outside the scope of this tutorial.

REFERENCES

P.G. de Gennes, "Scaling Concepts in Polymer Physics", Cornell University Press, New York (1979).

L. Leibler, "Theory of Microphase Separation in Block Copolymers", Macromolecules 13, 1602-1617 (1980).

M. Benmouna, H. Benoit, R. Borsali, M. Duval, "Theory of dynamic scattering from copolymer solutions using the random phase approximation ", Macromolecules 20, 2620-2624 (1987).

A.Z. Akcasu and M. Tombakoglu, "Dynamics of Copolymer and Homopolymer Mixtures in Bulk and in Solution via the Random Phase Approximation", Macromolecules 23, 607-612 (1990).

A.Z. Akcasu, R. Klein and B. Hammouda, "Dynamics of Multicomponent Polymer Mixtures via the Random Phase Approximation Including Hydrodynamic Onteractions", Macromolecules 26, 4136-4143 (1993).

B. Hammouda, "SANS from Homogeneous polymer Mixtures: A Unified Overview", Advances in Polymer Science 106, 87 (1993). B. Hammouda, "Scattering from Mixtures of Flexible and Stiff Polymers", J. Chem. Phys. 98, 3439-3444 (1993).

QUESTIONS

1. Write down the generalized Random Phase Approximation formula for multi-component incompressible polymer mixtures. Does it apply to pure copolymers?
2. Write down the scattering cross section for a multi-component polymer mixture of arbitrary composition in matrix form.
3. What is the size of the matrix to be inverted for an incompressible mixture with four polymer components.
4. Write down the so-called de Gennes formula for scattering from a binary polymer blend mixture. Define the various terms.
5. Write down the $S_{11}(Q)$ interacting structure factor for a ternary polymer blend mixture.
6. Write down the so-called Leibler formula for scattering from a diblock copolymer.
7. Stiff (rodlike) polymers are characterized by orientational phase transitions beside the spinodal and binodal lines. Name the two best known transitions.

ANSWERS

1. The Random Phase Approximation general formula for multi-component incompressible polymer mixtures expresses the fully interacting structure factor $\underline{\underline{S}}(Q)$ in terms of the "bare" (non-interacting) structure factor $\underline{\underline{S}}_0(Q)$ and the various interaction factors $\underline{v}(Q)$ as $\underline{\underline{S}}^{-1}(Q) = \underline{\underline{S}}_0^{-1}(Q) + \underline{v}(Q)$. This does not apply to pure copolymers since a "background" component (either a homopolymer or a solvent) is required.

2. The scattering cross section for a multi-component polymer mixture of arbitray composition is expressed as $\dfrac{d\Sigma(Q)}{d\Omega} = \vec{\rho}^T.\underline{\underline{S}}(Q).\vec{\rho}$ where $.\vec{\rho}$ is a column vector containing all of the scattering length densities and $\underline{S}(Q)$ is a matrix containing all of the structure factors.

3. A homogeneous polymer mixture with four components generates a 3*3 RPA matrix to be inverted. The fourth component is taken to be the background component.

4. The de Gennes formula for scattering from a binary polymer blend mixture is expressed as

$$\frac{1}{S_{11}(Q)} = \frac{1}{S^0{}_{11}(Q)} + \frac{1}{S^0{}_{22}(Q)} - \frac{2\chi_{12}}{v_0}.$$ Here $S^0{}_{11}(Q)$ and $S^0{}_{22}(Q)$ are the bare structure

factors, χ_{12} is the Flory-Huggins interaction parameter and v_0 is a reference volume usually

expressed as $v_0 = \sqrt{v_1 v_2}$ where v_1 and v_2 are the specific monomer volumes.

5. The structure factor for a ternary polymer blend mixture is given by

$$S_{11}(Q) = \frac{S^0{}_{11}(Q)\left(1 + v_{22}S^0{}_{22}(Q)\right)}{\left(1 + v_{11}S^0{}_{11}(Q)\right)\left(1 + v_{22}S^0{}_{22}(Q)\right) - v_{12}{}^2 S^0{}_{11}(Q)S^0{}_{22}(Q)}.$$ The various factors are

defined in the text.

6. The Leibler formula is expressed as $S_{11}(Q) = W(Q) \Big/ \left[S(Q) - \frac{2\chi_{12}}{v_0} W(Q) \right]$ where

$W(Q) = S^0{}_{11}(Q)S^0{}_{22}(Q) - S^0{}_{12}(Q)S^0{}_{21}(Q)$ and $S(Q) = S^0{}_{11}(Q) + S^0{}_{22}(Q) + 2S^0{}_{12}(Q)$.

7. Stiff polymers are characterized by the spinodal and binodal temperatures as well as orientational transitions leading from the isotropic to the nematic or smectic phases.

Part H – SANS FROM POLYMERS

Chapter 35 - **INTRODUCTION TO POLYMERS**

Polymer research makes up a good fraction of beamtime use on SANS instruments. Using the partial deuteration method, SANS has been useful for investigations of chain conformations and miscibility in polymer solutions and polymer blend mixtures as well as in other polymeric systems. Many aspects of polymer research have benefited from the SANS technique.

1. WHAT ARE POLYMERS?

Polymers are synthetic macromolecules that make up a great deal of what we use in our daily lives. They include low-cost disposable conveniences (like milk containers or soda bottles) to high-tech structural materials (like hip joint replacement or computer CDs). Polymers are split into "bunching" categories like solutions or blends (alloyed polymers), thermoplastics (that can deform) or thermosets (that are hard to deform), with linear or branched architectures, that are amorphous or crystalline, etc. (Bandrup-Immergut 1975; Kawakatsu, 2004). Liquid crystal polymers contain stiff mesogen groups that increase material toughness. Their high degree of alignment makes them useful in optical devices. Polyolefins (polymers that containing C=C double bonds) are at the heart of petroleum chemistry. Much SANS research has been performed on polyolefins. SANS from polymers research is broad and deep. Only the simplest aspects of this research are covered here.

Polymer research has bloomed over the past fifty years (Flory, 1969; de Gennes, 1979; Higgins-Benoit, 1994). The development of light scattering in the 1960s and of neutron scattering in the 1970s along with advances in polymer synthesis and computational power have greatly benefited polymer research. Impact of the SANS technique has been substantial in many areas of research.

2. SANS FROM POLYMERS

Polymer research has benefited greatly from the SANS technique which matured in the 1970s and 1980s. SANS was first developed to the scale of a user program at the ILL (Grenoble, France) then spread to most neutron scattering facilities. Polymer research accounted for the largest share of SANS beamtime. The advent of judicious sample environments brought about renewed interest. These include temperature and pressure control, the application of in-situ shear, etc. The development of scattering theory for polymer systems such as the Random Phase Approximation helped promote growth in the use of the technique. Most neutron scattering facilities maintain SANS instruments that are overbooked. SANS from polymers research has developed from cutting edge research for hardcore users into a routine characterization method for laboratories that have access to the technique. For example, the Exxon Mobil company has maintained constant use of the SANS technique and its constant funding at the NCNR for almost twenty years. Moreover, The National Science Foundation has copiously funded the SANS program at many US facilities.

3. POLYMER CHAIN CONFORMATIONS

The partial deuteration method helps observe the conformation of polymer chains in the environment of a solvent or of other polymers. This is similar to the staining method in microscopy. An apparent radius of gyration is often estimated from SANS data in the Guinier region. The Porod region yields chain conformation details such as the degree of chain swelling or solvent quality in polymer solutions. This region also shows the onset of chain stiffness whereby the polymer chain persistence length can be measured.

The SANS technique has permitted measurements of the radius of gyration of polymer chains in various polymer systems whether in solution or in blends. The contrast match method has helped the separation of single-chain properties even in concentrated mixtures. It was found for example that polymer chains follow random walk statistics in "theta" solvents, in concentrated solutions as well as in polymer melts.

4. THERMODYNAMICS OF POLYMER MISCIBILITY

SANS intensity increases close to phase separation lines due to enhanced composition fluctuations. This makes SANS an effective tool for the investigation of miscibility thermodynamics. Polymeric systems phase separate either through heating and are characterized by a lower critical solution (or spinodal) temperature (LCST) or through cooling and are characterized by an upper critical solution temperature (UCST). Some polymer solutions or polymer blend mixtures are known to phase separate through both heating and cooling and are characterized by a miscibility gap. Others phase separate only within a specific temperature region and are characterized by a phase separation island. Polymer solutions in organic solvents tend to be characterized by UCSTs whereas water soluble polymers tend to be characterized by LCSTs. The four major types of phase diagrams are summarized in a figure. Combination of these basic types is also possible; for example UCST at low temperature and closed loop immiscibility at high temperature.
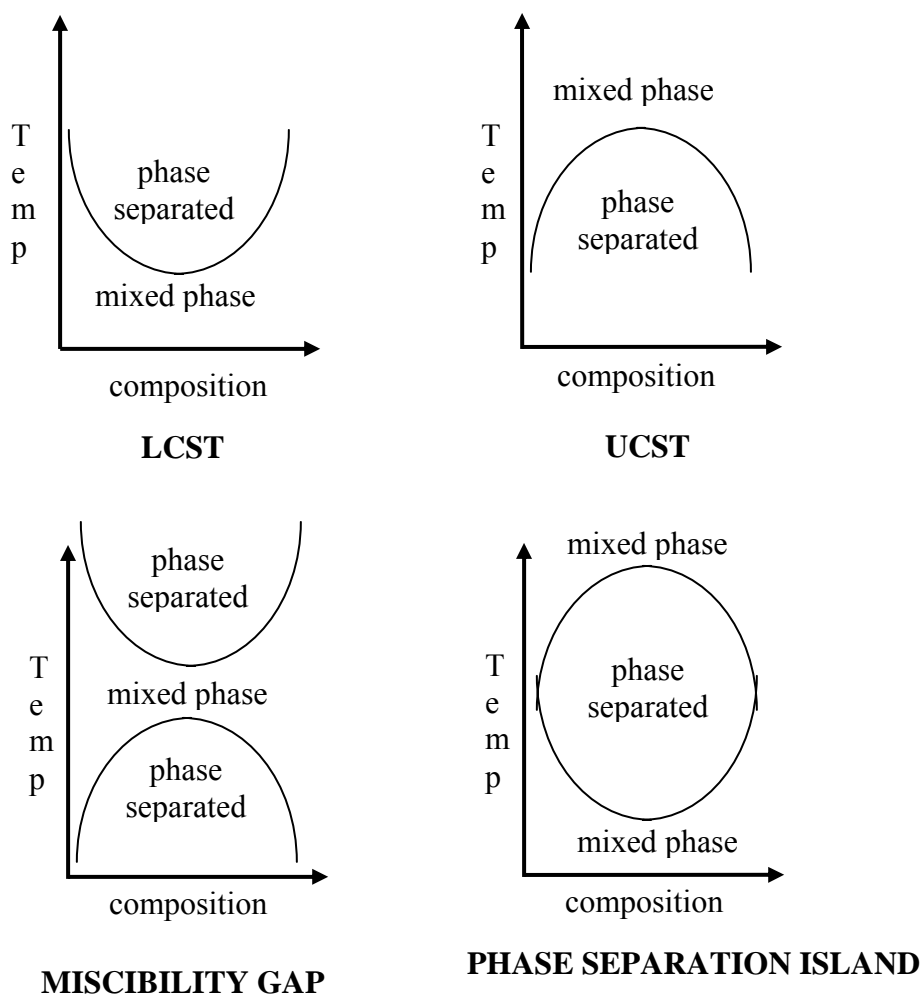
Figure 1: The four main types of phase separation diagrams for polymer blends showing the variation of the phase separation temperatures with polymer composition. Upper left: LCST, upper right: UCST, lower left: miscibility gap, lower right: closed loop immiscibility.

The SANS technique has permitted the determination of Flory-Huggins interaction parameters and the mapping out of miscibility phase diagrams. The advent of in-situ pressure and temperature control has brought about a better understanding of polymer thermodynamics.

5. CRYSTALLINE POLYMERS

The SANS technique probes density fluctuations (just like SAXS using x-rays) as well as composition fluctuations. Crystalline polymers are characterized by a strong low-Q signal below the crystallization temperature. This is due to the density fluctuations component. The use of partially deuterated chains allows the monitoring of chain conformation inside crystallites. Early findings have found, for instance, that polymer chains follow Gaussian chain statistics in the crystalline lamellae as well as in the melt state. It was also found that melt crystallization is characterized by "random re-entry" of the polymer chains from one

lamella to another. Solution crystallized polymers, however, are characterized by an "adjacent re-entry" scheme.

REFERENCES

P.J. Flory, "Statistical Mechanics of Chain Molecules", Wiley & Sons (1969)

J. Bandrup and E.H. Immergut, Editors, "Polymer Handbook", John Wiley & Sons (1975).

P.G. de Gennes, "Scaling Concepts in Polymer Physics", Cornell University Press, New York (1979).

J.S. Higgins and H. Benoit, "Polymers and Neutron Scattering", Oxford (1994).

T. Kawakatsu, "Statistical Physics of Polymers: an Introduction", Springer (2004)

QUESTIONS

1. When was the "golden age" for polymers research?
2. What are thermoplastics? How about thermosets?
3. Name some contributions of the SANS technique to polymer research.
4. Why is the SANS technique a good probe for thermodynamics investigations? How is this manifested?

ANSWERS

1. Polymers research was very strong for the past 50 years. Lots of progress was made in the 1970s and 1980s.
2. Thermoplastics can recover their original shapes when they are deformed. Thermosets are highly cross linked. It is hard to deform them.
3. The SANS technique has had broad impact on polymer research. A few examples follow: single-chain conformations in polymeric materials, phase separation thermodynamics, chain properties in crystalline polymers, clustering in water-soluble polymer solutions, etc.
4. The SANS technique is a good thermodynamics probe since it can monitor density and composition fluctuation. The intensity increases close to phase transition boundaries.

Chapter 36 - **POLYMER CONTRAST FACTORS**

The SANS scattering intensity is proportional to the neutron scattering contrast factor. The contrast factor for a polymer in solution or a polymer blend mixture is defined as $(b_M/v_M - b_S/v_S)^2$. Here b_M and v_P are the neutron scattering length and specific volume for the monomer that forms the polymer. b_S and v_S are for the solvent molecule or for another monomer in the polymer mixture.

1. COHERENT SCATTERING LENGTHS FOR A FEW MONOMERS

The following table summarizes scattering lengths for a few monomers (Bandrup-Immergut, 1975). These have been calculated using tabulated values for the scattering lengths of the various elements and their relative amounts.

Table 1: Coherent scattering lengths for a few synthetic monomers in fm (1 fermi=10^{-13} cm).

Polymer Name	Formula	Hydrogenated (fm)	Deuterated (fm)
Polystyrene	$[CH_2-CH(C_6H_5)]$	23.30	106.62
Polymethylmethacrylate	$[CH_2-C(CH_3)(CO_2CH_3)]$	14.95	98.27
Polymethylacrylate	$[CH_2-CH(CO_2CH_3)]$	15.78	78.27
Polyvinylchloride	$[CH_2CH(Cl)]$	13.78	45.03
Polyethylene	$[CH_2-CH_2]$	-1.66	40.0
Polycarbonate	$[C_6H_4-C(CH_3)_2C_6H_4-O-CO_2]$	71.50	217.30
Polyvinylmethylether	$[CH_2OH(OCH_3)]$	3.32	65.81
Polytetrahydrofuran	$[C_4OH_6]$	9.97	72.46
Poly α chlorostyrene	$[CH_2-CH(C_6H_4Cl)]$	38.74	111.64
Polyurethane (Ethylcarbonate)	$[NH-CO_2-CH_2-CH_2]$	22.23	74.31
Polyethylene oxide	$[CH_2CH_2O]$	4.139	45.78
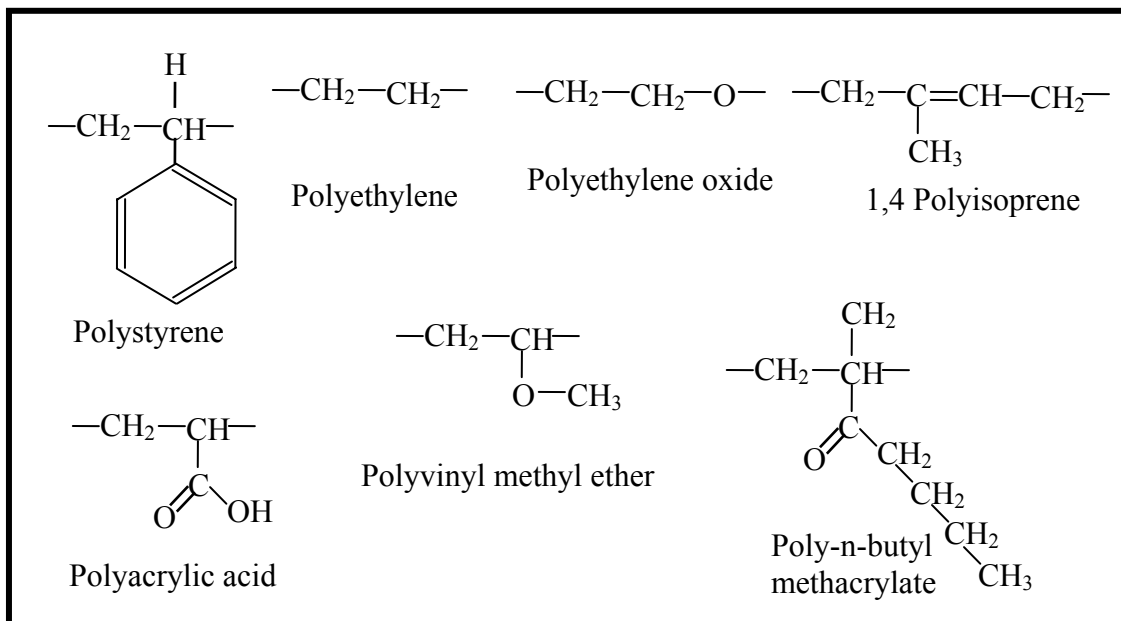
Figure 1: Chemical formulas for a few monomers.

2. COHERENT SCATTERING LENGTHS FOR A FEW SOLVENTS

The following table summarizes scattering lengths for a few commonly used solvents.

Table 2: Coherent scattering lengths for a few solvents.

Solvent Name	Formula	Hydrogenated (fm)	Deuterated (fm)
Toluene	$C_6H_5CH_3$	16.64	99.96
Benzene	C_6H_6	17.47	79.96
Cyclohexane	C_6H_{12}	-4.97	120.01
Acetone	$CH_3\text{-}COCH_3$	3.32	65.821
Chloroform	$CHCl_3$	31.60	42.05
Methylene Chloride	CH_2Cl_2	22.57	43.40
Carbon Disulfide	CS_2	12.26	------
Tetrahydrofurane	C_4OH_8	2.47	85.81
Tri-m-Tolylphosphate	$CH_3\text{-}C_6H_2P_3$	43.26	95.53
Trimethylbenzene	$C_6H_3(CH_3)_3$	14.98	139.96
Water	H_2O	-1.675	19.145
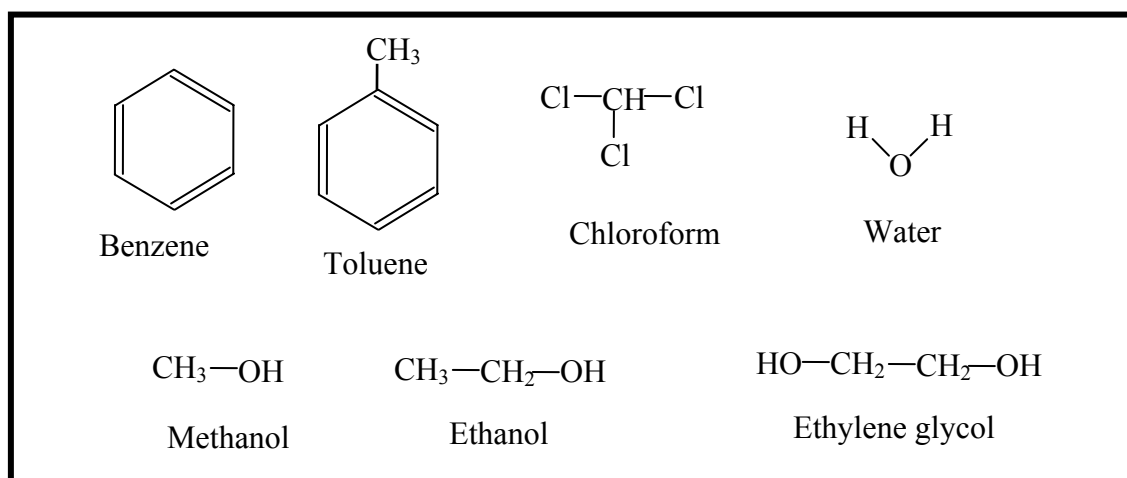
Figure 2: Chemical formulas for a few solvent molecules.

Table 3: Coherent scattering length densities for a few deuterated solvents.

Solvent Name	Formula	Molar Mass (g/mol)	Density (g/cm³)	Scattering Length Density (Å⁻²)
d-Ethylene Glycol	$C_2O_2D_6$	66	1.113	$4.47*10^{-6}$
d-Dioxane1-4	$C_4D_8O_2$	96	1.129	$6.46*10^{-6}$
d-Toluene	C_7D_8	100	0.943	$5.66*10^{-6}$
d-Benzene	C_6D_6	84	0.950	$5.43*10^{-6}$
d-Ethanol	C_2D_6O	52	0.888	$6.07*10^{-6}$
d-Methanol	CD_4O	36	0.888	$5.8*10^{-6}$
d-Water	D_2O	20	1.107	$6.37*10^{-6}$
d-Chloroform	$CDCl_3$	120.35	1.50	$6.16*10^{-6}$
d-DMF	NC_3D_7O	80	1.03	$6.33*10^{-6}$
d-Xylene	C_8D_{10}	116	0.953	$5.92*10^{-6}$

3. A FEW NEUTRON CONTRAST FACTORS FOR POLYMER MIXTURES

Consider a two-component polymer system (say component 1 homogeneously mixed in component 2). The neutron contrast is defined as the square of the difference between two scattering length densities $(b_1/v_1 - b_2/v_2)^2$ where b_1 and b_2 are the scattering lengths for monomers 1 and 2 and v_1 and v_2 are the monomer molar volumes for the two components. Component 2 could represent a solvent for polymer solutions. A few contrast factors have been calculated for the following polymer mixtures.

Table 4: Poly(ethylene oxide)/Deuterated Water (hPEO/D₂O) Solution.

Substance	Notation	Formula	Scattering Length (cm)	Specific Volume (cm³/mol)

Poly(ethylene oxide)	hPEO	C_2H_4O	$4.139*10^{-13}$	38.94
Deuterated water	d-water	D_2O	$19.14*10^{-13}$	18

Contrast Factor: $\left(\dfrac{b_{hPEO}}{v_{hPEO}} - \dfrac{b_{D_2O}}{v_{D_2O}} \right)^2 N_{av} = 5.498*10^{-3}$ mol/cm^4

N_{av} is Avogadro's number

Table 5: Deuterated Poly(ethylene oxide)/Water (dPEO/H$_2$O) Solution.

Substance	Notation	Formula	Scattering Length (cm)	Specific Volume (cm^3/mol)
Deuterated Poly(ethylene oxide)	dPEO	C_2D_4O	$45.78*10^{-13}$	38.94
Water	h-water	H_2O	$-1.67*10^{-13}$	18

Contrast Factor: $\left(\dfrac{b_{dPEO}}{v_{dPEO}} - \dfrac{b_{H_2O}}{v_{H_2O}} \right)^2 N_{av} = 9.657*10^{-3}$ mol/cm^4

Table 6: Deuterated Polystyrene/Polyvinylmethyether (dPS/PVME) Blend.

Substance	Notation	Formula	Scattering Length (cm)	Specific Volume (cm^3/mol)
Deuterated Polystyrene	dPS	C_8D_8	$1.06*10^{-11}$	100
Poly(vinyl methyl ether)	PVME	C_3H_6O	$3.30*10^{-13}$	55.4

Contrast Factor: $\left(\dfrac{b_{dPS}}{v_{dPS}} - \dfrac{b_{PVME}}{v_{PVME}} \right)^2 N_{av} = 6.07*10^{-3}$ mol/cm^4

Table 7: Deuterated Polystyrene/Hydrogenated Polystyrene (dPS/hPS) Blend.

Substance	Notation	Formula	Scattering Length (cm)	Specific Volume (cm^3/mol)
Deuterated Polystyrene	dPS	C_8D_8	$1.06*10^{-11}$	100
Polystyrene	hPS	C_8H_8	$0.23*10^{-11}$	100

$$\text{Contrast Factor: } \left(\frac{b_{dPS}}{v_{dPS}} - \frac{b_{hPS}}{v_{hPS}} \right)^2 N_{av} = 4.18*10^{-3} \text{ mol/cm}^4$$

Table 8: Deuterated Polystyrene/Polybutylmethacrylate (dPS/PBMA) Blend.

Substance	Notation	Formula	Scattering Length (cm)	Specific Volume (cm^3/mol)
Deuterated Polystyrene	dPS	C_8D_8	$1.06*10^{-11}$	100
Poly(butyl methacrylate)	hPBMA	$C_8H_{14}O_2$	$1.24*10^{-12}$	133
Contrast Factor: $\left(\frac{b_{dPS}}{v_{dPS}} - \frac{b_{hPBMA}}{v_{hPBMA}} \right)^2 N_{av} = 5.61*10^{-3}$ mol/cm^4				

Table 9: Polystyrene/Polyisoprene (PS/PI) Blend.

Substance	Notation	Formula	Scattering Length (cm)	Specific Volume (cm^3/mol)
Deuterated Polystyrene	dPS	C_8D_8	$1.06*10^{-11}$	100
Polystyrene	hPS	C_8H_{14}	$0.23*10^{-11}$	100
Poly(isoprene)	hPBMA	C_5H_8	$0.33*10^{-12}$	76
Contrast Factor: $\left(\frac{b_{hPS}}{v_{hPS}} - \frac{b_{hPI}}{v_{hPI}} \right)^2 N_{av} = 2.09*10^{-4}$ mol/cm^4 Contrast Factor: $\left(\frac{b_{dPS}}{v_{dPS}} - \frac{b_{hPI}}{v_{hPI}} \right)^2 N_{av} = 6.20*10^{-3}$ mol/cm^4				

Table 10: Deuterated Polystyrene/Dioctylphthalate (dPS/DOP) Solution.

Substance	Notation	Formula	Scattering Length (cm)	Specific Volume (cm^3/mol)
Deuterated Polystyrene	dPS	C_8D_8	$1.06*10^{-11}$	100

Dioctylphthalate	DOP	$C_{24}H_{38}O_4$	$4.07*10^{-12}$	390
Contrast Factor: $\left(\dfrac{b_{dPS}}{v_{dPS}} - \dfrac{b_{DOP}}{v_{DOP}}\right)^2 N_{av} = 5.48*10^{-3}$ mol/cm^4				

REFERENCES

http://www.ncnr.nist.gov/resources/sldcalc.html contains a scattering length density calculator.

J. Bandrup and E.H. Immergut, Editors, "Polymer Handbook", John Wiley & Sons (1975).

QUESTIONS

1. Which contrast factor is greater, for a deuterated polymer in hydrogenated solvent or for a hydrogenated polymer in deuterated solvent?
2. Which one of the two following dilute solution samples would you rather prepare for a SANS experiment: a deuterated polymer in hydrogenated solvent or a hydrogenated polymer in deuterated solvent?
3. Scattering from a non-deuterated polymer mixture is dominated by what type of fluctuations?

ANSWERS

1. The contrast factor for a deuterated polymer in hydrogenated solvent is equal to that for a hydrogenated polymer in deuterated solvent. This is the so-called Babinet principle.
2. The best sample to prepare for a SANS experiment from a dilute solution is a hydrogenated polymer in deuterated solvent. This minimizes the amount of hydrogen (and therefore incoherent background) in the sample.
3. Scattering from a non-deuterated polymer mixture is dominated by density fluctuations. The same would be observed using x-ray scattering.

Solubility is a determining factor in the synthesis, mixing ability and end-use of polymers. A general model for describing solubility is discussed here with an emphasis on what information is obtained from SANS measurements from polymer solutions (Flory, 1953). SANS data from specific polymer solutions are discussed in some detail.

1. POLYMER SOLUTIONS BASICS

Most non-polar polymers dissolve in organic solvents and some polar polymers dissolve in water. Concentration ranges vary from dilute to semi-dilute to concentrated solutions. The borderline between the dilute and the semi-dilute regimes is referred to as the overlap concentration (c*) which is estimated as $c* \sim M_w /(4\pi/3)R_g^3$ (M_w is the molecular weight and R_g is the radius of gyration). The polymer concentration c is related to the volume fraction ϕ through the density d as $c = \phi d$.

2. CASE OF A SIMPLE POLYMER SOLUTION

As an example of a polymer solution, the case of poly(ethylene oxide) PEO in water is discussed (Hammouda et al, 2002; Hammouda-Ho, 2007). The PEO monomeric unit -(CH_2CH_2O)- is the simplest one for a water-soluble polymer . When dissolved in water, PEO is characterized by hydrophilic interactions (hydrogen bonding of water molecules to the oxygen atoms on the polymer) and hydrophobic interactions (the CH_2CH_2 groups repel water). PEO dissolves in water for a wide range of temperatures and concentrations. Its homologues, PMO (-CH_2O-) and PPO (-$CH(CH_3)CH_2O$-) do not dissolve in water an ambient temperature. This may be due to the fact that the oxygen-oxygen inter-distance on the PEO chain matches the oxygen-oxygen inter-distance in the structure of pure water.

A typical SANS spectrum from a 4 % PEO/d-water (weight average and number average molecular weights of M_w = 100,000 and M_n = 96,000 g/mol respectively) is plotted for the T = 10° C temperature. This sample is well in the semi-dilute region (c* is estimated to be 0.0275 g/cm^3 which corresponds to 2.4 % volume fraction). The low-Q feature characterizes large size clusters (of no interest to us here) and the high-Q feature characterizes the polymer chains.

4% PEO/d-water, M$_w$=100,000 g/mole, T=10°C
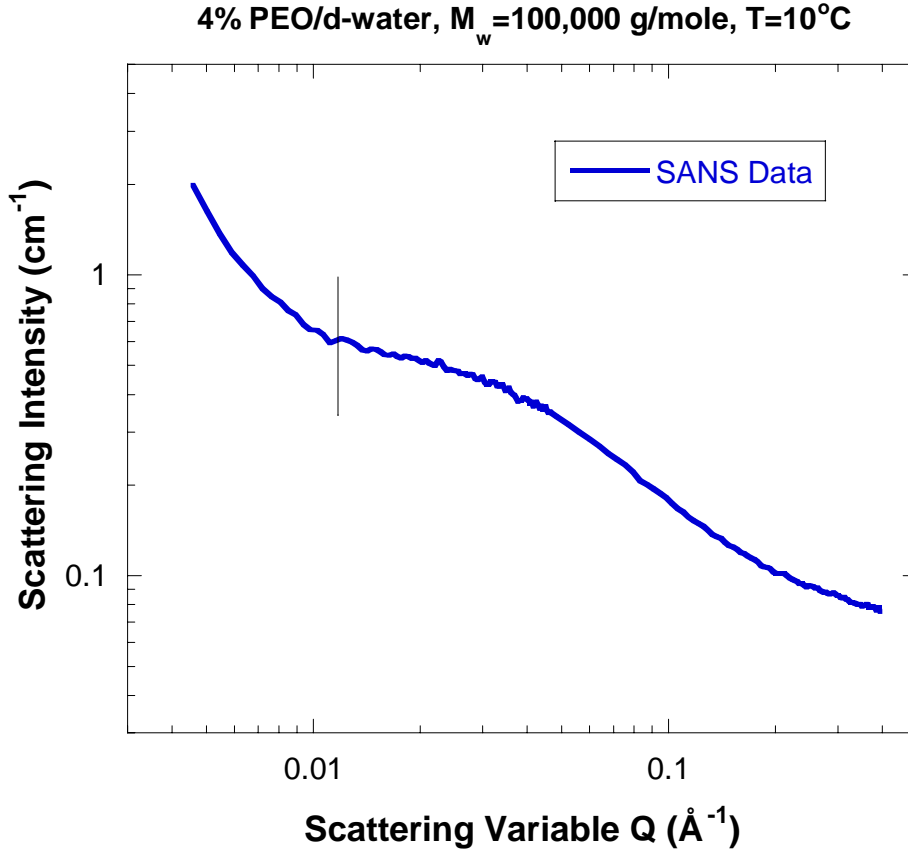
Figure 1: SANS data for a PEO/d-water sample over a wide Q range showing a low-Q feature and a high-Q feature. Only the tail of the low-Q feature is observed. Focus here is on the high-Q feature.

3. FIT TO A SIMPLE MODEL

In order to characterize our results, the following empirical functional form is fitted to the data:

$$I(Q) = \frac{A}{Q^n} + \frac{C}{1+(Q\xi)^m} + B. \tag{1}$$

The first term describes Porod scattering from clusters and the second term describes scattering from polymer chains. This second term characterizes the polymer/solvent interactions and therefore the thermodynamics and is of interest here. The two multiplicative factors A and C, the incoherent background B and the two exponents n and m are used as fitting parameters. The final parameter ξ is a correlation length for the entangled polymer chains. It gives an estimate of the entanglement length (average distance between entanglements). Non-linear least squares fits to the empirical functional form yields $\xi = 20$ Å, and m = 1.9 for the 4 % PEO/d-water sample.

4. THE CORRELATION LENGTH

The correlation length ξ decreases with increasing polymer volume fraction because the entanglement length increases. ξ goes from close to 80 Å at low polymer volume fraction to under 10 Å at high volume fraction. At low polymer volume fraction and at high-Q, the chains radius of gyration is given by $R_g = \sqrt{2} \, \xi = 113$ Å and the end-to-end chain distance is $R_{1n} = \sqrt{6} \, R_g = 277$ Å.

PEO/D$_2$O, M$_w$ = 100,000 g/mole
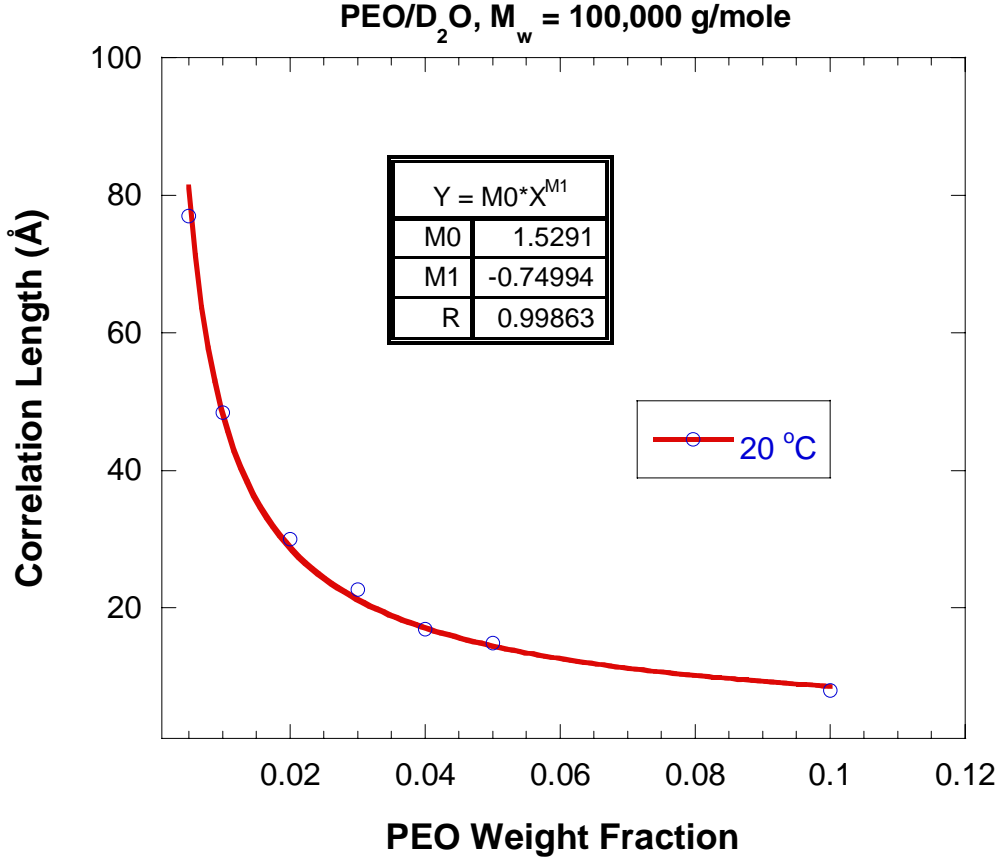
Figure 2: Variation of the correlation length with polymer volume fraction.

5. THE SPINODAL TEMPERATURE

The correlation length ξ and the coefficient C increase with increasing temperature T due to increased composition fluctuations when approaching phase separation. The PEO/d-water system is characterized by a lower critical solution temperature (LCST), i.e., it phase separates upon heating. The spinodal (phase separation) temperature T_s is obtained when C diverges; it can be accurately estimated from the intercept of a C^{-1} *vs* T^{-1} plot of data taken at various temperatures. In this case of 1 % PEO/d-water, one finds $T_s = 127$ °C.
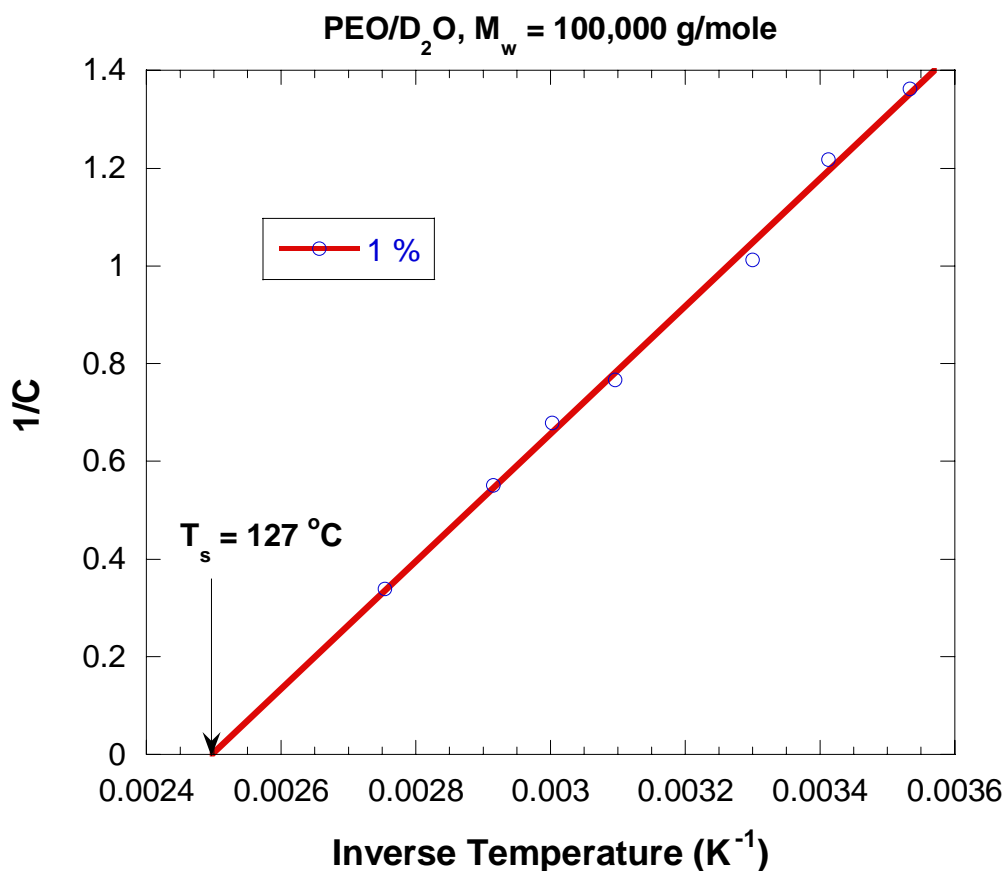
Figure 3: Variation of the high-Q inverse intensity C^{-1} with inverse temperature T^{-1}. The intercept represents the spinodal (phase separation) boundary line.

6. THE EXCLUDED VOLUME PARAMETER

Our fitting results (high-Q Porod exponent) for the 1 % PEO/d-water solution show that chains are mostly swollen at low temperatures (m = 1.85 which corresponds to an excluded volume parameter around $\nu = 1/m = 0.54$) and change to theta conditions at high temperatures (m = 2.02 which corresponds to an excluded volume parameter around $\nu = 0.5$) as the spinodal temperature is approached.

PEO/D$_2$O, M$_w$ = 100,000 g/mole
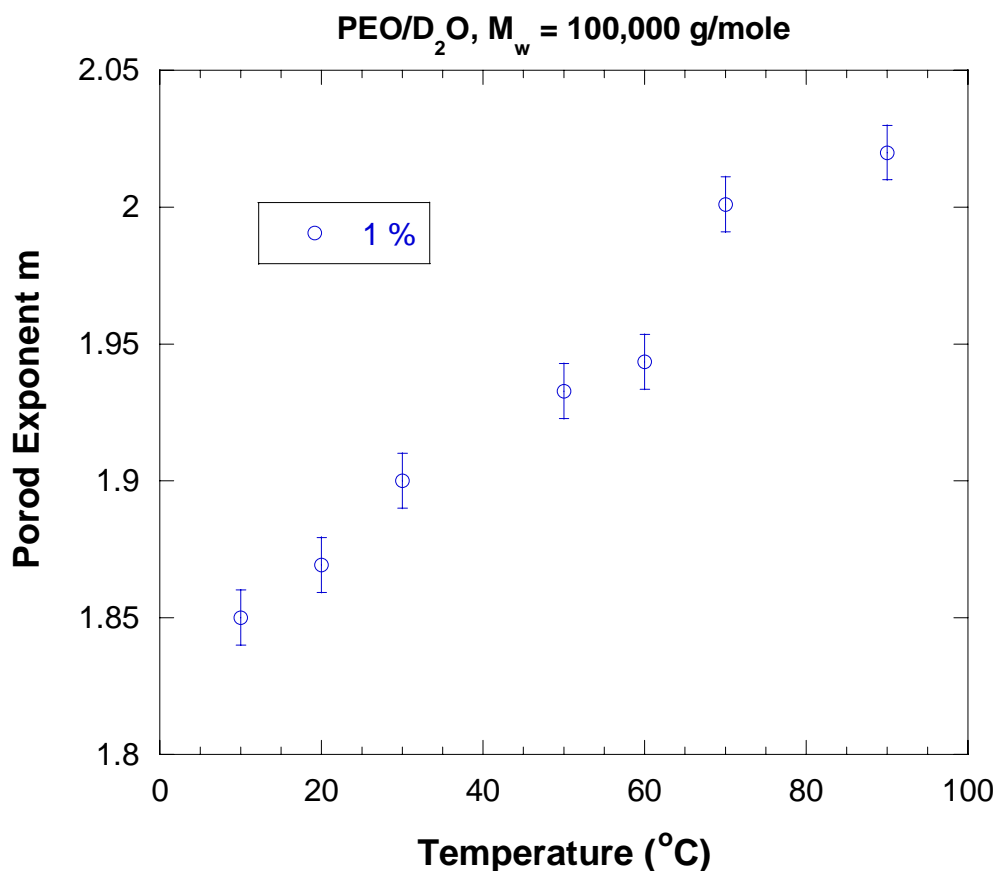
Figure 4: Variation of the Porod exponent with temperature. Polymer chains change from a swollen state to a "theta" condition as the spinodal temperature is approached.

7. BRANCH OF THE PHASE DIAGRAM

The spinodal temperature T_s was obtained from the various PEO volume fraction samples that were measured. A branch of the LCST phase diagram was obtained. What is interesting is that the phase boundary line T_s is estimated through extrapolation (i.e., before reaching it). For some of our samples, T_s happens to be above the boiling temperature of water (and therefore unreachable except when measurements are made inside a pressure cell). The SANS technique is a good monitor of phase separation because it is sensitive to composition fluctuations which get enhanced close to phase boundary lines.

PEO/D$_2$O, M$_w$ = 100,000 g/mole
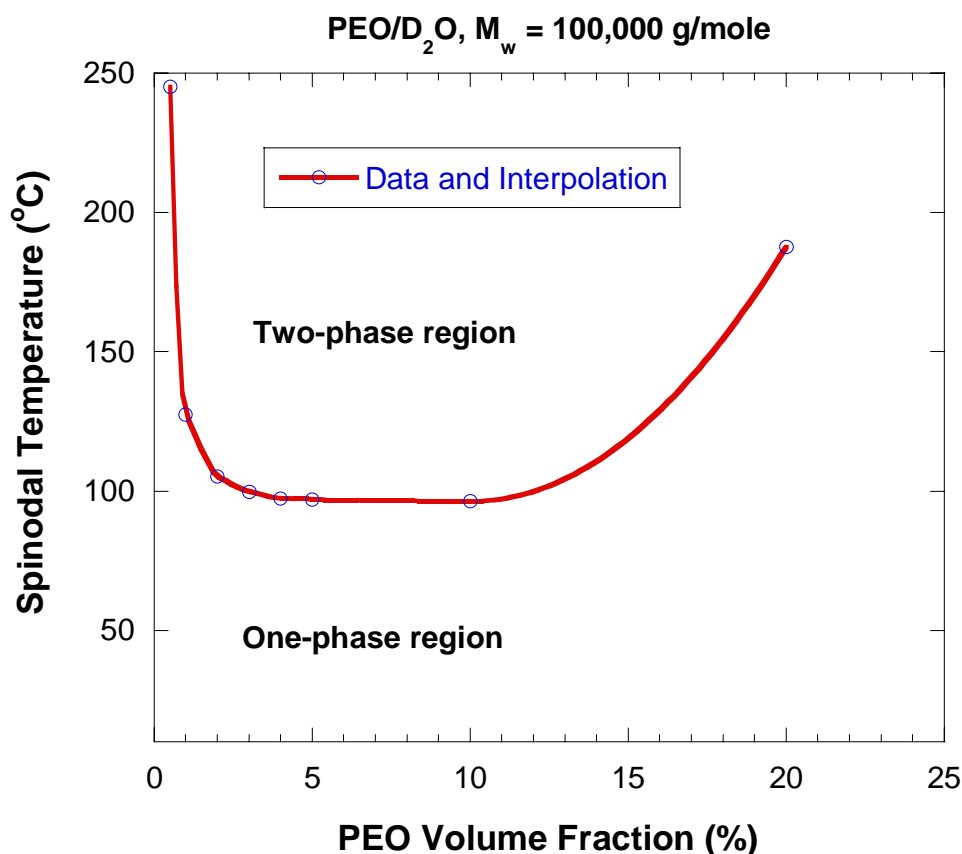
Figure 5: Limited branch of the phase diagram for the PEO/d-water polymer solution system. Phase separation is obtained upon heating (LCST behavior).

8. POLYMER SOLUTION THERMODYNAMICS

Polymer solutions can phase separate upon heating (LCST behavior) or upon cooling (UCST behavior). Polymers that dissolve in organic solvents tend to be characterized by a UCST whereas water-soluble polymers tend to follow LCST thermodynamics. The Flory-Huggins approach is a mean-field theoretical model to predict phase separation behavior. This model will be discussed later for polymer blends.

9. THE ZERO AVERAGE CONTRAST MATCH METHOD

The zero average contrast method (also called "high concentration" method) uses variation of the fraction of deuterated polymer and deuterated solvent but keeping the total polymer concentration (or volume fraction) constant to measure the single-chain form factor even at high concentrations because the interchain term cancels out.

A series of PEO/water solutions were prepared whereby the total polymer fraction was kept constant (volume fraction of 4 %) but the relative amount of dPEO/hPEO was varied. In order to isolate the single-chain contribution, we used mixtures of D$_2$O and H$_2$O solvent

molecules that match the average polymer scattering-length density in each case. For such hPEO/dPEO/H$_2$O/D$_2$O mixtures, the scattering intensity is given by:

$$\frac{d\Sigma(Q)}{d\Omega} = \left(\left\{\Delta B_P{}^2\right\} - \left\{\Delta B_P\right\}^2\right)n_P\phi_P v_P P_S(Q) + \left\{\Delta B_P\right\}^2 n_P\phi_P v_P P_T(Q) \quad (2)$$

$$\left\{\Delta B_P{}^2\right\} = \left[\Delta\rho_D{}^2\frac{\phi_D}{\phi_P} + \Delta\rho_H{}^2\frac{\phi_H}{\phi_P}\right]$$

$$\left\{\Delta B_P\right\}^2 = \left[\Delta\rho_D\frac{\phi_D}{\phi_P} + \Delta\rho_H\frac{\phi_H}{\phi_P}\right]^2$$

$$\Delta\rho_D = (\rho_D - \rho_S) = \left(\frac{b_D}{v_D} - \frac{b_S}{v_S}\right)$$

$$\Delta\rho_H = (\rho_H - \rho_S) = \left(\frac{b_H}{v_H} - \frac{b_S}{v_S}\right).$$

Here, b_H and b_D are the scattering lengths for the hPEO and dPEO monomers, v_H and v_D are the corresponding specific volumes, and ϕ_H and ϕ_D are the corresponding polymer volume fractions (and similarly for the solvent scattering length density b_S/v_S). In order to arrive at this formula, it was assumed that the protonated and deuterated polymer degrees of polymerization and specific volumes are matched. The degree of polymerization used here, n_P, represents the value for the two mixed polymer species ($n_H = n_D = n_P$). The total polymer volume fraction ϕ_P ($\phi_P = \phi_H + \phi_D$) and polymer specific volume v_P ($v_P = v_H = v_D$) have also been defined. The single-chain structure factor $P_S(Q)$ and the total-chain structure factor (including intra-chain and inter-chain contributions) $P_T(Q)$ have also been defined. The average contrast match condition zeroes the second term in the cross section equation leaving only the first term proportional to $P_S(Q)$.

This formula assumes that deuteration does not affect chain structure or interactions. This is obviously an assumption for our hydrogen-bonded system.
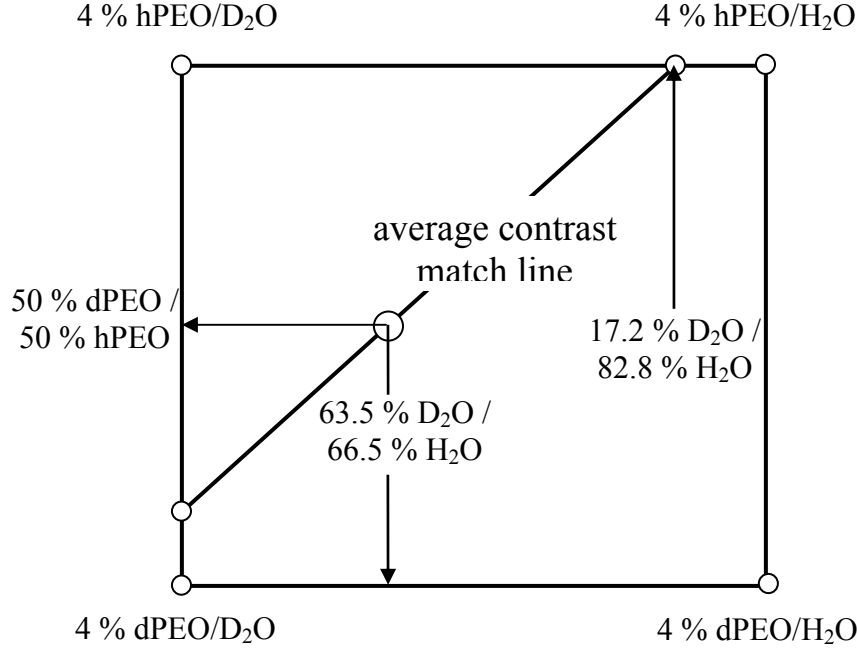
Figure 6: The series of PEO/water solutions for the average contrast match series. Mixtures of deuterated and non-deuterated polymers (dPEO and hPEO) and solvents (D_2O and H_2O) are used.

Specific values for the defined parameters for our system are as follows.

$$n_{hPEO} = 2273, \ n_{dPEO} = 2125, \tag{3}$$
$$b_{hPEO} = 4.14*10^{-13} \ cm, \ b_{dPEO} = 45.78*10^{-13} \ cm,$$
$$b_{H_2O} = -1.67*10^{-13} \ cm, \ b_{D_2O} = 19.14*10^{-13} \ cm,$$
$$v_{hPEO} = v_{dPEO} = 38.94 \ cm^3/mol,$$
$$v_{H_2O} = v_{D_2O} = 18 \ cm^3/mol.$$

The four possible contrast factors corresponding to the 4 corners in the figure are as follows:

$$\left(\frac{b_{dPEO}}{V_{dPEO}} - \frac{b_{H2O}}{V_{H2O}} \right)^2 N_{av} = 9.66*10^{-3} \ mol/cm^4 \tag{4}$$

$$\left(\frac{b_{hPEO}}{V_{hPEO}} - \frac{b_{D2O}}{V_{D2O}} \right)^2 N_{av} = 5.50*10^{-3} \ mol/cm^4$$

$$\left(\frac{b_{hPEO}}{V_{hPEO}} - \frac{b_{H2O}}{V_{H2O}} \right)^2 N_{av} = 2.38*10^{-4} \ mol/cm^4$$

$$\left(\frac{b_{dPEO}}{V_{dPEO}} - \frac{b_{D2O}}{V_{D2O}} \right)^2 N_{av} = 7.53*10^{-5} \ mol/cm^4 .$$

Here we have multiplied by Avogadro's number ($N_{av} = 6.022*10^{23}$ molecules/mol) for

convenience. The strongest neutron contrasts correspond to the two mixtures: dPEO/H$_2$O and hPEO/D$_2$O. Contrasts corresponding to the other two mixtures are much lower. The higher incoherent background is found in the samples with the most hydrogen (i.e., with non-deuterated solvent).

Data from a specific 4 % PEO/water mixture with 50 % dPEO/50 % hPEO and 63.5 % D$_2$O / 36.5 % H$_2$O are shown in a figure. This mixture is represented by a circle on the average contrast match line in the same figure. This sample is characterized by the single-chain scattering feature only. The low-Q feature representing clustering has mostly disappeared. This method is useful for isolating single-chain properties in semi-dilute (and even concentrated) polymer solutions.
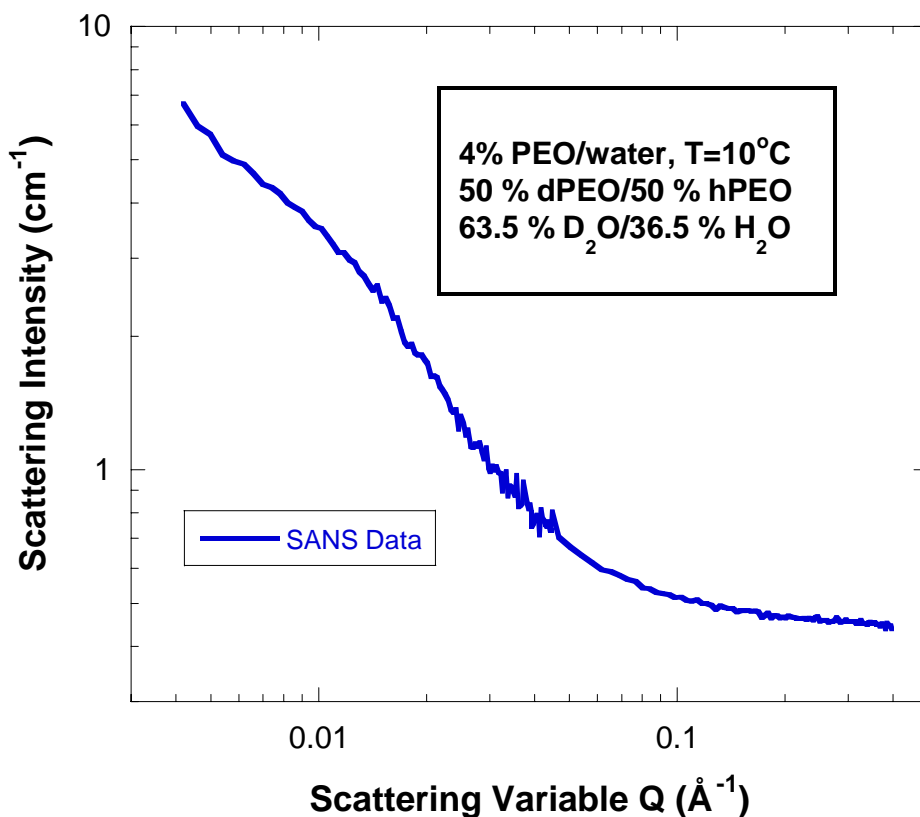
Figure 7: SANS data from a PEO/water sample on the average contrast match line. Mixtures of dPEO/hPEO and D$_2$O/H$_2$O are used to cancel out scattering from the clusters leaving scattering from single polymer chains only. M$_w$ = 100,000 g/mol for both the dPEO (deuterated) and hPEO (non-deuterated) polymers.

Nonlinear least-squares fit of this data to the Gaussian chain model with excluded volume (described before) gave a segment length of a$_{PEO}$ = 6.7 Å and an excluded volume parameter of ν = 0.51. Based on these numbers, the radius of gyration can be estimated as

$$R_g = \frac{a_{PEO} n_{PEO}^{0.51}}{\sqrt{(2\nu+1)(2\nu+2)}} = 137 \text{ Å}.$$ The PEO chain degree of polymerization $n_{PEO} = 2200$ has been used.

Fit to the "simple model" form (described before) gave a correlation length $\xi = 92.8$ Å and a Porod exponent $m = 2.06$. The radius of gyration can be estimated here also as $R_g = \sqrt{2}\,\xi = 131$ Å. This shows acceptable agreement.

REFERENCES

P. Flory, "Principles of Polymer Chemistry", Cornell University Press, Ithaca, 1953.

B. Hammouda, D. Ho, and S. Kline, "SANS from Poly(ethylene Oxide)/Water Systems", Macromolecules, 35, 8578-8585 (2002).

B. Hammouda and D. Ho, "Insight into Chain Dimensions in PEO/Water Solutions", J. Polym. Sci., Polym. Phys. Ed. 45, 2196-2200 (2007).

QUESTIONS

1. What is the high-Q expansion of the Debye function (structure factor for Gaussian coil)?
2. What standard plot is used to obtain the radius of gyration, the correlation length, the persistence length?
3. What is the meaning of the correlation length?
4. What does it mean to say the PEO/water solution is characterized by an LCST phase diagram?
5. A Porod exponent of 5/3 is an indication of what type of polymer chains?
6. The high-Q SANS data is characteristic of what type of interactions in polymer solutions?

ANSWERS

1. The high-Q expansion of the Debye function is: $\text{Lim } P(Q \to \infty) = 2/(Q^2 R_g^2)$.

2. The Guinier plot is used to obtain the radius of gyration, the Zimm plot is used to obtain the correlation length, and the Kratky-Porod plot is used to obtain the persistence length.

3. The correlation length is the average distance between entanglement points.

4. The PEO/water solution is characterized by a Lower Critical Solution Temperature phase diagram means that phase separation occurs upon heating.

5. A Porod exponent of 5/3 is an indication of fully swollen polymer chains.

6. The high-Q SANS data is characteristic of solvent/polymer interactions (the so-called salvation shell) and therefore of the thermodynamics of mixing.

Polymer blends are mixtures of homopolymers where mixing happens at the molecular level. Two polymers mix only when they are compatible with each other (i.e., when their chemical units are similar) and when they correspond to conditions in the mixed region of the phase diagram. The process of polymer blends demixing (phase separation) is discussed.

1. THE FLORY-HUGGINS MODEL

Polymer thermodynamics are described by the Gibbs free energy which consists of two main contributions: an entropic part (combinatorial mixing of the monomers) and an enthalpic part (interactions between monomers). The Flory-Huggins equation for polymer blends gives a simple expression for the Gibbs free energy:

$$\frac{G}{k_B T} = \frac{\phi_1}{n_1 v_1} \ln(\phi_1) + \frac{\phi_2}{n_2 v_2} \ln(\phi_2) + \frac{\chi_{12}(T)}{v_0} \phi_1 \phi_2 . \qquad (1)$$

n_1, ϕ_1 and v_1 are the degree of polymerization (i.e., number of monomers per chain), volume fraction and specific volume for monomer 1 and n_2, ϕ_2 and v_2 are the equivalent quantities for monomer 2. χ_{12} is the usual Flory-Huggins interaction parameter and v_0 is a "reference" volume. Note that $\phi_1 + \phi_2 = 1$.

The SANS technique is sensitive to composition fluctuations and is therefore a good monitor of phase separation thermodynamics. The scattering intensity is related to the second derivative of the Gibbs free energy with respect to composition. The scattering function in the forward direction ($Q = 0$) is given by:

$$S^{-1}(Q=0) = \frac{1}{k_B T} \frac{\partial^2 G}{\partial \phi_1^2} = \frac{1}{n_1 \phi_1 v_1} + \frac{1}{n_2 \phi_2 v_2} - 2\frac{\chi_{12}(T)}{v_0} . \qquad (2)$$

Phase separation thermodynamics are buried in the temperature-dependent Flory-Huggins parameter χ_{12}.
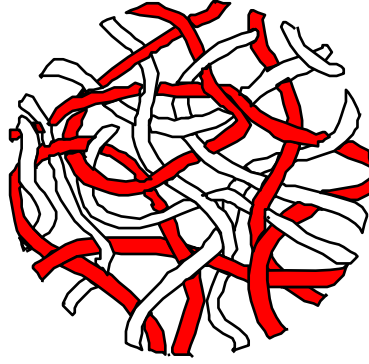
Polymers Blend

Figure 1: Schematic representation of a polymer blend mixture.

2. BINODAL AND SPINODAL LINES

The phase separation thermodynamics of polymer mixtures is characterized by two lines: the binodal and the spinodal lines. The binodal line corresponds to generalized phase separation (at large length scales) and the spinodal line corresponds to the onset of density fluctuations (at local length scales) leading the phase separation. The region between the binodal and spinodal lines is referred to as the nucleation-and-growth region.

The chemical potential μ_1 is the first derivative of the Gibbs free energy G with respect to the volume fraction ϕ_1:

$$\frac{\mu_1}{k_B T} = \frac{1}{k_B T} \frac{\partial G}{\partial \phi_1} \qquad (3)$$

$$\frac{\mu_1}{k_B T} = \frac{1}{n_1 v_1} \log(\phi_1) + \frac{1}{n_1 v_1} - \frac{1}{n_2 v_2} \log(1-\phi_1) - \frac{1}{n_2 v_2} + \frac{\chi_{12}(T)}{v_0}(1-\phi_1) - \frac{\chi_{12}(T)}{v_0}\phi_1$$

The binodal phase separation line is obtained when the two minima of $G(\phi_1)$ have the same tangent slope line.

The osmotic pressure π_1 corresponds to the second derivative of G with respect to ϕ_1:

$$\frac{\pi_1}{k_B T} = \frac{1}{k_B T} \frac{\partial^2 G}{\partial \phi_1^2} = \frac{1}{n_1 \phi_1 v_1} + \frac{1}{n_2(1-\phi_1)v_2} - 2\frac{\chi_{12}(T)}{v_0}. \qquad (4)$$

This expression also represents the inverse of the structure factor in the forward direction $S^{-1}(Q=0)$. The spinodal phase transition line is obtained when the condition $\pi_1=0$ (or $S(Q=0) \to \infty$) is met, i.e., it corresponds to the inflection points on the $G(\phi_1)$ curve.

3. THE RANDOM PHASE APPROXIMATION

The Random Phase Approximation (RPA) model is a mean field theory to describe polymer mixtures in the homogeneous phase region. It is a generalization of the Flory-Higgins equation to finite momentum transfer Q.

$$S^{-1}(Q) = \frac{1}{n_1 \phi_1 v_1 P_1(Q)} + \frac{1}{n_2 (1-\phi_1) v_2 P_2(Q)} - 2\frac{\chi_{12}(T)}{v_0} \qquad (5)$$

$P_1(Q)$ is the so-called Debye function for Gaussian random polymer coils.

$$P_1(Q) = \frac{2}{Q^4 R_{g1}^4}\left[\exp(-Q^2 R_{g1}^2) - 1 + Q^2 R_{g1}^2\right]. \qquad (6)$$

R_{g1} is the radius of gyration for component 1. The radius of gyration can be expressed in terms of the statistical segment length a_1 (think monomer size) as $R_{g1}^2 = na_1^2/6$. Precisely, the statistical segment length is the length for which the polymer chain is represented by a random walk. The Debye function is used because chains in compatible polymer blends do not swell or collapse.

The SANS scattering cross section is given in terms of an absolute macroscopic cross section (units of cm^{-1}) as:

$$\frac{d\Sigma(Q)}{d\Omega} = \left(\frac{b_1}{v_1} - \frac{b_2}{v_2}\right)^2 S(Q) \qquad (7)$$

where b_1/v_1 is the scattering length density for monomer 1 and the term $(b_1/v_1-b_2/v_2)^2$ is the contrast factor. This scattering cross section is also referred to as the scattering intensity I(Q).

4. POLYOLEFIN BLENDS

Polyolefins are a wide class of polymeric materials that find uses in many aspects of our daily lives. These are polymers containing C=C double bonds either in an aromatic ring or in the aliphatic chain. These double bonds can be saturated (i.e., broken) through the hydrogenation process. Gentle interactions among polyolefin blend mixtures make them ideal "mean field" systems to investigate phase separation thermodynamics. The mixed one-phase region is easily accessible for a wide range of temperatures and compositions.

Polyolefin blends are characterized by an Upper Critical Spinodal Temperature (UCST); i.e., they phase separate upon cooling. Phase separation occurs either by spinodal decomposition (sinusoidal composition fluctuations) or by nucleation and growth (phase coarsening around

nucleating centers). The SANS method is used here to map out the spinodal temperature for a polyolefin blend mixture.

5. A POLYOLEFIN BLEND

The polyolefin blend system considered here is polyethylbutylene mixed with deuterated polymethylbutylene (hPEB/dPMB) (Lefebvre et al, 2000). The PMB polymer is deuterated for enhanced neutron contrast. The chemical formula for hPEB is $[-CH_2-CH(C_2H_5)-CH_2-CH_2]-$ and for dPMB is $[-CHD-CD(CH_3)-CD_2-CHD]-$. An hPEB/dPMB polymer blend with molecular weights of $M_w = 40,100$ g/mol and $88,400$ g/mol and composition of $\phi_{hPEB} = 0.57$ and $\phi_{dPMB} = 0.43$ was measured by SANS. The stoichiometry of this sample is C_6H_{12} for hPEB and close to $C_5H_{4.5}D_{5.5}$ for dPMB as measured by NMR.

The scattering intensity at various temperatures is shown below. Scattering increases for decreasing temperature, due to the approach to the phase transition (spinodal) line.
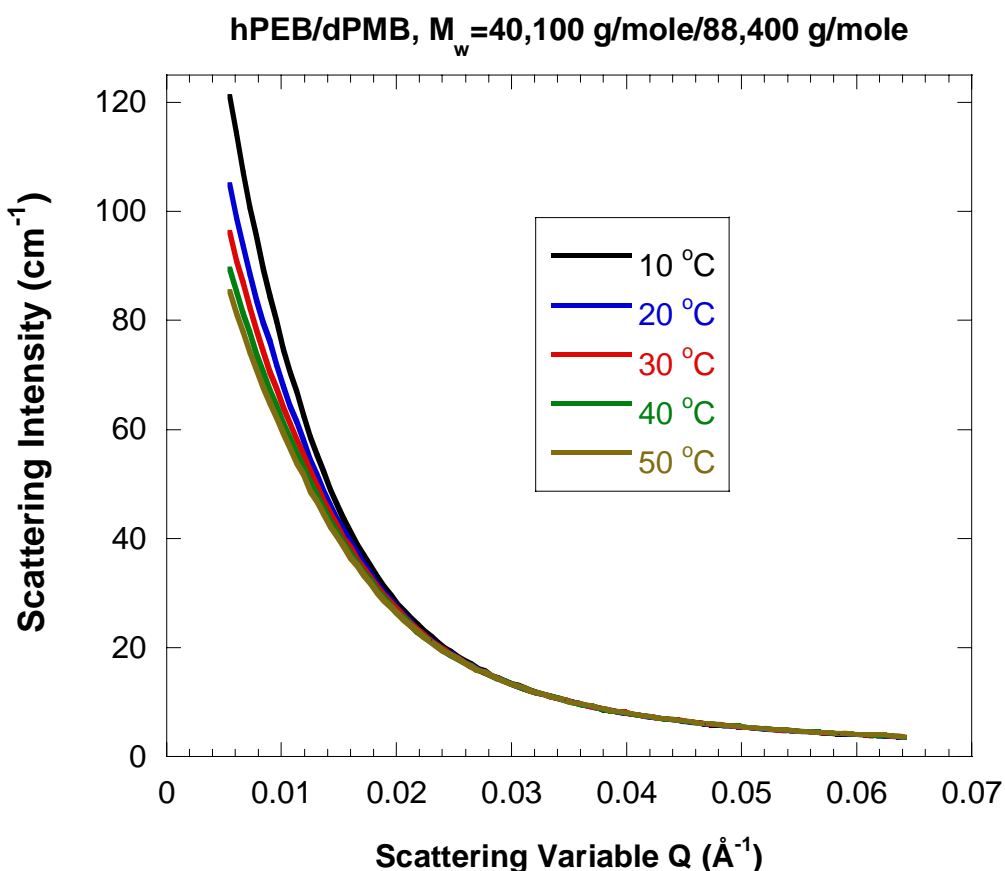
Figure 2: SANS scattered intensity for the hPEB/dPMB sample at various temperatures. The intensity increases as the temperature is lowered (UCST system)

The Zimm plot ($I^{-1}(Q)$ vs Q^2) yields an extrapolated value of the forward scattering $I(Q = 0)$.
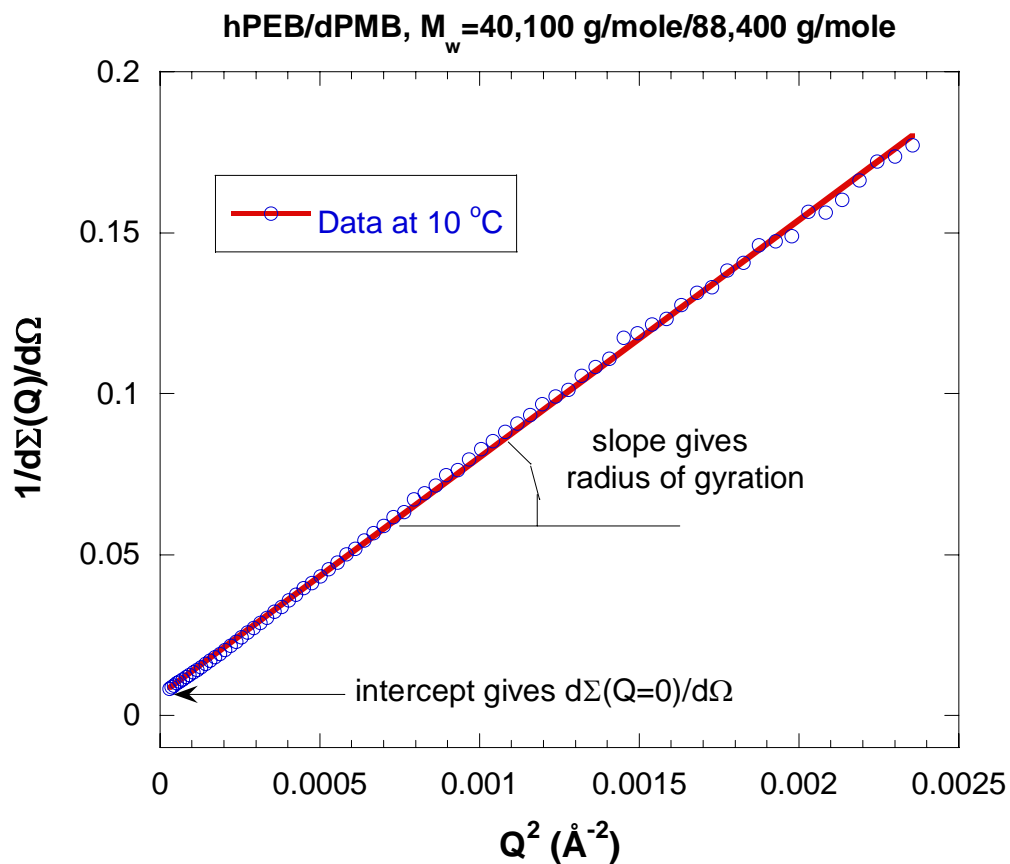
Figure 3: The Zimm plot yields I(Q=0) from the intercept.

A plot of $I^{-1}(Q=0)$ vs T^{-1} (T is in K) yields the spinodal temperature from the intercept; i.e., when I(Q=0) diverges or $I^{-1}(Q=0)$ is equal to zero. An estimated spinodal temperature of 220 K = -53 $^{\circ}$C is obtained for this sample.

hPEB/dPMB, M$_w$=40,100 g/mole/88,400 g/mole
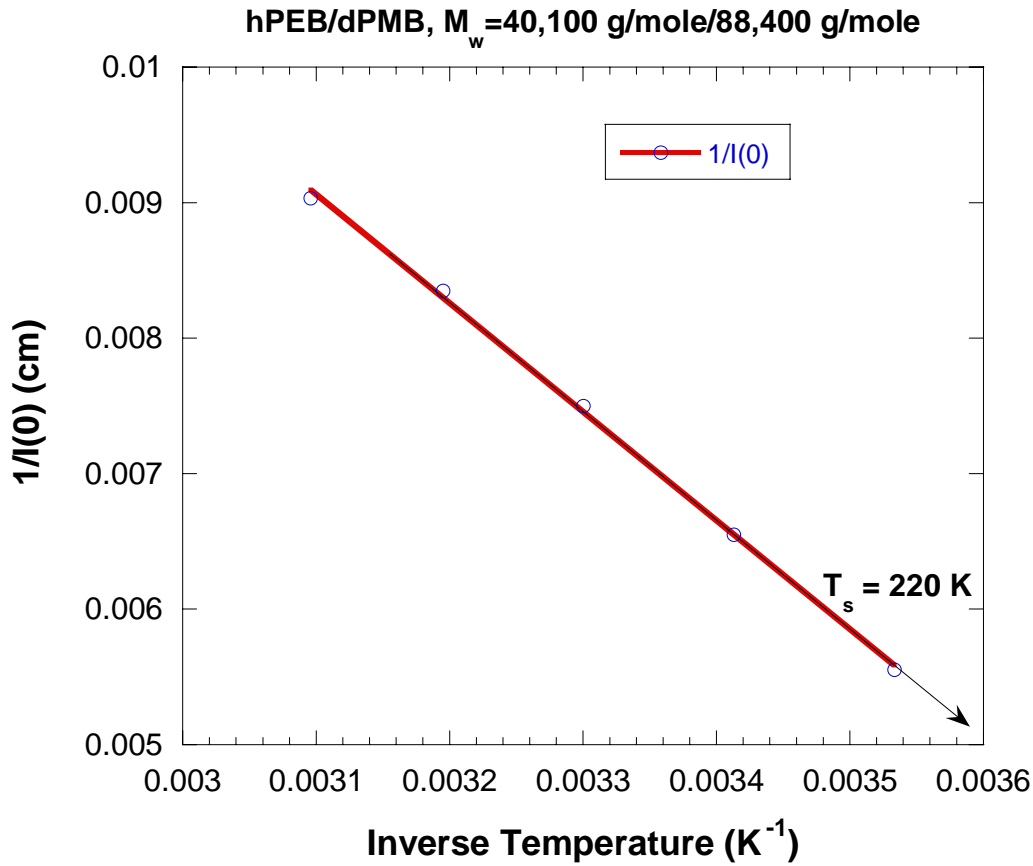
Figure 4: Variation of the inverse intensity (extrapolated to Q = 0) with the inverse temperature (in degree K). The spinodal temperature is obtained for 1/I(0)=0.

The reduced SANS data for every temperature were fit to the RPA functional form for the binary blend mixture with the following input parameters:

Degrees of polymerization:	$n_1 = 525$	$n_2 = 1105$
Volume fractions:	$\phi_1 = 0.57$	$\phi_2 = 0.43$
Specific volumes:	$v_1 = 97.5$ cm^3/mol	$v_2 = 81.9$ cm^3/mol
Scattering lengths:	$b_1 = -4.99*10^{-13}$ cm	$b_2 = 53.1*10^{-13}$ cm.

The specific volumes were obtained as the ratios of the monomer molecular weight to their densities. Note that the scattering length for hPEB is negative whereas that for dPMB is positive.

Fit results are:

Segment lengths:	$a_1 = 8$ Å	$a_2 = 8$ Å
Interaction parameter:	$\dfrac{\chi_{12}(T)}{v_0} = \dfrac{0.0106}{T} - 1.84*10^{-5}$ (T in deg K).	

The approach used here is approximate. The specific volumes were assumed to be independent of temperature. The purpose of the argument being made here is to show how the Flory-Huggins theory could be used to obtain a phase diagram. Note that in this approach, the "reference" volume v_0 needs to be specified only if $\chi_{12}(T)$ needs to be known. In this case, v_0 is approximated as $v_0 = \sqrt{v_1 v_2}$.
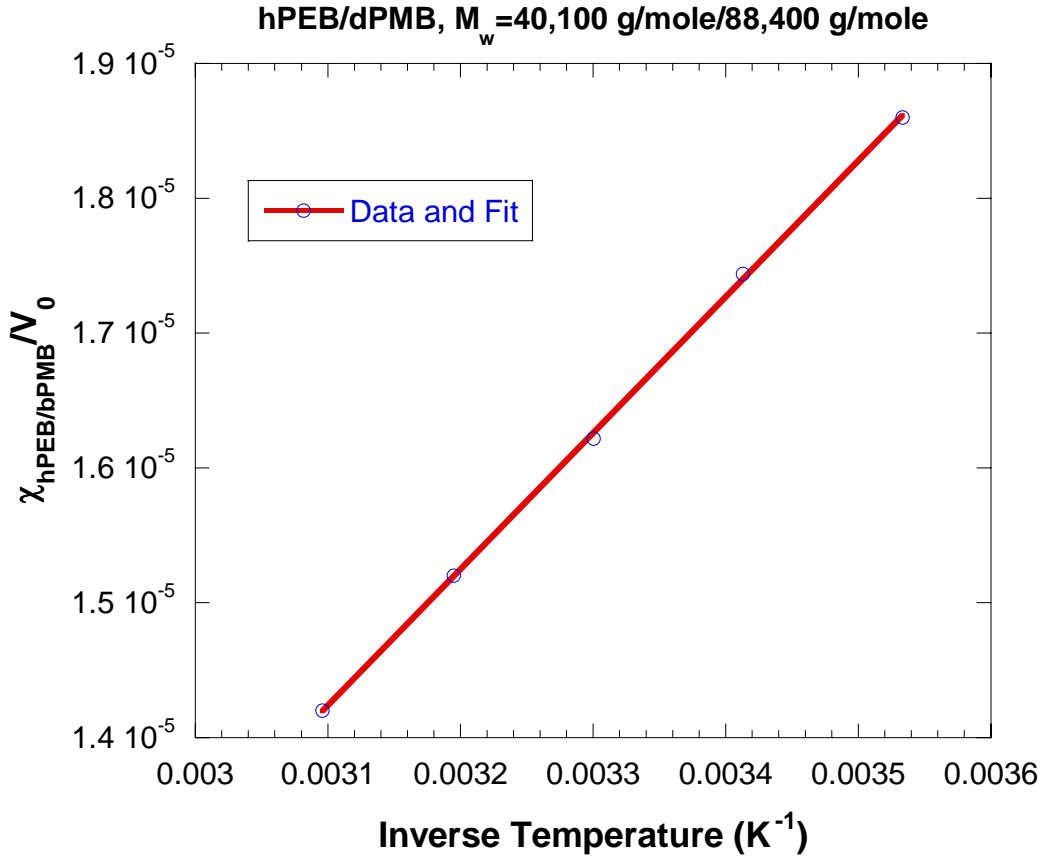
Figure 5: Variation of the Flory-Huggins $\dfrac{\chi_{12}(T)}{v_0}$ parameter with inverse temperature.

6. GIBBS FREE ENERGY AND PHASE DIAGRAM

Based on the Flory-Huggins parameter obtained from one hPEB/dPMB sample, the Gibbs free energy and the phase diagram can be constructed. This assumes that the Flory-Huggins parameter does not depend on polymer blend composition. This is a fairly good assumption for polyolefin blends.

Based on the figure showing the Gibbs free energy, the 220 K (= -53 $^{\circ}$C) temperature corresponding to the spinodal temperature of this sample is also the critical temperature of the phase diagram. The 270 K temperature is well in the one-phase region and the 200 K temperature is well into the spinodal region. The spinodal points are located at the two inflection points (where the second derivation of the free energy is zero). The two binodal

points correspond to two-points on the curve that share the same tangent as shown in the figure.

Recall that the spinodal condition is given by:

$$\frac{1}{k_B T} \frac{\partial^2 G}{\partial \phi_1{}^2} = \frac{1}{n_1 \phi_1 v_1} + \frac{1}{n_2 \phi_2 v_2} - 2 \frac{\chi_{12}(T)}{v_0} = 0 . \tag{8}$$

The binodal condition is obtained for:

$$\frac{G(\phi_A) - G(\phi_B)}{\phi_A - \phi_B} = \frac{\partial G(\phi_A)}{\partial \phi_1} - \frac{\partial G(\phi_B)}{\partial \phi_1} . \tag{9}$$

At fixed T, the two binodal volume fractions are called ϕ_A and ϕ_B.
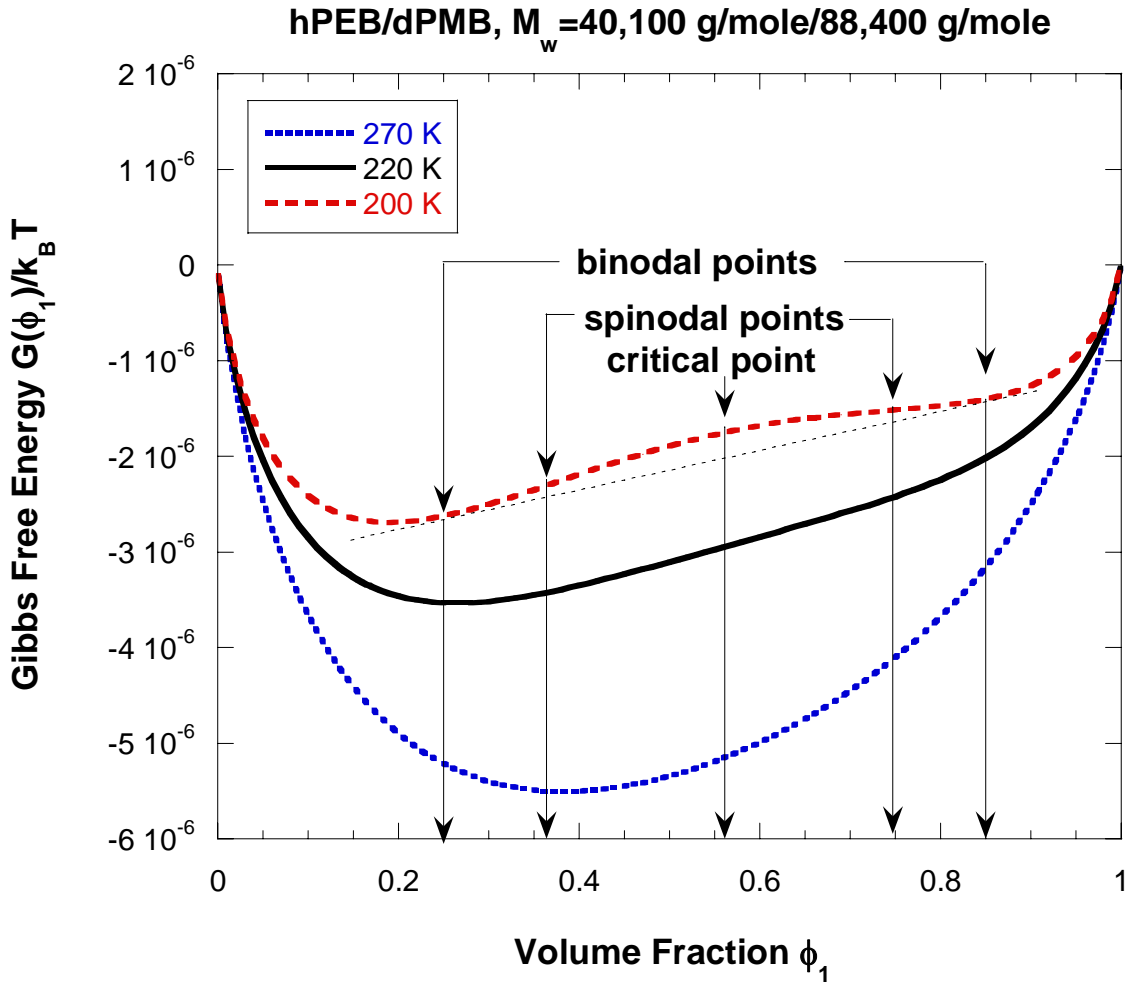
Figure 6: Variation of the Gibbs free energy with volume fraction $\phi_1 = \phi_{hPEB}$ for hPEO/dPMB blends. The measured sample with 0.57/0.43 volume fraction is at the critical point.

Once the Gibbs free energy is known, the demixing phase diagram can be mapped out.

hPEB/dPMB, M_w=40,100 g/mole/88,400 g/mole
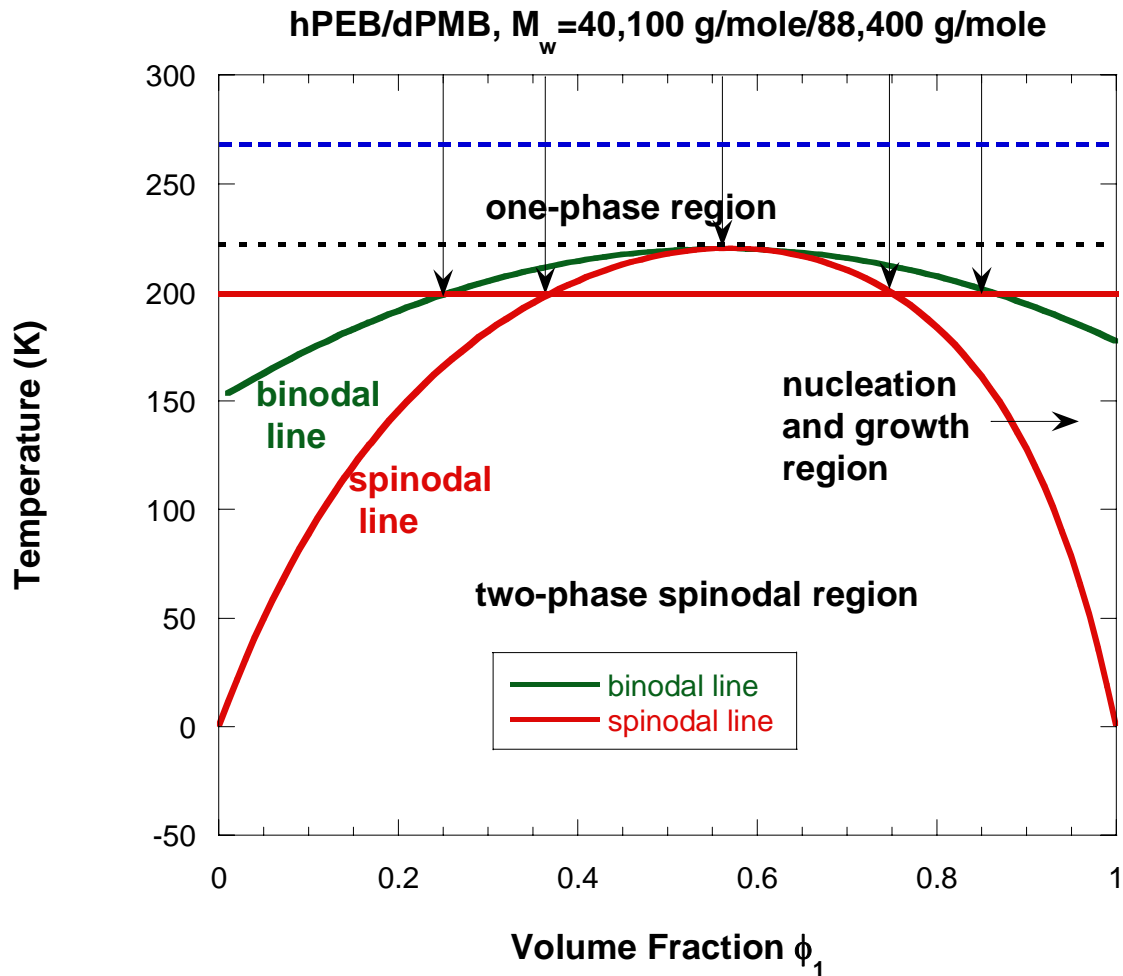
Figure 7: Variation of the spinodal and binodal temperatures with volume fraction $\phi_1 = \phi_{hPEB}$ for hPEO/dPMB blends. The spinodal region is underneath the binodal line. Vertical lines continue from the previous figure.

REFERENCES

A.A. Lefebvre, J.H. Lee, N.P. Balsara, B. Hammouda, "Fluctuations in Highly Metastable Polymer Blends", J. Polym. Sci., Polym. Phys. Ed. <u>38</u>, 1926-1930 (2000).

QUESTIONS

1. What scattering method detects the spinodal temperature? How about the binodal temperature?
2. What equation relates scattering methods and polymer mixture thermodynamics?
3. What relation defines the spinodal condition?
4. Based on the Flory-Huggins theory of phase separation, can you guess what would be the main difference between phase diagrams for a polymer blend and a polymer solution?

5. Polymer phase separation occurs either through spinodal decomposition or nucleation and growth? Define these two regions of the phase diagram.
6. Does the RPA apply when the sample is in the two-phase region?
7. What is the morphology characteristic of a fully phase separated polymer blend?

ANSWERS

1. The spinodal temperature corresponds to phase separation through local scale fluctuations. It is best detected by the SANS method. The binodal temperature corresponds to phase separation at a large length scale. It is best detected by light scattering. The binodal temperature can also be detected by SANS.
2. Scattering and polymer mixture thermodynamics are related by the following equation: $(1/k_B T)(\partial^2 G/\partial\phi_1^2) = S^{-1}(Q = 0)$. Here G is Gibbs free energy, ϕ_1 is the volume fraction of component 1 and S(Q=0) is the structure factor for Q=0 (i.e., in the thermodynamics limit).
3. The spinodal condition is defined by the inflection point of $G(\phi_1)$ *vs* ϕ_1 where G is the Gibbs free energy. This condition is expressed as $\partial^2 G/\partial\phi_1^2 = 0$.
4. The thermodynamics of phase separation of a polymer solution can be described by the Flory Huggins theory with $n_2 = 1$ (assuming that component 2 is the solvent). This tends to skew the phase diagram for polymer solutions towards the dilute limit. The critical point for polymer solutions takes place at low polymer volume fractions.
5. The spinodal region is underneath the spinodal line in the phase diagram (temperature T *vs* volume fraction ϕ_1). The nucleation and growth region is between the binodal and spinodal lines.
6. The RPA breaks down when the sample is in the two-phase region.
7. A fully phase separated polymer blend is characterized by a droplet morphology (droplets of one component in the medium of the other). A fully phase separated sample is also "hazy" since the droplets' size becomes comparable to the wavelength of visible light (fraction of a micron).

Scattering from block copolymer systems is characterized by a scattering peak representing the average inter-distance between domains in the ordered phase region. The scattering peak persists in the disordered phase region where it represents the "correlation hole" effect (Leibler, 1980). Scattering from a diblock copolymer solution is discussed here.

1. POLYSTYRENE-POLYISOPRENE COPOLYMER IN DOP SOLUTION

The polystyrene-polyisoprene (hPS-hPI) diblock copolymer considered here has typical molecular weights (M_w=11,000 for hPS and M_w=17,000 g/mol for hPI). Since the order-to-disorder (ODT) phase transition temperature for this copolymer is high, it was dissolved in dioctyl phthalate (DOP) at a copolymer volume fraction of 0.65. This brought the ODT down to an easily reachable value. DOP is a non-volatile good solvent for both hPS and hPI.

Even though none of the blocks is deuterated, the hPS-hPI copolymer is characterized by a reasonable "natural" neutron contrast in DOP.

Table 1: Summary of the scattering lengths and specific volumes.

	Notation	Formula	Scattering Length (cm)	Density (g/cm^3)	Specific Volume (cm^3/mol)
Polystyrene	hPS	C_8H_8	$0.23*10^{-11}$	1.04	100
Polyisoprene	hPI	C_5H_8	$0.33*10^{-12}$	0.91	75
Dioctylphthalate	DOP	$C_{24}H_{38}O_4$	$4.07*10^{-12}$	0.98	397

The three contrast factors are given by:

$$\left(\frac{b_{hPS}}{v_{hPS}} - \frac{b_{hPI}}{v_{hPI}} \right)^2 N_{av} = 2.08*10^{-4} \, \text{mol/cm}^4. \qquad (1)$$

$$\left(\frac{b_{hPS}}{v_{hPS}} - \frac{b_{DOP}}{v_{DOP}} \right)^2 N_{av} = 9.75*10^{-5} \, \text{mol/cm}^4.$$

$$\left(\frac{b_{hPI}}{v_{hPI}} - \frac{b_{DOP}}{v_{DOP}} \right)^2 N_{av} = 2.05*10^{-5} \, \text{mol/cm}^4.$$

The contrast factors were multiplied by Avogadro's number N_{av} in order to keep the order of magnitude reasonable. Some of these contrast factors are used in the data analysis process.

2. SANS DATA

SANS data was acquired using one instrument configuration for which the prominent scattering peak occurs in the middle of the scattering window. Sample temperature was varied between 20 °C and 70 °C at 10 °C intervals.
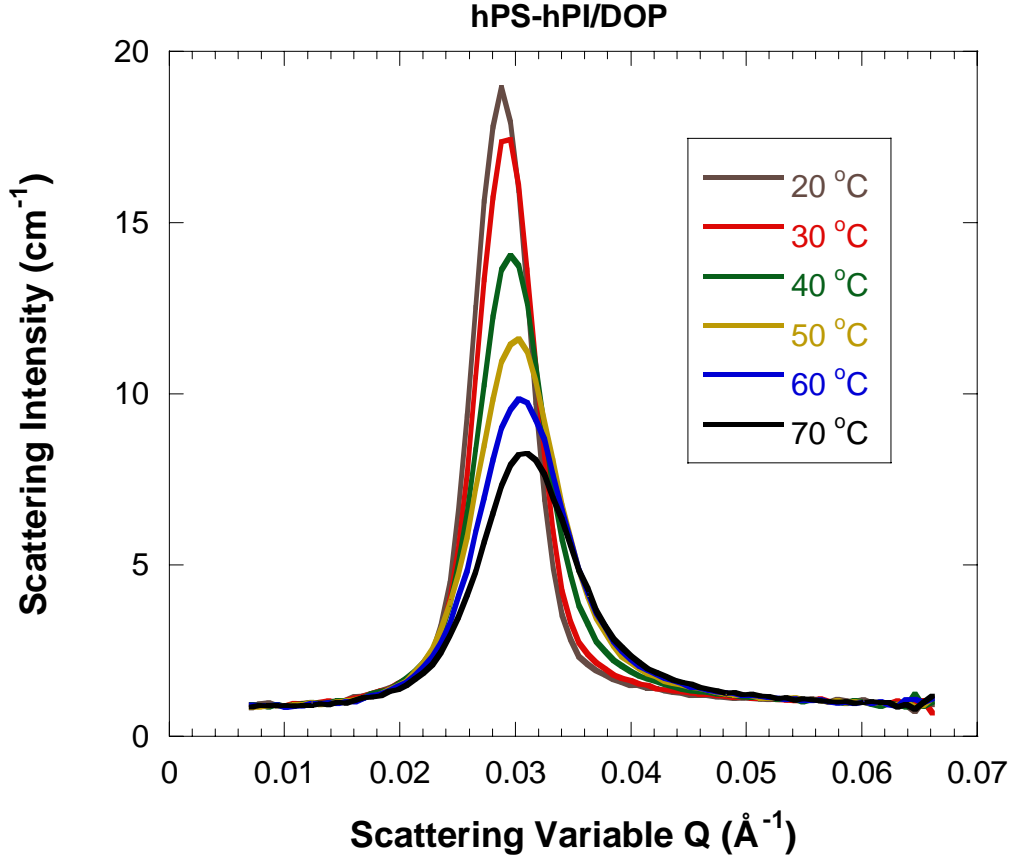
Figure 1: SANS data from the hPS-hPI/DOP diblock copolymer solution at various sample temperatures.

This Order-to-Disorder (ODT) temperature is the equivalent of the spinodal temperature for polymer blends displaying a UCST behavior. When temperature is raised, the copolymer ordered phase melts into a disordered phase.

An empirical model characterized by a peaked behavior is used first to fit the SANS data:

$$I(Q) = \frac{C}{1 + \left(| Q - Q_0 | L\right)^m} + B \ .$$

(2)

The fitting parameter C is a measure of composition fluctuations. C is high in the ordered phase and decreases in the disordered phase. A simple way of estimating the ODT is through a plot of $1/C$ vs $1/T$ (T is the absolute temperature). Extrapolation to the condition where the

scattering peak intensity C blows up yields an ODT of 29 °C. The hPS-hPI/DOP is ordered below that temperature. The measured sample phase separates into a lamellar morphology.

hPS-hPI/DOP
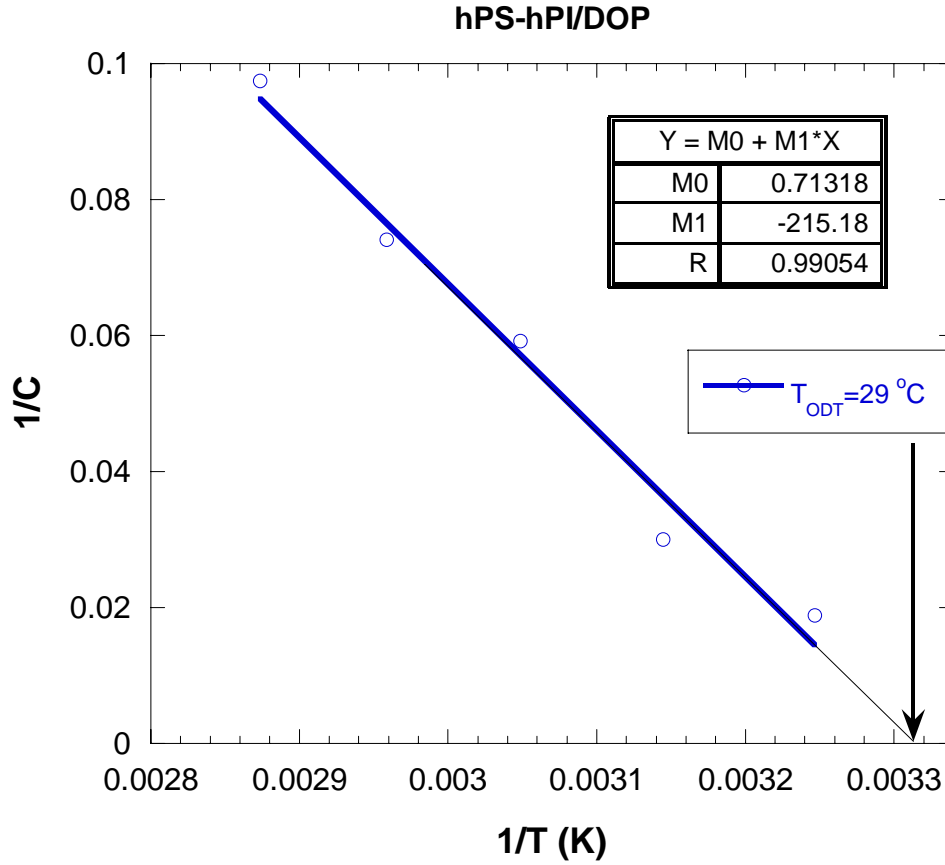
Figure 2: Determination of the Order-to-Disorder temperature.

3. THE RPA MODEL FOR A DIBLOCK COPOLYMER SOLUTION

Consider the DOP solvent (component 3) as the background component in the Random Phase Approximation (RPA) model (Akcasu-Tombakoglu, 1990; Hammouda, 1993). The RPA model applies to the disordered phase only. The relevant equations in matrix form are reproduced here as a review.

$$\underline{\underline{S}}^{-1}(Q) = \underline{\underline{S}}_0^{-1}(Q) + \underline{\underline{v}}(Q) \tag{2}$$

$$\underline{\underline{S}}(Q) = \left(\underline{\underline{1}} + \underline{\underline{S}}_0(Q).\underline{\underline{v}}(Q)\right)^{-1}.\underline{\underline{S}}_0(Q)$$

$$S_0(Q) = \begin{bmatrix} S^0_{11}(Q) & S^0_{12}(Q) & 0 \\ S^0_{21}(Q) & S^0_{22}(Q) & 0 \\ 0 & 0 & S^0_{33}(Q) \end{bmatrix}$$

$$S^0_{ii}(Q) = n_i \phi_i v_i P_i(Q)$$

$$S^0_{ij}(Q) = \sqrt{n_i \phi_i v_i n_j \phi_j v_j} \, P_{ij}(Q)$$

$$P_i(Q) = \frac{2}{Q^4 R_{gi}^4} \left[\exp(-Q^2 R_{gi}^2) - 1 + Q^2 R_{gi}^2 \right]$$

$$P_{ij}(Q) = F_i(Q)F_j(Q) = \left(\frac{1 - \exp\left(-Q^2 R_{gi}^2\right)}{Q^2 R_{gi}^2} \right) \left(\frac{1 - \exp\left(-Q^2 R_{gj}^2\right)}{Q^2 R_{gj}^2} \right)$$

$$R_{gi}^2 = \frac{n_i a_i^2}{6}$$

$$v_{11}(Q) = \frac{1}{S^0_{33}(Q)} - 2\frac{\chi_{13}}{v_0}$$

$$v_{22}(Q) = \frac{1}{S^0_{33}(Q)} - 2\frac{\chi_{23}}{v_0}$$

$$v_{12}(Q) = \frac{1}{S^0_{33}(Q)} + \frac{\chi_{12}}{v_0} - \frac{\chi_{13}}{v_0} - \frac{\chi_{23}}{v_0}$$

$$S_{11}(Q) = \frac{S^0_{11}\left(1 + v_{21}S^0_{12} + v_{22}S^0_{22}\right) - S^0_{12}\left(v_{21}S^0_{11} + v_{22}S^0_{21}\right)}{\left(1 + v_{11}S^0_{11} + v_{12}S^0_{21}\right)\left(1 + v_{21}S^0_{12} + v_{22}S^0_{22}\right) - \left(v_{11}S^0_{12} + v_{12}S^0_{22}\right)\left(v_{21}S^0_{11} + v_{22}S^0_{21}\right)}$$

$$S_{22}(Q) = \frac{S^0_{22}\left(1 + v_{12}S^0_{21} + v_{11}S^0_{11}\right) - S^0_{21}\left(v_{12}S^0_{22} + v_{11}S^0_{12}\right)}{\left(1 + v_{11}S^0_{11} + v_{12}S^0_{21}\right)\left(1 + v_{21}S^0_{12} + v_{22}S^0_{22}\right) - \left(v_{11}S^0_{12} + v_{12}S^0_{22}\right)\left(v_{21}S^0_{11} + v_{22}S^0_{21}\right)}$$

$$S_{12}(Q) = \frac{-S^0_{11}\left(v_{11}S^0_{12} + v_{12}S^0_{22}\right) + S^0_{12}\left(1 + v_{11}S^0_{11} + v_{12}S^0_{21}\right)}{\left(1 + v_{11}S^0_{11} + v_{12}S^0_{21}\right)\left(1 + v_{21}S^0_{12} + v_{22}S^0_{22}\right) - \left(v_{11}S^0_{12} + v_{12}S^0_{22}\right)\left(v_{21}S^0_{11} + v_{22}S^0_{21}\right)}$$

$$\frac{d\Sigma(Q)}{d\Omega} = \Delta\rho_1^2 S_{11}(Q) + \Delta\rho_2^2 S_{22}(Q) + 2\Delta\rho_1\Delta\rho_2 S_{12}(Q) + B.$$

Note that a Q-independent constant has been added to the scattering intensity to account for the incoherent scattering background. These equations are used to fit the SANS data in the disordered phase.

4. SANS DATA ANALYSIS

Analysis of the SANS data was performed using the RPA model and the following input parameters:

Component 1: hPS, $n_{hPS}=106$, $\phi_{hPS}=0.23$, $v_{hPS}=100$ cm^3/mol   (3)
Component 2: hPI, $n_{hPI}=250$, $\phi_{hPI}=0.42$, $v_{hPI}=75$ cm^3/mol
Component 3: DOP, $n_{DOP}=1$, $\phi_{DOP}=0.35$, $v_{DOP}=397$ cm^3/mol.

The fitting parameters obtained for the 70 $^{\mathrm{o}}$C temperature are included here:

$$a_{hPS} = 8.45 \text{ Å} \qquad\qquad\qquad (4)$$
$$a_{hPI} = 6.44 \text{ Å}$$
$$a_{DOP} = 29.15 \text{ Å}$$

$$\frac{\chi_{hPS/DOP}}{v_0} = 0.0104 \text{ mol/cm}^3$$

$$\frac{\chi_{hPI/DOP}}{v_0} = 0.040 \text{ mol/cm}^3$$

$$\frac{\chi_{hPS/hPI}}{v_0} = 0.013 \text{ mol/cm}^3$$

$$B = 0.828 \text{ cm}^{-1}.$$

These parameters are reasonable estimates given the fact that so many parameters were floated at the same time. More precise parameters could be obtained if pure hPS/DOP, hPI/DOP and/or hPS/hPI samples were measured first. The 70 $^{\mathrm{o}}$C temperature is above the ODT (of 29 $^{\mathrm{o}}$C) and well within the single-phase region whereby the copolymer microstructure has melted. The observed SANS peak is due to the correlation hole effect.

hPS-hPI/DOP at 70 °C
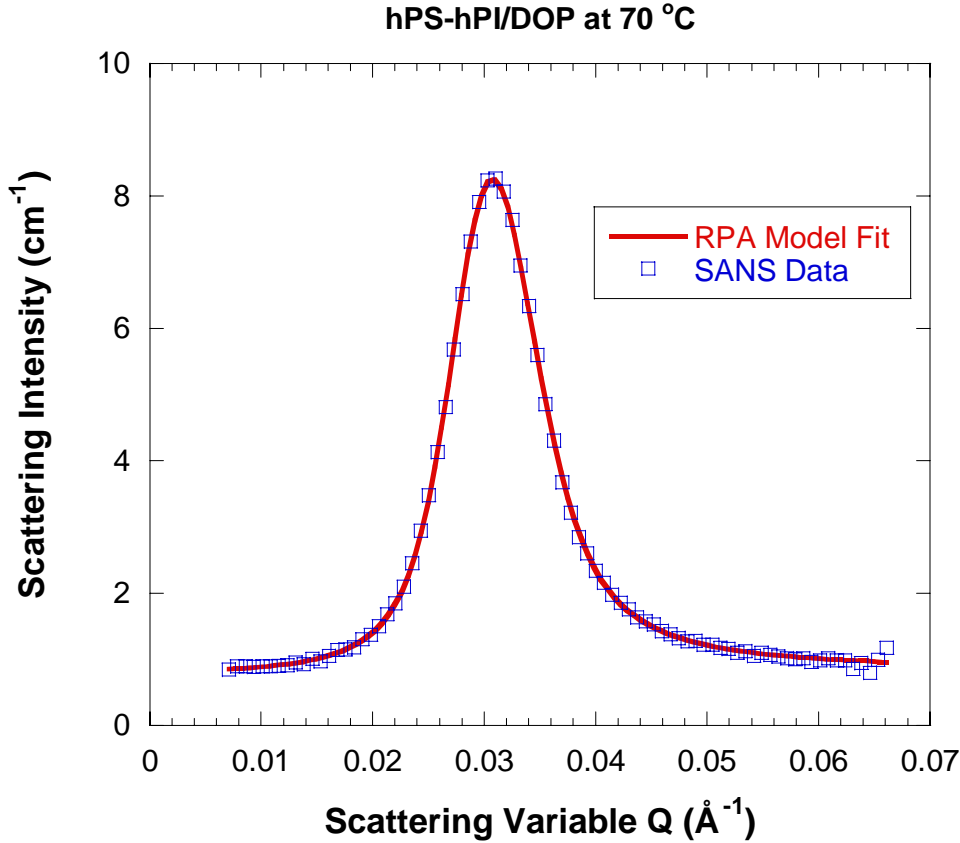
Figure 3: Superposition of the RPA model fit and the SANS data for the 70 °C temperature.

5. THE ORDERED PHASE

The ordered phase is characterized by three main morphologies: spherical, cylindrical or lamellar domains. Other morphologies such as the gyroid and double-diamond phases are also known. The RPA model can predict the ODT line but does not apply in the ordered phase region. It yields predictions from the disordered phase region. Other more sophisticated models such as the self-consistent filed theory can predict the various phases in the ordered phase region. The critical condition for a symmetric diblock copolymer is given by $\chi n = 10.5$. Here χ is the Flory-Huggins interaction parameter and n is the degree of polymerization. Recall that this condition is $\chi n = 2$ for symmetric polymer blends. Above that condition, phase separation occurs. Both the spinodal phase separation in polymer blends and the Order-to-Disorder Transition (ODT) in copolymers are second order phase transitions since they involve the second derivative of the Gibbs free energy $k_B T / S(0) = \partial^2 G / \partial \phi_1^2 = 0$ where ϕ_1 is the order parameter (polymer composition). The ODT is also referred to as a "weak" first order phase transition.

Disordered Block Copolymer
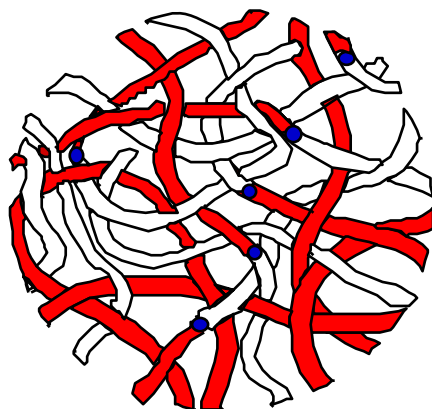
Ordered Block Copolymer
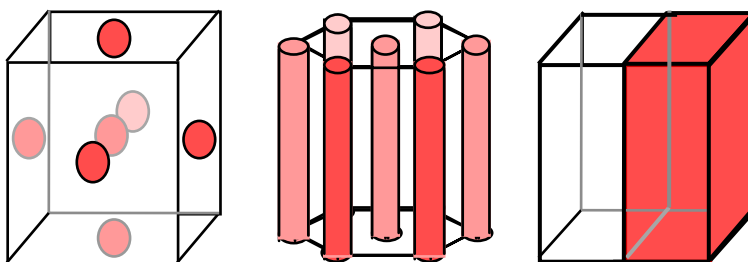
Figure 4: Representation of the disordered phase and the ordered phases.

Copolymer Phase Diagram
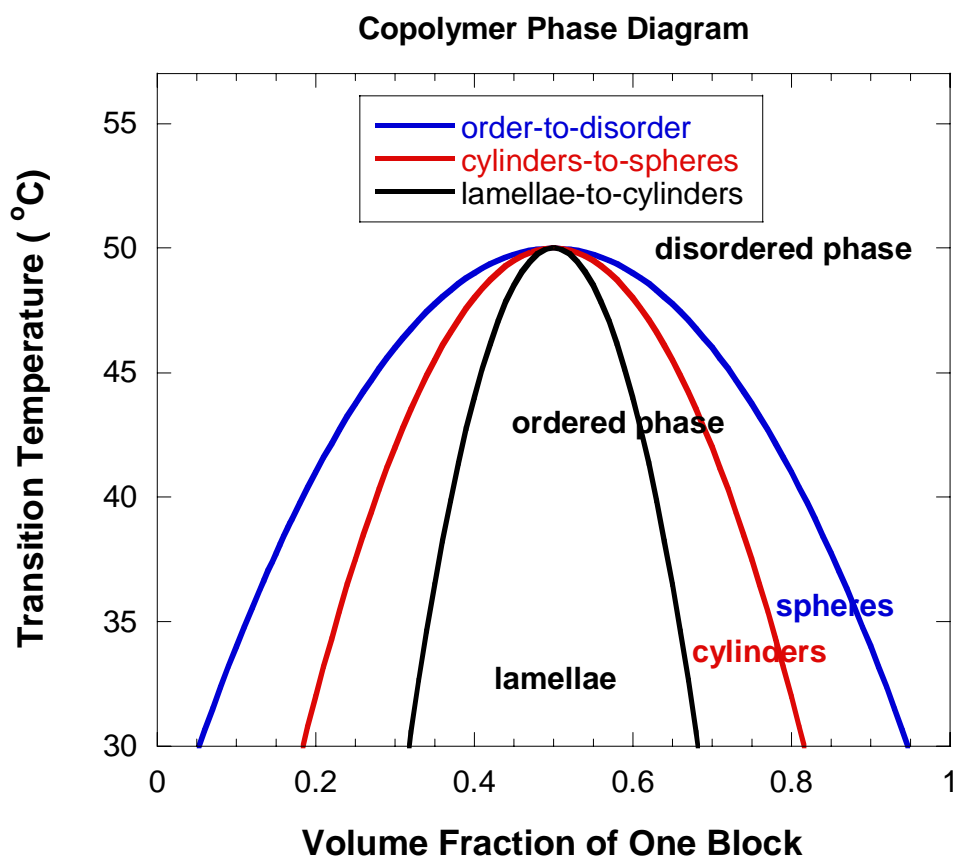
Figure 5: Schematic representation of the copolymer phase boundaries for the main morphologies.

The position of higher order peaks (relative to the first order peak) varies for the various copolymer morphologies. The first order peaks occur as follows:

-- $1, \sqrt{2}, \sqrt{3}$ for the spherical morphology.

-- $1, \sqrt{3}, \sqrt{4}$ for the cylindrical morphology.

-- $1, 2, 3$ for the lamellar morphology.

Due to the broad wavelength spread characterizing SANS (and therefore of the Q resolution standard deviation), higher order peaks are smeared and hard to resolve.

REFERENCES

L. Leibler, "Theory of Microphase Separation in Block Copolymers", Macromolecules 13, 1602-1617 (1980).

A.Z. Akcasu and M. Tombakoglu, "Dynamics of Copolymer and Homopolymer Mixtures in Bulk and in Solution via the Random Phase Approximation", Macromolecules 23, 607-612 (1990).

B. Hammouda, "SANS from Homogeneous polymer Mixtures: A Unified Overview", Advances in Polymer Science 106, 87 (1993).

QUESTIONS

1. The SANS data from copolymers are characterized by a peak in what phase (ordered or disordered or both)? Why?
2. What is the correlation hole effect?
3. What are the main morphologies formed in the ordered phase region?
4. What is the most likely morphology formed by a symmetric diblock copolymer? Why?
5. What is critical condition (for phase separation) for χn for symmetric diblock copolymers. Here χ is the Flory-Huggins interaction parameter and n is the degree of polymerization. What is that condition for symmetric polymer blends?
6. What is the order of the spinodal and Order-to-Disorder phase transitions?

ANSWERS

1. The SANS data from copolymers are characterized by a peak in both the ordered and the disordered phases. The peak in the ordered phase is due to the periodic microphase separated morphology whereas the peak in the disordered phase region is due to the correlation hole effect.
2. The correlation hole effect occurs when the nearest neighbors are excluded from the region right next to a particle. In copolymers, the second block excludes regions containing the first block.
3. The main morphologies formed in the ordered phase region are spherical, cylindrical and lamellar.
4. The most likely morphology formed by a symmetric diblock copolymer is lamellar because there is 50 % of each block.
5. The critical condition (for phase separation) for symmetric diblock copolymers is $\chi n = 10.5$. That condition is $\chi n = 2$ for symmetric polymer blends.
6. The spinodal transition for polymer blends and the Order-to-Disorder phase transition for copolymers are both second order phase transitions. The ODT is also referred to as a "weak" first order transition.

A ternary polymer blend is a mixture of three polymers. The thermodynamics of mixing and phase separation can be investigated for ternary blends using the SANS technique and the Random Phase Approximation.

1. SANS FROM A TERNARY POLYMER BLEND

Consider a ternary polymer blend consisting of deuterated polystyrene (dPS), non-deuterated polystyrene (hPS) and poly(vinyl methyl ether) (PVME) (Hammouda et al, 1992). The binary blend dPS/PVME is characterized by a Lower Critical Spinodal Temperature (LCST) whereas the binary blend dPS/hPS is characterized by a weak Upper Critical Spinodal Temperature (UCST). Here, the ternary blend was investigated with the goal of testing the RPA model for multi-component mixtures and investigating the phase separation of the binary hPS/PVME blend. This blend does not contain any deuteration and could not be investigated by SANS directly.

A series of three samples were prepared. The characterization of the polymers used and of the volume fractions of the three samples that were prepared are summarized in two tables.

Table 1: Characterization of the polymers used.

	Mw (g/mol)	Mw/Mn	Degree of Polymerization	Specific Volume (cm3/mol)
dPS	1.95×10^5	1.02	1741	100
hPS	1.90×10^5	1.04	1827	100
PVME	1.59×10^5	1.30	2741	55.4

Table 2: Volume fractions for the three measured samples.

Sample Number	ϕ_{dPS}	ϕ_{PVME}	ϕ_{hPS}
1	0.484	0.516	0
2	0.360	0.511	0.129
3	0.238	0.506	0.256

SANS data were taken from the three samples for a range of temperatures above the polystyrene glass transition temperature (i.e., above 100 $^{oC).}$ SANS data from sample 3 for a range of temperatures in the homogeneous phase region are show in a figure. The intensity is seen to increase when temperature is increased. This is a sign of LCST behavior.
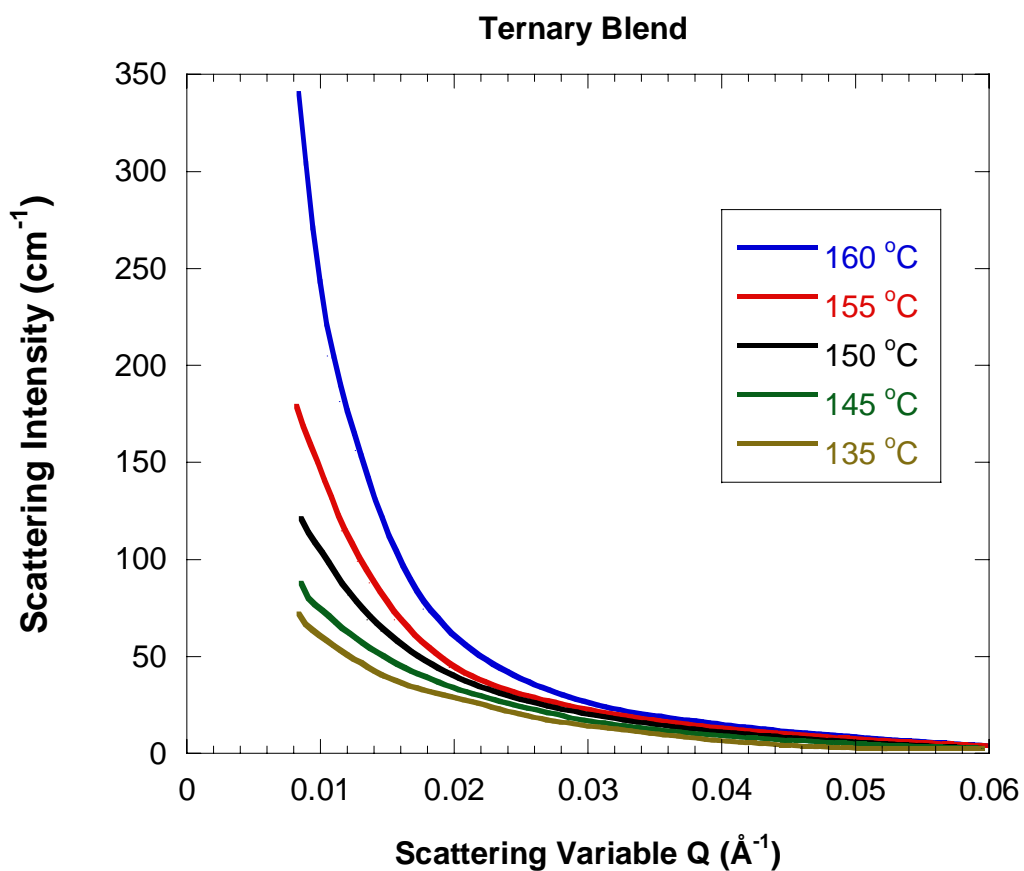
Figure 1: SANS data taken from sample 3 for a range of temperatures.

Variation of the forward scattering intensity with increasing temperature shows an interesting variation for the 3 samples.
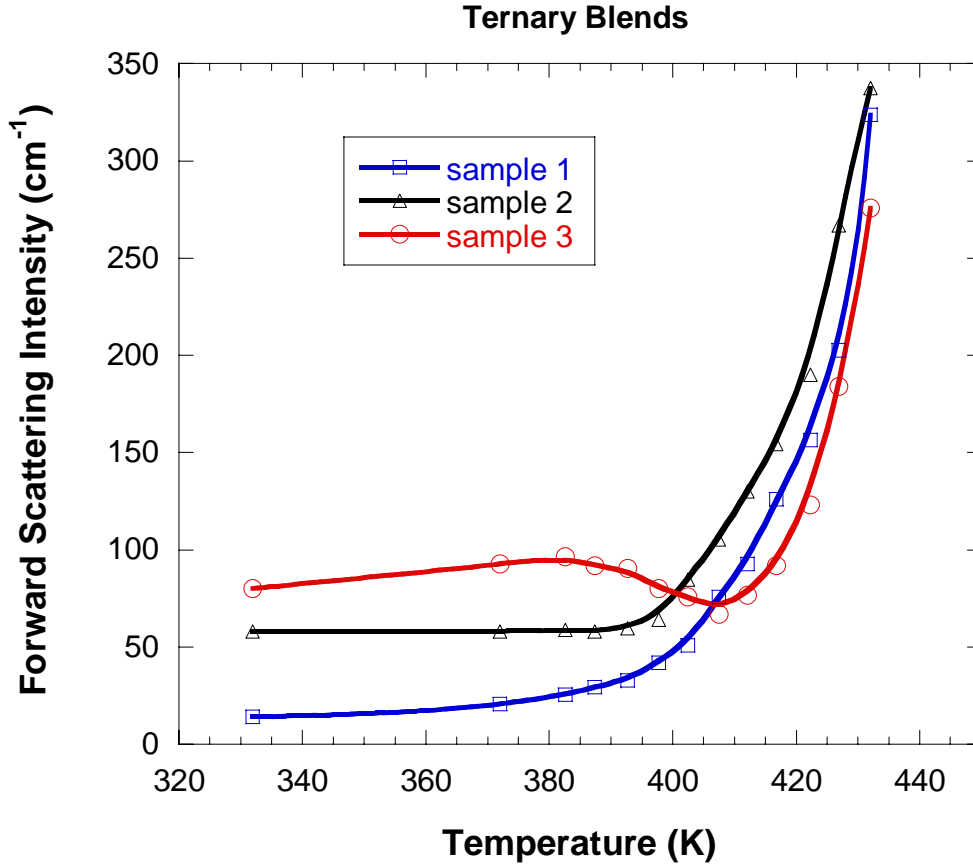
Ternary Blends

Figure 2: Variation of the forward scattering intensity $d\Sigma(Q = 0)/d\Omega$ with increasing temperature for the three ternary blends. The lowest value of Q = 0.0085 Å-1 is used to represent the forward scattering value.

Sample 3 shows a decrease in intensity at first then an increase. This is due to the interplay between the LCST behavior for dPS/PVME and hPS/PVME and the UCST behavior for the dPS/hPS.

2. THE TERNARY RPA MODEL

The ternary RPA equations are summarized here. Consider a ternary blend consisting of polymer 1, polymer 2 and polymer 3. The degrees of polymerization are noted n1, n2 and n3, the volume fractions are ϕ_1, ϕ_2 and ϕ_3, the specific monomer volumes are v1, v2 and v3, the radii of gyration are Rg1, Rg2 and Rg3, the form factors are P1(Q), P2(Q) and P3(Q) and the Flory-Huggins interaction parameters are χ_{12}, χ_{23} and χ_{13}.

The RPA equations for a ternary blend in the homogeneous phase are as follows. The non-interacting structure factors are given by:

$$S^0_{11}(Q) = n_1\phi_1v_1P_1(Q) \tag{1}$$

377

$$S^0_{22}(Q) = n_2 \phi_2 v_2 P_2(Q)$$
$$S^0_{33}(Q) = n_3 \phi_3 v_3 P_3(Q)$$

The form factors are given by the Debye function:

$$P_1(Q) = \frac{2}{Q^4 R_{g1}^4} \left[\exp(-Q^2 R_{g1}^2) - 1 + Q^2 R_{g1}^2 \right]$$

$$P_2(Q) = \frac{2}{Q^4 R_{g2}^4} \left[\exp(-Q^2 R_{g2}^2) - 1 + Q^2 R_{g2}^2 \right] \tag{2}$$

$$P_3(Q) = \frac{2}{Q^4 R_{g3}^4} \left[\exp(-Q^2 R_{g3}^2) - 1 + Q^2 R_{g3}^2 \right]$$

The excluded volume factors are:

$$v_{11}(Q) = \frac{1}{S^0_{33}(Q)} - 2\frac{\chi_{13}}{v_0}$$

$$v_{22}(Q) = \frac{1}{S^0_{33}(Q)} - 2\frac{\chi_{23}}{v_0} \tag{3}$$

$$v_{12}(Q) = \frac{1}{S^0_{33}(Q)} + \frac{\chi_{12}}{v_0} - \frac{\chi_{13}}{v_0} - \frac{\chi_{23}}{v_0}$$

The partial structure factors for the fully interacting mixture are given by:

$$S_{11}(Q) = \frac{S^0_{11}(Q)\left(1 + v_{22}S^0_{22}(Q)\right)}{\left(1 + v_{11}S^0_{11}(Q)\right)\left(1 + v_{22}S^0_{22}(Q)\right) - v_{12}^2 S^0_{11}(Q)S^0_{22}(Q)} \tag{4}$$

$$S_{22}(Q) = \frac{S^0_{22}(Q)\left(1 + v_{11}S^0_{11}(Q)\right)}{\left(1 + v_{11}S^0_{11}(Q)\right)\left(1 + v_{22}S^0_{22}(Q)\right) - v_{12}^2 S^0_{11}(Q)S^0_{22}(Q)}$$

$$S_{12}(Q) = \frac{-S^0_{11}(Q)v_{12}S^0_{22}(Q)}{\left(1 + v_{11}S^0_{11}(Q)\right)\left(1 + v_{22}S^0_{22}(Q)\right) - v_{12}^2 S^0_{11}(Q)S^0_{22}(Q)}$$

The scattering cross section is given by:

$$\frac{d\Sigma(Q)}{d\Omega} = \Delta\rho_1^2 S_{11}(Q) + \Delta\rho_2^2 S_{22}(Q) + 2\Delta\rho_1\Delta\rho_2 S_{12}(Q) \tag{5}$$

The relevant contrast factors are:

$$\Delta\rho_1{}^2 = (\rho_1 - \rho_3)^2 = \left(\frac{b_1}{v_1} - \frac{b_3}{v_3}\right)^2$$

$$\Delta\rho_2{}^2 = (\rho_2 - \rho_3)^2 = \left(\frac{b_2}{v_2} - \frac{b_3}{v_3}\right)^2 .$$

(6)

Note that the scattering cross section for incompressible blends is independent of the $(\rho_1 - \rho_2)^2$ contrast factor.

3. FITTING OF THE SANS DATA

The SANS data were fitted to the RPA model for ternary blends with the various known parameters (n_i, ϕ_i, v_i, $\Delta\rho_{i2}$) with index i representing either dPS, hPS or PVME. The radii of gyration R_{gdPS}, R_{ghPS} and R_{gPVME} and the Flory-Huggins interaction parameters $\chi_{dPS/PVME}/v_0$, $\chi_{hPS/PVME}/v_0$ and $\chi_{dPS/hPS}/v_0$ were allowed to vary during the nonlinear least-squares fits.

The various contrast factors are:

$$\left(\frac{b_{hPS}}{v_{hPS}} - \frac{b_{PVME}}{v_{PVME}}\right)^2 N_{av} = 1.79*10^{-4} \, mol/cm^4$$

$$\left(\frac{b_{dPS}}{v_{dPS}} - \frac{b_{PVME}}{v_{PVME}}\right)^2 N_{av} = 6.07*10^{-3} \, mol/cm^4$$

$$\left(\frac{b_{dPS}}{v_{dPS}} - \frac{b_{hPS}}{v_{hPS}}\right)^2 N_{av} = 4.16*10^{-3} \, mol/cm^4 .$$

(7)

Only two of these contrast factors are needed. Note that deuteration enhances the contrast factor and that Avogadro's number N_{av} has been introduced to keep from handling very small numbers.

Results of the fits are included here. The binary dPS/PVME blend (sample 1) gave a reliable estimate of the Flory-Huggins interaction parameter:

$$\left(\frac{\chi}{v_0}\right)_{dPS/PVME} = 9.73*10^{-4} - \frac{0.416}{T} .$$

(8)

This interaction parameter decreases with inverse temperature (1/T) which is a signature of the LCST behavior.

Previous measurements from a dPS/hPS binary blend and these measurements from ternary blends yielded:

$$\left(\frac{\chi}{v_0}\right)_{dPS/hPS} = -2.9*10^{-6} + \frac{0.0020}{T}$$. (9)

This interaction parameter for an isotopic blend is orders of magnitude smaller than typical ones for other blends. It increases with (1/T) which means that the dPS/hPS is characterized by a UCST behavior.

The third interaction parameter obtained from fits of the data taken from samples 2 and 3 are:

$$\left(\frac{\chi}{v_0}\right)_{hPS/PVME} = 10.3*10^{-4} - \frac{0.422}{T}$$ from sample 2 (10)

$$\left(\frac{\chi}{v_0}\right)_{hPS/PVME} = 10.6*10^{-4} - \frac{0.436}{T}$$ from sample 3.

These values agree fairly well. The units of (χ/v0) are in cm3/mol.
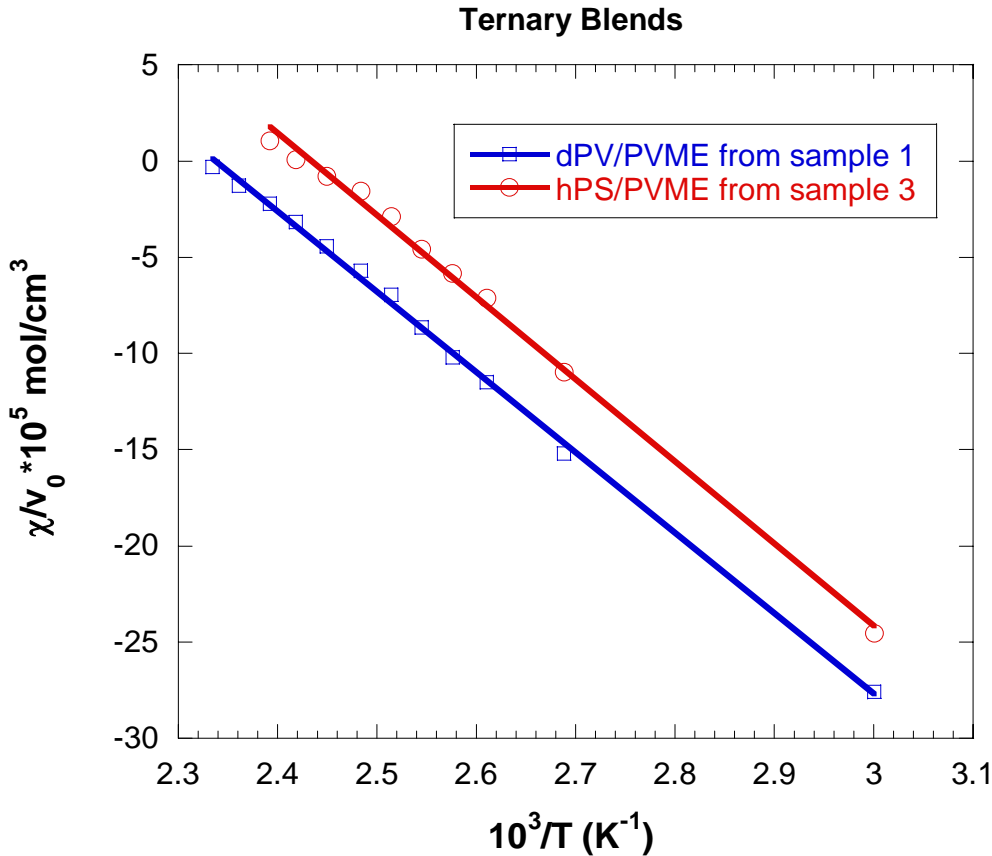
Figure 3: Variation of the Flory-Huggins interaction parameters for dPS/PVME obtained from sample 1 and for hPS/PVME obtained from sample 3.

The interaction parameters for the dPS/PVME and the hPS/PVME are close but not identical. The difference is due to the isotopic effect.

4. SPINODAL TEMPERATURE

The spinodal temperature is reached when the denominator of the structure factors (for Q = 0) goes to zero.

$$\left(1 + v_{11}S^0{}_{11}(0)\right)\left(1 + v_{22}S^0{}_{22}(0)\right) - v_{12}{}^2 S^0{}_{11}(0)S^0{}_{22}(0) = 0 \qquad (11)$$

This gives the following estimates for the spinodal temperatures:

Ts = 433 K = 160 ^oC for Sample 1
Ts = 421 K = 148 ^oC for Sample 2
Ts = 416 K = 143 ^oC for Sample 3.

Note that this method is based on estimating the spinodal temperature from the one-phase (i.e., mixed phase) region.

5. DISCUSSION

Using ternary blend mixtures allowed measurement of the Flory-Huggins interaction parameter for a pair of non-deuterated polymers (hPS/PVME). This binary blend mixture could not have been measured directly by SANS due to the very small contrast factor and to the overwhelming incoherent scattering background. The method presented here is a reliable method to measure the small isotopic effect on the polymer-polymer interaction parameter.

When supplemented with the RPA model, the SANS technique is useful for the investigation of the demixing (i.e., spinodal) phase transition. This method has been used to investigate many homogeneous polymer mixtures.

REFERENCES

B. Hammouda, R. Briber and B. Bauer, "SANS from dPS/PVME/hPS Ternary Polymer Blends", Polymer 33, 1785-1787 (1992).

QUESTIONS

1. How does the scattering intensity vary for increasing temperature for a Lower Critical Spinodal Temperature (LCST) polymer blend mixture? How about for an Upper CST?
2. In the Random Phase Approximation (RPA) model, what is the size of the matrices for an incompressible ternary polymer blend?

3. Does the RPA model apply in the two-phase (i.e., phase separated) region?

4. Using the RPA model, could one work out the phase diagram for a ternary blend mixture?

ANSWERS

1. The scattering intensity increases for increasing temperature for an LCST polymer blend. The scattering intensity decreases for increasing temperature for a UCST blend. The scattering intensity always increases when approaching the spinodal temperature due to the buildup of composition fluctuations.

2. A ternary polymer blend contains three components. The incompressibility assumption allows the elimination of one component (referred to as the "background" component). Therefore, the size of the RPA matrices is two.

3. The RPA model does not apply in the two-phase region. It applies only in the homogeneous (i.e., mixed phase) region and breaks down at the spinodal line.

4. The RPA model could be used to map out the phase separation lines (spinodal temperatures) for a ternary blend mixture. The phase diagram is triangular with one component at each corner and temperature as the third dimension.

Chapter 41 - **SANS FROM POLYMERS LITERATURE REVIEW**

A focused review of the literature on "SANS from Polymers" is included here. It draws heavily from publications that resulted from the use of the NIST Center for Neutron Research facility. This author sifted through some 190 publications (published over the past seven years) and summarized those with which he is most familiar. These have been categorized into broad sub-topics in a concise and descriptive format.

1. BRANCHED POLYMERS

A good number of SANS investigations have focused on characterizing branched polymer systems. Theses include star polymers, dendrimers and graft polymers. Star polymers with a large number of arms are synthesized starting from a compact dendrimer core that provides a high number of functionalized groups upon which arms are grafted.

Amphiphilic poly(dimethylsiloxane)-graft-polyether copolymer micelles were investigated using many measurement methods including UV-Visible spectroscopy to characterize the Critical Micelles Concentration and SANS to characterize the micellar structure (Lin-Alexandridis, 2002, Paper 093)

Hydrophobically modified dendrimers forming cylindrical micelles have been studied by SANS and SAXS. Micellar shapes and sizes have been determined from the pair correlation function; i.e., the Fourier transform of the proper scattering intensity (Grohn et al, 2002, Paper 208).

Conformations and size information were obtained from poly(ethylene oxide) star polymers with a PAMAM dendrimer core. Samples ranging from 30 arms (generation 3 dendrimer) to 150 arms (generation 10 dendrimer) were synthesized and characterized by SANS. Radii of gyration of the stars were measured in dilute solution. Guinier and Kratky standard plots were used (Hedden-Bauer, 2003, Paper 049).

A series of publications focused on the thermodynamics of mixing of star branched and linear polymers. The Flory-Huggins interaction chi parameters were determined for a number of branching architectures and polymer chemistry. For instance, it was found that chi increases with the number of branch points and with the number of chain ends. This may be understood based on chain topology (Lee et al, 2006, Paper 481).

The contribution of chi due to chain architecture increases with star functionality (number of arms) for a blend mixture of star branched and linear polymers (Greenberg et al, 2001, Paper 036). The thermodynamics of miscibility of star-star polymers have also been investigated. This included isotopic mixtures of stars with different number of arms (T. Martter et al, 2002, Paper 104).

Other SANS investigations involved stars with dendrimer cores and deuterated arms in solution. The solvent scattering length density was matched to that of the arms (zero contrast condition) in order to obtain characteristic sizes (radius of gyration) and Porod (fractal)

exponents. It was found that these properties depend strongly on core branching architecture in the dilute region. Inter-particle structure factors were obtained for semi-dilute solutions (Stancik et al, 2003, Paper 159). The Beaucage model was applied to branched dendrimers in solution in order to characterize the degree of branching and its regularity (Rathgeber et al 2002, Paper 137).

Star polymers with a dendrimer core have also been investigated in the bulk state (without any solvent). These form many characteristic morphologies observed in other phase separated polymer systems. The use of TEM, SAXS and SANS resolved some of the ordered structures formed (Mackay et al, 2002, Paper 100).

Arborescent polymers are comb-like structures with many side branches for each generation. This synthesis method yields high molecular weights quickly (much faster than for dendrimers). Simple core-shell model with uniform density or with varying density in the shell produced a density profile from the SANS data. The second virial coefficient (obtained from the Zimm plot) decreased with generation number. The radius of gyration was found to increase with molecular weight as $R_g \sim M_w^{2.4}$ (Yun et al, 2003, Paper 192).

Macrocyclic dendritic spin clusters have been synthesized and characterized by many methods including SANS. These are organic molecules with high quantum spin number in the electronic ground state and are models for polymers with magnetic ordering. Shape reconstruction software packages were used in order to infer the shape of the scattering particles (Rajca, 2004 et al, Paper 323).

2. COPOLYMERS

A great deal of SANS research has been performed on copolymer systems. The focus was on the compatibilization function of copolymers, on the microphase separation and on investigating the various microphases that form.

A blend/copolymer mixture A/B/A-C containing repulsive interactions forms micellar phases (due to the A-C "surfactant") as well as the typical polymer blends spinodal phase decomposition. This leads to microphase separation at low temperatures, homogeneous phase at intermediate temperatures and macrophase separation at high temperatures. Interpretation of the SANS data was performed using the Flory-Huggins theory, the self-consistent field theory and the random phase approximation. Reasonable agreements were found (Ruegg et al, 2007, Paper 483)

The effect of quench depth on ordered block copolymers was investigated using both time-resolved depolarized light scattering, rheology and SANS. Temperature jumps from the disordered phase to the shallow part of the ordered phase show that a few "regular" grains nucleate and grow to form the ordered phase. Deep quenches, on the other hand, show more nucleating centers of less regular shapes (Kim et al, 2004, Paper 234).

The phase diagram of ternary blends containing two homopolymers and the corresponding diblock A/B/A-B has been investigated using DLS and SANS. The transition between a disordered phase (at high temperature) and a bicontinuous microemulsion phase (at lower

temperature) occurs at the Lifshitz transition line. The Teubner-Strey model showed the transition from a $1/Q^2$ dependence to a $1/Q^4$ dependence (Morkved et al, 2001, Paper 212).

Another investigation involving an ABC triblock blended with an A/C homopolymer blend was carried out using SAXS, electron microscopy and SANS. Hexagonally-packed core-shell cylinders and core-shell gyroid phase were observed (Sugiyama et al, 2001, Paper 220).

Polyelectrolyte block copolymers that form micelles have been investigated using fluorescence microscopy, SANS and USANS. Large, highly polydisperse aggregates with rough surfaces were observed (Crichton et al, 2005, Paper 525).

Another polyelectrolyte block copolymer micelle project focused on structural changes with change in the ionic strength (pH). Drastic modification of the micellar corona was observed and related to electrostatic charge interactions (Lee et al, 2002, Paper 259).

Block copolymer microdomains have been templated by mixing layered silicates. These nanometer thick layers induce large scale mesoscopic ordering of cylindrical and spherical microdomains in asymmetric diblock copolymers. Rheology, electron microscopy and SANS have been applied to this research effort. Growth kinetics were investigated. Silicates were seen to enhance the kinetics for spherical domains; whereas for cylindrical domains, they have no effect (Silva, 2001 et al, Paper 252).

The order-to-disorder transition (ODT) and the critical micelle temperature were investigated in concentrated block copolymer solutions in selective solvents. The micelles were found to dissociate into free chains at a temperature above the ODT. Two transitions were documented: spherical (body-centered cubic) phase to disordered phase and cylindrical (hexagonal) phase to disordered phase (Park et al, 2005, Paper 395).

Amorphous-crystalline polyolefin random copolymers are known to form rodlike aggregates whereas amorphous-crystalline diblock copolymers form lamellar morphology instead. These materials are used as nucleating agents for wax crystal size control in commercial distilled fuels. The random copolymers co-crystallize with the wax into thin sheets surrounded by amorphous polymer hairs (Schwahn et al, 2002, Paper 146).

The inter-domain d-spacing of concentrated diblock copolymer solutions in supercritical CO_2 solvent was investigated in an in-situ pressure cell. This d-spacing was found to obey a modified scaling law as function of the copolymer volume fraction (Francis et al, 2007, Paper 591).

Organisilicates templated by triblock copolymers act as nanoporous media with ultra low dielectric constant. Solid-state NMR, SANS and positron annihilation spectroscopy have been employed to characterize the morphology (Yang et al, 2002, Paper 370).

3. CRYSTALLINE POLYMERS

Time resolved SANS was used to investigate the crystallization kinetics of polyethylene in solution. The detection limit of the volume fraction of the crystalline phase was pushed down

to 10^{-5}, therefore allowing the monitoring of the very early stages of crystallization. It was concluded that there is no diverging or spinodal-like decomposition density fluctuation during the early stages (Wang, 2006, Paper 518).

A model polymer system used for the study of polymer dispersion at the molecular level forms the matrix of the MALDI characterization method (used to measure sharp molecular weight distributions). This system forms a crystalline or an amorphous phase. Characteristic temperatures were measured by DSC and the structure was determined by SANS (Bauer et al, 2002, Paper 198).

4. IONOMERS

Ionomers are polymers with charges at specific sites like at the ends or in the middle of the macromolecule. Investigations of structural changes in the Nafion fuel cell membrane induced by various solvents were made using SANS. Two maxima were observed: one due to charge-charge interactions and one characterizing interspacing between crystalline domains. Positions of these maxima correlated well with solvent content (Young et al, 2002, Paper 190).

The effect of arm length on the aggregation structure of fullerene-based star ionomers has been investigation using both SAXS and SANS. These were found to form rodlike aggregates in water solution. The information obtained included the arm distribution, the aggregation number and the rod radius and length. The Mean Spherical Approximation was used to obtain an ionization factor (Lin et al, 2004, Paper 365).

The thermodynamics of phase separation in strongly interacting polyamide/ionomer blends were investigated using SANS. The LCST was found to increase with increasing sulfonation of the ionomer. Ion dipoles form physical crosslinks turning the blend into a network. The RPA model for demixing of cross-linked blends yielded a Flory-Huggins chi parameter which increased with increasing sulfonation level and with increasing ionomer composition (Tucker et al, 2003, Paper 174).

5. POLYELECTROLYTES

Polyelectrolytes are charged polymers (one charge per monomer). A calcium ion-induced transition in polyelectrolyte gels was studied by osmotic measurements and SANS. An interesting length scale characteristic of frozen-in structural inhomogeneities was observed. The concentration dependence of the osmotic pressure displays a power law behavior (Horkay et al, 2003, Paper 057).

Polyelectrolyte chain conformation and concentration fluctuations have been investigated near a demixing phase boundary. It was found that the addition of salt lowers the LCST down. Power laws were obtained for the variation of the correlation length with polymer concentration and of the radius of gyration with degree of polymerization (Prabhu et al, 2003, Paper 132).

Clustering and solvation characteristics of a model polyelectrolyte solution were investigated by SANS. It was found that solvent mixtures are better solvation agents than individual solvents (Hammouda et al, 2005, Paper 377).

SANS and rheology have been applied to the investigation of a block copolymer polyelectrolyte. These form micellar gels reminiscent of disordered colloidal glasses. At the gel point, rheological properties follow the scaling predicted by the percolation theory (Bhatia-Mourchid, 2002, Paper 006).

6. POLYMER BLENDS

The effect of in-situ pressure on the phase boundary of polyolefin blends has been investigated by SANS along with the Flory-Huggins theory and the RPA model. The spinodal (UCST) temperature is seen to increase with pressure. The binodal temperature has also been mapped out (Lefebvre et al, 2002, Paper 085).

The kinetics of liquid-liquid phase separation in off-critical polymer blends was investigated in the nucleation and growth region of the phase diagram. A critical nucleus size was measured and was found to depend on the quench depth (Balsara et al, 2004, Paper 297).

In order to enhance miscibility of immiscible polymer blends, balanced surfactants (diblock copolymers) are used. The "fish" type phase diagram contains the various phases (micellar, lamellar, demixed two-phase and three-phase regions). The Flory-Huggins theory helps predictions from the mixed phase region (Lee et al, 2001, Paper 236).

Phase separation of polymer blends near the limit of metastability has been investigation through temperature quenches from the mixed phase. The Cahn-Hilliard-Cook model was used to investigate the kinetics of phase separation (Lefebvre et al, 2002, Paper 088).

The binary blend of liquid-crystalline polyurethane with a flexible amorphous polymer was investigated. These mix together due to hydrogen-bonding. Anisotropic aggregates were seen to form (Mehta-Dadmun, 2006, Paper 556).

A free energy model has been developed to predict the phase behavior of ternary polymer blends using pure component properties such as coefficients of thermal expansion, densities and solubility parameters. This model calculate the SANS scattering function (Gonzales-Leon-Mayes, 2003, Paper 035).

A complex phase behavior was observed for a weakly interacting polymer blend. A miscibility gap was observed between the UCST and the LCST lines. A glass-rubber transition temperature (T_g) was observed at low temperature and a closed loop immiscibility island was observed at high temperature (Ryu et al, 2004, Paper 367).

7. POLYMER CLUSTERING

Most water-soluble macromolecular systems tend to form clusters. Careful measurements using both DLS and SANS showed that clustering in PEO/d-water are broken up by filtering. However, clusters reform over a couple of days. Moreover, it was found that the addition of a small amount of chloroform reduces clustering (Ho et al, 2003, Paper 230).

A clustering transition of PPE molecules into large flat clusters has been observed for rodlike molecules. When the clusters become too large, they form a constrained gel-like phase (Perahia et al, 2002, Paper 122).

Aggregated structures form during the polymerization of butadiene and isoprene in d-heptane. The propagation of butadiene during reaction was accompanied by the formation of large scale structures. These structures then decreased in size and were replaced by reacted star-like aggregates (Stellbrink et al, 2002, Paper 264).

8. POLYMER NANOCOMPOSITES

Composites are mixtures of polymers and other substances. This mixing is performed in order to enhance the physical properties of these materials. The structure of silica-filled polymers was investigated by SAXS and SANS. Contrast variation allowed the scattering from the crosslinked elastomer to be distinguished from that of the silica filler. Such measurements yield the surface-to-volume ratio for the filler particles as well the fraction of the surface which is in contact with the polymer (Geissler et al, 2002, Paper 030).

Nanocomposites containing polymers and clays have been investigated by SANS. The thermodynamics of phase separation of polymer blends were found to change with the addition of clay silicates. Both the morphology and kinetics of phase separation were studied (Yurelki et al, 2004, Paper 193).

The addition of silica nanoparticles was found to leave polymer chain conformations unmodified. These retained their Gaussian chain character regardless of the polymer molecular weight and silica particle filler composition (Sen et al, 2007, Paper 511).

Shear-induced structures have been investigated in polymer-clay nanocomposite solutions using SANS, SAXS and WAXS. Shear-induced orientation of the clay platelets was investigated. Two major orientations of the platelets were observed: one with its normal parallel to the vorticity direction and one parallel to the shear gradient direction (Malwitz et al, 2003, Paper 101).

9. POLYMER GELS

Gels are formed though physical crosslinking due to hydrogen bonding, hydrophobic interactions or other specific interactions. Lots of water-soluble macromolecules form hydrogels. Ionic microgels based on PAA networks which were bonded to pluronics copolymers have been investigated by SANS, USANS and DSC. Microgel particles and fractal structures have been observed (Bromberg et al, 2004, Paper 300).

Structural investigations of a neutralized polyelectrolyte gel and of an associating neutral hydrogel have been conducted. Hydrogen bonding and chemical cross linking are two driving forces for gel formation. Osmotic measurements of the elastic modulus and SANS measurements allowed the characterization of the two length scales involved (Horkay et al, 2005, Paper 407).

Electro-osmotic flow driven by an electric filed applied across a gel doped with charged colloidal particles has been investigated. Silica gel particles of various sizes were used. Solute flux enhancements were found to be strongest with applied electric field and small silica particles (Matos et al, 2006, Paper 517).

Gels formed of low-molecular mass organic gelators and perfluorinated liquids have been investigated. WAXS, Polarizing Optical Microscopy, IR spectroscopy and SANS have been used. These gels are thermally reversible and require small amounts of gelator. The incompatibility of the fluorocarbon and hydrocarbon segments causes the gelotor to segregate into lamellae within the fibrils that form the gel network (George et al, 2005, Paper 380).

Clustering and structural properties of depletion gels and thermogels have been investigated. Depletion gels are formed of dense clusters and voids whereas thermal gels are devoid of clusters. Shear breaks up clusters in depletion gels but induces clustering in thermal gels (Ramakrishnan et al, 2005, Paper 434).

10. POLYMER MICELLES

Quite a bit of research has been performed on pluronics and pluronics containing systems using SANS. Carbon added to pluronics forms an adsorbed monolayer. Zero contrast experiments yielded the size of this monolayer (Lin-Alexandridis, 2002, Paper 094).

Polymer micelles form when mixing a diblock copolymer A-C with two homopolymers A/B. The A/B interactions are repulsive whereas the A-C interactions are attractive. The demixing phase diagram contains many of the features of ternary micelle-forming microemulsions (Lee et al, 2003, Paper 084).

The kinetics of microemulsion polymerization have been investigated. Monomer partitioning between micelles and polymer particles during polymerization have been investigated with SANS. It turns out that monomer partitioning results from the competition between polymer effects (included in the Gibbs free energy) and the Helfrich curvature elastic free energy of the surfactant monolayers (Co et al, 2001, Paper 019).

11. POLYMER NETWORKS

The conformations of guest polymer chains in elastomeric networks have been investigated using NMR and SANS. Short guest chains tend not to disturb the network characteristics too much whereas long guest chains tend to phase separate into the amorphous phase region. The

radius of gyration of the (deuterated) guest chains remains unchanged upon stretching of the network (Batra et al, 2003, Paper 004).

A real time SANS study of the formation of Inter-Penetrating Networks (IPN) shows an ordered lamellar structure at the initial stage. As network formation proceeded, "diffraction" peaks appeared indicative of domain formation. These domains got sharper with time (Burford et al, 2006, Paper 537).

Elastomeric polypropylene has been investigated under in-situ stretch condition. Partially deuterated elastomer in the melt state (160 ^{o}C) shows uniform morphology. Slow cooling down to ambient temperature causes segregation into amorphous and crystalline regions (Wiyatno et al, 2003, Paper 186).

A polyurethane elastomer of low hard segment content has been investigated by SANS, SAXS and WAXS. SANS indicated the existence of hard segment crystalline domains. Their size, shape and aggregation number have been determined (Sun et al, 2006, Paper 540).

12. POLYMER SOLUTIONS

A great deal of research has been performed using PEO. PEO forms helical structures in mixtures of isobutyric acid and water. The helical structures have been confirmed by SANS and other methods. At temperatures above 60 ^{o}C, the helices become random coils (Alessi et al, 2005, Paper 443).

The clustering and solvation characteristics of PEO have been investigated in d-water and in mixed solvents. It was found that solvent mixtures are better solvating agents than any of the individual solvents (Hammouda, 2006, Paper 564).

PEO forms crystalline lamellae when dissolved in ethanol. Structure of the lamellar morphology has been investigated by SANS. Concentration and temperature have been varied. Adding a small amount of water eliminates the crystalline morphology (Ho et al, 2006). Paper 452.

Some water-soluble polymers form hydrate crystals in THF/water mixtures. Polymer chains adsorb on the hydrate crystal surfaces. This inhibits crystal growth. The SANS intensity is characterized by a low-Q signal due to aggregation/clustering and a high-Q signal due to solvation characteristics. The low-Q signal was correlated to the polymer's ability to inhibit crystal growth (King et al, 2000, Paper 073).

Stiff polymer solutions have been investigated using SANS and DLS. The Zimm plot and the wormlike chain model have been used to obtain the radius of gyration and the persistence length. The effect of temperature has also been investigated (Yun et al, 2006, Paper 471).

Polymers can be dissolved in supercritical fluid solvents. Polyethylene butane solutions in supercritical d-ethane have been investigated. In-situ pressure was used to approach the critical phase boundary. As the critical conditions were approached, the chain radius of gyration increased and the correlation length decreased (DiNoia et al, 2005, Paper 436).

13. POLYMERS UNDER PRESSURE

The effect of pressure on the order-to-disorder phase transition has been investigated in a series of polystyrene/poly-n-alkyl methacrylate diblock copolymers. In this homologous series, the length of the alkyl chain in the methacrylate block was increased. For short lengths and long lengths, pressure favors demixing whereas for intermediate lengths, it favors mixing. A free energy model can predict most of the observed trends (Ruzette et al, 2003, Paper 141).

Two of the diblocks in this series have been investigated in pressurized CO_2 solvent. It was found that pressure increases miscibility in PS-PHMA and decreases miscibility in PS-PBMA. The lower disorder-to-order temperature (LDOT) is entropically driven. Pressure tends to reduce the amount of "free volume" present and therefore tends to increase the LDOT. The upper DOT, on the other hand is controlled by monomer-monomer enthalpic interactions and could go either way depending on the enthalpy change and volume change upon mixing. The so-called Clausius-Clapeyron equation predicts the variation of the transition temperature for varying pressure dT_s/dP (Vogt et al, 2003, Paper 175).

14. POLYMERS UNDER SHEAR

A shear-induced network-to-network transition has been observed in a block copolymer melt. Application of shear transforms the self-assembled soft material into single crystal texture while preserving the short-range three-fold network connectivity. Both phases (with and without shear) are stable under annealing (Cochran-Bates, 2004, Paper 267).

The effects of shear flow on the structure and morphology of a polymeric microemulsion PEE/PDMS/PEE-PDMS have been investigated using DLS, microscopy, rheology and SANS. At equilibrium, the microemulsion contains two percolating microphases, one rich in PEE and the other rich in PDMS. When shear is increased, there is a breakdown of the bicontinuous structure resulting in a shear-induced phase transition. DLS revealed the existence of the string phase. At even higher shear rates, complete demixing takes place (Krishnan et al, 2002, Paper 162).

15. THIN POLYMER FILMS

Structural characterization of a low dielectric constant thin film has been performed using X-ray reflectivity and SANS. Both the depth profile and pore structure have been determined. A scattering invariant analysis of the SANS data helped determine the average chord length of the pores independent of the depth profile (Lin et al, 2002, Paper 165).

A low dielectric constant thin film has been investigated by SANS using the contrast variation method. This was done using a mixture of deuterated and non-deuterated toluene gas vapor that fills the pores. The partial pressure of the solvent vapor was increased. Pores

filled with liquid solvent progressively. The size distribution of the empty pores was determined (Hedden et al, 2004, Paper 319).

Investigations of the conformation of polymer chains confined in Vycor glass have been carried out. It was found that confinement in the porous medium did not affect chain dimensions. This result was at variance with simulation results (Nieh et al, 2002, Paper 118).

Diblock copolymer thin films (coating a silicon substrate) have been aligned using an electric field. The orientation of cylindrical microdomains has been monitored by SANS. Cylindrical domains tend to orient parallel to the surface. The application of an E-field and annealing got the cylinders to orient parallel to the applied E-field (Xu et al, 2005, Paper 475).

REFERENCES

Y.N. Lin and P. Alexandridis, "Small-Angle Neutron Scattering Characterization of Micelles Formed by Poly(dimethylsiloxane)-graft-polyether Copolymers in Mixed Polar Solvents", Journal of Physical Chemistry B 106, 12124-12132 (2002). Paper 093.

F. Grohn, B. Bauer and E. Amis, "Hydrophobically Modified Dendrimers as Inverse Micelles: Formation of Cylindrical Multi-dendrimer Nanostructures", Macromolecules 34, 6701-6707 (2001). Paper 208.

R. Hedden and B. Bauer, "Structure and Dimensions of PAMAM/PEG Dendrimer Star Polymers", Macromolecules 36, 1829-1835 (2003). Paper 049.

J.S. Lee, M. Foster and D.T. Wu, "Effect of Butadiene End-capping of Arms in a Star Polystyrene on Solution Properties, Bulk Dynamics and Bulk Thermodynamic Interactions in Binary Blends" Macromolecules 39, 5113-5121 (2006). Paper 481.

C.C. Greenberg, M. Foster, C.M. Turner, S. Corona-Galvan, E. Cloutet, R.P. Quirk, P. Butler and C. Hawker, "Effective Interaction Parameter Between Branched and Linear Polystyrene", J. Polym. Sci. Polym. Phys. Ed. 39, 2549-2561 (2001). Paper 036.

T. Martter, M.D. Foster, T. Yoo, S. Xu, G. Lizarraga and R.P. Quirk, "Thermodynamic Interaction Parameter of Star-Star Polybutadiene Blends", J. Polym. Sci. Polym. Phys. Ed. 41, 247-257 (2003). Paper 104.

C.M. Stancik, J.A. Pople, M. Trollsas, P. Lindner, J.L. Hedrick and A.P. Gast, "Impact of Core Architecture on Solution Properties of Dendrimer-Like Star Copolymers", Macromolecules 36, 5765-5775 (2003). Paper 159.

S. Rathgeber, A.P. Gast and J.L. Hendrick, "Structural Properties of Star-like Dendrimers in Solution", Applied Physics A 74, S396-S398 (2002). Paper 137.

M. Mackay, Y. Hong, M. Jeong, B.M. Tande, N.J. Wagner, S. Hong, S.P. Gido, R. Vestberg, C.J. Hawker, ""Microphase Separation of Hybrid Dendron-Linear Diblock Copolymers into Ordered Structures", Macromolecules 35 8391-8399 (2002), Paper 100.

392

S.I. Yun, R.M. Briber, R.A. Kee and M. Gauthier, "Small-Angle Neutron Scattering of Arborescent Polystyrene-graft-Poly(2-vinylpyridine) Copolymers", Polymer <u>44</u>, 6579-6587 (2003). Paper 192.

A. Rajca, J. Wongsriratanakul and S. Rajca, "Organic Spin Clusters: Macrocyclic-Macrocyclic Polyarylmethyl Polyradicals with Very High Spin S=5-13", J. Amer. Chem. Soc. <u>126</u>, 6608-6626 (2004). Paper 323.

M. Ruegg, B.J. Reynolds, M.Y. Lin, D.J. Lohse and N.P. Balsara, "Microphase and Macrophase Separation in Multicomponent A/B/A-C Polymer Blends with Attractive and Repulsive Interactions", Macromolecules <u>39</u>, 1125-1134 (2007). Paper 483.

W.G. Kim, M.Y. Chang, B.A. Garetz, M.C. Newstein, N.P. Balsara, J.H. Lee, H. Hahn and S.S. Patel, "Effect of Quench Depth on Grain Structure in Quiescently Ordered Block Copolymers", J. Chem. Phys. <u>114</u>, 10191-10211 (2001). Paper 234.

Morkved TL, P. Stepanek, K. Krishnan, F.S. Bates, T.P. Lodge, "Static and Dynamic Scattering from Ternary Polymer Blends: Bicontinuous Microemulsions, Lifshitz lines, and Amphiphilicity", J. Chem. Phys. <u>114</u>, 7247-7259 (2001). Paper 212.

M. Sujiyama, T.A. Shefelbine, M.E. Vigild and F.S. Bates, "Phase Behavior of an ABC Triblock Copolymer Blended with A and C Homopolymers", J. Phys. Chem. B <u>105</u>, 12448-12460 (2001). Paper 220.

M.A. Crichton, N.S. Forbes and S.R. Bhatia, "USANS as a Probe of Large-Scale Structure in Attractive Colloidal Glasses of Block Copolymer Micelles", Materials Research Society Symposium Proceedings <u>840</u>, Q7.11.1 (2005)

A.S. Lee, V. Butun, M. Vamvakaki, S.P. Armes, J.A. Pople and A.P. Gast, "Structure of pH-Dependent Block Copolymer Micelles: Charge and Ionic Strength Dependence", Macromolecules <u>35</u>, 8540-8551 (2002). Paper 259.

A.S. Silva, C.A. Mitchell, M.F. Tse, H.C. Wang and R. Krishnamoorti, "Templating of Cylindrical and Spherical Block Copolymers Microdomains by Layered Silicates", J. Chem. Phys. <u>115</u>, 7166- (2001). Paper 252.

M.J. Park, K. Char, J. Bang and T.P. Lodge, "Order-Disorder Transition and Critical Micelle Temperature in Concentrated Block Copolymer Solutions", Macromolecules 38, 2449-2459 (2005), Paper 395.

D. Schwahn, D. Richter, M.Y. Lin and L.J. Fetters, "Co-crystallization of a Poly(ethylene-Butene) Random Copolymer with C-24 in n-Decane", Macromolecules <u>35</u>, 3762-3768 (2002). Paper 146.

T.J. Francis, B.D. Vogt, M.X. Wang, and J.J. Watkins, "Scaling of Interdomain Spacing of Diblock Coploymers in a Selective Diluent", Macromolecules <u>40</u>, 2515-2519 (2007). Paper 591.

S. Yang, P.A. Mirau, C.S. Pai, O. Nalamasu, E. Reichmanis, J.C. Pai, Y.S. Obeng, J. Seputro, E.K. Lin, H.J. Lee, J. Sun and D.W. Gidley, "Nanoporous Ultralow Dielectric Constant Organisilicates Templated by Triblock Copolymers", Chem. Mater. 14, 369-374 (2002). Paper 370.

H. Wang, "SANS Study of the Early Stages of Crystallization in Polyethylene Solutions", Polymer 47, 4897-4900 (2006). Paper 518.

B. Bauer, C.M. Guttman, D.W. Liu, and W.R. Blair, "Tri-alpha-naphthylbenzene as a Crystalline or Glassy Matrix for Matrix-Assisted Laser Desorption/Ionization: a Model System for the Study of Effects of Dispersion of Polymer Samples at a Molecular Level", Rapid Communications on Mass Spectroscopy 16, 1192-1198 (2002). Paper 198.

S.K. Young, S.F. Trevino and N.C. Beck Tan, "Small-Angle Neutron Scattering Investigation of Structural Changes in Nafion Membranes Induced by Swelling with Various Solvents", Journal of Polym. Sci., Polym. Phys. Ed. 40, 387-399 (2002). Paper 190.

T.L. Lin, U. Jeng, C.S. Tsao, W.J. Liu, T. Canteenwala, and L.Y. Chiang, "Effect of Arm Length on the Aggregation Structure of Fullerene-Based Star Ionomers", Journal of Physical Chemistry B 108, 14884-14888 (2004). Paper 365.

R. Tucker, C.C. Han, A.V. Dobrynin, and R.A. Weiss, "Small-Angle Neutron Scattering Analysis of Blends with Very Strong Intermolecular Interactions: Polyamide/Ionomer Blends", Macromolecules 36, 4404-4410 (2003). Paper 174.

F. Horkay, P.J. Basser, A.M. Hecht and E. Geissler, "Calcium Induced Volume Transition in Polyelectrolyte Gels", Macromol. Symp. 200, 21-30 (2003). Paper 057.

V. Prabhu, M. Muthukumar, G.D. Wignal and Y. Melnichenko, "Polyelectrolyte Chain Dimensions and Concentration Fluctuations near Phase Boundaries", J. Chem. Phys. 119, 4085-4098 (2003). Paper 132.

B. Hammouda, M. Becker and F. Horkay, "Clustering and Solvation in Poly(acrylic acid) Polyelectrolyte Solutions", Macromolecules 38, 2019-2021 (2005). Paper 377.

S. Bhatia and A. Mourchid, "Gelation of Micellar Block Polyelectrolytes: Evidence of Glassy Behavior in an Attractive System", Langmuir 18, 6469-6472 (2002). Paper 006.

A.A. Lefebvre, N.P. Balsara, J.H. Lee, and C. Vaidyanathan, "Determination of the Phase Boundary of High Molecular Weight Polymer Blends", Macromolecules 35, 7758-7764 (2002). Paper 085.

N.P. Balsara, T.J. Rappl, and A.A. Lefebvre, "Does Conventional Nucleation Occur During Phase Separation in Polymer Blends?", J. Polym. Sci., Polym. Phys. Ed. 42, 1793-1809 (2004). Paper 297.

J.H. Lee, N.P. Balsara, R. Krishnamoorti, H.S. Jeon and B. Hammouda, "Designing Balanced Surfactants for Mixtures of Immiscible Polymers", Macromolecules <u>34</u>, 6557-6560 (2001). Paper 236.

A.A. Lefebvre, J.H. Lee, N.P. Balsara, and C. Vaidyanathan, "Fluctuation Mediated Phase Separation in Polymer Blends near the Limit of Metastability", J. Chem. Phys. <u>117</u>, 9074-9083 (2002). Paper 088.

R. Mehta and M.D. Dadmun, "Small Angle Neutron Scattering Studies on Miscible Blends of Poly(styrene-ran-vinyl phenol) with Liquid Crystalline Polyurethane", Macromolecules <u>39</u>, 8799-8807 (2006). Paper 556.

J.A. Gonzales-Leon and A.M. Mayes "Phase Behavior Prediction of Ternary Polymer Mixtures", Macromolecules <u>36</u>, 2508-2515 (2003). Paper 035.

D.Y. Ryu, D.H. Lee, J. Jang, K.A. Lavery and T. Russell, "Complex Phase Behavior of a Weakly Interacting Binary Blend", Macromolecules <u>37</u>, 5851-5855 (2004). Paper 367.

D. Ho, B. Hammouda and S.R. Kline, "Clustering of Poly(ethylene oxide) in Water Revisited", J. Polym. Sci.., Polym. Phys. Ed. <u>41</u>, 135-138 (2003). Paper 230.

D. Perahia, R. Traiphol and U.H. Bunz, "From Single Molecules to Aggregates to Gels in Dilute Solution: Self-Organization of Nanoscale Rodlike Molecules", J. Chem. Phys. <u>117</u>, 1827-1832 (2002). Paper 122.

J. Stellbrink, J. Allgaier, L. Willner, D. Richter, T. Slawecki and L.J. Fetters, "Real Time SANS Study on Head Group Self-Assembly for Lithium Based Anionic Polymerizations", Polymer <u>43</u>, 7101-7109 (2002). Paper 264.

E. Geissler, A.M. Hecht, C. Rochas, F. Horkay, F. Bley and F. Livet, "Structure and Dynamics of Silica-Filled Polymers by SANS and Coherent SAXS", Macromol. Symp. <u>190</u>, 23-32 (2002). Paper 030.

K. Yurelki, A. Karim, E.J. Amis amd R. Krishnamoorti, "Phase Behavior of PS-PVME Nanocomposites", Macromol. <u>37</u>, 507-515 (2004). Paper 193.

S. Sen, Y. Xie, S. Kumar, H. Yang, A. Bansil, D. Ho, L. Hall, J.B. Hooper and K.S. Schweizer, "Chain Conformations and Bound Layer Correlations in Polymer Nanocomposites", Phys. Rev. Lett. <u>98</u>, 128302-1-4 (2007). Paper 511.

M.M. Malwitz, S. Lin-Gibson, E.K. Hobbie, P. Butler and G. Schmidt, "Orientation of Platelets in Multilayered Nanocomposite Polymer Films", J. Polym. Sci., Polym. Phys. Ed. <u>41</u>, 3237-3248 (2003). Paper 101.

L. Bromberg, M. Temchenko, G.D. Moeser and T.A. Hatton, "Thermodynamics of Temperature-Sensitive Polyether-Modified Poly(acrylic acid) Microgels", Langmuir <u>20</u> 5683-5692 (2004). Paper 300.

F. Horkay, P.J. Basser, A.M. Hecht and E. Geissler, "Structural Investigations of a Neutralized Polyelectrolyte Gel and an Associating Neutral Hydrogel", Polymer 46, 4242-4247 (2005). Paper 407.

M.A. Matos, L.R. White and R.D. Tilton, "Electro-Osmotically Enhanced Mass Transfer through Polyacrylamide Gels", J. Colloid and Interf. Sci., 300, 429-436 (2006). Paper 517.

M. George, S.L. Snyder, P. Terech and R.G. Weiss, "Gelation of Perfluorinated Liquids by N-Alkyl Perfluoroalkanamides", Langmuir 21, 9970-9977 (2005). Paper 380.

S. Ramakrishnan, V. Gopalakrishnan and C.F. Zukoski, "Clustering and Mechanics in Dense Depletion and Thermal Gels", Langmuir 21, 9917-9925 (2005). Paper 434.

Y. Lin and P. Alexandridis, "Temperature-Dependent Adsorption of Pluronic F127 Block Copolymers onto Carbon Black Particles Dispersed in Aqueous Media", J. Chem. Phys. 106, 10834-10844 (2002). Paper 094.

J.H. Lee, M.L. Ruegg, N.P. Balsara, Y. Zhu, S.P. Gido, R. Krishnamoorti and M.H. Kim, "Phase Behavior of Highly Immiscible Polymer Blends Stabilized by a Balanced Block Copolymer Surfactant", Macromolecules 36, 6537-6548 (2003). Paper 084.

C.C. Co, R. de Vries and E.W. Kaler, "Microemulsion Polymerization. 1. Small-angle Neutron Scattering Study of Monomer Partitioning", Macromolecules 34, 3224-3232 (2001). Paper 019.

A. Batra, R.C. Hedden, P. Schofield, A. Barnes, C. Cohen and T.M. Duncan, "Conformational Behavior of Guest Chains in Uniaxially Stretched Poly(diethylsiloxane) Elastomers: H-2 NMR and SANS", Macromolecules 36, 9458-9466 (2003). Paper 004.

R.P. Burford, M.G. Markotsis and R.B. Knott, "Real-time SANS Study of Interpenetrating Polymer Network (IPN) Formation", Physica B 385-386, 766-769 (2006). Paper 537.

W. Wiyatno, G.G. Fuller, J.A. Pople, A.P. Gast, Z. Chen, R.M. Waymouth, and C.L. Myers, "Component Stress-Strain Behavior and Small-Angle Neutron Scattering Investigation of Stereoblock Elastomeric Polypropylene", Macromolecules 36, 1178-1187 (2003). Paper 186.

Y.S. Sun, U.S. Jeng, Y.S. Huang, K.S. Liang, T.L. Lin and C.S. Tsao, "Complementary SAXS and SANS for Structural Characteristics of a Polyurethethane Elastomer of Low Hard-Segment Content", Physica B 385-386, 650-652 (2006). Paper 540.

M.L. Alessi, A.I. Norman, S.E. Knowlton, D.L. Ho and S.C. Greer, "Helical and Coil Conformations of Poly(ethylene glycol) in Isobutyric Acid and Water", Macromolecules 38, 9333-9340 (2005). Paper 443.

B. Hammouda, "Solvation Characteristics of a Model Water-Soluble Polymer", J. Polym. Sci., Polym. Phys. Ed. 44, 3195-3199 (2006). Paper 564.

D.L. Ho, B. Hammouda and S.R. Kline, "Unusual Phase Behavior in Mixtures of Poly(ethylene oxide) and Ethyl Alcohol", J. Polym. Sci., Polym. Phys. Ed. <u>44</u>, 557-564 (2006). Paper 452.

H.E. King, J.L. Hutter, M.Y. Lin and T. Sun, "Polymer Conformations of Gas-Hydrate Kinetic Inhibitors: A Small-Angle Neutron Scattering Study", J. Chem. Phys. <u>112</u>, 2523-2532 (2000). Paper 073.

S.I. Yun, K. Terao, K. Hong, Y.B. Melnichenko, G.D. Wignall, P.F. Britt and J.W. Mays, "Solution Properties of 1,3-Cyclohexadiene Polymers by Laser Light Scattering and Small-Angle Neutron Scattering", Macromolecules <u>39</u>, 897-899 (2006). Paper 471.

T.P. DiNoia, I.H. Park, M.A. McHugh and J.H. van Zanten, "Observation of Polymer Chain Contraction near the Overlap Concentration", Macromolecules <u>38</u>, 9393-9395 (2005). Paper 436.

A.V. Ruzette, A.M. Mayes, M. Pollard, T.P. Russell and B. Hammouda, "Pressure Effects on the Phase Behavior of Styrene/n-alkyl methacrylate Block Copolymers", Macromolecules <u>36</u>, 3351-3356 (2003). Paper 141.

B.D. Vogt, V.S. RamachandraRao, R.G. Gupta, K.A. Lavery, T.J. Francis, T.P. Russell and J.J. Watkins, "Phase Behavior of Polystyrene-block-poly(n-alkyl methacrylate)s Dilated with Carbon Dioxide", Macromolecules <u>36</u>, 4029-4036 (2003). Paper 175.

E.W. Cochran and F.S. Bates, "Shear-Induced -to-Network Transition in a Block Copolymer Melt", Phys. Rev. Lett. <u>93</u>, 087802-1 to 087802-4 (2004). Paper 267.

K. Krishnan, B. Chapman, F.S. Bates, T.P. Lodge, K. Almdahl and W. Burghardt, "Effects of Shear Flow on a Polymeric Bicontinuous Microemulsion: Equilibrium and Steady State Behavior", J. of Rheology <u>46</u>, 529-554 (2002). Paper 162.

E.K. Lin, H.J. Lee, G.W. Lynn, W.L. Wu and M.L. O'Neill, "Structural Characterization of a Porous Low-Dielectric-Constant Thin Film with a Non-uniform Depth Profile", Applied Physics Letters <u>81</u>, 607-609 (2002). Paper 165.

R.C. Hedden, H.J. Lee, C.L. Soles and B.J. Bauer, "Characterization of Pore Structure in a Nanoporous Low-Dielectric-Constant Thin Film by Neutron Porosimetry and X-ray Porosimetry", Langmiur <u>20</u>, 6658-6667 (1004). Paper 319.

M.P. Nieh, S.K. Kumar, D.L. Ho and R. Briber, "Neutron Scattering Study of Chain Conformations in the Energetically Neutral Pores of Vycor Glass", Macromolecules <u>35</u>, 6384-6391 (2002). Paper 118.

T. Xu, A.V. Zvelindovsky, G.J.A. Sevink, K.S. Lyakhova, H. Jinnai and T.P. Russell, "Electric Field Alignment of Asymmetric Diblock Copolymer Thin Films", Macromolecules <u>38</u>, 10788-10798 (2005). Paper 475.

Part I – SANS FROM COMPLEX FLUIDS

Chapter 42 – **PHASE DIAGRAMS FOR MICELLAR SYSTEMS**

A substantial fraction of SANS research is performed on "complex fluids". These include micelles, colloids, gels, networks, etc, and could be referred to as "micellar systems". Phase diagrams for micellar systems are discussed in this chapter (Kahlweit-Strey, 1985). Following Kahlweit-Strey, this topic is treated at a descriptive level.

1. BASICS OF MICELLAR SYSTEMS

Micellar systems consist of mixtures of water/oil and an amphiphile surfactant that increases their miscibility. The amphiphile surfactant is either not charged (i.e., is nonionic) or consists of an ionic (charged) headgroup. The focus here will be on nonionic micellar systems and their mixing and phase separation phase diagram.

The phase diagram of the ternary micellar system is represented by a triangle (A: water, B: oil and C: surfactant). The three binary systems A-B, A-C and B-C are represented by their characteristic mixed-phase (1-phase) and phase separated (2-phase) regions. The oil-surfactant (B-C) binary mixture is characterized by an upper critical solution temperature (UCST); i.e., it phase separates upon cooling. The water-oil (A-B) binary mixture is also characterized by a UCST behavior but is mostly phase separated (water and oil do not mix). The phase diagram for the water-surfactant (A-C) binary solution is more complex and is characterized by a UCST behavior at low temperatures and a closed loop immiscibility island at high temperatures; i.e., it phase separates both upon cooling and upon heating. The closed loop is due to the breaking of hydrogen bonds upon heating and shows up for strong amphiphile surfactants.
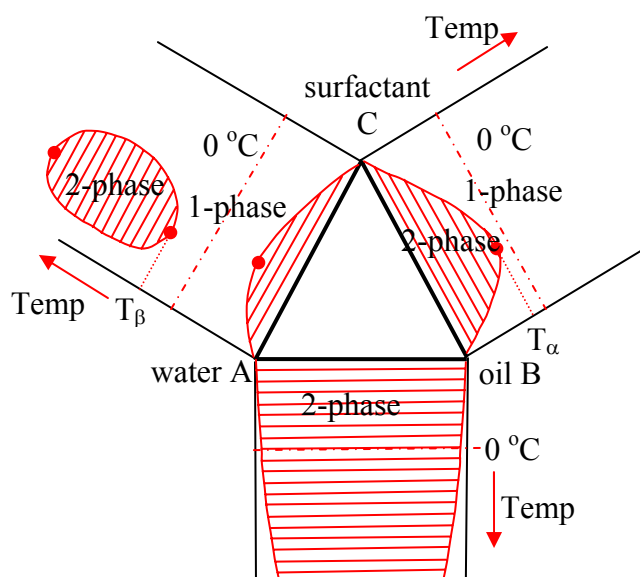
Figure 1: Phase diagram for the three binary mixtures (B-C, A-B, and A-C). The phase separation lines and temperatures are shown. The 0 °C water-freezing line has also been marked.

Phase separation occurs upon jumping from the phase mixed (1-phase) region to the phase separated (2-phase) region. Phase separation proceeds along tie lines and produces a phase rich in the A component (left side) and a phase rich in the C component (right side). The points at which the phase separation lines have a horizontal slope are the critical points. The A-C binary phase diagram shows three critical points. Note that the lower UCST may lie below the freezing point of the mixture.
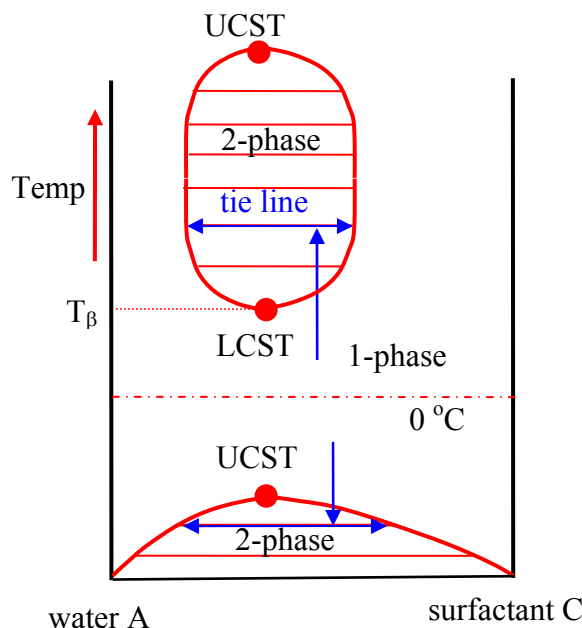
Figure 2: The water/surfactant (A-C) binary phase diagram.

Given the three generic binary mixtures phase diagrams, the phase diagram for the ternary A-B-C mixture is discussed next.

2. PHASE DIAGRAM FOR THE TERNARY MIXTURE

The ABC triangle is obtained by combining the three binary mixtures phase diagrams. It contains a micelle-formation phase (m-phase also referred to as "1-phase") region and a 2-phase region. The m-phase region contains oil-in-water and water-in-oil micelles. The 2-phase region contains a phase containing water and surfactant and another phase containing mostly oil at low temperatures. Note that micelles can form in the 2-phase region since binary mixtures (water/surfactant or oil/surfactant) can form micelles. The m-phase region is inhomogeneous (contains micelles) in the nanometer size scale but homogeneous in the

micrometer (optical range) size scale. The m-phase region is "clear" for light but "cloudy" for neutrons.

Now consider the temperature axis (vertical variable out of the page). A jump from the m-phase region to the 2-phase region prompts phase separation that proceeds along tie lines (that are no longer horizontal). The critical condition for the ternary mixture is referred to as the "plait" point (equivalent to 'critical" point for binary mixtures).

surfactant C

m-phase

plait
point

2-phase

water A   oil B
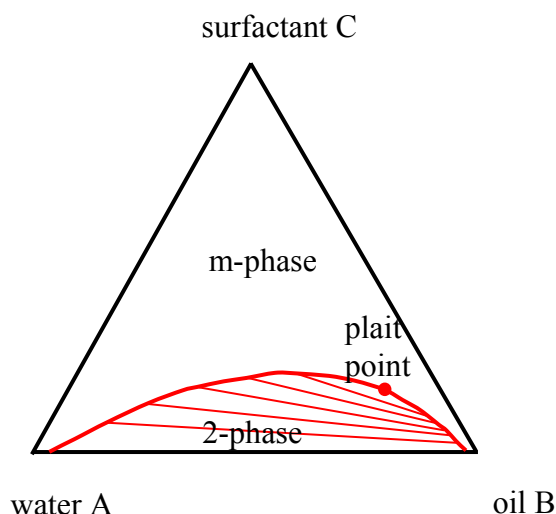
Figure 3: Schematic representation of a generic ternary mixture phase diagram. The m-phase is the micelle-formation phase.

This simple representation of the ternary phase diagram is valid for low temperatures; i.e., before reaching the closed loop region. When the closed loop region is reached and with strong amphiphilic surfactants, there is an interplay of interactions which adds two 2-phase regions (one water-rich and one oil-rich) and two plait points. The slopes of the tie lines are different. This type of phase diagram is characterized by a 3-phase region inside the triangle that cuts through both 2-phase regions.
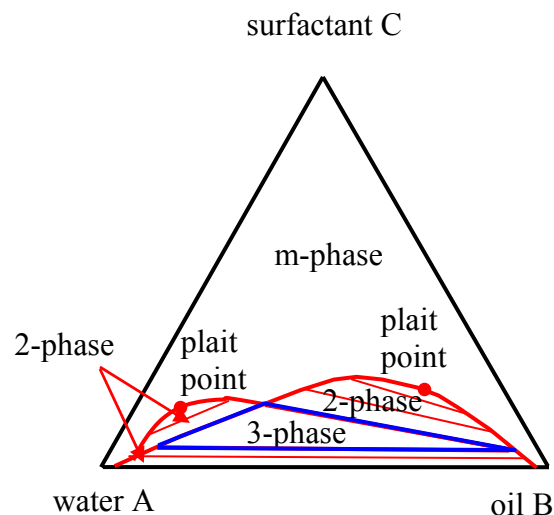
Figure 4: Ternary phase diagram that shows the 3-phase region.

There are three types of "Windsor" phase diagrams: type I corresponding to a 2-phase region where the surfactant is dissolved mainly in the water phase, type II corresponding to a 2-phase region where the surfactant is dissolved mainly in the oil phase and type III corresponding to a 3-phase region where the surfactant forms a phase of its own between the (bottom) water phase and (top) oil phase.

In order to appreciate the cause of the formation of the 3-phase, the temperature dependence of the phase diagram is explored in more detail.

3. THE CRITICAL POINTS LINE

Consider first the simple case without a closed loop for the water-surfactant binary mixture phase diagram. The 3D phase diagram (referred to as the "prism") is shown here. The plait points form line that ascends from the oil-rich region.
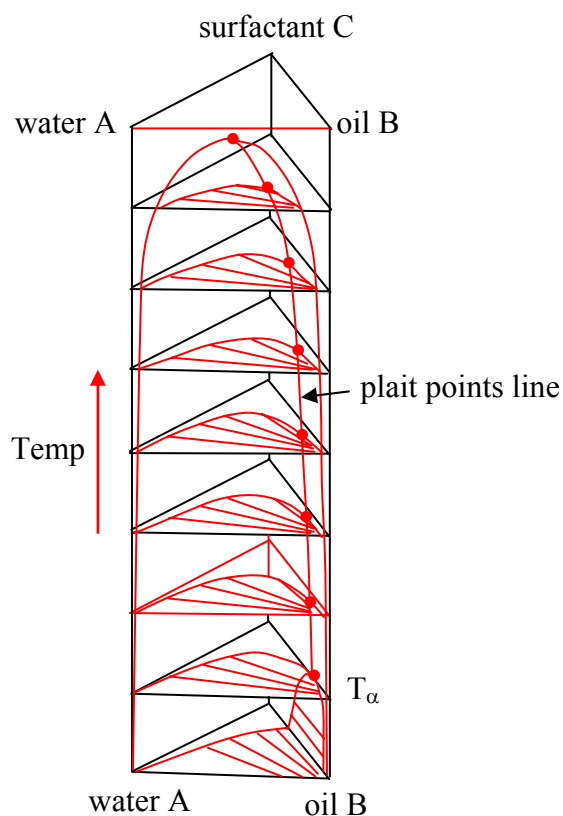
Figure 5: The prism phase diagram for a simple ternary mixture.

When the surfactant becomes more amphiphile, a closed loop appears. This modifies the prism phase diagram to show plait point lines both on the oil-rich (right) side and on the water-rich (left) side. Up to now, there are still the m-phase and the 2-phase regions only; the 3-phase region has not shown up yet. Note that the tie lines slopes change with temperature for this case.

The water/oil phase volume (relative amount) varies with increasing temperature. At low temperature, the 2-phase consists of a water-surfactant phase (called a) and an oil phase (called b). As temperature is increased, surfactant is distributed equally between a water phase (a) and an oil phase (b). This temperature corresponds to the inflection point in the variation of the plait points line (also called critical points line). As temperature is increased further, the 2-phase mixture becomes an oil-surfactant phase (b) and a water phase (a).
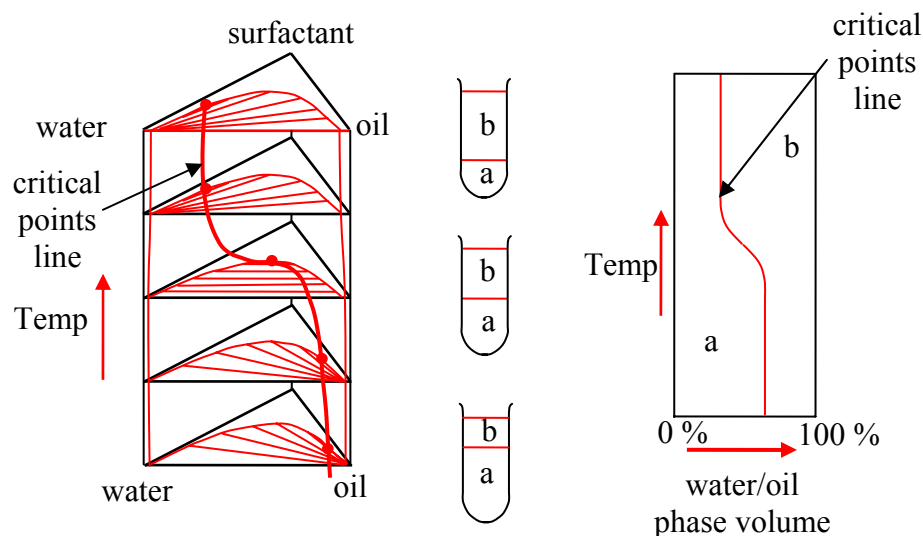
Figure 6: The prism phase diagram when a closed loop is present. The composition of the 2-phase mixtures is represented for increasing temperature.

4. THE THREE-PHASE REGION

Depending on the chemical nature of the amphiphile surfactant and oil used, one could obtain a 3-phase region. In order to understand its origin, consider the variation of the critical points line when the surfactant becomes more amphiphile or when the oil becomes more hydrophobic. The slope at the inflection point becomes steeper till it becomes horizontal. This corresponds to a so-called "tricritical" condition. Beyond that, the critical points line breaks which leads to the formation of a 3-phase region.
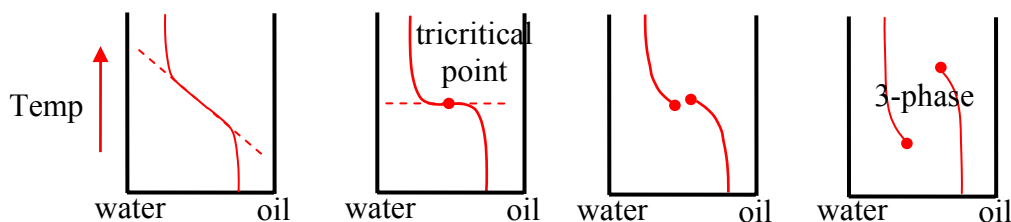
Figure 7: Variation of the critical points line with increasing amphiphile character of the surfactant and/or increasing the hydrophobic nature of the oil.

The critical points line changes drastically when a 3-phase region is present. That line "breaks"and a "sigmoid" (i.e., s-shaped) behavior appears. The 2-phase regions at low temperature and high temperature are almost unchanged but a 3-phase region appears at intermediate temperatures.
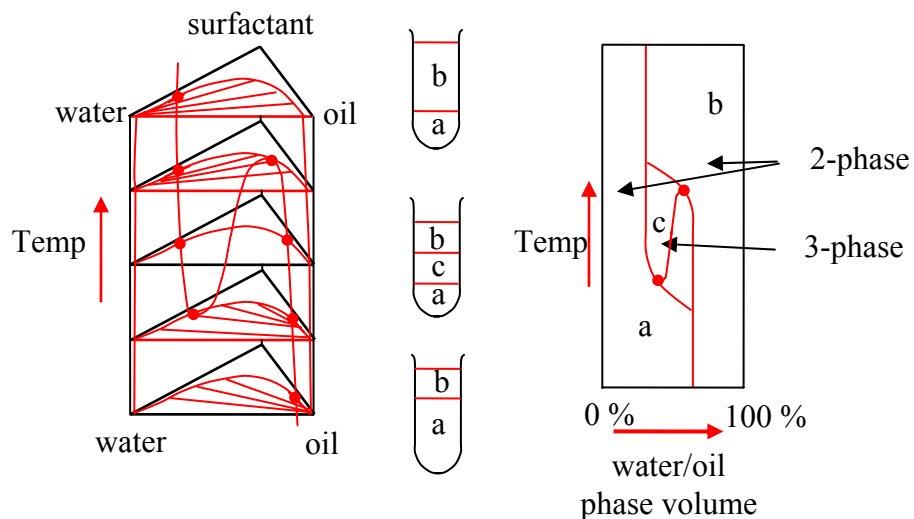
Figure 8: Representation of the prism phase diagram when a 3-phase region is present.

The surfactant is transferred continuously from the water-rich phase to the oil-rich phase as temperature is increased. Consider a triangle phase diagram at a temperature for which a 3-phase region exists. The 1-phase region is close to the surfactant corner. The 2-phase regions are on each of the three sides of the 3-phase region. The 3-phase region itself is a triangle within the triangle. The 3-phase triangle size varies depending on the ternary system used and on the temperature considered.
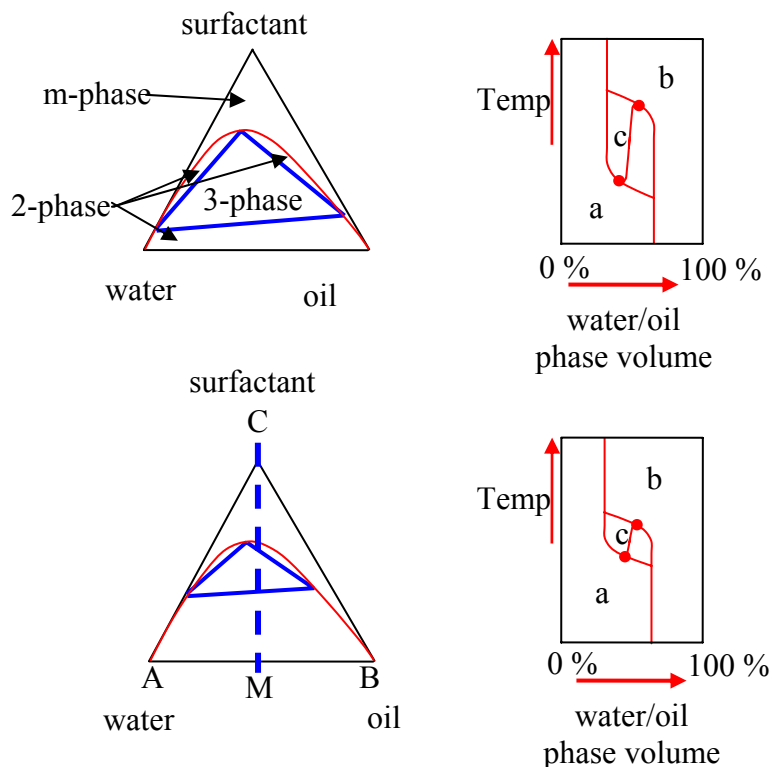
Figure 9: The triangle delimiting the 3-phase region.

Consider a vertical cut MC through the ABC triangle. Representing the phase diagram along the MC cut gives the "fish" phase diagram.

5. THE FISH PHASE DIAGRAM

The "fish" phase diagram is obtained when an MC cut is taken across the ABC triangle phase diagram. This cut corresponds to increasing the surfactant concentration but keeping the amount or water and oil constant. Representation of the temperature/ surfactant concentration phase diagram comprises the m-phase region at high surfactant concentration, two 2-phase regions (at low and high temperatures) and a 3-phase region at intermediate temperatures. The name "fish" stems from the shape of the phase diagram with the 3-phase as the fish head.
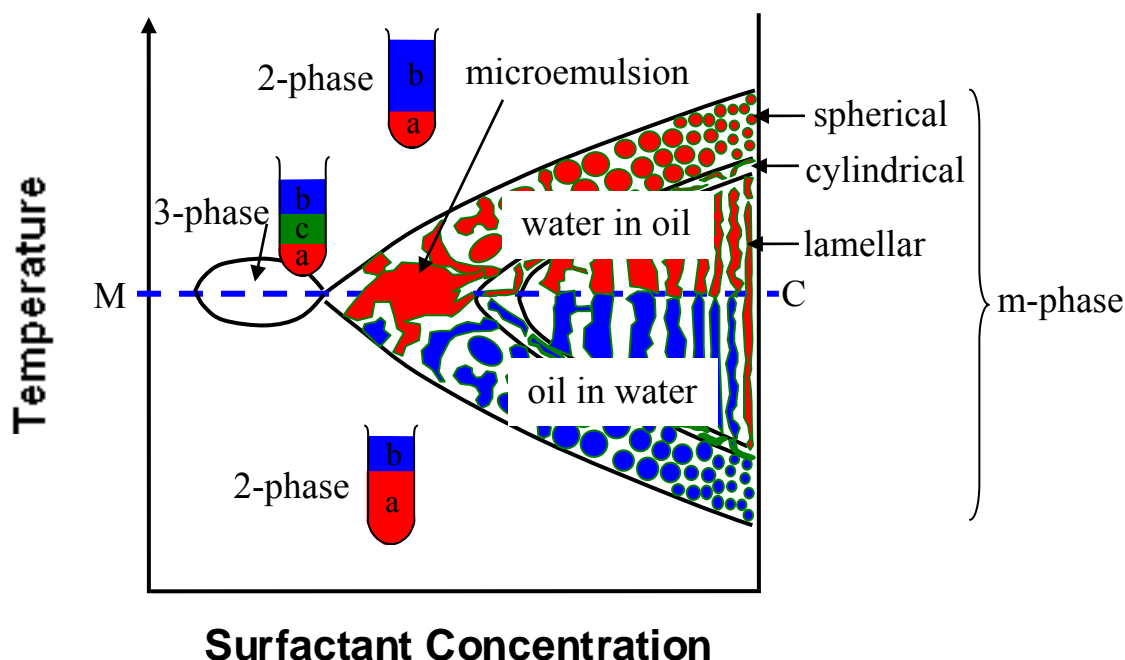
Figure 10: The fish phase diagram.

The m-phase region (right side) of the fish phase diagram is described next.

6. THE MICELLE-FORMATION PHASE

The m-phase region is the focus of most SANS investigations since it is the region of micelle formation and micelles are of nanometer size. The m-phase region is rich in mesophases (with various morphologies). It contains spherical, cylindrical (also called wormlike) and lamellar micelles depending on the temperature range. Structures for these mesophases correspond to cubic, hexagonal and lamellar symmetry respectively. Note also the "microemulsion" (also called bicontinuous) phase. Moreover, oil-in-water micelles are obtained at low temperature and "reverse" (water-in-oil) micelles are obtained at high temperatures.

Water-in-oil and oil-in-water micelles form in the m-phase region. Micelles can also form in the 2-phase region as well. These micelles are different from those found in the m-phase region and would be formed of surfactant/water (or surfactant/oil) only. Micelles form above a critical micelle temperature (CMT) and/or critical micelle concentration (CMC).

SANS data for a nonionic surfactant (pluronics P85) mixed with d-water are shown. The pluronics molecule is a triblock copolymer PPO-PEO-PPO which forms micelles above a critical temperature and concentration. PPO is hydrophilic and PEO is hydrophilic. P85 is different from a ternary water-oil-surfactant system, but the overall trends remain the same. Unimers (dissolved macromolecules) are obtained at low temperature and micelles form at high temperature. The critical micelle temperature and concentration are referred to as the

CMT and CMC. At fixed surfactant concentration, micelles form as shown by an increase in the low-Q SANS intensity.

P85 Pluronics in d-Water
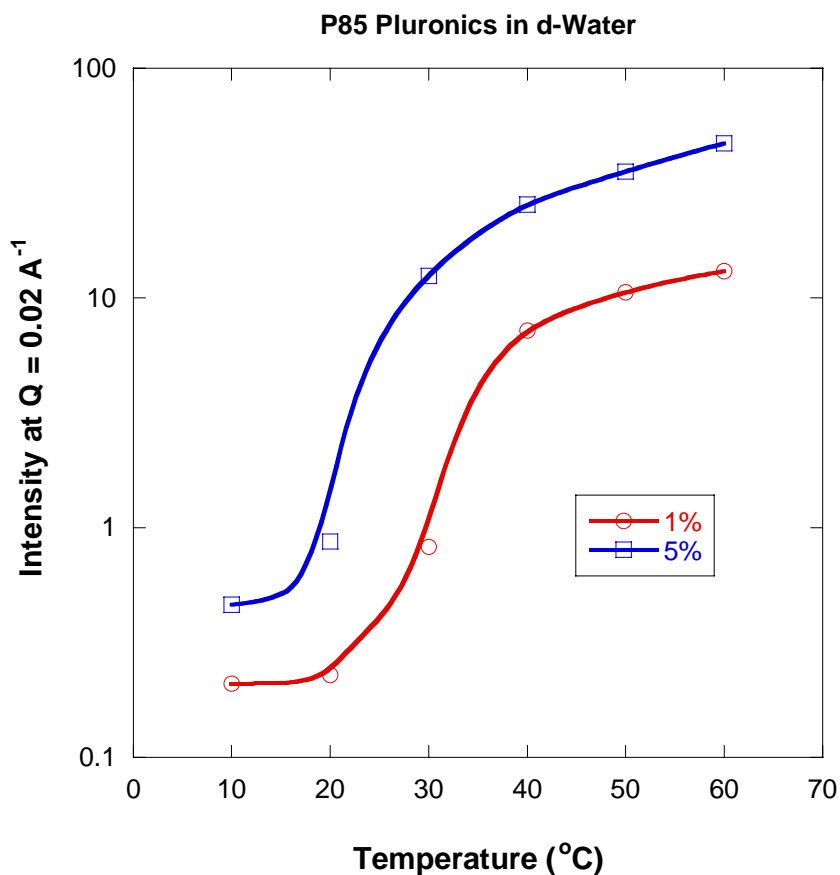
Figure 12: Low-Q SANS data from P85 pluronics in d-water at two difference concentrations. The sigmoid shape function characterizes the critical micelle temperature (CMT).

Varying temperature for a fixed P85 mass fraction shows a transition from a spherical to a cylindrical morphology in the micelle-formation region.
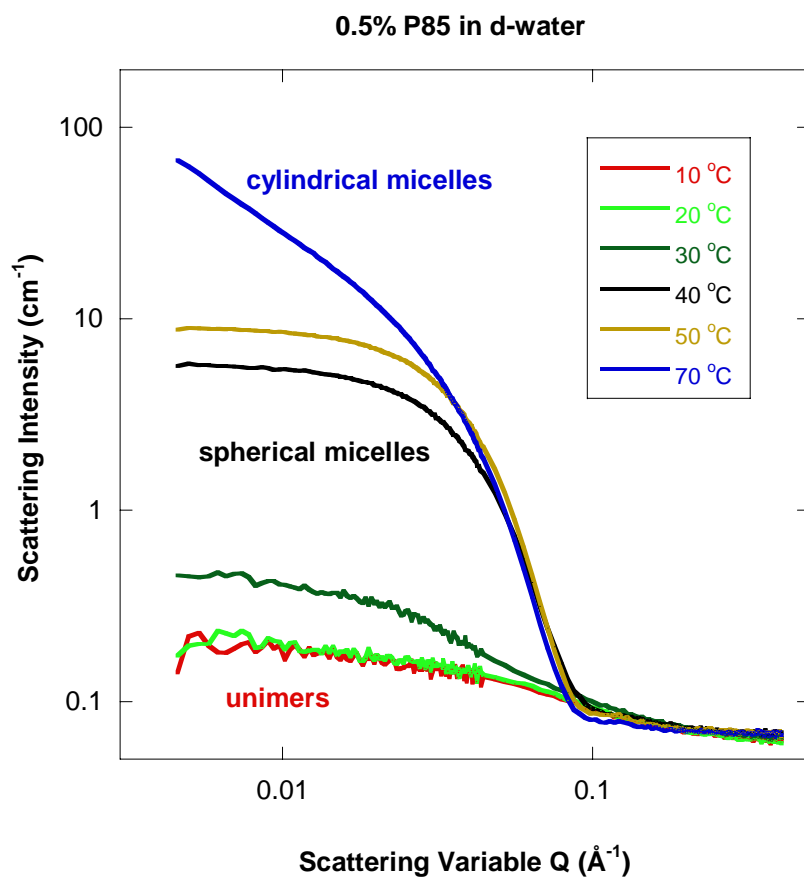
0.5% P85 in d-water

Figure 13: Transition from the unimers to the spherical micelles phase to the cylindrical micelles phase regions as temperature is increased for 0.5 % P85 in d-water.

The transitions from the unimers region to the spherical micelles region, then to the cylindrical micelles region are clearly seen in the next figure as well. The heating/cooling cycle shows no hysteresis.
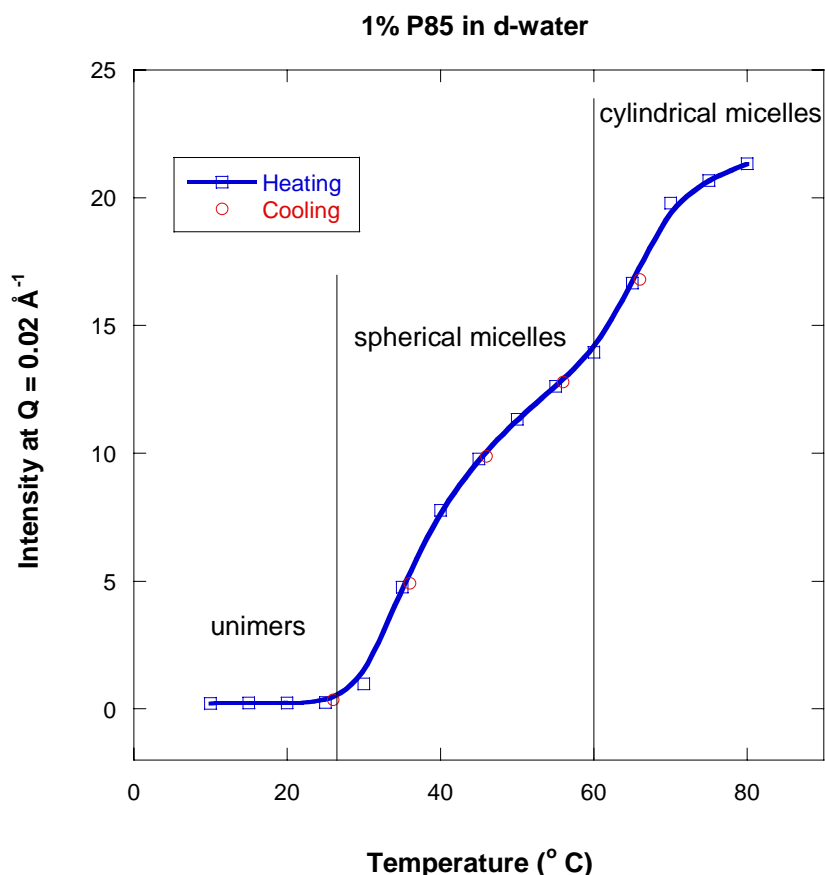
Figure 14: The unimers to spherical micelles and then to cylindrical micelles transitions are clearly seen.

7. TYPICAL SURFACTANTS

P85 was used as a typical nonionic surfactant. A class of nonionic surfactants is denoted C_iE_j. They are comprised of a hydrophobic alkyl chain containing i carbons $H(CH_2)_i$- and a hydrophilic ethoxy containing j alkylpolyglycol ethers $–(OCH_2CH_2)_jH$.

Ionic surfactants contain a charged headgroup and a hydrophobic tail. Model ionic surfactants include cetyletrimethylammonium bromide (CTAB), sodium dodecyl sulfate (SDS), bis(2-ethylhexyl) sodium sulfosuccinate (AOT) also called diocyl sulfosuccinate, sodium salt, etc. The phase diagram for water/oil/ionic surfactant case is similar (but not identical) to the nonionic surfactant case.

A table summarizes the chemical formulas and scattering length densities for some common surfactants. Deuterated water and a typical deuterated oil (d-decane) have also been included. Note that some of the densities have been estimated.

Table 1: Typical ionic surfactants and their scattering length densities.

Surfactant	Chemical Formula	Density (g/cm^3)	Scattering Length Density (Å^{-2})
CTAB	$CH_3(CH_2)_{15}N(CH_3)_3Br^-Na^+$	0.9	$-1.54*10^{-7}$
SDS	$H(CH_2)_{12}OSO_3^-Na^+$	0.9	$3.72*10^{-7}$
AOT	$CH_3(CH_2)_3CH(C_2H_5)CH_2O_2CCH_2CH(SO_3^- Na^+)CO_2CH_2CH(C_2H_5)(CH_2)_3CH_3$	0.9	$5.08*10^{-7}$
d-water	D_2O	1.11	$6.39*10^{-6}$
d-decane	$CD_3(CD_2)_8CD_3$	0.73	$5.7*10^{-6}$

8. SELF-ASSEMBLING SYSTEMS

A slightly more general category than "complex fluids" could be referred to as "self-assembling systems". These include a large class of molecular systems that do not stay dissolved. The following couple of chapters cover "self-assembling" systems. Two nonionic systems will be considered: crystalline lamellae in solution and spherical micelle-forming pluronics. An ionic system forming wormlike micelles will also be included.

Soft materials include gels and networks that trap solvent and form regular amorphous structures. Strong driving forces such as hydrophobic/hydrophilic or Coulombic interactions and other specific interactions (such as hydrogen bonding or dipolar interactions) form self-assembling systems.

Various salts are added to micellar systems in order to control solubility. For example, lyotropic salts decrease the mutual solubility of water and amphiphiles (they increase the closed loop immiscibility island) whereas hydrotropic salts increase solubility (they shrink the closed loop).

Micellar systems are part of main-stream chemical-engineering. They find applications in detergents and cosmetics formulation, drug design and delivery, pharmaceuticals, oil recovery and treatment and in the food industry.

REFERENCES

M. Kahlweit and R. Strey, "Phase Behavior of Ternary Systems of the Type H_2O-Oil-Nonionic Amphiphile (Microemulsions)**,** Angewandte Chemie International Edition in English 24, 654–668 (1985).

http://www.ncnr.nist.gov/resources/sldcalc.html contains a scattering length density calculator.

QUESTIONS

1. What is the difference between an LCST and a UCST phase separation?
2. What is a miscibility gap? How about an immiscibility island?
3. What is a tie line?
4. Define the critical point for a binary mixture.
5. What name replaces the critical point for a ternary mixture?
6. Define the 2-phase and the 3-phase compositions for a ternary water/oil/surfactant system.
7. Describe the 1-phase for binary and for ternary mixtures. Contrast the main difference.
8. How many types of surfactant are there? Name them.
9. What is referred to as the "fish" phase diagram?
10. What is the "prism" phase diagram?
11. What are the two main criteria for the formation of a 3-phase region?
12. In which part of the phase diagram is the SANS technique most effective for a ternary system? Why?

ANSWERS

1. Phase separation occurs upon cooling for a UCST system and upon heating for an LCST system.
2. A miscibility gap is a miscibility region between a UCST at low temperature and an LCST at high temperature. A closed loop immiscibility island is a phase separation region between an LCST at low temperature and a UCST at high temperature.
3. A tie line is the line in the temperature-concentration phase diagram along which phase separation proceeds. The final product is a 2-phase mixture.
4. The critical point for a binary mixture (say water and surfactant) is the maximum point on the binodal line (also called coexistence curve) in the temperature-concentration phase diagram.
5. The plait point is used to refer to the critical point for a ternary mixture.
6. The 2-phase for a ternary system consists of a mixture of two phases (one rich in water and one rich in oil).
7. The 1-phase region for binary systems consists of a homogeneously mixed phase (i.e., mixed at the molecular level). The micelle-formation phase (m-phase) is sometime referred to as the 1-phase for ternary systems. This m-phase is mixed at the micrometer (so-called optical) scale but shows micellar structure at the nanometer (SANS) scale.
8. There are two types of surfactants: nonionic and ionic (i.e., charged).

9. The "fish" phase diagram maps out the 2-phase, the 3-phase and the m-phase regions in a temperature/surfactant concentration plot.

10. The "prism" phase diagram is the extension of the ABS triangle phase diagram to 3D by adding the temperature variable (out of the page). A prism shape is obtained.

11. A 3-phase region forms when the water-surfactant binary phase diagram contains a closed loop immiscibility island and the surfactant is a strong amphiphile.

12. The SANS technique is most effective in the micelle-formation phase since micelles are of nanometer sizes. The 2-phase and the 3-phase regions are characterized by huge (micrometer scale or larger) droplets.

Polymers with regular structures can crystallize whether in solution or in the melt state. Solution crystallization forms regular lamellar structures and is the focus here.

1. A CRYSTALLINE POLYMER SOLUTION

Scattering from poly(ethylene oxide) (PEO) in d-ethanol (deuterated ethanol) solutions shows a strong low-Q signal at low temperatures (below 40 $^{\circ}$C). A low-Q SANS signal could be due to many effects including aggregation, clustering, phase separation, crystallization or just undesired bubbles in the sample.

4 % PEO/d-ethanol, M$_w$ = 50,000 g/mol
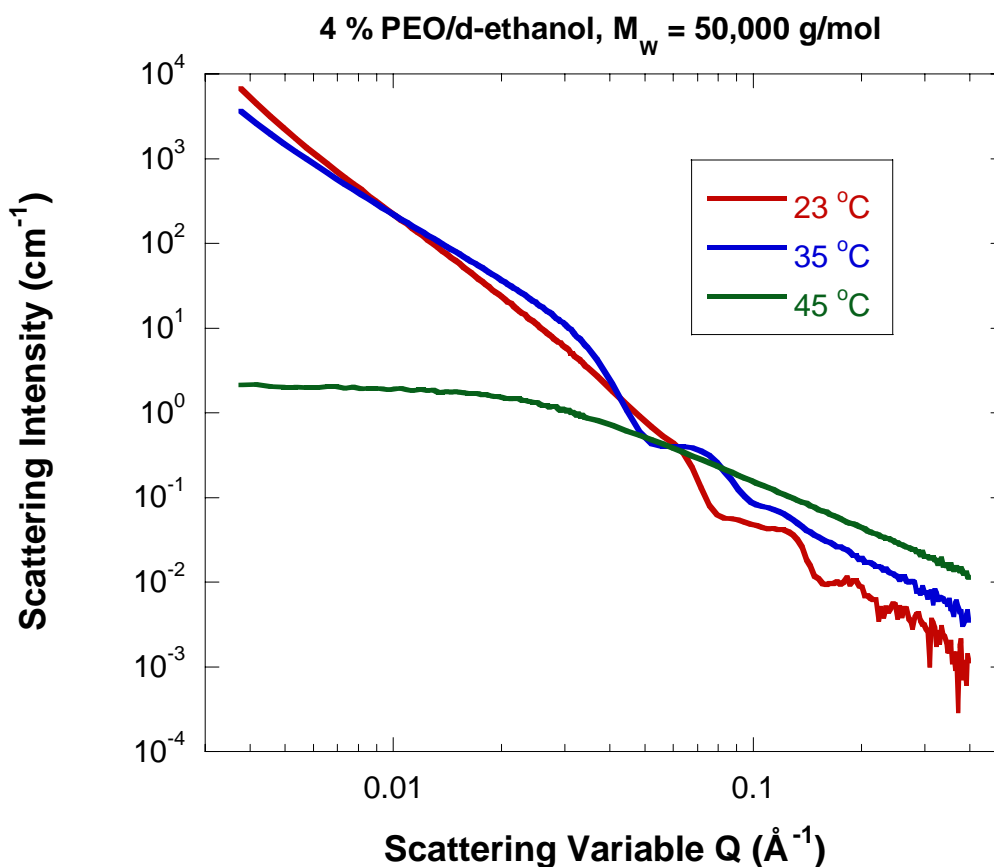
Figure 1: SANS from 4 % PEO/d-ethanol (mass fraction) measured at temperatures below and above the crystal melting temperature. The incoherent background component has been subtracted.
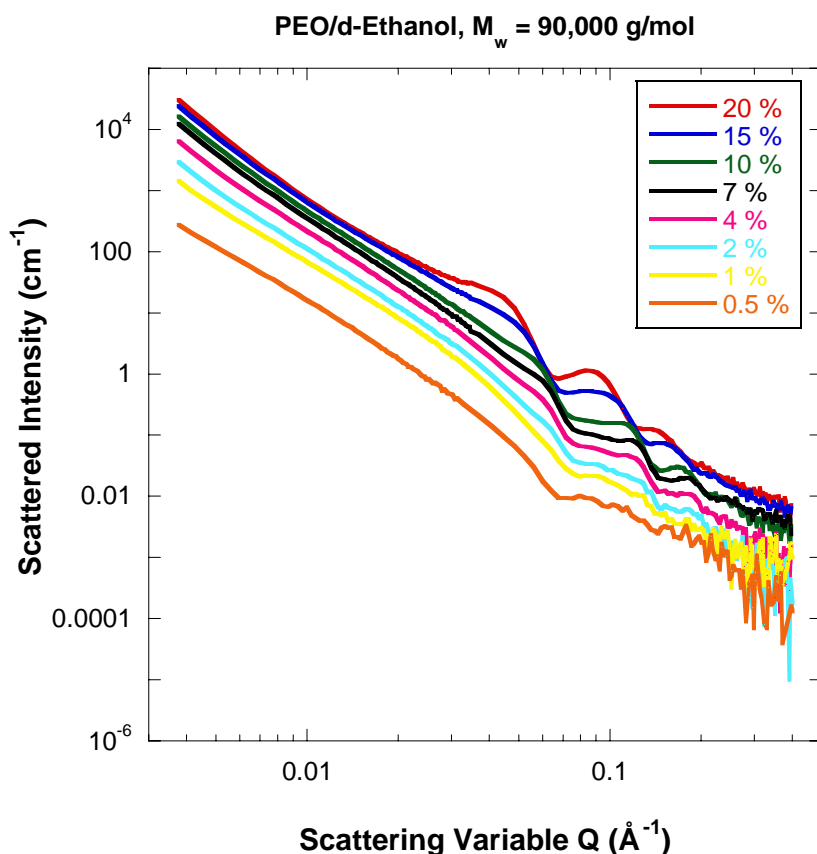
Figure 2: SANS data from PEO/d-ethanol for the various mass fractions measured. Measurements were taken at 23 °C, i.e., well into the crystalline region. The incoherent background component has been subtracted.

In order to discriminate among the various effects that could cause the strong low-Q signal, two standard characterization methods are used. These methods can detect crystallization. The first method is Differential Scanning Calorimetry (DSC) which clearly shows a crystal melting process upon heating and a crystallization process upon cooling.
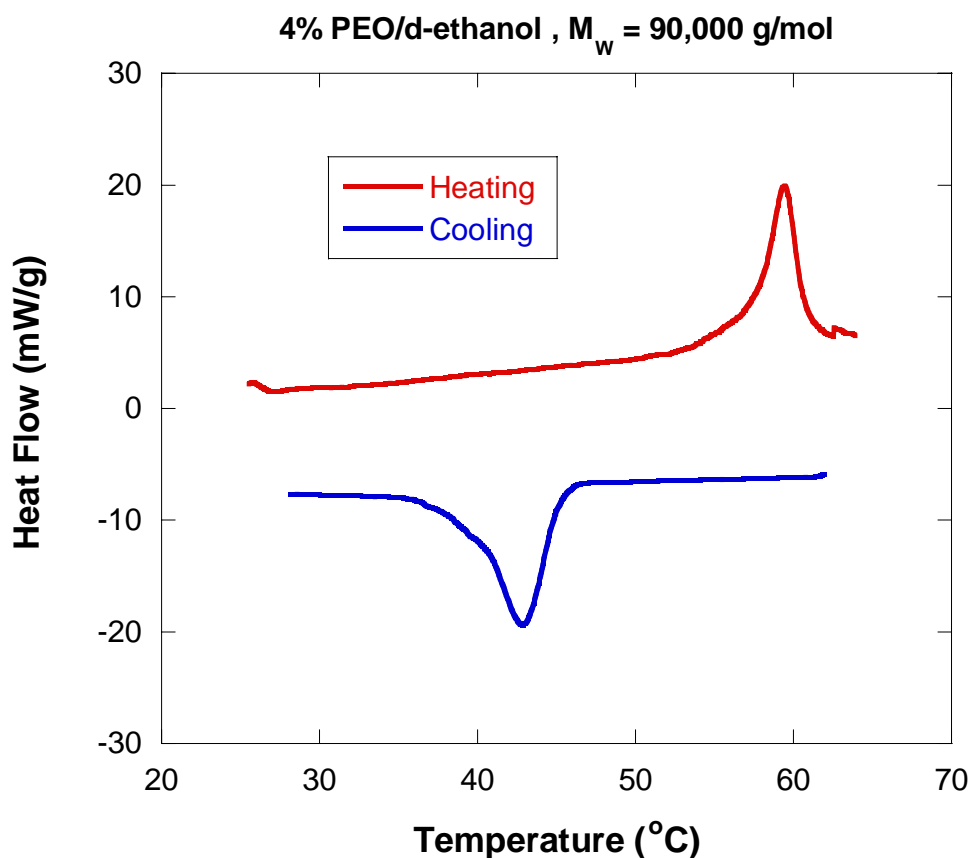
Figure 3: Differential Scanning Calorimetry (DSC) measurements from 4 % PEO/d-ethanol showing the crystalline nature. The heating and cooling curves show the effect of melting and crystallization.

The second good monitor of sample crystallization is Wide-Angle X-ray Scattering (WAXS). This method clearly shows crystalline peaks even at low PEO mass fraction.
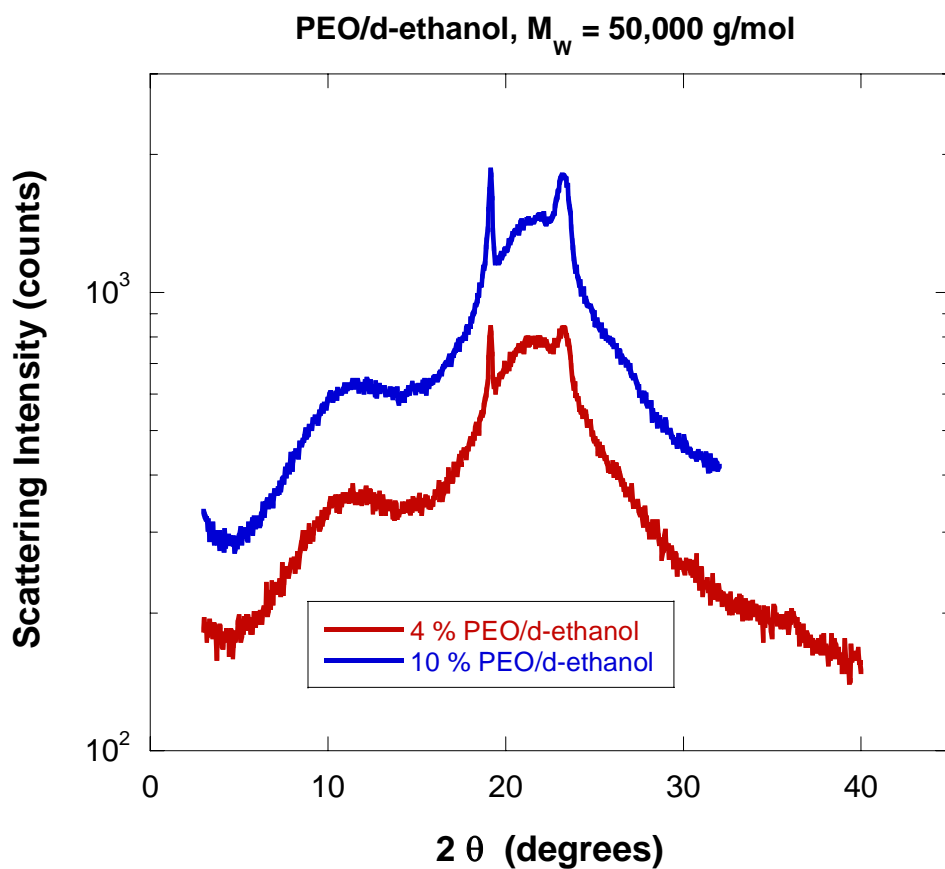
Figure 4: Wide-Angle X-ray Scattering (WAXS) spectra from PEO/ethanol showing crystallinity in the sample. Note that most of the spectrum consists of amorphous halos but two crystalline peaks are observed. The second spectrum was shifted upward.

Another method for determining crystal melting temperatures (while heating) and crystallization temperatures (while cooling) consists in precise density measurements.
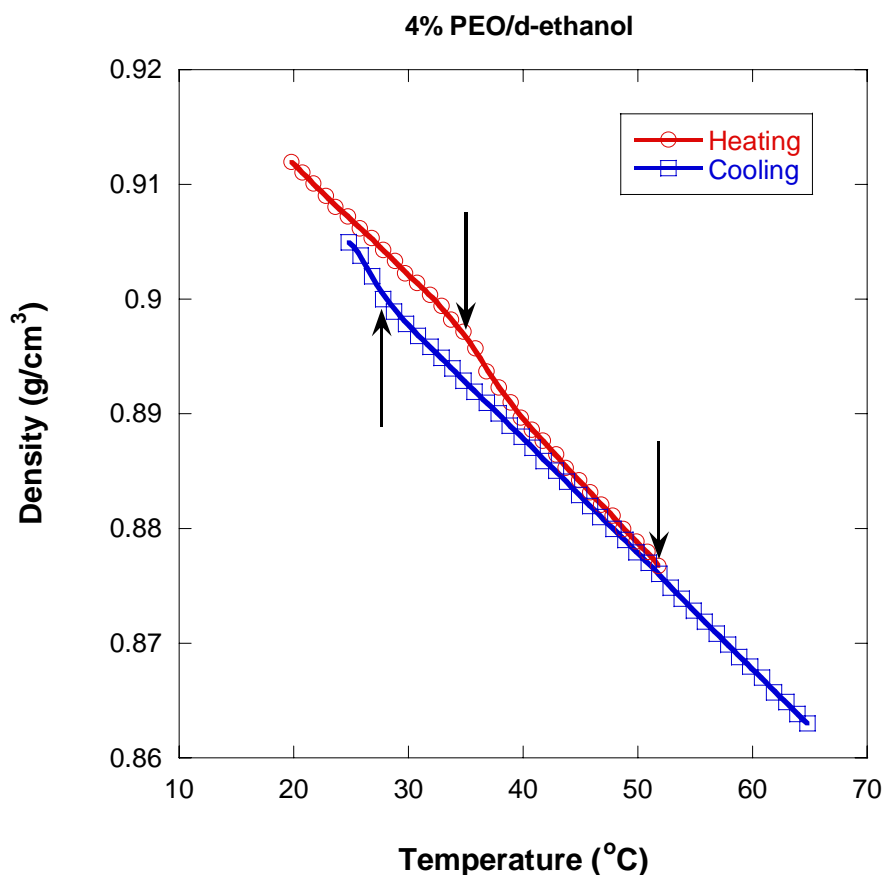
4% PEO/d-ethanol

Figure 5: Density measurements for 4% PEO/d-ethanol. The heating and cooling cycles are shown. Arrows show breaks in the data trend corresponding to melting and crystallization transitions.

2. CLUES ABOUT THE PEO/D-ETHANOL SYSTEM

PEO crystallizes in ethanol even at low mass fractions. Minutes after mixing PEO and ethanol, the solution turns white and gel-like; it does not flow when turned upside-down. When probed using a needle, the structure feels sponge-like. This structure could be referred to as a lamellar sponge.

In order to analyze the measured SANS data, the following model in used.

3. FORM FACTOR FOR A SINGLE LAMELLA
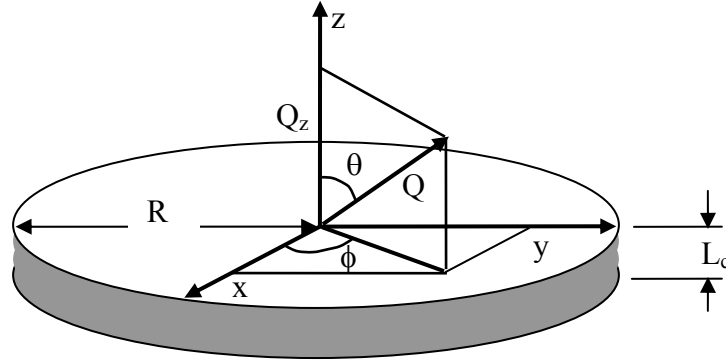
Figure 6: Coordinates parametrization of a single lamella.

The form factor amplitude $F(Q,\mu)$ for a single-lamella has two contributions: one for the Q component parallel to the z-axis and one in the horizontal plane.

$$F(Q,\mu) = F_z(Q,\mu)F_\perp(Q,\mu) \tag{1}$$

$$F_z(Q,\mu) = \frac{1}{L_c}\int_{-L_c/2}^{L_c/2} dz\,\exp[iQ\mu z] = \frac{\sin(Q\mu L_c/2)}{Q\mu L_c/2} \tag{2}$$

$$F_\perp(Q,\mu) = \frac{1}{\pi R^2}\int_0^R d\rho\rho \int_0^{2\pi} d\phi \exp[iQ\sqrt{1-\mu^2}\,\cos(\phi)\rho]. \tag{3}$$

Here $\mu = \cos(\theta)$ and θ is the inclination angle. After manipulations described elsewhere, one obtains:

$$F_\perp(Q,\mu) = \frac{2J_1(Q\sqrt{1-\mu^2}R)}{Q\sqrt{1-\mu^2}R}. \tag{4}$$

J_1 is the cylindrical Bessel function. The final result for the form factor amplitude for a single lamella is:

$$F(Q,\mu) = \left[\frac{\sin(Q\mu L_c/2)}{Q\mu L_c/2}\right]\left[\frac{2J_1(Q\sqrt{1-\mu^2}R)}{Q\sqrt{1-\mu^2}R}\right]. \tag{5}$$

The form factor for a single isolated lamella is therefore given by the following orientational average:

$$P(Q) = \frac{1}{2} \int_{-1}^{1} d\mu \, | F(Q,\mu) |^2 . \tag{6}$$

Lamellae form in stacks. Here the lamellae are not isolated so that the orientational averaging is not performed until the inter-lamellae stack structure factor is included.

4. INTER-LAMELLAE STRUCTURE FACTOR

Consider a stack of N lamellae consisting of alternating crystalline and amorphous regions. L is the inter-lamellar distance (also called long period), L_C is the lamella thickness and R is the radius (Richter et al, 1997; Ho et al, 2006).
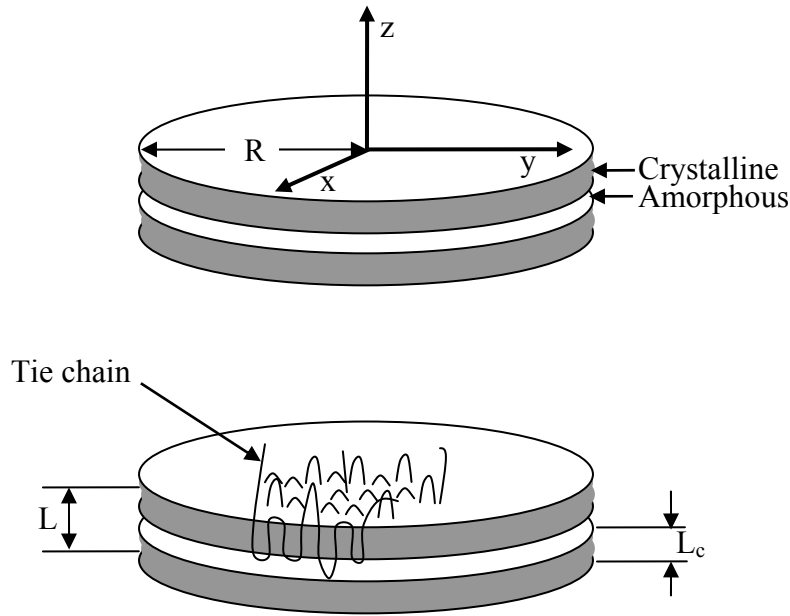
Figure 7: Stack of multiple lamellae.

Consider the following inter-lamellae Gaussian distribution function:

$$W_k(z, L) = \frac{1}{\sqrt{2\pi k \sigma_L^2}} \exp\left[-\frac{(z - kL)^2}{2k\sigma_L^2} \right]. \tag{7}$$

Note that the variance $k\sigma_L^2$ gets larger and the Gaussian peak height gets smaller with increasing lamellar order k within a stack.

The structure factor for a stack of N lamellae is given by:

$$S_I(Q,\mu) = \frac{1}{N^2} \sum_{i,j=0}^{N} < \exp[iQ\mu z] > \tag{8}$$

$$= \frac{1}{N^2} \sum_{i,j=0}^{N} \frac{1}{L} \int dz \exp[iQ\mu z] W_{|i-j|}(z, L).$$

Here $Q_z = Q\mu$ is the projection along the vertical (z) axis and the "I" subscript stands for "inter-lamellae". The z integration is readily performed:

$$\frac{1}{L} \int dz \frac{\exp[iQ\mu z]}{\sqrt{2\pi |i-j|\sigma_L^2}} \exp\left[-\frac{(z-|i-j|L)^2}{2|i-j|\sigma_L^2}\right] = \exp[iQ\mu |i-j|L]\exp\left[-\frac{Q^2\mu^2 |i-j|\sigma_L^2}{2}\right]$$
(9)

Use the following summation identity:

$$\sum_{i,j=1}^{N} F(|i-j|) = N + 2\sum_{k=1}^{N} (N-k)F(k).$$
(10)

And obtain:

$$S_I(Q,\mu) = \frac{1}{N} + \frac{2}{N^2} \sum_{k=1}^{N} (N-k)\exp[iQ\mu kL]\exp\left[-\frac{Q^2\mu^2 k\sigma_L^2}{2}\right].$$
(11)

This result is general and applies for a finite stack of lamellae.

Note that the hypothetical (unrealistic) case where L = 0 yields the following familiar function:

$$S_I(Q,\mu) = \frac{1}{N} + 2\left[\frac{\exp(-A) - 1 + A}{A^2}\right].$$
(12)

This is the Debye function encountered when calculating the form factor for a Gaussian coil along with $A = Q^2\mu^2\sigma_L^2/2$.

The infinite stack case is obtained by taking the $N \rightarrow \infty$ limit. The following result is obtained:

$$S_I(Q,\mu) = \frac{1}{N} + \frac{\exp(Q^2\mu^2\sigma_L^2/2) - \exp(-Q^2\mu^2\sigma_L^2/2)}{\exp(Q^2\mu^2\sigma_L^2/2) + \exp(-Q^2\mu^2\sigma_L^2/2) - 2\cos(Q\mu L)}$$
(13)

$$S_I(Q,\mu) = \frac{1}{N} + \frac{\sinh(Q^2\mu^2\sigma_L^2/2)}{\cosh(Q^2\mu^2\sigma_L^2/2) - \cos(Q\mu L)}.$$

This is a more compact result but applies only for stacks with infinite number of lamellae.

5. THE SCATTERING FACTOR

Putting the single-lamella form factor and the inter-lamella structure factor together gives the following scattering factor:

$$S(Q) = \frac{1}{2} \int_{-1}^{1} d\mu P(Q,\mu) S_1(Q,\mu) \qquad (14)$$

$$S(Q) = \frac{1}{2} \int_{-1}^{1} d\mu \left[\frac{\sin(Q\mu L_c/2)}{Q\mu L_c/2} \right]^2 \left[\frac{2J_1(Q\sqrt{1-\mu^2}R)}{Q\sqrt{1-\mu^2}R} \right]^2 S_1(Q,\mu).$$

This model assumes uniform crystalline density within each lamella and neglects completely scattering from the amorphous phase between the lamellae. Note that in writing down this scattering factor, we did not worry too much about normalization factors. These factors are included in the next section where the scattering cross section is written down.

6. THE STACKED LAMELLAE MODEL

Consider a scattering system consisting of a sponge-like structure where the lamellae trap solvent. A few lamellae packed into stacks form the partitions. Each stack contains a number of crystalline lamellae and amorphous regions in-between the lamellae. Solvent dissolves the amorphous regions and fills the pockets of the sponge-like structure. Note that the extent of the stack (its radius) is not well-defined. It is large and could be thought of as the average distance between bifurcation points.
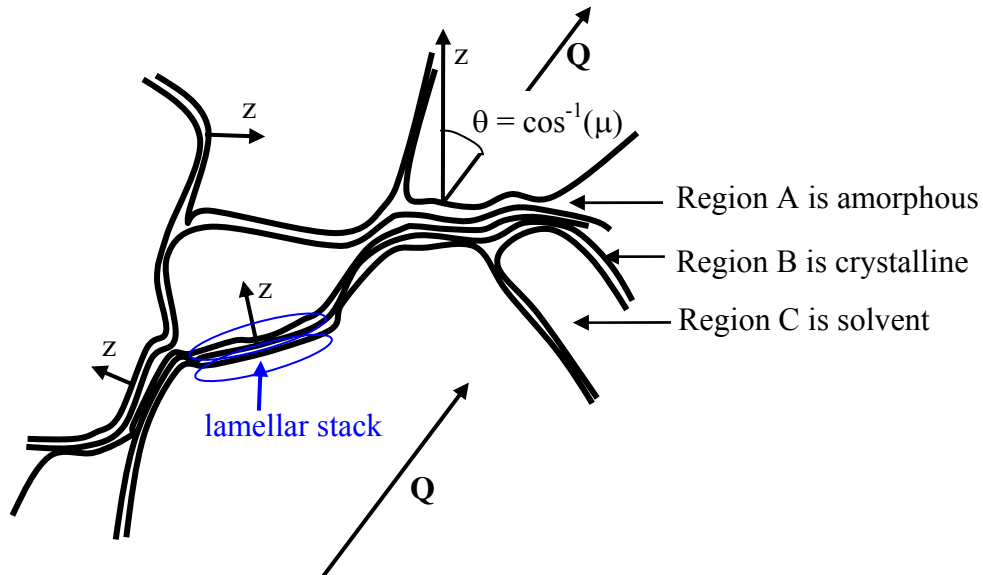
Figure 8: The stacked lamellae model consists of alternating amorphous and crystalline regions that surround solvent pockets.

The following parameters are used in the model.

L_A: thickness of the amorphous region
L_B: thickness of the crystalline region
L: lamellar spacing ($L = L_A + L_B$)
N: number of lamellae per stack
σ_L: standard deviation of lamellar spacing
$V_A = \pi R^2 L_A$: volume of one amorphous region
$V_B = \pi R^2 L_B$: volume of one crystalline region
R: average radius of the lamellar stack
$V_{A+B} = \pi R^2 L$: volume of one crystalline and one amorphous regions
$\rho_A = b_A / v_A$: scattering length density of the amorphous region (region A)
$\rho_B = b_B / v_B$: scattering length density of the crystalline region (region B)
$\rho_C = b_C / v_C$: scattering length density of the solvent region (region C)
N_S/V: lamellar stacks number density.

The orientation-dependent cross section is given by:

$$\left[\frac{d\Sigma(Q,\mu)}{d\Omega} \right] = \left(\frac{\phi_S}{V_S} \right) \left[\left(\frac{b_A}{v_A} - \frac{b_C}{v_C} \right) V_A F_A(Q,\mu) + \left(\frac{b_B}{v_B} - \frac{b_C}{v_C} \right) \left[V_{A+B} F_{AB}(Q,\mu) - V_A F_A(Q,\mu) \right] \right]^2 S_I(Q,\mu)$$

(15)

$$\left[\frac{d\Sigma(Q,\mu)}{d\Omega} \right] = \left(\frac{\phi_S}{V_S} \right) \left[\left(\frac{b_A}{v_A} - \frac{b_B}{v_B} \right) V_A F_A(Q,\mu) + \left(\frac{b_B}{v_B} - \frac{b_C}{v_C} \right) V_{A+B} F_{AB}(Q,\mu) \right]^2 S_I(Q,\mu).$$

Note that the number density of the lamellar stacks N_S/V has been expressed in terms of the stacks volume fraction ϕ_S and stack volume V_S as $N_S/V = \phi_S/V_S$.

The form factors are:

$$F_A(Q,\mu) = \left[\frac{\sin(Q\mu L_A/2)}{Q\mu L_A/2} \right] \left[\frac{2J_1(Q\sqrt{1-\mu^2}R)}{Q\sqrt{1-\mu^2}R} \right]$$

(16)

$$F_{AB}(Q,\mu) = \left[\frac{\sin(Q\mu L/2)}{Q\mu L/2} \right] \left[\frac{2J_1(Q\sqrt{1-\mu^2}R)}{Q\sqrt{1-\mu^2}R} \right].$$

The inter-lamellae structure factor for each stack is given by:

$$S_I(Q,\mu) = \frac{1}{N} + \frac{2}{N^2} \sum_{k=1}^{N} (N-k) \exp[iQ\mu kL] \exp\left[-\frac{Q^2\mu^2 k\sigma_L^2}{2} \right].$$

(17)

424

The orientationally averaged cross section is obtained as:

$$\frac{d\Sigma(Q)}{d\Omega} = \frac{1}{2} \int_{-1}^{1} d\mu \frac{d\Sigma(Q,\mu)}{d\Omega} . \qquad (18)$$

The scattering intensity consists of the following contributions:

$$I(Q) = \frac{A}{Q^n} + \frac{d\Sigma(Q)}{d\Omega} + B . \qquad (19)$$

The lamellar stacks represent only the crystalline-amorphous regions forming the walls of the sponge-like structure. Scattering comprises also scattering from the sponge-like structure itself. A term A/Q^n term has been added to represent the lamellar non-stack scattering component. This component has contributions from the clustering network of the sponge-like structure (mass fractal network and surface fractal lamellae). B is a Q-independent (mostly incoherent) scattering background.

7. MODEL FITTING

The stacked lamellae model is smeared with the instrumental resolution function and used to fit SANS data from PEO/d-ethanol samples in the crystalline region.

425
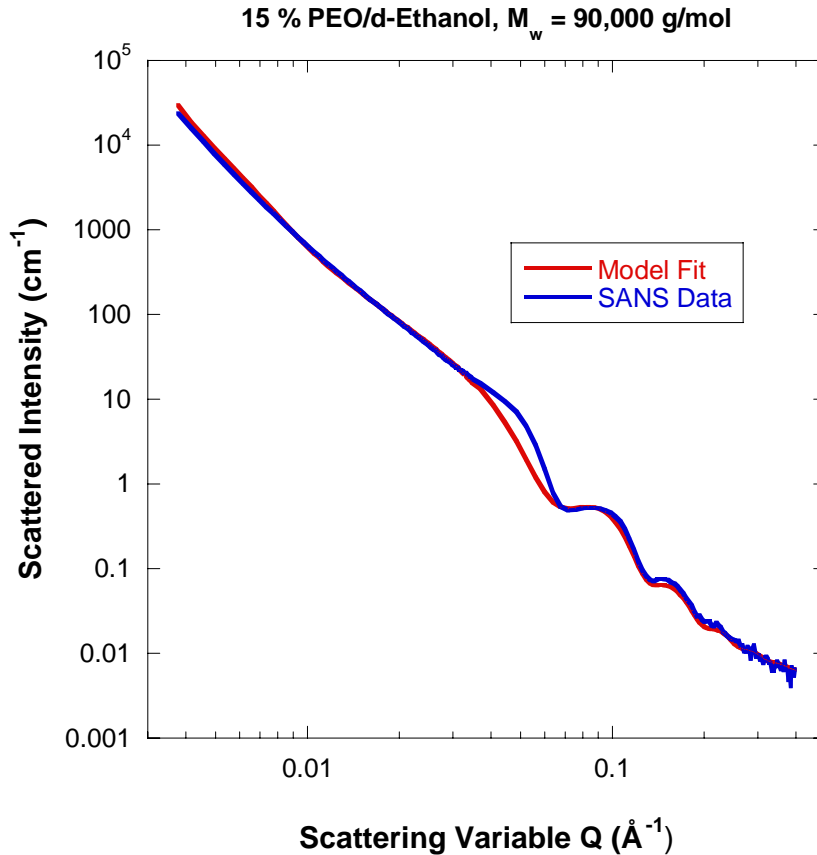
Figure 9: Comparison of the SANS data and the stacked lamellae smeared model for the 15 % PEO/d-ethanol sample at 23 $^\circ$C. The model fits the data fairly well except for a region in the middle of the window.

Results of the fit follow.

Lamellar stacks volume fraction $\phi_S = 0.36$
Lamellae radius $R = 10{,}757$ Å
Thickness of the amorphous region $L_A = 3$ Å
Lamellar thickness $L_B = 50$ Å
Scattering length density of the amorphous region $\rho_A = 4.15*10^{-6}$ Å^{-2}
Scattering length density of the crystalline region $\rho_B = 7.67*10^{-7}$ Å^{-2}
Scattering length density of the d-ethanol solvent region $\rho_S = 6.07*10^{-6}$ Å^{-2}
Number of lamellae per stack $N_L = 6.86$
Standard deviation of the inter-lamellar distance $\sigma_L = 0.56$ Å
Clustering scaling factor $A = 282*10^{-6}$ cm^{-1}
Clustering Porod exponent $n = 2.8$
Constant (incoherent) background level $B = 0.004$ cm^{-1}.

The solvent scattering length density ρ_S was fixed. All other 11 fitting parameters were varied. With so many varying parameters, it is difficult to find a unique solution. The one presented here gives an idea of the magnitude of the various parameters. Constraints such as ordering the various scattering length densities as $\rho_{EO} < \rho_B < \rho_A < \rho_{dEth}$ help the fitting.

15 % PEO/d-Ethanol, M_w = 90,000 g/mol
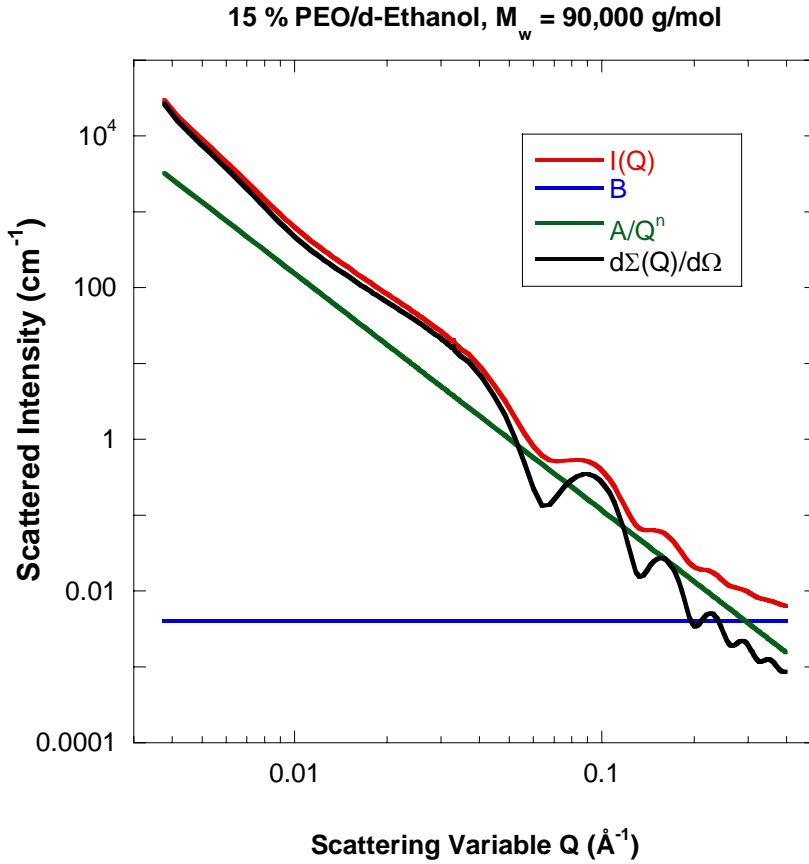
Figure 10: Breakdown of the various terms forming the fitting model functional form. Note that $I(Q) = d\Sigma(Q)/d\Omega + A/Q^n + B$.

8. THE MATERIAL BALANCE EQUATIONS

Consider a solution consisting of lamellar stacks comprising alternating amorphous and crystalline regions. We assume that D_2O exists in the amorphous and crystalline regions; i.e., that there are y_A d-ethanol molecules per ethylene oxide (EO) monomer in the amorphous region (region A) and y_B d-ethanol molecules per EO monomer in the crystalline region (region B). Note that most of the solvent exists in the sponge-like pockets outside of the lamellar stacks. Define N_{agg} as the aggregation number, i.e., the number of PEO macromolecules per lamellar stack and note that there are n EO monomers per macromolecule. These are distributed as $n_A = nf_A$ monomers in region A and $n_B = nf_B$ in region B.

The fitting parameters are L_A, L_B, ρ_A, ρ_B, R, N, and σ_L. Other known quantities are the specific volumes v_{EO}^A (EO in the amorphous region), v_{EO}^B (EO in the crystalline region) and v_{dEth} and the scattering lengths b_{EO} and b_{dEth}. The unknown parameters are y_A, y_B, f_A, and N_{ag}. Note that $f_B = 1-f_A$.

The material balance equations are:

$$(1) \quad \pi L_A R^2 N_L = N_{ag} f_A n \left(v_{EO}^A + v_{dEth} y_A \right) \tag{20}$$

$$(2) \quad \pi L_B R^2 N_L = N_{ag} f_B n \left(v_{EO}^B + v_{dEth} y_B \right)$$

$$(3) \quad \rho_A = \frac{N_{ag} f_A n \left(b_{EO} + b_{dEth} y_A \right)}{4 \pi L_A R^2 N_L}$$

$$(4) \quad \rho_B = \frac{N_{ag} f_B n \left(b_{EO} + b_{dEth} y_B \right)}{4 \pi L_B R^2 N_L} \, .$$

These four linear equations can be solved to obtain:

$$y_A = \frac{\rho_A v_{EO}^A - b_{EO}}{b_{dEth} - \rho_A v_{dEth}} \tag{21}$$

$$y_B = \frac{\rho_B v_{EO}^B - b_{EO}}{b_{dEth} - \rho_B v_{dEth}}$$

$$f_A = \frac{\left(v_{EO}^B + y_B v_{dEth} \right) \dfrac{L_A}{L_B}}{\left(v_{EO}^A + y_A v_{dEth} \right) + \left(v_{EO}^B + y_B v_{dEth} \right) \dfrac{L_A}{L_B}}$$

$$f_B = 1 - f_A$$

$$N_{ag} = \frac{4 \pi R^2 L_A N_L}{n f_A \left(v_{EO}^A + y_A v_{dEth} \right)} \, .$$

We have transformed the four fitting parameters L_A, L_B, ρ_A and ρ_B into four meaningful parameters y_A, y_B, f_A and N_{ag}. This set of solutions is unique. Note that only N_{ag} depends on the ill-defined stack radius R.

9. NUMERICAL APPLICATION

Consider the PEO/d-ethanol system described earlier. Some of the known parameters follow:

$$v_{EO}^A = 42.82 \text{ cm}^3 / \text{mol} \tag{23}$$
$$v_{EO}^B = 38.93 \text{ cm}^3 / \text{mol}$$
$$v_{dEth} = 58.56 \text{ cm}^3 / \text{mol}$$

$$b_{EO} = 4.14*10^{-13}\,cm$$
$$b_{dEth} = 59.12*10^{-13}\,cm.$$

Note that the amorphous region's specific volume has been taken to be 10 % higher than that for the crystalline region. Using these parameters along with the following fitting parameters:

$$\phi_S = 0.36 \qquad\qquad\qquad (24)$$
$$R = 10{,}757\ \text{Å}$$
$$L_A = 3\ \text{Å}$$
$$L_B = 50\ \text{Å}$$
$$\rho_A = 4.15*10^{-6}\ \text{Å}^{-2}$$
$$\rho_B = 7.67*10^{-7}\ \text{Å}^{-2}$$
$$\rho_S = 6.07*10^{-6}\ \text{Å}^{-2}$$
$$N_L = 6.86$$
$$\sigma_L = 0.56\ \text{Å}.$$

The material balance equations yield:

$$y_A = 3.7 \qquad\qquad\qquad (25)$$
$$y_B = 0.02$$
$$f_A = 0.01$$
$$f_B = 0.99$$
$$N_{ag} = 926{,}000$$

Fit results yield 3.7 solvent molecules per EO monomer in the amorphous region and no solvent in the crystalline region. Moreover, most of the EO monomers are found in the crystalline regions.
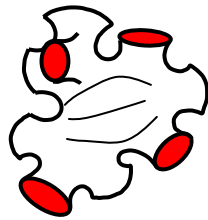
Figure 11: Schematic representation of the sponge-like structure. The sponge walls are formed of lamellar stacks that trap pockets of solvent.
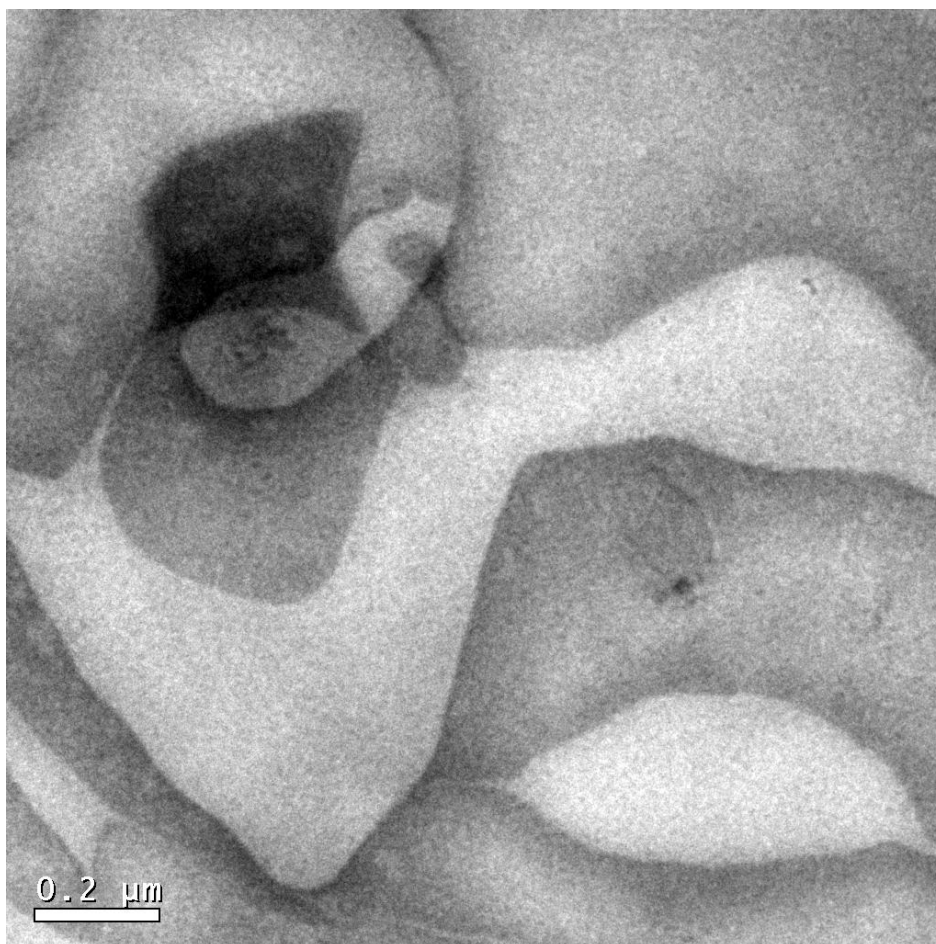
Figure 12: Transmission Electron Micrograph (TEM) of a 4 % PEO/ethanol crystalline sample. The sample was stained. The sponge-like crystalline structure traps pockets of solvent.

The exercise described here gives an idea of what it takes to understand some SANS data: clues about the sample, model fitting and a great deal of common sense.

REFERENCES

D. Richter, D. Schneiders, M. Monkenbush, L. Willner, L.J. Fetters, J.S. Huang, M. Lin, K. Mortensen and B. Farago, "Polymer Aggregates with Crystalline Cores: The System Polyethylene-Poly(ethylenepropylene)", Macromolecules 30, 1053-1068 (1997).

D.L Ho, B. Hammouda, S.R. Kline and W-R Chen, "Unusual Phase Behavior in Mixtures of Poly(ethylene oxide) and Ethyl Alcohol", J. Polym. Sci., Polym. Phys. Ed. 55, 557-564 (2006)

QUESTIONS

1. Crystalline lamellar morphology is formed in what conditions?
2. What are the main pieces used to work out the scattering from a lamellar system?
3. Why is the scattering from crystalline lamellae characterized by SANS oscillations at high-Q?
4. Why is the inter-lamellae scattering (also called long period) characterized by a Bragg peak?
5. Lamellar growth occurs either following the "adjacent" or the "random switchboard" re-entry. Which occurs in solution crystallization and which occurs in melt crystallization?
6. Are the crystallization and the crystal melting temperatures the same? Which is lower? Why?

ANSWERS

1. Crystalline polymers form lamellar morphology in solution as well as in the melt state. In the melt state, however, lamellae organize into spherulitic structures.
2. Scattering from a lamellar system is calculated using the form factor for a lamella and the inter-lamellar structure factor.
3. SANS scattering from crystalline lamellae is characterized by oscillations at high-Q because of the sharp (highly monodisperse) lamellar size.
4. The inter-lamellae scattering is characterized by a Bragg peak because of the well-defined characteristic d-spacing between lamellae.
5. Adjacent re-entry occurs in solution crystallization and random switchboard occurs in melt crystallization. This is due to the slower crystalline growth kinetics in solution crystallization.
6. Crystallization is obtained through cooling whereas crystal melting happens though heating. For this, the crystallization temperature is lower than the melting temperature due to the "hysteresis" effect. This effect is seen on the DSC spectra included earlier.

Chapter 44 - SANS FROM PLURONICS

1. WHAT ARE PLURONICS?

Poly(ethylene oxide) (referred to as PEO) is the simplest water soluble polymer. Its structure $-CH_2CH_2O-$ consists of a hydrophobic ethylene $-CH_2CH_2-$ group and a hydrophilic $-O-$ oxygen. Its neighbors in the homologous series poly(methylene oxide) (or PMO) and poly(propylene oxide) (or PPO) do not dissolve in water at ambient temperature. This behavior can be traced to the just-right balance between hydrophobic and hydrophilic interactions in PEO. For instance, the oxygen-oxygen inter-distance of 4.7 Å in PEO corresponds to the oxygen-oxygen next-nearest neighbor inter-distance in the structure of pure water.

Pluronics are triblock copolymers composed of one PPO block connected to two PEO blocks. The PEO blocks dissolve well in aqueous media because they are mostly hydrophilic while the PPO block does not dissolve because it is mostly hydrophobic at ambient temperature. This amphiphilic nature of pluronics molecules makes them form micelles at ambient temperature. At low temperatures, this balance does not hold and both PEO and PPO blocks dissolve in water thereby breaking down the micellar structure. The Critical Micelle formation Temperature (CMT) is a temperature at which micelles form. The CMT is the Critical Micelle formation Concentration. CMT and CMC vary depending on the block composition of the various pluronics.

Pluronics are commercially available materials used in the cosmetics and pharmaceutical industries. The P85 pluronic considered here consists of 26 EO monomers in each of the outside blocks and 40 PPO monomers in the middle block. P85 is referred to as $EO_{26}PO_{40}EO_{26}$. The molecular weight of P85 is around 4,600 g/mol (Slawecki et al, 1998).

2. SANS FROM P85 PLURONIC

SANS data were taken from 10 % P85 at various temperatures (from 20 ^oC to 60 ^oC). Two instrument configurations (one low-Q and one high-Q) were used. Micelles are well formed by 30 ^oC. When micelles are formed, the scattering is characterized by two features: a peak characteristic of inter-micelles interactions, and decay at high Q characterizing the tail of the single-particle form factor. In-between these two features, the hint of a second peak (shoulder around Q = 0.15 $Å^{-1}$) can be observed. This shoulder is also characteristic of the single particle form factor (oscillation of the spherical Bessel function) and is affected by polydispersity effects.
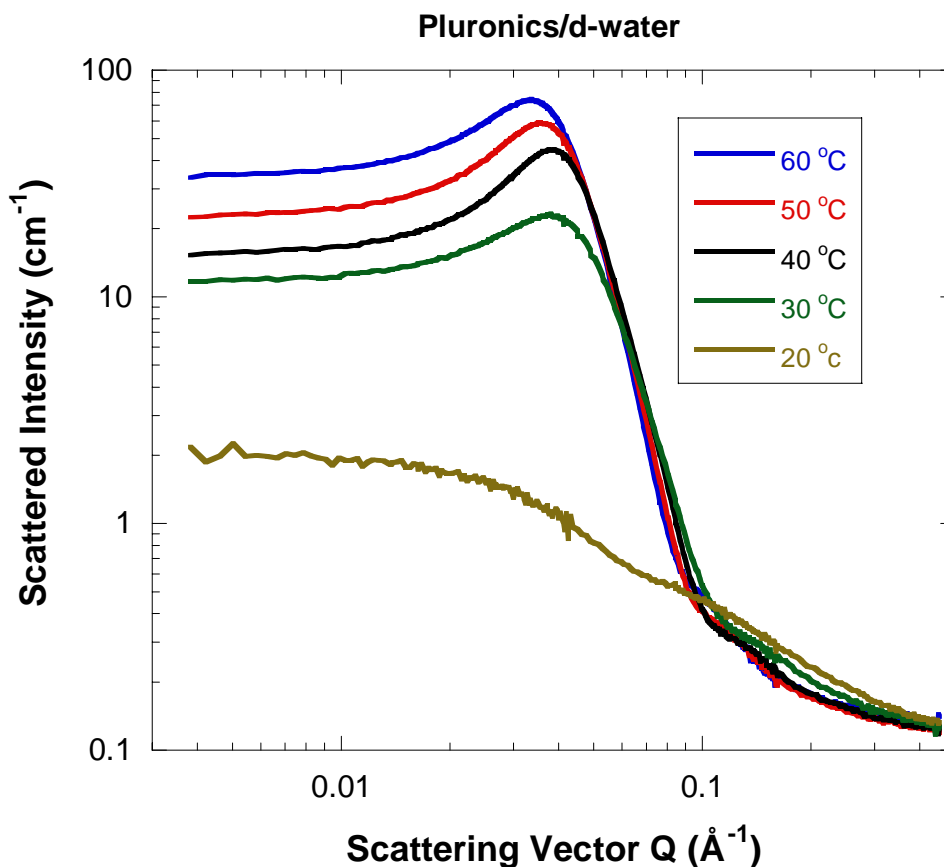
Figure 1: SANS data from the 10 % P85 in D_2O at various temperatures. Data statistics are different for the two instrument configurations. The overlap region for the two configurations is between 0.03 Å $^{-1}$ and 0.04 Å $^{-1}$.

3. THE CORE-SHELL PARTICLE MODEL

The P85 pluronic forms micelles above the CMT and CMC. The simple core-shell model is used to analyze the SANS data from P85 (Kline-Hammouda, 2004). This model is reviewed here. Consider three regions: a core (region A) of radius R_A, a shell (region B) of thickness R_B-R_A and the solvent (region C).
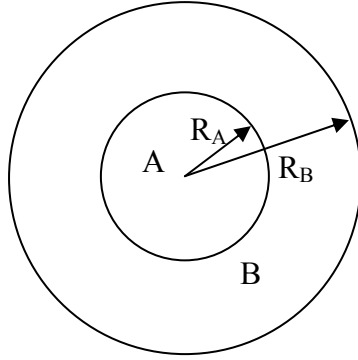
Figure 2: Schematic representation of the P85 micelle as a core-shell particle.

The following parameters are defined:

N: number of core-shell particles in the solution.
b_A: scattering length for region A.
b_B: scattering length for region B.
b_C: scattering length for region C.
v_A: specific volume in region A (= density/molar mass).
v_B: specific volume in region B (= density/molar mass).
V_A: volume of region A. $V_A = (4\pi/3)R_A^3$.
V_{A+B}: volume of regions A and B. $V_{A+B} = (4\pi/3)R_B^3$.
V: total volume of the solution.

At first, assume that the particles do not interact, i.e., consider the very infinite dilution case.

Assuming uniform densities in the core and shell regions, the macroscopic scattering cross section is given as the particle number density multiplied by the square of the single-particle form factor.

$$\left[\frac{d\Sigma(Q)}{d\Omega}\right]_{ID} = \frac{N}{V}\left[\left(\frac{b_A}{v_A} - \frac{b_C}{v_C}\right)V_A\frac{3j_1(QR_A)}{QR_A} + \left(\frac{b_B}{v_B} - \frac{b_C}{v_C}\right)\left(V_{A+B}\frac{3j_1(QR_B)}{QR_B} - V_A\frac{3j_1(QR_A)}{QR_A}\right)\right]^2$$

(1)

The VD subscript stands for infinite dilution. The first part is for the core contribution (integration between 0 and R_A) with the right scattering length density difference and the second part is for the shell contribution (integration between R_A and R_B). The single-particle form factor for a sphere (of radius R_A) is expressed in terms of the familiar spherical Bessel function

$$j_1(QR_A) = \left(\frac{\sin(QR_A)}{(QR_A)^2} - \frac{\cos(QR_A)}{QR_A}\right).$$ (2)

Another form for the same cross section is:

$$\left[\frac{d\Sigma(Q)}{d\Omega}\right]_{ID} = \frac{N}{V}\left[\left(\frac{b_A}{v_A} - \frac{b_B}{v_B}\right)V_A\frac{3j_1(QR_A)}{QR_A} + \left(\frac{b_B}{v_B} - \frac{b_C}{v_C}\right)V_{A+B}\left(\frac{3j_1(QR_B)}{QR_B}\right)\right]^2.$$

(3)

These forms reproduce the limit of the scattering cross section for uniform density spheres (of radius R_A) by assuming either $b_B/v_B = b_C/v_C$ or $R_B = R_A$.

4. CONCENTRATION EFFECTS

When the particle concentration is finite (i.e., non zero), the scattering cross section contains contributions from the inter-particle structure factor $S_I(Q)$. The simplest analytical form for expressing $S_I(Q)$ is through the Percus-Yevick approximation for spheres interacting through a hard sphere potential. The Percus-Yevick approximation was introduced as a "closure" relation to the Ornstein-Zernike equation. Within the Percus-Yevick approximation, $S_I(Q)$ for a finite concentration of spheres (of diameter D) is expressed as:

$$S_I(Q) = \frac{1}{1 - \overline{NC(Q)}}.$$

(4)

$\overline{NC(Q)}$ is the Fourier transform of the direct correlation function given by:

$$\overline{NC(Q)} = -24\phi\left\{\lambda_1\left[\frac{\sin(QD) - (QD)\cos(QD)}{(QD)^3}\right] - 6\phi\lambda_2\left[\frac{(QD)^2\cos(QD) - 2(QD)\sin(QD) - 2\cos(QD) + 2}{(QD)^4}\right]\right.$$

$$\left. -\phi\frac{\lambda_2}{2}\left[\frac{(QD)^4\cos(QD) - 4(QD)^3\sin(QD) - 12(QD)^2\cos(QD) + 24(QD)\sin(QD) + 24\cos(QD) - 24}{(QD)^6}\right]\right\}$$

(5)

The parameters λ_1 and λ_2 are given by:

$$\lambda_1 = \frac{(1+2\phi)^2}{(1-\phi)^4}$$

(6)

$$\lambda_2 = \frac{-(1+\phi/2)^2}{(1-\phi)^4}.$$

ϕ is the packing fraction which can be expressed in terms of the particle number density (N/V) and particle radius R (R = D/2) and is defined as: $\phi = \left(\dfrac{N}{V}\right)\left(\dfrac{4\pi}{3}R^3\right)$. Note that in the core-shell particle model $R = R_B$.

The scattering cross section for a concentrated solution of hard spheres is obtained by multiplying the infinite dilution result by $S_I(Q)$:

$$\frac{d\Sigma(Q)}{d\Omega} = \left[\frac{d\Sigma(Q)}{d\Omega}\right]_{ID} S_I(Q). \tag{7}$$

The single-particle and inter-particle structure factors are the main pieces of the scattering cross section for the P85 micelles.

5. FIT RESULTS

Fits of the P85 SANS data were performed using the non-dilute solution of core-shell particles. Results for the 10 % P85 in D_2O are presented here for the 40 ^{o}C temperature case where the micelles are well formed.

Packing volume fraction $\phi = 0.248$ (8)
Core radius $R_A = 43.96$ Å.
Polydispersity parameter $\sigma_A/R_A = 0.16$
Shell outer radius $R_B = 72.91$ Å.
$\left(\dfrac{b}{v}\right)_A = 7.563*10^{-7} \, \text{Å}^{-2}$
$\left(\dfrac{b}{v}\right)_B = 5.940*10^{-6} \, \text{Å}^{-2}$
$\left(\dfrac{b}{v}\right)_C = 6.40*10^{-6}$ Fixed.

These fit results are used to obtain detailed information about the P85 micelles using the material balance equations.

10% P85 Pluronic in D$_2$O at 40 ^{o}C
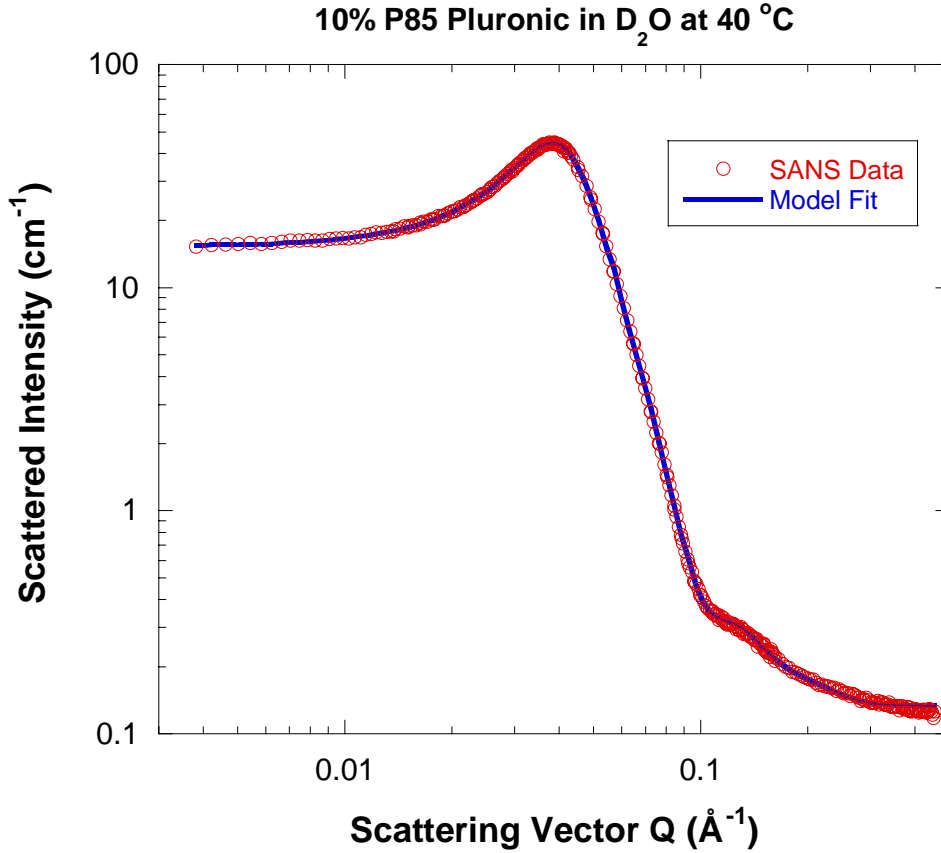
Figure 3: SANS data and model fit for the 10 % P85 in D$_2$O sample at 40 ^{o}C. The two curves are indistinguishable.

6. MATERIAL BALANCE EQUATIONS

Consider a model whereby the micelle core contains PO blocks and a fraction f of the EO blocks and the shell contains the remaining fraction (1-f) of the EO blocks. Moreover assume that D$_2$O exists in the core and in the shell to hydrate the EO blocks. Assume that there are y$_A$ D$_2$O molecules per EO monomer in the core (region A) and y$_B$ D$_2$O molecules per EO monomer in the shell (region B). Define N$_{agg}$ as the aggregation number, i.e., the number of P85 molecules per micelle and recall that there are 40 PO monomers per block and 26*2 = 52 EO monomers per macromolecule.

The material balance equations are:

(1) $\dfrac{4\pi}{3} R_A{}^3 = N_{ag}.[40.v_{PO} + 52.f.v_{EO} + 52.f.v_{D2O}.y_A]$ (9)

(2) $\dfrac{4\pi}{3} (R_B{}^3 - R_A{}^3) = N_{ag}.[52.(1-f).v_{EO} + 52.(1-f).v_{D2O}.y_B]$

$$(3) \quad \left(\frac{b_A}{v_A}\right) = \frac{N_{ag}[40b_{PO} + 52.b_{EO}.f + 52b_{D2O}.f.y_A]}{\frac{4\pi}{3}R_A{}^3}$$

$$(4) \quad \left(\frac{b_B}{v_B}\right) = \frac{N_{ag}[40.b_{EO}.(1-f) + 52.b_{D2O}.(1-f).y_B]}{\frac{4\pi}{3}(R_B{}^3 - R_A{}^3))} \cdot$$

Specific volumes and scattering length densities have been defined for EO, PO and D$_2$O.

These four linear equations can be solved to obtain:

$$y_B = \frac{b_{EO} - v_{EO}\left(\frac{b}{v}\right)_B}{-b_{D2O} + v_{D2O}\left(\frac{b}{v}\right)_B} \qquad (10)$$

$$y_A = \frac{A + Bf}{f}$$

where:

$$A = \frac{[52v_{EO} + 52y_B v_{D2O}]\frac{R_A{}^3}{R_B{}^3 - R_A{}^3} - 40v_{PO}}{52v_{D2O}} \qquad (11)$$

$$B = \frac{[-v_{EO} - y_B v_{D2O}]\frac{R_A{}^3}{R_B{}^3 - R_A{}^3} - v_{EO}}{v_{D2O}}$$

$$f = \frac{E - C}{D - F}$$

And:

$$C = [40v_{PO} + 52.A.v_{D2O}]\left(\frac{b}{v}\right)_A \qquad (12)$$

$$D = [52v_{EO} + 52.B.v_{D2O}]\left(\frac{b}{v}\right)_A$$

$$E = [40b_{PO} + 52.A.b_{D2O}]$$

$$F = [52b_{EO} + 51.B.b_{D2O}]$$

The last parameter is given by:

$$N_{ag} = \frac{\frac{4\pi}{3}R_A{}^3}{40v_{PO} + 52v_{EO}.f + 52v_{D2O}.f.y_A} .$$

We have transformed the four fitting parameters R_A, R_B, $(b/v)_A$ and $(b/v)_B$ into four meaningful parameters N_{ag}, f, y_A and y_B. This set of solutions is unique.

7. RESULTS FOR THE 10 % P85 IN D_2O AT 40 °C

The following results are obtained for the 10 % P85 in D_2O at 40 °C.

Table 1: Scattering lengths and specific volumes for PO, EO and D_2O.

	Density g/cm^3		m_w g/mol	Molar volume cm^3/mol	Scattering Lenghts cm
PO	1.004	C_3H_6O	58	$v_{PO} = 57.77$	$b_{PO} = 3.307 \times 10^{-13}$
EO	1.127	C_2H_4O	44	$v_{EO} = 39.04$	$b_{EO} = 4.139 \times 10^{-13}$
D_2O	1.111	D_2O	20	$v_{D2O} = 18.02$	$b_{D2O} = 19.145 \times 10^{-13}$

Using the table of scattering lengths and specific volumes for the various components, and taking care of expressing everything consistently in units of Å or cm, the following results are obtained.

f = 0.53 (53 % of the EO monomers are in the core).
y_A = 0.39 (there is less than one D_2O molecule per EO monomer in the core).
y_B = 26.44 (there are 26.44 D_2O molecules per EO monomer in the shell).
N_{agg} = 59.80 (there are 59.80 P85 molecules per micelle).

The finding that 53 % of the EO monomers can be found in the micelle core is surprising. Not much D_2O makes it to the core region as expected even with the presence of a fraction of the EO monomers. The micellar shell region is swollen by quite a bit of D_2O as expected. Note that in this simple model we have assumed that the various specific volumes are constant with temperature.

The micelles number density $\left(\dfrac{N}{V}\right)$ (i.e., number of micelles per cm^3) can be obtained from the packing volume fraction ϕ as:

$$\left(\frac{N}{V}\right) = \frac{\phi}{\left(\frac{4\pi}{3}R_B{}^3\right)}. \qquad (13)$$

The estimated P85 volume fraction can be obtained as:

$$\phi_{P85} = \left(\frac{N}{V}\right)N_{agg}.(40.v_{PO}+52.v_{EO}). \qquad (14)$$

In the case considered here, one obtains $\left(\dfrac{N}{V}\right) = 1.53*10^{17}$ cm^{-3} and $\phi_{P85} = 0.066$ which is lower than the real mixing fraction $\phi_{Mix} = 0.1$.

With a rather simple (core-shell) model, one can obtain quite a bit of information from the SANS data. The purpose of this exercise is not to prove that the core-shell model used is correct, but to show an example of the mass balance equations that relates the fitted parameters to more meaningful properties.

solvent region C

shell region B

core region A

In the core:
2,392 PO monomers
1,648 EO monomers
1,213 D$_2$O molecules

In the shell:
1,462 EO monomers
38,642 D$_2$O molecules

$\left(\dfrac{b}{v}\right)_C = 6.400*10^{-6}$

$\left(\dfrac{b}{v}\right)_B = 5.940*10^{-6}$

$\left(\dfrac{b}{v}\right)_A = 7.563*10^{-7}$

$R_A = 43.96$ Å

$R_B = 72.91$ Å
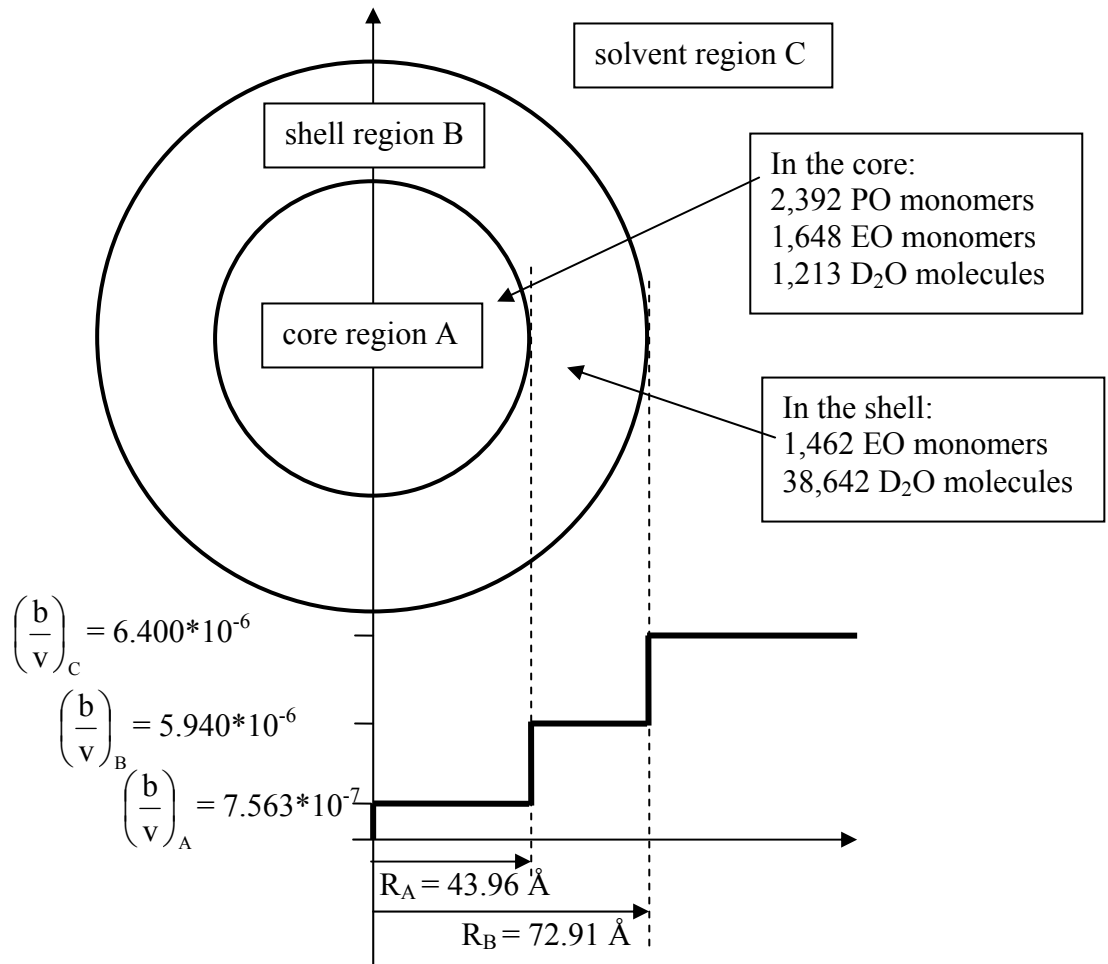
Figure 4: Schematic representation of a micelle with sizes, scattering length densities and contents.

8. POLYDISPERSITY EFFECTS

The polydispersity parameter obtained from the fit to the SANS data for the 10 % P85 sample at 40 $^{\circ}$C was $\sigma_A/R_A = 0.16$, where σ_A is the standard deviation of the core radius size distribution. This distribution was assumed to correspond to the Schulz distribution.

$$f(R) = (z+1)^{z+1} \left(\frac{R}{R_A} \right)^z \frac{\exp\left[-(z+1)\dfrac{R}{R_A} \right]}{R_A \Gamma(z+1)}. \tag{15}$$

R_A is the average value for the peaked distribution and the standard deviation σ_A is related to z as:

$$\frac{\sigma_A}{R_A} = \frac{1}{\sqrt{(z+1)}}. \tag{16}$$

The integration over the Schulz distribution is performed over the macroscopic cross section for the core-shell particle model.

$$\left[\frac{d\Sigma(Q)}{d\Omega} \right]_{polydisperse} = \int_0^\infty dR\, f(R) \left[\frac{d\Sigma(Q)}{d\Omega} \right]_{monodisperse}. \tag{17}$$

This integration can be performed numerically and is available analytically. Due to the lengthy expression, the analytical form is not reproduced here.

10% P85 Pluronic in D$_2$O at 40 ^{o}C
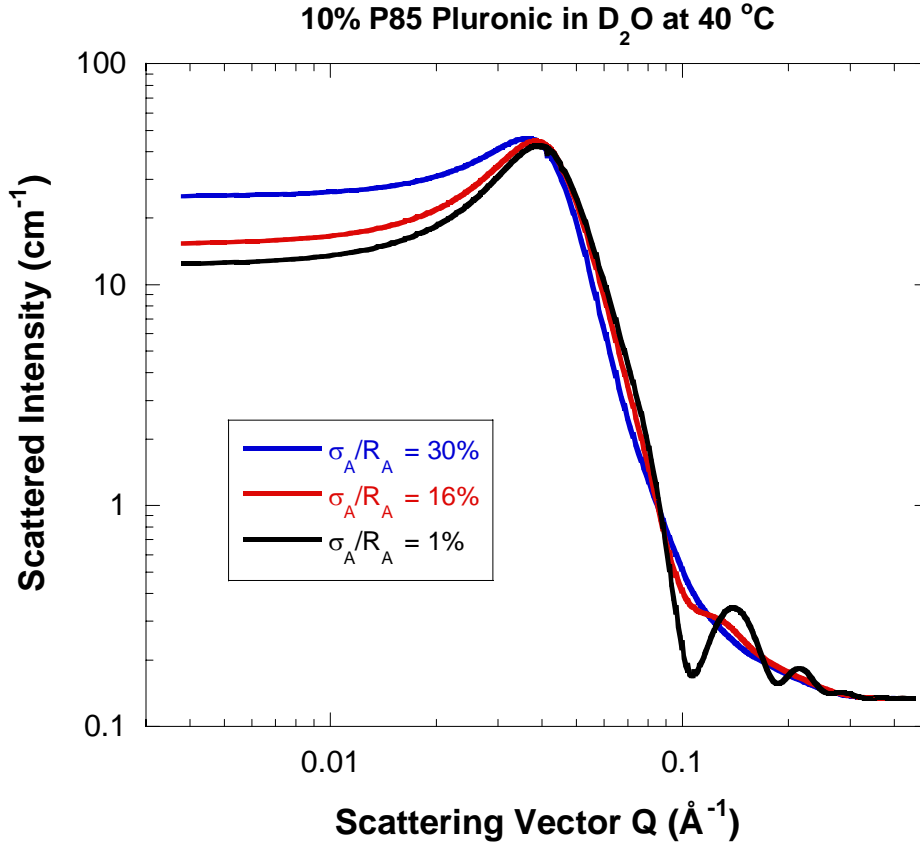
Figure 5: Simulated data corresponding to parameters for the 10 % P85 sample at 40 ^{o}C. The polydispersity parameter has been varied to see its effect. All other parameters were kept the same. The effect of polydispersity is seen to broaden peaked features.

Note that the particle core volume averaged over the polydisperse size distribution is given by:

$$V_A = \frac{4\pi}{3}\langle R^3 \rangle = \frac{4\pi}{3} R_A{}^3 \frac{(z+2)(z+3)}{(z+1)^2}$$

In practice the average volume ($4\pi R_A{}^3/3$) is often used for low polydispersity.

9. TEMPERATURE EFFECTS

SANS data were taken from the 10 % P85 in D$_2$O at various temperatures going from the partly dissolved copolymer phase at 20 ^{o}C to the fully formed micelles at temperatures of 30°C and above. The above described model was applied to the SANS data for 40 ^{o}C, 44 ^{o}C, 50 ^{o}C, 55 ^{o}C, and 60 ^{o}C. For simplicity, the specific molar volumes were assumed to be independent of temperature. The results are presented in a series of figures.

When temperature is increased both R_A and R_B increase while the micelle packing volume fraction decreases. This is due to the fact that the aggregation number increases because the driving force for micelle formation gets stronger. As this happens, D_2O gets squeezed out of the shell region. As temperature increases, the micelles packing volume fraction decreases because there are fewer larger micelles.

10% P85 Pluronic in D_2O
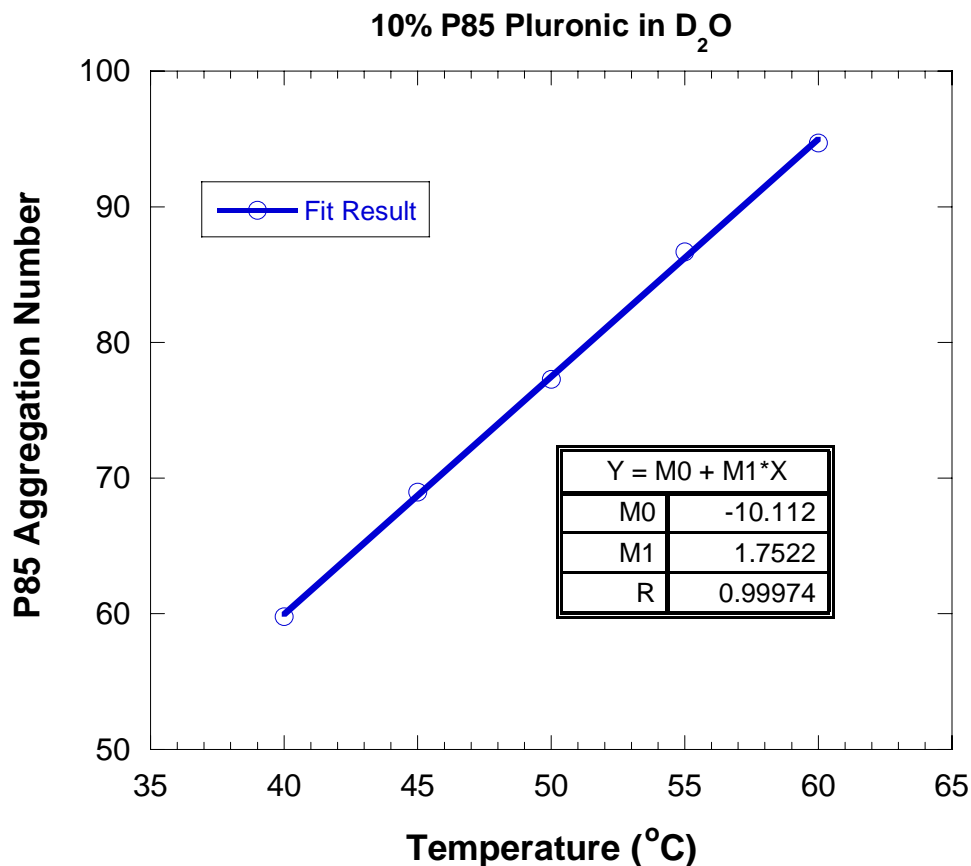
Figure 6: Variation of the aggregation number with temperature.
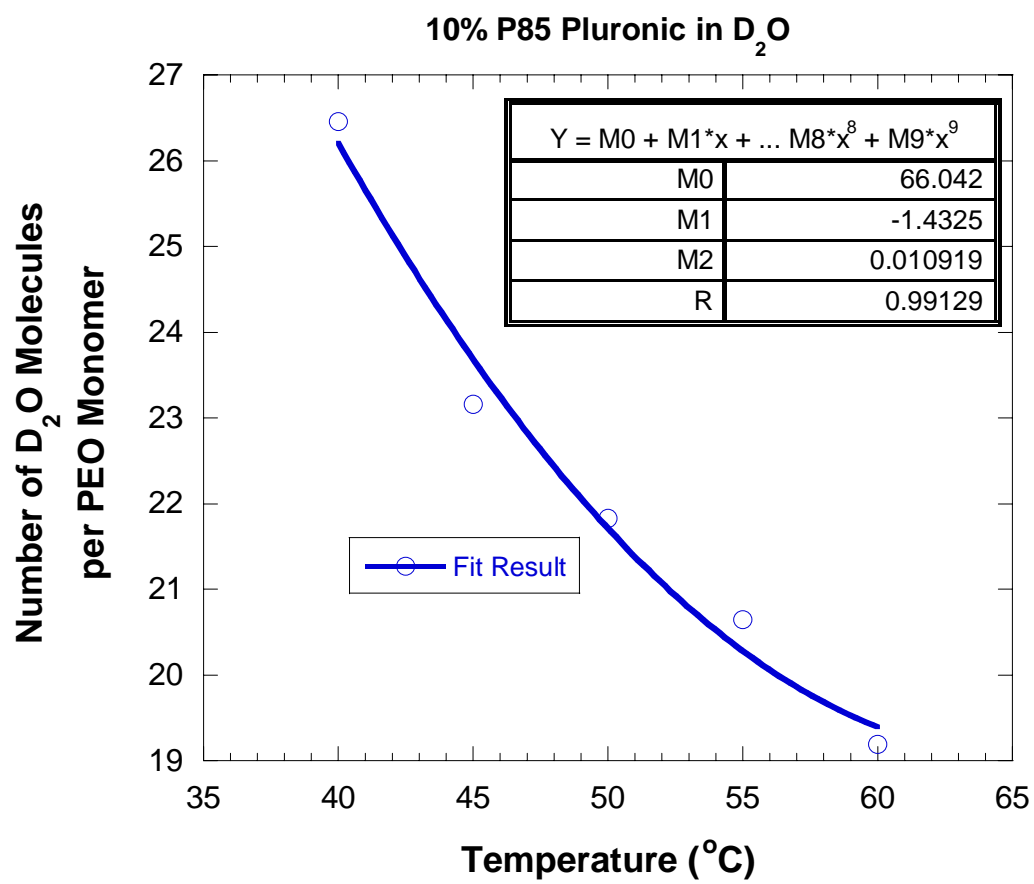
Figure 7: Variation of the number of D_2O molecules per EO monomer in the shell region with increasing temperature.

10% P85 Pluronic in D_2O

$Y = M0 + M1 \cdot x + \dots M8 \cdot x^8 + M9 \cdot x^9$	
M0	2.9167e+17
M1	-4.2162e+15
M2	1.8671e+13
R	0.99923
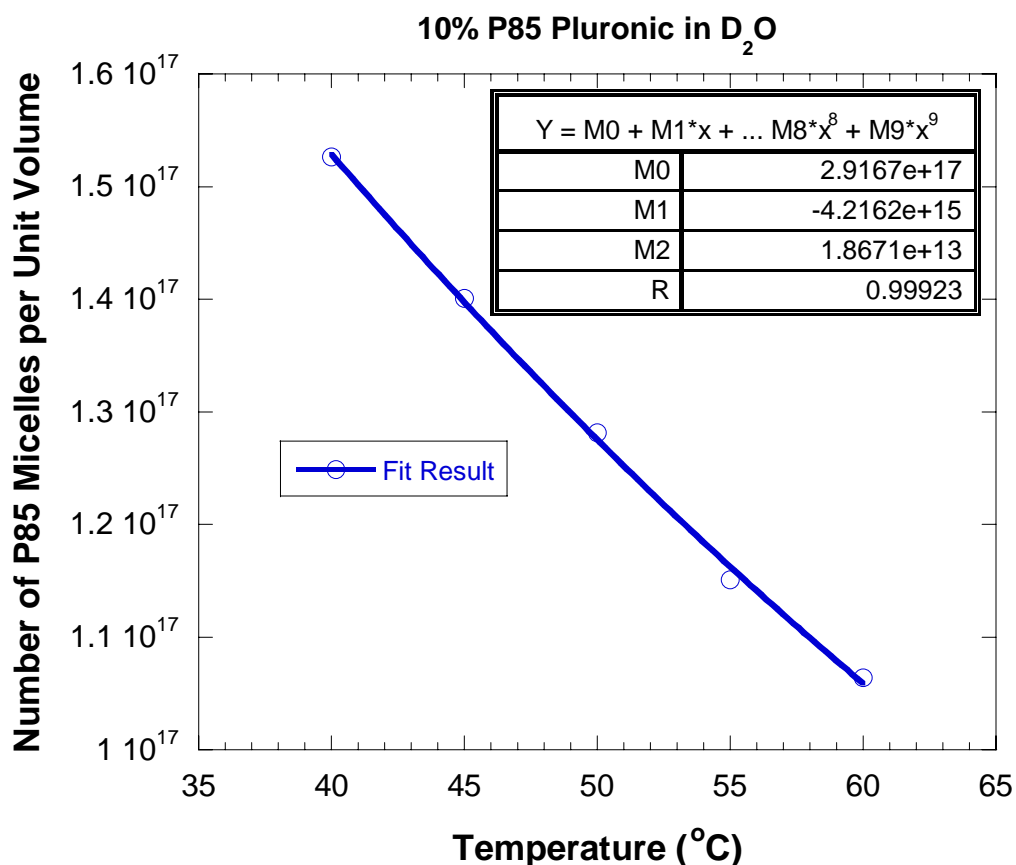
Figure 8: Variation of the micelles number density with temperature.

10. DISCUSSION

P85 is a typical nonionic micellar system comprising hydrophilic EO blocks and hydrophobic PO blocks. SANS data from P85 micelles were fitted to a core-shell model in order to obtain core sizes and shell thicknesses, scattering length densities of these two regions, fitted volume fractions and core polydispersity characteristics. Using a materials balance equation, useful information such as the fraction of EO blocks in the core, the aggregation number, and the number of D_2O molecules per EO monomer in the two regions. The purpose of this last exercise was not to prove the correctness of the core-shell model but to show how useful material balance equations could be.

REFERENCES

T. Slawecki, C. Glinka and B. Hammouda, "Shear-Induced Micellar Crystal Structures in an Aqueous Triblock Copolymer Solution", Phys Rev E 58, R4084-4086 (1998).

S. Kline and B. Hammouda "Free Chains and Micelles of a Triblock Copolymer in Water", NCNR Summer School (2004).

QUESTIONS

1. Do Pluronics form ionic or nonionic micelles?
2. What is the CMC? How about the CMT?
3. Are micelles always spherical?
4. What is the Percus-Yevick approximation?

ANSWERS

1. Pluronics are not charged. They form nonionic micelles.
2. The CMC is the Critical Micelles (formation) Concentration. The CMT is the Critical Micelles (formation) Temperature. These are conditions at which micelles form.
3. No, micelles are not necessarily spherical. Micelles come in many shapes including elongated wormlike micelles.
4. The Percus-Yevick approximation is a closure relation that allows the analytical solution of the Ornstein-Zernike equation for hard sphere interaction potential.

Ionic micelles use surfactants with charged head groups. When mixed with hydrophilic and hydrophobic molecules, these self-assemble into micelles of various shapes. Micelles form in order to screen the hydrophobic groups and avoid their contact with water. Coulomb interactions help in micelle formation. A system that forms rodlike ionic micelles is described here.

1. AN IONIC RODLIKE MICELLES SYSTEM

Consider the following ionic micellar system: cationic surfactant cetyltrimethyl ammonium 4-vinylbenzoate (CTVB) in aqueous (d-water) solution (Kline, 1999; Kim et al, 2006). These form rodlike micelles. Free radical polymerization is performed on the VB groups in order to obtain polymerized micelles. After polymerization, negative charges (VB⁻) are on the outer surface and positive charges (CTA⁺) are on the inner surface of the rodlike polymerized micelles.

- VB⁻

- CTA⁺ $CH_3(CH_2)_{15}N^+(CH_3)_3$
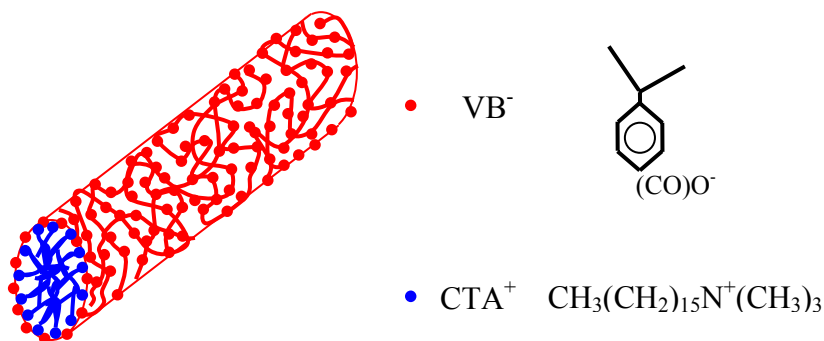
Figure 1: Schematic representation of the CTVB polymerized rodlike micelle.

A set of four CTVB/d-water samples were prepared varying the micelles fraction. These correspond to 0.25 %, 0.5 %, 1 % and 1.9 % CTVB mass fractions. SANS measurements were made at 25 °C. As the mass fraction increases, a peak is seen to develop.
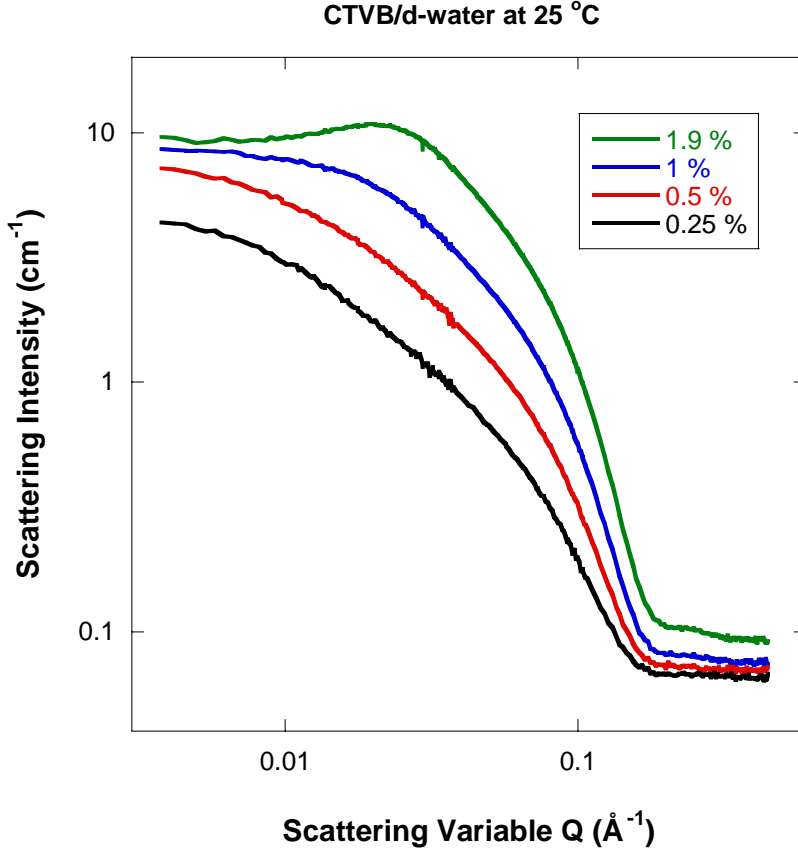
CTVB/d-water at 25 °C

Figure 2: SANS data from CTVB/d-water for increasing concentration.

2. SCATTERING MODEL

A scattering model consisting of a solution of interacting rodlike particles is used to fit the SANS data. The scattering cross section is given by:

$$\frac{d\Sigma(Q)}{d\Omega} = \Delta\rho^2 \phi V_P P(Q) S_I(Q) + B . \qquad (1)$$

Here $\Delta\rho^2$ is the contrast factor, ϕ is the particles volume fraction, V_P is the particle volume and B is a constant used to represent the Q-independent (mostly incoherent scattering) background.

The form factor for a cylinder is given by the following orientational average:

$$P(Q) = \frac{1}{2} \int_{-1}^{1} d\mu \, | F(Q,\mu) |^2 . \qquad (2)$$

$$F(Q,\mu) = \left[\frac{\sin(Q\mu L/2)}{Q\mu L/2}\right]\left[\frac{2J_1(Q\sqrt{1-\mu^2}R)}{Q\sqrt{1-\mu^2}R}\right]. \tag{3}$$

μ represents the rod orientation with respect to the scattering vector direction. R is the cylinder radius and L is its length. J_1 is the cylindrical Bessel function.

The structure factor for a solution of charged particles is obtained from the Ornstein-Zernike (OZ) equation solved with the Mean Spherical Approximation (MSA) closure relation. The MSA approach was used to account for the Coulomb interactions. Note that that MSA solution was originally introduced for spherical particles. Since there is no simple analytical approach that can model the structure factor for rodlike particles, the MSA is used here for lack of a better model. The structure factor is given by:

$$S_I(Q) = \frac{1}{1-\overline{NC}(K)} \tag{4}$$

$$\frac{\overline{NC}(K)}{24\phi} = \frac{A(\sin(K)-K\cos(K))}{K^3} + \frac{B\left[\left(\frac{2}{K^2}-1\right)K\cos(K)+2\sin(K)-\frac{2}{K}\right]}{K^3}$$

$$+ \frac{\phi A\left[\frac{24}{K^3}+4\left(1-\frac{6}{K^2}\right)\sin(K)-\left(1-\frac{12}{K^2}+\frac{24}{K^4}\right)K\cos(K)\right]}{2K^3}$$

$$+ \frac{C(k\cosh(k)\sin(K)-K\sinh(k)\cos(K))}{K(K^2+k^2)}$$

$$+ \frac{F[k\sinh(k)\sin(K)-K(\cosh(k)\cos(K)-1)]}{K(K^2+k^2)}$$

$$+ \frac{F(\cos(K)-1)}{K^2} - \frac{\gamma\exp(-k)(k\sin(K)+K\cos(K))}{K(K^2+k^2)}.$$

Here K = QD is the reduced scattering variable and D is the rodlike micelle diameter.

Note that it is difficult to model overlapping rods since these could form liquid crystalline (such as nematic or smectic) phases. Only the isotropic phase (obtained for a low concentration of rods) can be modeled by the MSA approach.

Isotropic Phase	Nematic Phase	Smectic Phase
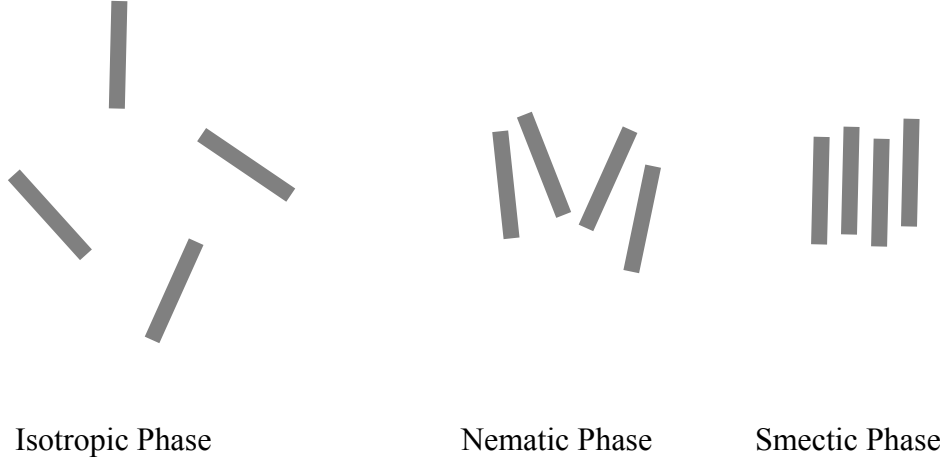
Figure 3: Schematic representation of the main liquid crystal phases for rodlike particles. These are the isotropic, nematic and smectic phases obtained when the rodlike particle concentration increases.

3. FITS OF THE SANS DATA

Fits of the model to the SANS data are performed. Results for the 1 % mass fraction sample are included here. The contrast factor for the CTVB/d-water mixture was fixed as well as the dielectric constant ε and the sample temperature T.

$$\Delta\rho = \rho_{d\text{-water}} - \rho_{CTVB} = 6.39*10^{-6} - 0.35*10^{-6} = 6.04*10^{-6} \text{ Å}^{-2} \quad (5)$$
$$\varepsilon = 77.94$$
$$T = 298 \text{ K}.$$

The remaining fitting parameters were varied and found to be:

$$\phi = 0.01 \qquad\qquad\qquad\qquad\qquad (6)$$
$$R = 20.9 \text{ Å}$$
$$L = 184 \text{ Å}$$
$$z_m = 0.06$$
$$B = 0.074 \text{ cm}^{-1}.$$

In order to appreciate the contributions from the form factor and the structure factor terms, SANS data are compared to the results of the model fits in the dilute limit (i.e., when $S_I(Q)=1$). The structure factor $S_I(Q)$ is also plotted. The effect of inter-particle interactions is small but finite.
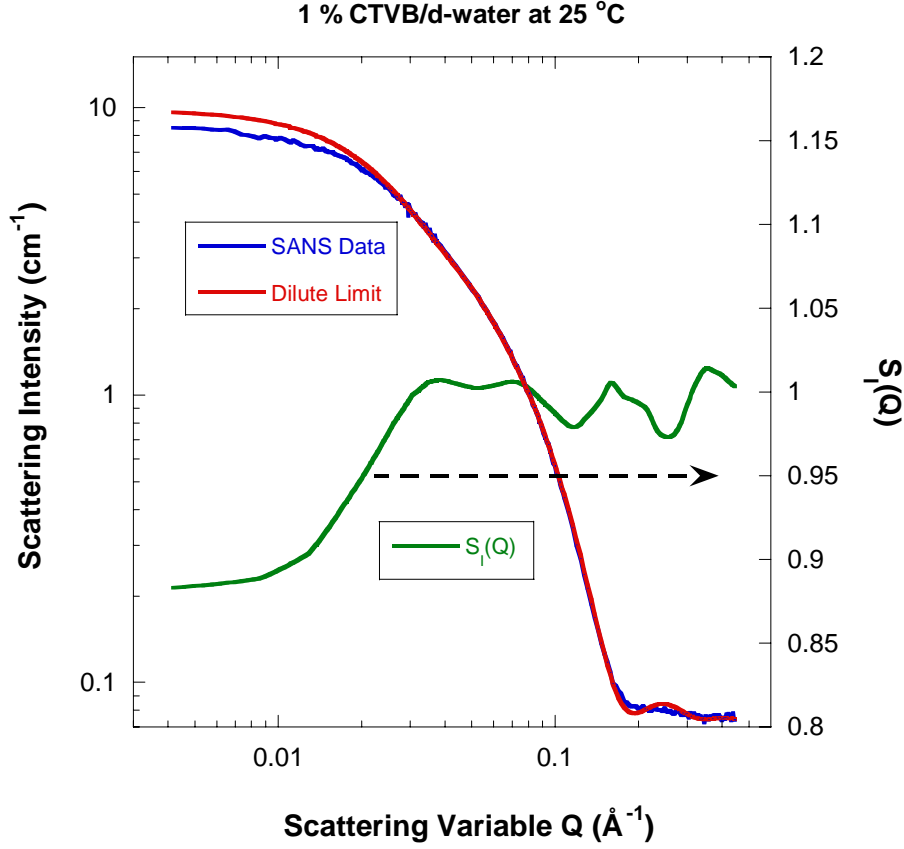
Figure 4: Comparison of the SANS data to the model fit in the dilute limit. The structure factor $S_I(Q)$ is also plotted.

The apparent radius of gyration for the rodlike cylinders of radius R and length L is calculated using:

$$R_g = \sqrt{\frac{R^2}{2} + \frac{L^2}{12}} \ . \tag{7}$$

Results are plotted for increasing CTVB mass fraction. A polynomial fit is performed and yields:

$$\left(R_g\right)_{app} = \left(R_g\right)_0 - m_1\phi + m^2\phi^2 + \tag{8}$$

This is sometime referred as a "virial expansion". The "real" radius of gyration is obtained at the infinite dilution limit as:

$$\left(R_g\right)_0 = 124 \ \text{Å} \ . \tag{9}$$

Note that the first dominant correction term in the expansion is negative. In the infinite dilution (subscript ID) limit, P(Q) decreases (and therefore R_g also decreases) with micelles fraction.

$$\frac{\left(\dfrac{d\Sigma(Q)}{d\Omega}\right)_{ID} - B}{\phi} = \Delta\rho^2 V_P P(Q) . \tag{10}$$
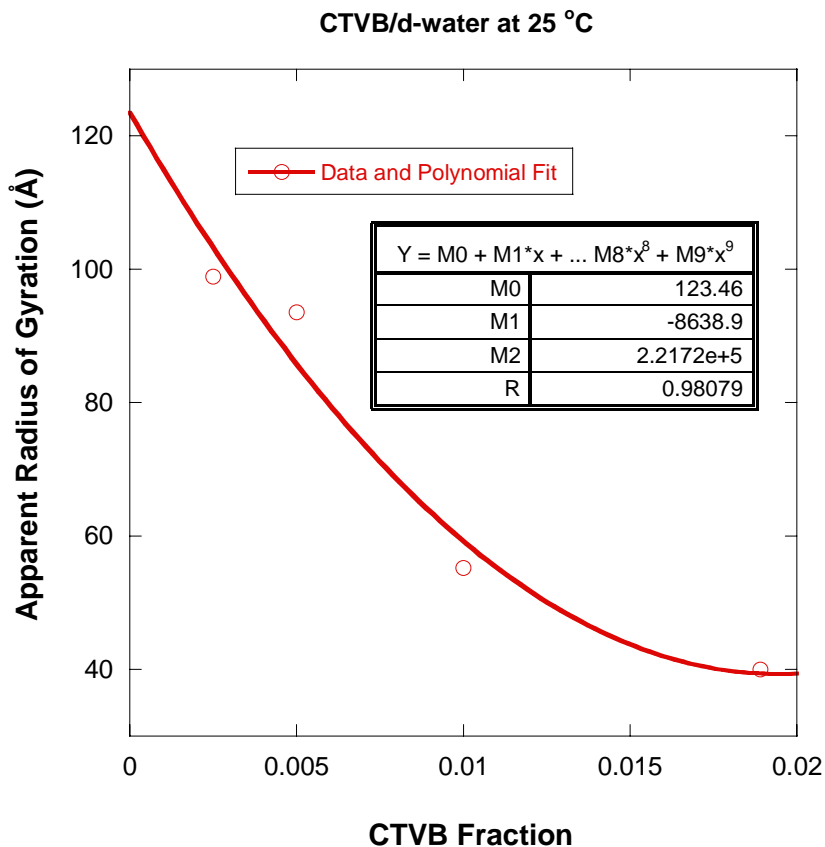
CTVB/d-water at 25 ^{o}C

Figure 5: Variation of the apparent radius of gyration for increasing CTVB fraction.

Temperature was varied for the 1 % CTVB/d-water sample. Rodlike particle dimensions (R and L) were obtained from the fits. Since the micelles are polymerized, there is very weak (to non-existent) temperature dependence of the radius R but noticeable temperature dependence of the rod length L.

1 % CTVB/d-water
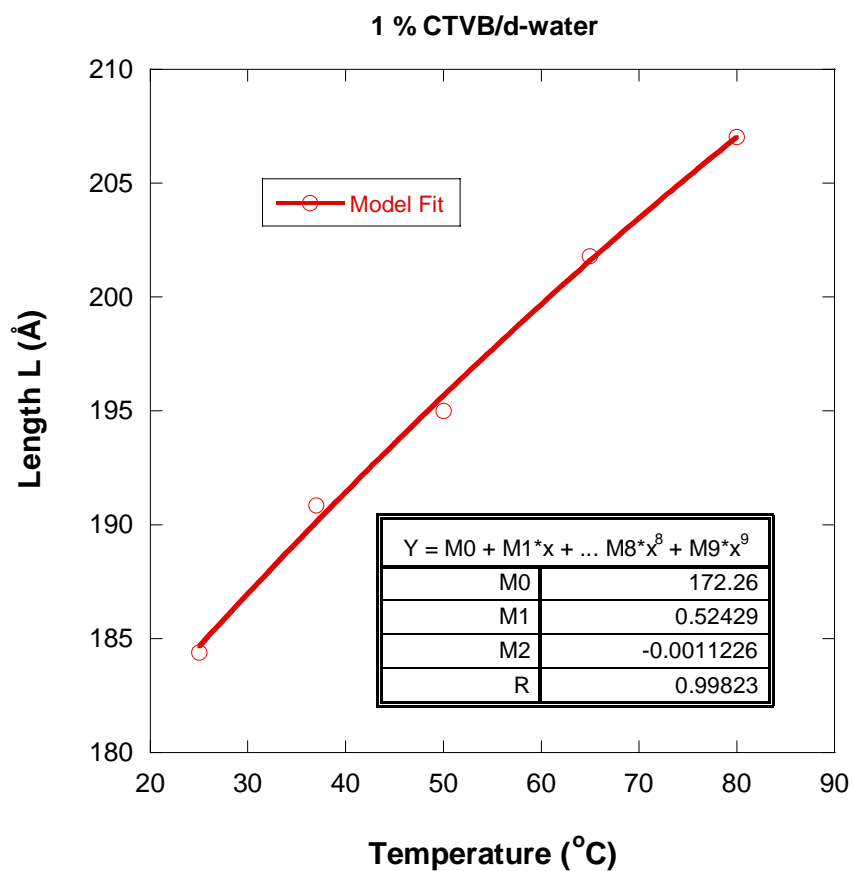
Figure 6: Temperature dependence of the rodlike particles length for increasing sample temperature.

In order to perform the fits to the SANS data when sample temperature was varied, temperature dependence of the dielectric constant for d-water was required. ε is seen to decrease with temperature as tabulated (CRC Handbook, 1984).

Y = M0 + M1*x + ... M8*x^8 + M9*x^9	
M0	87.679
M1	-0.4249
M2	0.0013677
M3	-3.6439e-6
R	0.99993
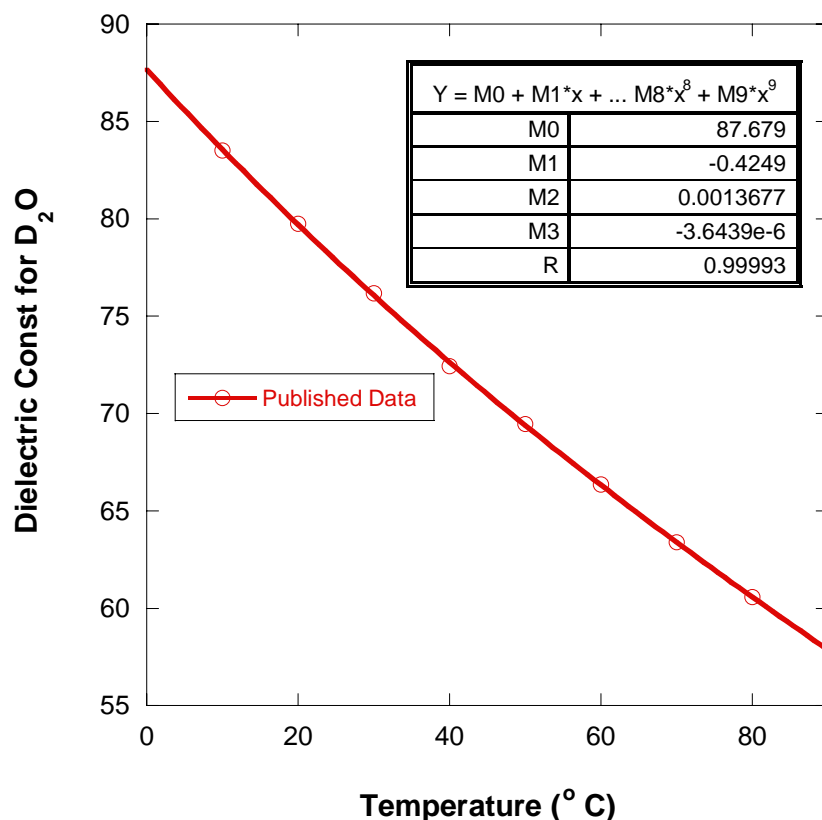
Figure 7: Temperature dependence of the dielectric constant for d-water.

4. DISCUSSION

SANS data from the CTVB/d-water ionic polymerized micelle system is characterized by varying features when the CTVB fraction increases. For low volume fractions, the MSA model developed for particulate systems with Coulomb interactions applies. A model consisting of the form factor for rodlike particles and the MSA structure factor was used to fit the SANS data. Fit results included rod dimensions (rod radius and length) in each case along with the macroion charge. This charge was found to be very small pointing to almost neutral rodlike particles.

REFERENCES

R.C. Weast, Editor-in-Chief, "CRC Handbook of Chemistry and Physics", 65th Edition, Page E57 (1884).

S.R. Kline, "Polymerization of Rodlike Micelles", Langmuir 15, 1726-1732 (1999)

T-H Kim, S-M Choi and S.R. Kline, "Polymerized Rodlike Nanoparticles with Controlled Surface Charge Density", Langmuir 22, 2844-2850, (2006)

QUESTIONS

1. What is the form factor for an infinitely thin rod of length L?
2. Name two possible closure relations used to solve the Ornstein-Zernike equation for particulate systems?
3. What is Debye-Huckel screening length? Define it for a neutral solution of macroions of charge $z_m e$ and electrons.
4. What is the CMC?
5. What is the radius of gyration for a cylindrical rod of radius R and length L?

ANSWERS

1. The form factor for an infinitely thin rod of length L is given by:

$$P(Q) = \frac{1}{2} \int_{-1}^{1} d\mu \left[\frac{\sin(Q\mu L / 2)}{Q\mu L / 2} \right]^2 .$$

2. Two possible closure relations used to solve the Ornstein-Zernike equation for particulate systems are: the Percus-Yevick and the Mean Spherical Approximation.
3. The Debye-Huckel screening length is the distance beyond which Coulomb interactions die out (are screened). The Debye-Huckel screening parameter (inverse length) is given by:

$$\kappa^2 = \frac{e^2}{k_B T} z_m \overline{N}$$ where e is the electron charge, $z_m e$ is the macroion charge, $\overline{N}$ is the

macroion number density (number per unit volume) and $k_B T$ is the sample temperature in absolute units.
4. The Critical Micelle Concentration (CMC) is the surfactant concentration for which micelles form.
5. The radius of gyration for a cylindrical rod of radius R and length L is given by:

$$R_g = \sqrt{\frac{R^2}{2} + \frac{L^2}{12}} .$$

Chapter 46 - **SANS FROM COMPLEX FLUIDS LITERATURE REVIEW**

The published literature on SANS from Complex Fluids is reviewed here. Focus will be on papers published over the past seven years and resulting from use of the NIST Center for Neutron Research SANS instruments. Some 151 papers have been reviewed. About one third are included here. If you find this chapter difficult to read, just imagine how painful it must have been to write. Readers have the option of skipping this chapter altogether.

1. TEMPLATING AND AGGREGATION

Self-organized systems can serve as templates for the structure-directed synthesis of organic compounds (for example polymerization). Depending on the template structure and the reaction conditions, the output product may be nanoparticles of various structures, shapes, sizes and interaction environments. There is a delicate balance between the reaction kinetics, phase behavior thermodynamics and mass transfer parameters (Hentze, 2003, Paper 053).

Early stages of glacial clustering in supercooled triphenyl phosphate were observed in the temperature range of 210 K to 214 K. The stages correspond to cluster formation, rapid nucleation, agglomeration and saturation. SANS was used to obtain particle sizes, volume fractions and polydispersity. Competition between increase in cluster size and increase in cluster number density was deduced (Schwickert et al, 2001, Paper 148).

A self-assembled organogel of aluminum isopropoxide and didodecyl phosphate surfactant in decane was investigated by SANS; cylindrical wormlike micelles were observed. Rheology confirmed the formation of a connected network with physical gel behavior. At large excess of aluminum, phase separation into a gel was observed along with a non-viscoelastic liquid (Page, 2004, Paper 305).

MD simulation and SANS were used to characterize aggregation in guanidinium carbonate solutions due to ion pairing. A molecular-level explanation for the contrasting denaturant properties of guanidinium salts in solution was presented (Mason, 2006, Paper 523).

2. ASPHALTENE

Structure and phase behavior of blends of asphaltenes in naturally occurring oils have been investigated using the SANS technique. The natural neutron contrast stems from the hydrogen-poor asphaltene in a "sea" of hydrogen-rich oil. When two compatible oils are blended together, the asphaltenes remain dispersed as colloidal nanoparticles; whereas when two incompatible oils are blended, the asphaltene nanoparticles aggregate to form micron size structures. Nanoparticle sizes and concentrations were obtained. This helps directly assess the compatibility of crude oils and diagnose refinery fouling problems (Mason-Lin, 2003, Paper 107).

Asphaltenes from different crude oils were fractionated in heptane/toluene solvent mixtures and subjected to chemical analysis, vapor osmometry and SANS. It was found that a

particular fraction with strong polar and hydrogen-bonding characteristics showed strong cooperative interactions (aggregation). Individual aggregates were also seen to flocculate. The addition of resin to asphaltene reduced the aggregate size by disrupting the π-π polar bonding interactions (Spiecker et al, 2003, Paper 156).

3. CLAY DISPERSIONS

SANS was used to characterize the dispersion of montmorillonite clay in toluene (plus a cation agent referred to as ditallow). The cluster sizes, the amount of ditallow adsorbed on montmorillonite platelets, and estimation of the adsorbed layer thickness were estimated (Hanley et al, 2003, Paper 043).

Using Hansen's solubility parameters, the correlation between the degree of exfoliation of organically modified clays and the solvent used has been analyzed. It was found that the dispersion component is the principal driving interaction for clay solubility. Organically modified clays were found to precipitate in solvents with hydrogen-bonding groups. This helped correctly identify trichloroethylene as a suitable solvent that completely exfoliates the organically modified montmorillonite clay (Ho-Glinka, 2003, Paper 056).

Surface tension, contact angle and SANS measurements were performed on a surfactant adsorbed on a clay surface. Aggregate formation appears at specific surfactant concentration and temperature. This is reminiscent to the critical micelle concentration and critical micelle temperature. Aggregation numbers were estimated (Cipriano et al, 2005, Paper 420).

4. COLLOIDAL SUSPENSIONS

SANS has been used to investigate gelatin/SDS complexes formed at the polystyrene latex sphere/water interface. SDS micelles act as buffer between the hydrophilic gelatin and the hydrophobic polystyrene. The adsorbed amount of gelatin peaks when there is one SDS micelle per gelatin chain. At high SDS concentration, gelatin takes the form of the SDS micelles (Marshall et al, 2002. Paper 103).

Shear thickening of colloidal dispersions was investigated by SANS with in-situ applied shear. The onset of shear thickening was found to scale inversely with colloidal particle volume. Quantitative comparisons of the low-shear viscosity and critical stress for shear thickening to the hard-sphere theory were made (Maranzano-Wagner, 2002, Paper 238).

SAXS and SANS have been employed to investigate structural characteristics of spherical colloid particles mixed with non-adsorbing polymers in solution. Measured inter-particle structure factors were obtained and compared to the reference interaction site theory. Agreement is obtained until the gel phase forms at high concentration. The following conclusion was reached: neither long wavelength fluctuations nor local cage structure can be the main process for gelation (Shah et al, 2003, Paper 263).

Near-surface SANS (NS-SANS) and neutron reflectometry (NR) were used to investigate the ordering of CTAB micelles in water solutions in the proximity of the shear cell wall as a function of concentration and temperature. These two techniques complement each other with higher resolution for NR and wider application of NS-SANS which can apply to thick layers as well as to the bulk (Hamilton, 2005, Paper 396).

SANS and USANS have been used to investigate an unstable emulsion of saturated ammonium nitrate in hexadecane and stabilized by a Pluronics surfactant. The water-oil droplet interfaces are coated with surfactant but a small amount of surfactant tends to aggregate into micron-size droplets with no oil phase inside (Zank et al, 2006, Paper 430).

Thermally reversible organogels were studied by IR, NMR, optical microscopy, X-ray diffraction, rheology, light scattering and SANS. Gelation is induced isothermally. In-situ polymerization forms self-assembled fibrillar networks that encapsulate and immobilize the organic liquid component. Gelator efficiencies have been determined. When heated, these gels revert to sols over wide temperature ranges (George et al, 2006, Paper 536).

5. GELS

Hydrogels are of biological interest and significance. They are formed when crosslinking occurs in macromolecular systems. For example, beta hairpin peptides tend to self-assemble into strands that form hydrogels. Hydrophobic collapse drives the self-assembly. Depending on the peptide used (various sequences for the two amino acids used), different network structures are obtained. Circular Dichroism (CD), IR spectroscopy, Cryo-TEM and SANS are used to characterize the gel structures (Schneider et al, 2002, Paper 262).

SANS studies have been conducted on dispersions of temperature-sensitive microgel particles. These are formed with crosslinked the NIPAM water-soluble polymer. The microgel particles are seen to contract at 32 $^\circ$C. A form factor characteristic of solid polymer nanospheres was observed (Mason, 2005, Paper 374).

SANS and osmotic swelling pressure measurements were performed on polyelectrolyte gels under physiological conditions. A few synthetic and biopolymers were compared and found to have similar gel-like structure leading to the conclusion that molecular architecture (for example the persistence length) is a weak factor in the gel self-assembly (Horkay et al, 2006, Paper 560).

6. MESOPHASES

A mixture of cationic (DDAB) and nonionic (C_8E_3) surfactants form efficient bicontinuous structures. Increase in DDAB causes the tightening of these elastic membrane structures as a result of electrostatic stiffening. SANS data for bicontinuous structures is characterized by a weak second order peak. The Teubner-Strey model was used to obtain a correlation length and a domain d-spacing (Silas-Kaler, 2001, Paper 150).

A microstructural transition from columar hexagonal to lamellar has been observed by SANS in solutions of AOT, lecithin and isooctane in water. Dramatic increase in viscosity and the formation of a rigid gel (lamellar morphology) occur when water content is increased (Simmons et al, 2002, Paper 153).

Shear-induced orientation of a rigid surfactant mesophase was investigated using the in-situ Couette shear cell. Shear helped sort out the columnar hexagonal microstructure at ambient temperature. The first couple of reflections were indexed and found to follow the cylindrical orientation (Singh et al, 2004, Paper 286).

Magnetic fluids comprising dispersed magnetite nanoparticles were investigated by SANS, SALS, DLS and Cryo-TEM. Fits of the SANS data to a core-shell model yielded the iron oxide core size and the surfactant shell. The magnetic colloidal particles form mass fractal structures as well (Shen et al, 2001, Paper 242).

Phospholipid unilamellar vesicles form discotic micelles at low temperature and extended lamellar morphology upon heating above a critical temperature. The discotic phase is formed of ellipsoidal shape vesicles filled with water (Nieh et al, 2005, Paper 413).

7. MICELLES

DLS and SANS were used to investigate vesicle microstructures formed in aqueous SDS solution where the photosensitive surfactant BTHA (trans isomer) was added. BTHA is located at the vesicle interface. Illumination with UV changes the BTHA isomeric state to the cis isomer thereby driving the reorganization of the vesicles into a cylindrical phase. This structural transition was found to be reversible (Hubbard et al, 2005, Paper 379).

SANS and Cryo-TEM have been used to determine the structure of aggregates formed by a photoresponsive surfactant. Under UV illumination condition, a phase transition is observed from unilamellar and bilamellar phase, then to a bicontinuous phase. This transition is driven by change in rigidity as a result of photoisomerization (trans to cis) (Shang et al, 2006, Paper 482).

Dimeric polyoxyethylene) (so-called gemini) surfactants form spherical micelles with long ethoxylated chain lengths and cylindrical micelles with short ones. These systems exhibit conventional cloud point behavior along with a sphere-to-cylinder transition at high temperature (FitzGerald et al, 2005, Paper 409).

8. MICROEMULSIONS

Sodium taurocholate (NaTC) bile salt cosurfactants modify the interfacial properties and aggregate size of AOT reversed micelles. At low concentration, NaTC monomers are randomly dispersed among AOT molecules. When the NaTC concentration is increased, it forms hydrogen-bonded dimers and becomes therefore a more effective cosurfactant (Freeman et al, 2001, Paper 027).

SDS micelles growth through the addition of a cationic salt (PTHC) was investigated by SANS. A generalized indirect Fourier transform method and fits to the rescaled mean spherical approximation (MSA) along with a Yukawa potential were performed; ellipsoidal form factors and inter-particle structure factors were obtained (Hassan et al, 2003, Paper 045).

The lamellar L_α sponge phase has been investigated in cetylpyridinium-hexanol/dextrose-brine system using the in-situ shear cell and time-resolved SANS. Structural relaxation times of order of seconds have been observed (Porcar et al, 2004, Paper 343).

Diblock copolymers of polystyrene (PS) and imidazolium-functionalized PS (IL) assemble into elongated micelles in toluene. The PS block forming the micellar shell exhibits a star-like or brush-like conformation upon the IL block used to form the micellar core. It was found that any added water can be sequestered in the core (Stancik et al, 2004, Paper 358).

EO_6BO_{11} (ethylene oxide-b-butylene oxide) diblock copolymers form vesicular structures that are predominantly unilamellar at low polymer concentration and become multilamellar at high copolymer concentrations or high temperature. The vesicles ultimately fuse into lamellar sheets (Norman et al, 2006, Paper 450).

9. NANOSTRUCTURES

Dense clusters form during cluster formation and gelation of attractive slippery nanoemulsion droplets. Time-resolved SANS was used to monitor the formation of dense clusters of droplets which then become dense rigid gel networks. The slippery attraction is turned on through a temperature quench. Universal long time behavior was observed independent of droplet volume fraction (Wilking et al, 2006, Paper 461).

The spatial distribution of components within an aerosol droplet was investigated by SANS. For water/n-butanol droplets, a core containing mostly water and a densely packed shell containing mostly butanol were observed (Wyslouzil et al, 2006, Paper 480).

The multilayered structures of poly(ethylene oxide)/montmorillonite clay nanocomposite films made from solution were investigated. Shear orientation of the polymer/clay network in solution followed by solvent evaporation lead to multilayered structures. Polymer chains were seen to bridge between clay domains as well as wrap around them (Stefanescu et al, 2006, Paper 494).

10. PLURONICS

The glass transition was investigated for copolymer micellar systems with a short-range attractive interparticle interaction. Two types of glass transitions were observed at different temperatures. The transition line between these two regions stops at an end point as predicted by mode-coupling theory (Chen et al, 2003, Paper 014).

The effects of oil solutes and alcohol cosolvents on the structure of oil-in-water microemulsions stabilized by PEO-PPO-PEO pluronics copolymers have been investigated. It was found that without pluronics addition, the addition of ethanol cosolvent decreased the micelles volume fraction whereas with the addition of pluronics, the addition of ethanol had the opposite effect (Lettow et al, 2005, Paper 393).

The structure of solutions of silica particles in highly ordered pluronics domains under in-situ shear have been investigated using SANS. The contrast variation method was used to investigate the structure of the nanoparticles when the pluronics template was made "invisible" through deuteration. The addition of silica particles was found to provoke an ordering transition for the pluronics spheres (Pozzo-Walker, 2007, Paper 544).

11. PRESSURE EFFECTS

Pressure induces the freezing of the hydrophobic core thereby leading to a phase transition for $C_{12}E_5$ micelles in D_2O from thread-like micelles to hexagonally ordered bundles of cylindrical micelles. The freezing up of the micellar hydrophobic core forms an amorphous solid (Bossev et al, 2001, Paper 008).

The effect of in-situ pressure on C_8E_5 Micelles in D_2O has been investigated. Pronounced decrease of the micelle radius of gyration and forward scattering intensity was observed over a wide pressure range. The effect of pressure is seen to induce a dehydratation of the surfactant headgroups (Lesemann et al, 2003, Paper 089).

12. SHEAR EFFECTS

Ordering of a surfactant membrane sponge phase has been investigated at the solid-liquid interface using neutron reflectometry and near surface (NS) SANS in the reflection geometry. NS-SANS measurements were found to agree with conventional bulk SANS measurements indicating that the skin layer close to the surface does not constitute an inherently 2D phase. Layering periodicity observed close to the surface corresponds to the same sponge phase structure observed in the bulk (Hamilton et al, 2002, Paper 247).

Shear thickening has been observed in a nanoparticle dispersion at high Couette shear rates. Micromechanical models that relate the sample parameters to the rheological response have been compared and found to agree with the observed reversible shear thickening transition (Lee-Wagner, 2006, Paper 530).

Phase separation in wormlike micelles has been investigated in an-situ shear cell for which the neutron beam is along the neutral (also called vorticity) direction. This shear cell probes the velocity-velocity gradient shear plane. Shear-induced microphase separation and shear banding were observed (Liberatore et al, 2006, Paper 495

13. WORMLIKE MICELLES

Highly viscoelastic wormlike micelles have been investigated by rheology, Cryo-TEM and SANS. The effects of surfactant concentration, added salt and temperature have been studied. The Kratky-Porod model for wormlike chains was used to fit the SANS data; a reasonable radius of gyration was obtained. Cryo-TEM images revealed structural changes upon salt addition (Croce et al, 2003, Paper 021).

The self-assembly of sodium oleate in the presence of both a binding salt and a simple salt has been investigated by SANS, rheology and cloud point measurements. Both forms of salt promote the growth of long wormlike micelles thereby increasing the viscosity. Cloud point measurements showed phase separation upon heating. Salt addition lowered the cloud point temperature (Kalur-Raghavan, 2005, Paper 410).

SANS was used to investigate cationic micellar solutions as a function of concentration and salt addition. Semiflexible chain models incorporationg excluded volume effects were used to analyze the data. The addition of an intermicellar interaction term was used. Influence of the headgroups and ionic strength on the contour length and micellar flexibility was shown (Chen et al, 2006, Paper 512).

REFERENCES

H.P. Hentze, and E.W. Kaler, "Polymerization of (and Within) Self-Organized Media", Current Opinion in Colloid & Interface Science 8, 164-178 (2003). Paper 053.

B.E. Schwickert, S.R. Kline, K. Zimmermann, K.M. Lantzky and J.L. Yarger, "Early Stages of Glacial Clustering in Supercooled triphenyl phosphate", Physical Review B 64, 045410-1 to -6 (2001). Paper 148.

M.G. Page and G.G. Warr, "Structure and Dynamics of Self-assembling Aluminum didodecyl phosphate Organogels" , Journal of Physical Chemistry B 108, 16983-16989 (2004). Paper 305.

P.E. Mason, G.W. Nielson, S.R. Kline, C.E. Dempsey and J.W. Brady, "Nanometer-Scale Ion Aggregates in Aqueous Electrolyte Solutions: Guanidinium Carbonate", Journal of Physical Chemistry B 110, 13477-13483 (2006). Paper 523.

T.G. Mason and M.Y. Lin, ""Asphaltene Nanoparticle Aggregation in Mixtures of Incompatible Crude Oils", Phys. Rev. E 67, 50401-1 to 4 (2003). Paper 107.

P.M. Spiecker, K.L Gawrys and P.K. Kilpatrick, "Aggregation and Solubility of Asphaltenes and their Subfractions", J. Colloid and Interface Science 267, 178-193 (2003). Paper156.

H.J.M. Hanley, C.D. Muzny, D.L. Ho and C.J. Glinka, "A SANS Study of a Commercial Organoclay Dispersion", Langmuir 19, 5575-5580 (2003). Paper 043.

D.L. Ho and C. Glinka, "Effects of Solvent Solubility Parameters on Organoclays Dispersions", Chem. Mater. 15, 1309-1312 (2003). Paper 056.

B.H. Cipriano, S.R. Raghavan and P.M. McGuiggan, "Surface Tension and Contact Angle Measurements of a Hexadecyl imidazolium Surfactant Adsorbed on a Clay Surface", Colloids and Surfaces A 262, 8-13 (2005). Paper 420.

J.C. Marshall, T. Cosgrove, K. Jack and A. Howe, "SANS of Gelatin/SDS Complexes at the Polystyrene/Water Interface", Langmuir 18, 9668-9675 (2002). Paper 103.

B.J. Maranzano and N.J. Wagner, "The Effect of Interparticle Interactions and Particle Size on Reversible Shear Thickening: Hard Sphere Colloidal Dispersions", J. Rheology 45, 1205-1222 (2001). Paper 238.

S.A. Shah, S. Ramakrishnan, Y.L. Chen, K.S. Schweizer and C.F. Zukoski, "Scattering Studies of the Structure of Colloid-Polymer Suspensions and Gels", Langmuir 19, 5128-5136 (2003). Paper 263.

W.A. Hamilton, L. Porcar and L.J. Magid, "Using Neutron Reflectometry and Reflection Geometry Near-Surface SANS to Investigate Surfactant Micelle Organization at a Solid-Solution Interface", Physica B 357, 88-93 (2005). Paper 396.

J. Zank, P.A. Reynolds, A.J. Jackson, K.J. Baranyai, A.W. Perriman, J.G. Barker, M.-H. Kim and J. White, "Aggregation in a High internal Phase Emulsion Oberved by SANS and USANS", Physica B 385-386, 776-779 (2006). Paper 430.

M. George, G.P. Funkhouser, P. Terech and R.G. Weiss, "Organogels with Fe(III) Complexes of Phosphorous-Containing Amphiphiles as Two-Component Isothermal Gelators", Langmuir 22, 7885-7893 (2006). Paper 536.

J.P. Schneider, D.J. Pochan, B. Ozbas, K. Rajagopal, L. Pakstis and J. Kretsinger, "Responsive Hydrogels from the Intramolecular Folding and Self-Assembly of a Designed Peptide", JACS 124, 15030-15037 (2002). Paper 262.

T.G. Mason and M.Y. Lin, "Density Profiles of Temperature-Sensitive Microgel Particles", Phys Rev E 71, 040801-1 to 4 (2005). Paper 374.

F. Horkay, A.M. Hecht and E. Geissler, "Similarities between Polyelectrolyte Gels and Biopolymer Solutions", J. Polym. Sci., Polym. Phys. Ed. 44, 3679-3686 (2006). Paper 560.

J.A. Silas and E.W. Kaler, "The Phase Behavior and Microstructure of Efficient Cationic-Nonionic Microemulsions", J. of Colloi and Interface Science 243, 248-254 (20010> Paper 150.

B.A. Simmons, G.C. Irvin, V. Agarwal, A. Bose, V.T. John, G.L. McPherson and N.P. Balsara, "SANS Study of Microstructural Transitions in a Surfactant-Based Gel Mesophase", Langmuir 18, 624-632 (2002). Paper 153.

M. Singh, V. Agarwal, D.D. kee, G. McPherson, V.T. John and A. Bose, "Shear-Induced Orientation of a Rigid Surfactant Mesophase", Langmuir 20, 5693-5702 (2004). Paper 286.

L. Shen, A. Stachowiak, A.E.K. Fateen, P.E. Laininis and T.A. Hatton, "Structure of Alkanoic Acid Stabilized Magnetic Fluids, A SANS and Light Scattering Analysis", Langmuir 17, 288-299 (2001). Paper 241.

M-P. Nieh, V.A. Raghunathan, S.R. Kline, T.A. Harroun, C-Y. Huang, J. Pencer and J. Katsaras, "Spontaneously Formed Unilamellar Vesicles with Path-Dependent Size Distribution", Langmuir 21, 6656-6661 (2005). Paper 413.

F.P. Hubbard, G. Santonicola, E.W. Kaler and N.L. Abbott, "SANS from Mixtures of SDS and a Cationic, Bolaform Surfactant Conatining Azobenzene", Langmuir 21, 6131-6136 (2005). Paper 379.

T. Shang, K.A. Smith and T.A. Hatton, "Self-Assembly of a Nonionic Photoresponsive Surfactant under Varying Irradiation Conditions: A SANS and Cryo-TEM Study", Langmuir 22, 1436-1442 (2006). Paper 482.

P.A. FitzGerald, T.W. Davey and G.G. Warr, "Micellar Structure in Gemini Nonionic Surfactants from SANS", Langmuir 21, 7121-7128 (2005). Paper 409.

K.S. Freeman, N.C. Beck Tan, S.F. Trevino, S.R. Kline, L.B. McGown and D.J. Kiserow, "Size and Polydispersity Determination of AOT/Bile Salt Reversed Micelles Obtained by SANS", Langmuir 17, 3912-3916 (2001). Paper 027.

P.A. Hassan, G. Fritz and E.W. Kaler, "SANS Study of SDS Micellar Growth Driven by Addition of a Hydrotropic Salt", J. Colloid and Interface Science 257, 154-162 (2003). Paper 045.

L. Porcar, W.A. Hamilton, P.D. Butler and G.W. Warr, "Relaxation of a Shear-Induced Lamellar Phase Measured with Time-Resolved SANS", Physica B 350, 963-966 (2004). Paper 343.

C.M. Stancik, A.R. Lavoir, P.A. Achurra, R.M. Waymouth and A.P. Gast, "A SANS Study of the Structure and Water Partitioning of Selectively Deuterated Copolymer Micelles", Langmuir 20, 8975-8987 (2004). Paper 358.

A.L. Norman, D.L. Ho, J-H. Lee and A. Karim, "Spontaneous Formation of Vesicles of Diblock Copolymer EO_6BO_{11} in Water: A SANS Study", J. Phys. Chem. 110, 62-67 (2006). Paper 450.

J.N. Wilking, S.M. Graves, C.B. Chang, K. Meleson, M.Y. Lin and T.G. Mason, "Dense Cluster Formation During Aggregation and Gelation of Attractive Slippery Nanoemulsion Droplets", Phys. Rev. Lett. 96, 015501-1 to -4 (2006). Paper 461.

B.E. Wyslouzil, G. Wilemski, R. Strey, C.H. Heath and U. Diergsweisler, "Experimental Evidence for Internal Structure in Aqueous-Organic Nanodroplets", Physical Chemistry Chemical Physics 8, 54-57 (2006). Paper 480.

E.A. Stefanescu, A. Dundigalla, V. Ferreiro, E. Loizou, L. Porcar, I. Negulescu, J. Garno and G. Schmidt, "Supramolecular Structures in Nanocomposite Multiplayered Films", Physical Chemistry Chemical Physics 8, 1739-1746 (2006). Paper 494.

S.H. Chen, W-R. Chen and F. Mallamace, "The Glass-to-Glass Transition and Its End Point in a Copolymer Micellar System", Science 300, 619-622 (2003). Paper 014.

J.S. Lettow, T.M. Lancaster, C.J. Glinka and J.Y. Ying, "SANS and Theoretical Investigation of PEO-PPO-PEO Stabilized Oil-in-Water Microemulsions", Langmuir 21, 5738-5746 (2005). Paper 393.

D.C. Pozzo and L.M. Walker, "SANS of Silica Nanoparticles Templated in PEO-PPO-PEO Cubic Crystals", Colloids and Interfaces A 294, 117-129 (2007). Paper 544.

D.P. Bossev, S.R. Kline, J.N. Israeachvili and M.E. Paulaitis, "Pressure-Induced Freezing of the Hydrophobic Core Leads to a L1 to H1 Phase Transition for $C_{12}E_5$ Micelles in D_2O", Langmuir 17, 7728-7731 (2001). Paper 008.

M. Lesemann, H. Nathan, T.P. DiNoia, C.F. Kirby, M.A. McHugh, J.H. van Zanten and M.E. Paulaitis, Self-Assembly at High Pressures: A SANS Study of the Effect of Pressure on Microstructure of $C_{12}E_5$ Micelles in Water", Ind. Eng. Chem. Res. 42, 6425-6430 (2003). Paper 089.

W.A. Hamilton, L. Porcar, P.D. Butler and G.G. Warr, "Local Membrane Ordering of Sponge Phases at a Solid-Solution Interface", J. Chem. Phys. 116, 8533-8546 (2002). Paper 247.

Y.S. Lee and N.J. Wagner, "Rheological Properties and SANS of a Shear Thickening Nanoparticle Dispersion at High Shear Rates", Ind. Eng. Chem. Res. 45, 7015-7024 (2006). Paper 530.

M.W. Liberatore, F. Nettesheim, N.J. Wagner and L. Porcar, "Spatially Resolved SANS in the 1-2 Plane: A Study of Shear-Induced Phase Separating Wormlike Micelles", Phys. Rev. E 73, 020504-1 to 4 (2006). Paper 495

V. Croce, T. Cosgrove, G. Maitland, T. Hughes and G. Karlsson, "Rheology, Cryo-TEM and SANS of Highly Viscoelastic Wormlike Micellar Solutions", Langmuir 19, 8536-8541 (2003). Paper 021.

G.C. Kalur and S.R. Raghavan, "Anionic Wormlike Micellar Fluids that Display Cloud Points: Rheology and Phase Behavior", J. Chem. Phys. B 109 (8599-8604 (2005). Paper 410.

W-R. Chen, P.D. Butler and L.J. Magid, "Incorporating Intermicellar Interactions in the Fitting of SANS Data from Cationic Wormlike Micelles", Langmuir 22, 6539-65-48 (2006). Paper 512.

Part J – **SANS IN BIOLOGY**

Chapter 47. Elements of Biology

Chapter 48. SANS from Phospholipid Bilayers under Pressure

Chapter 49: SANS from DNA

Chapter 50: SANS from a Protein Complex

Chapter 51: SANS in Biology Literature Review

52.3 Proteins
References

Biology is the science of life. The word microbiology refers to the observation of biological systems in the optical (micrometer) size scale. Molecular biology is the science of biology at the molecular level. The new term nanobiology could refer to investigations in the nanometer scale. This is our focus.

1. CELL BIOLOGY

Understanding the cell drives a great deal of biology research. Microbiology is moving from a mode driven by clinical research to new developments in bio-genetics. The human genone has been mapped out some ten years ago. The 23 pairs of chromosomes contain DNA which codes for some 20,000 to 25,000 genes involving millions of base pairs. These control the synthesis of all proteins. The order of the nucleotides in DNA controls the order of amino acids in protein synthesis. Proteins perform most of the biological functions essential for life (Becker et al, 1999).

Cells contain organelles which perform specific functions. One of these, the nucleus, contains the DNA double helix packed into chromosomes. The same DNA is contained in every nucleus of every cell in the body. Cell division involves DNA replication whereby new copies are made.

Cells are bounded by a membrane with a hydrophobic interior and a hydrophilic exterior. Lipids containing (hydrophobic) hydrocarbon tails and polar (hydrophilic) head groups form the cell membrane. Special proteins help in the transport of essential ingredients into and out of the cell. The passage of small molecules (such as CO_2 and H_2O) and of essential ionic groups also occurs.

The interplay of hydrophobic and hydrophilic interactions is a major diving force in the working of membranes, in the assembly of cellular structures as well as in the folding of macromolecules such as DNA and proteins. Proteins are folded into helical and sheet portions in their active form which is essential for specific functions.

Polysaccharides perform storage and structural functions in cells. Starch and cellulose are typical plant polysaccharides. They are formed of repeating sugar glucose units.

2. LIPIDS

The simplest components of a cell are the lipid molecules forming the membranes. These are amphiphile (surfactant) molecules with hydrophilic head groups and hydrophobic tails. Membranes surround the cell as well as the organelles inside the cell. Proteins form channels across the membrane and other structures in membranes.

468

MEMBRANE

lipids

proteins

0   5 nm
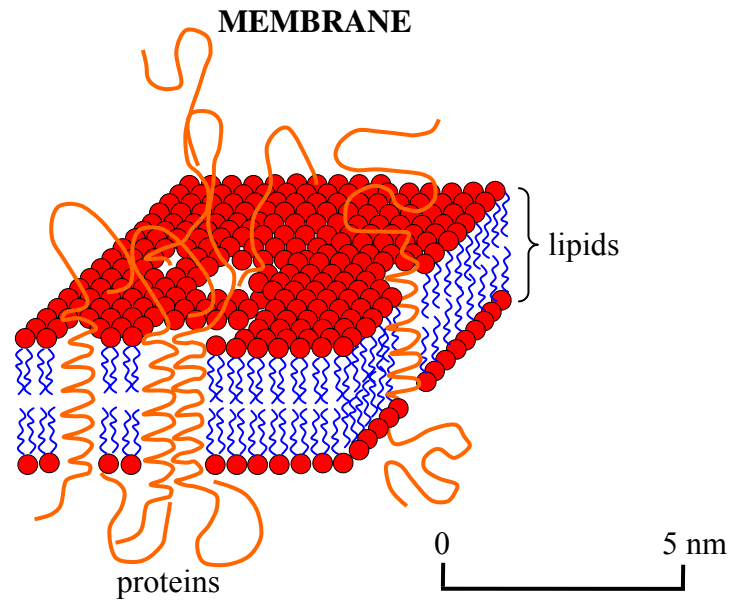
Figure 1: Schematic representation of a membrane.

Lipids are formed from a glycerol backbone and fatty acid side chains. These two undergo a condensation reaction that removes a water molecule.


```
        H
        |
    H-C-OH      HOOC ~~~~~~~~~~~
        |
    H-C-OH          Fatty acid
        |
    H-C-OH
        |
        H

    Glycerol
```
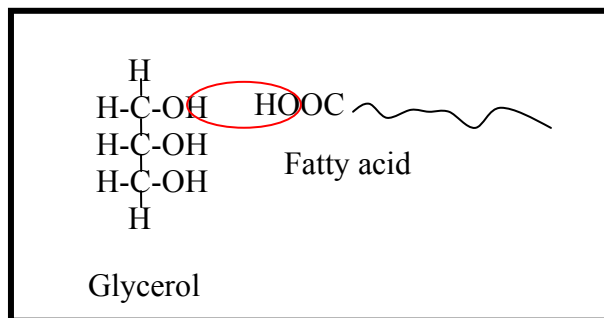
Figure 2: Reaction that forms lipids.

One specific lipid corresponding to a C17 hydrocarbon tail is included here.
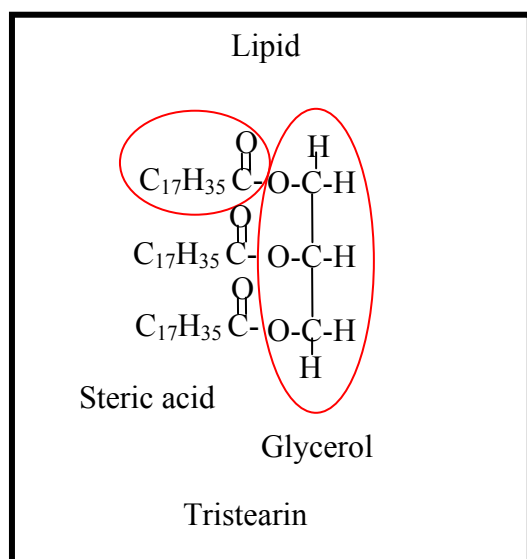
Figure 3: Example of a lipid molecule.

The fatty acids forming the lipid tails contain either C=C double bonds or saturated C-C single bonds. The double bonds produce kinks in the fatty acid chain.

3. DNA AND RNA

DNA is the key component for the expression and transmission of genetic information. It is composed of nucleic acid sequences that form the genetic code. RNA plays an intermediate role in reading the DNA code. The deoxyribonucleic acid (DNA) and the ribonucleic acid (RNA) molecules are identical except for a small difference on the sugar ring. DNA contains desoxyribose whereas RNA contains ribose. The DNA chain is synthesized through a condensation reaction as well.
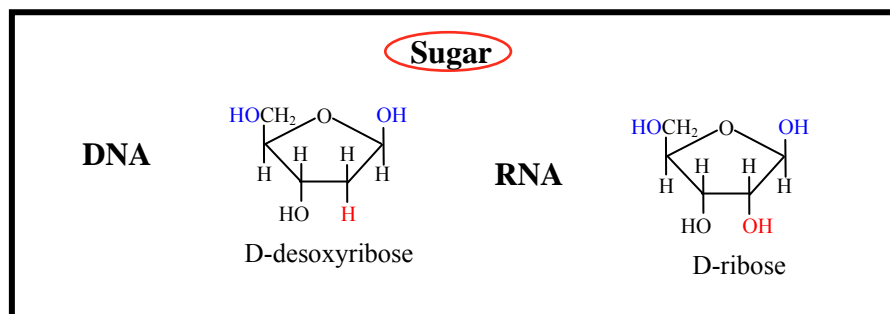
Figure 4: Chemical formula for the sugar ring in DNA and in NA.

Messenger RNA contains the genetic information (transcribed from DNA) that dictates the amino acid sequence during the synthesis of polypeptides. Transfer RNA brings the correct amino acid to the next site during this synthesis process on ribosomes.

Each DNA nucleotide is formed of a phosphate group, a five-carbon sugar, and an amine base. Different nucleotides contain different amine bases. Please note that the DNA chain runs either from the 5' position to the 3' position on the sugar or in the other direction (position 3' to 5').
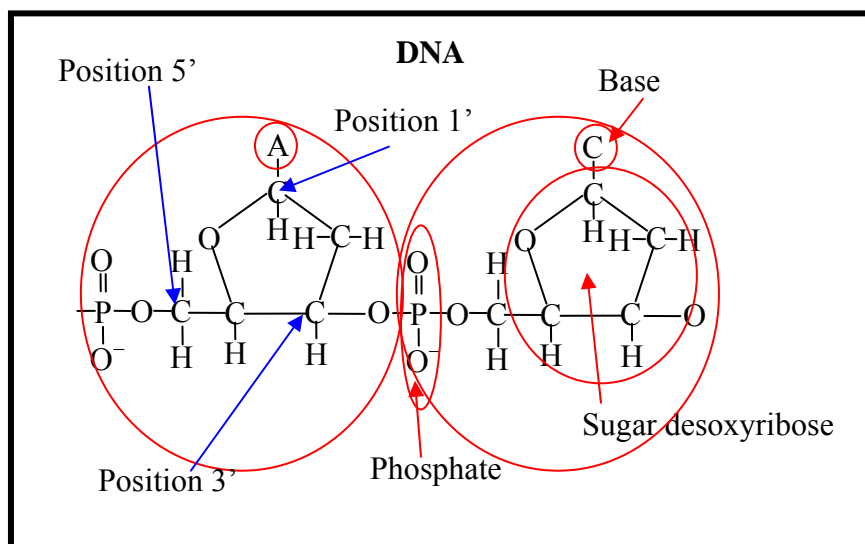
Figure 5: Components of the DNA nucleotide.

There are four amine bases in DNA: Adenine (A), Thymine (T), Guanine (G) and Cytosine (C). In RNA, Thymine is replaced by Uracil (U).

THE DNA MOLECULE
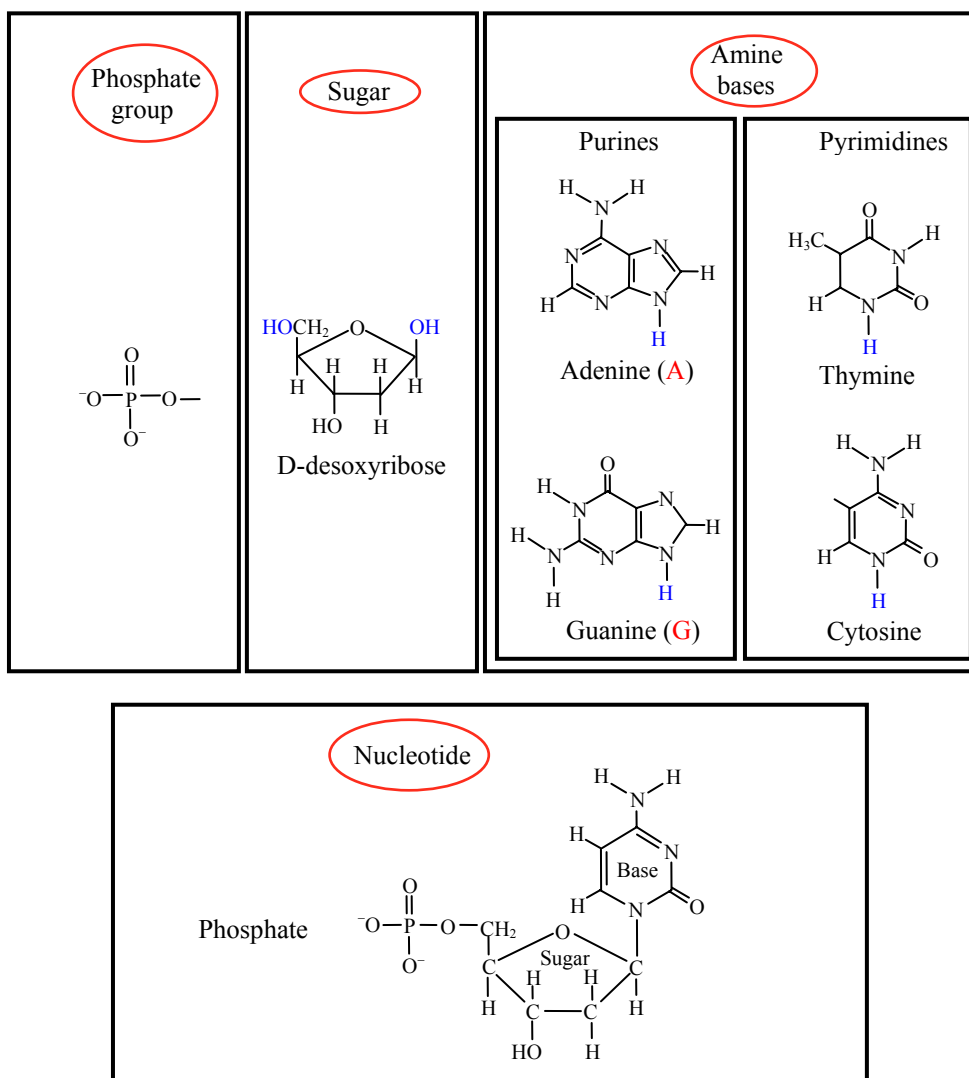
Figure 6: Components of the DNA molecule.

DNA folds into a double helix structure whereby the amine bases are stacked and hydrogen bonded. The pair A-T has two hydrogen bonds whereas the pair C-G has three hydrogen bonds. The two DNA chains forming the double helix run in opposite direction. Stacking of the amine bases and hydrogen bonding between them is the key driving force for the helix formation. Water hydrates the outside phosphate groups as well as produces hydrogen bonding between the base pairs.
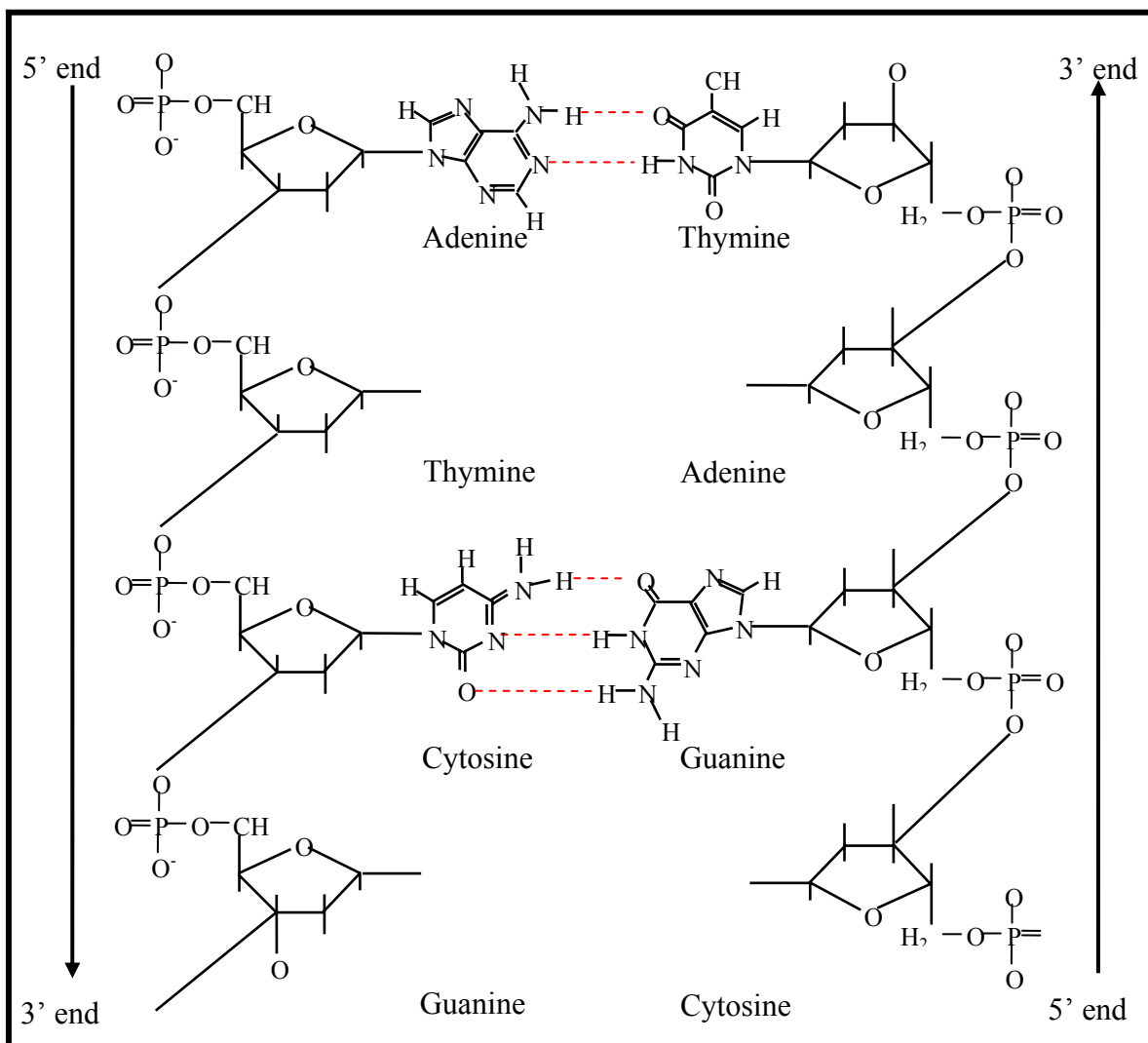
Figure 7: Amine base stacking and hydrogen bonding that form the DNA double helix.

X-ray diffraction helped in the determination of the precise structure of the DNA double helix. Information like the repeat distance per base pair (3.4 Å) and the helix pitch (34 Å) were determined.

THE DNA DOUBLE HELIX
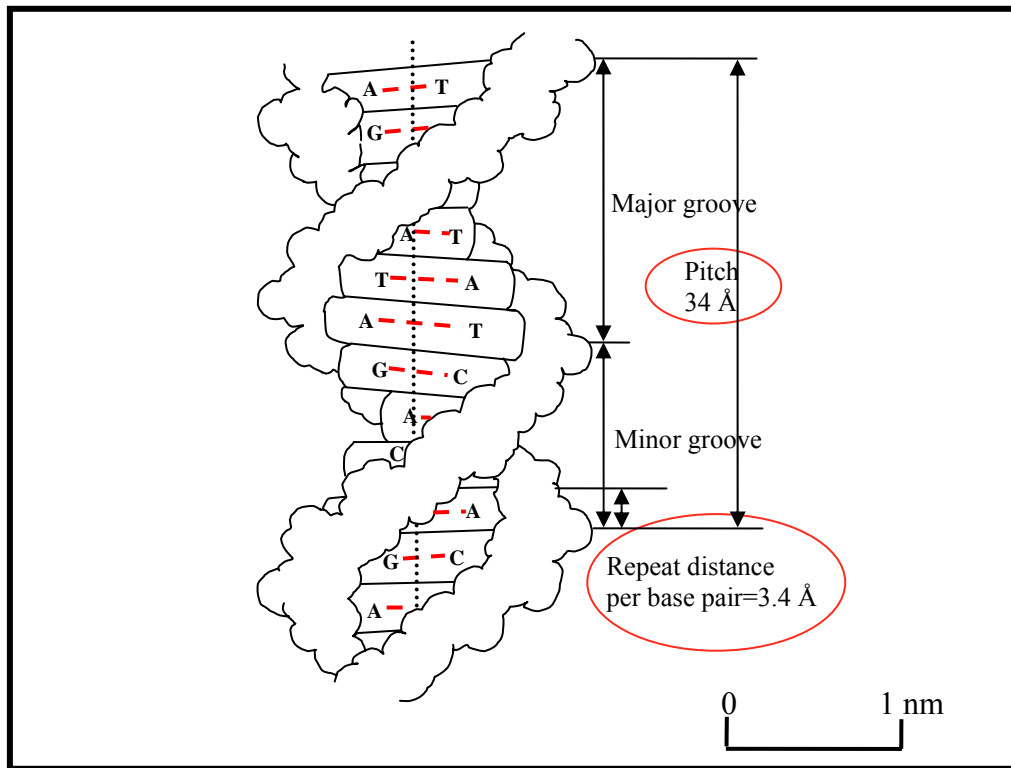
Figure 8: The DNA double helix. Structure for the dominant form of DNA (the B type) is schematically represented here.

4. PROTEINS

Proteins are responsible for the enzymatic (or catalytic), structural and regulatory functions of the cell. Most of the cell processes are mediated by proteins. Proteins are formed of polypeptide chains which are coiled and folded in a precise way dictated by the amino acid sequence. Unfolding (denaturation) leads to loss of biological activity. Each polypeptide consists of a specific amino acid sequence. No two long amino acid sequences are alike. Peptides are synthesized through a condensation reaction of two amino acids to form the amide (also called peptide) bond. A water molecule is a byproduct. Energy is provided for this chemical reaction. RNA plays the messenger (mRNA), adapter or transfer (tRNA), and linker or ribosomal (rRNA) roles in order to transcribe the DNA code into a correct amino acid sequence.
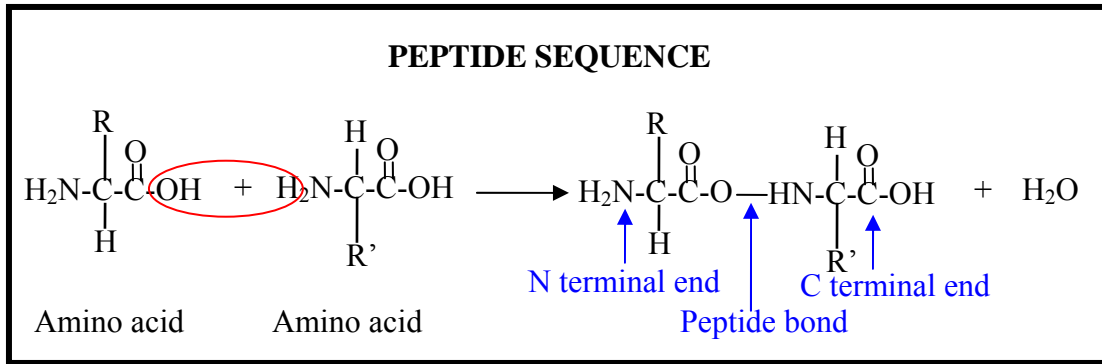
Figure 9: A peptide sequence of two amino acids.

There are 20 amino acids involved in protein synthesis. These consist in a (1) nonpolar (hydrophobic) group, a (2) polar (hydrophilic) uncharged group and a (3) polar (hydrophilic) charged group. The hydrophobic groups tend to be buried in the middle of proteins out of contact with water.
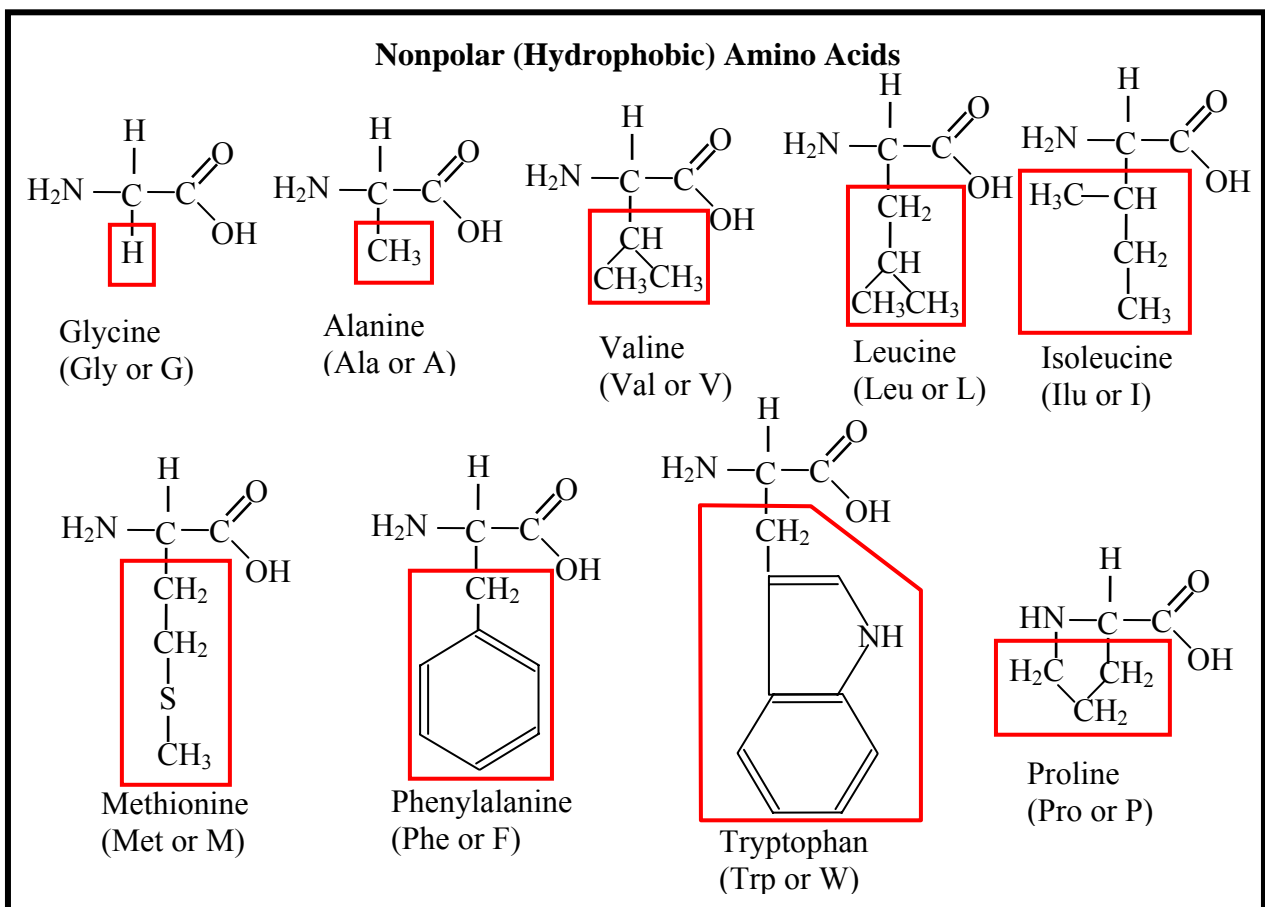
Figure 10a: The group of nonpolar (hydrophobic) amino acids.

Polar (Hydrophilic) Uncharged Amino Acids

Serine
(Ser or S)

Cysteine
(Cys or C)

Tyrosine
(Tyr or Y)

Glutamine
(Gln or Q)

Threonine
(Thr or T)

Asparagine
(Asn or N)
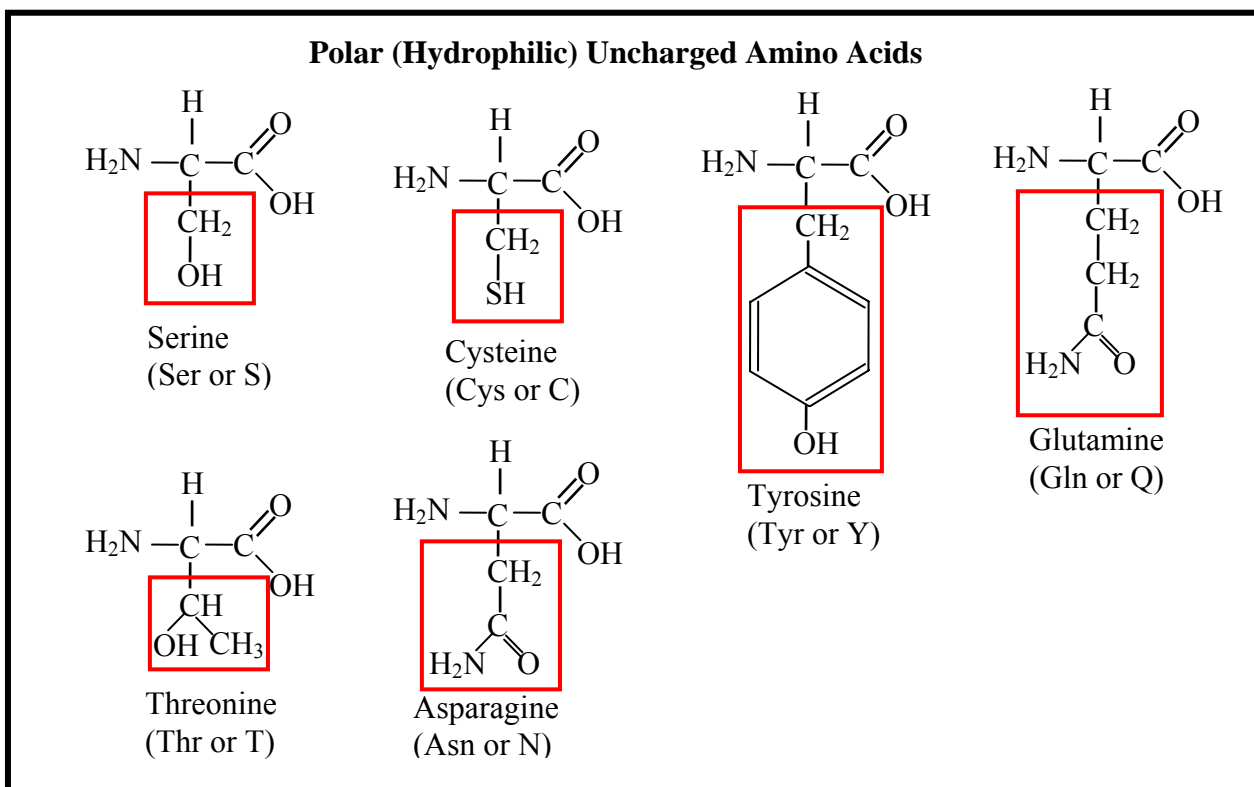
Figure 10b: The group of polar (hydrophilic) uncharged amino acids.

Polar (Hydrophilic) Charged Amino Acids

Aspatate
(Asp or D)

Glutamate
(Glu or E)

Lysine
(Lys or K)

Arginine
(Arg or R)

Histidine
(His or H)

Acidic

Basic
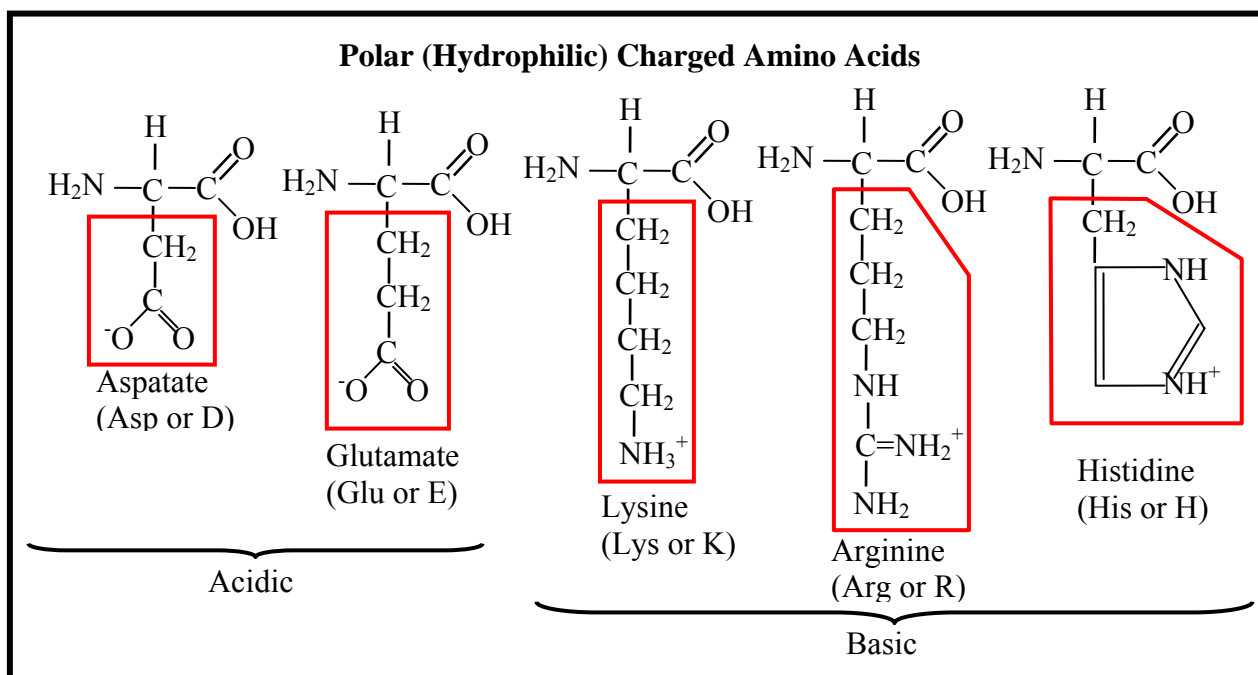
Figure 10c: The group of polar (hydrophilic) charged amino acids.

Molecular chaperones are needed in the folding of proteins in order to prevent incorrect molecular conformations. Proteins comprise four hierarchical self-assembling structures. These are the primary, secondary, tertiary and quaternary structures.

The primary structure refers to the amino acid sequence along the peptide chains. mRNA, tRNA and rRNA play the role of transcribing, transferring and linking the amino acid sequence. The secondary structure dictates the folding strategy based on amino acid interactions. Folding occurs in the form of alpha helix, beta sheet or random coil. The alpha helix contains 3.6 amino acids per helical turn bridging the peptide bond of every fourth amino acid. For example leucine forms alpha helices. The beta sheet is a planar structure involving –CO to HN– hydrogen bonds between two polypeptides. For example, valine forms beta sheets.

The tertiary structure involves interaction between the R groups of amino acids. Electrostatic, hydrophobic and hydrogen bonding interactions as well as S-S covalent bonds contribute to the structure formation. Polypeptides are folded, coiled and twisted into the desired protein's native configuration. A domain of 50 to 350 amino acids is required to fulfill a specific function. Some proteins consist of multiple functions played by multiple domains. The quaternary structure is mode of two or more chains. Each chain can have two or more domains.

Information included in the DNA gene sequence (A, G, T, C bases) is used to set the amino acid sequence in protein synthesis. For example an AAG sequence in a DNA strand (running from 5' to 3' positions) transcribes to an AAG sequence in the mRNA and to the addition of Lys (lysine) amino acid in the polypeptide synthesis. The beginning (start) and end (stop) of a gene sequence are also included in the DNA code.

Ribonuclease Protein
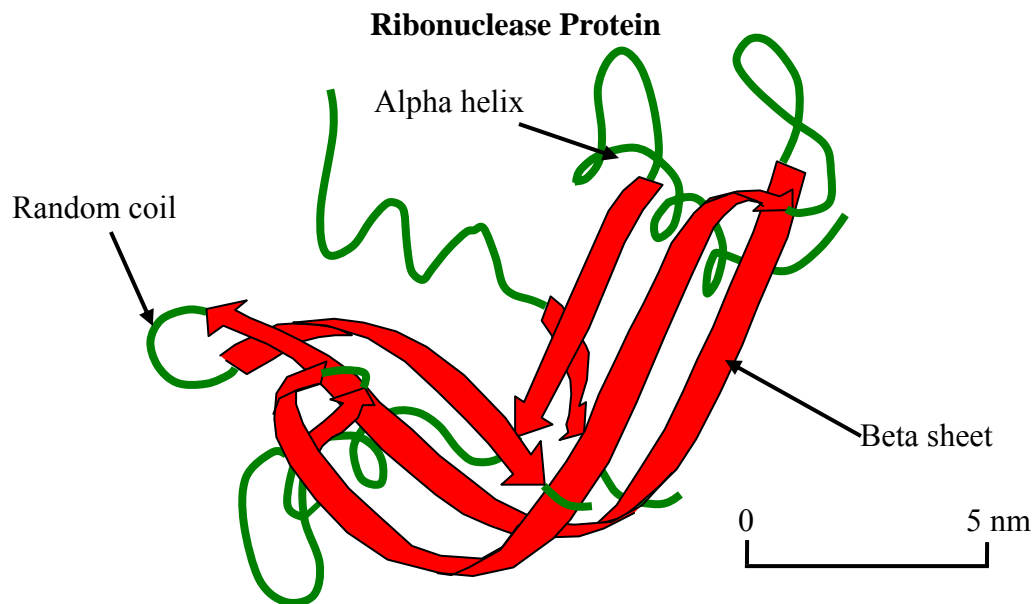
Figure 11: Schematic representation of Ribonuclease which is a globular protein containing beta sheet, alpha helix and random coil secondary structures. Ribonuclease is an enzyme that catalyses the hydrolysis of RNA into smaller components.

477

5. POLYSACCHARIDES

Polysaccharides are polymers formed of monosaccharides (Greek for "single sugar") joined together by glycosidic bonds. There are two categories of sugars: the aldosugars and the ketosugars.
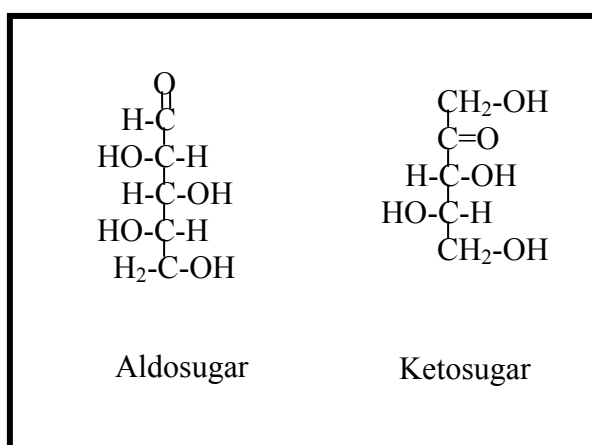
Figure 12: The two categories of sugar molecules

The most common form of aldosugar is the D-glucose ($C_6H_{12}O_6$) which occurs in linear and cyclic forms. The general formula $C_nH_{2n}O_n$ is characteristic of sugars. These are also referred to as carbohydrates.
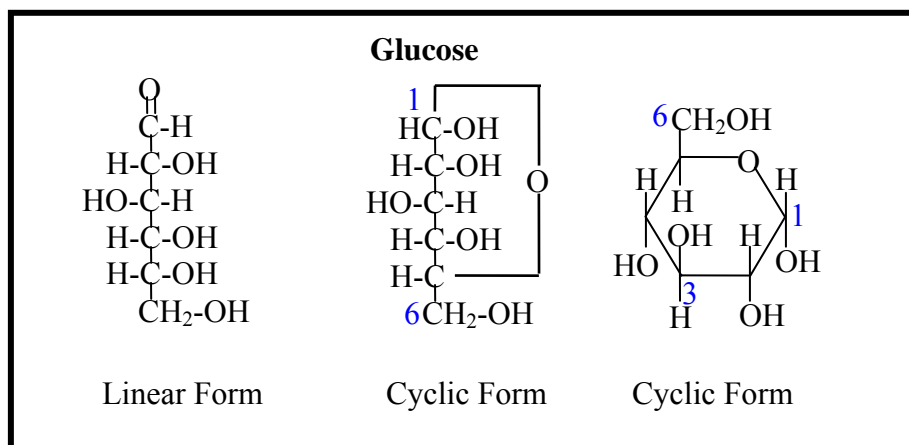
Figure 13: The linear and cyclic forms of D-glucose.

Two well known polysaccharides in plant cells are starch and cellulose. Two well known polysaccharides in animal cells are glycogen and chitin. Starch and glycogen contain alpha glycosidic bonds whereas cellulose and chitin contain beta glycosidic bonds. Polysaccharides

478

are often branched and are represented by the chemical formula $(C_6H_{10}O_5)_n$ with n being a large number (hundreds to thousands).
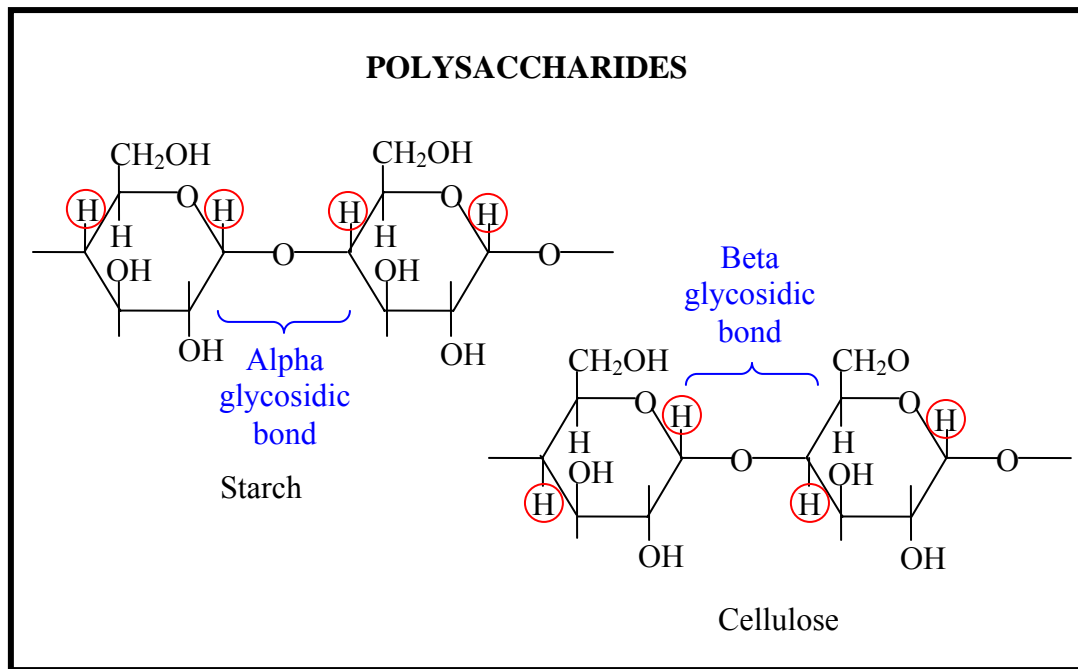
Figure 14: Chemical formulas for two plant polysaccharides.

Mammals do not possess enzymes that can hydrolyze the beta glycosidic bonds and can not therefore digest cellulose.

6. CELLS AND ORGANELLES

The basic unit in biology is the cell. Eukaryotes include most living beings and are characterized by a nucleus and well defined membranes around the organelles (such as the nucleus) in all cells. In contrast, bacteria have no nucleus or organelles and are termed prokaryotes.
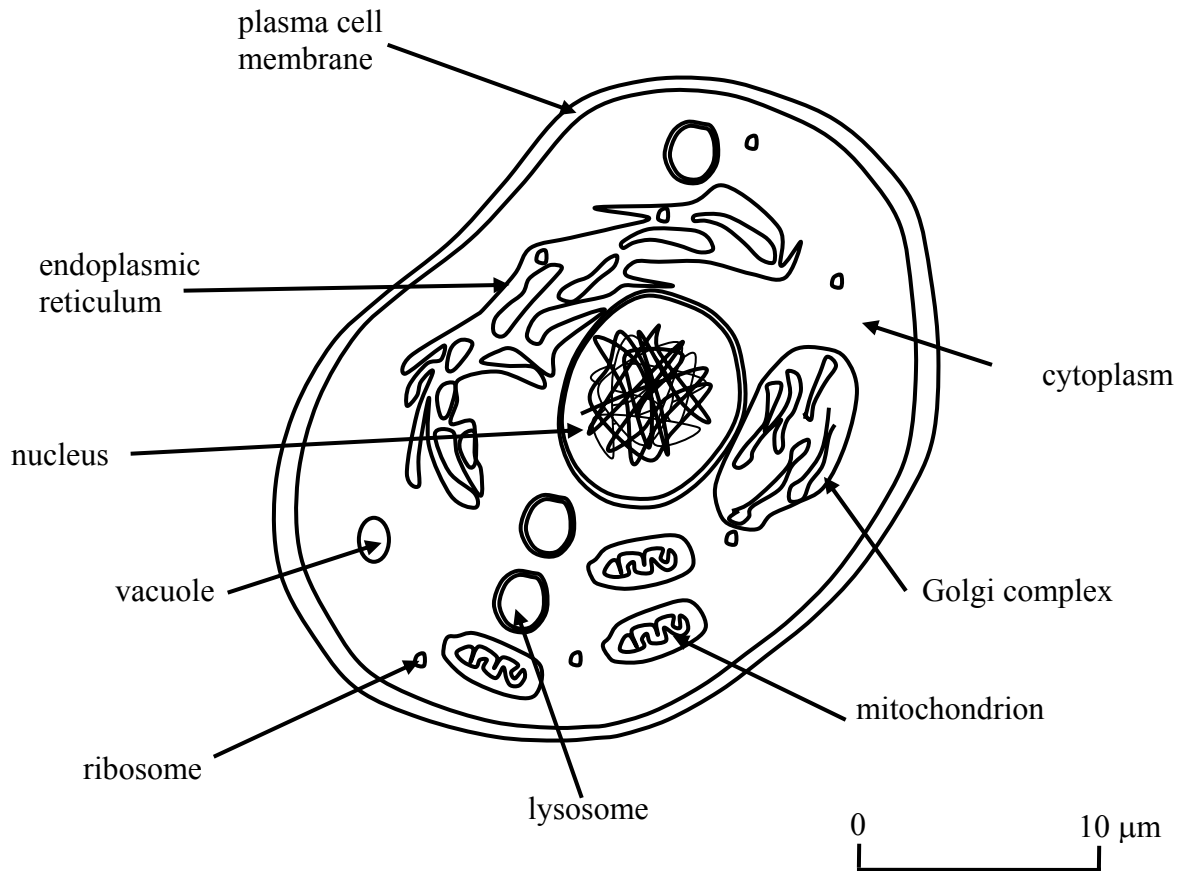
Figure 15: Schematic representation of an animal cell showing the various organelles.

A brief description of the various organelles is included here. These include the nucleus, the endoplasmic reticulum, the Golgi complex, the mitochondria, the lysosomes, the peroxisomes, the vacuoles and vesicles.

The cell nucleus contains the chromosomes where DNA is tightly packed. The nucleus is bounded by a double membrane that keeps its contents separate from the cytoplasm. Membrane pores allow the free movement of small molecules and ions. The movement of larger molecules such as proteins is controlled by specialized carrier proteins (enzymes)

The endoplasmic reticulum (ER) consists of an interconnected network of tubular membranes and vesicles and is the site of protein synthesis and transport. The ER is also the site for the sequestration of calcium and the production and storage of glycogen and steroids.

The Golgi complex serves in the processing and packaging of secretory proteins, in the synthesis of polysaccharides and in the processing of lipids.

Mitochondria play an important role in the oxidation of sugars which are the main source of energy for the cell. It is the site for the generation of adenosine triphosphate (ATP) which is

the energy currency within the cell. The cell localizes most of the enzymes in the mitochondrion. Some proteins are synthesized in the mitochondria. In addition to being the energy production center, mitochondria are also involved in cell signaling, cell differentiation as well as cell growth. Mitochondria have their own DNA which is independent of the DNA in the nucleus.

Lysosomes contain digestive enzymes along with carbohydrates. The membrane surrounding the lysosome prevents the digestive enzymes from destroying the cell. Lysosomal proteins are made in the ER and Golgi apparatus. Peroxisomes lay a role in breaking down fatty acids.

Vacuoles are used for temporary storage or transport. They remove and export unwanted substances, maintain the proper internal cell hydrostatic pressure and pH and enable cell flexibility. Vacuoles are important components of plant cells.

The cell contains many other components. Vesicles are used for storage. Plant cells contain chloroplasts where photosynthesis takes place. The cytoplasm contains tubules and filaments for flexibility and mobility of the cell. Chaperones help in the correct assembly of proteins. Enzymes are synthesized in the rough ER, packaged in the Golgi complex and released by vesicle transport.

7. CHARACTERIZATION METHODS

There are many characterization methods used in biology. Some of the routine techniques include: mass spectroscopy to measure molecular weights, circular dichroism (CD) to distinguish between coil, beta sheet and alpha helix configurations, Cryo-Transmission Electron Microscopy (TEM) to visualize down to the molecular level, Vis-UV absorption spectroscopy to detect the existence of DNA or proteins in the sample, Electrophoresis to determine fragment sizes, etc. For example, UV absorption spectroscopy is sensitive to π bonding in the amine bases in DNA (260 nm line) and to the existence of Tryptophan amino acid in proteins (280 nm line). Wide-angle x-ray diffraction is used to determine crystalline structures. When crystalline bio-material can not be obtained, as small-angle x-ray scattering (SAXS) and small-angle neutron scattering (SANS) are used in order to determine amorphous structures. Dynamic Light Scattering (DLS) is also used to estimate particle sizes.

8. NEUTRON SCATTERING LENGTHS

Neutron scattering works best when deuteration is possible. Deuteration is achieved either by using a deuterated solvent or by deuterium labeling the macromolecules. Due to the complex "natural" processes involved, deuterium labeling is not easy to achieve in biology. Synthesis using deuterated amino acids is achieved for short polypeptide sequences of less than 50 amino acids. That process is complex and time consuming even with the use of automatic equipment. Another more involved route for obtaining deuterated bio-macromolecules is to grow organisms in a d-water culture then separate the deuterated proteins.

Water is the solvent of choice in biology research since it is the major component in the cell. The dialysis process allows the exchange of H by D and vice versa. This helps enhance the neutron contrast and is accompanied by deuterium exchange on the macromolecules. C-H bonds do not exchange but O-H and N-H bonds exchange into O-D and N-D.

The tabulated values for the scattering lengths of the light chemical elements found in proteins and DNA are included:

$b_H = -3.739*10^{-13}$ cm, $b_D = 6.671*10^{-13}$ cm, $b_C = 6.646*10^{-13}$ cm
$b_O = 5.803*10^{-13}$ cm, $b_P = 5.130*10^{-13}$ cm, $b_S = 2.847*10^{-13}$ cm.

The scattering lengths, densities and molecular volumes for water and d-water are:

$b_{H_2O} = -1.675*10^{-13}$ cm, $b_{D_2O} = 19.145*10^{-13}$ cm
$d_{H_2O} = 1$ g/cm^3, $d_{D_2O} = 1.11$ g/cm^3
$v_{H_2O} = 29.9$ Å^3, $v_{D_2O} = 29.9$ Å^3

The scattering length densities are given by:

$$\rho_{H_2O} = \frac{b_{H_2O}}{v_{H_2O}} = -5.702*10^{-7} \text{ Å}^{-2}, \quad \rho_{D_2O} = \frac{b_{D_2O}}{v_{H_2O}} = 6.403*10^{-6} \text{ Å}^{-2}$$

A table summarizes the chemical formulas, the scattering lengths and scattering length densities for the various amino acids (Jacrot, 1976). Four cases are considered: (1) the case of hydrogenated molecules (amino acids or nucleotides), (2) the case of hydrogenated molecules with H-D exchange, (3) the case of deuterated molecules, and (4) the case of deuterated molecules with D/H exchange. The same information is included for the DNA and the RNA nucleotides These numbers are estimates for thermal neutron scattering and will vary with neutron wavelength and solution conditions (such as pH, etc).

Table 1: Scattering lengths for amino acids and deuterated amino acids after H/D or D/H exchange. Scattering lengths for nucleotides and deuterated nucleotides are also included.

Name	H/D Content	Formula	Scattering Length (10^{-12} cm)	Density (g/cm^3)	Scattering Length Density (10^{-6} Å^{-2})

Amino Acids

	Hydrogenated	C_2NOH_3	1.72	1.43	2.60
	H/D Exchange	C_2NOH_2D	2.77	1.45	4.16
Glycine (Gly or G)	Deuterated	C_2NOD_3	4.85	1.50	7.30
	D/H Exchange	C_2NOHD_2	3.81	1.48	5.73
	Hydrogenated	C_3NOH_5	1.64	1.29	1.79

	H/D Exchange	C_3NOH_4D	2.68	1.31	2.93
Alanine (Ala or A)	Deuterated	C_3NOD_5	6.85	1.38	7.48
	D/H Exchange	C_3NOHD_4	5.80	1.36	6.34
	Hydrogenated	C_5NOH_9	1.47	1.16	1.04
Valine (Val or V)	H/D Exchange	C_5NOH_8D	2.52	1.17	1.78
	Deuterated	C_5NOD_9	10.84	1.27	7.65
	D/H Exchange	C_5NOHD_8	9.80	1.25	6.92
	Hydrogenated	C_6NOH_{11}	1.39	1.12	8.28
Leucine (Leu or L)	H/D Exchange	$C_6NOH_{10}D$	2.43	1.13	1.45
	Deuterated	C_6NOD_{11}	12.84	1.23	7.65
	D/H Exchange	C_6NOHD_{10}	11.80	1.22	7.03
	Hydrogenated	C_6NOH_{11}	1.39	1.11	8.24
Isoleucine (Ilu or I)	H/D Exchange	$C_6NOH_{10}D$	2.43	1.12	1.44
	Deuterated	C_6NOD_{11}	12.84	1.22	7.61
	D/H Exchange	C_6NOHD_{10}	11.80	1.21	6.99
	Hydrogenated	C_9NOH_9	4.13	1.20	2.03
Phenylalanine (Phe or F)	H/D Exchange	C_9NOH_8D	5.17	1.21	2.54
	Deuterated	C_9NOD_9	13.50	1.27	6.64
	D/H Exchange	C_9NOHD_8	12.46	1.27	6.13
	Hydrogenated	$C_9NO_2H_9$	4.71	1.33	2.31
Tyrosine (Tyr or Y)	H/D Exchange	$C_9NO_2H_7D_2$	6.79	1.35	3.34
	Deuterated	$C_9NO_2D_9$	14.08	1.40	6.92
	D/H Exchange	$C_9NO_2H_2D_7$	12.00	1.39	5.89
	Hydrogenated	$C_{11}N_2OH_{10}$	6.02	1.30	2.54
Tryptophan (Trp or W)	H/D Exchange	$C_{11}N_2OH_8D_2$	8.11	1.32	3.41
	Deuterated	$C_{11}N_2OD_{10}$	16.43	1.37	6.92
	D/H Exchange	$C_{11}N_2OH_2D_8$	14.35	1.36	6.04
	Hydrogenated	$C_4NO_3H_4$	3.84	1.67	3.38
Aspartate (Asp or D)	H/D Exchange	$C_4NO_3H_3D$	4.88	1.68	4.30
	Deuterated	$C_4NO_3D_4$	8.00	1.73	7.05
	D/H Exchange	$C_4NO_3HD_3$	6.96	1.71	6.13
	Hydrogenated	$C_5NO_3H_6$	3.76	1.51	2.67
Glutamate (Glu or E)	H/D Exchange	$C_5NO_3H_5D$	4.80	1.52	3.41
	Deuterated	$C_5NO_3D_6$	10.00	1.58	7.11
	D/H Exchange	$C_5NO_3HD_5$	8.96	1.57	6.37
	Hydrogenated	$C_3NO_2H_5$	2.22	1.46	2.24
	H/D Exchange	$C_3NO_2H_3D_2$	4.30	1.49	4.34

Serine (Ser or S)	Deuterated	$C_3NO_2D_5$	7.43	1.54	7.49
	D/H Exchange	$C_3NO_2H_2D_3$	5.34	1.51	5.39
Threonine (Thr or T)	Hydrogenated	$C_4NO_2H_7$	2.14	1.37	1.75
	H/D Exchange	$C_4NO_2H_5D_2$	4.22	1.40	3.46
	Deuterated	$C_4NO_2D_7$	9.43	1.47	7.72
	D/H Exchange	$C_4NO_2H_2D_5$	7.34	1.44	6.01
Asparagine (Asn or N)	Hydrogenated	$C_4N_2O_2H_6$	3.45	1.40	2.55
	H/D Exchange	$C_4N_2O_2H_3D_3$	6.57	1.44	4.86
	Deuterated	$C_4N_2O_2D_6$	9.69	1.47	7.17
	D/H Exchange	$C_4N_2O_2H_3D_3$	6.57	1.44	4.86
Glutamine (Gln or Q)	Hydrogenated	$C_5N_2O_2H_8$	3.36	1.32	2.09
	H/D Exchange	$C_5N_2O_2H_5D_3$	6.49	1.35	4.03
	Deuterated	$C_5N_2O_2D_8$	11.69	1.40	7.26
	D/H Exchange	$C_5N_2O_2H_3D_5$	8.57	1.37	5.32
Lysine (Lys or K)	Hydrogenated	$C_6N_2OH_{13}$	1.58	1.22	8.96
	H/D Exchange	$C_6N_2OH_9D_4$	5.74	1.25	3.26
	Deuterated	$C_6N_2OD_{13}$	15.11	1.34	8.58
	D/H Exchange	$C_6N_2OH_4D_9$	10.95	1.30	6.21
Arginine (Arg or R)	Hydrogenated	$C_6N_4OH_{13}$	3.45	1.44	1.91
	H/D Exchange	$C_6N_4OH_8D_5$	9.70	1.50	5.36
	Deuterated	$C_6N_4OD_{13}$	16.984	1.56	9.39
	D/H Exchange	$C_6N_4OH_5D_8$	10.74	1.51	5.94
Histidine (His or H)	Hydrogenated	$C_6N_3OH_7$	4.96	1.36	2.84
	H/D Exchange	$C_6N_3OH_5D_2$	6.84	1.38	4.09
	Deuterated	$C_6N_3OD_7$	12.05	1.43	7.20
	D/H Exchange	$C_6N_3OH_2D_5$	9.96	1.41	5.96
Methionine (Met or M)	Hydrogenated	C_5NOSH_9	1.76	1.28	1.03
	H/D Exchange	C_5NOSH_8D	2.80	1.29	1.64
	Deuterated	C_5NOSD_9	11.13	1.36	6.52
	D/H Exchange	C_5NOSHD_8	10.09	1.35	5.91
Cysteine (Cys or C)	Hydrogenated	C_3NOSH_5	1.93	1.62	1.82
	H/D Exchange	$C_3NOSH_3D_2$	4.00	1.65	3.79
	Deuterated	C_3NOSD_5	7.13	1.70	6.75
	D/H Exchange	$C_3NOSH_2D_3$	5.05	1.67	4.78
	Hydrogenated	C_5NOH_7	2.22	1.25	1.72
	H/D Exchange	C_5NOH_7	2.22	1.25	1.72

Proline (Pro or P)	Deuterated	C_5NOD_7	9.51	1.34	7.36
	D/H Exchange	C_5NOD_7	9.51	1.34	7.35

DNA Nucleotides

Adenine	Hydrogenated	$PN_5O_5C_{10}H_{11}$	10.63
	H/D Exchange	$PN_5O_5C_{10}H_9D_2$	12.71
	Deuterated	$PN_5O_5C_{10}D_{11}$	22.08
	D/H Exchange	$PN_5O_5C_{10}H_2D_9$	20.00
Guanine	Hydrogenated	$PN_5O_6C_{10}H_{11}$	11.21
	H/D Exchange	$PN_5O_6C_{10}H_8D_3$	14.33
	Deuterated	$PN_5O_6C_{10}D_{11}$	22.66
	D/H Exchange	$PN_5O_6C_{10}H_3D_8$	19.54
Cytosine	Hydrogenated	$PN_3O_6C_9H_{11}$	8.67
	H/D Exchange	$PN_3O_6C_9H_9D_2$	10.75
	Deuterated	$PN_3O_6C_9D_{11}$	20.12
	D/H Exchange	$PN_3O_6C_9H_2D_9$	18.04
Thymine	Hydrogenated	$PN_2O_7C_{10}H_{12}$	8.61
	H/D Exchange	$PN_2O_7C_{10}H_{11}D_1$	9.65
	Deuterated	$PN_2O_7C_{10}D_{12}$	21.10
	D/H Exchange	$PN_2O_7C_{10}H_1D_{11}$	20.06

RNA Nucleotides

Adenine	Hydrogenated	$PN_5O_6C_{10}H_{11}$	11.21
	H/D Exchange	$PN_5O_6C_{10}H_8D_3$	14.33
	Deuterated	$PN_5O_6C_{10}D_{11}$	22.66
	D/H Exchange	$PN_5O_6C_{10}H_3D_8$	19.54
Guanine	Hydrogenated	$PN_5O_7C_{10}H_{11}$	11.79
	H/D Exchange	$PN_5O_7C_{10}H_7D_4$	15.95
	Deuterated	$PN_5O_7C_{10}D_{11}$	23.24
	D/H Exchange	$PN_5O_7C_{10}H_4D_7$	19.08
Cytosine	Hydrogenated	$PN_3O_7C_9H_{11}$	9.25
	H/D Exchange	$PN_3O_7C_9H_8D_3$	12.37
	Deuterated	$PN_3O_7C_9D_{11}$	20.70
	D/H Exchange	$PN_3O_7C_9H_3D_8$	17.58

Urasil	Hydrogenated	$PN_2O_8C_9H_{10}$	9.27
	H/D Exchange	$PN_2O_8C_9H_8D_2$	11.35
	Deuterated	$PN_2O_8C_9D_{10}$	19.68
	D/H Exchange	$PN_2O_8C_9H_2D_8$	17.60

Note that the density of nucleotides is estimated to be between 1.73 g/cm^3 and 1.78 g/cm^3. This gives scattering length densities for hydrogenated nucleotides between $3.18*10^{-6}$ Å^{-2} and $3.66*10^{-6}$ Å^{-2}.

A figure summarizes the average scattering length densities (ρ = b/v where b is the scattering length and v is the molecular volume) values for hydrogenated proteins and DNA without H/D exchange (left axis) and with H/D exchange (right axis). Average values for deuterated proteins and deuterated DNA without and with D/H exchange are also included (Jacrot, 1976).

Note that the neutron contrast $\Delta\rho^2$ is defined as the difference in scattering length densities (squared) between the macromolecules (proteins or DNA) and the solvent (water). Note that the average scattering length density for hydrogenated proteins is $1.8*10^{-6}$ Å^{-2} (left axis) whereas after H/D exchange (in D_2O) it is $3*10^{-6}$ Å^{-2} (right axis). Note for example that proteins are contrast matched in mixtures of 40 % D_2O and 60 % H_2O.
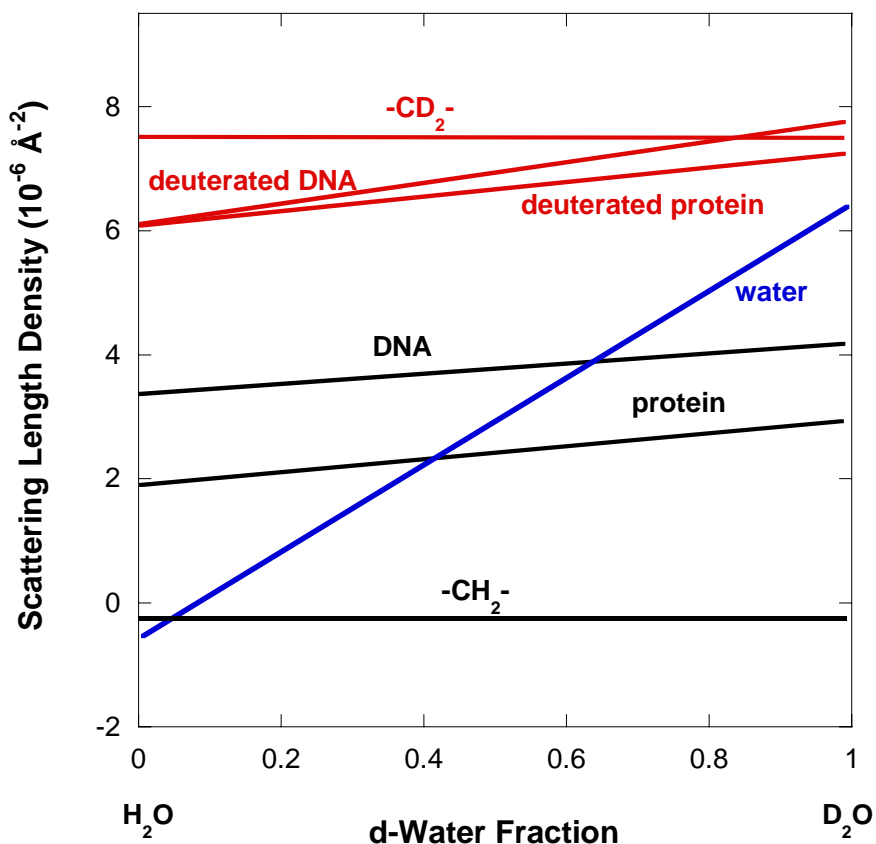
Figure 16: Average scattering length densities for DNA and proteins following H exchange in H_2O (left) or D_2O (right).

REFERENCES

W.M. Becker, L.J., Kleinsmith and J. Hardin, "The World of the Cell", Benjamin/Cummings Publishing (1999)

B. Jacrot, "The Study of Biological Structures by Neutron Scattering from Solution", Rep. Prog. Phys. <u>39</u>, 911-953 (1976)

QUESTIONS

1. What are biological membranes made out of?
2. What is a condensation reaction? Where do condensation reactions take place?
3. What are the main components of DNA? How many amine bases are there? Name them.
4. What is the difference between DNA and RNA?
5. What are the main conformations of proteins?
6. How many amino acids are used in the synthesis of proteins?
7. How is the genetic DNA code used for the synthesis of proteins?
8. What is the prominent component of polysaccharide? Name a couple of polysaccharides.
9. Which cell organelle is the center of energy production?
10. How is dialysis used to enhance the neutron contrast?

ANSWERS

1. Biological membranes are made out of lipids with hydrophilic heads and hydrophobic tails. Lipids are produced through the condensation reaction of glycerol and a fatty acid group.
2. A chemical reaction is referred to as a "condensation reaction" when a water molecule is a byproduct. Condensation reactions occur during the synthesis of lipids, of DNA and of proteins.
3. DNA is formed of phosphate groups, sugars and amine bases. There are four amine bases. These are Adenine (A), Thymine (T), Guanine (G) and Cytosine (C).
4. The main difference between DNA and RNA is in the sugar group. DNA contains desoxyribose wheareas RNA contains ribose. Moreover, in RNA, Thymine is replaced by Urasil (U).
5. Proteins conformations are the alpha helix, the beta sheet and the randon coil.
6. There are 20 amino acids involved in the synthesis of proteins.
7. The sequence of three nucleotides codes for the addition of a specific amino acid in the synthesis of a peptide sequence.
8. Polysaccharides are made through the polymerization of sugars. Starch and cellulose are plant polysaccharides. Glycogen and chitin are animal polysaccharides.
9. The mitochondrion is the center of energy production. Energy is produced through the oxidation mainly of sugars.

10. A dialysis bag (containing the macromolecules) is used inside a container full of d-water in order to enhance deuterium exchange. This results in partially deuterated macromolecules (DNA or proteins) by deuterium exchange on O and N atoms.

Membranes are essential biological components for the integrity of cells and cell constituents. They create a barrier between the outside and the inside and regulate the input and output processes. Cells membranes are composed of surfactant bilayers with hydrophilic head groups and hydrophobic tails. Phospholipids are typical amphiphile surfactants that form biological membranes.

1. PHOSPHOLIPIDS

Phospholipids form a chemical homologous series with increasing hydrocarbon tail. Dimyristoylphosphatidylcholine (DMPC) has C14 carbon tail, dipalmitoylphosphatidylcholine (DPPC) has C16 carbon tail, distearoylphosphatidylcholine (DSPC) has C18 carbon tail, and diactylphosphatidylcholine (DAPC) has C20 acyl hydrocarbon tail, etc. These are membrane lipids that contain two saturated symmetric hydrocarbon chains. The choline group is charged and acts as the surfactant head group which interfaces with water. The acyl fatty acid groups form the hydrophobic bulk of the lipid layers.
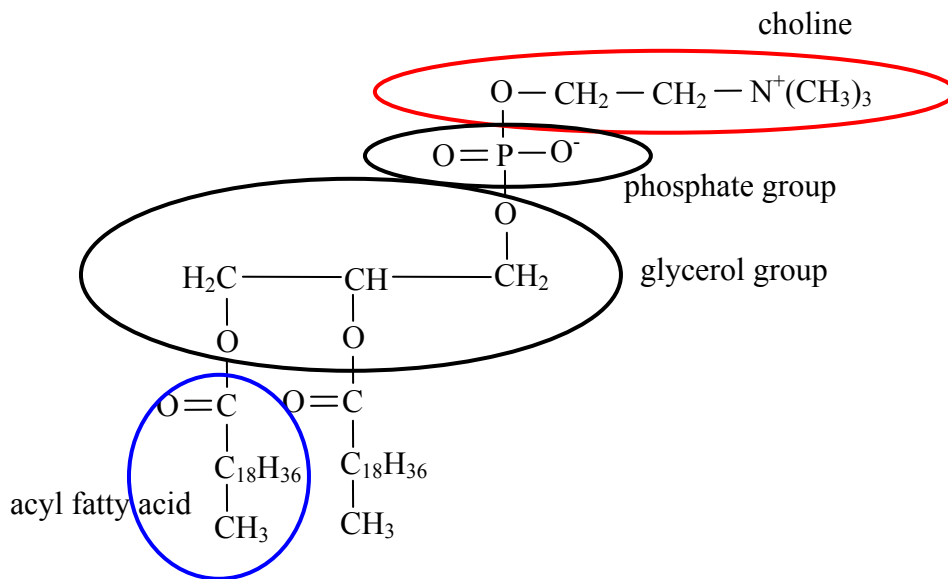
Diacyl-phosphatidylcholine (DAPC)

Figure 1: The various groups that form DAPC.

2. PHOSPHOLIPID BILAYERS PHASES

Phospholipids form smectic phase bilayers in the presence of water. The bilayers are formed of alternating hydrophilic and hydrophobic layers. Many phases have been identified using optical and diffraction methods. Some of these phases are: the liquid crystalline phase (L_α)

obtained at high temperature, the ripple gel phase (P_β) obtained at intermediate temperature, the lamellar gel phase (L_β) obtained at low temperature, and the lamellar crystalline phase (L_c) obtained at even lower temperature. Note that similar primed phases such as $L_{\beta'}$ and $P_{\beta'}$ correspond to tilted hydrocarbon tails forming the structures. A variation of the L_β phase is the interdigitated phase ($L_{\beta I}$).

L_β

Lamellar gel phase

$L_{\beta I}$

Interdigitated phase

P_β

Ripple phase

L_α

Liquid crystalline phase

L_c

Lamellar crystalline phase
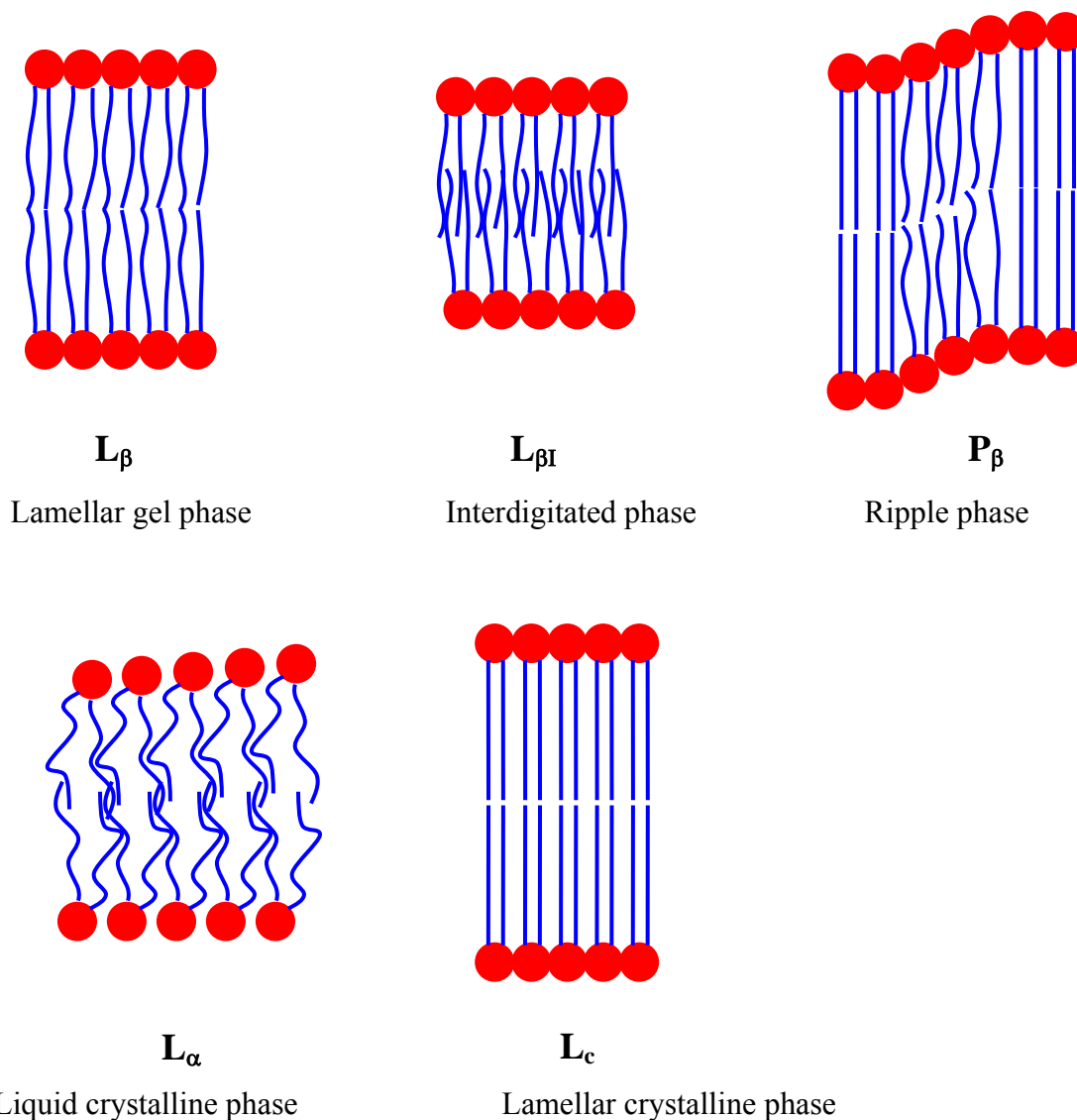
Figure 2: The main phospholipid bilayer phases.

The interdigitated phase is induced by a number of factors including (1) small amphiphilic (cosurfactant) molecules such as ethanol, ethylene glycol, etc and (2) pressure. The effect of hydrostatic pressure is described here when used in conjunction with small-angle neutron scattering (SANS).

3. SANS UNDER PRESSURE

The SANS technique was used to investigate the transitions between the various bilayer phases in DAPC (characterized by C20) and with in-situ pressure and temperature control (Worcester-Hammouda, 1997). The sample contained about 2 % DAPC (mass fraction) in d-water and was formed of multi-lamellar vesicles. Pressure was varied up to 1 kbar (14.7 kpsi) and temperature was varied from 50 ^{o}C to 85 ^{o}C. A figure shows the case corresponding to 70 ^{o}C. The liquid crystalline phase L_α, the ripple gel phase P_β and the interdigitated phase $L_{\beta I}$ are clearly observed. They are identified by widely different structural features.

DAPC at 70 ^{o}C
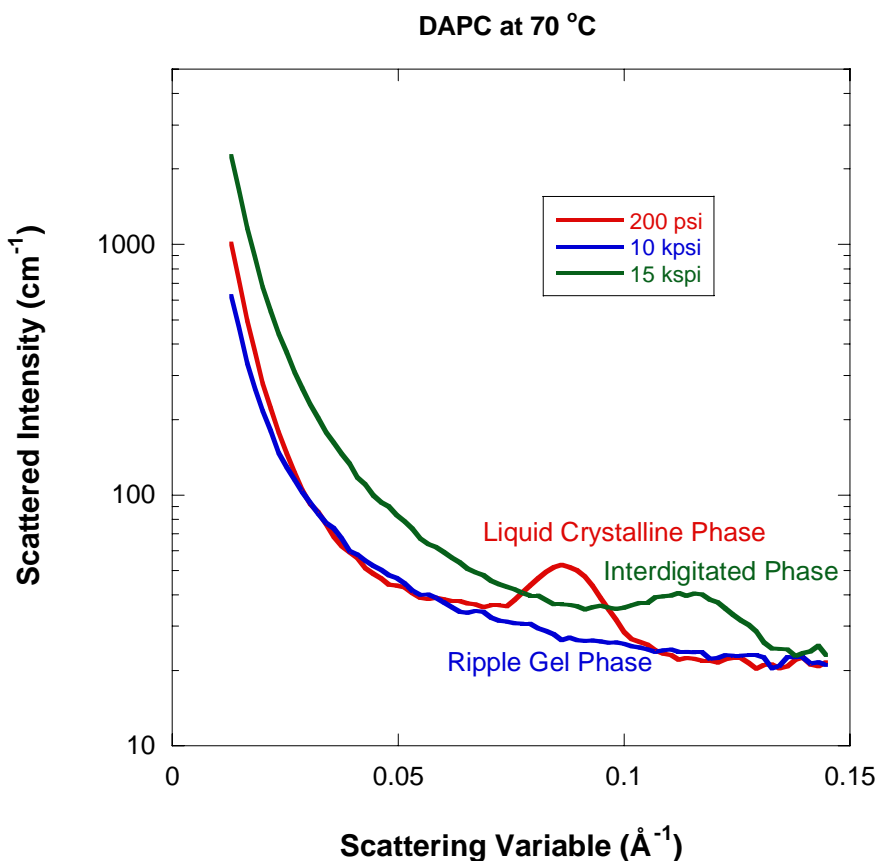
Figure 3: SANS from DAPC phospholipid bilayers at 70 ^{o}C. Increasing pressure induces structural phase transitions.

The following peak positions are obtained for the P_α and $L_{\beta I}$ spectra $Q_0 = 0.085$ Å^{-1} and $Q_0 = 0.114$ Å^{-1} respectively. These correspond to inter-layer d-spacings (= $2\pi/Q_0$) of 73.57 Å and 54.92 Å for the P_α and $L_{\beta I}$ phases respectively at 70 ^{o}C.

4. THE PHASE DIAGRAM

Using this method of identifying the various phases by their SANS diffraction pattern, an entire phase diagram has been constructed by varying pressure and temperature. The interdigitated phase forms only at high pressure.

Formation of the interdigitated phase by hydrostatic pressure is largely driven by the packing of acyl chains. This is otherwise difficult to achieve because of the large cross-sectional areas of the polar head groups. The curved phase boundary for interdigitation demonstrates complex properties for this packing.

DAPC (C20) Phospholipid Bilayers
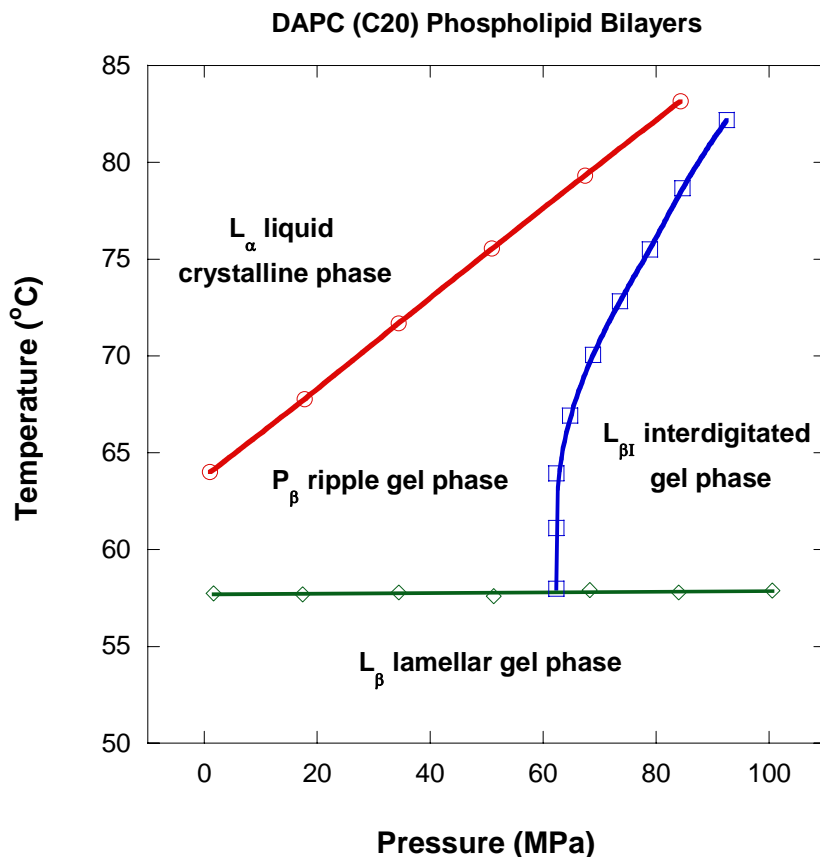
Figure 4: The temperature-pressure phase diagram for DAPC. Note that 14.7 kpsi = 1 kbar = 100 MPa.

Similar temperature-pressure phase diagrams have been mapped out for other phospholipid/d-water systems (for example DPPC and DSPC).

5. COMMENTS

This exercise shows once again that the SANS technique is a useful tool for resolving structures and mapping out phase boundaries. It also demonstrates the advantage of SANS measurements with in-situ pressure.

The field of membrane research has benefited from SANS as well as Neutron Reflectometry (NR). Just like SANS, NR can probe in-plane structures through the so-called off-specular scattering component.

REFERENCES

D. Worcester and B. Hammouda, "Interdigitated Hydrocarbon Chains in C20 and C22 Phosphatidylcholines Induced by Hydrostatic Pressure", Physica B: Condensed Matter 241-243, 1175-1177 (1997).

QUESTIONS

1. What are the major components of a biological membrane?
2. What is a surfactant?
3. What is the difference between DMPC, DPPC, DSPC and DAPC?
4. What is a smectic phase? How about a nematic phase? How about an isotopic phase?

ANSWERS

1. A biological membrane is formed of phospholipid bilayers.
2. Phospholipids are surfactant molecules containing a hydrophilic head and a hydrophobic tail.
3. The difference between the various phospholipids in the series is the length of the hydrocarbon tail with DMPC (has C14), DPPC (has C16), DSPC (has C18) and DAPC (has C20).
4. A smectic phase is a liquid crystalline phase with both translational and orientational order. A nematic phase is characterized by translational order and orientational disorder. An isotopic phase has translational and orientational disorder.

1. THE DNA DOUBLE HELIX

Desoxyribo-nucleic acid (DNA) is the basic building block for life. It codes for the synthesis of proteins inside living cells by controlling the amino acid sequences that form the genes. DNA is formed of backbone phosphates, linked to desoxyribose sugars and side group amine bases. The charged phosphate groups are hydrophilic, the desoxyribose sugar groups are mostly hydrophobic, and the amine bases contain both hydrophobic and hydrophilic groups. DNA forms a helical structure which is stable because of the stacking of the amine bases and of the hydrogen bonding between them. The helical structure is effective at "hiding" the hydrophobic sugar groups from contact with water. The helix phase melts into disordered coils under various conditions including temperature increase.

Helix   Coil
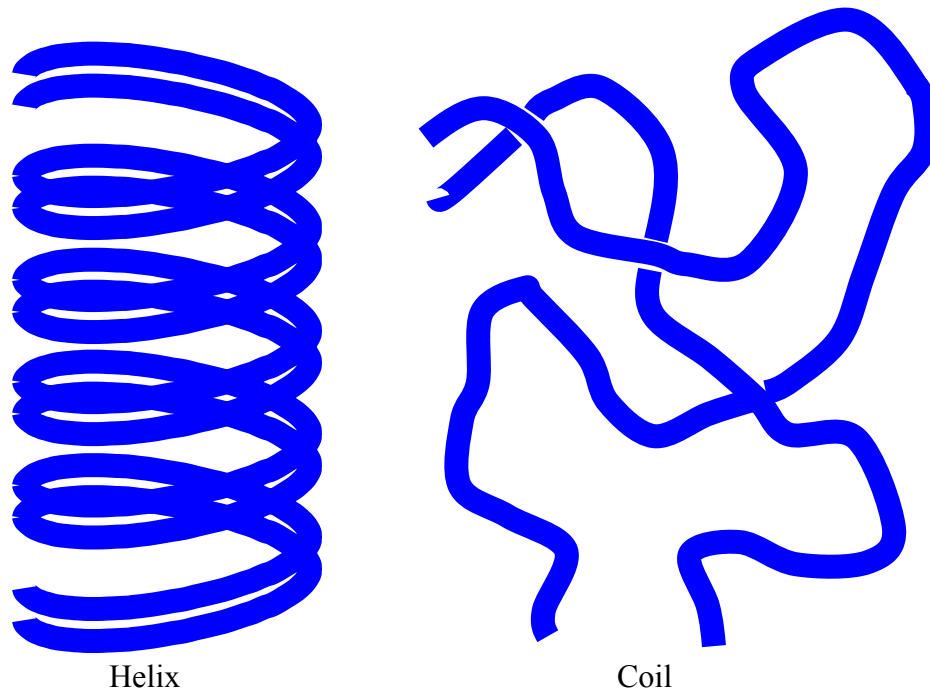
Figure 1: Schematic representation of the DNA helix and coil conformations

DNA macromolecules form helical structures in their active form and melt to a random coil phase in their denatured form. The denaturation transition consists in a helix-to-coil transition that can be promoted either using denaturing agents or through heating. Here, the simpler heating route is discussed using two characterization methods: the UV absorption spectroscopy and SANS.

2. UV ABSORPTION SPECTROSCOPY

Ultra-violet (UV) light absorption spectroscopy is sensitive to the stacking of π-bonded groups such as the amine bases in DNA. It is an effective method to monitor the helix-to-coil transition.

UV Absorption Spectroscopy
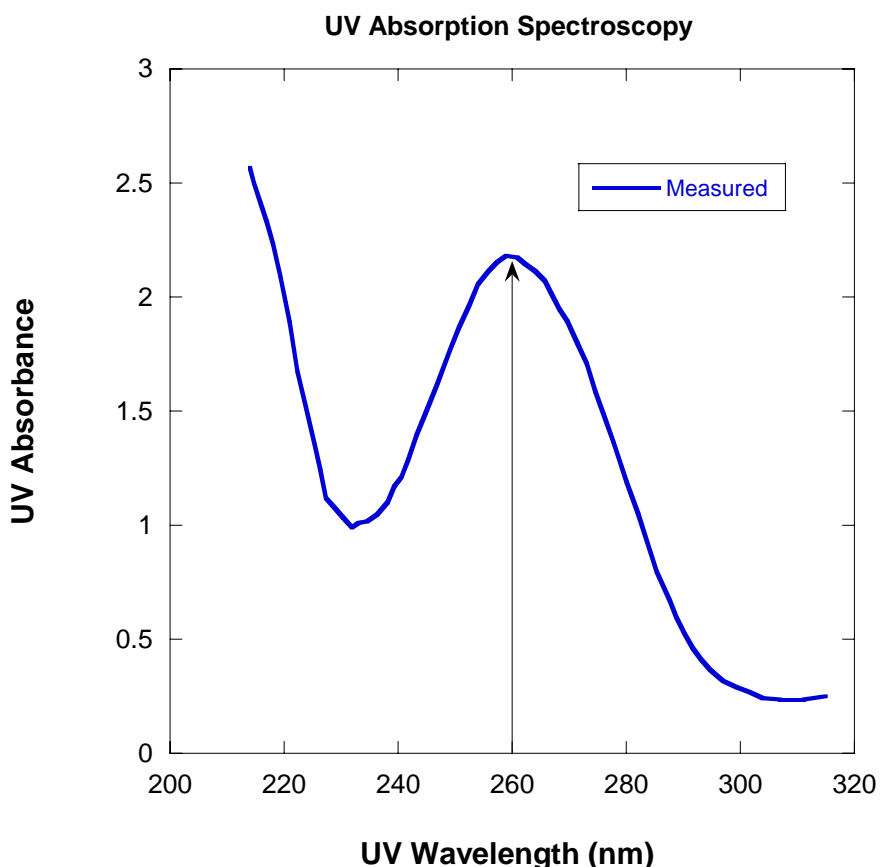
Figure 2: Typical UV absorption spectrum from DNA showing a characteristic peak at a wavelength of 260 nm.

The monitoring of the intensity at the peak position (260 nm) with increasing temperature yields a sigmoid function centered at the helix-to-coil transition temperature. The helix-to-coil transition is mediated by the un-stacking of the amine bases and the breaking of the hydrogen bonds between these bases.

A sample containing 4% salmon DNA (molecular weight of $1.3 *10^6$ g/mol) in water is characterized by a helix-to-coil transition temperature of 94 ^{o}C. Since this temperature is too close to the boiling temperature for water (100 ^{o}C), another solvent was considered as well. A 4% DNA in ethylene glycol is characterized by a more convenient helix-to-coil transition temperature of 38 ^{o}C. The characteristic sigmoid shape function was obtained in each case. The inflection point corresponds to the helix-to-coil melting temperature. In order to avoid saturation of the UV absorbance, 50 μm thin samples were measured.

Since the same DNA samples were investigated by UV absorption spectroscopy and SANS, deuterated solvents were used with both characterization methods. Moreover a 100 mM

NaCl salt content was added throughout in order to screen the charges on the DNA phosphate groups.
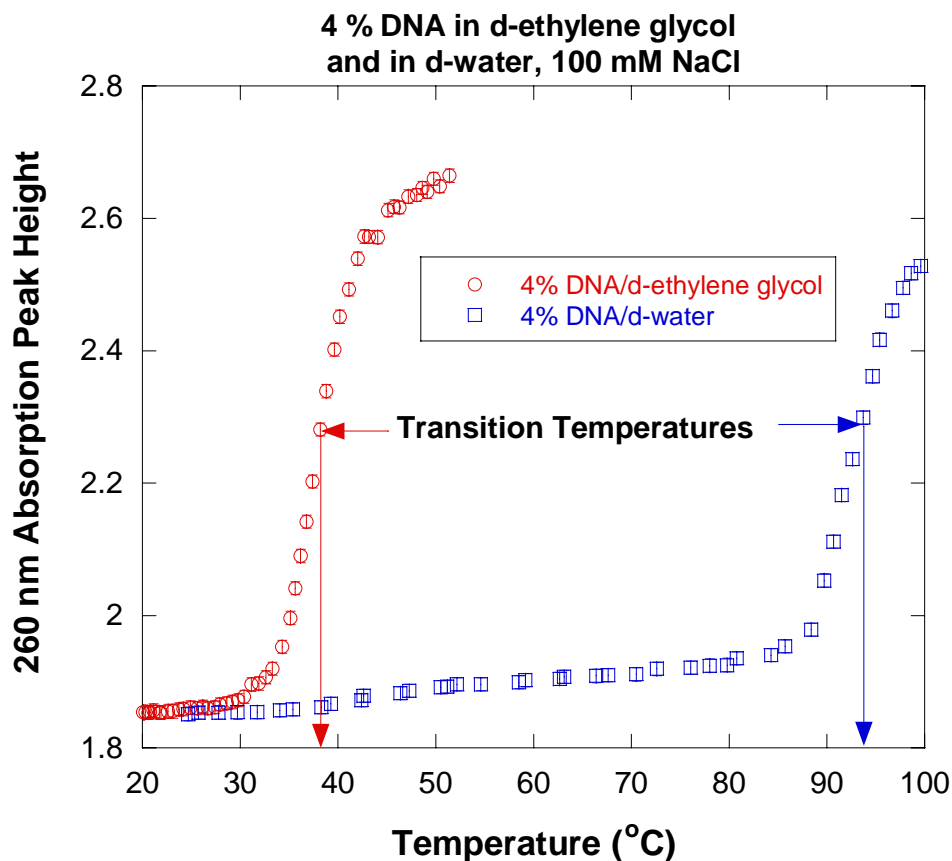
Figure 3: Variation of the UV absorption spectroscopy peak intensities at 260 nm with increasing temperature for 4% DNA in d-water or in d-ethylene glycol. The helix-to-coil transitions can be observed clearly.

3. HELIX-TO-COIL TRANSITION IN MIXED SOLVENTS

The UV absorption spectroscopy provides an effective way to monitor the helix-to-coil transition in d-water/d-ethylene glycol mixed solvents. The same 4% salmon DNA weight fraction and 100 mM NaCl salt content were used.
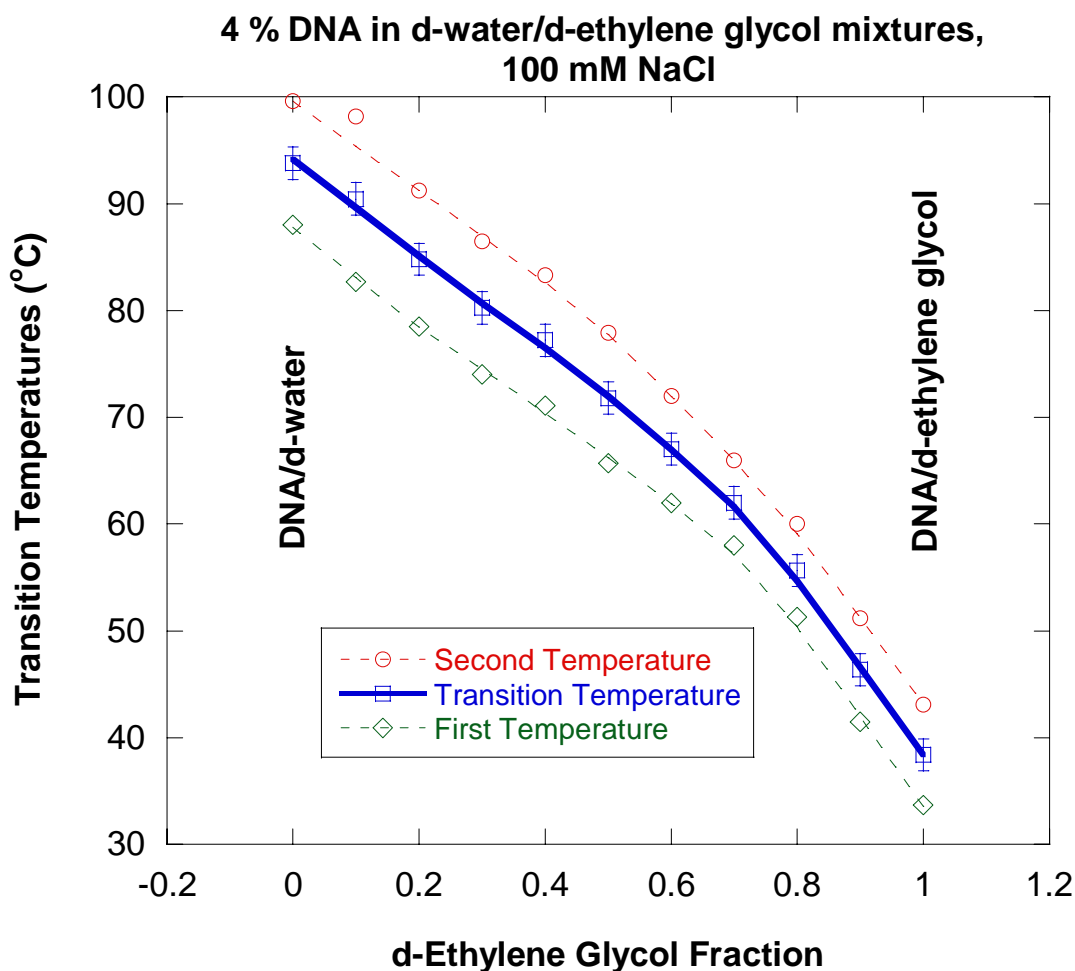
Figure 4: Variation of the helix-to-coil transition temperature for 4 % DNA in mixed d-water/d-ethylene glycol mixed solvents.

The monotonic linear variation is attributed to the fact that the transition was approached from the helix side whereby solvents mix randomly (ideal solvent mixing behavior). The fact that the melting temperature decreases with d-ethylene glycol fraction points to the conclusion that the hydrophobic groups CD_2 in d-ethylene glycol play an important role in the melting transition. They help solvent molecules cross the hydrophobic zone of the desoxyribose sugar groups thereby loosening the helical structure. This argument helps understand the micellar nature of the DNA macromolecules in terms of a hydrophobic sugar region and hydrophilic phosphate and amine base regions. The ability of the solvent to cross the hydrophobic region controls the stability of the helix phase.
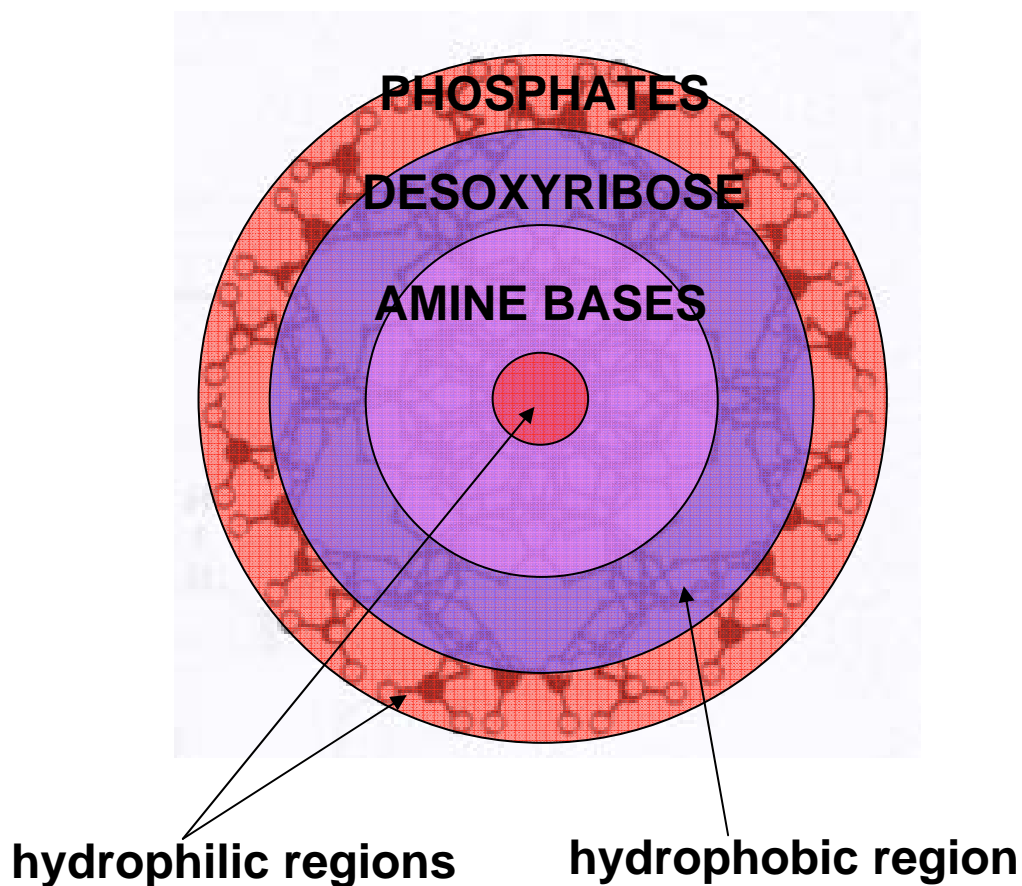
Figure 5: Simple representation of a cross section of the DNA macromolecule.

4. THE HELIX-TO-COIL TRANSITION BY SANS

The SANS technique is effective at determining macromolecular structures. A series of measurements were performed from a 4 % DNA/d-ethylene glycol/100 mM NaCl sample at temperatures ranging from 10 ^{o}C to 80 ^{o}C (at 5 ^{o}C intervals). A figure shows a typical SANS spectrum at two temperatures; one below (25 ^{o}C) and the other one above (50 ^{o}C) the helix-to-coil transition. This temperature is known to be 38 ^{o}C based on US absorption measurements (Hammouda-Worcester, 2006).

4 % DNA in d-ethylene glycol, 100 mM NaCl
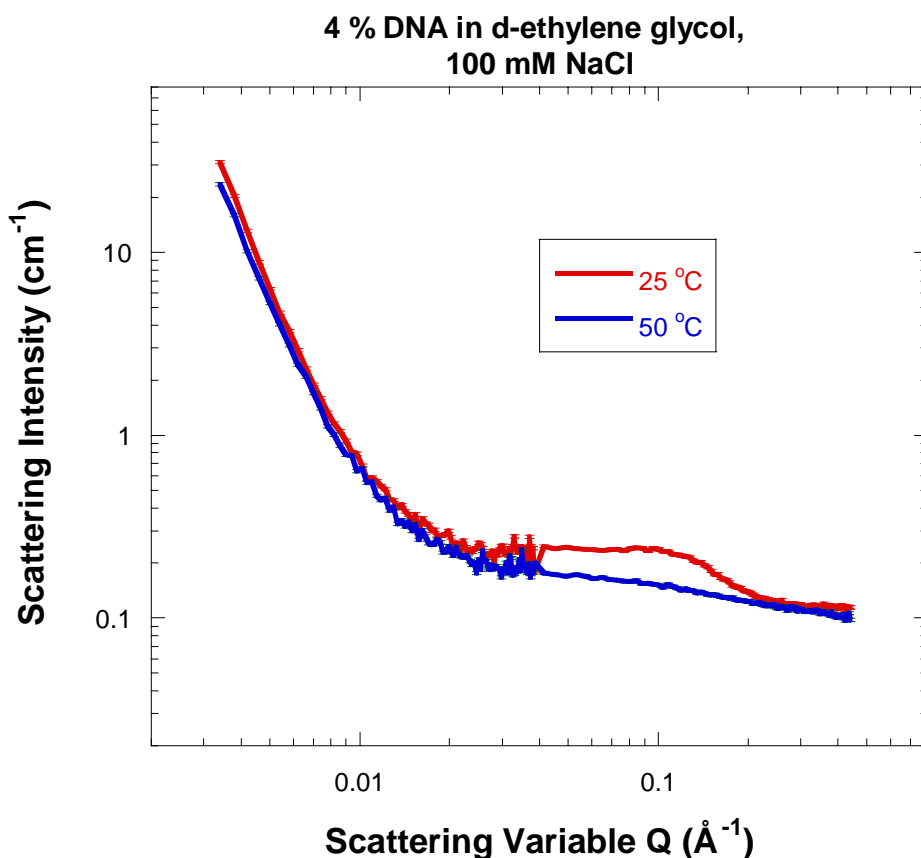
Figure 6: SANS from a 4 % mass fraction DNA/d-ethylene glycol/100 mM NaCl sample measured at temperatures below (25 °C) and above (50 °C) the helix-to-coil melting temperature.

The high-Q signal is distinctively different in the two cases. The data show an abrupt decrease in the high-Q intensity for the helix phase but a gradual decrease for the coil phase.

The SANS data were fit to the following empirical functional form that reproduces the main data features:

$$I(Q) = \frac{A}{Q^n} + \frac{C}{1+(Q\xi)^m} + B.$$

(1)

The term A/Q^n represents the low-Q clustering (network) scattering part and the term $C/[1+(Q\xi)^m]$ represents the high-Q solvation part. B represents a Q-independent (mostly incoherent) background. The low-Q part represents scattering from a large gel network structure. It does not change much across the melting transition. Our focus here is on the high-Q signal exclusively.

A figure shows the variation of the "solvation intensity" (the fitted quantity C) for increasing temperature. The intensity drop between 25 °C and 40 °C characterizes the helix melting transition. Lowering temperature shows that this transition is weakly reversible with

substantial hysteresis. Further temperature increase beyond the melting transition increases the solvation intensity. This result is typical of water-soluble polymers which are characterized by a Lower Critical Solution Temperature (LCST).
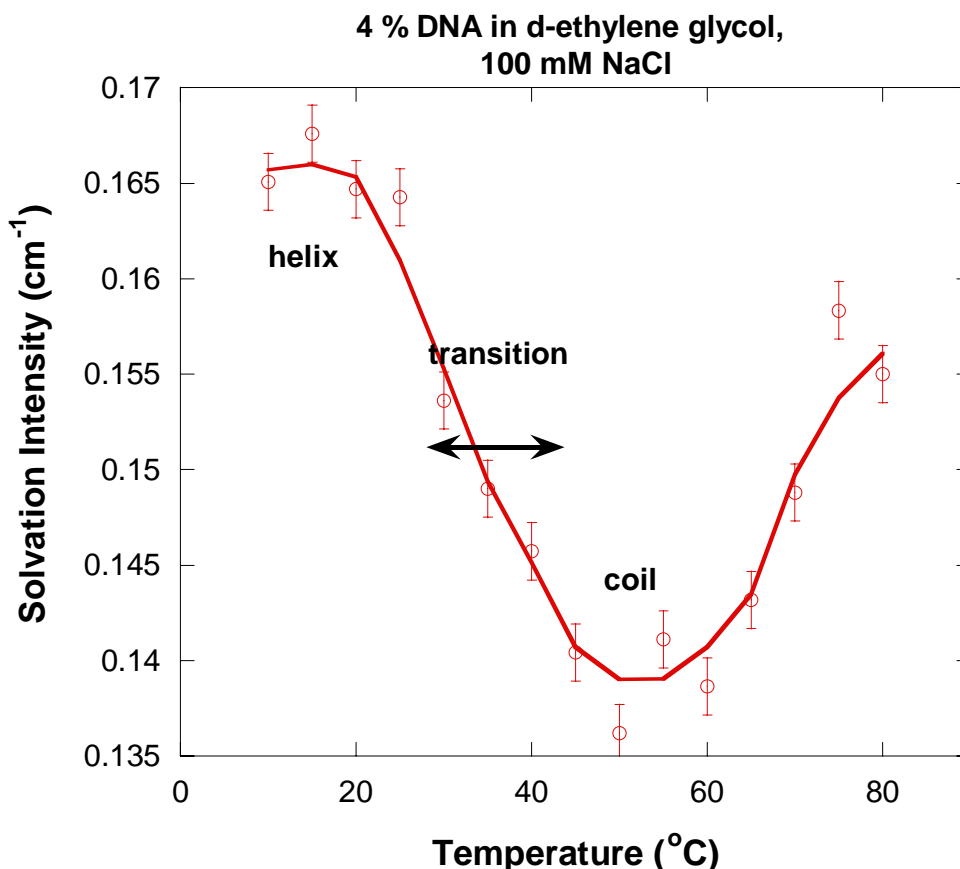
Figure 7: Variation of the SANS solvation intensity (the quantity C in the empirical model) for increasing temperature. For temperatures beyond the melting transition, the solvation intensity increases.

The correlation length ξ also varies across the melting transition. This correlation length represents a weighted-average inter-distance between the hydrogen-containing (sugar-amine base) groups. It is around 8.5 Å in the helix phase and increases to 12.3 Å in the coil phase. In the helix phase the sugar-amine base groups are closer together than in the coil phase. This increase in ξ is due to the opening of the tight helical structure into a loser coil configuration. This correlation length is not a measure of the DNA radius. Raising the temperature further in the coil phase increases the correlation length even further; this is a familiar trend for LCST systems.
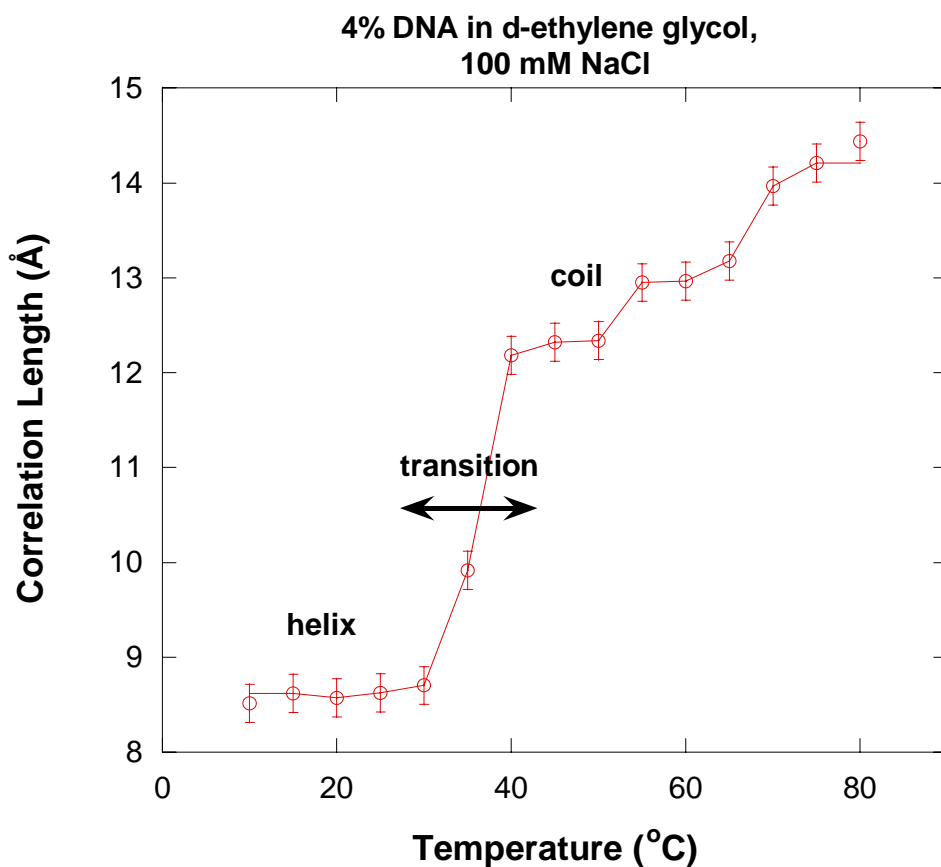
Figure 8: Variation of the correlation length (the quantity ξ in the empirical model) for increasing temperature. After melting, DNA coils swell with further temperature increase.

Finally the high-Q Porod exponent m is seen to vary between values around 3.7 in the helix phase to values close to 1.7 in the coil phase. DNA helices are appearing like cylinders with fairly smooth surfaces (Porod exponents close to 4) and DNA coils behave like polymer chains in good solvent conditions or in a fully swollen chain configuration (Porod exponent of 5/3 = 1.67).

4 % DNA in d-ethylene glycol, 100 mM NaCl
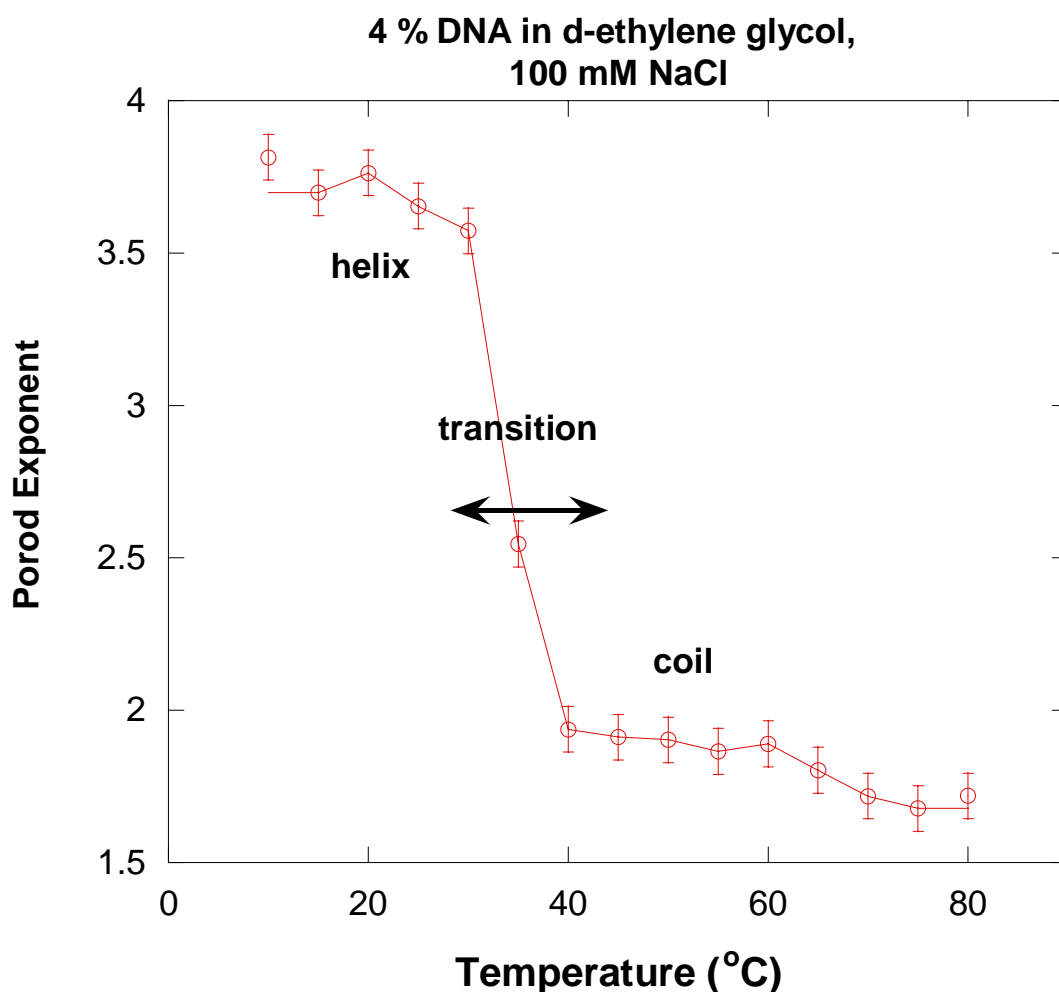
Figure 9: Variation of the high-Q Porod exponent m for increasing temperature. This exponent varies from 3.7 (cylinder) to 1.7 (swollen coil).

It is noted that the rod-like nature of DNA (Porod exponent around 1) has not been seen due to the clustering signal overwhelming the low-Q scattering. It is also noted that once the melting transition has taken place, DNA coils behave like typical water-soluble synthetic polymer chains.

5. A HELIX-TO-COIL TRANSITION MODEL

Helix-to-coil transition models have been published by many authors including Zimm (Zimm, 1959). The formulation from Flory's book (Flory, 1969) will be followed closely here.

Consider a macromolecule consisting of N units (think residues) comprising ν helical sequences. There is a total of N_H helical units and $N_C = N - N_H$ coil units. Define the partition function for the melting of one helical unit as $s = \exp(\Delta H_m/RT)$ where ΔH_m is the enthalpy needed, R is the molar gas constant (related to the Boltzman constant k_B through Avogadro's

number N_{Av} as $R = k_B N_{Av}$) and T is the temperature in absolute units. Assume that it takes no enthalpy to form a coil so that the partition function for a coil unit is equal to 1. Define the partition function for the removal of one helical sequence as σ. The partition function for the helix-to-coil melting process is:

$$Z = \sum \prod s^{N_H} \sigma^v . \tag{2}$$

The product $\prod$ is taken over all helical units N_H and all helical sequences v and the summation $\sum$ is taken over all possible configurations (i.e., over all possible unit arrangements to form the macromolecule with N units).

helical unit

helical sequence
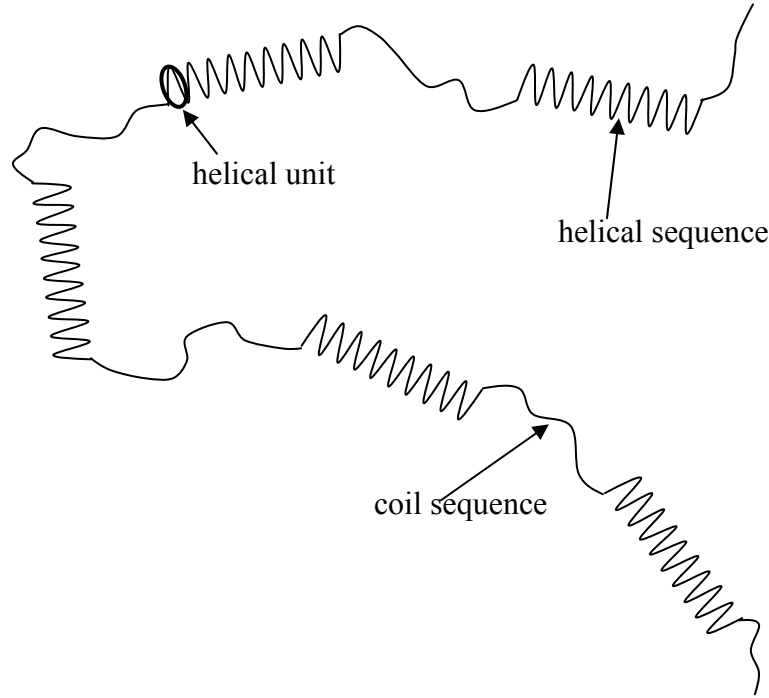
coil sequence

Figure 10: Schematic representation of the helical and coil sequences.

The partition function can be expressed in matrix notation as:

$$Z = J^* \, U^N \, J. \tag{3}$$

With:

$$J^* = \begin{bmatrix} 1 & 0 \end{bmatrix} \qquad U = \begin{bmatrix} 1 & s\sigma \\ 1 & s \end{bmatrix} \qquad J = \begin{bmatrix} 1 \\ 1 \end{bmatrix}. \tag{4}$$

J^* means that the macromolecule starts with a coil unit and J means that it finishes with either a coil or a helical unit. In order to perform the U^N product, the configuration matrix U is diagonalized into the form $U = A \Lambda A^{-1}$ where Λ is a diagonal matrix. U^N simplifies as $U^N = A \Lambda^N A^{-1}$. The eigenvalues λ_1 and λ_2 (diagonal elements of matrix Λ) are given by:

$$\lambda_1 = \frac{(1+s) + \sqrt{(1-s)^2 + 4\sigma s}}{2} \qquad \lambda_2 = \frac{(1+s) - \sqrt{(1-s)^2 + 4\sigma s}}{2}. \tag{5}$$

The partition function can then be summed up to become:

$$Z = \frac{(1-\lambda_2)}{(\lambda_1 - \lambda_2)} \lambda_1^{N+1} + \frac{(\lambda_1 - 1)}{(\lambda_1 - \lambda_2)} \lambda_2^{N+1}. \tag{6}$$

The fraction of units in the helical state is given by:

$$p_H = \frac{1}{N} \frac{\partial \ln(Z)}{\partial \ln(s)} \tag{7}$$

The fraction of units in the coil state is $p_C = 1 - p_H$. In the case of long macromolecules ($N \gg 1/2\sqrt{\sigma}$), p_H simplifies to:

$$p_H = \frac{\partial \ln(\lambda_1)}{\partial \ln(s)} = \frac{(\lambda_1 - 1)}{(\lambda_1 - \lambda_2)}. \tag{8}$$

The relative number of helical sequences is given by:

$$p_\sigma = \frac{\partial \ln(\lambda_1)}{\partial \ln(\sigma)} = \frac{(\lambda_1 - 1)(1 - \lambda_2)}{\lambda_1 (\lambda_1 - \lambda_2)}. \tag{9}$$

The average number of helical units per helical sequence y_H is given by the ratio:

$$y_H = \frac{p_H}{p_\sigma} = \frac{\lambda_1}{(1 - \lambda_2)}. \tag{10}$$

In the notation used here, the total number of helical units is $N_H = N\, p_H$ and the number of helical sequences is $\nu = N\, p_\sigma$.

The meaning of the various parameters is discussed here. First what is the meaning of parameter s? The helix-to-coil transition is driven by heating of the sample, i.e., by the enthalpy needed to melt one unit ΔH_m. From the definition of s, one can express the deviation from the melting temperature T_m as:

$$T_m - T = \frac{RTT_m}{\Delta H_m} (s-1). \tag{11}$$

This simple relation is obtained by expanding the exponential in the definition of s. The dimensionless variable s can be used instead of T. How to understand the meaning of

parameter σ? Note that at s = 1 (middle of the helix-to-coil melting transition corresponding to temperature T_m) the preceding results simplify to:

$$p_H = \frac{1}{2}, \qquad p_\sigma \cong \frac{\sqrt{\sigma}}{2}, \qquad y_H \cong \frac{1}{\sqrt{\sigma}}. \qquad (12)$$

Right at the transition point (i.e., at $T = T_m$), $v = N\sqrt{\sigma}/2$ represents the number of helical sequences. One can think of σ as a helical sequence "nucleation" parameter. The helix-to-coil transition happens through either a few or many helix-to-coil sequences (think "nucleation centers") depending on the temperature conditions. This transition is similar to the melting transition of crystalline materials that happens through nucleation centers.

Note that this simple model applies to the simplest form of helix-to-coil transition involving single-strand helical structures and "isolated" macromolecules. This would apply to very dilute polypeptide sequences. The case of double-strand helical structures (as in DNA) would involve larger configuration matrices U with enthalpies for the various processes (hydrogen bonding and base stacking for AT or GC pairs). The results described here are approximate but still give useful results for the DNA case. They are applied to some of our UV absorption data.

6. APPLICATION OF THE MODEL TO UV ABSORPTION DATA

Consider the helix-to-coil transition UV absorption data obtained for 4% DNA/100 mM NaCl in d-ethylene glycol. In order to apply the simple model described above, two rescalings of the UV data have are performed: (1) modification of the horizontal temperature axis into the variable s axis using the relationship between T and s given in the previous section and (2) rescaling of the UV data vertical axis to a variation between 0 and 1. Moreover the values R = 1.989 cal/mol.K and 1 cal = 4.18 J are used. The model described here is not sensitive enough to let both ΔH_m and σ float. The melting temperature (T= T_m = 38°C) corresponds to s = 1. A reasonable value for the enthalpy of melting ΔH_m is taken to be ΔH_m = -6 kcal/mole. The data are plotted along with model best fit for the predicted p_C using this value and the best fit value of σ = 0.0037. This simple model reproduces the sigmoid shape of the UV absorption data well.
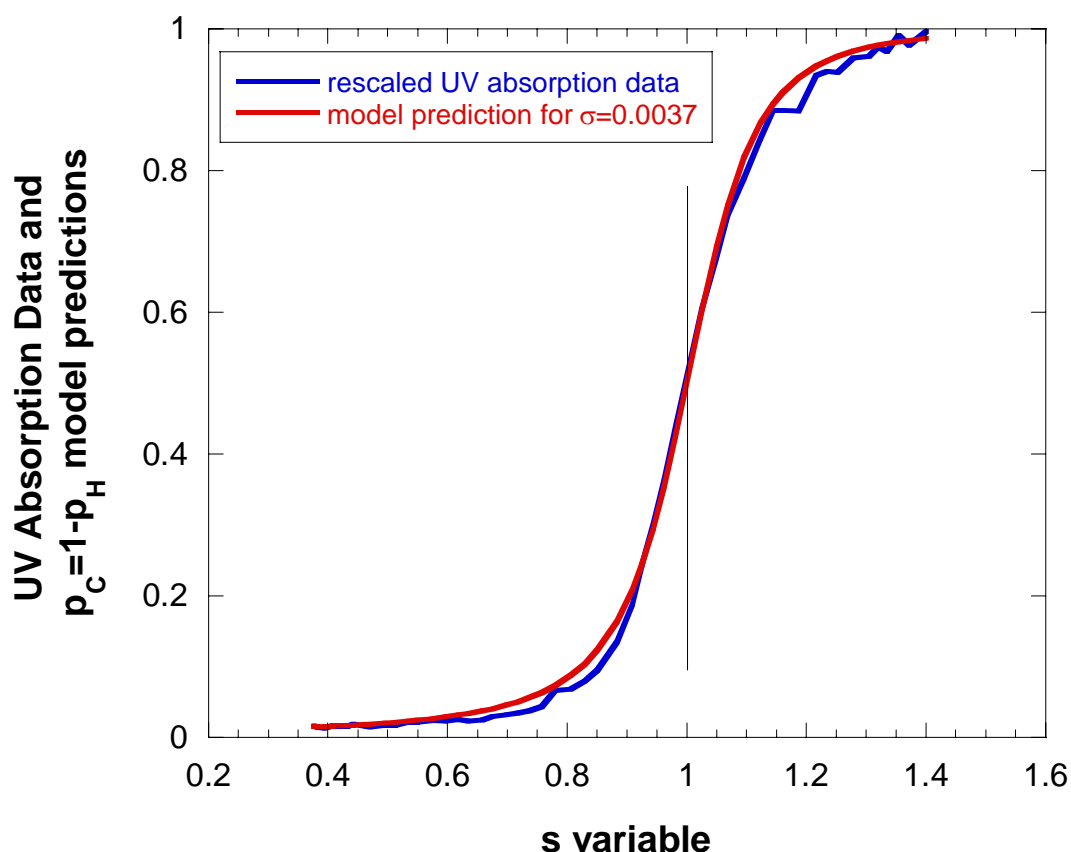
Figure 11: The UV absorption data across the helix-to-coil transition is compared to model prediction for $p_C = 1-p_H$ with the best fit parameter $\sigma = 0.0037$. $\Delta H_m = -6$ kcal/mole has been used.

The relative number of helical sequences p_σ increases, reaches a maximum at s=1 (or $T=T_m$) then decreases. Note that at the melting transition (i.e., for $T=T_m$), $N_H = N/2$ and $p_\sigma = 0.029$ which means that there are 29 helical sequences per 1000 base units.

REFERENCES

B.H. Zimm, and J.K. Bragg, "Theory of the Phase Transition between Helix and Random Coil in Polypeptide Chains", J. Chem. Phys. 31, 526-535 (1959).

P.J. Flory, "Statistical Mechanics of Chain Molecules", Interscience Publishers (1969). Look up mostly Chapter VII.

B. Hammouda and D.L. Worcester, "The Denaturation Transition of DNA in Mixed Solvents", Biophysical Journal 91, 2237-2242 (2006).

QUESTIONS

1. DNA is formed of what units?
2. What drives the formation of the helical structure of DNA?
3. What is the analytical measurement method of choice for observing the helix-to-coil transition?
4. What is the typical helix-to-coil transition temperature for DNA/water? How about for DNA/ethylene glycol?
5. What is the SANS Porod exponent for the helical structure? How about for the coil structure? What do these exponents mean?
6. What is the activation enthalpy for the melting of a helical unit?

ANSWERS

1. DNA is formed of nucleotides.
2. The helical structure of DNA is driven by the stacking of the amine bases and the hydrogen-bonding between them.
3. UV absorption spectroscopy is the analytical measurement method of choice for observing the helix-to-coil transition.
4. A typical helix-to-coil transition temperature of 94 ^{o}C characterizes DNA/water. That temperature is around 38 ^{o}C for DNA/ethylene glycol.
5. A SANS Porod exponent close to 4 characterizes the helical structure and an exponent close to 5/3 characterizes the coil structure. A Porod exponent of 4 is for a cylinder with smooth surface whereas an exponent of 5/3 is for a fully swollen coil.
6. The melting of a helical unit is characterized by an activation enthalpy of -6 kcal/mol.

1. INTRODUCTION

Proteins perform the basic tasks essential for life. Enzymes are proteins that catalyze reactions and perform specialized cell functions. Kinases are a large class of enzymes that add phosphate groups to protein and other biomolecules. In bacteria, kinases coordinate cellular responses to external signals. The function of histidine kinases is to transfer a phosphate group from an ATP molecule to a specific amino acid (histidine) site on the kinase. This transfer mechanism is referred to as phosphorylation. The phosphate is further transferred from the histidine site to another protein.

A histidine kinase named KinA is essential in the sporulation mechanism of bacteria. Sporulation is the formation of spores which are capable of surviving dormant for a long time before reproducing again when external conditions become more favorable. KinA functions in concert with a response regulator named Sda which can halt sporulation when DNA damage is detected. Sda binds onto KinA to stop its autokinase activity thereby stopping its sporulation function by halting the phosphate transfer mechanism.

Histidine kinases are comprised of two domains: (1) a "sensor" domain which recognizes the sporulation signal and (2) an "autokinase" domain which performs the phosphotransfer function.
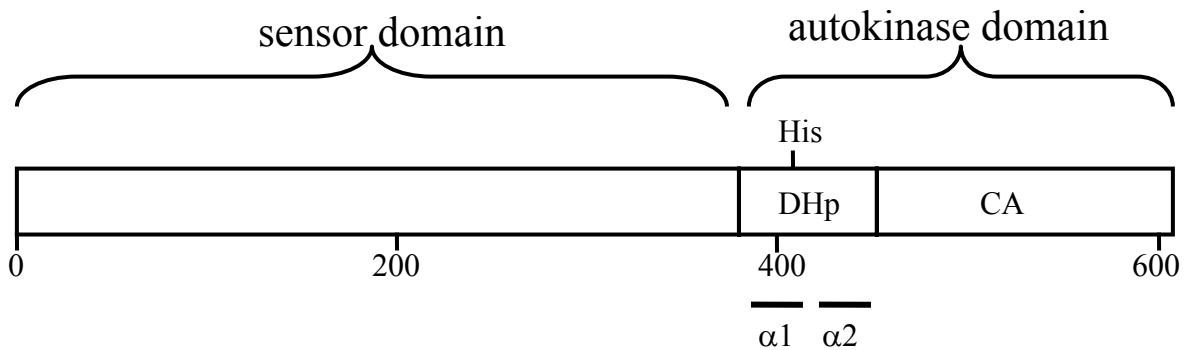
Figure 1: Representation of the two domains that form KinA. The 606 amino acid sequence is marked. The histidine used in the phosphate transfer mechanism is located in position 405.

The autokinase domain is further divided into two sub-domains: two catalytic and ATP binding parts named the CA dimer and a histidine phosphotransfer part named the DHp stalk.
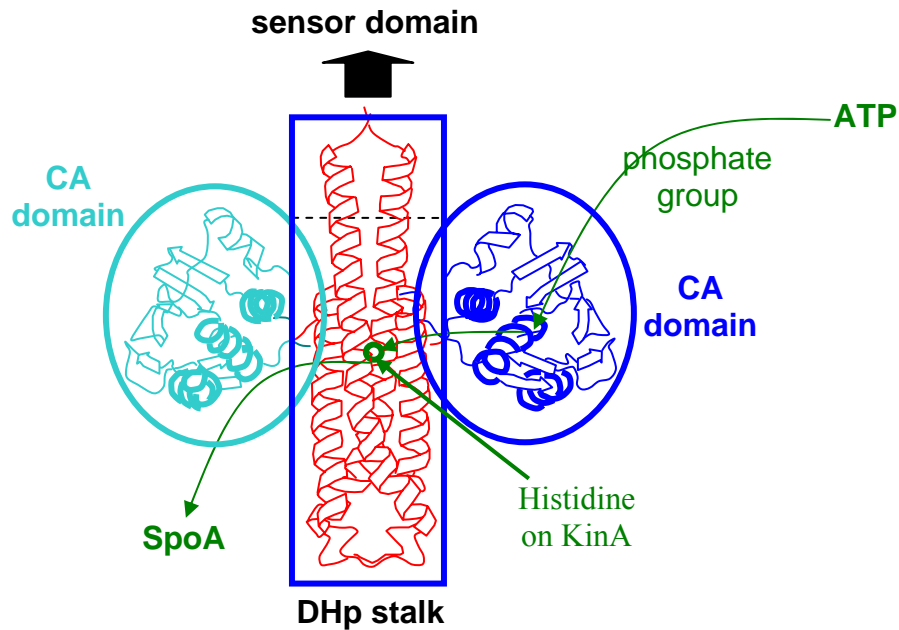
Figure 2: Representation of the dimeric KinA protein comprising the two CA domains and the DHp stalk. One of the two histidine amino acids used in the phosphate transfer mechanism is shown in green. The other one is behind.

KinA is comprised of 606 amino acid residues. The first 383 constitute the sensor domain with three PAS regions and the next 223 constitute the autokinase domain with residues 383-465 for the DHp region and residues 456-606 for the CA dimer region. The amino acid sequence for KinA has been only partly resolved.
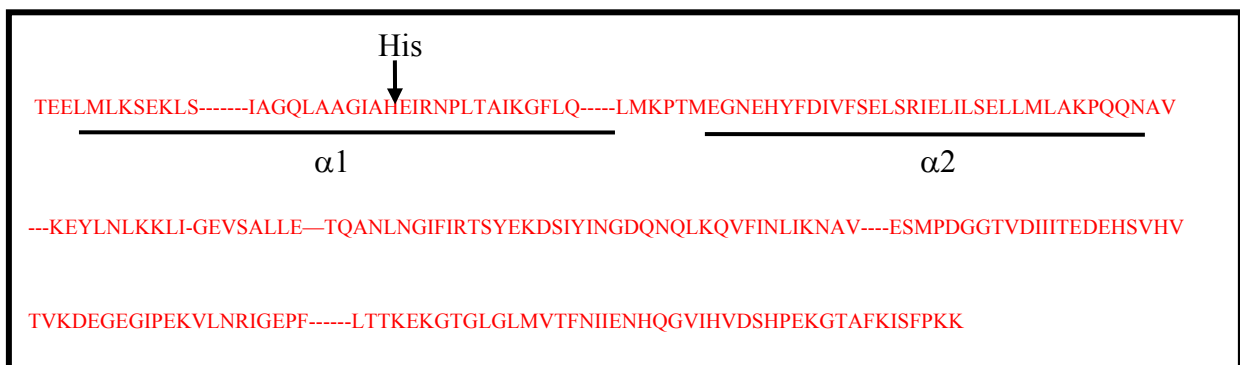
Figure 3: Spelling out of the amino acid residue sequence (383-606) showing two helices α1 and α2 located in the DHp stalk. The histidine used in the phosphate transfer mechanism is shown at position 405. Dash marks corresponds to the sequences that have not been resolved.

The DHp stalk is formed of a bundle of four helices. The two histidine phosphorylation active sites are located halfway along the stalk (helices α1 and α'1). When the sensor domain receives the signal to sporulate, each of the two CA domains transfers a phosphate

group from an adenosine triphosphate (ATP) molecule to one of the two histidine active sites. This is performed through a hinge-like motion of the CA domains; these domains pivot to transfer the phosphate groups.

The response regulator Sda halts (inhibits) the sporulation mechanism performed by KinA when necessary. When Sda binds onto KinA, the phosphotransfer mechanism performed by the CA domains is stopped. The Sda binding region on KinA has been identified as located toward the lower part of the DHp stalk with no direct interaction with the CA domains.

The purpose of the investigations reported here is to understand the positioning of the KinA and Sda parts of the protein complex and to get insight into the sporulation inhibition mechanism (Whitten et al, 2007). This is performed using the SAXS and the SANS techniques.

2. SAXS FROM THE PROTEIN COMPLEX

The KinA and the Sda parts of the protein complex have been characterized by standard methods. The molecular weights have been determined using mass spectrometry and size exclusion chromatography (SEC). These showed the dimer nature of Sda. Kinase assay identified the Sda surface involved in binding the KinA protein. Characterization was performed both on the protein complex and on its individual components.

SAXS was performed on KinA and Sda alone and on the KinA-Sda complex. Two protein complex concentrations in the dilute regime in water were measured.

SAXS from Protein Complex
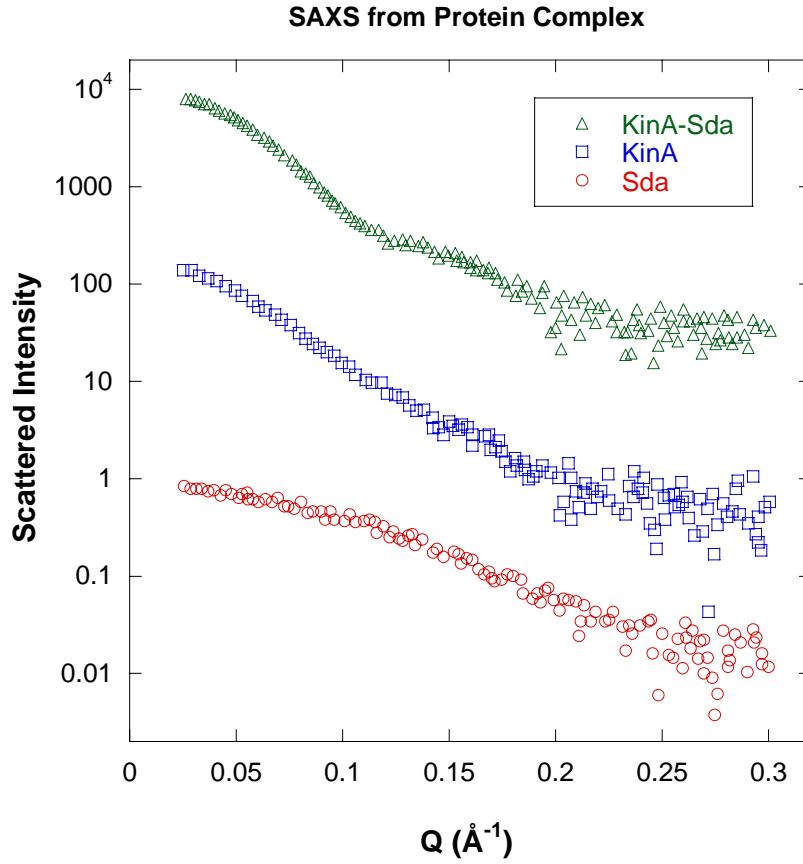
Figure 4: SAXS from dilute solutions of KinA and Sda alone and of the KinA-Sda complex. Curves have been shifted arbitrarily upward not to overlap.

The pair-distance probability distribution function $P(\vec{r})$ is the inverse Fourier transform of the scattering form factor P(Q).

$$P(Q) = \int d\vec{r} \exp(i\vec{Q}.\vec{r})P(\vec{r}) = \int_0^\infty dr 4\pi r^2 \left(\frac{\sin(Qr)}{Qr} \right) P(\vec{r}). \qquad (1)$$

The distance distribution function $4\pi r^2 P(\vec{r})$ (also referred to as the pair correlation function) was obtained and plotted. It gives an estimate of the average size of the KinA, Sda and KinA/Sda complex (peak position) and goes to zero at the particle edge (at D_{max}).
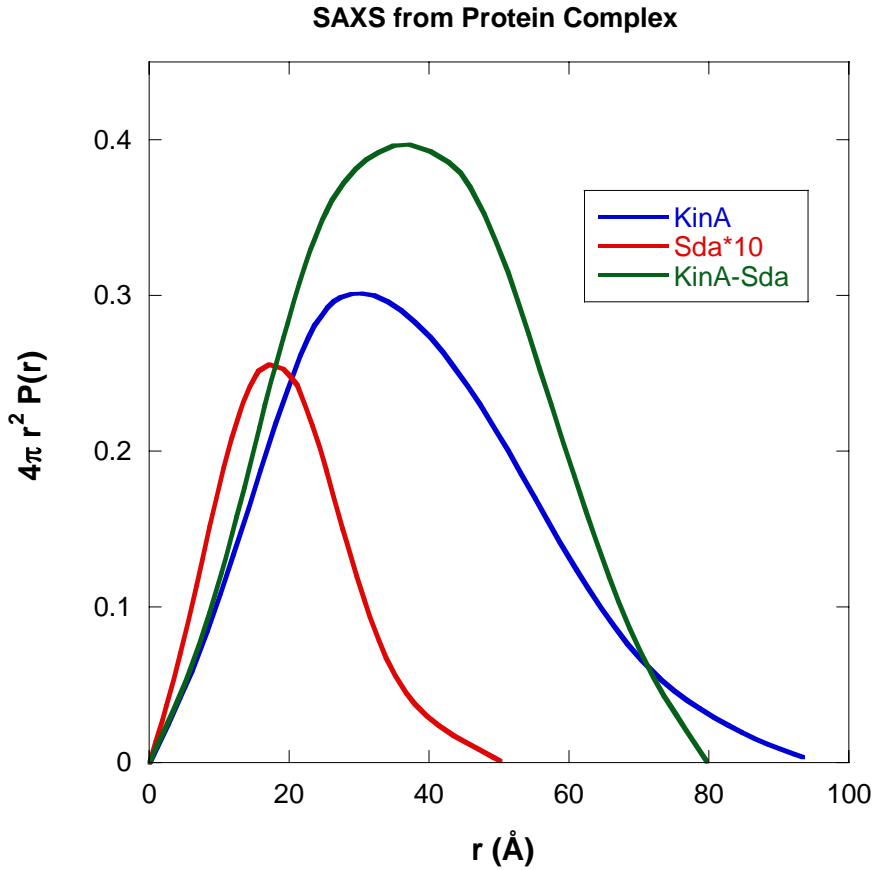
Figure 5: Distance distribution functions obtained from SAXS data from the individual protein and from the protein complex. Scattering from Sda was scaled up (*10).

The radius of gyration is obtained as the second moment of $P(\vec{r})$:

$$R_g^2 = -\frac{3}{2}\left[\frac{\partial^2 \exp(-Q^2 R_g^2/3)}{\partial Q^2}\right]_{Q=0} = -\frac{3}{2}\left[\frac{\partial^2}{\partial Q^2}\left(\int d\vec{r} \exp(i\vec{Q}.\vec{r})P(\vec{r})\right)\right]_{Q=0}$$

$$R_g^2 = \frac{3}{2}\int d\vec{r} \exp(i\vec{Q}.\vec{r})r^2 P(\vec{r}) = \frac{3}{2}\int_0^\infty dr 4\pi r^2 \left(\frac{\sin(Qr)}{Qr}\right)r^2 P(\vec{r}) . \quad (2)$$

R_gs for KinA and Sda were obtained from the Guinier analysis and from the second moment of P(r) analysis and are summarized in a table. Sizes obtained for the KinA/Sda complex showed a compaction of KinA after Sda binding.

Table 1: Size parameters derived from the SAXS Guinier and P(r) data analyses.

Sample	Concentration (mg/ml)	Guinier R_g (Å)	P(r) R_g (Å)	P(r) D_{max} (Å)
KinA	3.7	29.3	29.6	95
Sda	5.2	15.3	15.4	52

| KinA/Sda | 4.4 | 29.2 | 29.1 | 80 |
| KinA/Sda | 3.7 | 29.4 | 29.1 | 80 |

3. SANS FROM THE PROTEIN COMPLEX

SANS measurements were performed with deuterated Sda (d-Sda) complexed with non-deuterated KinA. Both KinA and Sda were overexpressed using E. coli cultures. D-Sda was obtained using a culture in d-water. Two dilute solution concentrations (3.5 mg/ml protein in 50 mM NaCl and 11.9 mg/ml in 200 mM NaCl) were measured. A contrast variation series was performed in each case using mixtures of water and d-water.

Radius of Gyration Analysis

Here also, radii of gyration were obtained for KinA, d-Sda and the KinA/d-Sda complex. In order to estimate the radius of gyration of the complex in terms of the individual radii of gyration, the following argument is used. Consider a compound object formed of two particles: particle 1 (for d-Sda) of volume V_1 and particle 2 (for KinA) of volume V_2 separated by a distance D (between the centers of mass) and define $\Delta\rho_1$ and $\Delta\rho_2$ for their excess scattering length densities ($\Delta\rho_1 = \rho_1 - \rho_0$ and $\Delta\rho_2 = \rho_2 - \rho_0$ where index 0 refers to the solvent).
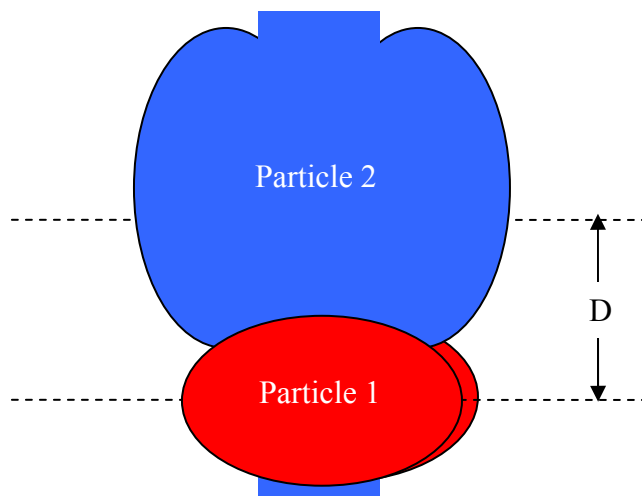
Figure 6: Schematic representation of a compound object formed of two distinct particles. The inter-distance between the centers of mass is D.

According to the parallel axis theorem, the radius of gyration of the compound object is expressed in terms of the individual radii of gyration R_{g1} and R_{g2} as follows:

$$R_g{}^2 = \frac{\Delta\rho_1 V_1}{\Delta\rho_1 V_1 + \Delta\rho_2 V_2} R_{g1}{}^2 + \frac{\Delta\rho_2 V_2}{\Delta\rho_1 V_1 + \Delta\rho_2 V_2} R_{g2}{}^2 + \left(\frac{\Delta\rho_1 V_1}{\Delta\rho_1 V_1 + \Delta\rho_2 V_2}\right)\left(\frac{\Delta\rho_2 V_2}{\Delta\rho_1 V_1 + \Delta\rho_2 V_2}\right) D^2$$

(3)

After a few straightforward manipulations, this can be put into the following Stuhrmann relation (Ibel-Stuhrmann, 1975):

$$R_g{}^2 = R_{gm}{}^2 + \frac{\alpha}{\Delta\bar\rho} - \frac{\beta}{\Delta\bar\rho^2}.$$

(4)

This is expressed in terms of the average neutron contrast $\Delta\bar\rho$ defined as:

$$\Delta\bar\rho = \frac{\Delta\rho_1 V_1 + \Delta\rho_2 V_2}{V_1 + V_2}.$$

(5)

The various parameters are defined as follows:

$$R_{gm}{}^2 = \frac{V_1}{V_1 + V_2} R_{g1}{}^2 + \frac{V_2}{V_1 + V_2} R_{g2}{}^2 + \left(\frac{V_1}{V_1 + V_2}\right)\left(\frac{V_2}{V_1 + V_2}\right) D^2$$

$$\alpha = (\rho_1 - \rho_2)\left(\frac{V_1}{V_1 + V_2}\right)\left(\frac{V_2}{V_1 + V_2}\right)\left[R_{g1}{}^2 - R_{g2}{}^2 + \left(\frac{V_2{}^2 - V_1{}^2}{(V_1 + V_2)^2}\right) D^2\right]$$

$$\beta = (\rho_1 - \rho_2)^2\left(\frac{V_1}{V_1 + V_2}\right)^2\left(\frac{V_2}{V_1 + V_2}\right)^2 D^2.$$

(6)

Variation of the measured radius of gyration (squared) with $1/\Delta\bar\rho$ yields three parameters ($R_{gm}{}^2$, α and β or R_{g1}, R_{g2} and D). The various points were obtained from the contrast variation series. $R_g{}^2$ values were obtained from Guinier plots.

SANS from Protein Complex
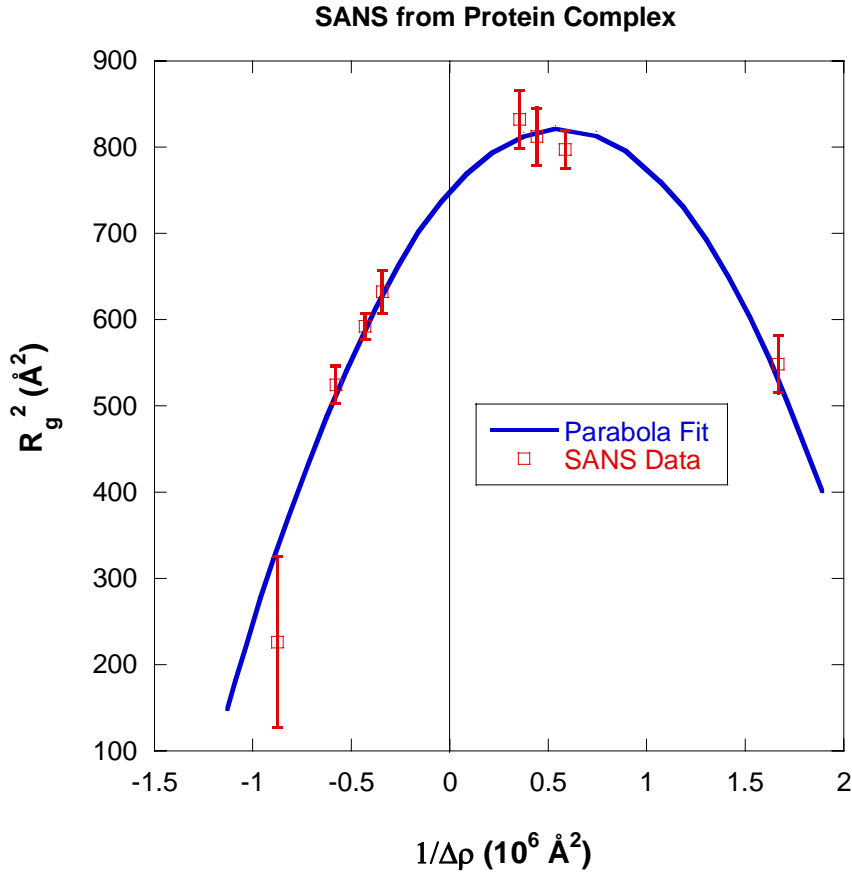
Figure 7: Stuhrmann plot for the KinA/d-Sda complex.

The positive sign for the coefficient α reveals that the higher contrast component (d-Sda) lies towards the periphery of the complex. This is due to the following relation:

$$\left(\frac{V_2^{\,2} - V_1^{\,2}}{(V_1 + V_2)^2}\right) D^2 > \left(R_{g2}^{\,2} - R_{g1}^{\,2}\right). \tag{7}$$

Moreover, it was found that the distance between the centers of mass is $D = 27.0$ Å along with $R_{g1} = 25.3$ Å for d-Sda and $R_{g2} = 25.4$ Å for KinA.

Pair Correlation Function Analysis

The SANS intensity for the contrast variation series from the KinA/d-Sda complex can be modeled as:

$$I(Q) = \Delta\rho_1^{\,2} I_{11}(Q) + \Delta\rho_2^{\,2} I_{22}(Q) + \Delta\rho_1 \Delta\rho_2 2 I_{12}(Q). \tag{8}$$

$I_{11}(Q)$ is the scattering from particle 1, $I_{22}(Q)$ is the scattering from particle 2 and $I_{12}(Q)$ is the cross term representing correlations between a pair of scatterers belonging to the two particles.

SANS from Protein Complex
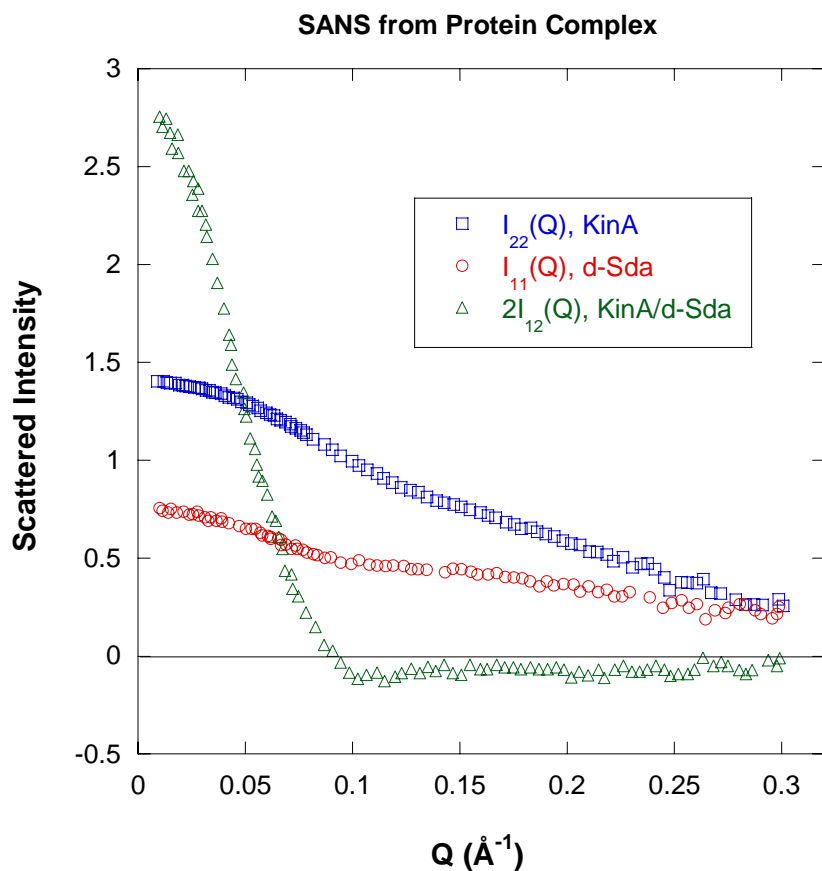
Figure 8: Single-particle and inter-particle form factors $I_{11}(Q)$, $I_{22}(Q)$ and $I_{12}(Q)$ obtained from SANS measurement. Scattered intensity is in arbitrary units.

The inverse Fourier transform for the self and cross terms has been obtained and plotted.
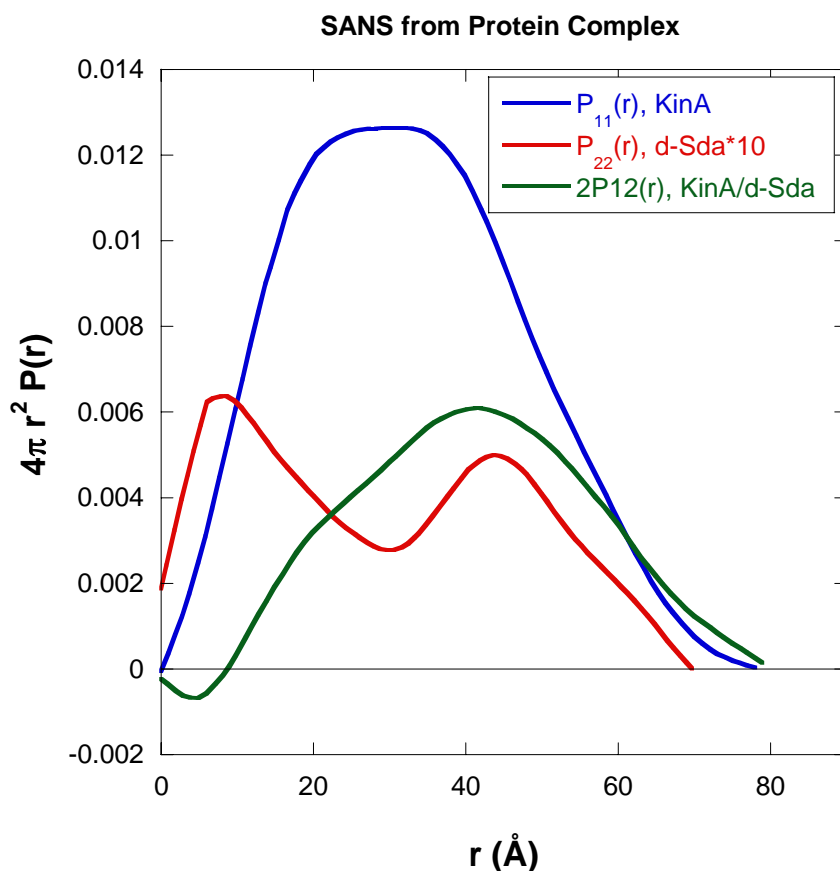
Figure 9: Single-particle and inter-particle pair correlation functions $P_{11}(r)$, $P_{22}(r)$ and $P_{12}(r)$ obtained as the inverse Fourier transform of the form factors.

The pair distribution function for the d-Sda component is characterized by two peaks. Although d-Sda forms dimers when it is alone in solution, it binds to KinA as two individual distinct monomers. The two peaks indicate that centers of mass of the two d-Sda monomers are separated by 45 Å. The KinA and the d-Sda molecules themselves are separated by 27 Å. It is noted that the KinA molecule appears more compact when d-Sda is bound to it. Size parameters obtained from SANS data analyses are summarized in a table.

Table 2: Size parameters derived from the SANS Guinier and P(r) analyses.

Sample	Concentration (mg/ml)	% H_2O	Guinier R_g (Å)	P(r) R_g (Å)	P(r) D_{max} (Å)
KinA/d-Sda	3.7	0	28.9	28.3	80
		10	28.3	28.5	80
		20	28.0	27.9	80
		80	22.5	22.7	80
		90	27.1	24.4	80
		100	25.7	25.1	80
KinA/d-Sda	11.9	0	28.3	28.9	80
		10	28.2	28.3	80

		20	29.1	28.2	80
		80	22.5	23.0	70
		90	24.3	24.2	75
		100	25.3	25.1	75
KinA/d-Sda	26.6	40	26.1	23.4	70

The cross term $P_{12}(r)$ (inverse Fourier transform of $I_{12}(Q)$) is characterized by one peak. This means that the two d-Sda monomers lie approximately equidistant from the two CA catalytic domains and must be located on opposite sides of the lower part of the DHp stalk. Even though the d-Sda monomers are nowhere near the CA domains, they affect their phosphorylation function. This must be performed through a remote (called allosteric) control through the four helix bundle. This bundle is probably disturbing the hinge motion of the CA domains necessary for the transfer of a phosphate group from an ATP molecule to the histidine location in the middle of the DHp stalk. The d-Sda inhibitor is therefore not acting as a molecular barrier to the autokinase motion of the CA domains.
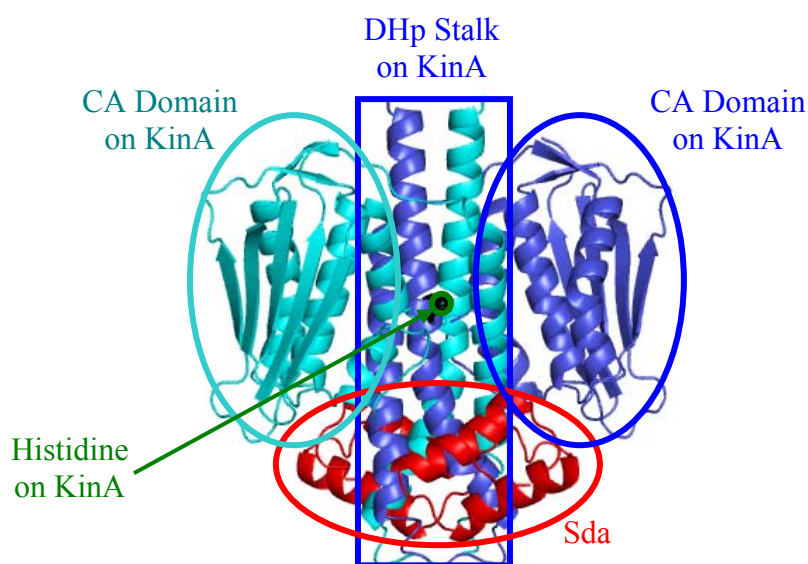
Figure 10: Computer rendering of the KinA/Sda protein complex consistent with the scattering results obtained. The second histidine and the second Sda monomer located on the back are not shown.

4. COMMENTS

The structure of amorphous protein complexes are hard to resolve since no single-crystal diffraction data can be obtained. Small-angle scattering helps resolve the main structural characteristics of such protein complexes. The SANS technique when used with contrast variation and deuterated macromolecules can map out sizes and inter-particle distances between the various components forming the complex. Information obtained from scattering methods and from other techniques helps in the understanding of the mechanisms involved.

A histidine kinase KinA and its inhibitor Sda have been investigated using SAXS and SANS. This protein complex is relevant to the sporulation mechanism in bacteria. Sporulation happens through the transfer of a phosphate group from an ATP molecule to a specific histidine site on the KinA stalk. This is performed by the hinge-like motion of the two CA domains of KinA. The phosphate is further transferred from the histidine site to a sporulation protein (SpoA) that docks onto KinA. The inhibition of the sporulation mechanism is performed when protein Sda forms a complex with KinA. Eevn though Sda is located at the bottom of the DHp stalk, it stops the sporulation mechanism of the KinA CA domains allosterically (i.e., remotely) through conformational changes in the four helix bundle of the DHp stalk.

REFERENCES

A.E. Whitten, D.A. Jacques, B. Hammouda, T. Hanley, G.F. King, J.M. Guss, J. Trewhella, D.B. Langley, "The Structure of the Sda-KinA Complex Suggests an Allosteric Mechanism of Histidine Kinase Inhibition", Journal of Molecular Biology 368, 407-420 (2007)

K. Ibel, H.B. Stuhrmann, "Comparison of Neutron and X-ray Scattering of Dilute Myoglobin Solutions", Journal of Molecular Biology 93, 255-265 (1975)

QUESTIONS

1. What is histidine?
2. What is a kinase?
3. What is an inhibitor? Name a kinase protein and its inhibitor.
4. What is sporulation?
5. What is the difference between a spore and a seed?
6. What is measured through the Guinier plot?
7. What is the pair correlation function $P(\bar{r})$? How about the size distribution function?
8. State the so-called Stuhrmann relation used to analyze SANS data.
9. What is the parallel axis theorem for the radius of gyration? What else is it used for?
10. How are deuterated proteins obtained?

ANSWERS

1. Histidine is one of the 20 amino acid residues. These are the building blocks for proteins.
2. A kinase is a protein that performs the function of phosphorylation. Phosphorylation is the transfer of a phosphate group from an ATP molecule to an active site on the kinase or other molecules.
3. An inhibitor is a protein that stops (inhibits) a specific function. KinA is a histidine kinase used in the sporulation function and Sda is its inhibitor; i.e., it stops that function.
4. Sporulation consists in the formation of spores which package the genetic material of a species. Spores are capable of surviving for a long time before reproducing when external conditions become more favorable.
5. Spores contain the genetic material for reproduction only. Seeds contain the genetic material as well as food for initial growth.
6. The Guinier plot measures the radius of gyration which is a measure of the particle density distribution around the center-of-mass.
7. The pair correlation function $P(\vec{r})$ is the inverse Fourier transform of the scattering intensity (form factor). It is the probability of finding a scatterer at position $\vec{r}$ given that there is a scatterer at the origin. The size distribution function is defined as $4\pi r^2 P(\vec{r})$.
8. The Stuhrmann relation is used to analyze R_g data when a contrast variation series is measured. It related R_g^2 to the average excess scattering length density $\Delta\bar{\rho}$ as follows:

$$R_g^2 = R_{gm}^2 + \frac{\alpha}{\Delta\bar{\rho}} - \frac{\beta}{\Delta\bar{\rho}^2} \cdot R_{gm}^2, \ \alpha \text{ and } \beta \text{ are related to structural parameters.}$$

9. The parallel axis theorem relates the radius of gyration of a compound particle to the radii of gyration of the individual components. The parallel axis theorem is used in cases where the second moment is used. The moment of inertia for compound particles is also calculated that way.
10. Deuterated proteins are obtained from E. coli cultures grown (overexpressed) in d-water.

Biology is the third major SANS research area. It has been growing steadily. This author has processed some 50 papers on SANS in biology published over the past 7 years. These have been sorted out into sub-categories. Some of these papers are included here.

1. DNA AND RNA

The transcription of enzymes that metabolize carbohydrates in E-coli is enhanced by the binding of cAMP receptor protein (CRP) to a specific site on the promoter adjacent to the RNA polymerase binding site. The interaction between CRP and RNA polymerase was investigated. It is entropically driven and increases the binding affinity of the RNA polymerase to the promoter. SANS measurements on the DNA-CRP/mutant complexes in D_2O/H_2O solutions showed an increase in the radius of gyration of the CRP/mutant component. A slight unwinding of the DNA in solution was also observed. This tends to enhance the activation of transcription (Krueger et al, 2003, Paper 079).

Counterions help in the self-assembly of the RNA tertiary structure by neutralizing the electrostatic interactions that oppose the folding process. SANS investigations have been conducted in salts containing Mg^{2+} and Na^+. The RNA was found to be expanded in low salt content and compacted at higher salt content. This result points to a first order collapse transition. Multivalent ions were found to contract RNA more efficiently than monovalent ones (Perez-Salas, 2004, Paper 124).

SANS was used to investigate conformational changes in single-strand DNA comprised of 9 nucleotides across the helix-to-coil transition. DSC scans yielded an estimate of the transition temperature. The transition was broad but reversible (Zhou et al, 2006, Paper 447).

The denaturation (helix-to-coil) transition of salmon DNA has been investigated in solvent mixtures by SANS and UV absorption spectroscopy. The transition temperature was found to be 94 ^{o}C in water and 38 ^{o}C in ethylene glycol. Conformational changes across the transition were reported (Hammouda-Worcester, 2006, Paper 532).

L11 is an important binding functional site in the ribosome. The structure of L11 as well as its complexes with RNA has been investigated by SANS (Lee et al, 2007, Paper 578).

2. LIPIDS AND MEMBRANES

SANS and DLS investigations have been conducted on unilamellar vesicles (ULV) formed of a short and long phospholipids (DHPC and DMPC) doped with DMPG. Focus was put on the effects of lipid concentration and salt content on ULV stability. These are stable for months without the addition of any stabilizer (Yue et al, 2005, Paper 387).

The presence of C_{60} fullerenes promotes structural changes when they are embedded in lipid bilayers. Bilayer orientation has been investigated by many surface and bulk techniques

including SANS, grazing-incidence SAXS and neutron reflectometry (Jeng et al, 2005, Paper 401).

DMPC phospholipids form unilamellar vesicles (ULV). The influence of cholesterol on the ULV bilayer thickness and membrane thermal area expansion have been documented using the SANS technique (Pencer et al, 2005, Paper 418).

SANS, cryo-TEM and DLS were used to study the metal-dependent phase behavior of microbially produced surfactants, the marinobactins. The marinobactins have six amino acid headgourps and fatty monoalkyl acid tail. These are siderophores that facilitate the acquisition of Fe(III). They form micelles that undergo a spramolecular transformation to form vesicles upon the addition of either Cd(II), Zn(II) or La(III). The micelles and vesicles sizes were characterized using standard SANS models (Owen et al, 2007, Paper 601).

3. PROTEINS

A phosphorylation-based switch is commonly used to activate as many as 40 different types of output domains in two-component response regulators. Biochemical and crystallographic studies showed that phosphorylation causes a switch between alternative dimeric forms. SANS was employed to determine the structure of two forms of receiver domains. The structure of one closely resembles that observed in the crystal structure and the fitting solution of the other eliminates two of the four possible dimeric conformations (Nixon et al, 2005, Paper 440).

Recombinant forms of the bacteriophage MS2 and its RNA-free capsid were studied in solution in order to determine if RNA content plays a role in the global arrangement of the protein shell around the virus. Wild-type MS2 and MS2 containing an A protein showed different shell thicknesses (Kuzmanovic et al, 2005, Paper 448).

The irreversible denaturation of pepsin was investigated using SANS, circular dichorism (CD) and differential scanning calorimetry (DSC). Moreover, the secondary and tertiary structures of native, unfolded (alkaline denatured) and acid refolded pepsin were also looked at (Dee et al, 2006, Paper 559).

The multi-domain viral protein HIV-1 named Gag is capable of assembly into a retrovirus-like particle in mammalian cells. SANS and atomic level simulation have been used in order to elucidate the structure and inter-relationship of the individual domains forming Gag. Models consistent with SANS data showed that Gag was folded over. This implies that gag undergoes a major conformational change upon virus assembly (Datta et al, 2007, Paper 567).

A histidine kinase KinA controls activation of the transcription factor governing sporulation. The decision to sporulate involves KinA transferring a phosphate group onto one of its histidine residues. The sporulation inhibitor called Sda halts sporulation by binding to KinA and blocking the autokinase reaction. SAXS and SANS were used to determine the structure of KinA and of the KinA-Sda complex. The use of deuterated Sda showed that this protein attached itself to the stalk (base) position on KinA. This implies that the inhibitory signal

must be transmitted through the four-helix bundle that forms the KinA stalk (Whitten et al, 2007, Paper 579).

Tubulin is a type of globular proteins. Tubulin and two similar peptides in solution have been measured by SANS. A simple bead ring model describes adequately the SANS data. Significant differences have been observed for the two types of similar peptides (Boukari et al, 2004, Paper 342).

REFERENCES

S. Krueger, S. Gregurick, Y. Shi, S. Wang, B.D. Wladkowski and F.P. Schwarz, "Entropic Nature of the Interaction Between Promoter Bound CRP Mutants and RNA Polymerase", Biochemistry 42, 1958-1968 (2003). Paper 079.

U.A. Perez-Salas, P. Rangan, S. Krueger, R.M. Briber, D. Thirumalai and S.A. Woodson, "Compaction of a Bacterial Group I Ribozyme Coincides with the Assembly of Core Helices", Biochemistry 43, 1746-1753 (2004). Paper 124.

J. Zhou, S.K. Gregurick, S. Krueger and F.P. Schwarz, "Conformational Changes in Single-Strand DNA as a Function of Temperature by SANS", Biophysical Journal 90, 544-551 (2006). Paper 447.

B. Hammouda and D. Worcester, "The Denaturation Transition of DNA in Mixed Solvents", Biophysical Journal 91, 2237-2242 (2006). Paper 532.

D. Lee, J.D. Walsh, P. Yu, M.A. Markus, T. Choli-Papadopoulou, C.D. Shieters, S. Krueger, D.E. Draper and Y-X. Wang, "The Structure of Free L11 and Functional Dynamics of L11 in Free, L11-rRNA Binary and L11-rRNA-Tiostrepton Ternary Complexes", J. Mol. Biol. 367, 1007-1022 (2007). Paper 578.

B. Yue, C-Y. Huang, M-P. Nieh, C.J. Glinka and J. Katsaras, "Spontaneously Forming Unilamellar Phospholipid Vesicles", Macromol. Symp. 219, 123-133 (2005). Paper 387.

U-S. Jeng, C-H Hsu, T-L. Lin, C-M. Wu, H-L. Chen, L-A. Tai and K-C. Hwang, "Dispersion of Fullerenes in Phospholipid Bilayers and the Subsequent Phase Changes in the Host Bilayers", Physica B 357, 193-198 (2005). Paper 401.

J. Pencer, M-P. Nieh, T. Harroun, S. Krueger, C. Adams and J. Katsaras, "Bilayer Thickness and Thermal Response of DMPC Unilamellar Vesicles Containing Sterols: A SANS Study", Biochim et Biophys. Acta 1720, 84-99 (2005). Paper 418.

T. Owen, R. Pynn, B. Hammouda and A. Butler, "Metal-Dependent Self-Assembly of a Microbial Surfactant", Langmuir 23, 9393 - 9400 (2007). Paper 601.

B.T. Nixon, H.P. Yennawar, M. Doucleff, J.G. Pelton, D.E. Wemmer, S. Krueger and E. Kondrashkina, "SAS Solution Structures of the Apo and Mg^{2+}/BeF_3^- Bound receiver Domain of DctD from *Sinothizibium Meliloti*", Biochemistry 44, 13962-13969 (2005). Paper 440.

D.A. Kuzmanovic, I. Elashvili, C. Wick, C. O'Connell and S. Krueger, "The MS2 Coat Protein Shell is Likely Assembled Under Tension: A Novel Role for the MS2 Bacteriophage A Protein as Revealed by SANS", J. Mol. Biol. 355, 1095-1111 (2006). Paper 448.

D. Dee, J. Pencer, M-P. Nieh, S. Krueger, J. Katsaras and R.Y. Yada, "Comparison of Solution Structures and Stabilities of Native, Partially Unfolded and Partially Refolded Pepsin", Biochemistry 45, 13982-13992 (2006). Paper 559.

S.A.K. Datta, J.E. Curtis, W. Ratcliff, P.K. Clark, R.M. Crist, J. Lebowitz, S. Krueger and A. Rein, "Conformation of the HIV-1 Gag Protein in Solution", J. Mol. Biol. 365, 812-824 (2007). Paper 567.

A.E. Whitten, D.A. Jacques, B. Hammouda. T. Hanley, G.F. King, J.M. Guss, J. Trewhella and D.B. Langley, "The Structure of the KinA-Sda Complex Suggests an Allosteric Mechanism of Histidine Kinase Inhibition", J. Mol. Biol. 368, 407-419 (2007). Paper 579.

H. Boukari, V. Chernomordik, S. Krueger, R. Nossal and D.L. Sackett, "SANS Studies of Tubulin Ring Polymers", Physica B 350, 533-535 (2004). Paper 342.

Part K – **OTHER SANS TOPICS**

Chapter 52. SANS from Polymer Blends under Pressure

Chapter 53. Solvation with Mixed Solvents

Chapter 54: SANS under Shear

Chapter 55: SANS from Polymeric Materials

Chapter 56: Neutron Scattering with Spin Polarization

Chapter 52 – **SANS FROM POLYMER BLENDS UNDER PRESSURE**

1. INTRODUCTION

Pressure is another parameter relevant to the understanding of the phase separation and thermodynamic behavior of polymer blends. Polymer blend mixtures phase separate either upon heating and are characterized by an Upper Critical Spinodal Temperature (UCST) behavior or upon cooling in which case they are characterized by a Lower Critical Spinodal Temperature (LCST) behavior. The UCST behavior is driven by enthalpic interactions between monomers whereas it is argued that the LCST behavior is due to "free volume". Free volume is related to the packing ability of monomers and is related to many factors among which polymer chemistry (side group bulkiness).

The mean field Flory-Huggins theory is a broadly used model that describes polymer blend miscibility. The chi parameter has two main contributions, one entropic and one enthalpic in nature. This theory is the basis for the Random Phase Approximation (RPA) approach used to model the scattering from homogeneous polymer blends. The commonly used RPA equations assume incompressible blends. Extension of the RPA equations to describe compressible blends will be discussed.

The goal here is to investigate the effect of hydrostatic pressure on the UCST and LCST phase behaviors and to account for equation-of-state (i.e., compressibility) effects using the SANS technique with in-situ pressure. Pressure can be controlled faster than temperature and is therefore more effective for thermodynamic studies. Pressure is also an important factor in polymer processing.

The in-situ pressure cell consists mainly of two sapphire windows separated by a fixed gap (typically 1 mm) in which a polymer wafer is confined inside an o-ring. Pressure is applied to the sample through the o-ring so that the pressurizing fluid never gets in contact with the sample. In-situ pressure can be varied typically up to a couple of atmospheres (note that 1 atm = 1 bar = 760 mm Hg = 14.7 psi = 100 kPa) and temperature can be varied up to 160 $^{\mathrm{o}}$C. This gives a wide window in parameter space.

2. THE DPS/PVME POLYMER BLEND UNDER PRESSURE

SANS with in-situ pressure has been applied to a series of deuterated polystyrene (dPS) and polyvinyl methyl ether (PVME) blends with various compositions (Hammouda-Bauer, 1995). Molecular weights were M_w = 188,000 g/mol (M_w/M_n = 1.02) for dPS and M_w = 201,000 g/mol (M_w/M_n = 1.49) for PVME. The dPS/PVME volume fractions were chosen as 10%, 30% and 50%. It is known that the dPS/PVME blend is characterized by an LCST behavior with a minimum (critical point) at around 20% dPS. The effect of pressure is to raise the LCST line since its effect is to damp out composition fluctuations. This is manifested as a lowering of the scattering intensity. In order to monitor composition fluctuations, the forward scattering intensity I(0) is obtained using a Zimm plot (plot of $I^{-1}(Q)$ *vs* Q^2). It was found that pressure favors mixing for the dPS/PVME blend in most cases.

10%/90% dPS/PVME Polymer Blend
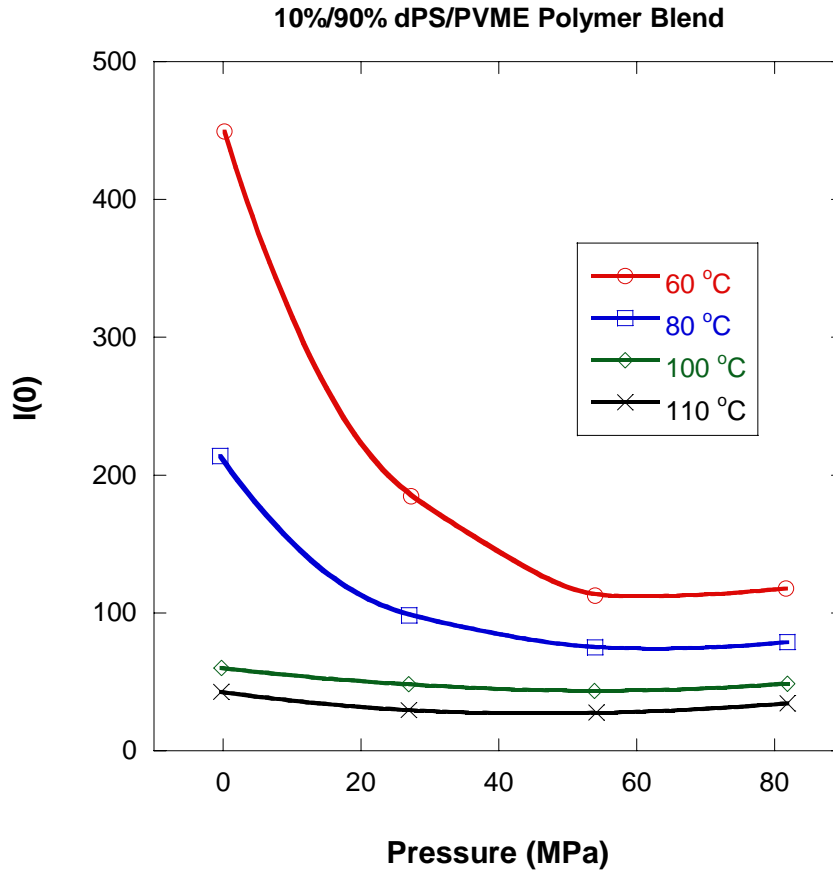
Figure 1: Variation of the forward scattering intensity I(0) with pressure for the 10%/90% dPS/PVME sample at various temperatures. A line through the points is included as a guide to the eye.

A pressure-induced increase of the spinodal line with pressure (evidenced by a decrease of the scattering intensity I(0)) of as much as 30 $^{\circ}$C/kbar was observed.

Since pressure can be changed fast, spinodal decomposition can be controlled at will even for this strongly interacting blend. Following pressure change strategies, one could get in and out of the spinodal phase demixing region. This is observed as the formation of a spinodal ring which quickly disappears under the beamstop.

As a first step in understanding the SANS data, recall the incompressible RPA equation for polymer blends:

$$\frac{(\rho_1 - \rho_2)^2}{I(Q)} = \frac{1}{n_1 \phi_1 v_1 P_1(Q)} + \frac{1}{n_2 \phi_2 v_2 P_2(Q)} - \frac{2\chi_{12}}{v_0}. \qquad (1)$$

Here the standard notation has been used for the degrees of polymerization (n_1 and n_2), volume fractions ϕ_1 and ϕ_2, monomer volumes v_1 and v_2, Debye functions $P_1(Q)$ and $P_2(Q)$, scattering length densities ρ_1 and ρ_2 and chi parameter χ_{12}/v_0.

The Flory-Huggins interaction parameter has two contributions: one entropic and one enthalpic in nature, $\chi_{12} = C + \dfrac{D}{T}$. Our measurements showed that both contributions increase with pressure. This interaction parameter is characterized by a composition-dependence. Our measurements also showed that this dependence is not due to compressibility effects.

The form factors can be expanded at low-Q as $\dfrac{1}{P_1(Q)} = 1 + \dfrac{Q^2 R_{g1}^{\;2}}{3}$. This changes the incompressible RPA equation to the low-Q expansion:

$$\frac{(\rho_1 - \rho_2)^2}{I(Q)} = \frac{1}{n_1\phi_1 v_1} + \frac{1}{n_2\phi_2 v_2} - \frac{2\chi_{12}}{v_0} + \left(\frac{1}{n_1\phi_1 v_1}\frac{R_{g1}^{\;2}}{3} + \frac{1}{n_2\phi_2 v_2}\frac{R_{g2}^{\;2}}{3} \right) Q^2 \,.\,(2)$$

The Zimm plot slope B in $I^{-1}(Q) = I^{-1}(0) + BQ^2$ is proportional to the radii of gyration.

30%/70% dPS/PVME Polymer Blend
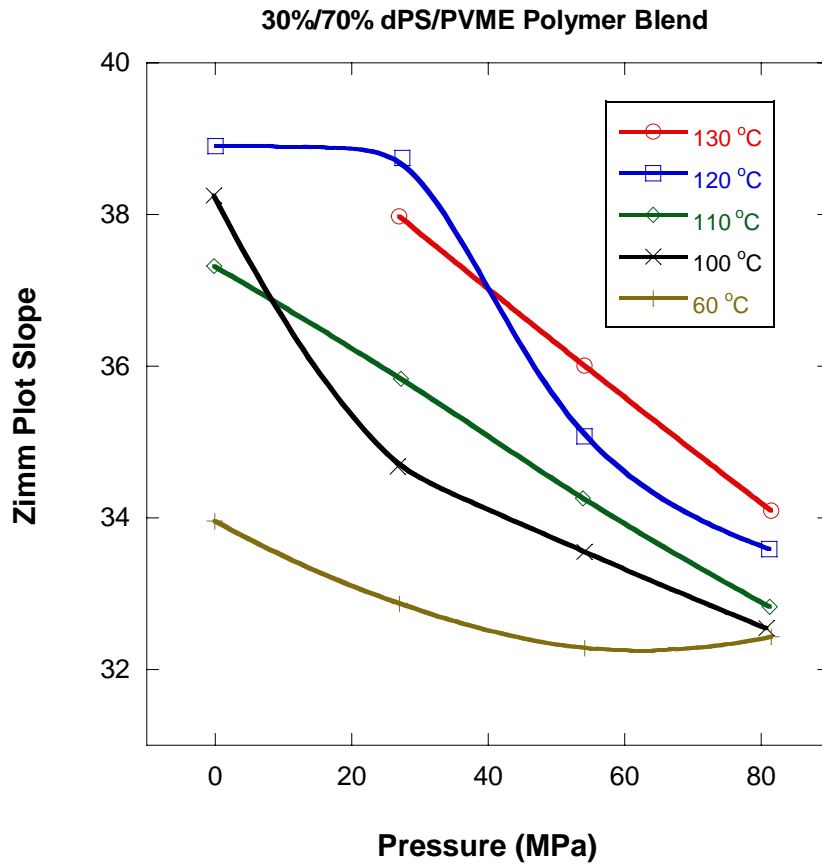
Figure 2: Variation of the Zimm plot slope B (obtained from $I^{-1}(Q) = I^{-1}(0) + BQ^2$) with pressure for the 30%/70% dPS/PVME sample measured at various temperatures.

This Zimm plot slope is seen to decrease with pressure. There is no reason for pressure to affect the radii of gyration. This artifact is due to the incompressible assumption in the RPA model. A compressible RPA model is described next.

3. COMPRESSIBLE POLYMER BLEND MODEL

In order to include compressibility effects, an equation-of-state is used. It describes density variation with temperature and pressure (using so-called PVT measurements). Various equation-of-state models are available to describe free volume effects in polymers (1) cell models associate a free volume component as part of the monomer volume, (2) lattice-fluid models assume free volume as a separate component, and (3) hole models assume a combination of the above two features. Here a simple lattice-fluid model is used (Sanchez-Bidkar, 1995).

Consider the "mixing" polymer volume fractions for the two polymer components ϕ_1 and ϕ_2 defined previously such that $\phi_1+\phi_2 = 1$. Introduce a free volume fraction f_0 and new fractions $f_1 = \phi_1(1-f_0)$ and $f_2 = \phi_2(1-f_0)$ such that $f_1+f_2+f_0 =1$. f_0 is not directly measurable but can be estimated through PVT (density) measurements. Define monomer "hard-core" volumes v_1* and v_2*, the statistical segment lengths a_1 and a_2, neutron scattering length densities ρ_1 and ρ_2 and degrees of polymerization n_1 and n_2.

The lattice-fluid equation-of-state uses a characteristic energy density (internal pressure) $P*$ and characteristic temperature $T*$ for each of the components. These are tabulated quantities for each polymer. The lattice-fluid equation-of-state reads:

$$(1-f_0)^2 + \frac{P}{P*} + \left[\ln(f_0)+1-f_0\right]\frac{T}{T*} = 0 . \tag{3}$$

The term $\dfrac{1}{n} = \dfrac{\phi_1}{n_1} + \dfrac{\phi_2}{n_2}$ appearing in the original model has been neglected for typical (large) degree of polymerization (n>>1).

Mixing rules are used to connect the two polymer components:

$$P* = \phi_1^{\,2}P_1* +2\phi_1\phi_2P_{12}* +\phi_2^{\,2}P_2* \tag{4}$$

$$\frac{P*}{k_BT*} = \frac{1}{v_0} = \frac{\phi_1P_1*}{k_BT_1*} + \frac{\phi_2P_2*}{k_BT_2*} .$$

These equations describe the compressibility part of the blend mixture.

The scattering intensity is obtained using a three component RPA approach whereby the third component represents "holes" (free volume). The ternary RPA equations have been discussed previously. They are repeated here for convenience. The SANS cross section for

compressible blends ($\frac{d\Sigma(Q)}{d\Omega}$ also called SANS intensity I(Q)) is given by the following set of equations (Hammouda-Benmouna, 1995):

$$\frac{d\Sigma(Q)}{d\Omega} = \rho_1{}^2 S_{11}(Q) + \rho_2{}^2 S_{22}(Q) + 2\rho_1\rho_2 S_{12}(Q) . \qquad (5)$$

$$S_{11}(Q) = \frac{S^0{}_{11}(Q)\left(1 + v_{22}S^0{}_{22}(Q)\right)}{\left(1 + v_{11}S^0{}_{11}(Q)\right)\left(1 + v_{22}S^0{}_{22}(Q)\right) - v_{12}{}^2 S^0{}_{11}(Q)S^0{}_{22}(Q)}$$

$$S_{22}(Q) = \frac{S^0{}_{22}(Q)\left(1 + v_{11}S^0{}_{11}(Q)\right)}{\left(1 + v_{11}S^0{}_{11}(Q)\right)\left(1 + v_{22}S^0{}_{22}(Q)\right) - v_{12}{}^2 S^0{}_{11}(Q)S^0{}_{22}(Q)}$$

$$S_{12}(Q) = \frac{-S^0{}_{11}(Q)v_{12}S^0{}_{22}(Q)}{\left(1 + v_{11}S^0{}_{11}(Q)\right)\left(1 + v_{22}S^0{}_{22}(Q)\right) - v_{12}{}^2 S^0{}_{11}(Q)S^0{}_{22}(Q)}$$

$$S^0{}_{11}(Q) = n_1 f_1 v_1 {}^* P_1(Q)$$
$$S^0{}_{22}(Q) = n_2 f_2 v_2 {}^* P_2(Q)$$
$$S^0{}_{00} = f_0 v_0$$

$$v_{11} = \frac{1}{S^0{}_{00}} - 2\frac{P_1{}^*}{k_B T} + C_{11}$$

$$v_{22} = \frac{1}{S^0{}_{00}} - 2\frac{P_2{}^*}{k_B T} + C_{22}$$

$$v_{12} = \frac{1}{S^0{}_{00}} - 2\frac{P_{12}{}^*}{k_B T} + C_{12}$$

$$C_{11} = -2\phi_2 \frac{[\ln(f_0) + (1 - f_0)]}{(1 - f_0)^2}\left(\frac{P_1{}^*}{k_B T_1{}^*} - \frac{P_2{}^*}{k_B T_2{}^*}\right)$$

$$C_{22} = 2\phi_1 \frac{[\ln(f_0) + (1 - f_0)]}{(1 - f_0)^2}\left(\frac{P_1{}^*}{k_B T_1{}^*} - \frac{P_2{}^*}{k_B T_2{}^*}\right)$$

$$C_{12} = (\phi_1 - \phi_2) \frac{[\ln(f_0) + (1 - f_0)]}{(1 - f_0)^2}\left(\frac{P_1{}^*}{k_B T_1{}^*} - \frac{P_2{}^*}{k_B T_2{}^*}\right) .$$

This formalism is tied up using the following bridging relation between the energy densities $P_{ij}{}^*$ and the monomer-monomer interaction parameters W_{ij}:

$$P_{ij}{}^* = -\frac{W_{ij}}{2v^*} . \qquad (6)$$

Here $v^* = \sqrt{v_1{}^* v_2{}^*}$ is a reference volume and $P_{11}{}^* = P_1{}^*$ is understood.

The lattice-fluid equation-of-state and the compressible RPA equations are solved self-consistently (i.e., iteratively till convergence is obtained). The iterative process is carried out using an initial guess: $P_{12}^* = \sqrt{P_1^* . P_2^*}$.

Input: ϕ_1, ϕ_2, v_1^*, v_2^*, P_1^*, P_2^*, T_1^*, T_2^*

Initial Guess: $P_{12}^* = \sqrt{P_1^* . P_2^*}$

Use Mixing Rule:
$P^* = \phi_1^2 P_1^* + 2\phi_1\phi_2 P_{12}^* + \phi_2^2 P_2^*$
$P^*/k_B T^* = \phi_1 P_1^*/k_B T_1^* + \phi_2 P_2^*/k_B T_2^*$

Solve Lattice Fluid Equation of State:
$(1-f_0)^2 + P/P^* + [\ln(f_0)+1-f_0]T/T^* = 0$

Obtain Free Volume: f_0

Iterate

Input: ρ_1, ρ_2, a_1, a_2

Fit RPA Equations to SANS Data:
$$\frac{d\Sigma(Q)}{d\Omega} = \rho_1^2 S_{11}(Q) + \rho_2^2 S_{22}(Q) + 2\rho_1\rho_2 S_{12}(Q)$$
Using expressions for $S_{11}(Q)$, $S_{22}(Q)$ and $S_{12}(Q)$ in terms of v_{11}, v_{22}, v_{12} and C_{11}, C_{22}, C_{12}, v_0, f_0

Obtain: P_{12}^*

Final f_0 and P_{12}^*

Figure 3: Self-consistent approach to calculate the scattering intensity for compressible polymer blends using the lattice-fluid equation-of-state and the compressible RPA equations.

This formalism is applied here to the dPS/PVME blend under pressure. Tabulated values for dPS are $P_1^* = 355$ MPa and $T_1^* = 731$ K and for PVME they are $P_2^* = 353$ MPa and $T_2^* = 657$ K. Some results for the free volume fraction for increasing temperature and pressure follow.

10%/90% dPS/PVME Polymer Blend
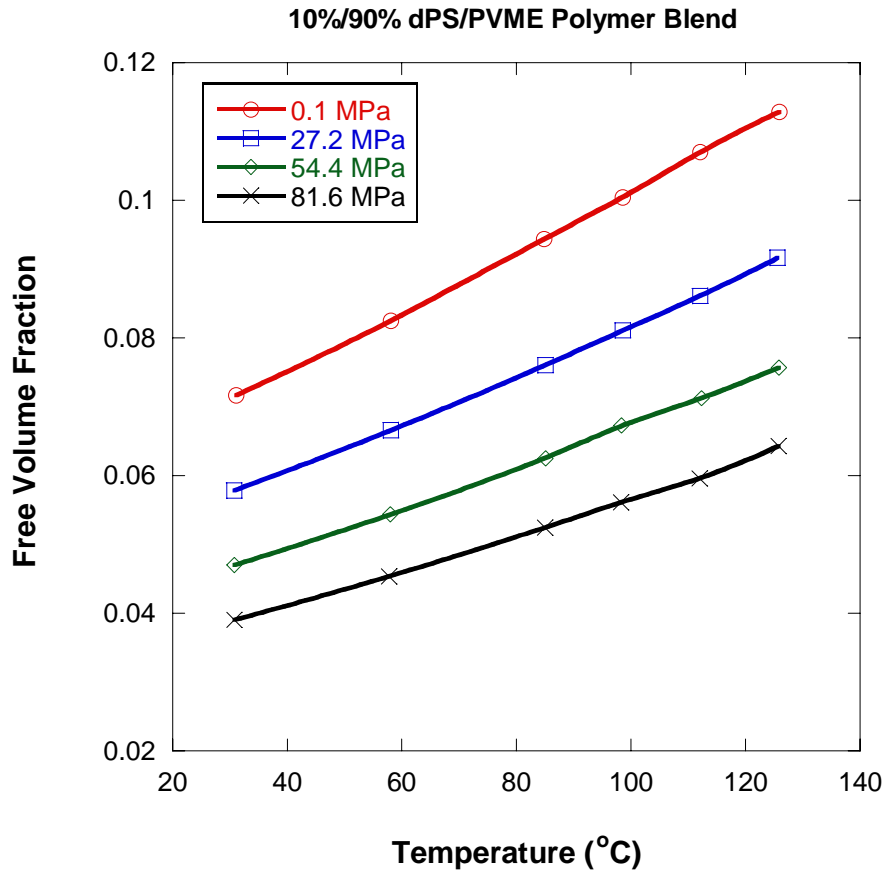
Figure 4: Variation of the free volume fraction f_0 for increasing temperature for the 10%/90% dPS/PVME polymer blend.
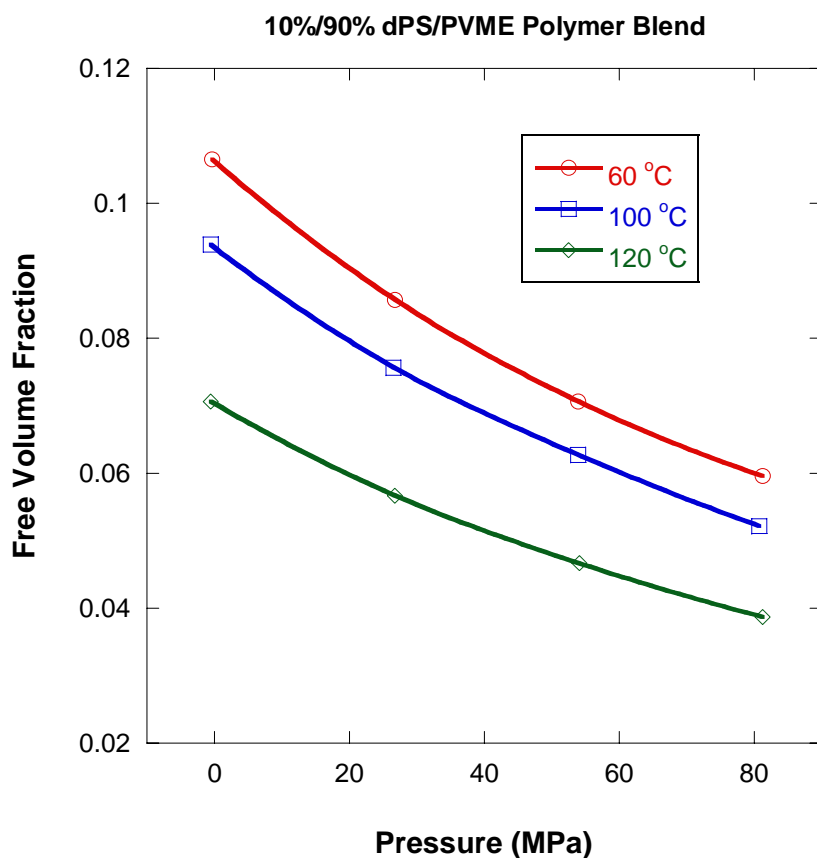
Figure 5: Variation of the free volume fraction f_0 for increasing pressure for the 10%/90% dPS/PVME polymer blend.

The free volume fraction f_0 is seen to increase with temperature and decrease with pressure as it should.

The inter-monomer interaction energy density $P_{12}*$ is plotted next with and without free volume (i.e., with $f_0 = 0$). This variation is seen to have weak variation for increasing pressure and to decrease consistently with increasing temperature. These results are reasonable since increasing temperature moves the blend closer to phase separation.
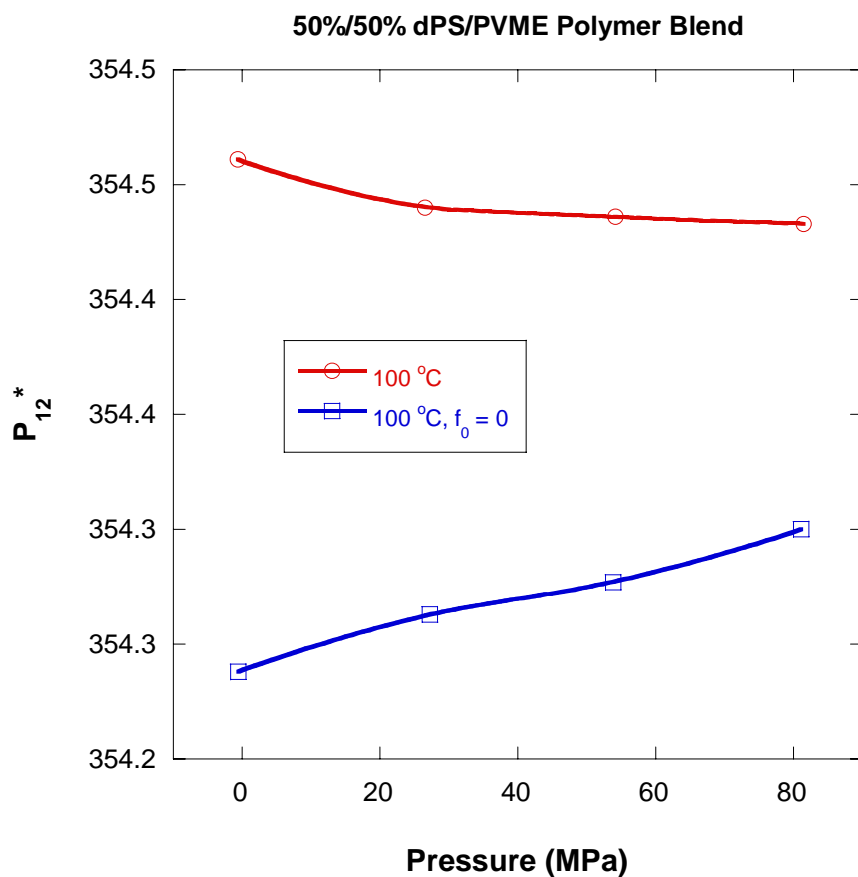
Figure 6: Variation of the inter-component interaction energy density P_{12}* for increasing pressure for the 50%/50% dPS/PVME.

50%/50% dPS/PVME Polymer Blend
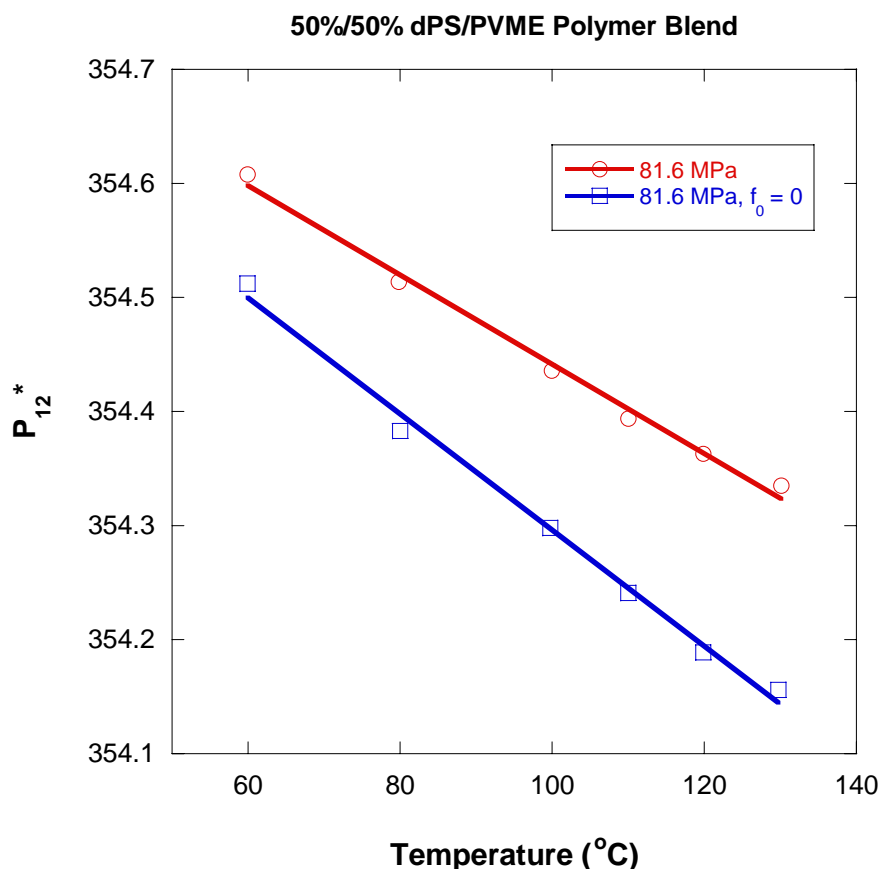
Figure 7: Variation of the inter-component interaction energy density $P_{12}*$ for increasing temperature for the 50%/50% dPS/PVME.

The incompressible RPA model used to fit the SANS data is highly nonlinear and yields wide variations in intensity for slight variation in interaction energy density $P_{12}*$. $P_{12}*$ was found to depend on pressure (weakly) and on temperature (linearly).

4. A POLYOLEFIN POLYMER BLEND UNDER PRESSURE

Model polyolefins of molecular weight around 200,000 g/mol consisting of deuterated polymethyl butylene (dPMB) and polyethyl butylene (PEB) were blended and investigated under pressure. A PMB-PEB diblock copolymer was added in order to adjust the phase diagram to a convenient temperature range. The degrees of polymerizations were 4260 for dPMB, 3350 for PEB and 3740 for the PMB-PEB diblock. The relative fraction of PEB monomers in the PMB-PEB diblock was 0.33. The dPMB/PEB relative volume fraction was also 0.33.

The SANS technique was used with in-situ pressure in order to investigate the effect of pressure on the spinodal and binodal temperatures for this polyolefin blend (Hammouda et al, 1997). The spinodal temperature T_s is obtained from an extrapolation of the plot of $I^{-1}(0)$ *vs* T^{-1} where $I(0)$ is the forward scattering intensity obtained from a Zimm plot and T is the absolute temperature (in K). The binodal temperature T_b on the other hand is obtained when

536

$I^{-1}(0)$ becomes negative. Note that the region between T_b and T_s is the nucleation and growth region. When pressure is increased, both T_s and T_b are seen to increase. In other words, pressure favors phase separation (demixing).

dPMB/PEB Polyolefin Blend
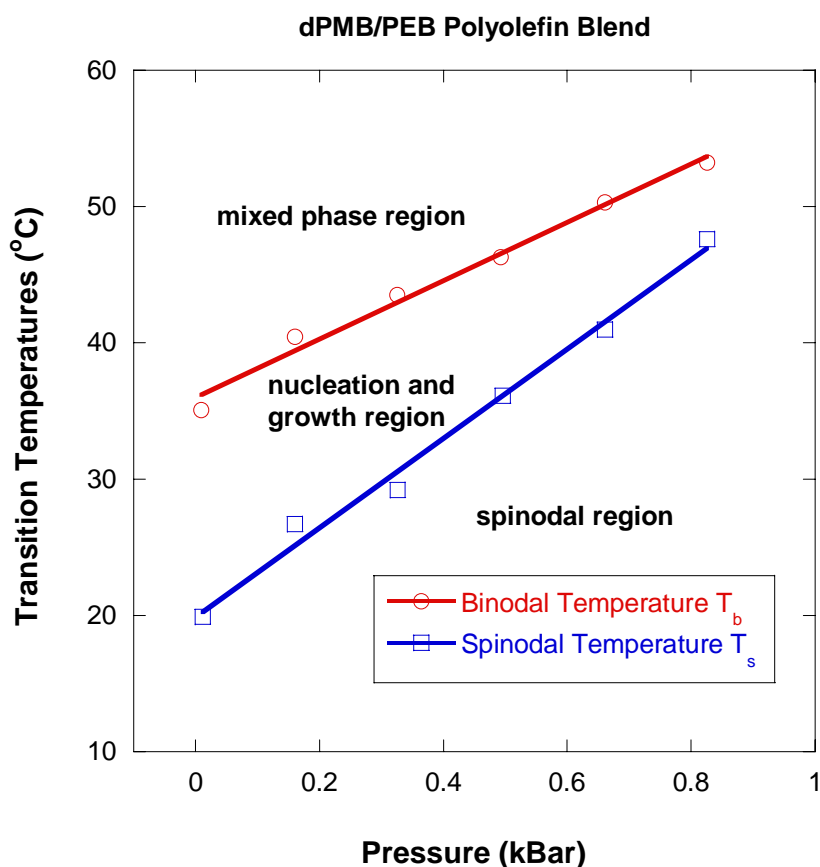
Figure 8: Variation of the binodal and spinodal transition temperatures with pressure for the dPMB/PEB polyolefin blend. The nucleation and growth and the spinodal regions combine to give the so-called phase separation region.

A simple description of compressibility effects through a pressure-dependent Flory-Huggins interaction parameter $\chi_{12} = E + FP$ showed that E (related to the internal energy change ΔU upon mixing) and F (related to the volume change ΔV upon mixing) are proportional. This means that the volume increase upon mixing is a linear response of the repulsive interactions between monomers (Lefebvre et al, 1999).

Here also, varying pressure gives a fast-response way for moving from the mixed phase region to the phase separated region of the phase diagram. This allows the monitoring of the phase separation kinetics during phase separation. The reverse phase-mixing kinetics have also been investigated (Hammouda et al, 1997).

5. THE DPS/PBMA POLYMER BLEND UNDER PRESSURE

Another polymer blend was investigated using in-situ pressure. It consisted of dPS blended with poly-n-butyl methacrylate noted PBMA for short (Hammouda-Bauer, 1995). The molecular weights were M_w = 10,000 g/mol (M_w/M_n = 1.03) for dPS and M_w = 34,000 g/mol (M_w/M_n = 1.96) for PBMA. This blend is characterized by a miscibility gap. In-situ pressure affects both the UCST and the LCST branches of the phase diagram. This is seen as a systematic decrease of the scattering intensity for all temperatures. Here also, pressure dampens composition fluctuations and widens the miscibility gap.

10%/90% dPS/PBMA Polymer Blend
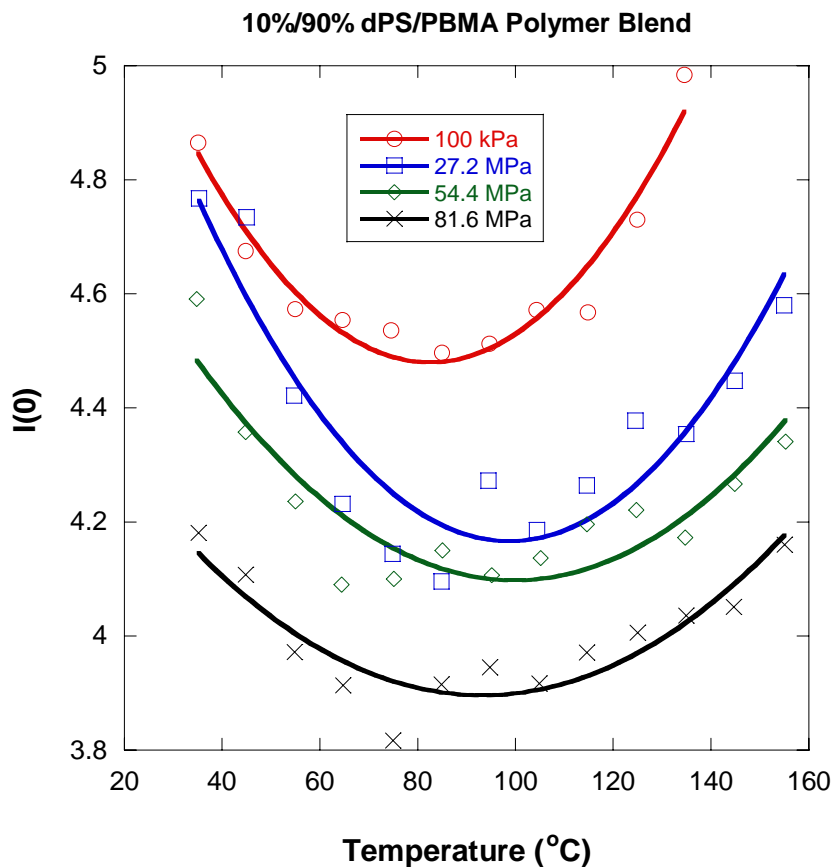
Figure 9: Variation of the forward scattered intensity I(0) with temperature for the 10%/90% dPS/PBMA sample for various pressures. The upturn variation is characteristic of a miscibility gap. The lines are parabolic fits included to better visualize the trends.

Pressure seems to affect the high temperature branch (LCST) more than the low temperature branch (UCST). It also shifts the miscibility gap to a slightly higher temperature.

6. SUMMARY AND DISCUSSION

Pressure affects both the UCST and the LCST branches of the phase diagram in polymer blends. Based on the blends considered here, a few conclusions can be summarized. Pressure can raise the LCST which is driven by free volume. It can either raise or lower the UCST (driven by monomer-monomer interactions). It should be noted that in other instances (not described here), pressure can lower the LCST such as in the case of solutions of poly(ethylene oxide) in deuterated water (PEO/d-water). In that case, the LCST is driven by specific interactions (hydrogen bonding) that soften under pressure. These points are summarized elsewhere (Hammouda, 2001).
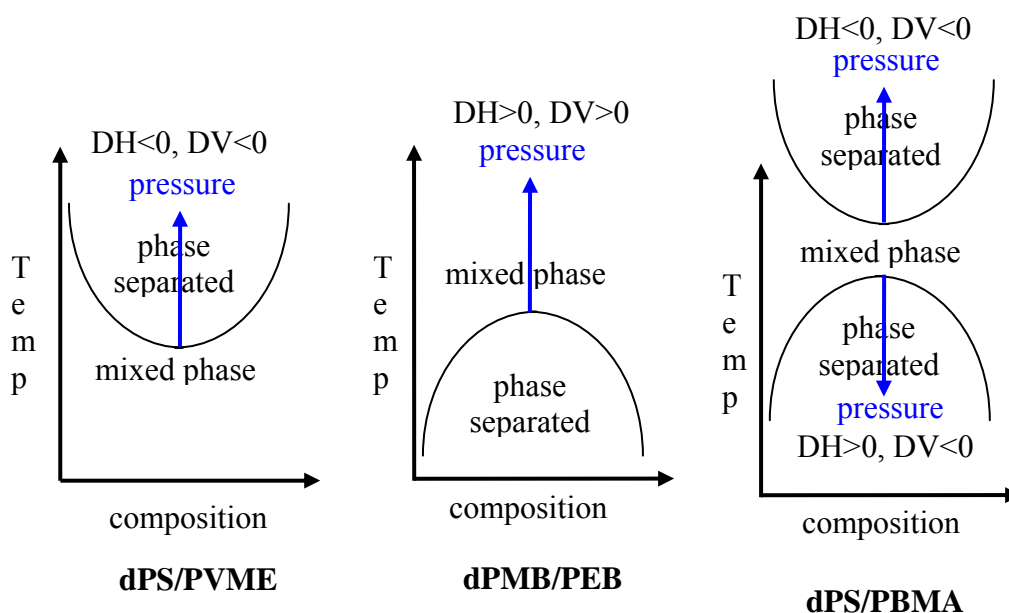
Figure 10: Pressure effects on the thermodynamics of phase-mixing for three polymer blends.

The phase separation lines can either increase or decrease with pressure. This can be understood in terms of the Clausius-Clapeyron equation:

$$\frac{dT}{dP} = \frac{\Delta V}{\Delta H}. \qquad (7)$$

Here dT/dP is the derivative of the temperature variation with pressure along the phase separation curve and ΔV and ΔH are the volume change and enthalpy change upon phase-mixing. For a UCST system, mixing happens upon heating ($\Delta H>0$). If the volume change upon mixing is positive $\Delta V>0$, then pressure increases the UCST line (as in the case of dPMB/PEB). If on the other hand $\Delta V<0$, then pressure decreases the UCST line (as in the case of dPS/PBMA). For an LCST system, mixing happens upon cooling ($\Delta H<0$). Similarly, if $\Delta V<0$ then dP/dT>0 and pressure increases the LCST line (as in the cases of dPS/PVME and dPS/PBMA). This is the case of LCST driven by free volume (which decreases upon

cooling). If on the other hand $\Delta V > 0$, then $dP/dT < 0$ and pressure decreases the LCST line as in the case of PEO/d-water (not shown here). This is the case of LCST due to hydrogen bonding (which causes the volume to increase upon cooling).

REFERENCES

B. Hammouda and B. Bauer, "Compressibility of Two Polymer Blend Mixtures", Macromolecules 28, 4505-4508 (1995)

U. Bidkar, and I. Sanchez, "Neutron Scattering from Compressible Polymer Blends: A Framework for Experimental Analysis and Interpretation of Interaction Parameters" Macromolecules 28, 3963-3972 (1995)

B. Hammouda and M. Benmouna, "Neutron Scattering from Polymer Blends Under Pressure", J. Polym. Sci., Polym. Phys. Ed. 33, 2359-2364 (1995)

B. Hammouda, N.P. Balsara and A.A. Lefebvre, "SANS from Pressurized Polyethylebutylene/Polymethylbutylene Blends", Macromolecules 30, 5572-5574 (1997)

A. Lefebvre, J. Lee, N. Balsara, B. Hammouda, and R. Krishnamoorti "Relationship Between Internal Energy and Volume Change on Mixing in a Simple Polymer Blend", Macromolecules 32, 5460-5462 (1999)

B. Hammouda, "SANS from Polymers under Pressure: a Short Review", Neutron News 12, 20-24 (2001)

QUESTIONS

1. How is pressure applied to the sample in an in-situ pressure cell?
2. Describe the LCST and UCST phase behaviors.
3. Describe a miscibility gap.
4. What is meant by "free volume" in polymer blends? What causes free volume?
5. What is the effect of pressure on an LCST system driven by free volume?
6. Does the UCST line increase or decrease with increasing pressure? Why?
7. What is an equation-of-state? Name an equation-of-state used for polymers.
8. State the Clausius-Clapeyron equation? Define the various terms.

ANSWERS

1. The in-situ pressure cell uses an o-ring confined between two sapphire windows. The sample itself is melt-pressed into the right volume and confined in the o-ring. The pressurizing fluid compresses the o-ring thereby pressurizing the sample.
2. Phase separation occurs through heating in a Lower Critical Spinodal Temperature (LCST) system whereas it occurs through cooling in a UCST system.

3. Phase separation occurs both though heating and cooling when a polymer blend is characterized by a miscibility gap with an LCST at high temperature and a UCST at low temperature.

4. Free volume means the less-than-perfect packing of monomers in the blend. Free volume decreases during densification. Free volume can be caused by bulky side groups that are hard to pack tightly.

5. Free volume is squeezed out when pressure is applied. This raises the LCST with increasing pressure.

6. The UCST could either increase or decrease with increasing pressure. This is due to the possibility of a positive or negative volume change upon mixing in blends.

7. An equation-of-state describes the variation of density with temperature and pressure. The lattice-fluid equation-of-state is used to describe polymers.

8. The Clausius-Clapeyron equation is stated as: $\dfrac{dT}{dP} = \dfrac{\Delta V}{\Delta H}$ where dT/dP is the derivative of the temperature variation with pressure along the phase separation curve and ΔV and ΔH are the volume change and enthalpy change upon phase-mixing.

1. SOLVATION OF MACROMOLECULES

Solvent interaction with macromolecules determines the miscibility characteristics and chain conformations. Macromolecules dissolve in good solvents, precipitate in poor solvents and cluster or aggregate in marginal solvents. Clustering characterizes water-soluble macromolecules. SANS measures both the clustering component at low-Q as well as the solvation component at high-Q. A typical SANS spectrum is shown from 4% PEO/d-water.

4% PEO/d-water, M_w = 100,000 g/mol, T = 10 ^{o}C
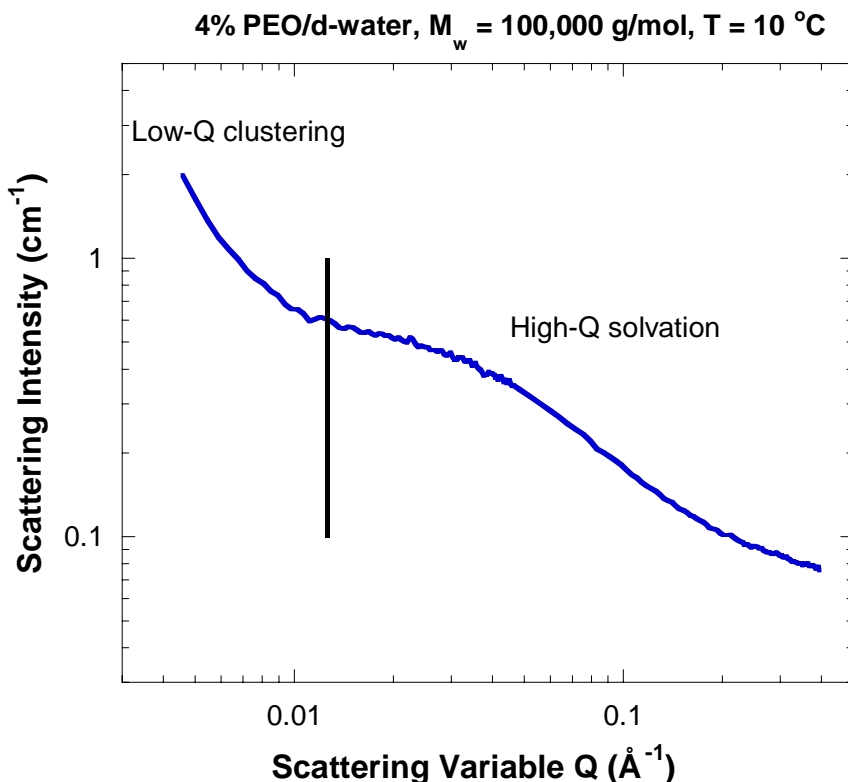
Figure 1: SANS data from 4% PEO/d-water.

The low-Q and high-Q features are separated through a fit to the following empirical functional form.

$$I(Q) = \frac{A}{Q^n} + \frac{C}{1 + (Q\xi)^m} + B \qquad (1)$$

The first term describes Porod scattering from clusters and the second term describes scattering from solvated polymer chains. B represents a constant incoherent scattering background. The solvation part is of interest here; parameter C is referred to as the solvation intensity.

2. POLY(ETHYLENE OXIDE) IN WATER/ETHANOL SOLVENT MIXTURES

PEO/d-water solution is characterized by an LCST phase separation behavior (it phase-separates upon heating) whereas PEO/d-ethanol solution is characterized by a UCST phase separation behavior (it phase separate upon cooling). Note that PEO crystallizes in d-ethanol at low temperature and that the UCST behavior is observed at higher temperature. Here, the solvation behavior of PEO in d-water/d-ethanol mixed solvent is described.

When the d-water fraction is increased, the solvation intensity (parameter C) is characterized by a minimum. It decreases then increases. This is the signature on non-ideal mixing behavior. Solvent molecules are not randomly mixed around the polymer chain. SANS can not resolve the local cage-like structure for the solvent molecules, but it is showing that the mixed solvents are more effective solvating agents than any of the individual solvents.

The solvation intensity is seen to decrease with increasing temperature at low d-water fractions (signature of UCST behavior) but increases with increasing temperature at high d-water fractions (signature of LCST behavior).
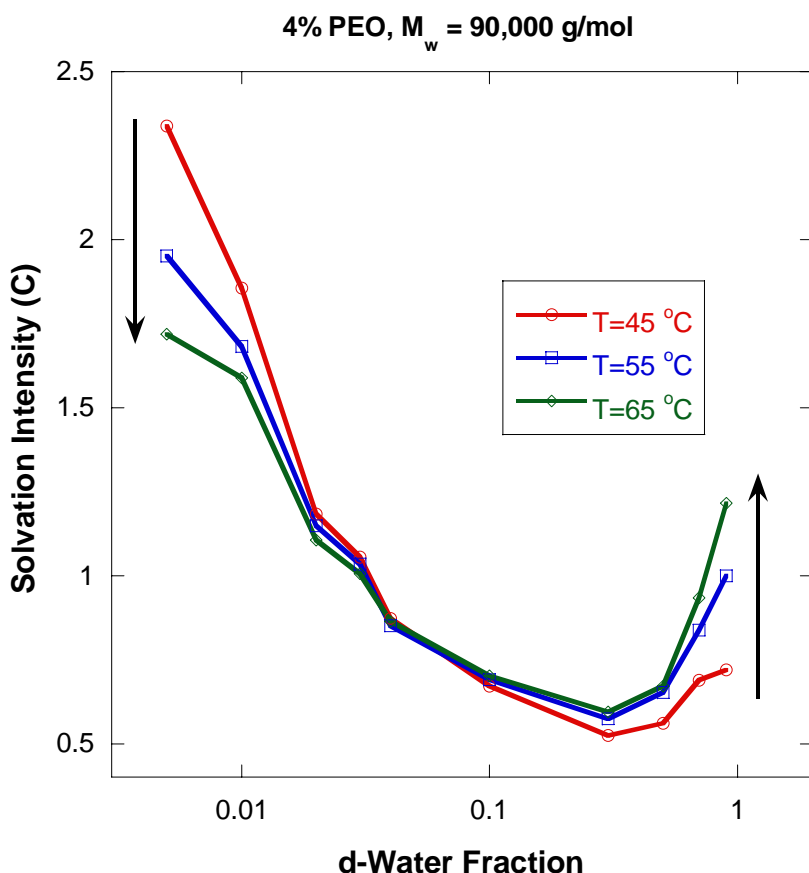
Figure 2: Variation of the solvation intensity (parameter C) with increasing d-water fraction for three temperatures.

Variation of 1/C with 1/T yields an estimate of the spinodal phase separation temperature through the familiar extrapolation procedure. With increasing d-water fraction, the spinodal temperature is seen to decrease, disappear at low temperatures then reappear at high temperatures.

4% PEO, M_w = 90,000 g/mol
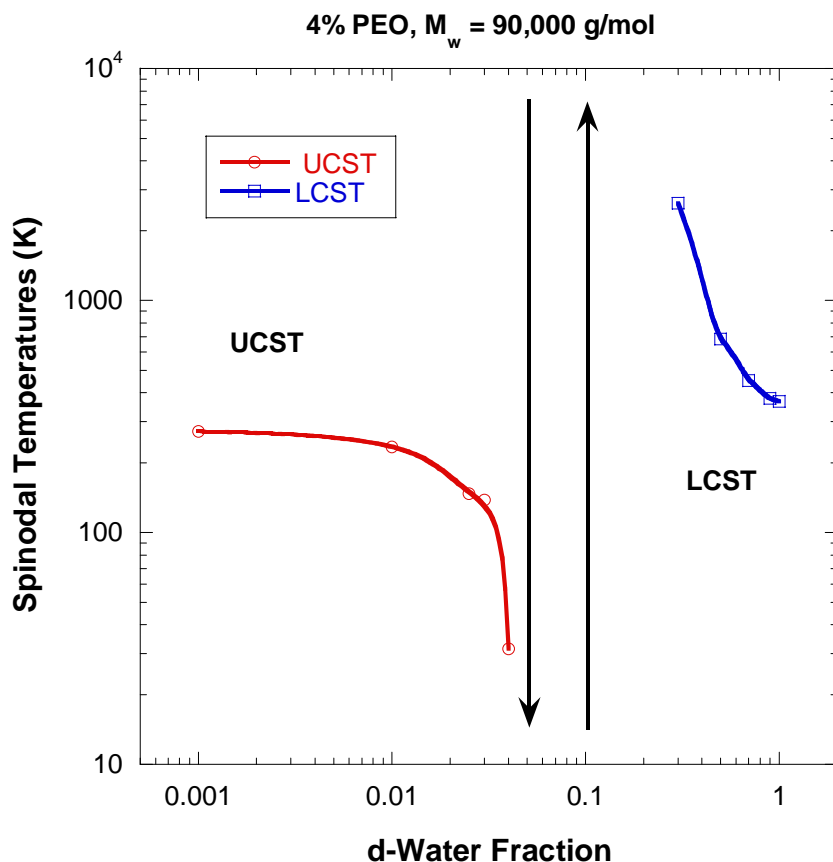
Figure 3: Variation of the spinodal phase separation temperature with increasing d-water fraction.

Similar SANS measurements were made for PEO in other mixed solvent pairs in which d-water is one of the solvents. The same non-ideal mixing trend was observed in d-water/d-methanol and d-water/d-ethylene glycol (Hammouda, 2006).

4% PEO/d-solvents,

M$_w$ = 42,900 g/mol, T = 50 ^{o}C
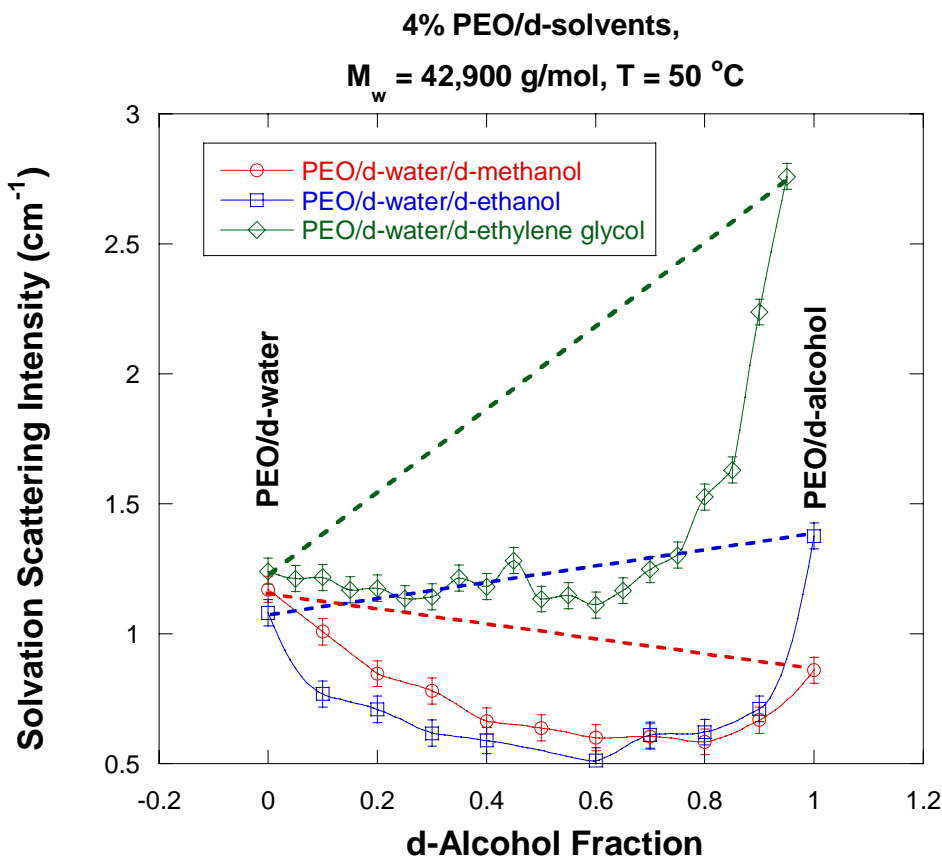
Figure 4: Variation of the solvation intensity with increasing d-alcohol fraction.

3. PEO/D-WATER/D-METHANOL TERNARY MIXTURES.

PEO/d-methanol solutions are also characterized by crystalline behavior for low temperatures. In order to avoid PEO crystallization, SANS data at the elevated temperature of 50 ^{o}C are discussed here. To analyze the SANS data from PEO in mixed (d-water/d-methanol) solvents, the ternary Random Phase Approximation (RPA) model is used. This mean-field model is highly approximate for polymer solutions. The ternary RPA equations are not reproduced here. The three components are chosen as: A = PEO, B = d-methanol and C = d-water.

The degrees of polymerization and specific volumes are:

N_A = 975, N_B = N_C = 1
$v_A N_{av}$ = 38.94 cm^3/mol, $v_B N_{av}$ = 40.54 cm^3/mol, $v_C N_{av}$ = 18.07 cm^3/mol,

Note that Avogadro's number (N_{av} = 6.02*10^{23} /mol) was used to multiply the specific volumes. The scattering lengths are:

b_A = 4.1326*10^{-13} cm, b_B = 3.9133*10^{-12} cm, b_C = 1.9145*10^{-12} cm.

545

The volume fractions for the three components are defined as ϕ_A, ϕ_B and ϕ_C. The two limiting cases of binary mixtures 4 % PEO/d-water and 4 % PEO/d-methanol (at T = 50 ^{o}C) are considered first. For the case of 100 % d-water ($\phi_B = 0$), the fit to the SANS data gives for the solvation intensity C = 1.171 cm^{-1}. This gives a Flory-Huggins interaction parameter of $\chi_{AC}/V_0 = \chi_{PEO/d-water}/V_0 = 0.0106$ mol/cm^3. For the case of 100 % d-methanol ($\phi_C = 0$), the fit to the SANS data gives C = 0.860 cm^{-1} which yields $\chi_{AB}/V_0 = \chi_{PEO/d-methanol}/V_0 = 0.0268$ mol/cm^3. The third Flory-Huggins interaction parameter χ_{BC}/V_0 is obtained (for example) from the case of 4 % PEO in 40 % d-methanol/60 % d-water solvent ($\phi_A = 0.04$, $\phi_B = 0.96*0.4 = 0.384$, $\phi_C = 0.96*0.6 = 0.576$). For this case C = 0.6648 cm^{-1} which yields $\chi_{BC}/V_0 = \chi_{d-methanol/d-water}/V_0 = 0.0099$ mol/cm^3.

This exercise shows that even-though it is highly approximate, the mean-field RPA approach provides a model for fitting SANS data from polymers in mixed-solvents.

4. DNA SOLVATION IN MIXED SOLVENTS

Salmon DNA undergoes a helix-to-coil transition in d-water at 94 ^{o}C and in d-ethylene glycol at 38 ^{o}C for 4% DNA volume fraction and with the addition of 0.1 M NaCl. In order to investigate solvation in mixed solvents, SANS data were taken from DNA (same conditions) in d-water/d-ethylene glycol mixed solvents. Variation of the solvation intensity C with increasing d-ethylene glycol fraction at three temperatures (25 ^{o}C, 50 ^{o}C and 75 ^{o}C) shows clearly the helix phase and the coil phase (Hammouda, 2007).

Note that the helix phase is characterized by ideal solvent mixing around the DNA phosphate groups whereas the coil phase is characterized by non-ideal solvent mixing just as for the PEO solution case.
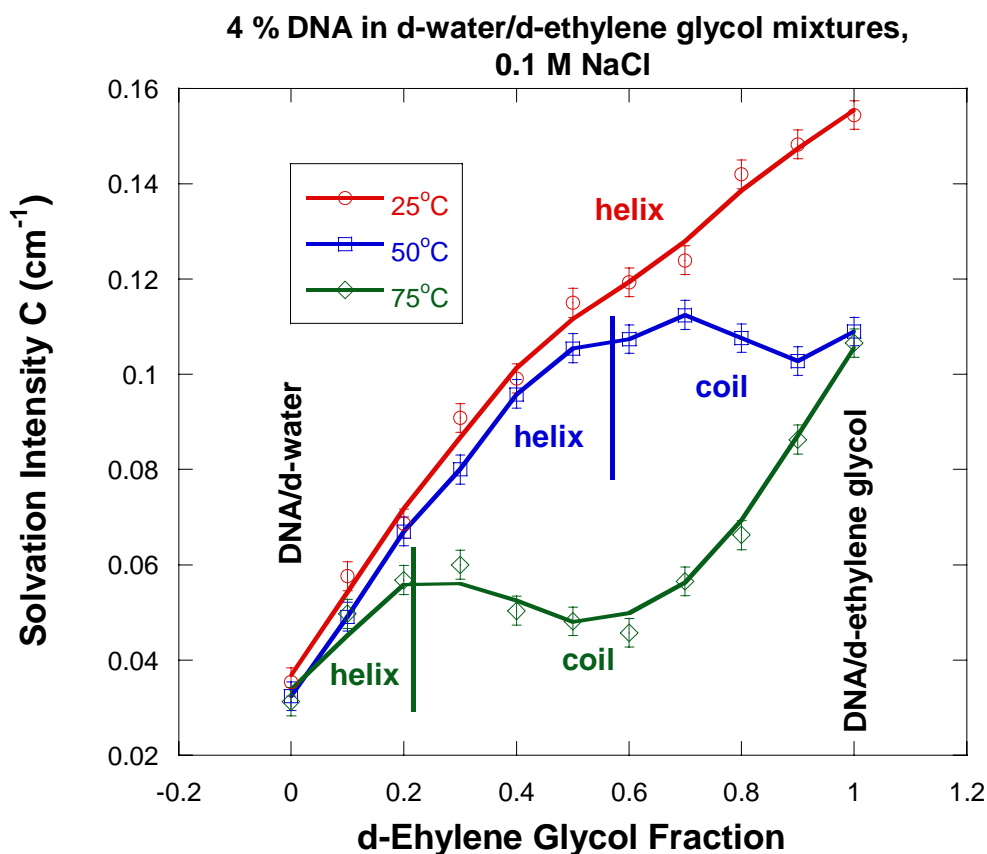
Figure 5: Variation of the SANS solvation intensity with increasing d-ethylene glycol fraction for DNA in d-water/d-ethylene glycol solvent mixtures shown for three temperatures.

REFERENCES

B. Hammouda, "Solvation Characteristics of a Model Water-Soluble Polymer", J. Polymer Science, Polymer Phys. Ed. <u>44</u>, 3195-3199 (2006)

B. Hammouda and DL Worcester, "The Denaturation Transition of DNA in Mixed Solvents", Biophysical Journal <u>91</u>, 2237-2242 (2006)

QUESTIONS

1. Is a PEO/d-water solution characterized by a Lower Critical Solution Temperature of an Upper Critical Solution Temperature? How about a PEO/d-ethanol solution?
2. What are the two main characteristic features of SANS data from water-soluble macromolecules?
3. How can one tell whether two solvents are mixed randomly or not around macromolecules?
4. Why is the DNA helix phase characterized by ideal solvent mixing?

ANSWERS

1. A PEO/d-water solution is characterized by a Lower Critical Solution Temperature; i.e., it phase separates upon heating. On the other hand, a PEO/d-ethanol solution is characterized by an Upper Critical Solution Temperature; i.e., it phase separates upon cooling.

2. SANS data from water-soluble macromolecules are characterized by a low-Q clustering feature and a high-Q solvation feature.

3. Two solvents are mixed randomly if the solvation intensity varies linearly between the two single solvent limits. Non-ideal mixing is characterized by nonlinear variation.

4. The DNA helix phase is characterized by random (ideal) solvent mixing because only the phosphate groups are in contact with the solvent. Different solvents interact similarly with the phosphate groups. The other groups (sugars and amine bases) are not in direct contact with the solvent.

Chapter 54 – SANS UNDER SHEAR

SANS is useful for investigating structures under shear. The orientation of layered structures can be monitored by SANS inside shear cells. Here, a couple of projects are described using in-situ shear cells. In-situ shear cells include the Couette type and the plate-plate geometry type.

1. SHEARED DISCOTIC LIQUID CRYSTAL MICELLES

A lyotropic mixture of cesium-perfluoro-octanoate (CsPFO) in water (55 % mass fraction) was investigated using a Couette shear cell (Mang et al, 1994; Hammouda et al, 1995). This mixture forms discotic liquid crystal micelles with a characteristic smectic-to-nematic transition temperature of 47 ^{o}C and a nematic-to-isotropic transition temperature of 52 ^{o}C.

The in-situ Couette shear cell consists of a cylindrical stator and rotor pair made out of quartz and separated by a 0.5 mm gap. The rotor diameter is 6 cm so that the sheared sample volume is around 12 ml. Its computer controlled rotation can be steady (for simple shear) or reciprocating (for oscillatory shear). Shear can be controlled up to a shear rate (or shear frequency) of 6000 Hz (note that 1 Hz corresponds to 1 rotation per second). Sample heating was performed using circulating fluid through the stator. The shear cell has two measurement configurations: one radial and one tangential. The radial configuration uses standard beam geometry with a 1.27 cm circular sample aperture diameter whereas the tangential configuration uses a vertical beam defining slit 0.5 mm in width. The oscillatory mode of operation uses 200 % strain, i.e., it oscillates by about 1 mm in each direction.

The SANS spectrum for the discotic micelles is characterized by two peaks: one at Q = 0.113 Å^{-1} and one at Q = 0.146 Å^{-1}. The first one represents the center-to-center inter-distance for micelles that lie planar in an edge-to-edge configuration while the second one corresponds to the face-to-face inter-distance for stacked disks. SANS measurements with the Couette shear cell were performed in the smectic phase at 45 ^{o}C, in the nematic phase at 49.7 ^{o}C and in the isotropic phase at 54 ^{o}C. Monitoring of the two peaks in the radial and tangential configurations gave clues as to the orientation of the discotic structures.
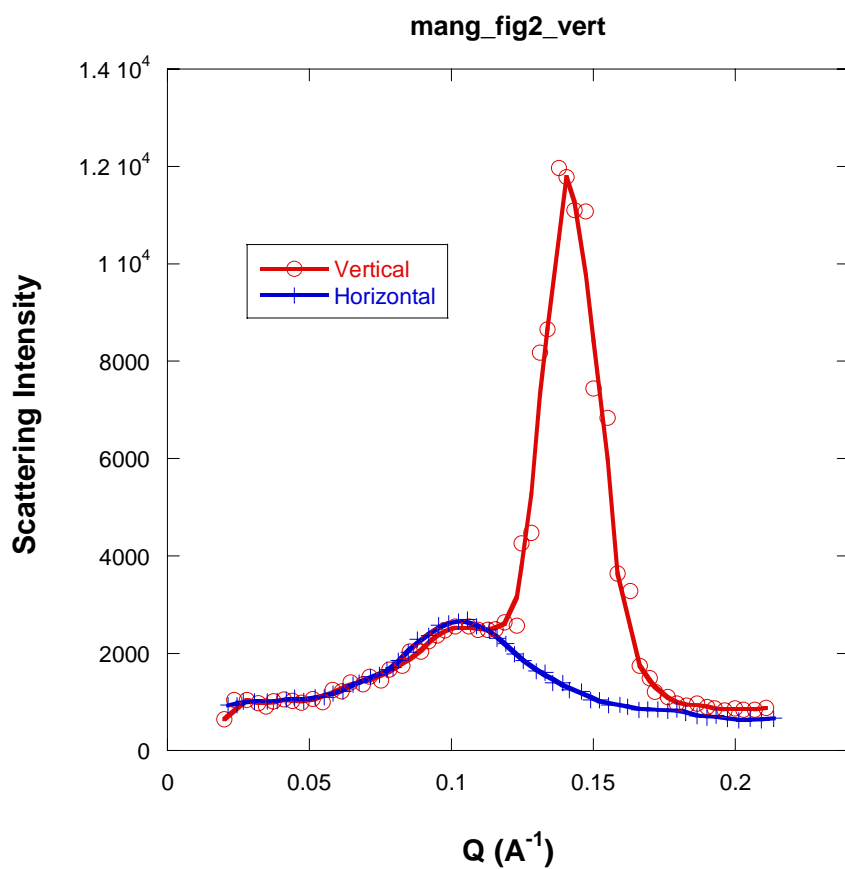
Figure 1: The two SANS peaks characterizing the discotic liquid crystal micelles structure.

The sheared discotic micelles orient mostly parallel to the moving shear cell (rotor) walls. This is referred to as the "C alignment" type.
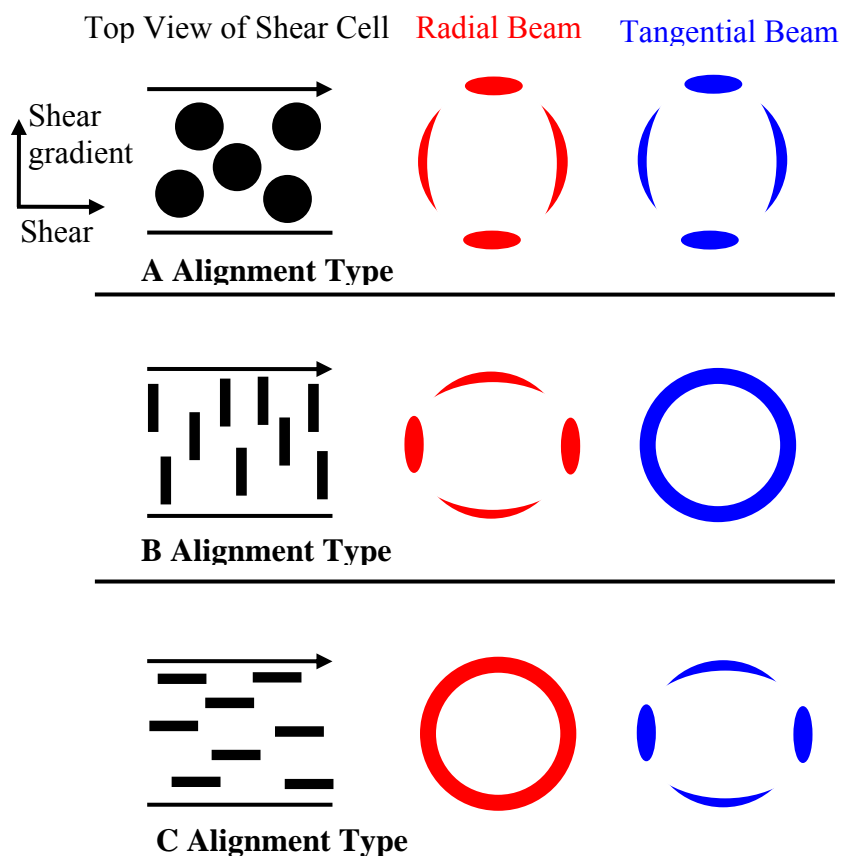
Figure 2: The three types of possible alignments as viewed using the radial and tangential configurations.

Flipping of the discotic structures was observed from the C type alignment observed in the nematic phase to the A type alignment observed in the smectic phase. The flipping transition has been observed with oscillatory shear either by varying temperature or shear rate. The flipping was not complete so that mixtures of A and C alignment types were often mixed.
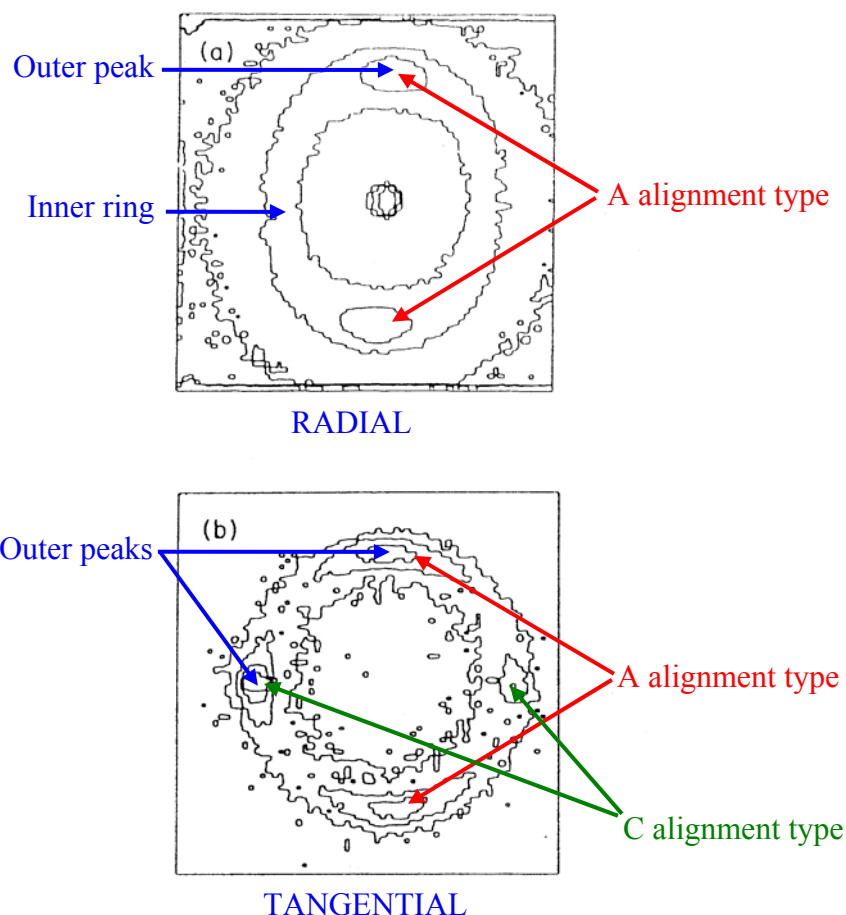
Figure 3: Iso-intensity contour plots for an oscillatory shear rate of 5835 s^{-1} at a temperature of 49.7 $^{\circ}$C (i.e., in the nematic phase) for radial (top) and tangential (bottom) beam geometries. The top contour plot shows an inner scattering ring and two outer scattering peaks in the vertical direction pointing to the A alignment type. The bottom contour plot shows four outer scattering peaks in the vertical and horizontal directions pointing to a mixture of A and C alignment types.

When oscillatory shear is used, shear-induced shifts of the phase transition temperatures were observed. These are interpreted as shear-induced damping of critical fluctuations that become stronger close to phase boundary lines. Moreover, interesting competing "bulk" and "wall" effects have also been observed. These effects were seen by changing the shear cell sample gap (from 0.5 mm to 1 mm).

2. SHEARED COPOLYMER LAMELLAE

Diblock copolymers form lamellar, cylindrical and spherical morphologies. Lamellar morphologies are amenable to investigations under shear. A polystyrene-polyisoprene (SI) diblock copolymer in concentrated DOP solution was investigated under Couette shear (Balsara-Hammouda, 1994; Balsara et al, 1994). The diblock molecular weights were M_w = 11,000 g/mol for the styrene block and M_w = 17,000 g/mol for the isoprene block. This

corresponds to a lamellar morphology. DOP solvent was added (65 % polymer concentration) in order to lower the order-disorder temperature (ODT) to an easily reachable value of 38 ^{o}C. Scattering from the SI diblock is characterized by a peak at Q = 0.032 Å^{-1}. Monitoring of this peak in the vertical and horizontal directions with radial or tangential beam configurations provides helpful clues to determine the lamellar orientation in each case.

The diblock thermal history was "erased" in each case by heating the sample above the ODT. The temperature was lowered before starting the shear. Some of the observations follow. Couette shear can orient the diblock lamellae even above the ODT as shown on an azimuthally averaged SANS data. This is due to a shear-induced shift of the phase boundary.
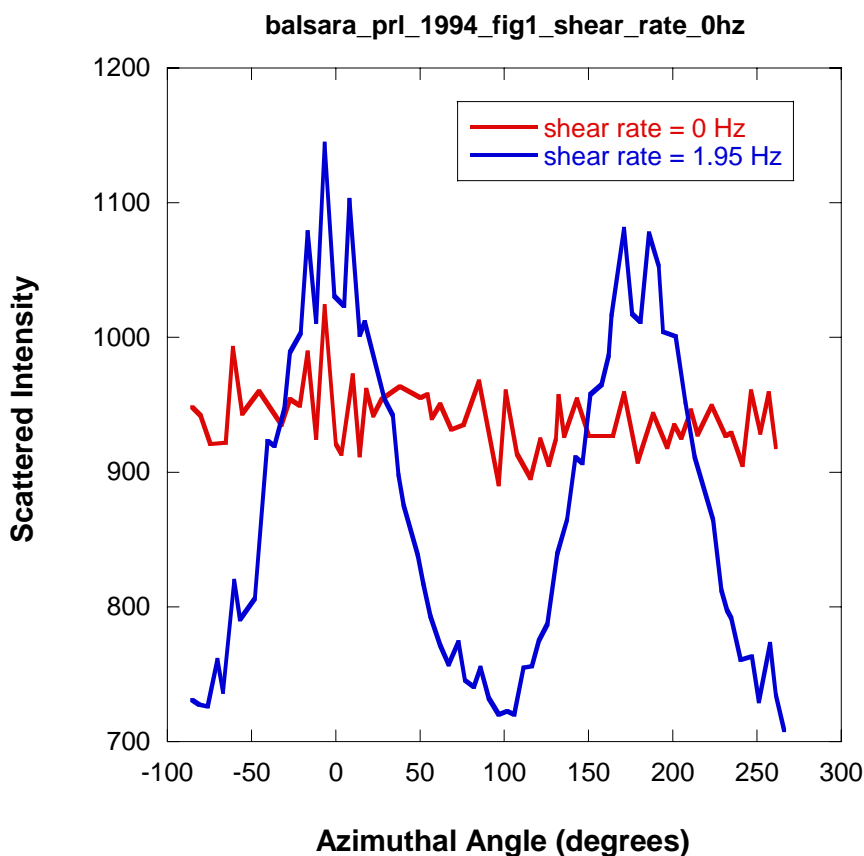
Figure 4: Effect of shear on azimuthally averaged SANS profiles obtained at 43 ^{o}C, i.e., above the quiescent ODT. The zero degree orientation is along the vertical axis.

The shear-induced orientation occurs above a critical shear rate $\dot{\gamma}_c$. The lamellar orientation is quantified through an anisotropy ratio ρ (ratio of the intensities in the vertical and horizontal directions). This ratio is seen to follow a universal behavior when plotted *vs* the scaled Couette shear rate $\dot{\gamma}/\dot{\gamma}_c$. Curves corresponding to different temperatures fall on a same master curve represented by $\rho \sim (\dot{\gamma}/\dot{\gamma}_c)^{0.19}$. This is reminiscent of the time-temperature superposition principle for polymer melts in the rubbery region.

balsara_prl_1994_fig3_38p3c
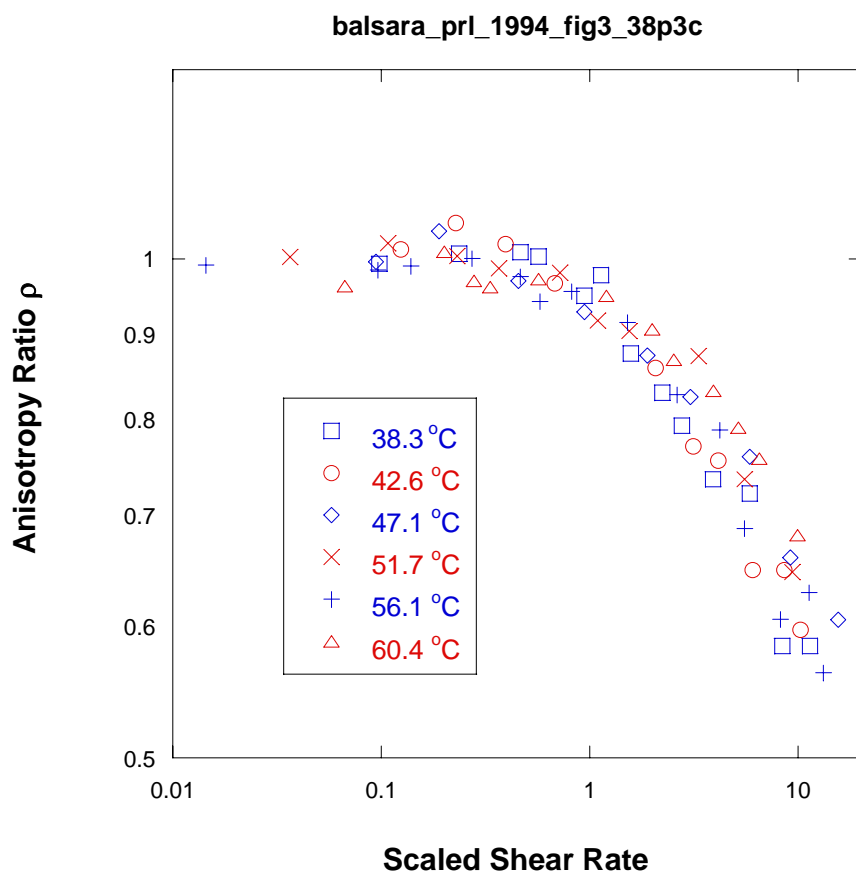
Figure 5: Master curve for the dependence of the peak anisotropy ρ with increasing scaled shear rate $\dot{\gamma}/\dot{\gamma}_c$ for various temperatures.

A 3D map of the SANS data under shear with the radial and tangential beam geometries lead to the following conclusions. The lamellar morphology is not perfect and contains lamellar "crumples" or "ripples" that are seen in the radial geometry (vertical peaks). The much higher intensity horizontal peaks in the tangential geometry show that the lamellae themselves are oriented mostly parallel to the shear cell walls (C type alignment).
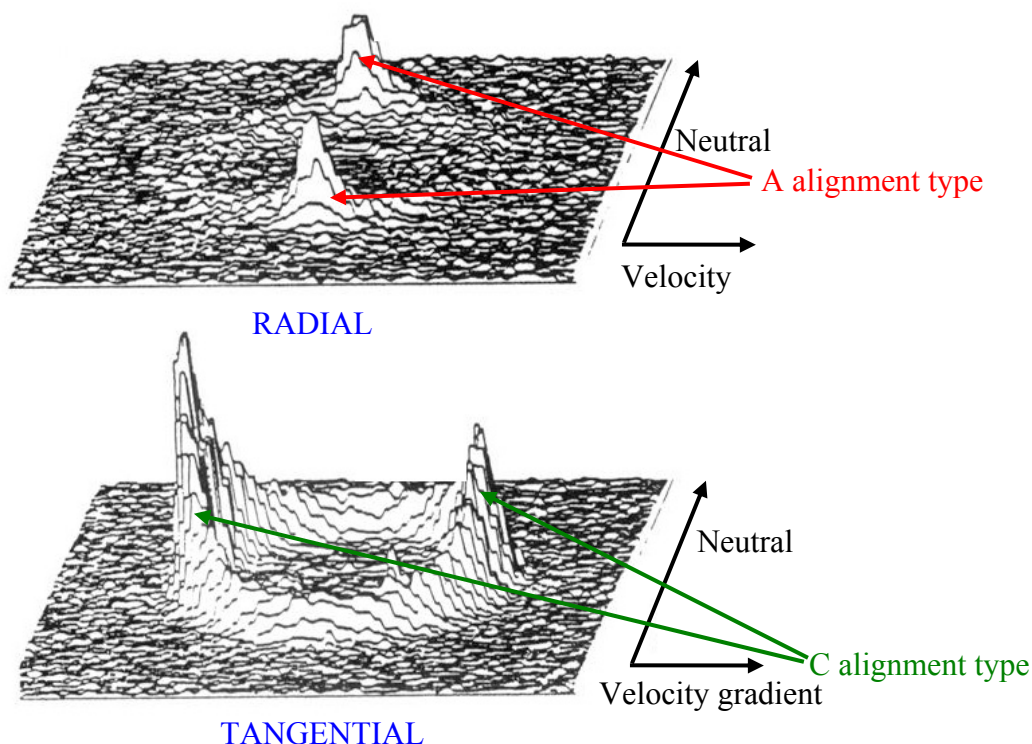
Figure 6: SANS iso-intensity contour plot obtained at ambient temperature (25 ^{o}C) and for a simple shear rate of 0.2 s^{-1} for the radial configuration (top) and tangential configuration (bottom). Note that the scattering volume is not uniform for the tangential configuration resulting in non-uniform peak heights.

Oscillatory shear produces lamellar alignment of the C type. Steady shear on the other hand produces lamellar alignment of the C type at high shear rates and of the A type at low shear rates. This is the "flipping" transition discussed before. The kinetics of lamellar flipping are characterized by time scales taking up to 90 minutes (Wang et al, 1999).

3. PLURONICS UNDER SHEAR

Pluronics are triblock copolymers of the type PEO-PPO-PEO containing poly(ethylene oxide) and poly(propylene oxide) blocks. They form micelles in water. P85 pluronics form spherical micelles in d-water in the mass fraction range of 25% or 30% (used here) and for temperatures above 20 ^{o}C. SANS investigations have been performed using SANS and the Couette shear cell. Interesting shear-induced texture of the packed spheres structure was observed (Slawecki et al, 1998). For example, a novel shear-induced structure with 2D hexagonal symmetry was observed. The unit cell of this "crystalline" structure was determined to be characterized by a = b=133 Å and c = 209 Å. This structure changes upon shear cessation.

Radial Beam **Tangential Beam**

sample gap

shear gradient

shear

0.5 mm

shear

shear gradient

20 s^{-1}

0 s^{-1}
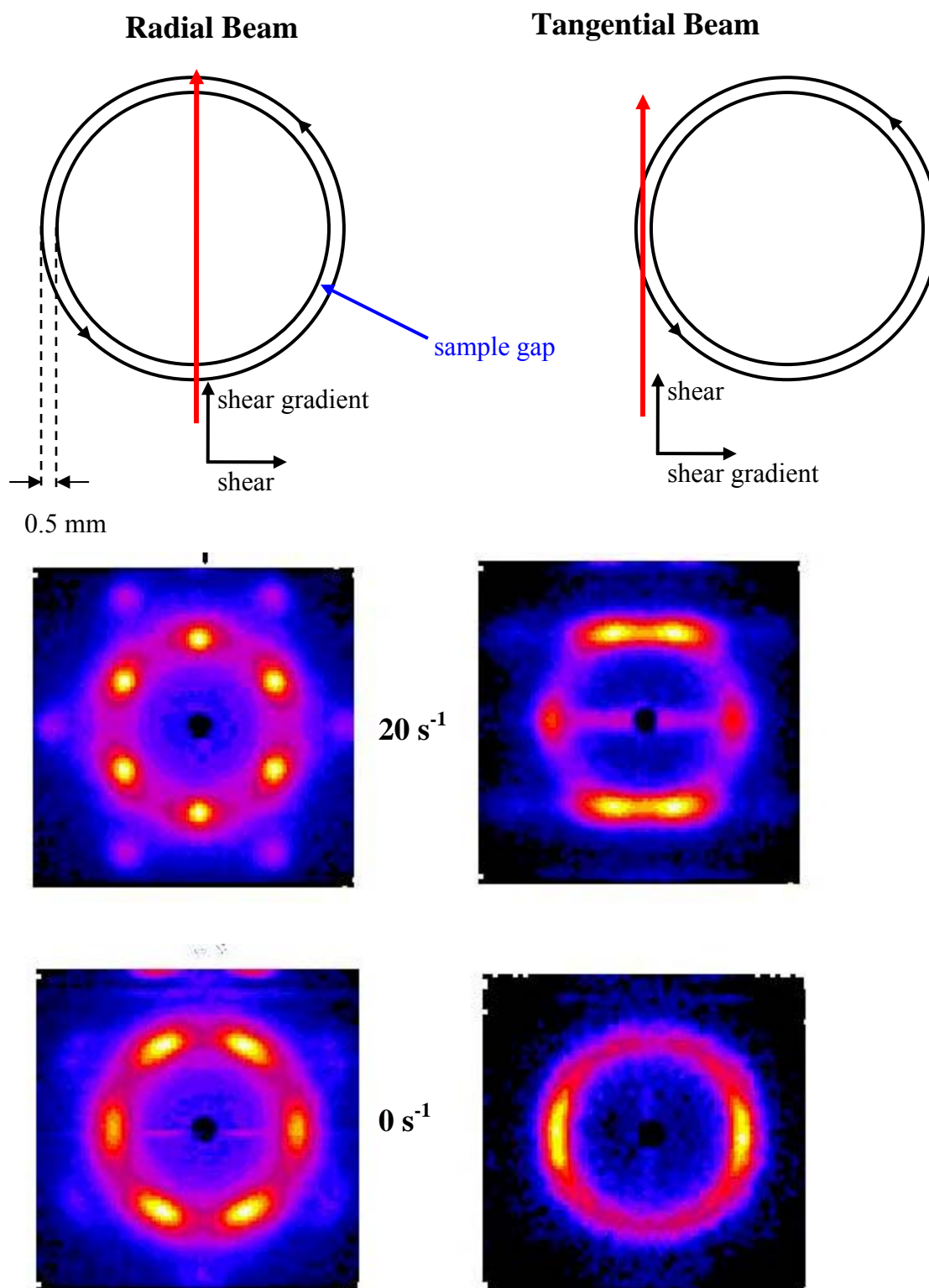
Figure 7: SANS patterns from 25% P85 in d-water under steady shear (20 s^{-1}) and after shear cessation. The left and right sides are for the radial and tangential beam geometries respectively. The schematics on the top show the Couette shear cell flow geometry.

4. MIXED COPOLYMER MORPHOLOGIES UNDER SHEAR

Individual lamellar and spherical copolymer morphologies have been investigated extensively under shear. A question comes to mind: what morphologies would be obtained when mixing samples with lamellar and spherical morphologies together? The answer to this question is addressed here.

The plate-plate shear cell is well suited for SANS investigations of copolymers under shear. It consists of sandwiching the copolymer sample in-between a sliding plate and a fixed one. The shear rate (or frequency) and the strain (or travel distance) are controlled. Note the three characteristic directions: shear, shear gradient and neutral.
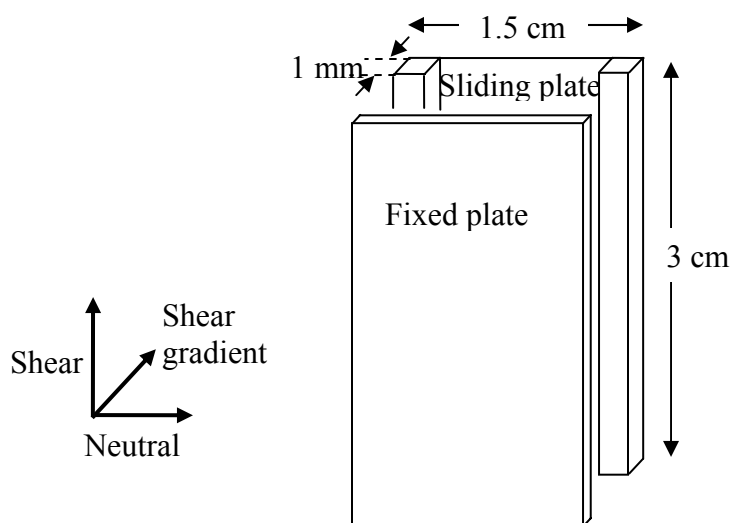
Figure 8: The plate-plate shear cell used for copolymers.

Asymmetric copolymer samples characterized by lamellar and spherical morphologies were homogeneously mixed and then investigated by SANS with in-situ plate-plate reciprocating shear. Two separate copolymers were measured (1) block copolymers of polystyrene and poly(ethylene-butene-1) (Krishnamoorti et al, 2000) and (2) block copolymers of polystyrene and polyisoprene (PS-PI) (Krishnamoorti et al, 2000).

Shearing at various temperatures (below the ODT) helps orient the sample morphology yielding scattering peaks in the horizontal and vertical directions. Two geometries were used (1) with a circular neutron beam along the shear gradient direction or (2) with a (vertical) slit-defined neutron beam along the neutral direction. Note that lamellae are characterized by a series of reflections at Q^*, $2Q^*$, $3Q^*$ where Q^* is the first reflection. Cylinders are characterized by Q^*, $\sqrt{3}\,Q^*$, $\sqrt{4}\,Q^*$ while spheres are characterized by Q^*, $\sqrt{2}\,Q^*$, $\sqrt{5}\,Q^*$. Monitoring the first peak sequence gives clues as to the sample structure.
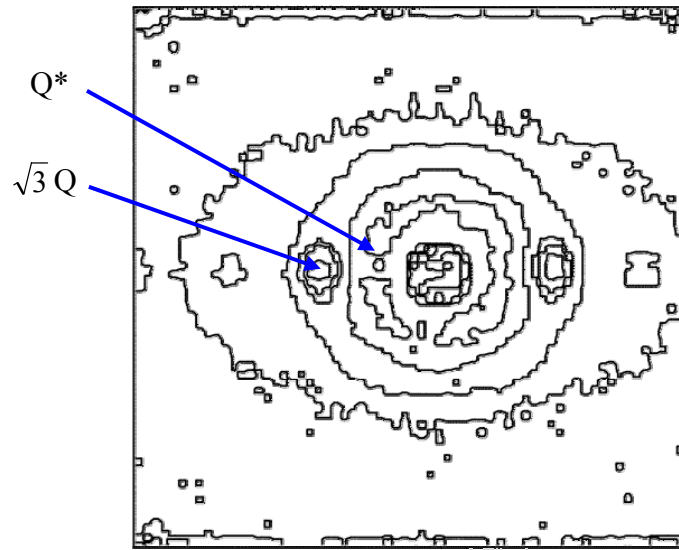
Figure 9: Shear aligned copolymer sample with cylindrical morphology characterized by a hexagonally close packed structure for cylinders aligned vertically with peaks at Q^*, $\sqrt{3}Q^*$, etc. The neutron beam is parallel to the shear gradient direction.

This technique yields a wide range or possible morphologies obtained by mixing lamellae and spheres. These include spheres, lamellae, cylinders and disordered phase morphology. Simple ideal mixing predictions are far from what was observed experimentally.
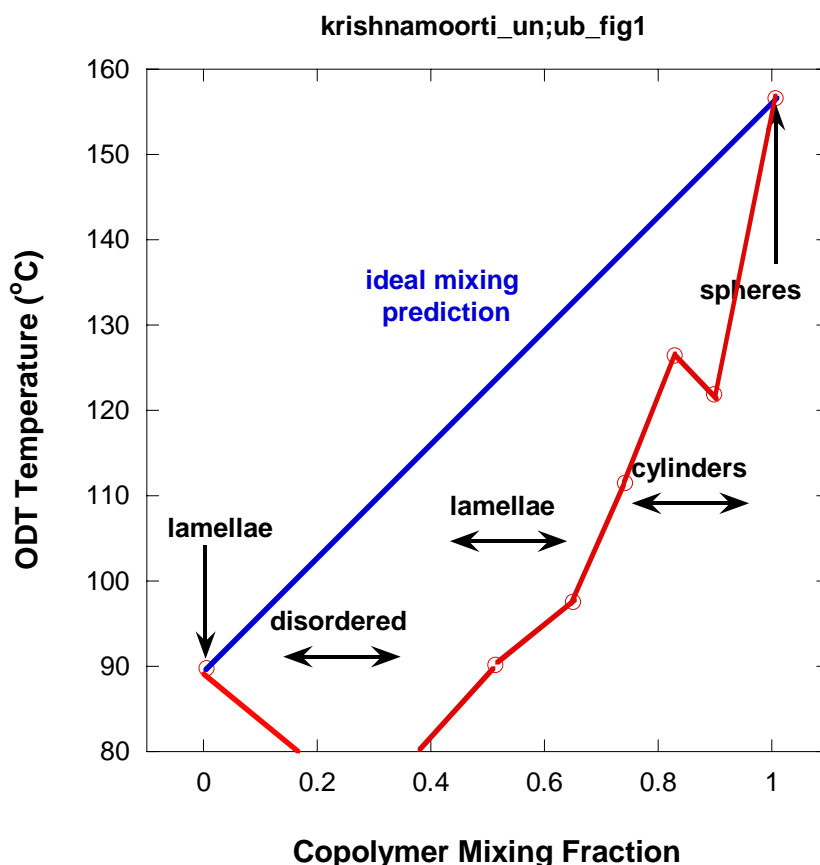
Figure 10: The range of different morphologies obtained by mixing PS-PI copolymer samples corresponding to lamellar and spherical morphologies at various fractions.

5. COMMENTS

Our focus here was on demonstrating the richness of possibilities afforded by the use of SANS with in-situ shear. We have described the effect of Couette and plate-plate shear on liquid crystal micelles and copolymer systems. Shear is useful for the investigation of various morphologies including lamellar, cylindrical and spherical. It is noted that the projects described here made use of in-situ shear cells with no regard to stress measurements; these are not rheometers. Rheometers have recently been adapted for SANS geometry.

REFERENCES

J. Mang, S. Kumar and B. Hammouda, "Discotic Micellar Nematic and Lamellar Phases under Shear Flow", Europhysics Lett. 28, 489-494 (1994)

B. Hammouda, J. Mang and S. Kumar, "Shear-Induced Orientational Effects in Discotic Liquid Crystal Micelles", PRE 51, 6282-6285 (1995)

N.P. Balsara and B. Hammouda, "Shear Effects on Solvated Block Copolymer Lamellae: PS-PI in DOP", PRL 72, 360-364 (1994)

N.P. Balsara, B. Hammouda, P.K. Kesani, S.V. Jonnalagadda and G.C. Straty, "In-Situ Small-Angle Neutron Scattering from a Block Copolymer Solution under Shear", Macromolecules 27, 2566-2573 (1994)

H. Wang, M.C. Newstein, A. Krishnan, N.P. Balsara, B.A. Garetz, B. Hammouda and R. Krishnamoorti, "Ordering Kinetics and Alignment of Block Copolymer Lamellae under Shear Flow", Macromolecules 32, 3695-3711 (1999)

T.M. Slawecki, C.J. Glinka and B. Hammouda, "Shear-Induced Micellar Crystal Structures in an Aqueous Triblock Copolymer Solution", PRE 58, R4084-R4087 (1998)

R. Krishnamoorti, A.S. Silva, M.A. Modi and B. Hammouda, "SANS Study of a Cylinder-to-Sphere Order-to-Order Transition in Block Copolymers", Macromolecules 33, 3803-3809 (2000).

R. Krishnamoorti and B. Hammouda, "Mixed Copolymer Morphologies under Shears", Unpublished Results (2000).

QUESTIONS

1. What is the difference between a shear rate and a shear frequency? How about a rotation frequency and an angular rotation frequency?
2. What are the various types of shear cells? Which ones were used here?
3. What is the most common orientation of layered (lamellar) structure under Couette shear?
4. Define the three main axes used with shear geometry.
5. Define the three (called A, B, and C) types of shear alignment.
6. Describe the "flipping" transition. What shear alignment types does it involve?
7. How much travel is required to shear a 0.5 mm thick sample to a strain of 200%?

ANSWERS

1. The shear rate and shear frequency are the same thing. This is the number of rotations per second (given in units of Hz). The rotation frequency ν (units of Hz) is related to the angular rotation frequency ω (units of rad/s) as $\omega = 2\pi\nu$.
2. Shear cells include the Couette type, the Poiseuille type, the plate-plate type and the cone-plate type among others. The Couette and the plate-plate were used here.
3. Layered (lamellar) structures tend to orient parallel to the moving shear cell walls under Couette flow.
4. The three main axes used in shear geometry are: the shear direction, the shear gradient direction and the neutral (also called the vorticity) direction.
5. The three types of shear alignment are described in Figure 2 in the text.

6. The flipping "transition" corresponds to a transition from the C alignment type to the A alignment type.

7. 1 mm of travel is required in order to shear a 0.5 mm thick sample to a strain of 200 %.

Chapter 55 – SANS FROM POLYMERIC MATERIALS

Materials Science is one of the major SANS research areas. A host of Materials Science projects are performed using the SANS technique. Here, a couple of projects in which this author was involved are described. Focus is on macromolecular orientation in polymeric materials associated with various types of deformation and processing. Macromolecular orientation affects the mechanical properties or polymeric materials.

1. MATERIALS AND METHOD

The projects described here use partially deuterated polystyrene to monitor macromolecular chain deformations associated with specific sample treatments. Deuterated atactic polystyrene (dPS) of $M_w = 338,000$ g/mol and $M_n = 239,000$ g/mol and hydrogenated (normal) polystyrene (hPS) of comparable molecular weight have been synthesized and characterized by GPC. A 5% dPS weight fraction was mixed to hPS in solution. The homogeneous mixture was then dried. Various partially deuterated PS plates of uniform thickness were produced using melt-pressing.

The SANS technique was used to monitor macromolecular chain orientation associated with various sample treatments such as hot-stretching, injection molding and shear band formation. The SANS instrument used (University of Missouri Research Reactor) was set to a neutron wavelength of 4.75 Å. This wavelength is obtained using a pyrolitic graphite monochromator with a 90° take-off angle. SANS data analysis consisted in a standard sector averaging method as well as in the elliptical averaging method which results in radii of gyration parallel and perpendicular to the orientation direction. The birefringence method was also used in some cases in order to compare chain orientations. The birefringence method averages over inter-chain contributions and can be measured over small spot sizes whereas the SANS technique is more sensitive to single-chain orientation. SANS sample thickness varied between 1 and 2 mm and the spot size diameter was 1 cm. Single-chain scattering was represented by the familiar Debye function for Gaussian polymer coils.

2. MACROMOLECULAR ORIENTATION WITH HOT STRETCHING

The 5% dPS/hPS homogeneous polymer mixture was compression molded into bars that were hot stretched in an Instron machine for stretching ratios from 1 to 4 under a temperature of 110 ^{o}C; i.e., slightly above the softening glass-rubber transition temperature T_g for PS. Upon reaching the desired External Draw Ratio (EDR) the samples were quenched in water at 23 ^{o}C.

SANS measurements were made from the hot stretched PS samples after and before hot stretching (Hammouda et al, 1986). Radii of gyration R_{gy} and R_{gx} along and perpendicular to the stretch direction after hot stretching and R_{g0} before hot stretching were obtained. Iso-intensity contour maps displayed elliptical asymmetry. The elliptical eccentricity ε is defined as the ratio $\varepsilon = R_{gx}/R_{gy}$. The Molecular Draw Ration (MDR) is defined as MDR = R_{gy}/R_{g0}.

Assuming that the molecular volume is conserved during deformation and that the x and z directions are equivalent, the MDR would also be given by $\sqrt{MDR} = R_{gx} / R_{g0}$.

Hot Stretched Polystyrene
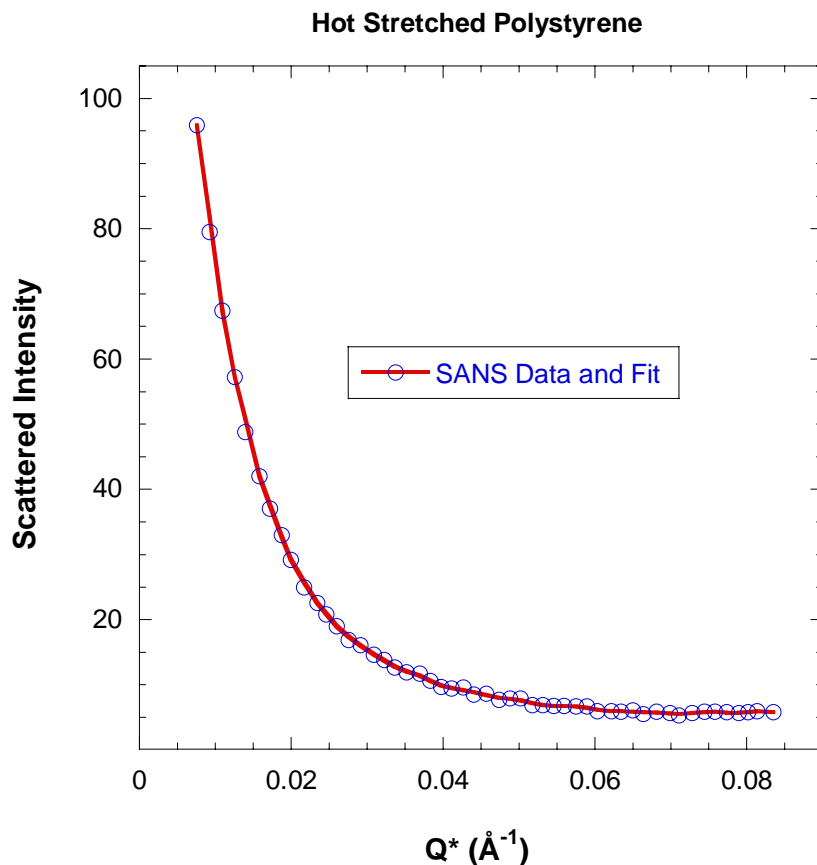
Figure 1: Typical SANS data from a hot stretched sample and fit to the Debye function.

A table summarizes the hot stretching conditions that produced the five samples and the radii of gyration results obtained from SANS measurements at ambient temperature. The birefringence measurements have also been included.

Table 1: Hot stretched samples and chain orientation results obtained from SANS and birefringence measurements

Sample	Load (lbs)	Stretch Rate (inch/min)	Temp (^{o}C)	EDR	Eccent. ε	R_{gy} (Å)	R_{gx} (Å)	MDR	Birefring. $*10^3$
CDS1	12.8	10	110	2.0	.45	249	112	1.70	5.74
CDS2	15.1	10	110	1.5	.75	170	127	1.21	1.78
CDS3	11	10	110	2.75	.33	293	97	2.09	8.80
CDS4	10	5	110	4	.30	330	99	2.23	10.02
CDS5	--	10	110	1.75	.54	214	116	1.51	4.21

A plot of the MDR vs EDR shows that chain deformations become nonlinear (i.e., non-affine) for large EDR values. Note that the trends obtained from SANS and birefringence measurements are similar.
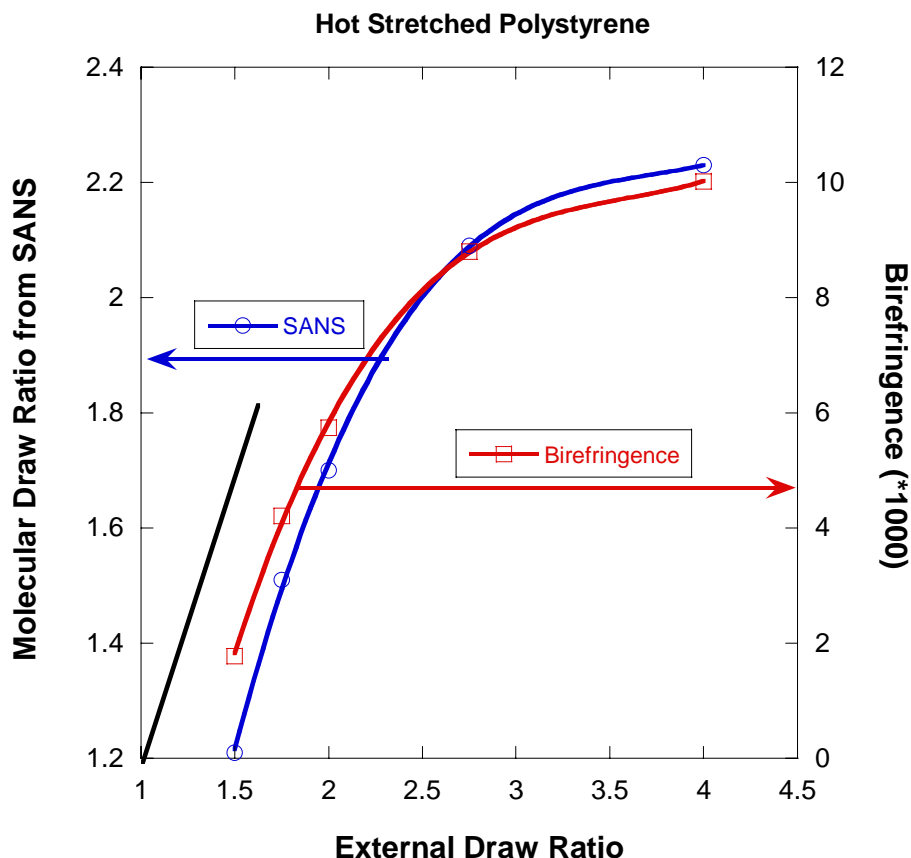
Figure 2: Plot of the MDR for varying EDR. Results from SANS and birefringence measurements are included. The line with a slope of 1 is also shown.

3. HOT STRETCHING REVISITED

Similar SANS measurements were performed on another series of partially deuterated hot stretched polystyrene bars (Schroeder, 1991). The deuteration level was increased to 20% for increased sensitivity. The MDR were obtained and plotted with increasing EDR. The SANS results were compared to rubber elasticity models. The simplest model assumes an affine deformation whereby $R_{gy} = R_{g0} * EDR$ and $R_{gx} = R_{g0} / \sqrt{EDR}$ where R_{gy}, R_{gx} and R_{g0} are the radii of gyration parallel, perpendicular and before stretching respectively. The prediction for the direction perpendicular to stretching falls on top of the data while the prediction parallel to the stretching direction is far from the data points. Polynomial fit to the data parallel to the stretch direction yielded a good fit for a second order polynomial.
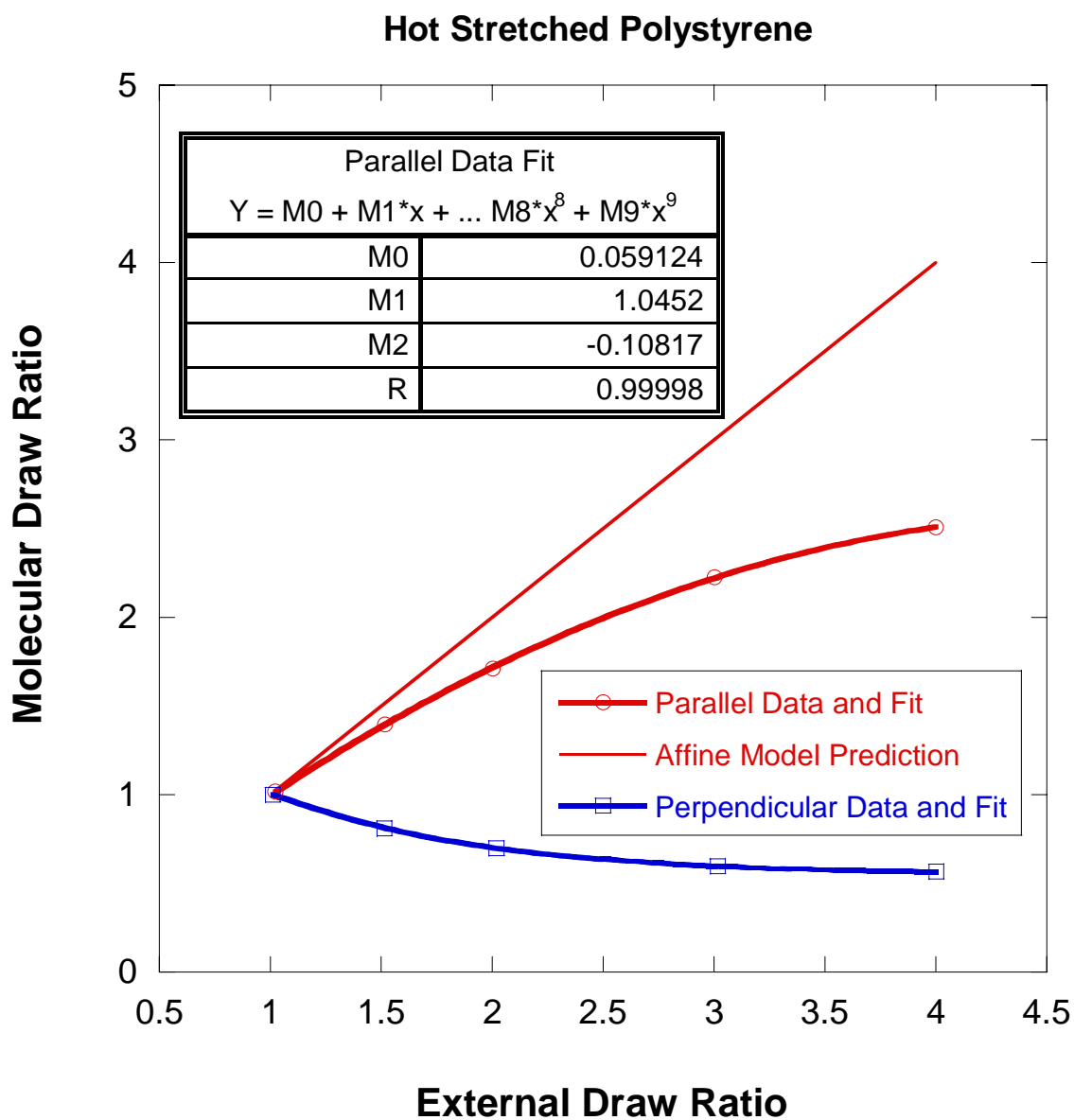
Figure 3: Variation of the MDR with EDR along with predictions of a rubber elasticity model.

More precise elliptical fitting of the iso-intensity contour maps showed that the eccentricity depends on the scattering variable Q, and therefore on the length scale in direct space.

4. MACROMOLECULAR ORIENTATION WITH INJECTION MOLDING

Injection molding is the most widely used method for polymer processing. It is characterized by high repetition rates, low cost and high precision. During the injection, packing and cooling stages of the molding process, flow and thermal stresses develop resulting in preferential orientation of the polymer chains. Macromolecular orientation associated with injection molding was investigated using the SANS technique on the same 5% dPS/hPS polystyrene mixture (Hammouda et al, 1986). 5 cm diameter disks and 2 cm wide by 15 cm long bars were injection molded using specific conditions.

Table 2: Injection molding conditions

	Cold Conditions	Hot Conditions
Melt Temperature	167 ^{o}C	229 ^{o}C
Pressure	3700 psi	2500 psi
Injection Time	8 s	8 s
Cooling Time	30 s	30 s
Band Temperature	176 ^{o}C	246 ^{o}C
Mold Temperature	24 ^{o}C	65 ^{o}C

Injection molded bars and disks were 3 mm thick. This thickness was chosen in order to be able to mill down a few spots in order to observe chain orientation close to the skin surface of deep inside the bulk. The milled down spots had an optimal thickness of 1.5 mm appropriate for SANS.
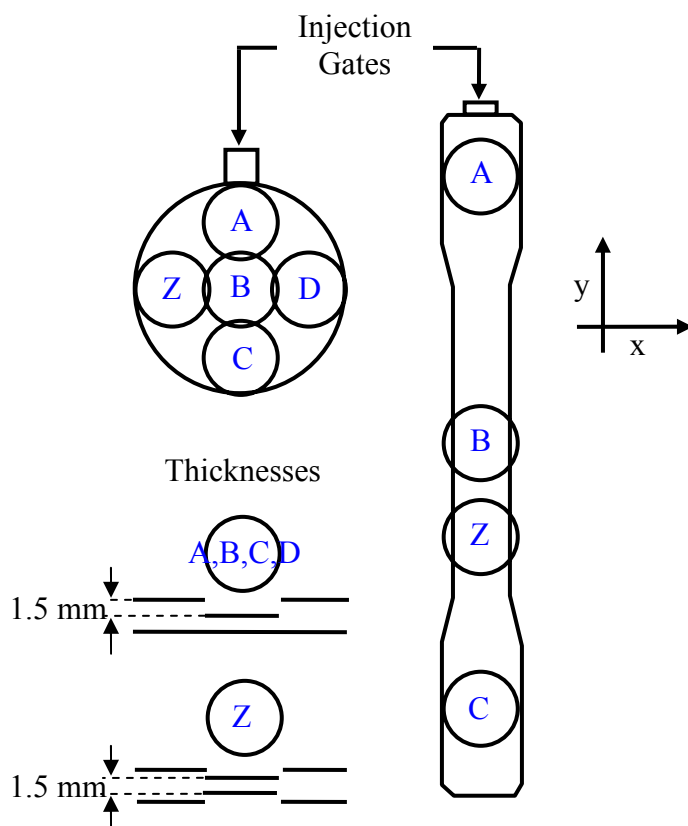
Figure 4: Injection molded disk and bar.

SANS measurements were performed and eccentricity factors (ε) and orientation angles of the iso-intensity contour maps were obtained. Representative results are included here.

Table 3: Eccentricity and orientation angle for one of the injection molded samples (cold molded disk).

	Eccentricity	Orientation Angle (degrees)
Spot A	.63	5
Spot B	.77	9
Spot C	.87	24
Spot D	.79	38
Spot Z	.92	40

Analysis of the SANS results yielded the following conclusions: there is more macromolecular chain orientation close the injection gate than away from it, close to the sample surface than deep inside, in open parts of the sample than in corners. Moreover, the "cold" condition injection molding showed more orientation than the "hot" condition.

5. MACROMOLECULAR ORIENTATION IN SHEAR BAND DEFORMATIONS

Polymeric materials have two main modes of deformation: the elastic and the plastic modes. The plastic mode is of interest since it involves irreversible mechanisms of deformation. Shear bands form in notched and compressed samples. Birefringence has been the main technique to investigate macromolecular chain orientation within shear bands. It was found that shear band packet propagates at 38° from the compression axis and that there is formation of a diffuse shear zone which propagates ahead of the shear band at 45°.

In order to investigate chain orientation within shear bands using the SANS technique, a 2 mm thick plaque of 5% dPS/hPS mixed polystyrene was molded. Identical rectangular plates (2 cm*4 cm) were cut out, sharply notched (notch was less than 1 mm deep) and compressed in a special device (Bubeck et al, 1986). Cases corresponding to fast and slow compression were considered. After compression schemes taking of order of minute(s) at various temperatures, the device was locked at the target strain, cooled to ambient temperature after which SANS data were taken. A new sample was used for each case. The compression was along the y axis making the x-y plane parallel to the scattering plane.

Four holes for heater probes

Cadmium internal lining

Holes for temperature control

Disk to center the device on the sample tray

Thin aluminum windows

Side spacers

Notched sample

Screws to block the device at the desired strain

Ruler to measure strains
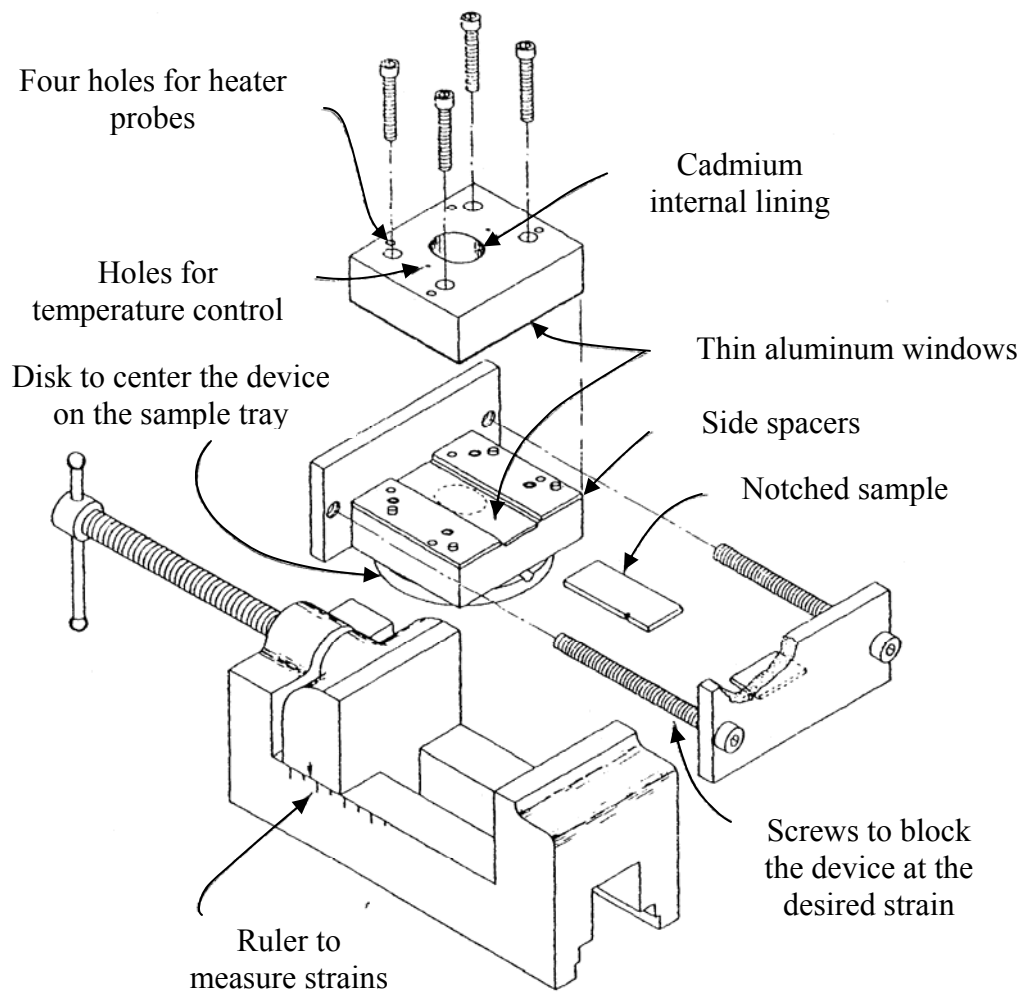
Figure 5: Representation of the device used to create shear bands.
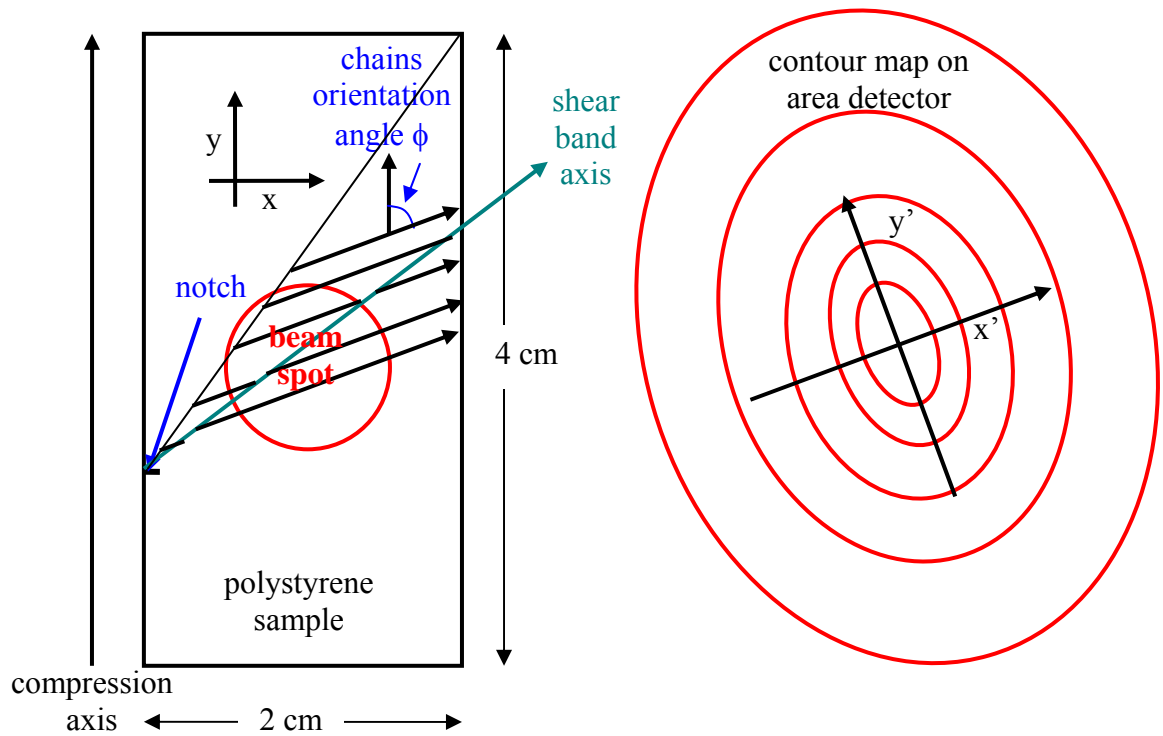
Figure 6: Representation of the sample plane (in direct space) and of the scattering plane (reciprocal space). Note that the neutron area detector is 64 cm*64 cm whereas the sample is 2 cm*4 cm.

Results of the SANS data analysis are summarized in a table. The radii of gyration parallel (y') and perpendicular (x') to the chain orientation axis were obtained using fits to the Debye functional form. An overall radius of gyration was also obtained as

$R_g = \sqrt{(R_{gy'}^2 + 2R_{gx'}^2)/3}$. The eccentricity was obtained as the ratio $\varepsilon = R_{gx'}/R_{gy'}$.

Table 4: Conditions used to create shear bands and SANS macromolecular orientation results.

Temperature (°C)	Strain (%)	Strain Rate (s⁻¹)	Eccentricity ε	Orientation Angle (degrees)	$R_{gy'}$ (Å)	$R_{gx'}$ (Å)	R_g (Å)
80	7.5	$5*10^{-3}$	.90	80	138	124	129
60	7.5	$5*10^{-3}$	.90	82	168	151	157
40	7.5	$5*10^{-3}$	.90	84	165	148	154
90	7.5	$5*10^{-4}$	.82	79	148	131	137
70	7.5	$5*10^{-4}$	.84	78	158	133	142
50	7.5	$5*10^{-4}$	.82	78	170	139	150
30	7.5	$5*10^{-4}$	.82	84	181	148	160

90	12.5	$4.6*10^{-4}$	.74	80	152	112	127
80	12.5	$4.6*10^{-4}$	.72	78	157	113	129
70	12.5	$4.6*10^{-4}$	.74	78	160	118	133
50	12.5	$4.6*10^{-4}$	.73	77	160	117	133
40	12.5	$4.6*10^{-4}$	.72	78	161	116	133
20	12.5	$4.6*10^{-4}$	.78	76	154	120	132

Some of the conclusions from the SANS results are included here. Macromolecules participating in the shear band are oriented at about 81° from the compression axis regardless of the compression conditions (temperature, strain and strain rate). This is in agreement with the birefringence measurements showing a $38^o+45^o = 83^o$ orientation angle. Only glide modes of deformation of elongated coils are observed in the shear bands. Diffusion modes are not prominent in our measurement conditions. Non-affine chain deformation was observed. These are plastic modes of deformation. Saturation was observed for the high strain rate case.

REFERENCES

B. Hammouda, R.A. Bubeck and D.F.R. Mildner, "Macromolecular Orientation in Hot Stretched and Injection Molded Polystyrene", Polymer 27, 393-397 (1986)

R.A. Bubeck, B. Hammouda and H. Kaiser, "Macromolecular Orientation Associated with Shear bands in Compressed Polystyrene", Polymer Communications 27, 354-356 (1986)

J.R. Schroeder, B. Hammouda, R.A. Bubeck and J.W. Chang, "SANS from Hot Stretched Polystyrene Revisited", J. Polym. Sci., Polym. Phys. Ed. 29, 1607-1612 (1991)

QUESTIONS

1. How to hot stretch a polymer bar? What instrument is used for that?
2. How is injection molding performed? What are the determining factors?
3. What are shear bands? How to obtain them?
4. Why is the Debye function adequate for the description of polymer chains in the melt?
5. Name two methods that are sensitive to macromolecular chain orientation.

ANSWERS

1. A polymer bar is hot stretched by heating slightly above the softening glass-rubber transition temperature (T_g), stretching to the desired external draw ration and quenching in cold water. The Instron machine is used for hot stretching.
 2. Injection molding is performed by melting the polymer, injecting the melt into a mold in a screw device, then cooling down. Temperature, pressure and injection rate are the determining factors.

3. Shear bands are a form of plastic deformation in polymeric materials. Shear bands are obtained by notching and compressing a sample which is confined in order to avoid buckling.

4. Polymer chains follow Gaussian chain statistics in the melt state; i.e., they follow a random walk with no excluded volume.

5. Two methods that are sensitive to macromolecular chain conformation are optical birefringence and SANS. SANS is more sensitive but requires partially deuterated samples.

Chapter 56 - **NEUTRON SCATTERING WITH SPIN POLARIZATION**

The neutron spin affects nuclear and magnetic scattering. Polarized neutrons are useful in magnetic systems as well as in the process of separation of incoherent and coherent scattering. In what follows, the spin dependent elastic neutron scattering cross section is derived and discussed. The approach used by Moon et al (1969) has been followed.

1. THE SPIN DEPENDENT ELASTIC NEUTRON SCATTERING CROSS SECTION

Consider an elastic scattering experiment with incident neutron spin s and nuclear spin I in the sample. Within the first Born approximation of Quantum Mechanics, the elastic neutron scattering cross section (per atom) is given in terms of the average of the potential V(Q) between the initial state |i> and final state |f>.

$$\frac{d\sigma(Q)}{d\Omega} = \left(\frac{2\pi m}{h^2}\right)^2 \frac{1}{N^2} \sum_{i,f} P_i \, |< f \,|\, V(Q) \,|\, i >|^2 \; . \tag{1}$$

Here m is the neutron mass. Averaging over the initial state and summing up over the final state have been performed. P_i is the probability of finding the neutron-nucleus system in the initial state. V(Q) is the Fourier transform of the Fermi pseudo-potential V(r):

$$V(r) = \left(\frac{h^2}{2\pi m}\right) \frac{1}{N} \sum_i (b_i + 2B\vec{s}.\vec{I}_i)\delta(\vec{r} - \vec{r}_i) \; . \tag{2}$$

Here b_i is the scattering length of the ith nucleus, $\vec{s}$ is the neutron spin operator. $\vec{I}_i$ and $\vec{r}_i$ are the spin operator and the position of the ith nucleus. B is related to the spin-incoherent scattering length b_{incoh} by the defining relation:

$$B = \frac{b_{incoh}}{\sqrt{I(I+1)}} \; . \tag{3}$$

The initial and final states are separated as |i>=|sI> and |f>=|s'I'> where |s> and |s'> are the initial and final neutron spin states and |I> and |I'> are the initial and final nuclear spin states. The spin-dependent cross section is given by:

$$\frac{d\sigma^{ss'}(Q)}{d\Omega} = \sum_{I,I'} P_I \, |< I's'|\, V(Q) \,|\, sI >|^2 \tag{4}$$

$$= \sum_{I,I'} P_I \, |< I's'|\, \frac{1}{N} \sum_i \exp(i\vec{Q}.\vec{r}_i)(b_i + 2B\vec{s}.\vec{I}_i) \,|\, sI >|^2 \; .$$

Neglecting isotopic incoherence makes b_i and $\vec{I}_i$ independent of the i index. Therefore:

$$\frac{d\sigma^{ss'}(Q)}{d\Omega} = \sum_{I,I'} P_I \left| < I' < s' | (b + 2B\vec{s}.\vec{I}) | s > \frac{1}{N} \sum_i \exp(i\vec{Q}.\vec{r}_i) | I > \right|^2 . \qquad (5)$$

In order to perform the neutron spin averages, we introduce the Pauli spin matrices $\vec{\sigma} = 2\vec{s}$ defined as:

$$\sigma_x = \begin{pmatrix} 0 & 1 \\ 1 & 0 \end{pmatrix} \qquad \sigma_y = \begin{pmatrix} 0 & -i \\ i & 0 \end{pmatrix} \qquad \sigma_z = \begin{pmatrix} 1 & 0 \\ 0 & -1 \end{pmatrix}. \qquad (6)$$

The neutron eigenstates $|s>$ and $|s'>$ correspond to the spin up $|+>$ and spin down $|->$ states which form a complete basis set:

$$|+> = \begin{pmatrix} 1 \\ 0 \end{pmatrix} \quad \text{and} \quad |-> = \begin{pmatrix} 0 \\ 1 \end{pmatrix}. \qquad (7)$$

Noting that $2\vec{s}.\vec{I} = \vec{\sigma}.\vec{I} = \sigma_x I_x + \sigma_y I_y + \sigma_z I_z$ and assuming that the neutron spin directions are along the z axis, the various averages can be worked out as:

$$< + | b + B\vec{\sigma}.\vec{I} | + > = b + B I_z \qquad (8)$$
$$< - | b + B\vec{\sigma}.\vec{I} | - > = b - B I_z$$
$$< - | b + B\vec{\sigma}.\vec{I} | + > = B(I_x + iI_y)$$
$$< + | b + B\vec{\sigma}.\vec{I} | - > = B(I_x - iI_y).$$

One specific spin-dependent cross section is as follows:

$$\frac{d\sigma^{++}(Q)}{d\Omega} = \sum_{I,I'} P_I \left| < I' | (b + B I_z) \frac{1}{N} \sum_i \exp(i\vec{Q}.\vec{r}_i) | I > \right|^2 \qquad (9)$$

$$= \sum_I P_I < I | (b + B I_z) \frac{1}{N} \sum_i \exp(i\vec{Q}.\vec{r}_i) \sum_{I'} | I' > < I' | (b + B I_z) \frac{1}{N} \sum_j \exp(-i\vec{Q}.\vec{r}_j) | I >.$$

Using the sum rule: $\sum_{I'} | I' > < I' | = 1$, this expression can be simplified to the form:

$$\frac{d\sigma^{++}(Q)}{d\Omega} = \sum_I P_I < I | (b + B I_z)^2 | I > \frac{1}{N^2} \sum_{i,j} < \exp\left(i\vec{Q}.(\vec{r}_i - \vec{r}_j)\right) > . \qquad (10)$$

Assume non polarized nuclei with $P_I = 1/(2I+1)$, define $\vec{r}_{ij} = \vec{r}_i - \vec{r}_j$, and use the following property:

$$I_z^2 | I > = \frac{1}{3}\vec{I}^2 | I > = \frac{1}{3}I(I+1) | I >. \qquad (11)$$

On the left hand side $\vec{I}^2$ is a spin operator while on the right-hand side $I(I+1)$ is its eigenvalue for eigenstate $|I\rangle$. Note that in $(b + BI_z)^2 = b^2 + B^2 I_z^2 + 2bBI_z$ only the first two terms contribute because $\sum_I P_I < I | I_z | I >= 0$.

Therefore:

$$\frac{d\sigma^{++}}{d\Omega} = b^2 \frac{1}{N^2} \sum_{i,j} \exp(i\vec{Q}.\vec{r}_{ij}) > + \frac{1}{3} b_{incoh}^2 . \qquad (12)$$

The other partial spin dependent cross sections can be obtained similarly as:

$$\frac{d\sigma^{--}}{d\Omega} = b^2 \frac{1}{N^2} \sum_{i,j} \exp(i\vec{Q}.\vec{r}_{ij}) > + \frac{1}{3} b_{incoh}^2 \qquad (13)$$

$$\frac{d\sigma^{+-}}{d\Omega} = \frac{2}{3} b_{incoh}^2$$

$$\frac{d\sigma^{-+}}{d\Omega} = \frac{2}{3} b_{incoh}^2 .$$

Use was made of the definition of B through $B^2 I(I+1) = b_{incoh}^2$. One can rewrite these results in terms of non-spin-flip (NSF), spin flip (SF), incoherent and coherent cross sections as follows:

$$\left[\frac{d\sigma}{d\Omega}\right]_{NSF} = \left[\frac{d\sigma}{d\Omega}\right]_{coh} + \frac{1}{3}\left[\frac{d\sigma}{d\Omega}\right]_{incoh} \qquad (14)$$

$$\left[\frac{d\sigma}{d\Omega}\right]_{SF} = \frac{2}{3}\left[\frac{d\sigma}{d\Omega}\right]_{incoh} .$$

Note that the coherent cross section depends on Q while the incoherent one does not.

2. SEPARATE-OUT THE COHERENT AND INCOHERENT CROSS SECTIONS

The previous results can be written in the following alternative form:

$$\left[\frac{d\sigma}{d\Omega}\right]_{coh} = \left[\frac{d\sigma}{d\Omega}\right]_{NSF} - \frac{1}{2}\left[\frac{d\sigma}{d\Omega}\right]_{SF} \qquad (15)$$

$$\left[\frac{d\sigma}{d\Omega}\right]_{incoh} = \frac{3}{2}\left[\frac{d\sigma}{d\Omega}\right]_{SF} .$$

These equations are used to separate out coherent from incoherent scattering using spin polarization and analysis.

3. SUM OF THE SPIN-DEPENDENT CROSS SECTIONS

Defining P_+ and P_- as the probabilities of finding the incident neutron in the up or down states, the sum of all spin-dependent cross sections is given by:

$$\frac{d\sigma}{d\Omega} = P_+\left(\frac{d\sigma^{++}}{d\Omega} + \frac{d\sigma^{+-}}{d\Omega}\right) + P_-\left(\frac{d\sigma^{-+}}{d\Omega} + \frac{d\sigma^{--}}{d\Omega}\right). \qquad (16)$$

For unpolarized neutrons ($P_+ = P_- = 1/2$) or for polarized neutrons (either $P_+=1$, $P_-=0$ or $P_+=0$, $P_-=1$), we have:

$$\frac{d\sigma}{d\Omega} = b^2 \frac{1}{N^2} \sum_{i,j} < \exp(i\vec{Q}.\vec{r}_{ij}) > + b_{incoh}^{\,2}. \qquad (17)$$

Note that the double summation of the phase factors still needs to be averaged over atomic positions and orientations (this average is noted $< ... >$). The coherent scattering length is referred to as b_{incoh} instead of b_i (usual notation) in order to avoid confusion with the "i" summation index. The cross sections σ can be obtained from the differential cross sections by integration over all solid angles as $\sigma = \int d\Omega \left(\frac{d\sigma}{d\Omega}\right)$. For example, the scattering cross section integrates to the sum of the coherent and incoherent cross sections:

$$\sigma_s = 4\pi(b^2 + b_{incoh}^{\,2}).$$

The treatment described here concerns only spin-incoherence. Contributions from isotopic and composition (disorder) incoherence are easily performed as described previously.

4. NEUTRON SPIN POLARIZATION FACTOR

The final neutron spin polarization P_f is defined as:

$$\frac{d\sigma}{d\Omega}P_f = P_+\left(\frac{d\sigma^{++}}{d\Omega} - \frac{d\sigma^{+-}}{d\Omega}\right) + P_-\left(\frac{d\sigma^{-+}}{d\Omega} - \frac{d\sigma^{--}}{d\Omega}\right). \qquad (18)$$

Assuming incident neutrons polarized in the up direction ($P_+=1$, $P_-=0$) or down direction ($P_+=0$, $P_-=1$), one obtains:

$$P_f = \frac{b^2 \dfrac{1}{N^2} \sum_{ij} < \exp(i\mathbf{Q}.\mathbf{r}_{ij}) > - \dfrac{1}{3} b_{incoh}^{\,2}}{b^2 \dfrac{1}{N^2} \sum_{ij} < \exp(i\mathbf{Q}.\mathbf{r}_{ij}) > + b_{incoh}^{\,2}}. \qquad (19)$$

For non-polarized neutrons ($P_+ = P_- = 1/2$) one obtains the trivial result of $P_f = 0$.

With the possibility of using a spin polarizer and spin analyzer, one could separate out the coherent from the spin-incoherent cross sections.

5. NUCLEAR SPIN POLARIZATION

Polarization of the nuclear spins is very difficult to achieve. It has been performed in rare-earth metals at very low temperatures (in the mK range). These are magnetic systems whereby strong electron spin moments transfer polarization to the nuclear spins. The low temperatures are required to damp out phonon modes thereby reducing strong lattice coupling which makes nuclear polarization difficult. Spin polarization has also been achieved through optical pumping of electronics states in He-3. Nuclear spin polarization is then achieved through collisions.

6. SUPERMIRROR NEUTRON SPIN POLARIZER

SANS polarizers are used in transmission geometry. These consist of supermirror coatings that transmit one spin state and reflect the other spin state. The large difference in the critical angles of the supermirror coating for the down spin state ($\theta_c \sim 2\theta_{Ni}$) and the up spin state ($\theta_c \sim 3\theta_{Ni}$) permit the polarization of a wide cross section neutron beam over a wide neutron wavelength range. θ_{Ni} is the critical angle for neutron reflection for Nickel.

A specific supermirror used on a SANS instrument at NIST consists of Fe/Si coating on 1 mm thick silicon plates aligned to form a V (1.92 ^{o} angle between the two plates) inside a copper-coated neutron guide. This polarizing cavity is 1.2 m long and polarizes a 4*5 cm^2 neutron beam in a wavelength range from 5 Å to 15 Å. Immediately following the polarizing cavity is a flat coil π spin flipper for reversing the direction of polarization. Permanent magnets maintain a 500 gauss vertical field to magnetize the supermirror coating and a 50 gauss field from the supermirror to the sample is used to maintain neutron polarization. This polarizing cavity is installed on a 30 m SANS instrument. It is characterized by a measured polarization of 89% for neutrons of wavelength $\lambda = 8$ Å and $\Delta\lambda/\lambda = 0.15$. The flipper polarization under spin reversal was measured to be 96% for the same wavelength condition.
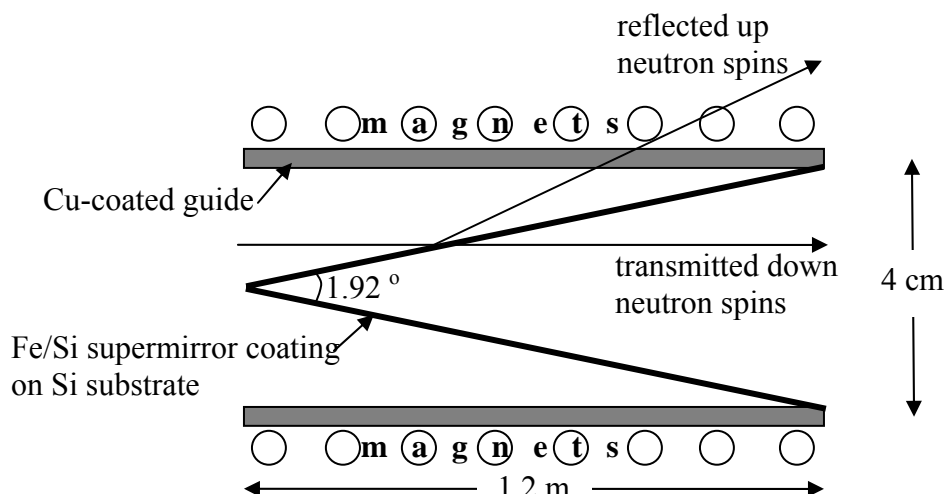
Figure 1: Schematic top view representation of the supermirror polarizing cavity. This figure is not to scale.

7. HE-3 GAS NEUTRON SPIN ANALYZER

Spin polarization analysis is also performed in transmission geometry in SANS instruments. The wide angular divergence of the scattered beam (as much as 20 degrees) prohibits the use of a supermirror polarizing cavity. A large number of these supermirrors would have to be used, each slightly misaligned in the vertical and horizontal directions in order to cover the wide angular divergence. This scheme is too complex to be of practical use. Instead, transmission geometry polarizing "bottles" can be used for polarization analysis. These contain a polarized gas that transmits only one spin state from a neutron beam with broad angular divergence.

A neutron spin analyzer uses polarized helium-3 (He-3) gas. He-3 has a large spin-dependence of the neutron absorption (capture) cross section. The absorption cross section is negligible for neutrons with spins parallel to the He-3 nuclear spins. Other orientations get absorbed. Two methods of polarizing He-3 are used. (1) The spin-exchange optical pumping method consists in polarizing electrons in rubidium (Rb) atoms (using circularly polarized laser light) that then transfer their polarization to He-3 nuclei. Rubidium is added to He-3 in very small amounts (ratio of Rb to He-3 is around 10^{-5}). (2) The metastability-exchange optical pumping method consists in using an electric discharge and a laser light to excite and polarize electrons in He-3 atoms that then transfer their electronic polarization to the He-3 nuclei. Pressures used in polarizing/analyzing bottles are a few bars of He-3 gas pressure. An axial holding magnetic field of 50 gauss is used to maintain polarization. If not constantly maintained, there is a slow exponential decay of the spin polarization inside the polarizing bottle over a period of a few hours to a couple of days. Reasonable neutron polarization has been achieved with the first generation of He-3 analyzer used on the NG3 SANS instrument at the NIST CNR (Gentile et al, 2000).

REFERENCES

R.M. Moon, T. Riste, and W.C. Koehler, "Polarization Analysis of Thermal Neutron Scattering", Physical Review 181, 920-931 (1969)

T.R. Gentile, G.L. Jones, A.K. Thompson, J. Barker, C.J. Glinka, B. Hammouda and J.W. Lynn, J. Appl. Cryst. 33, 771-774 (2000)

QUESTIONS

1. What is the value of the neutron spin? Does that make the neutron a Fermion or a Boson?
2. What is the first Born approximation? What type of neutron scattering does this approximation apply to?
3. What type of scattering are polarized neutrons used for?
4. What is the advantage of using polarized neutrons and polarization analysis?
5. What particle's spins are polarized in magnetic materials? Is it easy to polarize the nuclear spins?
6. Is the incoherent scattering cross section related solely to the non spin flip (NSF) or spin flip (SF) cross section?

ANSWERS

1. The value of the neutron spin is ½. This half integer value makes the neutron a Fermion. Full integer spins characterize bosons (for example photons).
2. The first Born approximation is a simple method for solving the Schrodinger equation. It consists in expanding the Green's function representation of the solution and keeping only the first term. This approximation applies to all types of neutron scattering where multiple scattering is not significant. The only notable exclusion is neutron reflectometry whereby the refraction limit (not diffraction limit) is used instead.
3. Polarized neutrons are used mainly to investigate spin-dependent magnetic scattering.
4. The main advantage of using polarized neutrons and polarization analysis is the sorting out of the various (++, --, +-, and -+) spin-dependent cross sections. These partial cross sections allow the separation of the coherent and incoherent cross sections.
5. The electrons spins are polarized in magnetic materials. It is so difficult to polarize the nuclear spins that it is an unpractical option. It involves very low temperatures and huge magnetic fields.
6. The incoherent scattering cross section is related solely to the spin flip (SF) cross section as $\left[\dfrac{d\sigma}{d\Omega}\right]_{incoh} = \dfrac{3}{2}\left[\dfrac{d\sigma}{d\Omega}\right]_{SF}$.

Chapter 57 – **OTHER SANS TOPICS LITERATURE REVIEW**

This chapter summarizes what is left of the SANS literature compiled over the past seven years from use of the NCNR. It contains a hodgepodge of topics other than polymers, complex fluids and biology. It is presented into three main categories: instrumentation, magnetism and materials science. Materials science itself contains many different subcategories such as carbon nanotubes, ceramics, fuel cell materials, geological materials, dielectric materials, metals and nanoscale materials. This tedious coverage of the SANS literature is meant to be searched for author or subject keyword. Some 126 papers have been reviewed, of which about one fourth has been included.

1. INSTRUMENTATION

An optical filter has been installed upstream of the NG3 SANS instrument in order to replace beryllium and bismuth crystal filters. This optical filter allows the neutron beam to get out of the direct line of sight from the neutron cold source. This eliminates epithermal neutrons and gammas from reaching the SANS instrument. The optical filter is a 30 m long tapered guide that raises the neutron beam by 14 cm. The entire instrument had to be raised by that height. The optical filter provides a current density gain factor of 1.8 for 15 Å neutrons and breaks even for 6 Å neutrons (Cook et al, 2005, Paper 376).

Neutron focusing lenses have been tested in order to monitor the variation of the neutron spot size (spatial resolution) with varying wavelength. The focusing condition has been determined and compared with theoretical predictions accounting for all major effects (including gravity neutron fall). The effect of shifting the lenses upward has also been investigated (Mildner et al, 2005, Paper 466).

When focusing lenses are placed after the sample, sample magnification is obtained just like with a magnifying glass. This "neutron microscope" was tested using 100 MgF_2 biconcave lenses and hydrogen-rich polymer samples. In order to achieve high spatial resolution, imaging plates were used for detection. A magnification factor of 22.5 was observed. The small acceptance angle of the lens system (placed after the sample) discriminates against scattered neutrons thereby producing the needed contrast for imaging (Cremer et al, 2005, Paper 468).

A software package for performing SANS data reduction and analysis has been developed based on Igor Pro. A graphical user interface has been included to visualize and reduce data online into 1D format. The data analysis package contains a multitude of models that are smeared before performing nonlinear least-squares fits. This package has been extended to handle USANS data and the required slit-smearing corrections (S.R. Kline, 2005, Paper 569).

The resolution of SANS instruments was reviewed in the case where refractive optics (lenses or prism) are used. The appropriate equations were derived to describe the position and spatial variance of the neutron beam at the detector in both the horizontal and vertical directions. The addition of lenses allows the increases of the sample aperture without penalty in resolution and enables an increase of neutron current at the sample. Gravity correcting

prisms shift the neutron beam in the vertical direction and eliminate anisotropic smearing of the beam spot (Hammouda-Mildner, 2007, Paper 586).

2. MAGNETISM

Ferromagnetic correlations in nanocrystalline electrodeposited Co and Ni have been investigated by SANS. The correlation length was found to be strongly dependent on the applied magnetic field. Correlation length variations lead to the conclusions that in Co, the main source of nonuniformity in the spin system is the anisotropic field of the individual crystals whereas in Ni, the main source of spin disorder originates from twin faults or defects at grain boundaries (Michels et al, 2003, Paper 110).

The magnetic cluster size distributions for several magnetic recording media have been investigated by SANS. It was found that the average magnetic cluster size is slightly larger than the grain size and is inversely correlated to the media signal-to-noise ratio (Toney et al, 2003, Paper 172).

Aggregates of iron-based nanoparticles were investigated by SANS. Marked differences were observed depending on particle size and degree of oxidation. Magnetic regions with spins perpendicular to the applied magnetic were observed. This result was interpreted in terms of an iron core coupled to an iron oxide shell region (Ijiri et al, 2005, Paper 372).

In $La_2(CuLi)O_4$ magnetic system, only a fraction of the antiferromagnetic correlations extending to neighboring planes freeze to form a spin glass. The remaining spins with only in-plane correlations remain a spin liquid at low temperature. Such a partial freezing of the 2D spin liquid is likely due to a delicate balance between disorder and quantum fluctuations in this Heisenberg spin system (Chen et al, 2005, Paper 453).

Type II superconductors are characterized by a first-order structural phase transition from hexagonal to square flux-line lattice. In V_3Si, this transition occurs for a magnetic field of 1 T. SANS measurements showed that the square phase reverts to hexagonal phase as the magnetic field approaches the second critical magnetic field. This behavior can be described by a nonlocal London theory with thermal fluctuations (Yethiraj et al, 2005, Paper 465).

3. CARBON NANOTUBES

Fullerenes come in two main categories: carbon nanotubes and buckyballs. They both are formed of cage-like structures containing only carbon (with ho hydrogen present).

Poly(urethane-ether) star polymers were synthesized starting from C_{60} buckyballs. The six arms of the star polymer were found to follow Gaussian statistics in toluene but are characterized by excluded volume interactions in DMF. The radius of gyration and the persistence length were obtained (Jeng et al, 2002, Paper 066).

Dilute solutions of single-wall carbon nanotube aqueous suspensions in the presence of SDS surfactant were characterized by SANS. The 1/Q behavior characterizing rod-like scattering

was observed at low Q. At lower Q, the $1/Q^2$ behavior characteristic of a mass fractal representing a network of rods was observed. Carbon nanotubes tend to form aggregates even at low concentration and in the presence of surfactant (Zhou et al, 2004, Paper 195).

SANS with in-situ shear and flow birefringence reveal weak alignment of single-wall carbon nanotubes dispersed using ionic surfactants. The alignment is along the shear direction and its degree is found to increase with shear rate. (Wang et al, 2005, Paper 419).

In an attempt to reduce single-wall carbon nanotube aggregation, nanotubes were dispersed by wrapping them with short single-strand DNA segments. SANS Porod exponents suggested clustered and not isolated nanotubes. Such wrapped nanotubes are used to stabilize dispersions of hydrophilic colloidal particles (Hobbie, et al, 2005, Paper 445).

The structure of single-wall carbon nanotube suspensions and gels was investigated by SANS and SAXS in the semidilute (overlap region). A correlation size (measure of the semidilute network mesh size) was obtained and found to decrease with increasing nanotube concentration (Hough et al, 2006, Paper 490).

Another method for obtaining isolated carbon nanotubes is through the use of a cationic surfactant with polymerizable counterions following by an in-situ polymerization or the micelles. Such systems were investigated by SANS (Kim et al, 2007, Paper 594).

4. CERAMICS MATERIALS

The microstructure of stabilized zirconia deposits that are plasma sprayed was investigated by using multiple SANS. This technique consists in using thick samples and a range of neutron wavelengths in order to quantify the amount of multiple scattering. Density measurements, electron microscopy, and elastic modulus measurements were also employed to characterize the microstructure as a function of sample content and annealing conditions for each of the three main porous components of these thermal barrier coatings: intrasplat cracks, interplat lamellar pores and globular pores (Allen et al, 2001, Paper 003).

The microstructure of thick plasma-sprayed yttria-stabilized zirconia deposits were studied using SANS and multiple SANS. Void characteristics such as average size, volume fraction, internal surface area and orientation distribution for each of the three void components within the deposits were determined. The effect of initial feedstock particle size and annealing temperature on the microstructure were also quantified (Boukari et al, 2003, Paper 009).

Thermal barrier coatings deposited onto turbine blades (using the electron-beam vapor deposition process) exhibit unique pore architectures. SAXS and SANS were used to characterize porosity anisotropy and pore sizes and gradients through the coatings (Kulkarni et al, 2006, Paper 516).

The primary binding reaction product of cement hydration, the calcium-silicate-hydrate gel, was investigated by SAXS and SANS. A calcium hydroxide phase that coexists with the gel

phase has been quantified. The following formula $(CaO)_{1.7}(SiO_2)(H_2O)_{1.8}$ and density of 2.604 g/cm^3 have been obtained (Allen et al, 2007, Paper 589).

5. FUEL CELLS MATERIALS

Fuel cells are energy production devices that combine stored hydrogen and atmospheric oxygen to produce water and electricity. Vigorous research is underway to assess various types of fuel cell membranes; these include Nafion and porous polymeric materials.

Transport and structural properties of membrane forming copolymers have been studied as potential fuel cell membrane material. Variation of the proton conductivity with humidity content has been quantified and compared to that of Nafion (Serpico et al, 2002, Paper 251).

Several Nafion fuel cell membranes were investigated with SANS under in-situ water vapor sorption in order to quantify the effect of relative humidity (RH). Other factors such as membrane processing (melt-extruded *vs* solution-cast), thermal history (preheated *vs* not) and membrane thickness have been considered. The sorption isotherm (water uptake with RH) of the membranes showed a strong correlation between the interionic domain distance and RH. The melt extruded membranes showed evidence of partial alignment and more effective ionic domain structures (Kim et al, 2006, Paper 524).

Block copolymer membranes comprising hydrophilic phases with microdomain widths lower than 50 A were found to become wetter as the temperature of the surrounding air is increased (at constant relative humidity). Both Cryo-TEM and (later) SANS were used to characterize humidity characteristics in such membranes (Park et al, 2007, Paper 600).

6. GEOLOGICAL MATERIALS

Scanning electron microscopy (SEM) and SANS were combined to quantify the microstructure of a porous solid in terms of continuous pore-size distribution spanning over five orders of magnitude in length scale (from 10 Å to 500 μm). This method was tested on a sample of natural sandstone and the results were compared against mercury porosimetry and nuclear magnetic resonance (NMR). The rock microstructure was found to follow fractal behavior (D = 2.47) for pore sizes in the range from 10 Å to 50 μm but follow Euclidean surface behavior (D = 2) for larger length scales. This new method furnishes new microstructural information that may facilitate the understanding of capillary phenomena in hydrocarbon reservoir rocks and other porous solids (Radlinski et al, 2004, Paper 324).

The structures of natural oil-bearing and synthetic rocks were investigated using the Ultra SANS (USANS) technique. Different thickness rocks were measured and analyzed using a Fourier transform method developed to remove multiple scattering effects. Both type of rocks were found to obey surface fractal behavior with fractal dimensions of D = 2.7 for the natural rocks and D = 2 for the synthetic rocks (Connolly et al, 2006, Paper 479).

7. DIELECTRIC MATERIALS

Nanoscale porosity is introduced into low-k dielectrics to achieve inter-level metal insulators with permittivities less than 2.0. Pore-formation in a polyphenylene low-k dielectric was investigated by x-ray reflectivity and SANS. This investigation included the nanoscale structure at various stages of pore formation through the use of deuterated porogen. Porogen degradation leads to pore-formation. During the degradation process, the smaller porogen domains collapse while the larger domains yield stable pores (Silverstein et al, 2005, Paper 378).

Ordered mesoporous silica films were synthesized using pre-organized PEO-PPO-PEO pluronics block copolymer templates in supercritical carbon dioxide. A battery of characterization methods including x-ray diffraction, spectroscopic ellipsometry, x-ray reflectivity, Rutherford backscattering, forward recoil elastic spectroscopy, transmission electron microscopy, and SANS were used. Two distinct populations of pores were found in the films. Spherical mesopores were templated by the hydrophilic copolymer domain; and an inter-penetrating network of smaller size pores were formed by the silicate network during condensation of the silica precursor (Vogt et al, 2005, Paper 388).

Specular x-ray reflectivity and SANS were used to characterize the structure of a thin film containing cylindrical mesopores. The film was found to be composed of a randomly packed core and surface layers within which the hollow cylinders are regularly packed and oriented along the surface. The cylinder packing was close to (but not quite) hexagonal (Vogt et al, 2005, Paper 422).

8. METALS

Multiple SANS was applied to thermally sprayed metallic deposits such as NiCrAlY coatings manufactured by different spray techniques. This technique consists in measuring neutron beam-broadening as a function of incident wavelength and can yield information about pore structure. Measurements were made in directions parallel and perpendicular to the surface. SEM micrographs of coating cross-sections were also taken. The pores surface area was obtained from the SANS Porod analysis (Keller et al, 2002, Paper 071).

Aluminum foils and single crystals were charged with hydrogen using a gas plasma method as well as electrochemical methods. This resulted in substantial amount of hydrogen introduced in aluminum. X-ray diffraction showed, however, no expansion of the aluminum lattice upon hydrogen loading. This meant that hydrogen does not enter the lattice as an interstitial but instead forms a hydrogen vacancy complex at grain boundaries and then diffuses to form hydrogen bubbles. SANS and USANS were employed to investigate the nature of the hydrogen bubbles in these aluminum foils (Buckley et al, 2001, Paper 309).

Oxidized silver-magnesium interfaces have been investigated by SANS. The composition was varied by exposing the sample to oxygen, hydrogen or to vacuum pumping in order to explore the structure for small MgO nanoprecipitates in a dilute Ag matrix. Hydrogen was found to segregate at the internal Ag/MgO interface. For each hydrogen atom localized at the interface, one Ag atom is removed from it (Kluthe et al, 2004, Paper 346).

9. NANOSCALE MATERIALS

SANS measurements have been performed in order to investigate the orientational ordering of a dispersion of rod-like ferromagnetic nanoparticles under applied shear and magnetic field. Anositropic scattering indicating orientational ordering was observed. At low shear rates, the particles were aligned in the magnetic field direction. When the shear rate was increased, the particles reverted to random orientation at a characteristic rate that depended on the magnetic field strength (Krishnamurthy et al, 2003, Paper 078).

Nanocrystalline MgO, CaO and SrO materials were prepared according to a modified aerogel process. SANS was used to investigate the nanoscale structure after the various stages of synthesis which include hydrolysis, supercritical drying and calcining. Guinier and Porod analyses were performed along with the maximum entropy method. It was found that the gel hydrolysis product suspended in methanol and toluene exhibits rod-like structures. This is consistent with a suspected filiform morphology. SANS data from air-dried alcogels indicate no evidence for rod-like structures (Hackley et al, 2005, Paper 454).

Nickel powders nanoscale structures were investigated using SANS with an interest in understanding the level of porosity. Nickel powders that had been exposed to various cycles of hydrogenation in an industrial refining process were measured. Results indicated general trends in the nanostructure pointing to a roughening of the particles surface (Knott et al, 2006, Paper 548).

REFERENCES

J.C. Cook, C. Glinka and I.G. Schroder, "Performance of the Vertical Optical Filter for the NG3 30 m SANS Instrument at the NIST-CNR", Rev. Sci. Instr. 76, 25108-1 to 8 (2005). Paper 376.

D.F.R. Mildner, B. Hammouda and S.R. Kline, "A Refractive Focusing lens System for SANS", J. Appl. Crys. 38, 979-987 (2005). Paper 466.

J.T. Cremer, M.A. Piestrup, H. Prask, C.K. Gary, R.H. Pantell, C.J. Glinka and J.B. Barker, "Imaging Hydrogeneous Materials with a Neutron Microscope", Appl. Phys. Lett. 87, 161913-1 to 3 (2005). Paper 468.

S.R. Kline, "Reduction and Analysis of SANS and USANS Data using Igor Pro", J. Appl. Crys. 39, 895-900 (2006). Paper 569.

B. Hammouda and D.F.R. Mildner, "SANS Resolution with Refracive Optics", J. Appl. Cryst. 40, 250-259 (2007). Paper 586.

A. Michels, R.N. Viswanath, J.G. Barker, R. Birringer and J. Weissmuller, "Range of Magnetic Correlations in Nanocrystalline Soft Magnets", Phys. Rev. Lett. 91, 267204-1 to 4 (2003). Paper 110.

M.F. Toney, K.A. Rubin, S-M. Choi and C.J. Glinka, "SANS Measurements of Magnetic Cluster Sizes in Magnetic Recording Disks", Appl. Phys. Lett. $\underline{82}$, 3050-3052 (2003). Paper 172.

Y. Ijiri, C.V. Kelly, J.A. Borchers, J.J. Rhydne, D.F. Farrell and S.A. Majetich, "Detection of Spin Coupling in Iron Nanoparticles with SANS", Appl. Phys. Lett. $\underline{86}$, 243102-1 to 3 (2005). Paper 372.

Y. Chen, W. Bao, Y. Qiu, J.E. Lorenzo, J.L. Sarrao, D.L. Ho and M.Y. Lin, "Slow Spin-Glass and Fast Spin-Liquid Components in Quasi 2D $La_2(Cu,Li)O_4$", Phys. Rev. B $\underline{72}$, 184401-1 to 6 (2005). Paper 453.

M. Yethiraj, D.K. Christen, A.A. Gapud, M.McK. Paul, S.J. Crowe, C.D. Dewhurst, R. Cubitt, L. Porcar and A. Gurevich, "Temperature and Field dependence of the Flux-Line Lattice Symmetry in V_3Si", Phys. Rev. B $\underline{72}$, 060504-1 to 4 (2005). Paper 465.

U-S. Jeng, T-L. Lin, L.Y. Wang, L.Y. Chiang, D.L. Ho and C.C. Han, "SANS Structural Characterization of Fullerene-derived Star Polymers in Solution", Appl. Phys. A $\underline{74}$, S487-S489 (2002). Paper 066.

W. Zhou, M.F. Islam, H. Wang, D.L. Ho, A.G. Yodh, K.I. Winey and J.E. Fischer, "SANS from Single-Wall Carbon Nanotube Suspensions: Evidence for Isolated Rigid Rods and Rod Networks", Chem. Phys. Lett. $\underline{384}$, 185-189 (2004). Paper 195.

H. Wang, G.T. Christopherson, Z.Y. Xu, L. Porcar, D.L. Ho, D. Fry and E.K. Hobbie, "Shear-SANS Study of Single-Walled Carbon Nanotube Suspensions", Chem. Phys. Lett. $\underline{416}$, 182-186 92005. Paper 419.

E.K. Hobbie, B.J. Bauer, J. Stephens, M.L. Becker, P. McGuiggan, S.D. Hudson and H. Wang, "Colloidal Particles Coated and Stabilized by DNA-Wrapped Carbon Nanotubes", Langmuir $\underline{21}$, 10284-10287 (2005). Paper 445.

L.A. Hough, M.F. Islam, B. Hammouda, A.G. Yodh and P.A. Heiney, "Structure of Semidilute Single-Wall Carbon Nanotube Suspensions and Gels" Nanoletters $\underline{6}$, 313-317 (2006). Paper 490.

T-H Kim, C. Doe, S.R. Kline and S-M. Choi, "Water-Redispersible Isolated Single-Walled Nanotubes Fabricated by In-Situ Polymerization of Micelles", Adv. Mat. $\underline{19}$, 929-933 (2007). Paper 594.

A.J. Allen, J. Ilasky, G.G. long, J.S. Wallace, C.C. Berndt and H. Herman, "Microstructure Characterization of Yttria-Stabilized Zirconia Plasma-Sprayed deposits Using MSANS", Acta Mater. $\underline{49}$, 1661-1675 (2001). Paper 003.

H. Boukari, A.J. Allen, G.C. Long J. Ilasky and J.S. Wallace, "SANS Study of the Role of Feedstock Particle Size on the Microstructural Behavior of Plasma-Sprayed Yttria-Stabilized Zirconia Deposits", J. Mat. Res. $\underline{18}$, 624-634 (2003). Paper 009.

A. Kulkarni, A. Goland, H. Herman, A.J. Allen, T. Dobbins, F. DeCarlo, J. Ilasky, G.C. Long, S. Fang and P. Lawton, "Advanced Neutron and X-Ray Techniques for Insight Into the Microstructure of EB-PVD Thermal Barrier Coatings", Mat. Sci. and Engin. A 426, 43-52 (2006). Paper 516.

A.J. Allen, J.J. Thomas, H.M. Hamlin, "Composition and Density of Nanoscale Calcium-Silicate-Hydrate in Cement", Nature Materials 6, 311-316 (2007). Paper 589.

J.M. Serpico, S.G. Ehrenberg, J.J. Fontanella, X. Jiao, D. Perahia, K.A. McGrady, E.H. Sanders, G.E. Kellogg and G.E. Wnek, "Transport and Structural Studies of Sulfonated Styrene-Ethylene Copolymer Membranes", Macromolecules 35, 5916-5921 (2002). Paper 251.

M-H. Kim, C.J. Glinka, A.A. Grot and W.G. Grot, "SANS Study of the Effect of Water Vapor Sorption on the Nanoscale Structure of Nafion Membranes", Macromolecules 39, 4775-4787 (2006). Paper 524.

M.J. Park, K.H. Downing, A. Jackson, E.D. Gomez, A.M. Minor, D. Cookson, A.Z. Weber and N.P. Balsara, "Increased Water Retention in Polymer Electrolyte Membranes at Elevated Temperatures Assisted by Capillary Condensation", Nanoletters 7, 3547-3552 (2007). Paper 600.

A.P. Radlinski, M.A. Ioannidis, A.L. Hinde, M. Hainbuchner, M. Baron, H. Rauch and S.R. Kline, "Angstrom-to-Millimeter Characterization of Sedimentary Rock Microstructure", J. Colloid and Interfaces Science 274, 607-612 (2004). Paper 324.

J. Connolly, W. Bertram, J. Barker, C. Buckley, T. Edwards and R. Knott, "Comparison of the Structure on the Nanoscale of natural Oil-Bearing and Synthetic Rocks", J. Petroleum Science and Engineering 53, 171-178 (2006). Paper 479.

M.S. Silverstein, M. Shach-Caplan, B.J. Bauer, R.C. Hedden, H-J. Lee and B.G. landes, "Nanopore Formation in a Polyphenylene Low-k Dielectric", Macromolecules 38, 4301-4310 (2005). Paper 378.

B.D. Vogt, R.A. Pai, H-J. Lee, R.C. Hedden, C.L. Soles, W-L. Wu, E.K. Lin, B.J. Bauer and J. Watkins, "Characterization of ordered Mesoporous Silica Films Using SANS and X-Ray Porosimetry". Chem. Mater. 17, 1398-1408 (2005). Paper 388.

B.D. Vogt, H-J. Lee, W-L. Wu and Y. Liu, "Specular X-Ray Reflectivity and SANS for Structure Determination of Ordered Mesoporous Dielectric Films", J. Phys. Chem. B 109, 18445-18450 92005). Paper 422.

T. Keller, W. Wagner, A. Allen, J. Ilasky, N. Margadant, S. Siegmann and G. Kostorz, "Characterization of Thermally Sprayed Metallic NiCrAlY Deposits by MSANS", Appl. Phys. A 74, S975-S977 (2003). Paper 071.

C.E. Buckley, H.K. Birnbaum, J.S. Lin, S. Spooner, D. bellman, P. Staron, T.J. Udovic, and E. Hollar, "Characterization of H Defects in the Aluminum-Hydrogen System Ysing SAS Techniques", J. Appl. Cryst. <u>34</u>, 119-129 (2001). Paper 309.

C. Kluthe, T. Al-Kassab, J. Barker, W. Pykhout-Hintzen and R. Kirchheim, "Segregation of Hydrogen at Internal Ag/MgO (Metal/Oxide) Interfaces as Observed by SANS", Acta Materialia <u>52</u>, 2701-2710 (2004). Paper 346.

V.V. Krishnamurthy, A.S. Bhandar, M. Piao, I. Zoto, A.M. Lane, D.E. Nikles, J.M. Wiest, G.J. mankey, L. Porcar and C.J. Glinka, Shear and Magnetic-Field Induced Ordering in Magnetic Nanoparticle Dispersion from SANS", Phys. Rev. E 67, 051406-1 to 6 (2003). Paper 078.

V.A. Hackley, P.K. Stoimenov, D.L. Ho, L.P. Sung and K.J. Klabunde, "Structure Development in Aerogel-Processed Nanocrystalline Alkaline Eartch Oxides as Revealed by SANS", J. Appl. Cryst. 38, 619-631 (2005). Paper 454.

R.B. Knott, M. Lin, H.J.M. Hanley and D. Muir, "Preliminary SANS Studies of the Structure of Nickel Powders on the Nanoscale", Physica B 385-386, 908-910 (2006). Paper 548.

Part L – **EVEN LOWER SANS SCALES**

Slit geometry is sometime used in order to obtain high resolution in one direction. This enhances the flux-on-sample but introduces drastic smearing in the other direction. The two instruments that use slit geometry are the VSANS instrument ("V" is for "very) and the Bonse-Hart USANS instrument ("U" is for "ultra"). The resolution function for slit geometry is discussed here.

1. VARIANCE OF THE Q RESOLUTION

Recall the following result that was derived for circular aperture geometry (Mildner-Carpenter, 1984):

$$\left[\sigma_Q^2\right]_{geo} = \frac{4\pi^2}{\lambda^2} \frac{\sigma_x^2 + \sigma_y^2}{L_2^2} \tag{1}$$

with:

$$\sigma_x^2 = \left(\frac{L_2}{L_1}\right)^2 <x^2>_1 + \left(\frac{L_1 + L_2}{L_1}\right)^2 <x^2>_2 + <x^2>_3$$

$$\sigma_y^2 = \left(\frac{L_2}{L_1}\right)^2 <y^2>_1 + \left(\frac{L_1 + L_2}{L_1}\right)^2 <y^2>_2 + <y^2>_3$$
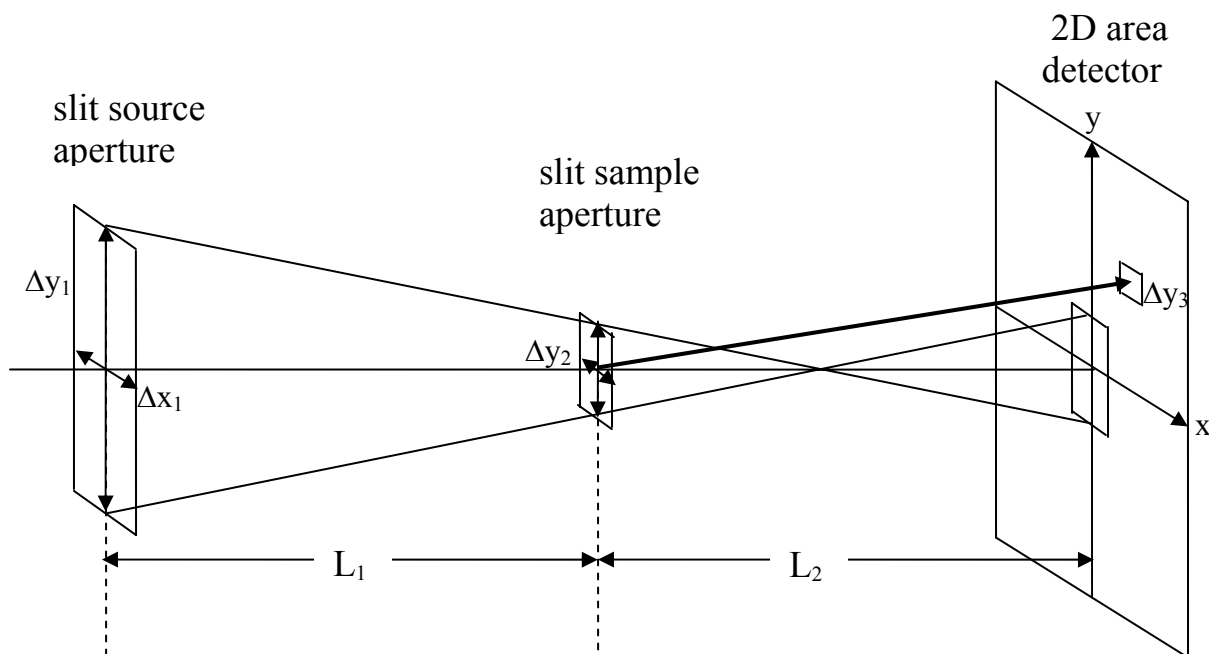
Figure 1: SANS slit geometry with rectangular source and sample apertures and 2D area detector cells. This figure is not to scale. Cartesian coordinates are used to characterize the three vertical (source, sample and detector) planes.

In the case of slit geometry, the various averages are calculated differently. The horizontal slit openings for the source and sample apertures are defined as Δx_1 and Δx_2 and the vertical slit openings are defined as Δy_1 and Δy_2. Δx_3 and Δy_3 represent the detector cell dimensions. The various averages can be readily calculated.

$$<x^2>_1 = \frac{\int\limits_{-\Delta x_1/2}^{\Delta x_1/2} dx\, x^2}{\int\limits_{-\Delta x_1/2}^{\Delta x_1/2} dx} = \frac{1}{3}\left(\frac{\Delta x_1}{2}\right)^2 = \frac{\Delta x_1^2}{12} \tag{2}$$

$$<x^2>_2 = \frac{\Delta x_2^2}{12}; \quad <x^2>_3 = \frac{\Delta x_3^2}{12}$$

$$<y^2>_1 = \frac{\Delta y_1^2}{12}; \quad <y^2>_2 = \frac{\Delta y_2^2}{12}; \quad <y^2>_3 = \frac{\Delta y_3^2}{12}.$$

The Q collimation for slit geometry is similar to that for pinhole collimation with slightly different terms for the geometry resolution. Note that the gravity term appears only in the vertical y direction. .

$$\sigma_Q^2 = \sigma_{Qx}^2 + \sigma_{Qy}^2 \tag{3}$$

$$\sigma_{Qx}^2 = \left(\frac{2\pi}{\lambda L_2}\right)^2 \left[\left(\frac{L_2}{L_1}\right)^2 \frac{\Delta x_1^2}{12} + \left(\frac{L_1+L_2}{L_1}\right)^2 \frac{\Delta x_2^2}{12} + \frac{\Delta x_3^2}{12}\right] + Q_x^2 \frac{1}{6}\left(\frac{\Delta\lambda}{\lambda}\right)^2$$

$$\sigma_{Qy}^2 = \left(\frac{2\pi}{\lambda L_2}\right)^2 \left[\left(\frac{L_2}{L_1}\right)^2 \frac{\Delta y_1^2}{12} + \left(\frac{L_1+L_2}{L_1}\right)^2 \frac{\Delta y_2^2}{12} + \frac{\Delta y_3^2}{12}\right] + Q_y^2 \frac{1}{6}\left(\frac{\Delta\lambda}{\lambda}\right)^2 + \frac{4\pi^2}{\lambda^2 L_2^2} A^2 \lambda^4 \frac{2}{3}\left(\frac{\Delta\lambda}{\lambda}\right)^2$$

$$A = L_2(L_1+L_2)\frac{gm^2}{2h^2}.$$

Here L_1 and L_2 are the source-to-sample and sample-to-detector distances.

This is the SANS resolution with slit geometry. Only the $<x^2>$ terms are different from the pinhole geometry case.

2. MINIMUM Q WITH SLIT GEOMETRY

The minimum Q achieved with slit geometry has horizontal and vertical components. The horizontal component is the lowest because collimation is often tightened in that direction. Slits are aligned in the vertical direction to avoid gravity effects. The Q_{min} values are similar to the case of pinhole geometry and are summarized here.

$$Q_{min}^X = \frac{2\pi}{\lambda} \frac{X_{min}}{L_2} \text{ and } Q_{min}^Y = \frac{2\pi}{\lambda} \frac{Y_{min}}{L_2} \tag{4}$$

$$X_{min} = \frac{L_2}{L_1} \Delta x_1 + \frac{L_1 + L_2}{L_1} \Delta x_2 + \frac{\Delta x_3}{2}$$

$$Y_{min} = Y_{min}^0 + 2A\lambda^2 \left(\frac{\Delta\lambda}{\lambda}\right)$$

$$Y_{min} = \frac{L_2}{L_1} \Delta y_1 + \frac{L_1 + L_2}{L_1} \Delta y_2 + \frac{\Delta y_3}{2}.$$

Gravity affects the vertical direction which is of no value because it is highly smeared due to the open collimation in that direction.

3. APPLICATION TO A SPECIFIC CASE

Consider the following instrument configuration with slit geometry:

$$\Delta x_1 = 0.25 \text{ cm} \tag{5}$$
$$\Delta y_1 = 2.5 \text{ cm}$$
$$\Delta x_2 = 0.05 \text{ cm}$$
$$\Delta y_2 = 0.5 \text{ cm}$$
$$\Delta x_3 = 0.05 \text{ cm}$$
$$\Delta y_3 = 0.5 \text{ cm}$$
$$L_1 = 15 \text{ m}$$
$$L_2 = 15 \text{ m}$$
$$\lambda = 12 \text{ Å}$$
$$\frac{\Delta\lambda}{\lambda} = 15\%.$$

Therefore:

$$A = 0.0138 \text{ cm/Å}^2 \tag{6}$$
$$\sigma_x^2 = 0.00625 \text{ cm}^2$$
$$\sigma_y^2 = 0.625 \text{ cm}^2.$$

So that:

$$\sigma_{Qx}{}^2 = 7.61 * 10^{-10} + 0.0037\, Q_x{}^2 \ \text{(in units of Å}^{-2}) \tag{7}$$

$$\sigma_{Qy}{}^2 = 8.34 * 10^{-8} + 0.0037\, Q_y{}^2 \ \text{(in units of Å}^{-2}).$$

Moreover,

$$Q_{min}{}^X = 0.00014 \ \text{Å}^{-1} \tag{8}$$

$$Q_{min}{}^Y = 0.0016 \ \text{Å}^{-1}.$$

In this case, the horizontal resolution is very good but the vertical one is poor.
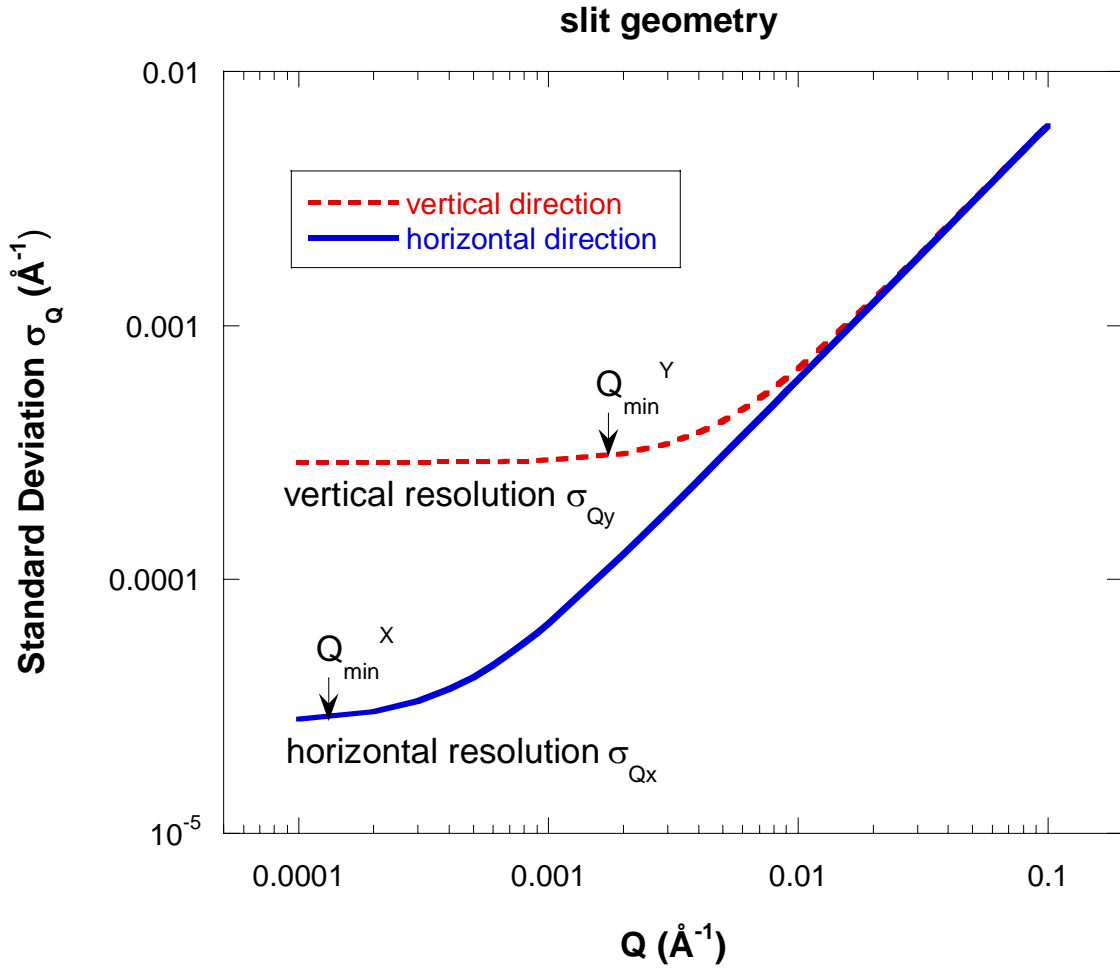

Figure 2: Standard deviation of the instrumental resolution for slit geometry. Resolution is tight in the horizontal direction and "opened up" in the vertical direction to enhance flux on sample. The values of Q_{min} are also indicated.

4. SLIT SMEARING CORRECTION

When correcting data with slit smearing, the horizontal and vertical directions are decoupled as follows:

$$R(Q,Q') = R(Q-Q') = R(Q_x-Q'_x) R(Q_y-Q'_y) \qquad (9)$$

$$R(Q_x - Q_x') = \sqrt{\frac{1}{2\pi\sigma_{Qx}^2}} \exp\left[-\frac{(Q_x - Q'_x)^2}{2\sigma_{Qx}^2}\right]$$

$$R(Q_y - Q_y') = \sqrt{\frac{1}{2\pi\sigma_{Qy}^2}} \exp\left[-\frac{(Q_y - Q'_y)^2}{2\sigma_{Qy}^2}\right].$$

The resolution integral becomes:

$$\left[\frac{d\Sigma(Q)}{d\Omega}\right]_{smeared} = \int_{-\infty}^{\infty} dQ'_x \int_{-\infty}^{\infty} dQ'_y R(Q_x - Q_x')R(Q_y - Q_y')\left[\frac{d\Sigma(Q'_x,Q'_y)}{d\Omega}\right]_{un-smeared} \qquad (10)$$

Slits are usually very small in the horizontal direction so that $R(Q_x-Q'_x) = \delta(Q_x-Q'_x)$ where δ is the Dirac Delta function. In the vertical direction the resolution is sometime replaced by a uniform "box" function (Barker et al, 2005):

$$R(Q_y-Q'_y) = 0 \text{ for } |Q_y-Q'_y| < \frac{-\Delta Q_y}{2} \text{ or } |Q_y-Q'_y| > \frac{\Delta Q_y}{2} \qquad (11)$$

$$R(Q_y-Q'_y) = \frac{1}{\Delta V} \text{ for } \frac{-\Delta Q_y}{2} \le |Q_y-Q'_y| \le \frac{\Delta Q_y}{2}.$$

Within this "infinitely thin slit" approximation, the resolution integral becomes simpler.

$$\left[\frac{d\Sigma(Q)}{d\Omega}\right]_{smeared} = \frac{1}{\Delta Q_y} \int_0^{\Delta Q_y} dQ'_y \left[\frac{d\Sigma(Q_x,Q'_y)}{d\Omega}\right]_{un-smeared} \qquad (12)$$

$$= \frac{1}{\Delta Q_y} \int_0^{\Delta Q_y} dQ'_y \left[\frac{d\Sigma(\sqrt{Q_x^2 + Q'_y^2})}{d\Omega}\right]_{un-smeared}.$$

We have made use of the following property of the Dirac Delta function:

$$\int_{-\infty}^{\infty} dQ'_x \delta(Q_x - Q'_x)\left[\frac{d\Sigma(Q'_x,Q'_y)}{d\Omega}\right]_{un-smeared} = \left[\frac{d\Sigma(Q_x,Q'_y)}{d\Omega}\right]_{un-smeared}. \qquad (13)$$

The desmearing procedure becomes a simple 1D integration.

REFERENCES

D.F.R. Mildner, and J.M. Carpenter, "Optimization of the Experimental Resolution for SAS", J. Appl. Cryst. <u>17</u>, 249-256 (1984)

J.G. Barker, C.J. Glinka, J.J. Moyer, M.H. Kim, A.R. Drews, and M. Agamalian," Design and Performance of a Thermal-Neutron Double-Crystal Diffractometer for USANS at NIST", J. Appl. Cryst. <u>38</u>: 1004-1011 (2005).

QUESTIONS

1. What is the main difference in the variance of the resolution function for the cases of circular apertures and slit geometry?
2. What are the main advantage and disadvantage of slit geometry?

ANSWERS

1. The main difference in the variance of the resolution function σ_Q for the cases of circular apertures and slit geometry is in the averaging involved to calculate the geometry contribution; for a circular aperture of radius R_1, $<x^2>_1 = \dfrac{R_1^2}{4}$, whereas for a slit of width Δx_1, $<x^2>_1 = \dfrac{1}{3}\left(\dfrac{\Delta x_1}{2}\right)^2$.

2. The advantage of slit geometry is increased flux-on-sample in the relaxed collimation direction. The disadvantage of the slit geometry is the drastic smearing effect.

Chapter 59 - **THE VSANS TECHNIQUE**

Very small-angle neutron scattering (VSANS) pushes the SANS small-Q limit down by an order of magnitude. It consists in using tighter collimation and a higher resolution detector combined with the usual long flight paths and the use of a velocity selector. SANS collimation can be tightened in one of two ways: either through multiple circular converging collimation or through multiple slit converging collimation. This last option enhances flux-on-sample but introduces slit smearing. VSANS falls between regular SANS and Ultra SANS (USANS). The three major figures of merit (minimum Q, flux on sample, and Q resolution) are discussed for possible VSANS configurations for an instrument under construction at the NIST CNR.

1. MULTIPLE CIRCULAR CONVERGING COLLIMATION

Resolution

Multiple circular (also called pinhole) converging collimation is appealing because it allows an improvement in the resolution without too much loss in the flux on sample. Overkill apertures are required in order to eliminate neutron cross collimation.
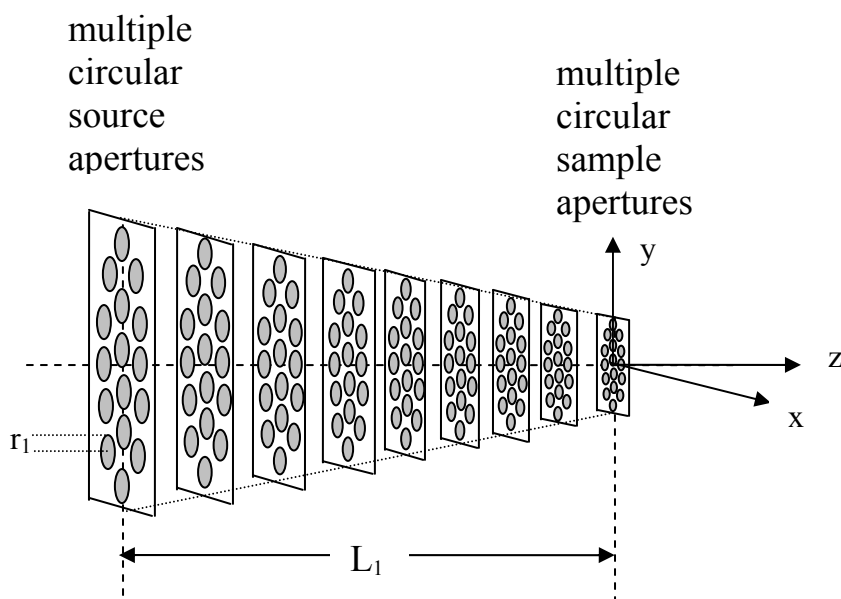

Figure 1: Multiple circular converging collimation. Intermediate apertures are placed so as to avoid cross collimation and keep neutrons in the same aperture channel. This figure is not to scale. Vertical scale is of order centimeters while horizontal scale is of order meters.

The main change to the variance of the Q resolution σ_Q^2 in going from a single large circular aperture to multiple small circular converging apertures is to change the radii of the source and sample apertures from R_1 and R_2 (large radii) to r_1 and r_2 (small hole radii) respectively. Everything else remains the same and will not be repeated here (Mildner-Carpenter, 1984; Mildner et al, 2005).

Similarly, the minimum scattering variable, Q_{min} for the single aperture and multiple apertures collimations are the same provided that the small circular aperture radii are used.

Resolution with Focusing Lenses

The addition of focusing lenses to the multiple converging collimation geometry allows the opening up of the sample apertures without penalty in resolution. Modification of the Q resolution equations to incorporate lenses involves replacing the sample aperture term

$\left(\dfrac{L_1+L_2}{L_1}\right)^2 \dfrac{r_2^2}{2}$ by the following term $\dfrac{2}{3}\left(\dfrac{\Delta\lambda}{\lambda}\right)^2 \left(\dfrac{L_1+L_2}{L_1}\right)^2 \dfrac{r_2^2}{2}$ where $\left(\dfrac{\Delta\lambda}{\lambda}\right)$ is the

wavelength spread and L_1 and L_2 are the source-to-sample and sample-to-detector distances. This corresponds to the condition where the neutron detector is located at the source image.

Similarly, modification of the Q_{min} equations to incorporate lenses involves replacing the

sample aperture term $\left(\dfrac{L_1+L_2}{L_1}\right)r_2$ by the equivalent term $2\left(\dfrac{\Delta\lambda}{\lambda}\right)\left(\dfrac{L_1+L_2}{L_1}\right)r_2$.

Flux-on-Sample

The neutron flux on sample can be approximated by the following estimate (based on measurements made at the NG3 30 m SANS instrument at the NIST CNR).

$$\phi(\lambda) = \frac{1.507*10^{15}}{\lambda^4}\exp\left[-\frac{30.25}{\lambda^2}\right]\left(\frac{\Delta\lambda}{\lambda}\right)\frac{A_1}{L_1^2} \quad \text{n/cm}^2\text{.s.} \qquad (1)$$

λ is the neutron wavelength, $\Delta\lambda$ is the wavelength spread, A_1 is the area of the source (small) aperture, and L_1 is the source-to-sample distance with $A_1 = \pi r_1^2$. The neutron count rate (or current) on sample is given by:

$$\Phi(\lambda) = \phi(\lambda)A_2 = \frac{1.507*10^{15}}{\lambda^4}\exp\left[-\frac{30.25}{\lambda^2}\right]\left(\frac{\Delta\lambda}{\lambda}\right)\frac{A_1 A_2}{L_1^2} . \qquad (2)$$

A_2 is the area of the sample aperture ($A_2 = \pi r_2^2$). For n small apertures, $\phi(\lambda)$ and $\Phi(\lambda)$ are multiplied by n.

Neutron Trajectories Constraint

Neutrons follow parabolic trajectories due to gravity. Neutrons climb up after crossing the source aperture, reach an apex half-way between the source and sample apertures, and fall back down to make it through the sample aperture. One constraint to consider for multiple circular converging collimation is the fact that all the neutron paths must make it through the overkill apertures especially the middle overkill aperture. After the sample aperture, neutrons keep on falling down till they reach the detector plane.
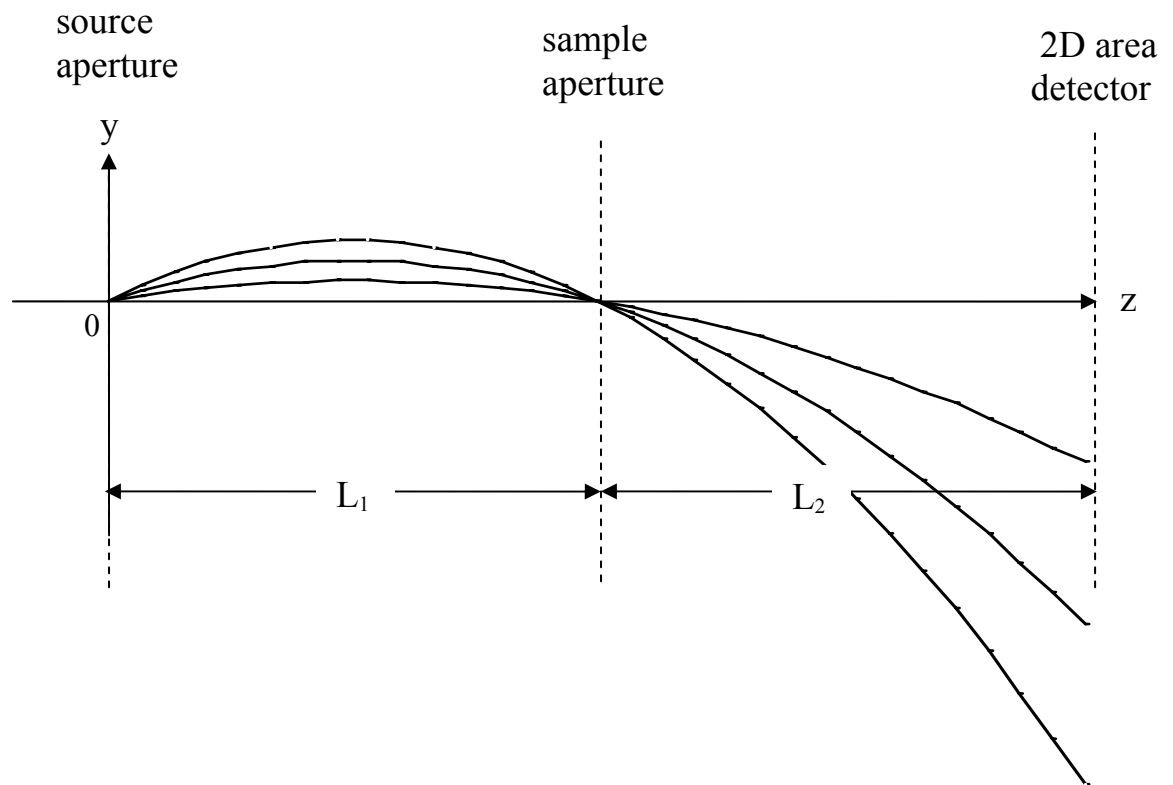

Figure 2: Trajectories of successfully transmitted neutrons corresponding to different wavelengths. Slower neutrons climb higher between the source and sample apertures.

Neutrons that are successfully transmitted through the source and sample apertures follow trajectories that depend on neutron wavelength. The maximum vertical beam spread occurs at mid-point between these two apertures. Neutrons follow parabolic trajectories that are described by the following parametric equation:

$$y(z) = [y(z)]_{geo} + [y(z)]_{grav} \tag{3}$$

$$[y(z)]_{grav} = -B\lambda^2 (z^2 - zL_1). $$

with:

$$B = \frac{gm^2}{2h^2} = 3.073 * 10^{-9} \, cm^{-1}.\text{Å}^{-2}. \tag{4}$$

Note that the related neutron fall constant at the detector location (i.e., for $z = L_1 + L_2$) is defined as:

$$A = L_2(L_1 + L_2)\frac{gm^2}{2h^2}. \tag{5}$$

The geometry part of the variance of the Q resolution corresponds to neutron trajectories without gravity effect. The effect of gravity is non-negligible for long wavelengths. The top neutron trajectory corresponds to $\lambda + \Delta\lambda$ whereas the bottom trajectory corresponds to $\lambda - \Delta\lambda$.

Constraining all neutrons within the wavelength spread to pass through the middle overkill aperture is performed by constraining the vertical neutron spread. The vertical beam spread corresponds to:

$$[\Delta y(z)]_{grav} = -B[(\lambda + \Delta\lambda)^2 - (\lambda - \Delta\lambda)^2](z^2 - zL_1) \tag{6}$$

$$= -B \, 4 \, \lambda^2 \left(\frac{\Delta\lambda}{\lambda}\right)(z^2 - zL_1). $$

And at the midpoint between the sample and source apertures (apex point where $z = L_1/2$), it is equal to:

$$[\Delta y(L_1/2)]_{grav} = B\lambda^2 \left(\frac{\Delta\lambda}{\lambda}\right)L_1^{\,2}. \tag{7}$$

The constraint that all neutrons within the wavelength spread make it through the middle overkill aperture (located at $z = L_1/2$) can be stated as:

$$2r_m \geq [\Delta y(L_1/2)]_{geo} + [\Delta y(L_1/2)]_{grav}. \tag{8}$$

r_m is the radius of the middle overkill aperture. This constraint translates to the condition:

$$r_m \geq \frac{r_1 + r_2}{2} + \frac{B\lambda^2 L_1^2}{2}\left(\frac{\Delta\lambda}{\lambda}\right). \tag{9}$$

This is a constraint on the size of the middle overkill aperture r_m in terms of the radii of the source and sample apertures r_1 and r_2, the source-to-sample distance L_1, the neutron wavelength λ and wavelength spread $\Delta\lambda$. An alternative criterion (not considered here) could be to constrain the variance of the beam spread instead.

2. SPECIFIC CASE OF MULTIPLE CIRCULAR CONVERGING COLLIMATION

Without Lenses

Consider the following possible VSANS instrumental conditions:

> Source circular aperture (hole) radius: $r_1 = 0.3$ cm $\qquad$ (10)
> Sample circular aperture (hole) radius: $r_2 = 0.15$ cm
> Number of apertures (holes): $n = 18$
> Detector cell horizontal size: $\Delta x_3 = 0.1$ cm
> Detector cell vertical size: $\Delta y_3 = 0.1$ cm
> Source-to-sample distance: $L_1 = 20$ m
> Sample-to-detector distance: $L_2 = 20$ m
> Neutron wavelength: $\lambda = 8.5$ Å
> Wavelength spread: $\dfrac{\Delta\lambda}{\lambda} = 0.13$.

This corresponds to a source aperture of 15 cm * 6 cm and a sample aperture (and a sample size) of 7.5 cm * 3 cm.

Therefore $A = 0.0246$ cm/Å^2 so that $\sigma_x^2 = \sigma_y^2 = 0.0458$ cm^2 and:

$$\sigma_{Qx}^2 = 6.26 * 10^{-9} + 0.0028\, Q_x^2 \text{ (in units of Å}^{-2}) \tag{11}$$
$$\sigma_{Qy}^2 = 1.11 * 10^{-8} + 0.0028\, Q_y^2 \text{ (in units of Å}^{-2}).$$

For this multiple circular converging collimation configuration,

$$Q_{min}^{\ X} = 0.00024 \text{ Å}^{-1} \tag{12}$$
$$Q_{min}^{\ Y} = 0.00041 \text{ Å}^{-1}.$$

Neutrons fall by 1.78 cm in the detector plane ($z = L_1+L_2$). At the apex position ($z = L_1/2$), neutron height corresponds to $y(L_1/2) = 0.22$ cm. This is the amount by which the middle overkill aperture has to be raised. Other overkill apertures are raised proportionally.

It is noted that a VSANS instrument with multiple circular converging collimation operates at preset discrete wavelengths because each wavelength requires different height adjustments

for the overkill apertures. Based on the constraint criterion used, the middle overkill aperture must have a radius of $r_m \geq 0.283$ cm for $\lambda = 8.5$ Å.

The neutron flux and count rate on sample are estimated for a neutron wavelength and wavelength spread of $\lambda = 8.5$ Å and $\Delta\lambda/\lambda = 0.13$. Using the source and sample areas of $A_1 = 0.283$ cm^2 and $A_2 = 0.0707$ cm^2, and n = 18, one obtains:

$$\phi(8.5 \text{ Å}) = 31,400 \text{ n/cm}^2.\text{s} \tag{13}$$
$$\Phi(8.5 \text{ Å}) = 2,218 \text{ n/s}.$$

These numbers are for a possible VSANS configuration characterized by a Q_{min} which is an order of magnitude lower than the similar SANS configuration.

With Lenses

When using focusing lenses, the sample aperture can be opened up. Consider now $r_2 = 0.5$ cm. This gives slightly lower resolution:

$$\sigma_{Qx}^2 = 3.57*10^{-9} + 0.0028\, Q_x^2 \text{ (in units of Å}^{-2}) \tag{14}$$
$$\sigma_{Qy}^2 = 8.43*10^{-9} + 0.0028\, Q_y^2 \text{ (in units of Å}^{-2}).$$

$$Q_{min}^X = 0.00022 \text{ Å}^{-1}$$
$$Q_{min}^Y = 0.00040 \text{ Å}^{-1}.$$

The neutron current is higher since the source aperture is larger.

$$\phi(8.5 \text{ Å}) = 31,400 \text{ n/cm}^2.\text{s} \tag{15}$$
$$\Phi(8.5 \text{ Å}) = 24,649 \text{ n/s}.$$

Use MgF$_2$ lenses (one stack of lenses per small aperture) and recall the following basic equations for MgF$_2$ lenses:

$$\frac{N\lambda^2}{R}\left(\frac{L_1 L_2}{L_1 + L_2}\right) = \frac{\pi}{\rho b_c} = 6.25*10^5 \text{ Å}^2. \tag{16}$$

Consider lenses of radius of curvature R that are thin at the center (0.5 mm thickness) in order to keep neutron transmission high. A multiple aperture configuration with $L_1 = L_2 = 20$ m yields a focal length of:

$$f = \left(\frac{L_1 L_2}{L_1 + L_2}\right) = 1000 \text{ cm}. \tag{17}$$

Therefore:

$$\frac{N\lambda^2}{R} = 625 \text{Å}^2. \tag{18}$$

For R = 0.5 cm and λ = 8.5 Å, it takes about 4.33 lenses to achieve the desired focal length.

In order to enhance flux-on-sample, multiple-slit converging collimation is discussed next.

3. MULTIPLE SLIT CONVERGING COLLIMATION

Multiple slit converging collimation has the advantage of increasing flux on sample by opening up the vertical resolution while tightening the horizontal resolution. The effect of gravity becomes irrelevant.
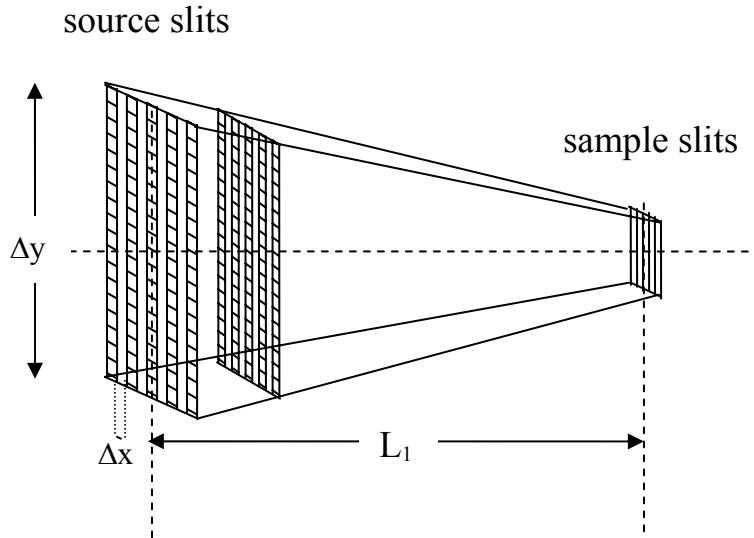

Figure 3: Multiple converging slit collimation. Intermediate apertures are placed so as to avoid cross collimation and keep neutrons in the same aperture channel.

The Q resolution for multiple slit converging collimation is similar to that for multiple circular converging collimation but with different "geometry" contributions σ_x^2 and σ_y^2. Also, the averages $<x^2>_1$ and $<x^2>_2$ over the beam defining apertures for slits are different from those for circular apertures. Recall that:

$$<x^2>_1 = \frac{1}{3}\left(\frac{\Delta x_1}{2}\right)^2 \text{ for slit of width } \Delta x_1 \tag{19}$$

$$<x^2>_1 = \frac{R_1^2}{4} \text{ for circular aperture of radius } R_1$$

Similarly, the Q_{min} value for multiple converging slit collimation in the horizontal (x-) direction is the same as that for multiple circular converging collimation. The same expression for the flux-on-sample applies for multiple circular collimation and multiple slit collimation.

4. PERFORMANCE OF THE VARIOUS VSANS CONFIGURATIONS

Comparison of the performance of various VSANS configurations for circular or slit apertures with or without lenses is presented in a table. These predictions assume the following:

Source-to-sample distance: $L_1 = 20$ m
Sample-to-detector distance: $L_2 = 20$ m
Neutron wavelength: $\lambda = 8.5$ Å
Wavelength spread: $\frac{\Delta\lambda}{\lambda} = 0.13$.
Source aperture of 15 cm * 6 cm
Sample aperture (and sample size) of 7.5 cm * 3 cm.

Table 1: Prediction of the performance of the VSANS instrument for various configurations

		Circular Apertures		Slit Apertures
	Small Aperture Sizes (cm)	Performance	Small Slit Sizes (cm)	Performance
Without Lenses	$r_1 = 0.3$ $r_2 = 0.15$ $n = 18$	$Q_{min}{}^X = 0.00024$ Å^{-1} $Q_{min}{}^Y = 0.00041$ Å^{-1} $\phi(8.5$ Å$)=31{,}400$ n/cm^2.s $\Phi(8.5$ Å$) = 2{,}218$ n/s	$\Delta x_1 = 0.6$ $\Delta y_1 = 15$ $\Delta x_2 = 0.3$ $\Delta y_2 = 7.5$ $n = 3$	$Q_{min}{}^X = 0.00024$ Å^{-1} $Q_{min}{}^Y = 0.0057$ Å^{-1} $\phi(8.5$ Å$)=1.67*10^5$ n/cm^2.s $\Phi(8.5$ Å$) = 3.75*10^5$ n/s
With Lenses	$r_1 = 0.3$ $r_2 = 0.5$ $n = 18$	$Q_{min}{}^X = 0.00022$ Å^{-1} $Q_{min}{}^Y = 0.00040$ Å^{-1} $\phi(8.5$ Å$)=31{,}400$ n/cm^2.s $\Phi(8.5$ Å$) = 24{,}649$ n/s	$\Delta x_1 = 0.6$ $\Delta y_1 = 15$ $\Delta x_2 = 1.0$ $\Delta y_2 = 7.5$ $n = 3$	$Q_{min}{}^X = 0.00022$ Å^{-1} $Q_{min}{}^Y = 0.0037$ Å^{-1} $\phi(8.5$ Å$)=1.67*10^5$ n/cm^2.s $\Phi(8.5$ Å$) = 1.25*10^6$ n/s

The configuration for circular apertures with lenses yields a slightly lower $Q_{min}{}^X$. This $Q_{min}{}^X$ is maintained when moving to slit collimation in the horizontal direction. Using lenses increases the neutron current. Using slits enhances the flux-on-sample. This, however, requires dealing with slit smearing corrections. Note that the neutron flux on sample and neutron current were estimated based on predictions for the NG3 guide.

The two main figures of merit (variance of the Q resolution and Q_{min}) are compared in a figure.
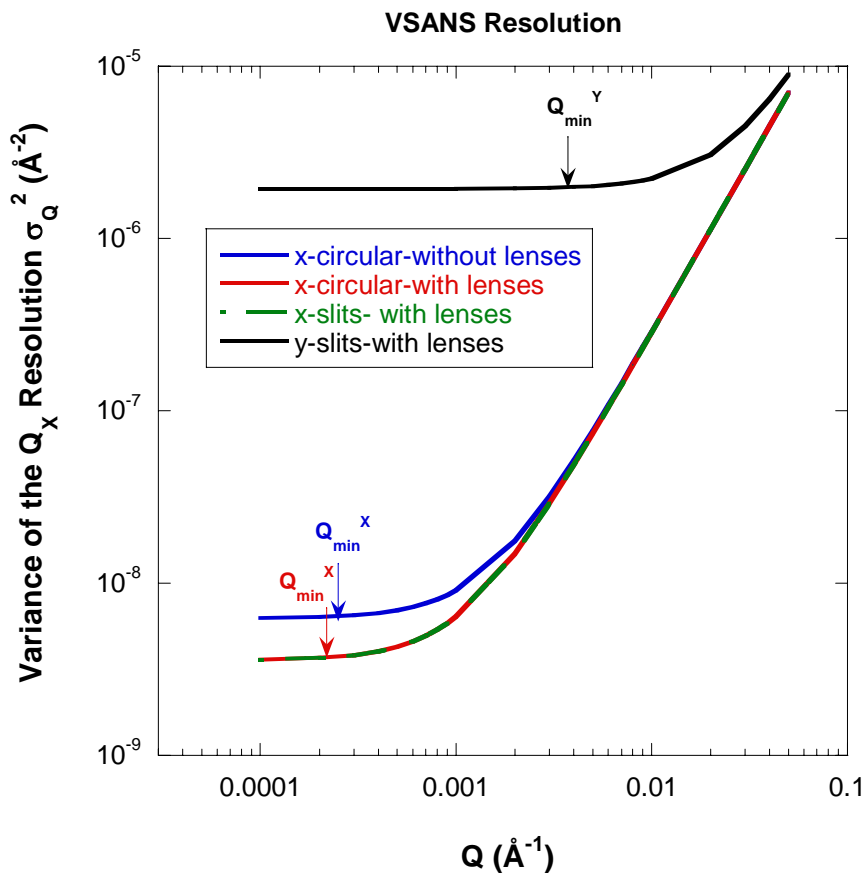
VSANS Resolution

Figure 4: Variation of the variance of the Q_x resolution and Q_{min} for various VSANS configurations. The x- and y- axes are the horizontal and vertical directions (the z- direction is along the neutron beam).

5. OVERKILL APERTURES

Spacing Scheme

Uniformly spacing the overkill apertures is not the most effective way of distributing them. Another scheme is discussed here. A similar scheme has been used to place disks on multidisk velocity selectors.
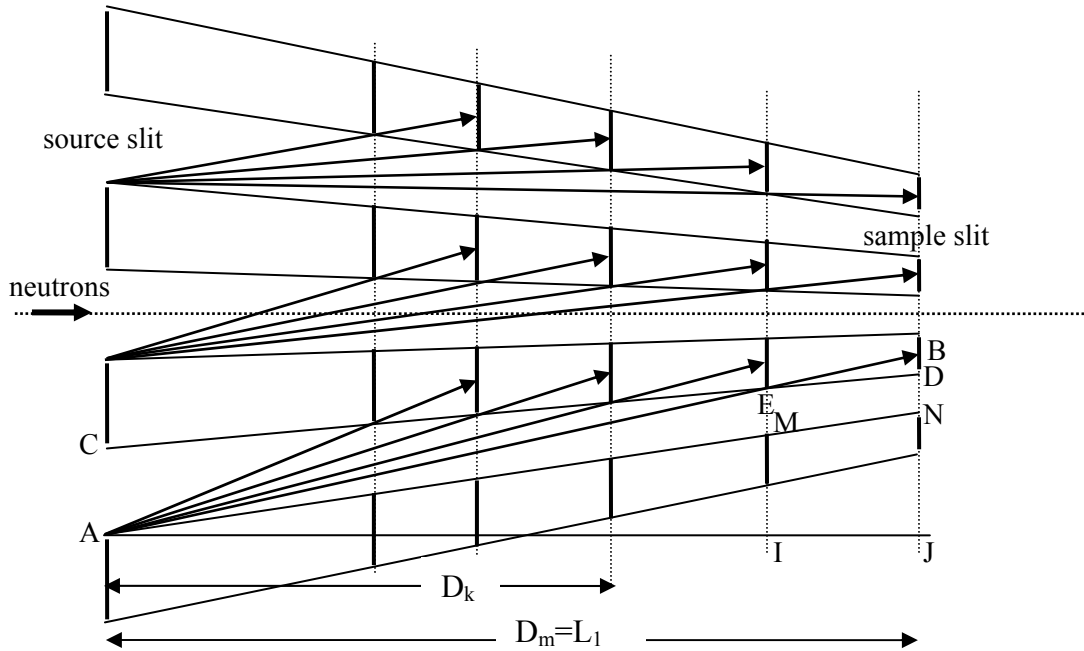
Figure 5: Top view of the distribution scheme proposed to place the overkill apertures along the neutron path. The neutron source aperture is located on the left and the sample aperture is located on the right.

The proposed scheme is illustrated in a figure. It consists in placing a series on m overkill apertures starting from the sample on the right side. A line AB is drawn to the middle of an absorbing region. It cuts line CD at a point E. This gives the location of aperture m-1 a distance D_{m-1} from the source (left) side.

Figure 6: Open slits and blocked regions on aperture k.

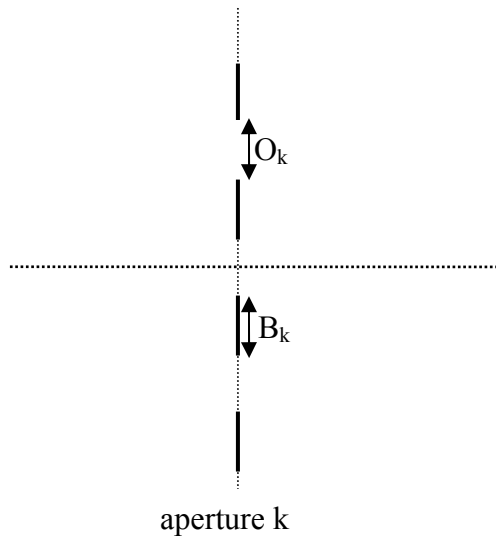Defining the sizes of the open (slit) and of the blocked parts of aperture k as O_k and B_k respectively, one can express the blocked to open ratio as:

$$w = \frac{B_m}{O_m} = \frac{B_k}{O_k} .$$ (20)

The distance D_{m-1} can be calculated from distance D_m based on a scaling argument working backward.

$$\frac{D_{m-1}}{D_m} = \frac{AI}{AJ} = \frac{IE}{JB} = \frac{ME}{NB} = \frac{O_{m-1}}{O_m + \frac{B_m}{2}} = \frac{O_{m-1}}{O_m} \frac{1}{1 + \frac{w}{2}}$$ (21)

$$D_{m-1} = D_m \frac{O_{m-1}}{O_m} K$$

Where:

$$K = \frac{1}{1 + \frac{w}{2}} .$$ (22)

D_m is the full source-to-sample distance (usually referred to as L_1). Similarly, one obtains for the location of subsequent slits:

$$D_{m-2} = D_m \left(\frac{O_{m-2}}{O_m} \right) K^2$$ (23)

The general formula is:

$$D_{m-k} = D_m \left(\frac{O_{m-k}}{O_m} \right) K^k .$$ (24)

The position of overkill apertures follows a geometric progression. This scheme ensures that no unwanted open channels are left open and guarantees more than single coverage of the blocked channels. In practice this scheme is used for a reasonable number of overkill slits.

The transmission factor for the apertures is given by:

$$T = \left(\frac{1}{1 + w} \right)$$ (25)

Slit Sizes

The following scaling relation applies:

$$\frac{O_{m-1}}{O_m} = \frac{O_1(D_m - D_{m-1}) + O_m D_{m-1}}{O_m D_m}. \qquad (26)$$

O_1 is the slit (open) size of the first (source) aperture and O_m is the slit (open) size of the last (sample) aperture. Replacing $D_{m-1} = D_m \left(\dfrac{O_{m-1}}{O_m} \right) K$, one obtains the following slit sizes relationship:

$$O_{m-1} = \frac{O_1}{1 + K \dfrac{O_1 - O_m}{O_m}}. \qquad (27)$$

Furthermore:

$$O_{m-k} = \frac{O_1}{1 + K^k \dfrac{O_1 - O_m}{O_m}}. \qquad (28)$$

This scheme would work for multiple slit converging apertures as well. For multiple circular converging apertures, vertical apertures sizes would have to be corrected for the gravity effect using the constraint discussed previously.

6. SPECIFIC CASE FOR OVERKILL APERTURES

Consider the following specific case for converging circular apertures without lenses.

> Slit opening on source aperture $O_1 = 0.6$ cm.
> Blocked area between slits on source aperture $B_1 = 0.6$ cm.
> Slit opening on sample aperture $O_m = 0.3$ cm.
> Blocked area between slits on sample aperture $B_m = 0.3$ cm.
> Source-to-sample distance $D_m = 20$ m.
> Consider $m = 9$; i.e., a total of 9 apertures.

In this case:

> Blocked to open ratio $w = 1$.
> Apertures transmission $T = 1/2 = 50$ %.
> Factor $K = 2/3 = 0.667$
> Factor $\dfrac{O_1 - O_m}{O_m} = 1$.

The apertures are located at the following distances from the source aperture:

$D_9 = 20$ m (sample aperture)
$D_8 = 16.00$ m
$D_7 = 12.32$ m
$D_6 = 9.15$ m
$D_5 = 6.61$ m
$D_4 = 4.66$ m
$D_3 = 3.24$ m
$D_2 = 2.22$ m
$D_1 = 0$ m (source aperture).

This is a possible placement sequence for the collimation apertures. This sequence can be used either in the forward or backward directions starting from the neutron source aperture.

Slit sizes in each aperture are as follows:

$O_9 = 0.30$ cm (sample aperture slit).
$O_8 = 0.36$ cm
$O_7 = 0.42$ cm
$O_6 = 0.46$ cm
$O_5 = 0.50$ cm
$O_4 = 0.53$ cm
$O_3 = 0.55$ cm
$O_2 = 0.57$ cm
$O_1 = 0.6$ cm (source aperture slit).

This is a possible sequence of slit sizes on the apertures.

7. SCATTERING ANGLE FOR MULTIPLE CONVERGING COLLIMATION

An issue worth discussing is whether the scattering angle would be the same for the various neutron scattering rays involved in the multiple converging collimation. As shown graphically all of the marked scattering angles are equal within the first order (small-angle) approximation. Higher order corrections may be needed when scattering angles are not small.
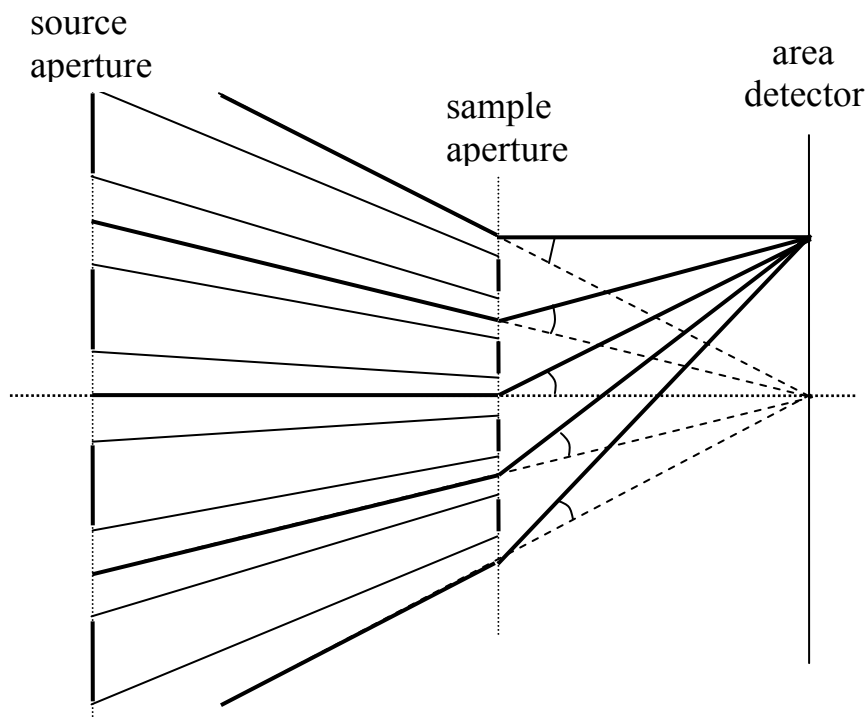
Figure 7: The marked angles are all equal to the scattering angle θ within the first order (small-angle) approximation.

8. DISCUSSION

The VSANS instrument combines the VSANS and SANS measurement ranges chosen in turn. Use of single-aperture collimation and coarse detector resolution measures the standard SANS range. Insertion of multiple apertures and of the high resolution neutron detector measures the VSANS range. The use of focusing lenses tightens the neutron beam spot on the detector while opening up the sample aperture. The use of multiple slits helps increase the neutron current substantially. This feature, however, works best with taller (rectangular) samples.

The VSANS instrument will use a couple of discrete wavelengths (for example 6 Å and 8.5 Å). These wavelengths must be higher than the Bragg cutoff (around 5 Å) for MgF_2 used for focusing lenses.

The VSANS instrument will use a "regular" area detector with resolution around 5 mm. A row of linear position sensitive detectors may replace the area detector or complement it by covering the larger angle areas. Linear "straw" detectors have the adventage of high count rate and robustness. Banks of such straw detectors could be placed on both sides of the main detector as well as at the top and bottom. This would cover a wide area.

The VSANS option requires a high resolution neutron detector as well. The technology for building high resolution (1 mm or 2 mm) detectors is improving. The Millimeter-resolution

Large Area Neutron Detectors (MILAND) project is an international focus group for improving such technology. Imaging plates and scintillation detectors can achieve that resolution. Imaging plates are sensitive to gammas and scintillation detectors can produce undesired gamma background.

The lens system when using multiple slits could be designed by incorporating holes in a slab cassette.
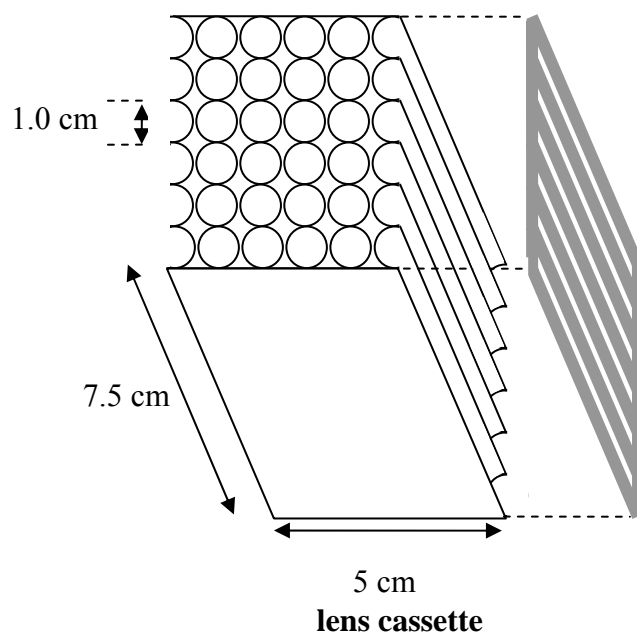
lens cassette

Figure 8: Schematic representation of the vertical lenses cassette that would comprise a number of slits. The cassette consists essentially of a slab with equally spaced vertical holes that are lined up. Two half holes make up one row of lenses, two half holes and four full holes in-between make up five rows of lenses.

The VSANS instrument would benefit from the use of two velocity selectors with typical and high resolution respectively.
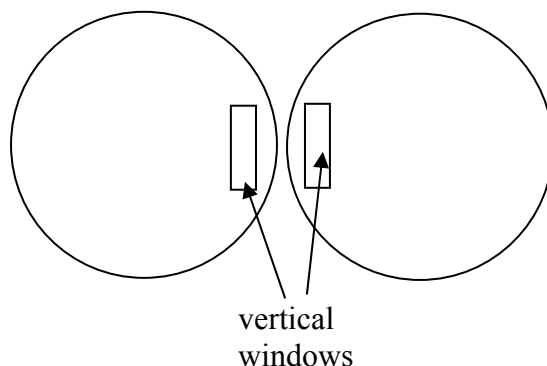
Two Velocity Selectors

vertical
windows

Figure 9: Two velocity selectors can be used, one characterized by $\Delta\lambda/\lambda \sim 0.15$ and the other one with $\Delta\lambda/\lambda \sim 0.05$.

Typical low-Q and high-Q configurations cover the following SANS Q range: 0.003 Å^{-1} < Q < 0.3 Å^{-1}. The USANS Q range is typically $3*10^{-5}$ Å^{-1} < Q < 0.005 Å^{-1}. A figure shows SANS and USANS data taken from 4 % poly(ethylene oxide) in d-ethanol. USANS requires high scattering cross section samples. The SANS data were acquired over a period of 30 minutes and the USANS data were acquired over a period of 5 hours. At the very low-Q, USANS statistics are very good, but for Q > 0.0004 A^{-1}, the USANS statistics become poor. This is where VSANS will improve data quality (counting statistics) in that region. The VSANS instrument will cover the Q range $3*10^{-4}$ Å^{-1} < Q < 0.009 Å^{-1}. The NIST CNR VSANS instrument is under construction (Barker, 2007).
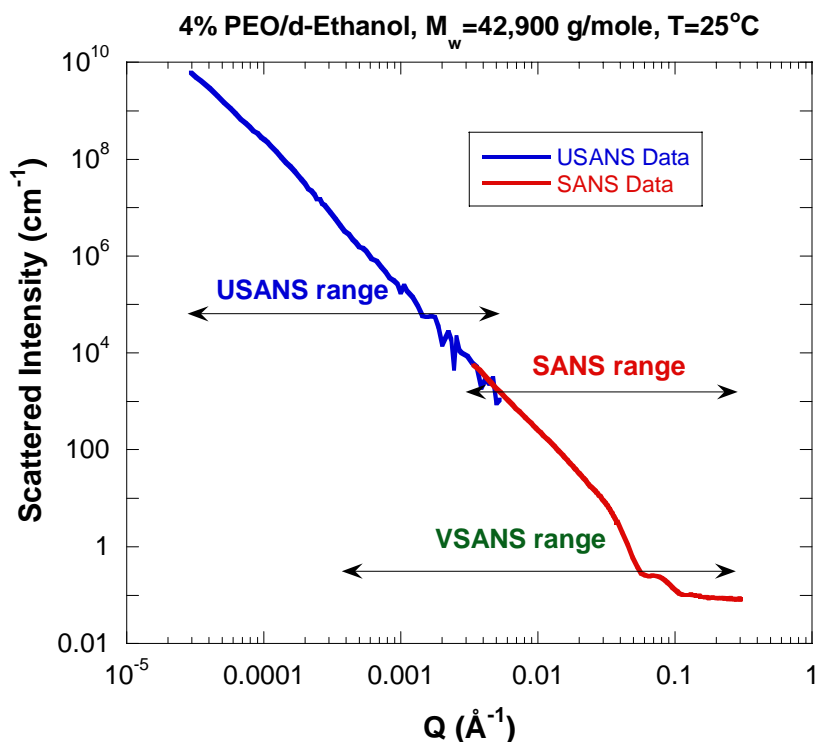
Figure 10: Compound plot of SANS data and USANS data from a 4 % poly(ethylene oxide) sample in d-ethanol. The Q range of the proposed VSANS technique is shown.

REFERENCES

D.F.R. Mildner, and J.M. Carpenter, "Optimization of the Experimental Resolution for SAS", J. Appl. Cryst. 17, 249-256 (1984).

D.F.R. Mildner, B. Hammouda, and S.R. Kline, "A Refractive Focussing Lens System for SANS", J. Appl. Cryst. 38, 979-987 (2005).

J.G. Barker, "VSANS Conceptual Design Report", NIST Center for Neutron Research Internal Report (2007)

QUESTIONS

1. What are the main components that make VSANS possible?
2. What is the main difference in the variance of the resolution function for circular and slit apertures?
3. What term changes in the variance of the resolution function when using focusing lenses?
4. What is the modification of the sample term in Q_{min} when using focusing lenses?

5. In going from SANS to VSANS, how much lower is Q_{min}?
6. Why is the VSANS option with multiple slits characterized by so much higher neutron current? What is the main drawback of using slit collimation?
7. What is the required detector resolution for VSANS to work?
8. What type of detectors could achieve 1 mm to 2 mm spatial resolution?

ANSWERS

1. The main components that make VSANS possible are: tight collimation through the use of multiple apertures and high resolution detector.
2. The main difference in the variance of the resolution function is in the averaging of the geometry contribution, $<x^2>_1 = R_1^2/4$ for a circular aperture of radius R_1 whereas $<x^2>_1 = (\Delta x_1/2)^2/3$ for a slit of width Δx_1.
3. The only term that changes in the variance of the resolution function is the sample aperture term which involves $< x^2+y^2>_2$. When using focusing lenses, this term is multiplied by $(2/3)(\Delta\lambda/\lambda)^2$.
4. The sample term in Q_{min} is multiplied by $2(\Delta\lambda/\lambda)$ when using focusing lenses.
5. Q_{min} is about an order of magnitude lower for VSANS than for SANS.
6. The VSANS option with multiple slits is characterized by a much higher neutron current because collimation in the vertical direction is opened up. The main drawback of this is slit smearing of the data.
7. For VSANS to work, the detector resolution must be 1 or 2 mm.
8. Imaging plates and scintillators could achieve sub-millimeter spatial resolution. These, however, are characterized by gamma background issues.

Chapter 60 - **THE USANS INSTRUMENT**

In order to achieve much lower Q ranges, an entirely different instrument concept is used. Instead of choosing long wavelengths and long flight paths (as done in conventional SANS instruments), thermal wavelength neutrons and perfect single crystals are used in the USANS instrument. The USANS instrument uses the Bonse-Hart method for achieving very narrow collimation through multiple bounce reflections.
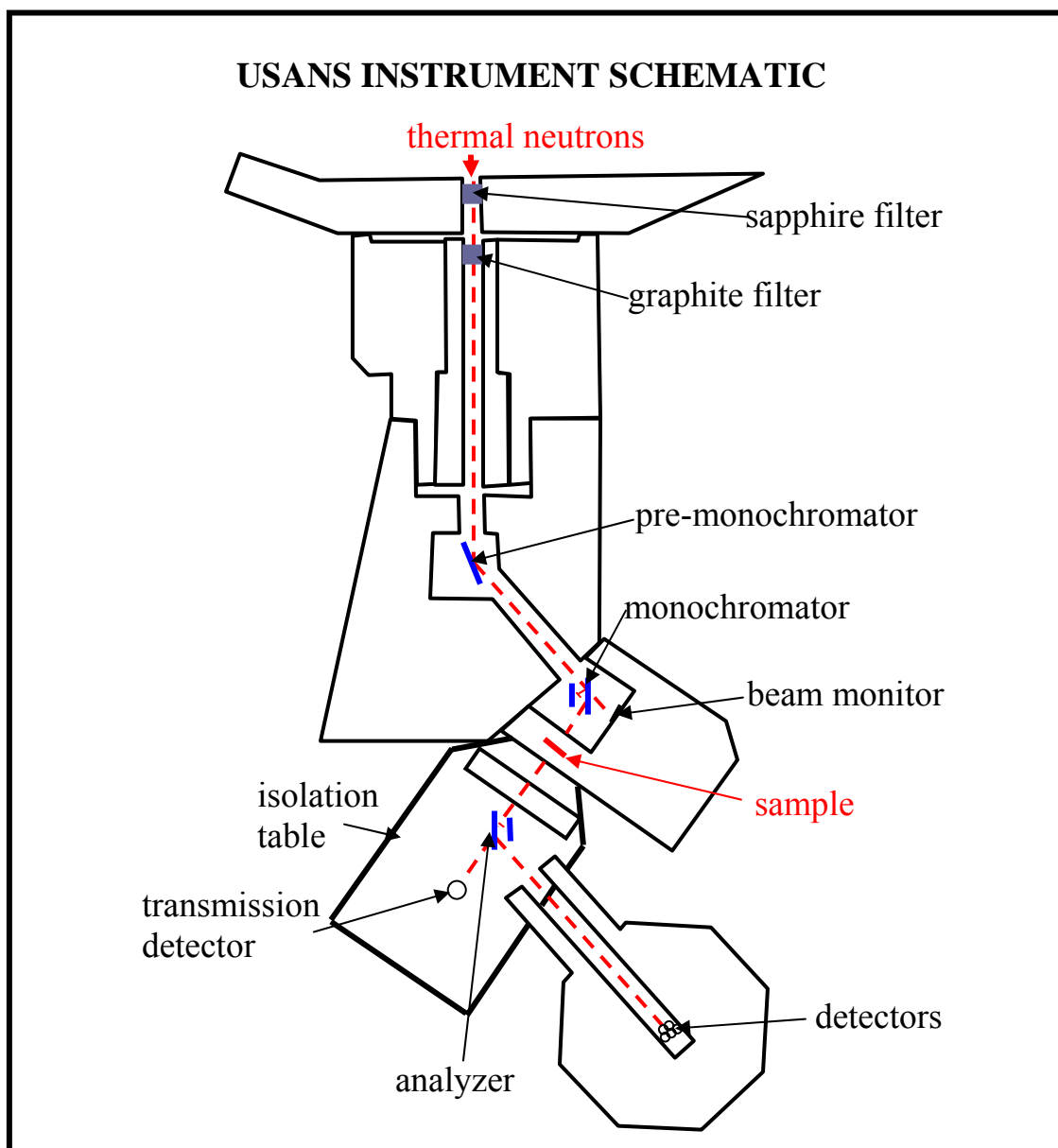
1. THE USANS INSTRUMENT COMPONENTS

Figure 1: Schematic representation of the USANS instrument at the NIST CNR.

Since the USANS instrument at the NIST CNR uses thermal neutrons, it is located inside the confinement building (not in the guide hall). It uses the silicon (220) reflection peaked at a neutron wavelength of $\lambda = 2.4$ Å. Neutron filters (sapphire and pyrolitic graphite) are used to filter out higher components of the energy spectrum. These eliminate neutrons with fractional wavelengths ($\lambda/2$, $\lambda/3$, etc). A pre-monochromator is used to reduce the radiation level on the monochromator and other components. Channel cut perfect silicon crystals are used for monochromator and analyzer. The three crystals (for the triple bounce) are cut from the same large silicon ingot. A set of five end-window counters are used as neutron detectors to step-scan the angular range (Barker et al, 2005).
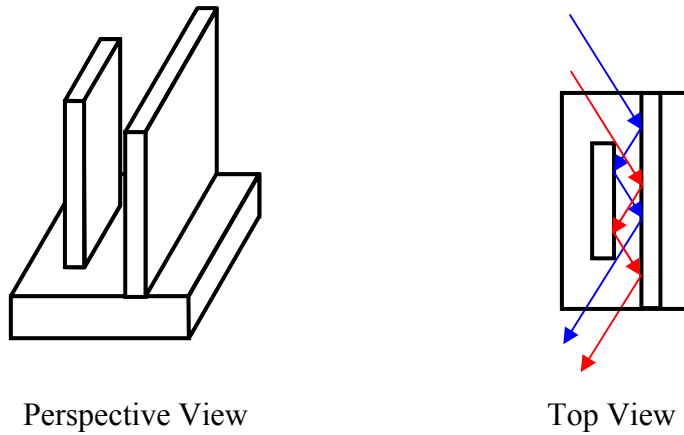

Perspective View   Top View

Figure 2: Triple bounce monochromator and analyzer single crystals. The three pieces are carved in the same single crystal silicon ingot.

2. THE USANS INSTRUMENT CHARACTERISTICS

The USANS instrument uses triple reflections from the single crystal silicon monochromator and analyzer in order to achieve very narrow $\Delta\lambda/\lambda$ and very high collimation (by reducing the beam angular divergence). It uses the slit geometry whereby the Q resolution if very tight in the vertical direction and opened up in the horizontal direction. The standard deviation of the Q resolution function is of order:

$$\sigma_Q{}^{ver} = 2.25 * 10^{-5} \text{ Å}^{-1} \qquad\qquad (1)$$
$$\sigma_Q{}^{hor} = 0.022 \text{ Å}^{-1}.$$

The coarse horizontal instrumental resolution allows the use of large sample sizes (5 cm diameter) and therefore large neutron beam currents.

The silicon (220) reflection is characterized by the $\lambda = 2.4$ Å (operating) USANS wavelength. Silicon has very narrow mosaic spread (a few arcsec FWHM). This low wavelength minimizes the multiple scattering effect so that standard (1 mm or 2 mm) sample thickness can be used. Low wavelength also minimizes gravity effects on the neutron trajectories.

The reflectivity profile from one silicon piece drops out like $R(Q) \sim 1/Q^2$. For three reflections in a row (triple bounce), $R(Q) \sim 1/Q^6$. The wings of the beam profile are substantially depressed making the Bonse-Hart adequate for ultra small-angle measurements.

The USANS instrument covers an ultra low-Q range: $4*10^{-5}$ Å$^{-1} < Q < 0.01$ Å^{-1}. This corresponds to the size range 7.8 μm > d-spacing > 628 Å that overlaps with optical microscopy. Microscopy measurements are performed in the real space whereas scattering measurements are performed in reciprocal space. Optical methods do not work on opaque samples whereas neutron scattering can measure opaque samples.

The main drawback of using slit geometry is the introduction of slit smearing of the data. The slit smearing integration of the scattering cross section (scattering intensity) is as follows:

$$\left(\frac{d\Sigma(Q)}{d\Omega} \right)_{smeared} = \frac{1}{\Delta Q_{ver}} \int_0^{\Delta Q_{ver}} dQ'_x \; \frac{d\Sigma(\sqrt{Q^2 + Q'_x{}^2})}{d\Omega} . \qquad (2)$$

Here the vertical integration window ΔQ_{ver} is proportional to $\sigma_Q{}^{ver}$. Integrating up to 2 or 3 standard deviations is reliable.

Two other figures of merit are the neutron current and the signal-to-noise ratio to insure low (acceptable) background level. The neutron current is $\Phi = 25{,}000$ n/sec for a horizontal sample slit size of $\Delta x_2 = 5$ cm. The signal-to-noise ratio is fairly low $5*10^5$ despite the fact that the USANS instrument at the NCNR is located inside the confinement building.

Assuming a Guinier-type function as a simple model for the scattering cross section at low-Q:

$$\frac{d\Sigma(Q)}{d\Omega} = \frac{d\Sigma(0)}{d\Omega} \exp\left(\frac{-Q^2 R_g{}^2}{3} \right). \qquad (3)$$

Here R_g is a characteristic radius of gyration. The smearing integral becomes:

$$\left(\frac{d\Sigma(Q)}{d\Omega} \right)_{smeared} = \frac{1}{\Delta Q_{ver}} \int_0^{\Delta Q_{ver}} dQ'_x \; \frac{d\Sigma(0)}{d\Omega} \exp\left(\frac{-(Q^2 + Q'_x{}^2) R_g{}^2}{3} \right). \qquad (4)$$

The following variable change is made $t = Q_x R_g / \sqrt{3}$ and the following integral is used:

$$\int_0^\infty dt \, \exp\exp\left(-t^2\right) = \frac{\sqrt{\pi}}{2}. \tag{5}$$

Assuming that the resolution window is wide-enough, one obtains the following low-Q limit.

$$\left(\frac{d\Sigma(0)}{d\Omega}\right)_{\text{smeared}} = \frac{d\Sigma(0)}{d\Omega} \frac{\sqrt{3\pi}}{2\Delta Q_{\text{ver}} R_g}. \tag{6}$$

Another simple function to model the scattering cross section is the Lorentzian function:

$$\frac{d\Sigma(Q)}{d\Omega} = \frac{d\Sigma(0)}{d\Omega} \frac{1}{1+Q^2\xi^2}. \tag{7}$$

Here also making the variable change $t = Q_x\xi$ and using the normalization integral:

$$\int_0^\infty dt \, \frac{1}{1+t^2} = \frac{\pi}{2}. \tag{8}$$

The following result is obtained for the low-Q limit:

$$\left(\frac{d\Sigma(0)}{d\Omega}\right)_{\text{smeared}} = \frac{d\Sigma(0)}{d\Omega} \frac{\pi}{2\Delta Q_{\text{ver}} R_g}. \tag{9}$$

3. THE FRAUNHOFFER DIFFRACTION

Fraunhoffer diffraction appears when aperture sizes become small. A circular aperture of radius R yields the following fringe pattern:

$$I(Q) = I(0)\left[\frac{2J_1(QR)}{QR}\right]^2. \tag{10}$$

Here J_1 is the cylindrical Bessel function or order 1 and I(0) constitutes the diffracted beam intensity through the aperture. Fraunhoffer fringes start at the edge of the direct beam on the detector. A slit aperture of width L yields the following fringe pattern:

$$I(Q) = I(0)\left[\frac{\sin(QL)}{QL}\right]^2. \tag{11}$$

These fringes constitute unwanted background when their Q range becomes comparable to the scattering features from the sample. This is the case of the USANS instrument whereby sub-millimeter slits are used and multi-micron size scales are probes.

Recall that $\left[\dfrac{2J_1(QR)}{QR} \right]^2$ and $\left[\dfrac{\sin(QL)}{QL} \right]^2$ are the form factors for a scattering disk of radius R and of a slab of width L provided that they are oriented perpendicular to the neutron beam. It is to be expected that the scattering from a particle of a specific shape be the same as the scattering from a sample of uniform density (think solvent) but with a beam defining mask of the same shape as the particle. This holds provided that the mask dimension is comparable to the size of the particle (nanometer to fraction of a micrometer scale).

4. TYPICAL USANS DATA

SANS and USANS data were taken from a 4 % poly(ethylene oxide) in d-ethanol. PEO crystallizes into lamellae that form a sponge-like structure. No Guinier region was observed in the SANS data, but its onset is visible in the USANS data. The scattering cross section is very large at low-Q, which yields good statistics. At intermediate-Q, the cross section is lower and the statistics are poor. It took 30 minutes to acquire the SANS data and 5 hours to acquire the USANS data.
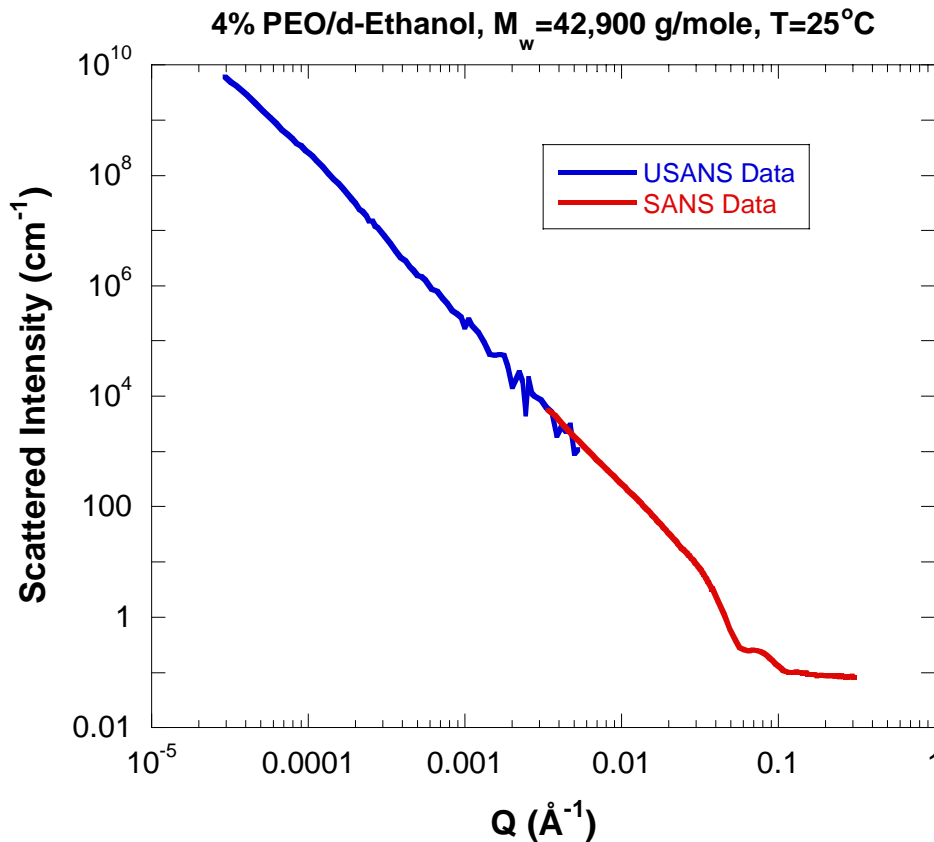

Figure 3: SANS and USANS data taken from a sample of 4 % poly(ethylene oxide) in d-ethanol.

More SANS and USANS data were taken from the PEO/d-ethanol at higher polymer weight fractions. The Guinier region is better defined and the high-Q oscillations from the lamellar structure occur at lower Q values (Ho et al, 2006). The high-Q Porod exponent is m = 3.5 which points to a mass fractal (sponge-like structure).
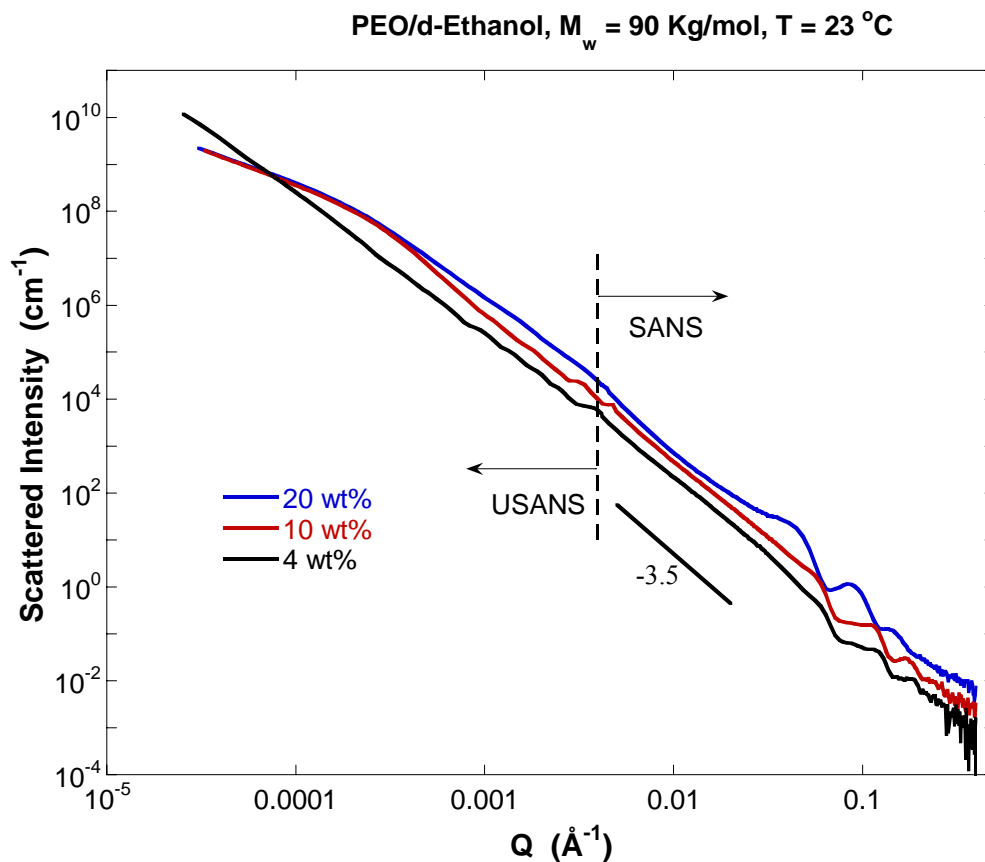

Figure 4: SANS and USANS data taken from crystalline PEO/d-ethanol. The incoherent background level has been subtracted.

A confocal optical micrograph was taken from 4 % hPEO/h-ethanol at ambient temperature. The sponge-like structure can be readily observed.
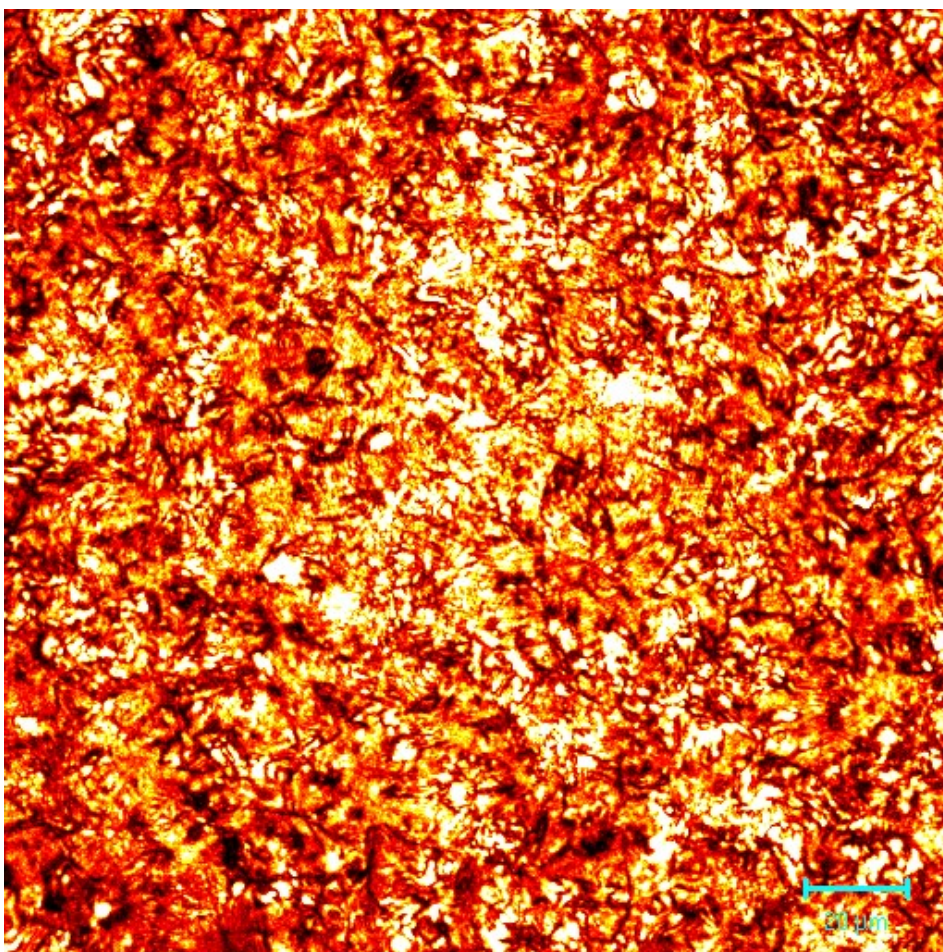
Figure 5: Confocal optical micrograph for a 4 % hPEO/h-ethanol sample. This picture represents data taken 28 μm underneath the sample surface. The scale bar represents a 20 μm length scale.

SANS and USANS data from a crosslinked gel are described next (Kim et al, 2006). Here also, the USANS data showed scattering information not observed by SANS. This system consisted of 1 % cetyltrimethylammonium 4-vinylbenzoate (CTVB) surfactant in d-water. Divinyl benzene crosslinker (0.8 mol crosslinker per 1 mol surfactant) was added to form a polymerized micelles soft gel. A slice of the gel was then equilibrated with excess oil (octane or toluene). The gel turns more opaque and white as it solubilizes oil. The USANS range shows that there are large "droplets" of oil present that can not be seen by SANS. Clearly, the gel can solubilize more toluene than octane.

Crosslinked CTVB Micelles
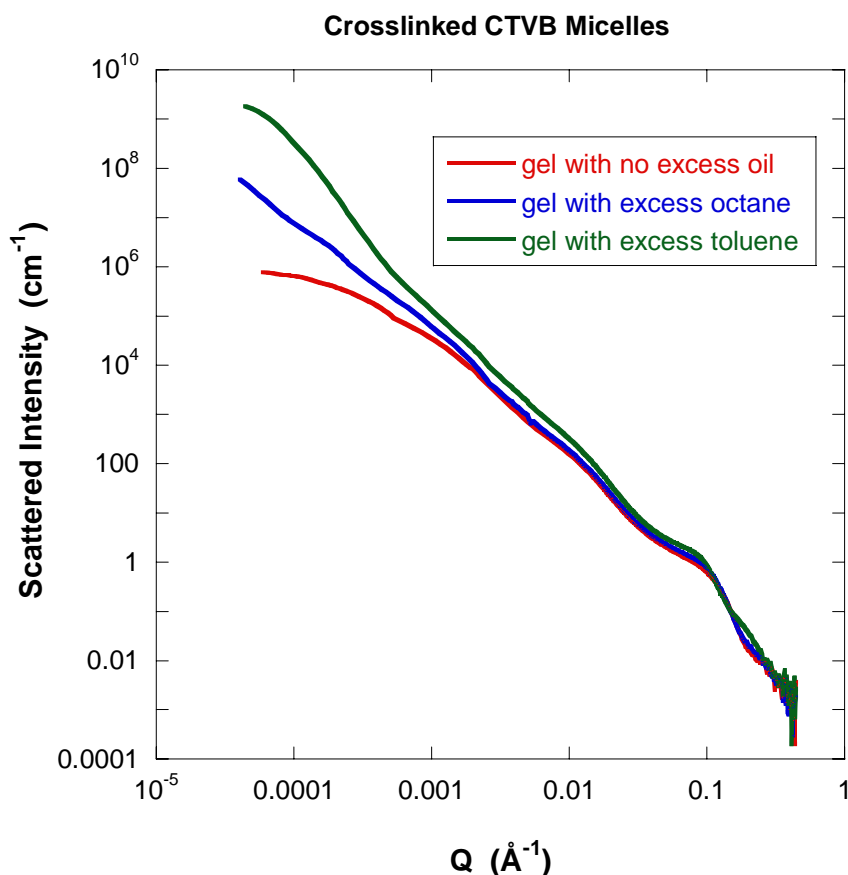
Figure 6: SANS and USANS data from CTVB wormlike micelles that were crosslinked to form a soft gel then swollen in oil.

REFERENCES

J.G. Barker, C.J. Glinka, J.J. Moyer, M.H. Kim, A.R. Drews, and M. Agamalian," Design and performance of a thermal-neutron double-crystal diffractometer for USANS at NIST", J. Appl. Cryst. <u>38</u>: 1004-1011 (2005).

D.L Ho, B. Hammouda, S.R. Kline and W-R Chen, "Unusual Phase Behavior in Mixtures of Poly(ethylene oxide) and Ethyl Alcohol", J. Polym. Sci., Polym. Phys. Ed. <u>55</u>, 557-564 (2006)

T-H Kim, S-M Choi and S.R. Kline, "Polymerized Rodlike Nanoparticles with Controlled Surface Charge Density", Langmuir <u>22</u>, 2844-2850, (2006)

QUESTIONS

1. Does the USANS instrument use cold or thermal neutrons?

2. What is the Q range for the USANS instrument? What is the corresponding d-spacing size range?
3. What is the main advantage of the USANS instrument?
4. What is the main difference between conventional SANS instruments and the USANS instrument?

ANSWERS

1. The USANS instrument uses thermal neutrons in order to avoid multiple scattering characterizing cold neutron wavelengths.
2. The USANS instrument covers the following Q range: $4*10^{-5}$ $\text{Å}^{-1} < Q < 0.01$ Å^{-1}. This corresponds to 7.8 μm > d-spacing > 628 Å.
3. The USANS instrument can observe structures in the optical (micrometer) size range in opaque samples. Optical methods can not probe opaque samples.
4. Conventional SANS instruments use velocity selectors for monochromation and long flight paths for collimation whereas the USANS instrument uses single crystal silicon for monochromation and triple bounce reflections (monochromator and analyzer) for improved resolution.

Part M – **FINAL ISSUES**

Chapter 61. Gallery of SANS Data Images

Chapter 62. Brief History and Future Prospect

This author has collected, over the years, a gallery of SANS data images from oriented samples. Some of these images are included here purely for their esthetic (artistic) value. A reference has been included in each case. This reference does not necessarily include the same SANS images, but is representative.

1. SHEARED MULTI-LAYER VESICLES

Multilayer vesicles (MLV) have an onion-skin type of structure. AOT surfactant in brine (i.e., salty) water solution forms MLVs. When sheared, MLVs yield characteristic SANS images dominated by orientation of the lamellae (Bergenholtz-Wagner, 1996). Couette shear is effective at orienting the lamellar structures. Oscillatory shear produces more orientation than simple shear. The tangential view (whereby the neutron beam is parallel to the shear direction) measures the shear gradient and neutral directions.
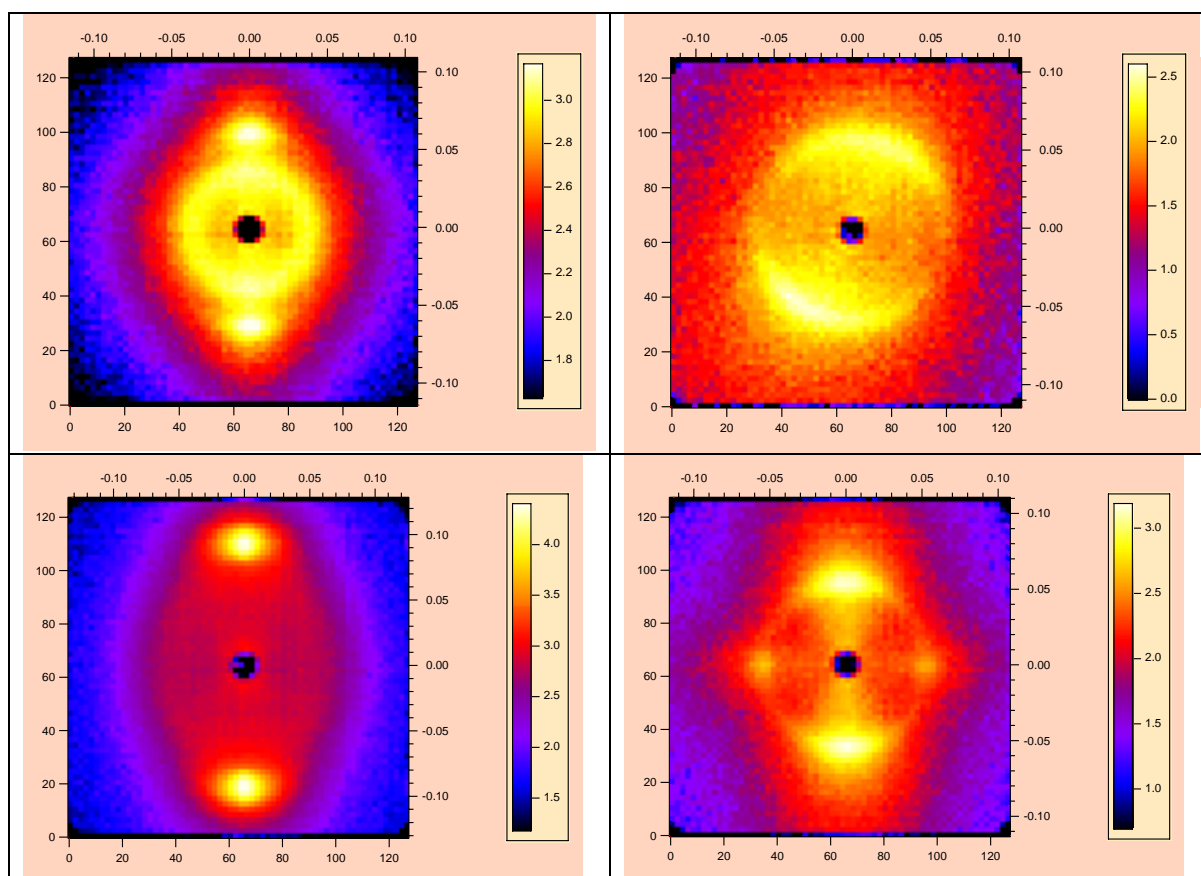

Figure 1: AOT in brine/D_2O multilayer vesicles sheared in a Couette shear cell. Top left: radial view under simple shear and low shear rate (0.025 rps), Top right: tangential view under simple shear and high shear rate (7.0 rps), Bottom left: radial view under oscillatory shear and high shear rate (15 rps), Bottom right: tangential view under oscillatory shear and

high shear rate (15 rps). The two SANS data sets shown in the bottom were taken at high temperature (50 ^{o}C).

2. THE BUTTERFLY PATTERN

SANS measurements are made in reciprocal space. When samples are oriented along the horizontal direction, they yield SANS patterns oriented along the vertical direction. This is due to the fact that reciprocal Q space and direct space form a conjugate pair. The exception to this is the case of the so-called "butterfly" pattern whereby orientation in direct space and in reciprocal space are along the same (here horizontal) direction. Cross linked polymer networks are characterized by a butterfly scattering pattern. Here a SANS image from a crosslinked and stretched poly(dimethyl siloxane) gel is included (Mendes et al, 1996).
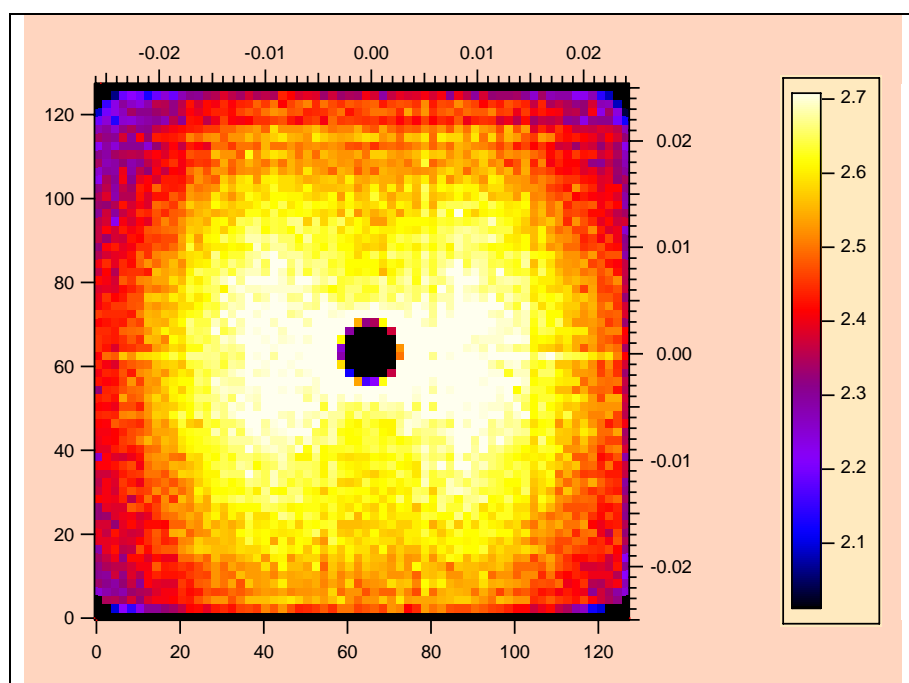
Figure 2: Butterfly SANS pattern from stretched poly(dimethyl siloxane) gel consisting of a mixture of crosslinked and (deuterated) linear polymer chains.

3. PACKED SPHERES

Highly packed silica particles in D_2O solution can form a "single crystal" texture characterized by bright diffraction spots under gentle shear (Butera et al, 1996). The SANS image shows 6-fold symmetry pointing to a cubic structure (body centered cubic). Four orders of diffraction spots are visible before the instrumental smearing becomes overwhelming (at high-Q).
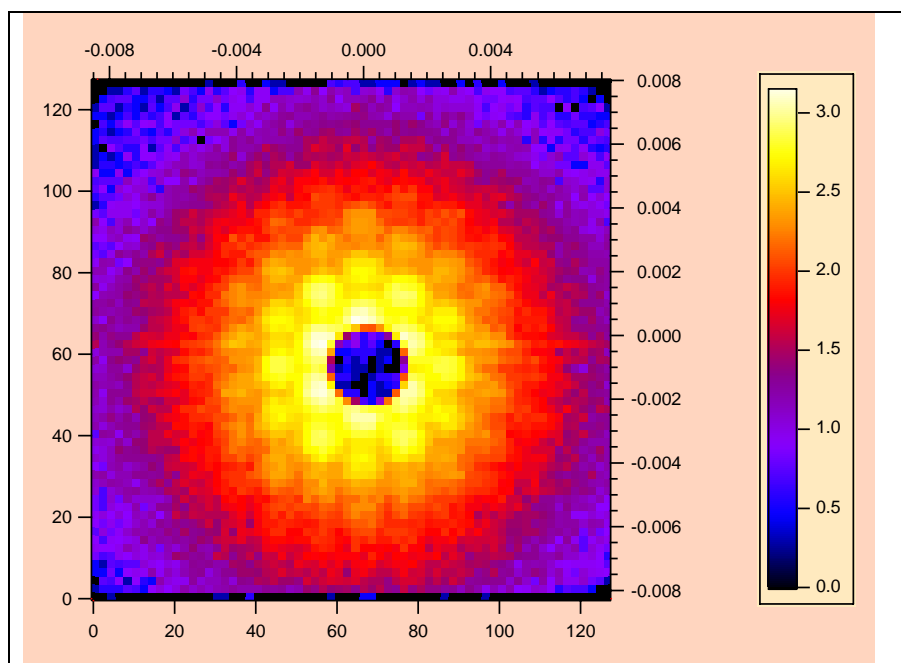
Figure 3: Single crystal diffraction pattern obtained from highly packed silica particles under gentle shear and in D_2O.

4. MULTI-PHASE ALUMINUM TEXTURE

SANS diffraction pattern obtained from a multi-grain aluminum sample is shown. Three major grains can be resolved. Note the dark blue spot on the middle-left part of the image. This is a damaged spot on the neutron detector produced by neutron over-exposure.
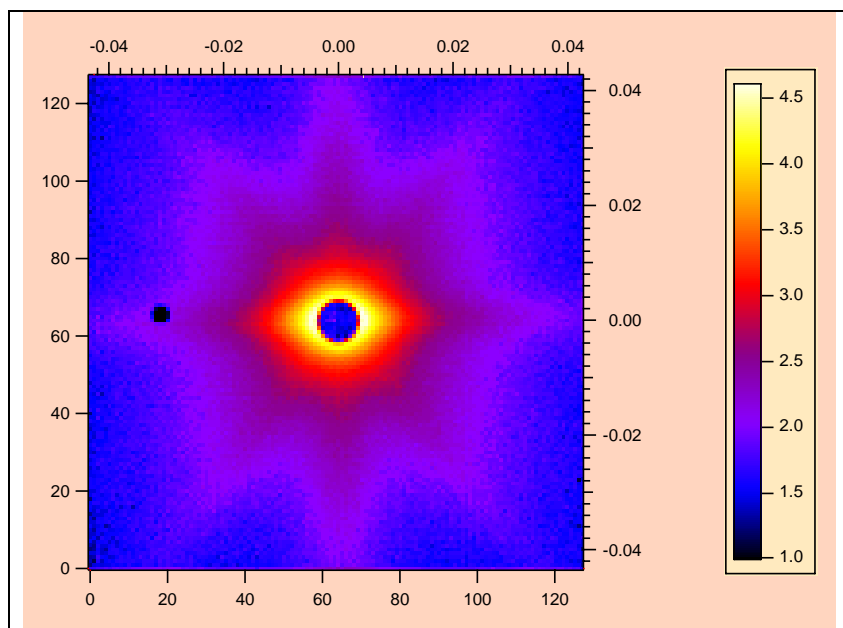
Figure 4: SANS diffraction pattern from multi-grain aluminum.

5. KANGAROO TAIL TENDON

Collagen from kangaroo tail tendon is a highly oriented fiber with crystalline structure along the fiber. Five order reflections can be resolved. Note that the second order reflection is extinct.
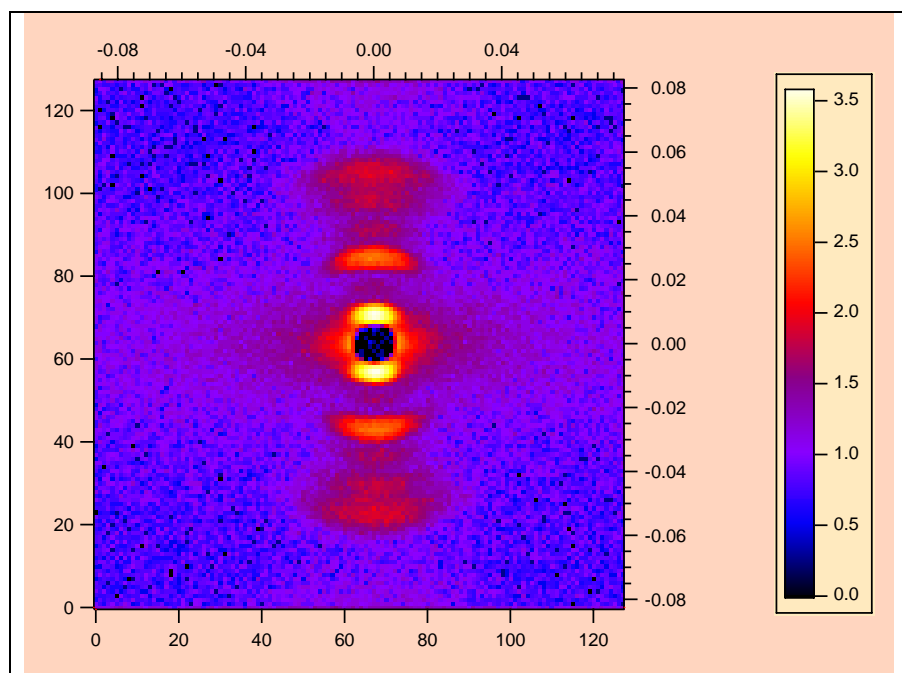
Figure 5: Scattering pattern from collagen from a kangaroo tail tendon showing the strong first and third reflection peaks as well as weak higher order reflection peaks; the second reflection peak is not allowed. The ordered structure is along the fibers and has a d-spacing of 667 Å.

6. TWINNED CRYSTAL

SANS from a twinned single-crystal of $NdBa_2Cu_3O_7$ (high T_c superconductor) is shown at 100 K. The twinned crystal grew along two orthogonal directions. Crystal boundaries occur when two crystals inter-grow with a highly symmetrical interface, often with one crystal being the mirror image of the other; atoms are shared by the two crystals at regular intervals. Scattering is mostly from nuclear (not magnetic) scattering (Lynn et al, 1987; Lynn et al, 1989).
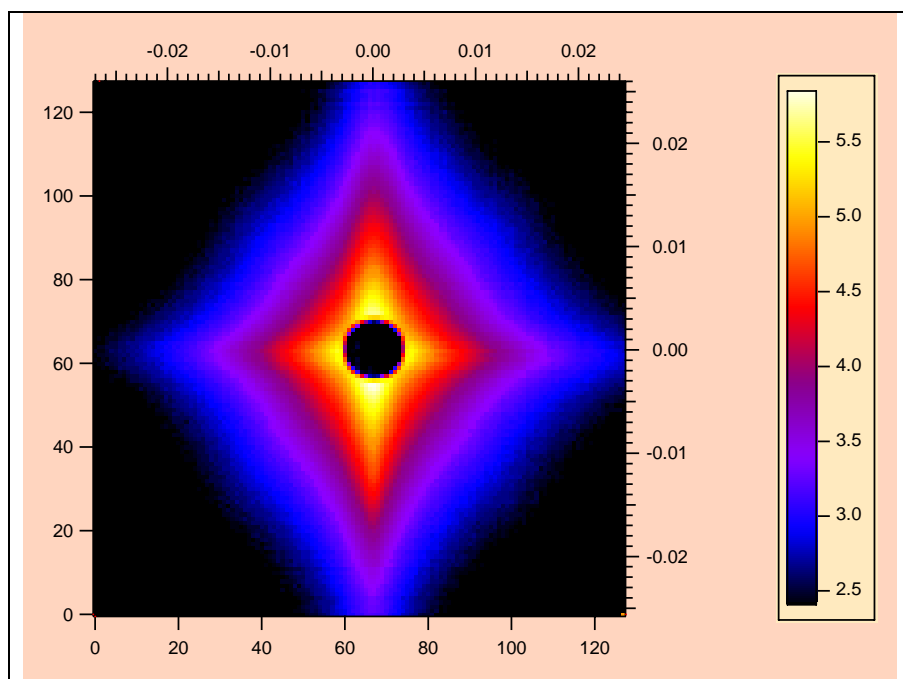
Figure 6: SANS data from the high T_c superconducting $NdBa_2Cu_3O_7$ cuprate at 100 K. The oriented structures characterizing the two crystals forming the twinned crystal are orthogonal (i.e, have orthorhombic symmetry) yielding the cross-like SANS patterns.

7. CORRELATIONS IN MULTIPHASE COMPOSITE

SANS data image taken from a multiphase aluminum oxide composite (Adolphs et al, 2002) is included. Distortion of the structure is observed. Further details are not available.
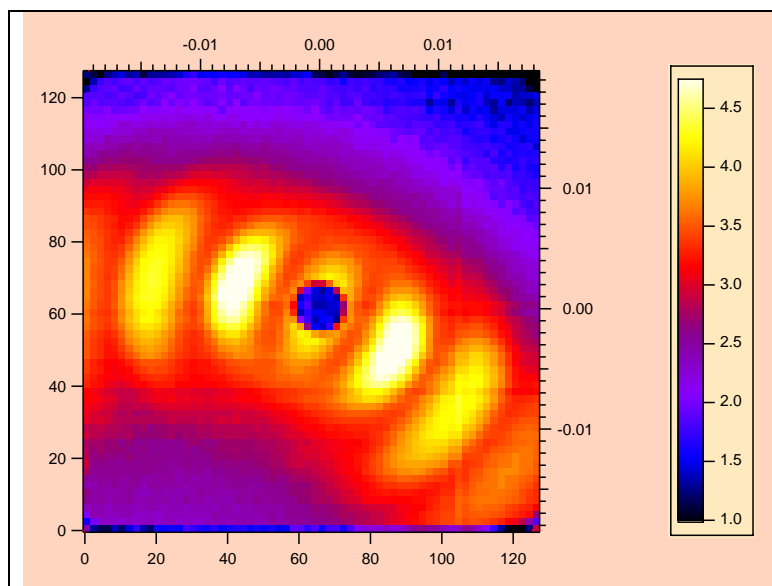
Figure 7: SANS from a multiphase aluminum oxide composite.

8. SHEARED SPHERICAL MICELLES

Anisotropic SANS data from P85 Pluronics micelles sheared in a Couette shear cell are shown. The characteristic hexagonal peak pattern (six fold symmetry) points to a cubic structure formed by the spherical micelles for 25 % mass fraction P85 in D_2O solutions. P85 is a triblock copolymer of poly(propylene) which is hydrophobic in the middle of the molecule and poly(ethylene oxide) which is hydrophilic on the outside of the molecule (PEO-PPO-PEO). P85 micelles are well formed at ambient temperature. Shearing helps the packing of the spherical micelles into a face centered cubic structure (Slawecki et al, 1998).
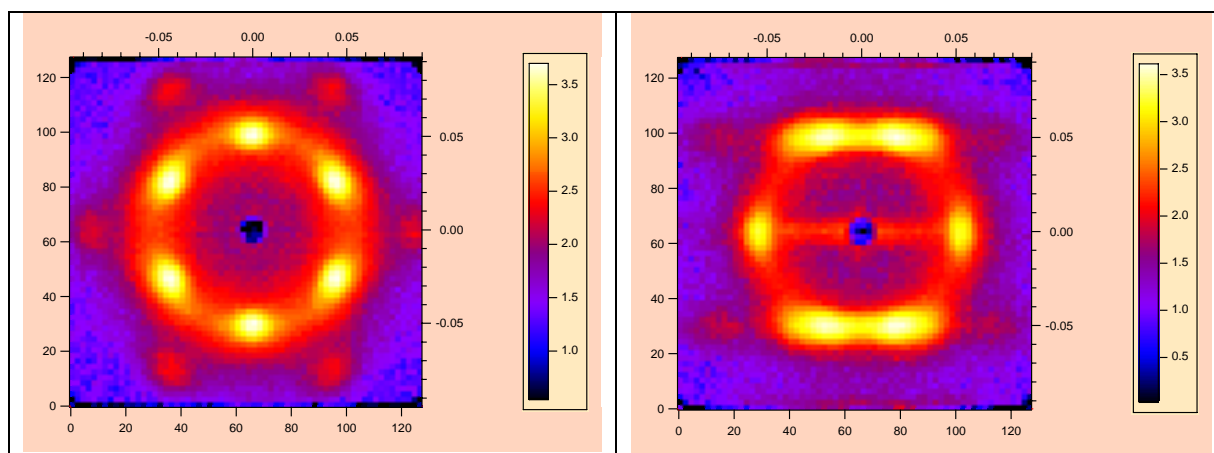
Figure 8: SANS data from 25 % P85 Pluronic (PEO-PPO-PEO triblock copolymer) in D_2O under Couette shear (5 Hz frequency) at 40 ^{o}C. The micelles form a cubic "single crystal" structure. Left: radial view. Right: Tangential view.

9. PEPTIDE ORIENTATION IN MEMBRANES

Peptides that are embedded in membranes produce highly oriented structures and yield a good harvest of interesting SANS images. Two antibiotic peptides (alamethicin or magainin) were investigated extensively. These were oriented between quartz slides and embedded into phopholipid bilayers forming the membrane. Deuterated water fills the inter-layer space for enhanced neutron contrast. Peptides form inter-layer "pores" that can be clearly observed. Temperature and relative humidity were controlled in order to monitor hydration effects on the structures. Fully hydrated samples show no inter-layer correlation. Dehydrated samples show strong such correlation that shows up as rich anisotropy in the SANS pattern characteristic of "single crystal" structure. In order to sample both the in-plane and the out-of-plane structure, the oriented membranes were tilted with respect to the neutron beam (Yang et al, 1998; Yang et al, 1999).
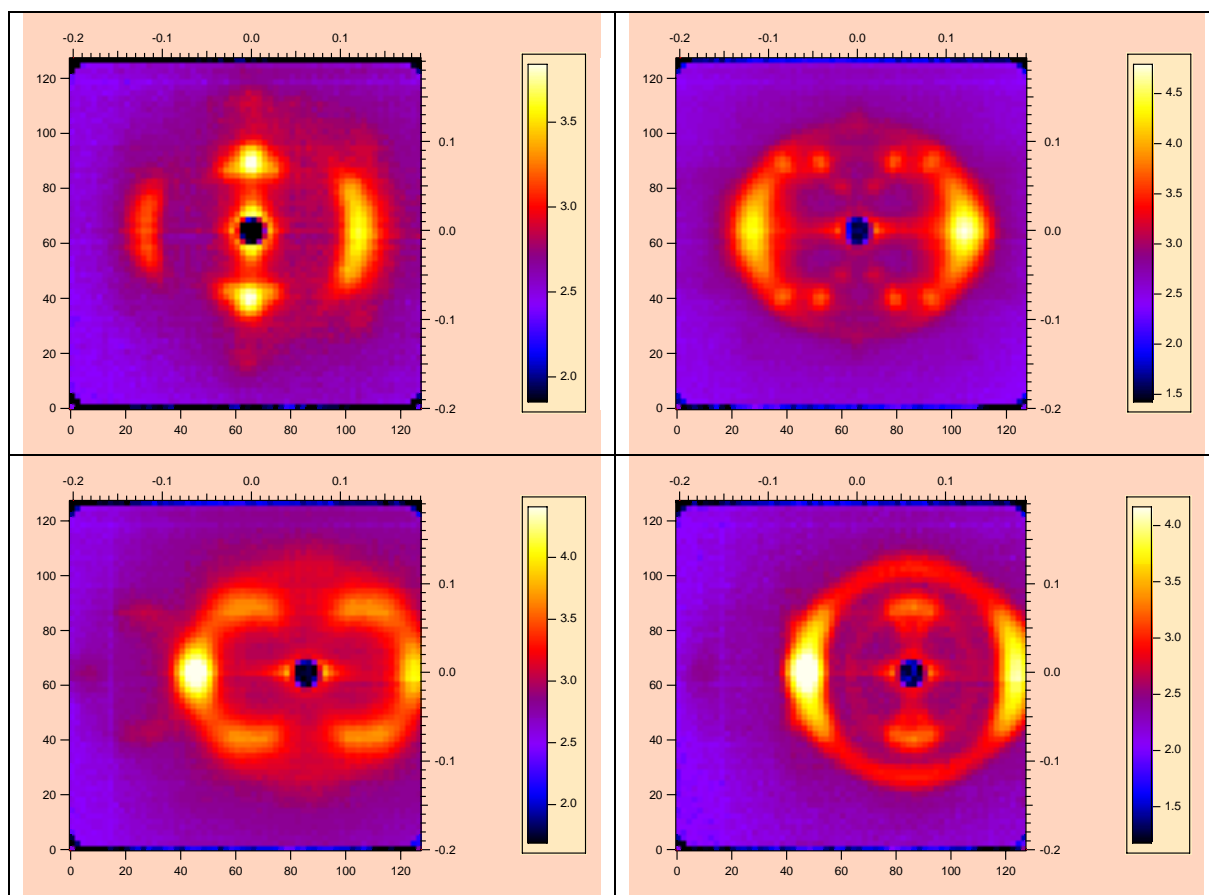
Figure 9: SANS data from peptides embedded into membranes and oriented between quartz slides. The sample was oriented at 60 ^{o} to the neutron beam in order to observe structures both parallel and perpendicular to the membrane surface. Top left: 60 ^{o} alignment angle. Top right: 80 ^{o} alignment angle. Bottom left: 80 ^{o} alignment angle and different hydration level. Bottom right: -80 ^{o} alignment angle. All patterns were obtained at 28 ^{o}C sample temperature but with different hydration level.

These images have a number of bright spots and more smeared diffuse features. The interlayer spots can be easily distinguished (specular scattering) since these are the brightest. The other spots and diffraction features are from the peptide structure. The major elements of that structure can be resolved based on the various clues available. It looks like there are two characteristic d-spacings throughout; one from the inter-layer spacing and one from the inter-peptide nearest neighbor (first coordination shell) d-spacing. This field of research has barely started (Yang et al, 1998; Yang et al, 1999).
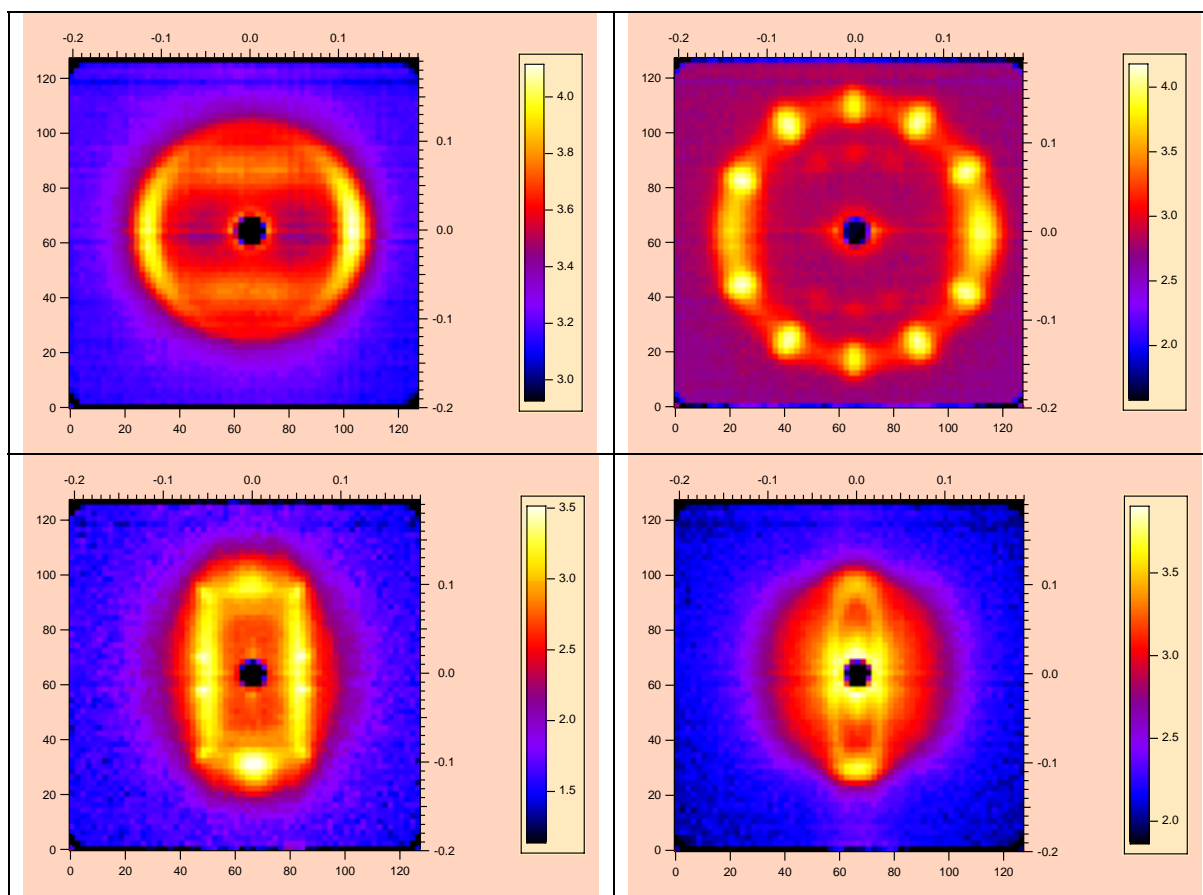
Figure 10: More patterns obtained from peptides embedded into membranes and oriented between quartz slides. The main features are understood. These structures, however, have not all been resolved yet.

Once the observed structures have been resolved in detail, one could think of using partially deuterated blocks within the peptides to nail down these structures in more detail. Nowadays, using deuterated amino acid sequences to synthesize specific peptides is possible.

REFERENCES

T. Slawecki, C. Glinka and B. Hammouda, "Shear-Induced Micellar Crystal Structures in an Aqueous Triblock Copolymer Solution", Phys Rev E 58, R4084-4086 (1998)

J Bergenholtz and N.J Wagner, "Formation of AOT/Brine Multilamellar Vesivles", Langmuir 12, 3122-3126 (1996)

L. Yang, T.A. Harroun, W.T. Heller, T.M. Weiss and H.W. Huang, "Neutron Off-Plane Scattering of Aligned Membranes; Method of Measurement", Biophysical Journal 75, 641-645 (1998).

L. Yang, T.M. Weiss, T.A. Harroun, W.T. Heller, and H.W. Huang, "Supramolecular Structures of Peptide Asemblies in Membranes by Neutron Off-Specular Scattering: Method of Analysis", Biophysical Journal <u>77</u>, 2648-2656 (1999).

J.W. Lynn, W-H Li, Q. Li, H.C. Ku, H.D. Yang and R.N. Shelton, "Magnetic Fluctuations and Two-Dimensional Ordering in ErBa2Cu3O7", Phys. Rev. B <u>36</u>, 2374-2377 (1987)

J.W. Lynn, T.W. Clinton, W.H. Li, R.W. Erwin, J.Z. Liu, K. Vandervoort, R.N. Shelton and P. Klavins, "2D and 3D Magnetic Ordering of Er in ErBa$_2$Cu$_3$O$_7$", Phys. Rev. Lett. <u>63</u>, 2606-2609 (1989)

E. Mendes, R. Oeser, C. Hayes, F. Boue, J. Bastide, "SANS Study of Swollen Elongated Gels", Macromolecules <u>29</u>, 5574-5584 (1996)

R.J. Butera, M.S. Wolfe, J. Bender and N.J. Wagner, "Formation of a Highly Ordered Colloidal Microstructure upon Flow Cessation for High Shear Rates", Phys. Rev. Lett. <u>77</u>, 2117-2120 (1996)

J. Adolphs, M.J. Setzer and P. Heine, "Changes in Pore Structure and Mercury Contact Angle of Hardened Cement Paste Depending on Relative Humidity", Materials and Structures <u>35</u>, 477-486 (2002).

QUESTIONS

1. When is the "butterfly" pattern obtained?
2. A diffraction pattern containing six-fold symmetry points to what possible structure?
3. What is the difference between "single crystal" diffraction and "powder" diffraction?
4. Fiber diffraction is characterized by what type of pattern?

ANSWERS

1. The butterfly pattern is obtained when the direction of orientation of the iso-intensity contour plots is the same as the orientation of the anisotropy in the sample.
2. The cubic and the hexagonal structures are characterized by six-fold diffraction patterns.
3. Single crystal diffraction is characterized by spots while powder diffraction is characterized by diffraction rings.
4. Fiber diffraction is characterized by spots aligned along one direction.

Chapter 62 - **BRIEF HISTORY AND FUTURE PROSPECT**

Over the past seventy years, we have come from the discovery of the neutron to the present stage of neutron sources, neutron scattering and small-angle neutron scattering (SANS) programs. Great progress has been made in the use of neutrons as a probe of nanoscale structures in a wide variety of research areas. A brief history timeline of major events leading to the present state is presented. Then a few kind comments about future prospects are offered.

1. BRIEF HISTORY TIMELINE

-- 1932: Discovery of the neutron by Chadwick.
-- 1942: Fist controlled nuclear reaction by Fermi's team at the University of Chicago stadium (called Chicago Pile 1 or CP1). Other reactors were constructed at US National Labs (CP2 to CP5) over the next ten years.
-- 1945: Sadly, first detonation then use of a nuclear weapon.
-- 1953: Launch of the "Atoms for Peace" program by President Eisenhower.
-- 1955: Construction of the first university-based nuclear research reactor at Penn State University.
-- 1950s: First neutron scattering experiments at Oak Ridge National Lab.
-- 1960s: First power-producing nuclear reactors.
-- 1972: First SANS instrument built at the ILL (Grenoble, France) using a cold neutron source.
-- 1975: First spallation source demonstrated at the Argonne National Lab.
-- 1980-1982: First SANS instruments built at the Oak Ridge National Lab, the National Institute of Standards and Technology and the University of Missouri. These instruments used thermal neutrons.
-- 1985: First operating spallation source in the US at the Intense Pulsed Neutron Source at Argonne National Lab.
-- 1985: First horizontal cold source (inside a beam tube) in the US at the Brookhaven National Lab.
-- 1998: First cold source at a spallation source in the US at the IPNS.
-- 1990: First optimized cold neutron source (in the reflector region) in the US at NIST.
-- 1994: Nobel Prize to Brockhouse and Shull for their pioneering work on neutron scattering.
-- 2000's: Major upgrades in most neutron scattering facilities.

2. SANS USER STATISTICS

Following are some user statistics based on the number of SANS beamtime proposals submitted to the NCNR for each research category and for three proposal rounds.

Proposal Rounds	10	15	20
Year	2000	2003	2006
	------	------	------

Polymers	18	15	12
Complex Fluids, Chemistry	4	10	13
Biology	5	8	12
Materials Science	19	14	16
Condensed Matter Physics, Magnetism, Physics	14	8	4
Total number of beamtime proposals:	60	55	57
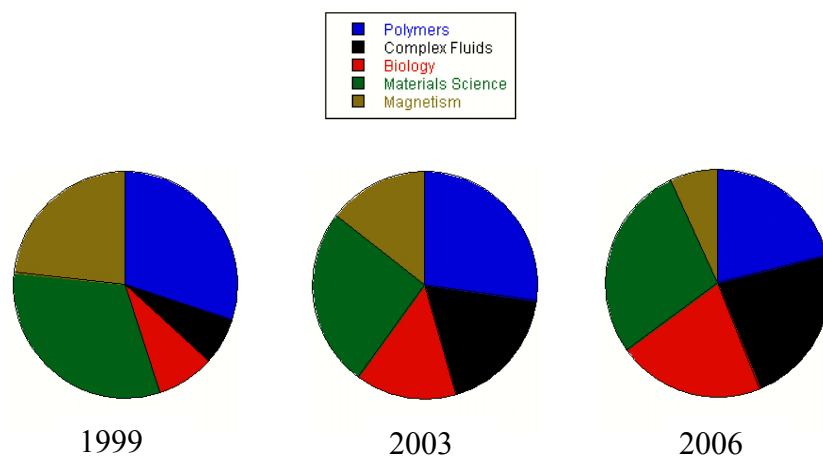
Figure 1: SANS user statistics at the NIST Center for Neutron Research for the years 1999, 2003 and 2006.

These are the total numbers of proposals that were allocated beamtime for three separate proposal rounds. Each proposal rounds covers a period of 7 months. This covers the full-time use of one 30 m SANS instrument. This amounts to about 250 days per year. The numbers of submitted proposals were 2 to 3 times higher. Each accepted proposal gets usually between 2 and 3 days of beamtime.

3. SANS PUBLICATIONS

The NIST CNR has two 30 m SANS instruments in operation: one on the outside users program (through the proposal system) and one on the internal users program (through the beam time request system). During the past six years (2001 to 2007), a total of 522 papers were published resulting from the use of the NCNR SANS instruments. This is an average of 70 to 80 SANS publications per year. Moreover, over the same period of six years, about 60 PhD theses have been successfully defended by students that used the SANS technique. These are from various colleges mostly in the US. Decidedly, the SANS program is highly productive.

Year	2001	2003	2006
	------	------	------
Polymers	38	28	16
Complex Fluids, Chemistry	14	28	25
Biology	3	6	9

Materials Science	12	12	27
Condensed Matter Physics, Magnetism, Physics	2	2	4
Total number of SANS publications:	69	76	81
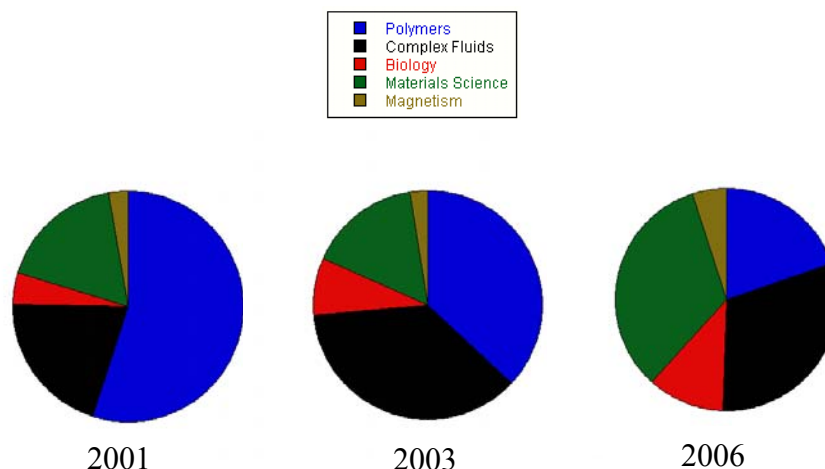
Figure 2: SANS publications resulting from the use of the NIST Center for Neutron Research for the years 2001, 2003 and 2006.

4. FUTURE PROSPECT

Future prospect for neutron scattering and its main SANS engine looks bright. In the US, the Spallation Neutron Source (Oak Ridge National Lab) went into operation. The NIST Center for Neutron Research is undergoing a major expansion including a second guide hall. Major upgrades are planned at most neutron scattering facilities in the world. In Europe, the ILL's second guide hall has been fully equipped and the construction of the ISIS second (low-frequency) target is almost complete. In Asia, most neutron sources have undergone (or are undergoing) upgrades to acquire cold sources and guide halls.

SANS research has traditionally been strong in the areas of polymer science and complex fluids. These two research areas have constituted the lion-share in the user community. Use of SANS in biology has been increasing steadily moving from 5 % of the beamtime proposals to 25 % in just 15 years at the NIST Center for Neutron Research. Biology research may become the primary focus of SANS research. Recent advances in the synthesis of peptide sequences and in the availability of deuterated amino acids are making a difference. Biologist are discovering the benefits of SANS.

5. THE NCNR EXPANSION

The NIST Center for Neutron Research is undergoing a major upgrade that includes the construction of a new guide hall. Both guide halls will be looking at the same optimized liquid hydrogen cold source. An assortment of new instruments will be constructed. These include a VSANS instrument that will cover the traditional SANS scattering range as well. Moreover, some instruments will be moved from the old guide hall to the new guide hall.
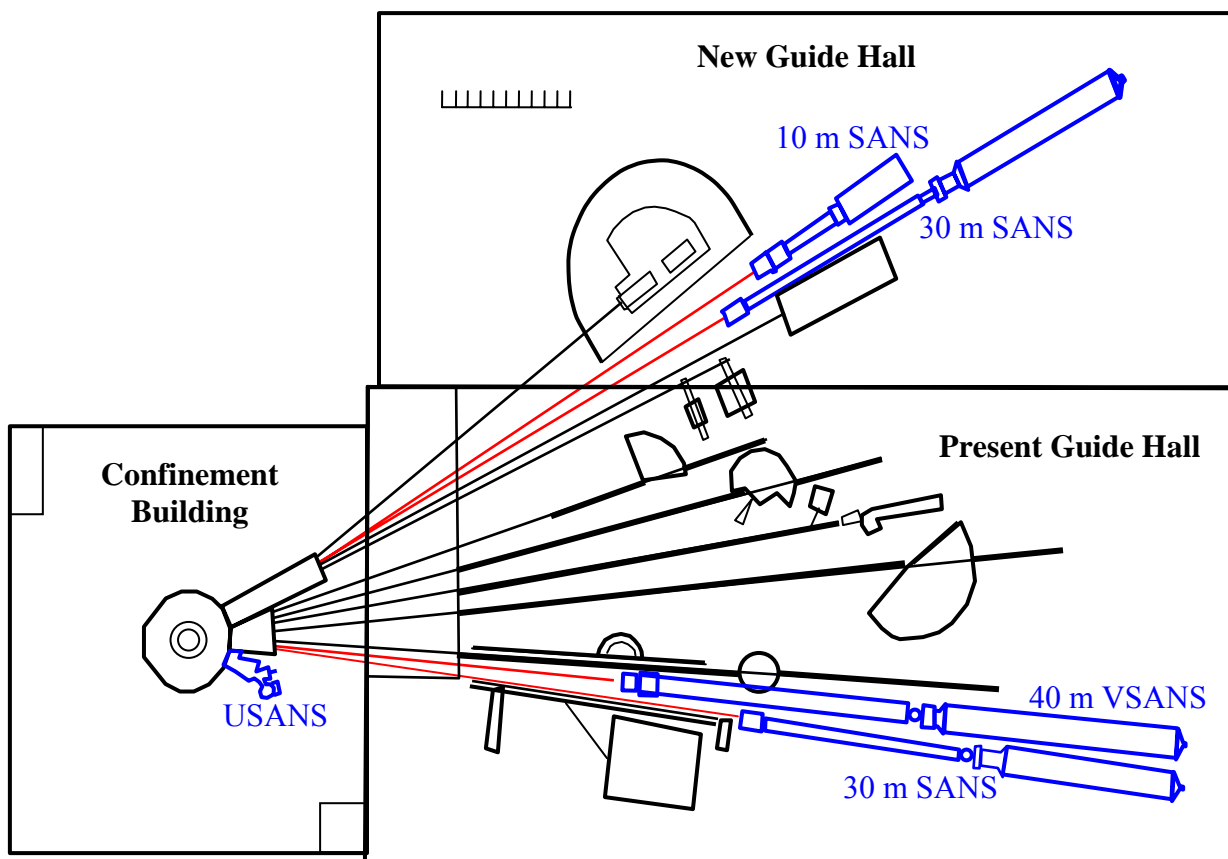
Figure 3: Schematics of the old and the new guide halls at the NIST Center for Neutron Research. The old guide hall is almost 20 years old and the new guide hall is under construction. Ultimately, there will be two 30 m SANS instruments, a 10 m SANS instrument, a 40 m VSANS instrument and a thermal neutrons Bonse-Hart USANS instrument.

This expansion will keep nanoscale research alive and well, and growing for the next two decades.

6. FINAL WORDS

The SANS technique has gained maturity in many research areas. To quote my dear mentor Prof. Walter Stockmayer (one of the founders of polymer science) who said: "Four great

636

developments have made polymer science what it is today; these are the (1) advent of lasers and optical methods that followed, (2) Small-Angle Neutron Scattering, (3) the development of NMR, and (4) advances in computer speed for simulation purposes". The SANS technique has managed to grow steadily over the past twenty-five years from a "follow the trends" technique to a sophisticated characterization method in morphology, thermodynamics, and rheology. Advances in the use of judicious sample environments (shear cells, magnets, pressure cells, temperature quench apparatuses, etc) have instilled new momentum.

Other characterization methods are often brought to bare and complement the SANS technique. Some of these include Transmission Electron Microscopy (TEM), Wide-Angle X-Ray Scattering (WAXS), Ultra-Violet (UV) Absorption Spectroscopy, Dynamic light Scattering (DLS), Differential Scanning Calorimetry (DSC), densitometry, etc.

The SANS technique has been a driving force justifying upgrades of neutron sources and enhancements of neutron scattering facilities. Its use has been ever growing. It has managed to generate new momentum through novel technological advances as well as better modeling capabilities. The need for higher fluxes and better resolution has kept us all in business for a good many years. SANS will undoubtedly outlive many careers.

7. DISCLAIMER

Naming products or brand-names does not imply endorsement by the National Institute of Standards and Technology. Contents of the literature review chapters is not guaranteed to be correct or of special significance by this author.

Part N – **APPENDICES**

Appendix 1. - Useful Mathematical Expressions
      1. Progressions
      2. Useful Identity
      3. Integration Trick
      4. The Convolution Integral
      5. Integration by Parts
      6. Bessel Functions
      7. The Gamma Function
      8. Some Other Integral Functions
      9. Laplace Transform of Trigonometric Functions
      10. Fourier Transform Integrals
      11. Dirac Delta Function
      12. The Gaussian Distribution
      13. Property of the Laplacian Operator
      14. Basic Matrix Manipulations
      15. Matrix Diagonalization
      References
      Questions
      Answers

Appendix 2. – Elements of Quantum Mechanics
      1. The Schrodinger Equation
      2. The Fermi Golden Rule
      3. The Bra-Ket Notation
      4. The Heisenberg Time Evolution Operator
      5. The Pauli Spin Matrices
      References
      Questions
      Answers

Appendix 1 - **USEFUL MATHEMATICAL EXPRESSIONS**

This appendix summarizes some mathematical expressions that have been used in this tutorial.

1. PROGRESSIONS

Arithmetic progression:

$$\sum_{k=0}^{N-1}(a+kr) = \frac{N}{2}\left[2a+(N-1)r\right]. \tag{1}$$

First three terms:

$$\sum_{k=1}^{N}k = \frac{N(N+1)}{2} \tag{2}$$

$$\sum_{k=1}^{N}k^2 = \frac{N(N+1)(2N+1)}{6} \tag{3}$$

$$\sum_{k=1}^{N}k^3 = \left[\frac{N(N+1)}{2}\right]^2. \tag{4}$$

Geometric progression:

$$\sum_{k=1}^{N}aq^{k-1} = \frac{a(q^N-1)}{q-1}; \; q \neq 1 \tag{5}$$

Arithmetico-geometric progression:

$$\sum_{k=1}^{N}(a+kr)q^k = \frac{a-[a+(N-1)r]q^N}{1-q} + \frac{rq(1-q^{N-1})}{(1-q)^2}; \; q \neq 1 \tag{6}$$

2. USEFUL IDENTITY

Consider the following identity:

$$\sum_{i,j=1}^{n}F(|i-j|) = n+2\sum_{k=1}^{n}(n-k)F(k). \tag{7}$$

In order to show this relation, consider an (i,j) plane for the summation variables where the limits are 1 and n for both axes.
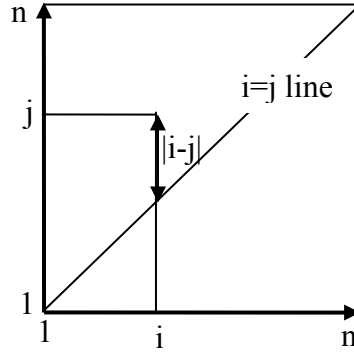
Figure 1: The (i,j) summation space.

The summation space consists of a line $i = j$ dividing the space into two equal square triangles. In order to scan one of these triangles entirely, one can choose another summation variable $k = |i-j|$. The $i = j$ line gives the first term n and the double sum is for the two triangles.

3. INTEGRATION TRICK

Consider the following integral trick that consists in switching the integration and differentiation steps:

$$2\int_0^1 dx(1-x)\exp[-Ax] = 2\int_0^1 dx\left(1+\frac{\partial}{\partial A}\right)\exp[-Ax] \qquad (8)$$

$$= 2\left(1+\frac{\partial}{\partial A}\right)\int_0^1 dx\,\exp[-Ax] = \left(1+\frac{\partial}{\partial A}\right)\left[\frac{\exp[-Ax]}{-A}\right]_0^1 =$$

$$= 2\left(1+\frac{\partial}{\partial A}\right)\left[\frac{\exp[-A]-1}{-A}\right] = 2\left[\frac{\exp[-A]-1}{-A}-\frac{\exp[-A]}{-A}+\frac{\exp[-A]-1}{A^2}\right]$$

$$= 2\left[\frac{\exp[-A]-1+A}{A^2}\right].$$

This property holds as long as the variable A does not depend on x. Note that this is a way to derive to so-called Debye function that represents the form factor for Gaussian coils with $A = Q^2 R_g^2$.

4. THE CONVOLUTION INTEGRAL

The convolution integral is used to smear a model function using the instrumental resolution. The following property has been used.

$$\frac{d\Sigma(Q_x)}{d\Omega} = \int_{-\infty}^{+\infty} dQ'_x \, P_{1D}(Q'_x) \frac{d\Sigma(|Q_x - Q'_x|)}{d\Omega} = \int_{-\infty}^{+\infty} dQ'_x P_{1D}(|Q_x - Q'_x|) \frac{d\Sigma(Q'_x)}{d\Omega} . \quad (9)$$

This can be shown through a variable change.

5. INTEGRATION BY PARTS

Integration by parts helps in the calculation of many integrals:

$$\int_a^b U dV = [UV]_a^b - \int_a^b V dU . \quad (10)$$

Integration by parts has been used to perform the following integral with $U = R^{z+N}$ and $dV = dR \exp[-(z+1)R/R_{av}]$:

$$\int_0^\infty dR R^{z+N} \exp[-(z+1)R/R_{av}] =$$

$$[R_{z+N} R_{av} \exp[-(z+1)R/R_{av}]]_0^\infty + \frac{(z+N)}{(z+1)} R_{av} \int_0^\infty dR R^{z+N} \exp[-(z+1)R/R_{av}] .$$

$$(11)$$

The first term is identically equal to zero.

6. BESSEL FUNCTIONS

There are two kinds of Bessel functions. These are the cylindrical Bessel functions $J_0(z)$, $J_1(z)$, etc and the spherical Bessel functions $j_0(z)$, $j_1(z)$, etc. The two are related through the following relashionship:

$$j_n(z) = \sqrt{\frac{\pi}{2z}} J_{n+1/2}(z) . \quad (12)$$

The cylindrical Bessel functions are of integer order and the spherical ones are of fractional order.

One definition of the cylindrical Bessel function is included here:

$$J_n(z) = \frac{i^{-n}}{\pi} \int_0^\pi d\phi \cos(n\phi) \exp[iz\cos(\phi)]. \qquad (13)$$

The zeroth order and the first order functions are simply:

$$J_0(z) = \frac{1}{\pi} \int_0^\pi d\phi \exp[iz\cos(\phi)] \qquad (14)$$

$$J_1(z) = \frac{1}{i\pi} \int_0^\pi d\phi \cos(\phi) \exp[iz\cos(\phi)].$$

These two functions are related by the following relation:

$$\int_0^1 dz z J_0(az) = \frac{1}{a} J_1(a) \qquad (15)$$

which in its general form reads:

$$\int_0^1 dz z^{v+1} J_v(az) = \frac{1}{a} J_{v+1}(a) \text{ with } \text{Re} v > -1. \qquad (16)$$

The spherical Bessel functions obey the following recursive relation:

$$j_n(z) = z^n \left(-\frac{1}{z}\frac{d}{dz} \right)^n j_0(z). \qquad (17)$$

The first three functions are:

$$j_0(z) = \frac{\sin(z)}{z} \qquad (18)$$

$$j_1(z) = \frac{\sin(z)}{z^2} - \frac{\cos(z)}{z}$$

$$j_2(z) = \left(\frac{3}{z^3} - \frac{1}{z} \right) \sin(z) - \frac{3}{z^2}\cos(z).$$

The following limit is known:

$$\text{Lim}\left(\frac{3j_1(z)}{z} \right) = 1 \text{ for } z \to 0. \qquad (19)$$

These are all Bessel function relations used in this tutorial.

7. THE GAMMA FUNCTION

The gamma function is defined as:

$$\Gamma(z) = \int_0^\infty dt \, \exp[-t] t^{z-1} \quad \text{for Re(z)>0.} \tag{20}$$

A few properties of the Gamma function follow:

$$\Gamma(z+1) = z\Gamma(z) = z! = z(z-1)! \tag{21}$$

$$\Gamma\left(\frac{1}{2}\right) = \sqrt{\pi}$$

$$\Gamma(1) = 1$$

z! refers to factorial z. The incomplete Gamma function is defined as:

$$\gamma(z,U) = \int_0^u dt \, \exp(-t) \, t^{z-1}. \tag{22}$$

Note that $\Gamma(z) = \gamma(z,\infty)$.

8. SOME OTHER INTEGRAL FUNCTIONS

Some other integral functions are described here. These have been used in this tutorial.

The Sine integral function Si(x) is defined as:

$$Si(x) = \int_0^x du \, \frac{\sin(u)}{u}. \tag{23}$$

The Dawson integral function D(U) is defined as:

$$D(U) = \exp(-U^2) \int_0^U dt \, \exp(t^2). \tag{24}$$

D(U) is sometime called F(U) instead.

Normalization of the Gaussian (also called Error) function:

$$\int_0^\infty dt \, \exp(-t^2) = \frac{\sqrt{\pi}}{2}. \tag{25}$$

Normalization of the Lorentzian function:

$$\int_0^\infty dt \, \frac{1}{1+t^2} = \frac{\pi}{2} \tag{26}$$

9. LAPLACE TRANSFORM OF TRIGONOMETRIC FUNCTIONS

Consider the following integrals that were used to calculate the polydispersity averages for dilute solution of spheres.

$$\int_0^\infty dX \, \exp(-AX)\sin^2(BX) = \frac{2B^2}{A(A^2+4B^2)} \tag{27}$$

$$\int_0^\infty dX \, \exp(-AX)\cos^2(BX) = \frac{A^2+2B^2}{A(A^2+4B^2)}$$

$$\int_0^\infty dX \, \exp(-AX)\sin(BX)\cos(BX) = \frac{B}{A^2+4B^2}$$

10. FOURIER TRANSFORM INTEGRALS

The Fourier transform integral is similar to the Laplace transform integral except that the integration limits are from $-\infty$ to $+\infty$.

The following integral is used to calculate the form factor for a uniform density sphere of radius R:

$$P(QR) = \frac{3}{4\pi R^3} \int_0^\infty dr \, 4\pi r^2 \, \frac{\sin(Qr)}{Qr} \left[1 - \frac{3}{4}\left(\frac{r}{R}\right) + \frac{1}{16}\left(\frac{r}{R}\right)^3 \right] \tag{28}$$

$$= \left[\frac{3j_1(QR)}{QR} \right]^3 = \left[\frac{3}{QR}\left(\frac{\sin(QR)}{(QR)^2} - \frac{\cos(QR)}{QR} \right) \right]^3.$$

11. DIRAC DELTA FUNCTION

Some properties of the Dirac Delta function follow:

$$\int_{-\infty}^{\infty} dx' f(x') \delta(x - x') = f(x) \qquad (29)$$

$$\int d\vec{r}' f(\vec{r}') \delta(\vec{r} - \vec{r}') = f(\vec{r}).$$

Integral representation of the Delta function:

$$\delta(\omega) = \frac{1}{2\pi} \int_{-\infty}^{\infty} dt \exp(-i\omega t) \qquad (30)$$

$$\delta(\vec{Q}) = \frac{1}{(2\pi)^3} \int d\vec{r} \exp(-i\vec{Q}.\vec{r}).$$

This last equation shows that the Dirac delta function is the 3D Fourier transform of unity.

12. THE GAUSSIAN DISTRIBUTION

The Gaussian distribution is a peaked function of the form:

$$P(\lambda) = \frac{1}{\sqrt{2\pi}\sigma} \exp\left(-\frac{(\lambda - \overline{\lambda})^2}{2\sigma^2}\right). \qquad (31)$$

Here $\overline{\lambda}$ is the average value and σ is the standard deviation of the distribution. The following moments can be calculated through integrations:

$$<\lambda> = \overline{\lambda} \qquad (32)$$

$$<\lambda^2> = \overline{\lambda}^2\left(1 + \frac{\sigma^2}{\overline{\lambda}^2}\right)$$

$$<\lambda^4> = \overline{\lambda}^2\left(1 + 6\frac{\sigma^2}{\overline{\lambda}^2} + 3\frac{\sigma^4}{\overline{\lambda}^4}\right).$$

In the calculation of the SANS resolution function, the wavelength distribution outputted by the velocity selector can be assumed to be triangular or Gaussian.

13. PROPERTY OF THE LAPLACIAN OPERATOR

In order to solve the Schrodinger equation for a square well potential, the following property of the Laplacian operator was used:

$$\Delta\left(\frac{1}{r}\right) = \nabla^2\left(\frac{1}{r}\right) = \delta(r) \tag{33}$$

14. BASIC MATRIX MANIPULATIONS

Consider a [3x3] square matrix $\underline{\underline{S}}$ with elements:

$$\underline{\underline{S}} = \begin{bmatrix} S_{11} & S_{12} & S_{13} \\ S_{21} & S_{22} & S_{23} \\ S_{31} & S_{32} & S_{33} \end{bmatrix}. \tag{34}$$

The transpose matrix is defined as:

$$\underline{\underline{S}}^T = \begin{bmatrix} S_{11} & S_{21} & S_{31} \\ S_{12} & S_{22} & S_{32} \\ S_{13} & S_{23} & S_{33} \end{bmatrix}. \tag{35}$$

Matrix $\underline{\underline{S}}$ can be inverted if $\text{Det}[\underline{\underline{S}}] \neq 0$. $\text{Det}[\underline{\underline{S}}]$ stands for the determinant of matrix $\underline{\underline{S}}$. It is also called $\left|\underline{\underline{S}}\right|$ or Δ.

$$\text{Det}[\underline{\underline{S}}] = \left|\underline{\underline{S}}\right| = \Delta = S_{11}\begin{vmatrix} S_{22} & S_{23} \\ S_{32} & S_{33} \end{vmatrix} - S_{12}\begin{vmatrix} S_{21} & S_{23} \\ S_{31} & S_{33} \end{vmatrix} + S_{13}\begin{vmatrix} S_{21} & S_{22} \\ S_{31} & S_{32} \end{vmatrix} \tag{36}$$

$$\Delta = S_{11}(S_{22}S_{33} - S_{23}S_{32}) - S_{12}(S_{21}S_{33} - S_{23}S_{31}) + S_{13}(S_{21}S_{32} - S_{22}S_{31}).$$

The inverse of matrix $\underline{\underline{S}}$ is given by:

$$\underline{\underline{S}}^{-1} = \frac{1}{\Delta}\begin{vmatrix} \Delta_{11} & -\Delta_{21} & \Delta_{31} \\ -\Delta_{12} & \Delta_{22} & -\Delta_{32} \\ \Delta_{13} & -\Delta_{23} & \Delta_{33} \end{vmatrix} \tag{37}$$

The various co-factors are defined as:

$$\Delta_{11} = \begin{vmatrix} S_{22} & S_{23} \\ S_{32} & S_{33} \end{vmatrix} = S_{22}S_{33} - S_{23}S_{32}, \text{ etc...} \tag{38}$$

The following properties apply to matrix inversion:

$$\left(\underline{\underline{A}} + \underline{\underline{B}}\right)^{-1} \neq \underline{\underline{A}}^{-1} + \underline{\underline{B}}^{-1} \tag{39}$$

$$\left(\underline{\underline{A}}.\underline{\underline{B}}\right)^{-1} = \underline{\underline{B}}^{-1}.\underline{\underline{A}}^{-1}$$

$$\left(\underline{\underline{A}} + \underline{\underline{B}}.\underline{\underline{C}}\right)^{-1} = \underline{\underline{C}}^{-1}\left(\underline{\underline{A}}.\underline{\underline{C}}^{-1} + \underline{\underline{B}}\right)^{-1}.$$

The bare minimum knowledge of Algebra and Calculus needed in this tutorial has been included here.

15. MATRIX DIAGONALIZATION

Consider a symmetric matrix $\underline{U}$ that can be inverted (i.e., for which $\mathrm{Det}\lfloor \underline{U} \rfloor \neq 0$). There is a unique transformation whereby $\underline{U}$ can be written as $\underline{U} = \underline{\underline{A}}\underline{\Lambda}\underline{\underline{A}}^{-1}$ in terms of a diagonal matrix $\underline{\Lambda}$. The eigenvalue matrix $\underline{\underline{A}}$ obeys the relationship $\underline{\underline{U}}\underline{\underline{A}} = \underline{\underline{A}}\underline{\underline{\Lambda}}$. This diagonalization of matrix $\underline{U}$ helps in the calculation of $\underline{U}^N$ which becomes $\underline{\underline{U}}^N = \underline{\underline{A}}\underline{\underline{\Lambda}}^N\underline{\underline{A}}^{-1}$. The diagonal elements of matrix $\underline{\Lambda}$ are the eigenvalues λ_1, λ_2, etc. Matrix $\underline{\underline{A}}$ is composed of two unit eigenvectors $\vec{\alpha}$ and $\vec{\beta}$ forming an orthogonal basis $\underline{\underline{A}} = [\vec{\alpha}, \vec{\beta}]$. These obey the following relations $\underline{\underline{U}}\vec{\alpha} = \lambda_1\vec{\alpha}$ and $\underline{\underline{U}}\vec{\beta} = \lambda_2\vec{\beta}$.

For example, consider the following matrix:

$$\underline{\underline{U}} = \begin{bmatrix} 1 & s\sigma \\ 1 & s \end{bmatrix}. \tag{40}$$

The two eigenvalues are:

$$\lambda_1 = \frac{(1+s) + \sqrt{(1-s)^2 + 4\sigma s}}{2} \tag{41}$$

$$\lambda_2 = \frac{(1+s) - \sqrt{(1-s)^2 + 4\sigma s}}{2}.$$

This formalism was used in the model describing the helix-to-coil transition in DNA.

REFERENCES

M. Abromowitz and I.A. Stegun, "Handbook of Matehmatical Functions", Dover Publications (New York, 1972)

I.S. Gradsteyn and I.M. Ryzhik, "Table of Integrals, Series, and Products", Academic Press (1980).

QUESTIONS

1. Give an example of where the useful identity $\sum_{i,j=1}^{n} F(|i-j|) = n + 2\sum_{k=1}^{n}(n-k)F(k)$ has been used.

2. Where was a convolution integral needed?

3. Which one is the "cylindrical" Bessel function, j_n or J_n? How are the j_n and J_n related?

4. Calculate $\Gamma(3)$? How about $\Gamma(n)$?

5. Where was the Sine integral function needed?

6. Where was the Dawson integral needed?

7. What is the main difference between the Laplace transform and the Fourier transform integrals?

8. How to invert a matrix product; i.e., how to calculate $\left(\underline{\underline{A}}.\underline{\underline{B}}\right)^{-1}$?

ANSWERS

1. The useful identity $\sum_{i,j=1}^{n} F(|i-j|) = n + 2\sum_{k=1}^{n}(n-k)F(k)$ was used, for instance, to calculate the form factor for a Gaussian coil (Debye function).

2. A convolution integral was needed in order to perform the smearing of a scattering model.

3. J_n is the cylindrical Bessel function, whereas j_n is the spherical one. These are related as follows $j_n(z) = \sqrt{\dfrac{\pi}{2z}} J_{n+1/2}(z)$.

4. $\Gamma(3) = \Gamma(2+1) = 2\Gamma(2) = 2\Gamma(1+1) = 2*1\Gamma(1) = 2$. Similarly, $\Gamma(n) = (n-1)(n-2)\ldots 1 = (n-1)!$.

5. The Sine integral function was needed to calculate the form factor for an infinitely thin rod.

6. The Dawson integral function was needed to calculate the form factor for a Gaussian ring.

7. The limits of the Laplace transform integral are from 0 to $+\infty$ whereas the limit of the Fourier transform integral are from $-\infty$ to $+\infty$.

8. A matrix product is inverted as follows: $\left(\underline{\underline{A}}.\underline{\underline{B}}\right)^{-1} = \underline{\underline{B}}^{-1}.\underline{\underline{A}}^{-1}$.

Appendix 2 - **ELEMENTS OF QUANTUM MECHANICS**

Quantum Mechanics tools are well suited to describe neutron scattering theory. Many elements of Quantum Mechanics have been used in this tutorial and will be summarized here.

1. THE SCHRODINGER EQUATION

The Schrodinger equation is expressed as follows:

$$H\psi = E\psi .$$

(1)

The scattering system Hamiltonian H contains a kinetic energy contribution and an interaction potential contribution:

$$H = -\frac{\hbar^2}{2m}\nabla^2 + V .$$

(2)

The momentum operator is defined as:

$$\vec{p} = -i\hbar\vec{\nabla} .$$

(3)

The eigenfunction Ψ and eigenvalue E are solutions to the integral Schrodinger equation.

The neutron current density (neutrons/cm^2.s) is given by:

$$\vec{J} = \frac{i\hbar}{2m}\left(\Psi\vec{\nabla}\Psi^* - \Psi^*\vec{\nabla}\Psi\right).$$

(4)

Where ψ^* is the complex conjugate of ψ .

The scattering amplitude is given by:

$$f(\theta) = \left(\frac{m}{2\pi\hbar^2}\right)\int d\vec{r}' \exp(-i\vec{Q}.\vec{r}')V(\vec{r}) .$$

(5)

The scattering cross section is given by:

$$\frac{d\sigma_s(\theta)}{d\Omega} = |f(\theta)|^2 .$$

(6)

2. THE FERMI GOLDEN RULE

To within the first order perturbation theory, the elastic scattering cross section is given by:

$$\frac{d\sigma_s(\theta)}{d\Omega} = \left| < s \left| \left(\frac{m}{2\pi\hbar^2} \right) \int dr' \exp(-i\vec{Q}.\vec{r}') V(\vec{r}') \right| i > \right|^2 . \qquad (7)$$

The quasielastic/inelastic double differential scattering cross section is more general:

$$\frac{d^2\sigma}{dEd\Omega} = \frac{k_s}{k_i} \left| < s \left| \left(\frac{m}{2\pi\hbar^2} \right) V \right| i > \right|^2 \delta(E - E_s + E_i) . \qquad (8)$$

Here |s> and |i> are the final and initial states.

3. THE BRA-KET NOTATION

The <bra|ket> is a useful and more compact notation. Consider the following definitions:

$$< \vec{r} | \vec{k}_i >= \exp(i\vec{k}_i.\vec{r}) \qquad (9)$$
$$< \vec{r} | \Psi >= \Psi(\vec{r})$$
$$< r | V = V(r)$$
$$< \vec{r} | G | \vec{r}') = G(\vec{r} - \vec{r}')$$
$$< \vec{r} | \vec{r}') = \delta(\vec{r} - \vec{r}') .$$

Define the following closure relations:

$$\int | \vec{r}'> d\vec{r}' < \vec{r}'|= 1 \qquad (10)$$
$$\int | \vec{k} > d\vec{k} < \vec{k} |= 1 .$$

The scattering amplitude is expressed as:

$$f(\theta) = \left(\frac{m}{2\pi\hbar^2} \right) < \vec{k}_s | V | \vec{k}_i > \qquad (11)$$

The scattering cross section is therefore given in terms of the transition probability $< s | V | i >$ as:

$$\frac{d\sigma_s(\theta)}{d\Omega} = \frac{k_s}{k_i} \left| < s \left| \left(\frac{m}{2\pi\hbar^2} \right) V \right| i > \right|^2 \delta(E - E_s + E_i) . \qquad (12)$$

This result applies to elastic as well as quasielastic/inelastic scattering. It can also describe magnetic scattering provided that the spin coupling term is included in the interaction potential.

4. THE HEISENBERG TIME EVOLUTION OPERATOR

The Heisenberg equation for a time-dependent operator $\vec{r}(t)$ is stated as follows:

$$i\hbar \frac{\partial \vec{r}(t)}{\partial t} = [H, \vec{r}(t)]. \tag{13}$$

Here $[H, \vec{r}(t)]$ is the commentator of the Hamiltonian H and the position operator $\vec{r}(t)$ and is defined as:

$$[H, \vec{r}(t)] = H.\vec{r}(t) - \vec{r}(t).H. \tag{14}$$

The Heisenberg time evolution operator helps represent the time dependence of an operator as follows:

$$\vec{r}(t) = \exp\left(\frac{-iHt}{\hbar}\right) \vec{r}(0) \exp\left(\frac{iHt}{\hbar}\right). \tag{15}$$

Note that two operators A and B are said to "commute" when: $[A, B] = A.B - B.A = 0$. Most Quantum Mechanics operators do not commute.

5. THE PAULI SPIN MATRICES

The Pauli spin matrices for the neutron spin $\vec{s} = \frac{\vec{1}}{2}$ are defined as $\vec{\sigma} = 2\vec{s}$ with:

$$\sigma_x = \begin{pmatrix} 0 & 1 \\ 1 & 0 \end{pmatrix} \quad \sigma_y = \begin{pmatrix} 0 & -i \\ i & 0 \end{pmatrix} \quad \sigma_z = \begin{pmatrix} 1 & 0 \\ 0 & -1 \end{pmatrix}. \tag{16}$$

Some of their properties follow:

$$\sigma_i = \sigma_i^+, \ Det(\sigma_i) = -1, \ \sigma_i^2 = 1 \text{ for any } i = x,y,z \tag{17}$$

$$[\sigma_y, \sigma_z] = 2i\sigma_x, \ [\sigma_z, \sigma_x] = 2i\sigma_y, \ [\sigma_x, \sigma_y] = 2i\sigma_z$$

$$\sigma_x \sigma_y \sigma_z = i, \ \sigma_x \sigma_y = i\sigma_z.$$

The spin up |α> and spin down |β> vector states are defined as:

$$|\alpha> = \begin{pmatrix} 1 \\ 0 \end{pmatrix} \quad \text{and} \quad |\beta> = \begin{pmatrix} 0 \\ 1 \end{pmatrix}. \tag{18}$$

These form an orthogonal basis such that $<\alpha|\alpha> = <\beta|\beta> = 1$ and $<\alpha|\beta> = 0$.

They also obey the following relations:

$$\sigma_z|\alpha> = |\alpha> \tag{19}$$
$$\sigma_z|\beta> = -|\beta>$$
$$\sigma_x|\alpha> = |\beta>$$
$$\sigma_y|\alpha> = i|\beta>, \text{ etc.}$$

Given a nuclear spin operator $\vec{I} = (I_x, I_y, I_z)$, the following averages can be calculated:

$$<\beta|\vec{\sigma}.\vec{I}|\alpha> = (I_x + iI_y) \tag{20}$$
$$<\alpha|\vec{\sigma}.\vec{I}|\beta> = (I_x - iI_y).$$

Assuming an eigenstate $|\tau>$ for the nuclear spin operator $\vec{I}$, the following relations hold:

$$I_z|\tau> = m|\tau>$$
$$\vec{I}^2|\tau> = I(I+1)|\tau>$$

Here I is an eigenvalue and m is the "magnetic" number.

REFERENCES

L.I. Schiff, "Quantum Mechanics", McGraw Hill (1955).

QUESTIONS

1. What are the two main parts of the Hamiltonian?
2. Write down the Schrodinger equation. Define the terms.
3. Describe the Fermi golden rule. What is it used for?
4. What type of neutron scattering obeys the Fermi golden rule? Which does not.
5. What are the Pauli spin matrices used for?
6. Given a spin operator $\vec{I}$ with eigenstate $|\tau>$, where was the following eigenvalue relation $\vec{I}^2|\tau> = I(I+1)|\tau>$ used?
7. Where were the Pauli spin matrices used?

ANSWERS

1. The two main parts of a Hamiltonian are the kinetic energy and the interaction (potential) energy.

2. The Schrodinger is given by $H\psi = E\psi$ where H is the Hamiltonian, ψ is the eigenstate (wavefunction) and E is the eigenvalue (energy).

3. The Fermi golden rule is a first order perturbation theory used to solve the Schrodinger equation. It is used to calculate the scattering cross section.

4. Single scattering methods (SANS, diffraction, elastic, quasielastic/inelastic scattering) all follow the Fermi golden rule. Methods that involve multiple scattering (or refraction) such as reflectometry do not follow the Fermi golden rule.

5. The Pauli matrices $\vec{\sigma} = 2\vec{s}$ are used to represent the neutron spin $\vec{s} = \dfrac{\vec{1}}{2}$.

6. The eigenvalue relation $\vec{I}^2 \, | \tau > = I(I+1) \, | \tau >$ was used when discussing spin incoherence during the scattering of a neutron and a nucleus.

7. The Pauli spin matrices were used to derive the neutron scattering cross section with spin polarization.

LIST OF SYMBOLS AND NOTATION

The various symbols used throughout are listed here in the order they occur.

$\phi(\lambda)$ Neutron flux (units of $neutron.cm^{-2}.s^{-1}$)

$\Phi(\lambda)$ Neutron current (units of $neutron.s^{-1}$)

b   Scattering length (units of fm)

v   Specific volume (units of cm^3)

$\rho = \dfrac{b}{v}$ Scattering length density (units of $Å^{-2}$)

$\Delta\rho^2$ Contrast factor

θ Scattering angle

Q   Scattering variable (units of Å)

$d\Omega$ Solid angle

$f(\theta)$ Scattering amplitude

I   Nuclear spin

$\dfrac{d\sigma(Q)}{d\Omega}$ Microscopic differential scattering cross section

$\dfrac{d\Sigma(Q)}{d\Omega}$ Macroscopic differential scattering cross section

σ Microscopic scattering cross section $\sigma = \int d\Omega\, d\sigma(Q)/d\Omega$ (units of barn)

Σ Microscopic scattering cross section $\Sigma = \int d\Omega\, d\Sigma(Q)/d\Omega$ (units of cm^{-1})

λ Neutron wavelength

E   Neutron kinetic energy

k   Neutron wavelenumber $k = 2\pi/\lambda$

$\dfrac{\Delta\lambda}{\lambda}$ Relative neutron wavelength spread

$\sigma_Q^{\;2}$ Variance of the Q resolution

L_1 Source-to-sample distance

L_2 Sample-to-detector distance

R_1 Source aperture radius

R_2 Sample aperture radius

Δx_3 Detector cell size

Q_{min} Minimum scattering variable

f   Focal length for neutron lenses

$T(\lambda)$ Sample transmission

g   Gravity constant $g = 9.81$ m.s^{-2}

F(Q)   Scattering form factor amplitude
$P(Q) = |F(Q)|^2$ Scattering form factor

$$P(Q) = \int d\vec{r} \exp(i\vec{Q}.\vec{r})P(\vec{r})$$

$$P(\vec{r}) = \int d\vec{Q} \exp(-i\vec{Q}.\vec{r})P(\vec{Q})$$ Probability distribution function

$$g(\vec{r})-1 = VP(\vec{r})$$ Pair correlation function

$$P(Q) = \frac{1}{R}\int_0^R dr \frac{\sin(Qr)}{Qr}p(r)$$

$$p(r) = 3\left(\frac{r}{R}\right)^2 \gamma(r)$$ $\gamma(r)$ the radial pair correlation function

E(Q)   Propagation scattering factor for polymers
F(Q)   Form factor amplitude
P(Q)   Form factor
$S_I(Q)$ Inter-particle structure factor
S(Q)   Scattering factor for polymers

$$S(Q) = \frac{1}{V}\int d\vec{r} \exp(i\vec{Q}.\vec{r})[g(\vec{r})-1]$$

$$g(r)-1 = VP(\vec{r})$$

R   Spherical particle radius
D   Spherical article diameter
L   Rodlike particle length

ξ Correlation length
n(r)   Fluctuating density
$\bar{n}$ Average density $= n/V$
V_P Particle volume
v   Specific volume
V   Sample volume

N   Number of particles or macromolecules in the sample
$\overline{N}$ Number density $= N/V$
n   Number of monomers per macromolecule (degree of polymerization)
ϕ Volume fraction
a   Statistical segment length for polymers

{...}   Average over composition or polydispersity average
$\{R^n\}$ n^{th} moment of R

$<...>$ Statistical average

$j_0(x)$ Spherical Bessel function of order 0
$j_1(x)$ Spherical Bessel function of order 1
$J_1(x)$ Cylindrical Bessel function of order 1

R_g radius of gyration
$f(R)$ Polydispersity distribution

χ Flory-Huggins interaction parameter in polymer blends

$C(Q)$ Ornstein-Zernike direct correlation function
$H(Q)$ Ornstein-Zernike total correlation function

z_m Macroion electric charge
ε: Dielectric constant
κ: Debye-Huckel inverse screening length

T Temperature
k_B Boltzman constant $k_B = 1.38*10^{-23}$ J.k^{-1}
N_{av} Avogadro's number $N_{av} = 6.02*10^{23}$ mol^{-1}
$\hbar$ Planck's constant $\hbar = 1.055*10^{-34}$ J.s

Unit Conversions:

1 Å $= 10^{-10}$ m
1 fm $= 10^{-13}$ cm
1 barn $= 10^{-24}$ cm^2
1 bar $=$ 1 torr $= 14.7$ psi $= 760$ mm Hg $= 10^5$ Pa

Acronyms of Characterization Methods

UV-Vis   Ultra Violet and Visible Absorption Spectroscopy
IR   Infra-Red Spectrocopy
CD   Circular Dichroism
NMR   Nuclear Magnetic Resonance
Mass-Spec   Mass Spectroscopy
Dens-Meas   Density Measurements
Visc-Meas   Viscosity Measurement
DSC   Differential Scanning Calorimetry
SEC   Size Exclusion Chromatography
Micros   Optical Microscopy
AFM   Atomic Force Microscopy
Cryo-TEM   Cryogenic Transmission Electron Microscopy
SALS   Small-Angle Light Scattering
DLS   Dynamic Light Scattering
Opt-Biref   Optical Birefringence

SAXS	Small-Angle X-Ray Scattering
WAXS	Wide-Angle X-Ray Scattering (Diffraction)
SANS	Small-Angle Neutron Scattering
WANS	Wide-Angle Neutron Scattering